MARTIN MARIETTA ENERGY SYSTEMS LIBRARIES
3 4456 0054025 2

ORNL-6111

ornl

OAK RIDGE
NATIONAL
LABORATORY

MARTIN MARIETTA

FUSION ENERGY DIVISION LIBRARY

FUSION ENERGY DIVISION

1984

FED LIBRARY SEP 17 1985

ANNUAL PROGRESS REPORT

OPERATED BY
MARTIN MARIETTA ENERGY SYSTEMS, INC.
FOR THE UNITED STATES
DEPARTMENT OF ENERGY

Period Ending December 31, 1984

Prepared for the Office of Science and Technology Policy. Available from
National Technical Information Service
U.S. Department of Commerce
5285 Port Royal Road, Springfield, Virginia 22161
NTIS price codes: Printed Copy [illegible] Microfiche $2.01

This report was prepared as an account of work sponsored by an agency of the United States Government. Neither the United States Government nor any agency thereof, nor any of their employees, makes any warranty, express or implied, or assumes any legal liability or responsibility for the accuracy, completeness, or usefulness of any information, apparatus, product, or process disclosed, or represents that its use would not infringe privately owned rights. Reference herein to any specific commercial product, process, or service by trade name, trademark, manufacturer, or otherwise, does not necessarily constitute or imply its endorsement, recommendation, or favoring by the United States Government or any agency thereof. [illegible] Any agency thereof.

ORNL-6111
Dist. Category UC-20

FUSION ENERGY DIVISION ANNUAL PROGRESS REPORT

Period Ending December 31, 1984

O. B. Morgan, Jr.
L. A. Berry
J. Sheffield

Date published—July 1985

Prepared by the
OAK RIDGE NATIONAL LABORATORY
Oak Ridge, Tennessee 37831
operated by
Martin Marietta Energy Systems, Inc.
for the
U.S. DEPARTMENT OF ENERGY
under Contract No. DE-AC05-84OR21400

MARTIN MARIETTA ENERGY SYSTEMS LIBRARIES
3 4456 0054025 2

Reports previously issued in this series are as follows:

ORNL-2693	Period Ending January 31, 1959
ORNL-2802	Period Ending July 31, 1959
ORNL-2926	Period Ending January 31, 1960
ORNL-3011	Period Ending July 31, 1960
ORNL-3104	Period Ending January 31, 1961
ORNL-3239	Period Ending October 31, 1961
ORNL-3315	Period Ending April 30, 1962
ORNL-3392	Period Ending October 31, 1962
ORNL-3472	Period Ending April 30, 1963
ORNL-3564	Period Ending October 31, 1963
ORNL-3652	Period Ending April 30, 1964
ORNL-3760	Period Ending October 31, 1964
ORNL-3836	Period Ending April 30, 1965
ORNL-3908	Period Ending October 31, 1965
ORNL-3989	Period Ending April 30, 1966
ORNL-4063	Period Ending October 31, 1966
ORNL-4150	Period Ending April 30, 1967
ORNL-4238	Period Ending October 31, 1967
ORNL-4401	Period Ending December 31, 1968
ORNL-4545	Period Ending December 31, 1969
ORNL-4688	Period Ending December 31, 1970
ORNL-4793	Period Ending December 31, 1971
ORNL-4896	Period Ending December 31, 1972
ORNL-4982	Period Ending December 31, 1973
ORNL-5053	Period Ending December 31, 1974
ORNL-5154	Period Ending December 31, 1975
ORNL-5275	Period Ending December 31, 1976
ORNL-5405	Period Ending December 31, 1977
ORNL-5549	Period Ending December 31, 1978
ORNL-5645	Period Ending December 31, 1979
ORNL-5674	Period Ending December 31, 1980
ORNL-5843	Period Ending December 31, 1981
ORNL-5919	Period Ending December 31, 1982
ORNL-6015	Period Ending December 31, 1983

CONTENTS

LIST OF TABLES vii

LIST OF FIGURES ix

SUMMARY xv

1. TOROIDAL CONFINEMENT EXPERIMENTS 1-1
   SUMMARY OF ACTIVITIES 1-5
   1.1 THE ISX-B EXPERIMENTAL PROGRAM 1-5
   1.2 THE ATF PROGRAM 1-27
   1.3 ADVANCED PROJECTS 1-41
   1.4 THE ORNL-JEN COLLABORATION ON TJ-II 1-50
   1.5 THE ORNL-PPPL COLLABORATION ON TFTR 1-57
   REFERENCES 1-59

2. EBT RESEARCH AND DEVELOPMENT 2-1
   SUMMARY OF ACTIVITIES 2-5
   2.1 EBT RESEARCH 2-5
   2.2 EBT-P PROJECT 2-44
   2.3 EBT ADVANCED CONCEPTS 2-45
   REFERENCES 2-52

3. ATOMIC PHYSICS AND PLASMA DIAGNOSTICS DEVELOPMENT 3-1
   SUMMARY OF ACTIVITIES 3-5
   3.1 EXPERIMENTAL ATOMIC COLLISIONS 3-6
   3.2 ATOMIC THEORY 3-25
   3.3 CONTROLLED FUSION ATOMIC DATA CENTER 3-33
   3.4 PLASMA DIAGNOSTICS DEVELOPMENT 3-34
   REFERENCES 3-46

4. PLASMA THEORY 4-1
   SUMMARY OF ACTIVITIES 4-9
   4.1 MHD EQUILIBRIUM, STABILITY, AND TURBULENCE 4-11
   4.2 TRANSPORT KINETICS: KINETIC THEORY 4-29
   4.3 RF HEATING AND CURRENT DRIVE 4-43
   4.4 CONFINEMENT OPTIMIZATION AND IMPROVEMENT 4-48
   4.5 PLASMA MODELING, BURN ANALYSIS, IMPURITIES, AND PELLETS 4-53
   4.6 ALPHA PARTICLE PHYSICS 4-59
   4.7 EXPERIMENT INTERPRETATION 4-61
   4.8 COMPUTING SUPPORT 4-70
   REFERENCES 4-74

5. PLASMA-MATERIALS INTERACTIONS 5-1
   SUMMARY OF ACTIVITIES 5-5
   5.1 SUMMARY OF "TIME-RESOLVED IMPURITY FLUXES IN THE TEXTOR PLASMA EDGE" 5-5

5.2 ABSTRACT OF "THE INFLUENCE OF IMPURITIES ON THE HIGH-TEMPERATURE SPUTTERING YIELD OF GRAPHITE" 5-8
5.3 IN SITU EROSION STUDIES WITH LASER FLUORESCENCE TECHNIQUES 5-10
5.4 WALL CONDITIONING AND CARBONIZATION FOR CONTROL OF IMPURITIES AND HYDROGEN RECYCLE 5-11
5.5 EXPERIMENTS ON IMPURITY AND PARTICLE CONTROL IN ISX-B 5-13
5.6 PLASMA-MATERIALS INTERACTION STUDIES DURING THE JET-ISX BERYLLIUM LIMITER EXPERIMENT 5-14
REFERENCES 5-19

6. PLASMA TECHNOLOGY 6-1
SUMMARY OF ACTIVITIES 6-5
6.1 NEUTRAL BEAM HEATING 6-6
6.2 PELLET FUELING 6-9
6.3 RF HEATING 6-22
6.4 GYROTRON DEVELOPMENT 6-33
REFERENCES 6-36

7. SUPERCONDUCTING MAGNET DEVELOPMENT 7-1
SUMMARY OF ACTIVITIES 7-5
7.1 INTRODUCTION 7-5
7.2 LARGE COIL TASK 7-6
7.3 ADVANCED CONDUCTOR DEVELOPMENT 7-13
7.4 MAGNET TECHNOLOGY 7-15
REFERENCES 7-18

8. ADVANCED SYSTEM STUDIES 8-1
SUMMARY OF ACTIVITIES 8-5
8.1 FUSION ENGINEERING DESIGN CENTER 8-5
8.2 FUSION ENVIRONMENTAL ASSESSMENT PROGRAM 8-67
REFERENCES 8-68

9. MATERIALS RESEARCH AND DEVELOPMENT 9-1
SUMMARY OF ACTIVITIES 9-5
9.1 ALLOY DEVELOPMENT FOR IRRADIATION PERFORMANCE 9-6
9.2 MATERIALS COMPATIBILITY—ABSTRACTS 9-11
9.3 DAMAGE ANALYSIS AND FUNDAMENTAL STUDIES—ABSTRACTS 9-11
REFERENCES 9-14

10. NEUTRON TRANSPORT 10-1
SUMMARY OF ACTIVITIES 10-5
10.1 ABSTRACTS 10-5
10.2 DATA EVALUATION AND PROCESSING FOR FUSION NEUTRONIC DATA NEEDS 10-7
10.3 RADIATION SHIELDING INFORMATION CENTER 10-8
REFERENCES 10-9

11. GENERIC MAGNETIC FUSION REACTOR ANALYSIS 11-1
SUMMARY OF ACTIVITIES 11-3
REFERENCE 11-6

12. MANAGEMENT SERVICES 12-1
SUMMARY OF ACTIVITIES 12-5
12.1 OFFICE OF THE MANAGER FOR GENERAL ADMINISTRATION AND PROCUREMENT 12-5
12.2 ENGINEERING SERVICES 12-6
12.3 FINANCE 12-7
12.4 LIBRARY 12-7
12.5 PUBLICATIONS OFFICE 12-9
12.6 SAFETY, EMERGENCY PLANNING, AND QUALITY ASSURANCE 12-11

Appendix 1. LIST OF ACRONYMS AND ABBREVIATIONS A-1
Appendix 2. PUBLICATIONS AND PRESENTATIONS A-5
Appendix 3. DIVISION ORGANIZATION CHART A-45

TABLES

Table 1.1. ATF device parameters 1-31
Table 1.2. Major coil characteristics 1-31
Table 1.3. ATF coil joint design limits 1-35
Table 1.4. ATF coil joint parameters 1-36
Table 1.5. Parameters of ATF-based torsatrons 1-44

Table 3.1. ORNL ECR source parameters 3-8

Table 4.1. Comparison of 3-D MHD inverse-coordinates codes 4-18

Table 5.1. Time-averaged retained impurity fluxes in the electron drift direction for ohmic hydrogen discharges in TEXTOR 5-6

Table 8.1. FPD engineering parameters 8-6
Table 8.2. TFCX option characteristics 8-16
Table 8.3. Plasma transport models 8-28
Table 8.4. TF coil requirements and parameters 8-34
Table 8.5. Nuclear heat capability for three cooling system configurations 8-38
Table 8.6. CCTF parameters 8-43
Table 8.7. Reference parameters for a nominal IST 8-50

Table 11.1. Parameters of improved fusion reactors with thermal power P_t of 3750 MW(t) 11-5

Table 12.1. Fusion Program expense funding—budget outlay 12-8
Table 12.2. Production and work-hours for CY 1984 12-10
Table 12.3. Volume of publication services 12-11

FIGURES

Fig. 1.1. Frequency spectrum of poloidal field fluctuations 1-8
Fig. 1.2. Correlation of energy confinement time and fluctuation level in scan of plasma current 1-9
Fig. 1.3. Correlation of energy confinement time and fluctuation level in scan of neutral beam injection power 1-10
Fig. 1.4. The two designs of the ISX-B pump limiter modules 1-12
Fig. 1.5. Pressure buildup in the limiter cavities as a function of line density in the scrapeoff layer for beam-heated discharges 1-12
Fig. 1.6. Plasma density before and after activation of the limiter pumps at constant gas flow rate for (a) ohmically heated and (b) beam-heated discharges 1-13
Fig. 1.7. Total radiated power from the plasma as a function of shot number before and after chromium gettering 1-14
Fig. 1.8. Line-averaged density as a function of shot number before and after chromium gettering 1-15
Fig. 1.9. Operating space in ISX-B with gettered torus 1-16
Fig. 1.10. Experimental arrangement of the beryllium limiter in ISX-B 1-18
Fig. 1.11. The beryllium limiter installed in ISX-B 1-19
Fig. 1.12. Bulk temperature rise per shot across the limiter for various plasma conditions 1-20
Fig. 1.13. The limiter surface after the experiment 1-21
Fig. 1.14. Radiation of oxygen and beryllium before and after self-gettering 1-22
Fig. 1.15. Energy deposition at the limiter with and without neon injection 1-23
Fig. 1.16. Time history of the beryllium limiter experiment 1-24
Fig. 1.17. ATF field line connection length vs vertical height Z in the $\phi = 0°$ plane 1-28
Fig. 1.18. Artist's conception of ATF 1-30
Fig. 1.19. Segmented helical coil concept 1-32
Fig. 1.20. View of lap joint joining helical coil segments 1-33
Fig. 1.21. Detail of lap joint for a single turn of the helical coils 1-34
Fig. 1.22. Peak temperature in a half-size coil joint as a function of current 1-35
Fig. 1.23. Top view of the ATF vacuum vessel 1-37
Fig. 1.24. Assembly concept 1-38
Fig. 1.25. HF power supply configured for (a) steady-state and (b) pulsed operation 1-40
Fig. 1.26. Neoclassical and anomalous transport 1-45
Fig. 1.27. Side view of Symmotron reactor with 24 identical, nonrotated twisted coils and 2 compensation (VF) coils 1-47

Fig. 1.28. Stress in the Symmotron reactor coil along the coil length 1-48
Fig. 1.29. Vacuum magnetic field line calculations for a torsatron with $R = 1.5$ m, $\ell = 2$, and $m = 9$ wound on a triangular cross-section torus 1-52
Fig. 1.30. Coil set for a flexible heliac 1-53
Fig. 1.31. Variable shear introduced in the rotational transform profile 1-54
Fig. 1.32. Variation of rotational transform value for nearly shearless profiles 1-55
Fig. 1.33. Vacuum flux surfaces at the beginning (0°) and halfway through (45°) a field period for flexible heliac configurations with different ι_0/M 1-56

Fig. 2.1. Electron temperature determined from three diagnostics (soft X-ray, aluminum line ratio, and Thomson scattering) vs neutral gas pressure for $P_\mu = 150$ kW 2-7
Fig. 2.2. Calculated intensity of two Al III lines vs T_{avg} for a simple Maxwellian distribution function and a two-component distribution function 2-8
Fig. 2.3. The number of photons collected in each of six polychrometer channels vs $\Delta\lambda^2$ 2-9
Fig. 2.4. $\langle Z^2 n_w \rangle / n_e(0)$ and F_w 2-10
Fig. 2.5. Ratios of throat to midplane electron densities 2-11
Fig. 2.6. Soft X-ray temperature measurement in the cavity midplane and throat vs neutral pressure for $P_\mu = 150$ kW 2-13
Fig. 2.7. Experimental setup and soft X-ray spectra for the three-cavity turnoff experiments 2-14
Fig. 2.8. The estimated toroidal plasma temperature from the measured induced toroidal currents, together with Thomson scattering measurements of temperatures in EBT-S 2-16
Fig. 2.9. Throat-launching antenna structure with rectangular polarizing grid 2-18
Fig. 2.10. High-field, polarized X-mode launcher snaked through the fundamental resonance 2-19
Fig. 2.11. Experimental setup for polarized microwave absorption tests 2-20
Fig. 2.12. Path attenuation and line density vs 18-GHz power 2-21
Fig. 2.13. Results of Bragg scattering of HeNe light in a plastic acoustic cell 2-26
Fig. 2.14. Change in fluctuation level at the cavity center with changing neutral pressure 2-26
Fig. 2.15. Signal level of FIR scattering from cavity center vs magnetic field strength 2-27
Fig. 2.16. Scattered signal vs spatial location 2-27
Fig. 2.17. Difference in scattered signal from the cavity center vs magnetic field 2-28

Fig. 2.18. Thomson scattering data showing the response of the bulk electron temperature following a step increase in the ECH power from 90 to 150 kW 2-33
Fig. 2.19. Amplitude and phase of the electron temperature perturbation as a function of modulation frequency 2-34
Fig. 2.20. The variation of the particle confinement time τ_p as a function of fill gas pressure with $P_\mu = 50$ MW 2-35
Fig. 2.21. Variation of τ_p as in Fig. 2.20 for $P_\mu = 100$ kW 2-35
Fig. 2.22. Variation of τ_p as in Fig. 2.20 for $P_\mu = 150$ kW 2-36
Fig. 2.23. Schematic diagram for the H_α scattering experiment performed on EBT 2-37
Fig. 2.24. Neutral atomic densities as determined by H_α fluorescence in the center of EBT, by H_α background measurements, by diagnostic neutral beams and by H_α spectroscopic measurements 2-40
Fig. 2.25. Neutral atomic density determined by H_α fluorescence scattering and neutral density measurements from charge-exchange measurements 2-41
Fig. 2.26. Neutral atomic hydrogen densities deduced from H_α fluorescence scattering measurements in the center of EBT, neutral densities measured by a diagnostic neutral beam, and neutral densities measured by spectroscopic methods 2-42
Fig. 2.27. Neutral atomic hydrogen densities as measured by H_α fluorescence from the center of EBT and H_α spectroscopic, line-of-sight measurements 2-42
Fig. 2.28. EBT-S and EBS reference configurations 2-46
Fig. 2.29. Trend to smaller EBT reactor systems exploited by EBT-S 2-47
Fig. 2.30. Geometry of an EBS configuration 2-49

Fig. 3.1. The ORNL ECR multicharged ion source 3-7
Fig. 3.2. Argon charge-state distribution from ECR ion source for 2.45-GHz operation 3-10
Fig. 3.3. Argon charge-state distribution from ECR ion source for 10.6-GHz operation 3-11
Fig. 3.4. Total electron-capture cross sections for O^{8+} and O^{7+} incident on H and H_2 vs energy 3-12
Fig. 3.5. Schematic of the ion-atom merged-beams apparatus 3-14
Fig. 3.6. Electron-impact ionization of Cu^{2+} 3-16
Fig. 3.7. Electron-impact ionization of Sb^{3+} 3-17
Fig. 3.8. Double ionization of Xe^{6+} by electron impact 3-18
Fig. 3.9. Triple ionization of Xe^{6+} by electron impact 3-19
Fig. 3.10. Measured cross section for single ionization of Xe^{6+} by electron impact 3-19
Fig. 3.11. Calculated energy levels of xenon ions 3-20
Fig. 3.12. New electron-ion crossed-beams apparatus with post-collision charge analyzer magnet 3-22

Fig. 3.13. Spectrometric measurement of the SXR and EUV light generated by 1.00 mA of 3.00-keV electrons incident on a tantalum target in the prototype radiometric source 3-23
Fig. 3.14. Dependence of bremsstrahlung signal strength on electron beam current 3-25
Fig. 3.15. Charge-exchange cross sections for multicharged ions on hydrogen atoms 3-26
Fig. 3.16. Charge-exchange cross sections for multicharged ions on hydrogen atoms 3-27
Fig. 3.17. Comparison of theory and experiment for electron-impact ionization of Ti^{2+} 3-29
Fig. 3.18. Predictions for electron-impact ionization of Fe^{4+} 3-30
Fig. 3.19. Predicted cross section for dielectronic recombination of B^{2+} 3-31
Fig. 3.20. Predicted dielectronic recombination cross section of Fe^{23+} convoluted into a 3-eV Gaussian electron energy distribution 3-32
Fig. 3.21. Schematic of the multichord FIR interferometer/polarimeter system 3-35
Fig. 3.22. Time variation of Faraday rotation and line-averaged electron density 3-37
Fig. 3.23. Typical display of time variation of line electron density and Faraday rotation signal 3-38
Fig. 3.24. The scattering geometry for the proposed CO_2 laser Thomson scattering diagnostic 3-41
Fig. 3.25. The total scattered spectrum from a TFTR-like plasma as a function of scattered frequency shift 3-42
Fig. 3.26. The scattered power vs the shifted frequency δf for three simple alpha particle distributions 3-43
Fig. 3.27. The scattered power integrated over a 2-GHz bandwidth as a function of the shifted frequency of a number of channels 3-45

Fig. 4.1. Approximate flux-conserving path to high beta 4-12
Fig. 4.2. Magnetic axis shift for the ATF helical-axis configuration 4-13
Fig. 4.3. Magnetic surfaces for the ATF helical-axis configuration, $\beta_0 = 5\%$ 4-13
Fig. 4.4. The effect of a radial electric field on transport in a model $\ell = 1$ stellarator with $\phi(\psi) = \phi(0)(1 - \psi)$ 4-34
Fig. 4.5. The functions Q and $\dot{S}_g$ vs $|e|a\phi'/T_e$, showing two stable states 4-36
Fig. 4.6. Flexible heliac coil configuration with additional $\ell = 1$ hardcore winding shown shaded 4-50
Fig. 4.7. Comparison of ι and V' profiles for $M = 4$, $R/a_c = 4$ heliacs with and without $\ell = 1$ hardcore winding 4-51
Fig. 4.8. Comparison of the standard EBT and the EBS configurations 4-68

Fig. 5.1. Time evolution of the radial dependence of retained impurity fluxes for Fe + Cr + Ni, molybdenum, and oxygen 5-7

Fig. 5.2. Dependence of the enhanced sublimation yield on titanium coverage for 50-keV argon bombardment of graphite at 1520°C 5-9
Fig. 5.3. Comparison of Ti I density for plasmas with and without neon injection 5-10
Fig. 5.4. $\bar{n}_e$ scan 5-12
Fig. 5.5. The decrease in surface-active impurities as carbon is increased by adding methane to the glow discharge 5-13
Fig. 5.6. Photomicrograph of the center part of limiter tile 8 5-15
Fig. 5.7. A section of Fig. 5.6 with magnification 10× 5-16
Fig. 5.8. Composition of the surface deposit on an aluminum cube as a function of depth 5-17
Fig. 5.9. Retention of beryllium and deuterium on long-term samples exposed in the ISX-B tokamak 5-18

Fig. 6.1. Reliability plot showing the beam parameters vs shot sequence 6-7
Fig. 6.2. Interrupt frequency vs percentage of shots at full power and pulse length 6-8
Fig. 6.3. Results of gun barrel length optimization studies, showing muzzle velocity vs barrel length 6-10
Fig. 6.4. Muzzle velocity vs supply pressure for 4-mm-diam hydrogen and deuterium pellets 6-11
Fig. 6.5. Side view of TFTR tritium pellet injector 6-12
Fig. 6.6. Top view of TFTR tritium pellet injector 6-13
Fig. 6.7. Tritium pellet injection system 6-14
Fig. 6.8. Interfaces between tritium pellet injector and TFTR tritium handling systems 6-15
Fig. 6.9. Data from pellet injection into ISX-B plasma, showing no increase in beta following pellet injection 6-17
Fig. 6.10. Data from pellet injection into ISX-B plasma, showing a 30% increase in beta following pellet injection 6-18
Fig. 6.11. Trajectory plots of plasma density vs beta for the two shots shown in Figs 6.9 and 6.10 6-19
Fig. 6.12. H_α emission profiles for the two shots shown in Figs. 6.9 and 6.10 6-19
Fig. 6.13. Bremsstrahlung radiation, density, and temperature in an ohmically heated and an ICRF-heated discharge in PLT 6-20
Fig. 6.14. T_e profile in an ohmically heated and an ICRF-heated discharge in PLT 6-21
Fig. 6.15. Neutron production in an ohmically heated and an ICRF-heated discharge in PLT 6-22
Fig. 6.16. Feedthrough configurations 6-25
Fig. 6.17. Equipotentials for the feedthrough configurations of Fig. 6.16 6-26
Fig. 6.18. Impedance as a function of length for cases 2–6A of Fig. 6.16 6-27
Fig. 6.19. VSWR for cases 2–6A of Fig. 6.16 6-28
Fig. 6.20. TE mode in a ridge waveguide 6-29

Fig. 6.21. Slow-wave launching structure 6-30
Fig. 6.22. Structure similar to that in Fig. 6.21, with a Faraday shield added to protect the antenna from the plasma 6-31
Fig. 6.23. Cutaway drawing of the RFTF 6-32
Fig. 6.24. RFTF vacuum vessel and magnet supports in place in enclosure 6-34
Fig. 6.25. RFTF enclosure during construction in Bldg. 9201-2 6-35

Fig. 8.1. Magnet configurations for FPD-I, FPD-II, and FPD-III 8-7
Fig. 8.2. Plan view of FPD-I 8-9
Fig. 8.3. Sectionalized plan view of FPD 8-11
Fig. 8.4. Central-cell module of FPD-II 8-12
Fig. 8.5. Plan and elevation views of FPD-III 8-13
Fig. 8.6. TFCX superconducting option, TFCX-S 8-17
Fig. 8.7. Elevation view of TFCX 8-19
Fig. 8.8. Plan view of TFCX-S 8-20
Fig. 8.9. Vacuum vessel and shield configuration 8-21
Fig. 8.10. Limiter erosion rate and lifetime 8-22
Fig. 8.11. Magnetics analysis flow chart 8-25
Fig. 8.12. Limiter scrapeoff profiles 8-26
Fig. 8.13. Divertor scrapeoff profiles 8-27
Fig. 8.14. Ignition contours 8-29
Fig. 8.15. Lower hybrid system 8-30
Fig. 8.16. Ion cyclotron system 8-32
Fig. 8.17. Cooling and manifolding for the high-performance case 8-35
Fig. 8.18. Achievable current density vs peak conductor temperature at 10 T and 12 T 8-37
Fig. 8.19. TFCX plot plan 8-39
Fig. 8.20. Longitudinal section of tokamak support buildings 8-41
Fig. 8.21. Elevation view of CCTF 8-44
Fig. 8.22. Midplane section to CCTF 8-45
Fig. 8.23. CCTF sector-to-sector arrangement 8-45
Fig. 8.24. The plasma configuration of a spherical torus 8-47
Fig. 8.25. Elevation view of IST 8-52
Fig. 8.26. Plan view of IST 8-53
Fig. 8.27. Flow diagram of TMRSC 8-54
Fig. 8.28. FEDC cost estimating methodology 8-63
Fig. 8.29. Methodology for refinement of component development cost data 8-65

Fig. 11.1 COE vs mass of fusion island 11-4

Fig. 12.1 Fusion Program expense funding 12-9

SUMMARY

The Fusion Program of Oak Ridge National Laboratory (ORNL), a major component of the national fusion program, encompasses nearly all aspects of magnetic fusion research. Collaboration among staff from ORNL, Martin Marietta Energy Systems, Inc., private industry, the academic community, and other fusion laboratories is aimed at the development of fusion energy for the future. The results of this collaboration during 1984 are documented in this report, which is issued as the annual progress report of the ORNL Fusion Energy Division and also contains information from those Fusion Program components external to the division (approximately 15% of the program effort).

The Fusion Program comprises work in a number of areas:

- experimental and theoretical research on three magnetic confinement concepts—the tokamak, the stellarator, and the ELMO Bumpy Torus (EBT);
- engineering and physics of existing and planned fusion devices;
- development and testing of diagnostic tools and techniques;
- assembly and distribution to the fusion community of data bases on atomic physics and radiation effects;
- development and testing of materials for fusion devices;
- development and testing of the technologies needed to heat and fuel fusion plasmas;
- development and testing of superconducting magnets to contain fusion plasmas;
- design of future devices;
- assessment of the environmental impact of fusion energy; and
- assessment of the economics of fusion power.

The interactions between these activities and their integration into a unified program are major factors in the success of each activity. The task of maintaining a balance among these activities was a challenging one for the Fusion Program in 1984, as some programs were completed and others underwent significant changes.

Toroidal Confinement Experiments

The Impurity Study Experiment (ISX-B) was shut down in August 1984 after eight years of operation. The program funded by the Department of Energy was successfully completed in April, and from June through August an additional program was carried out to test a beryllium limiter for the Joint European Torus (JET). Following completion of this experiment, efforts began to prepare the ISX-B facility and many of the diagnostics for use on the Advanced Toroidal Facility (ATF).

Work on ATF proceeded smoothly. An increasingly detailed understanding of the physics issues is emerging and confirms our initial estimates of device performance. The construction project continued on schedule and at cost, with most major contracts let by year's end. Detailed planning for the required facility modifications was initiated.

A great deal of effort was devoted to advanced projects. These included an extension of the performance of ATF into the long-pulse/steady-state regime; the definition of a next-generation ATF, ATF-II; and a proposal for the Spherical Torus Experiment, a low-aspect-ratio tokamak.

Division staff collaborated with personnel from the Junta de Energia Nuclear of Spain in defining a toroidal confinement experiment, TJ-II, and were assigned to Princeton Plasma Physics Laboratory to work on the Tokamak Fusion Test Reactor (TFTR).

EBT Research and Development

The EBT research program in 1984 strongly reinforced the conclusions reached in 1983 regarding the limits on performance of the circular bumpy torus configuration. However, investigation of the ELMO Bumpy Square (EBS) configuration led to predictions of much better confinement conditions, and the EBS was shown to have high potential for development into a competitive fusion reactor. It was determined that the existing EBT device could be converted to an EBS in 18 months at a cost of less than $5 million. However, these developments were not sufficient to sustain 1985 funding for the EBS program in the face of reductions in the national fusion program. As a result, the program was phased down; the EBT-Scale (EBT-S) device was decommissioned, and staff members were reassigned to other activities. Studies of EBS will continue into 1985 with the aim of obtaining 1986 funding.

Atomics Physics and Plasma Diagnostics Development

The activities of the Atomic Physics and Plasma Diagnostics Development Program, which is supported by the Fusion Program within the ORNL Physics Division, are divided between atomic collisions research and development of plasma diagnostics.

Experimental atomic collisions research concentrates on improving the basic understanding of the complex collision processes involving partially ionized atoms at the relatively low kinetic energies characteristic of fusion plasmas. During 1984, significant progress was made in the understanding of electron-impact ionization. A new electron cyclotron resonance source of low-energy, highly charged ions was implemented and has considerably expanded the range of highly ionized systems available to investigators. The Controlled Fusion Atomic Data Center continued to provide bibliographies and compilations of atomic data to the fusion community.

The plasma diagnostics program concentrated on developing steady-state, optically pumped laser systems in the far infrared. A five-channel interferometer/polarimeter was successfully operated on ISX-B. The feasibility of pulsed CO_2 laser Thomson scattering as a diagnostic for fusion-produced alpha particles was studied, and development of this diagnostic began. The Diagnostics Development Center awarded a subcontract to the Georgia Institute of Technology for the development of a diagnostic to measure static and time-varying electric fields in plasmas.

Plasma Theory

The goals of the plasma theory effort, which concentrates on toroidal confinement theory, are to understand, improve, and optimize the confinement of plasmas for fusion reactors. The approach is to identify critical problems and then to integrate the necessary plasma physics disciplines to solve them. Collaboration with ORNL experimental groups, university groups, and the international fusion community is strongly emphasized.

Key results during 1984 include definition of ways to increase the flexibility and improve the confinement of ATF, invention of the flexible heliac concept, improvement in understanding of confinement in ISX-B and of electron cyclotron heating and confinement in EBT-S, development of EBS, and successful application of pellet models to TFTR and Doublet III.

Plasma-Materials Interactions

The Plasma-Materials Interactions Program addresses the interaction of fusion plasmas with surrounding material surfaces, with the goals of (1) understanding the fundamental phenomena related to impurity control, erosion and redeposition of wall and limiter materials, recycling and retention of hydrogen, and particle handling and (2) developing techniques and components for impurity control and particle handling. The program combines laboratory studies with applications in fusion devices.

Laboratory studies in 1984 concentrated on the influence of impurities on the high-temperature sputtering yield of graphite and on wall conditioning. Techniques were developed to reduce impurity radiation and improve plasma performance.

Studies of impurity fluxes in the edge plasma of the TEXTOR tokamak continued; time-resolved and *in situ* erosion studies were performed on a reference limiter in ISX-B, using laser fluorescence; and particle handling with pumped limiters in beam-heated plasmas was demonstrated in ISX-B. The test of the JET beryllium limiter on ISX-B afforded opportunities for intensive studies of beryllium gettering, transport of wall material to the limiter, erosion and redeposition of limiter material, and deuterium retention in beryllium.

Plasma Technology

The technology for heating and fueling fusion plasmas is developed by the Plasma Technology Section. Areas of work are neutral beams, pellet fueling, radio-frequency (rf) heating, and gyrotrons.

In 1984, development and testing of the Advanced Positive Ion Source were successfully completed, demonstrating a high atomic ion fraction and low beam divergence. Optics codes were developed and used to design accelerator structures for both positive- and negative-ion beams.

A mechanical centrifuge-type pellet injector was operated on Doublet III. The repeating pneumatic injector was modified to produce 4-mm-diam, high-velocity pellets and will be used on TFTR in 1985. The preliminary design of a tritium pellet injector for use on TFTR in 1986 was concluded.

Development progressed on a single-tube rf power source that will deliver over 2 MW of power at 40-80 GHz. Antennas for heating plasmas at the ion cyclotron resonant frequency have been built and tested. Faraday shields to protect these antennas were designed, and shield materials were tested. Improved current feedthroughs were developed to couple rf power through the wall of a fusion device. Construction has started on the Radio Frequency Test Facility, which will provide the plasma environment needed to test rf heating components.

Contracts to develop 60-GHz gyrotrons were successfully concluded. Another contract was let for a 140-GHz gyrotron power source.

Superconducting Magnet Development

The Magnetics and Superconductivity Section and the Large Coil Program carry out the development of superconducting coils needed to confine fusion plasmas through the Large Coil Task (LCT), an international collaboration between the United States, Japan, Switzerland, and the European Atomic Energy Commission. During 1984, three more coils were delivered to the International Fusion Superconducting Magnet Test Facility; shakedown of the facility was accomplished; and preliminary operational tests were performed on three coils. In these tests, the U.S. General Dynamics coil and the Japanese coil were operated at full current, and the Swiss coil was successfully cooled. Numerous research and development tasks were accomplished in support of the LCT, and work on advanced conductors and magnet technology also progressed.

Advanced System Studies

The Fusion Engineering Design Center and the Fusion Environmental Assessment Program carry out advanced system studies for the Fusion Program. The activities of the Design Center during 1984 included work on the Tokamak Fusion Core Experiment, the Fusion Power Demonstration tandem-mirror reactor studies, and the Ignition Spherical Torus. The Design Center also developed a tandem-mirror systems code, contributed to the International Tokamak Reactor effort, developed a data base and methodology for evaluating fusion costs, and assessed the availability of fusion reactors.

The Environmental Assessment Program focused on developing the generic environmental impact statement for fusion. A revised preliminary draft prepared in 1984 addressed issues related to the place of fusion power plants in the U.S. energy economy.

Materials Research and Development

Materials research and development are carried out in three major task areas: Alloy Development for Irradiation Performance (ADIP), Damage Analysis and Fundamental Studies (DAFS), and Special-Purpose Materials (SPM). The ADIP and DAFS programs are concerned with understanding the mechanisms involved in radiation damage and corrosion, providing the information on materials needed to design near-term fusion devices and to study fusion power reactors, and developing a sound basis for development of materials for fusion.

In the ADIP program, research on austenitic stainless steels has focused on development of microstructures that are stable at high temperatures to high irradiation damage levels. Exploratory research began in 1984 on manganese-stabilized austenitic stainless steels. Research on vanadium alloys showed that the resistance of these alloys to helium embrittlement can be improved through further alloy development. Studies of the effects of doping ferritic steels with small concentrations of nickel show that the basic metallurgical response of the tempered martensitic structure is retained. Corrosion studies address the compatibility of materials used for structure, coolant, and breeders and the mechanisms of corrosion and mass transfer.

The DAFS research has focused on understanding the effects of helium on microstructural evolution, swelling, and mechanical properties. The program includes theory, modeling, and experiments.

The SPM program has focused on providing facilities at the National Low-Temperature Neutron Irradiation Facility for research into the effects of radiation on magnet materials. This facility will produce temperatures and irradiation conditions similar to those at the magnets of a fusion reactor.

Neutron Transport

The neutron transport program carries out both experiments and analyses. The experiments are designed to provide the data needed for verifying the analytic method and the cross-section data used for fusion reactor neutronics design calculations. The analytic program supports the design of the experiments and compares calculated and experimental data. Work is also performed in the areas of nuclear data evaluation and cross-section processing. The Radiation Shielding Information Center supplies a broad range of services to the fusion community.

Generic Magnetic Fusion Reactor Analysis

A new activity within the Fusion Program during 1984 was the study of a "generic" magnetic fusion reactor model. The model, which incorporates the elements common to a number of configurations, is used to evaluate the self-consistent requirements for a fusion reactor and to determine whether fusion power can be a cost-competitive source of energy. This study has led to the conclusion that the cost of fusion power will be close to that of fossil and fission energy if certain physics and technology requirements, which represent only a moderate advance over present achievements, are met.

The many achievements summarized in this report clearly illustrate the diversity of these activities and the strengths of the Fusion Program. These contributions were formally acknowledged with the presentation to the Fusion Energy Division of the ORNL Director's Award in recognition of outstanding accomplishments in 1984.

O. B. Morgan
Director, Fusion Energy Division

L. A. Berry
Associate Director for Development and Technology,
Fusion Energy Division

J. Sheffield
Associate Director for Confinement,
Fusion Energy Division

Chapter 1

Toroidal Confinement Experiments

J. L. Dunlap, Toroidal Confinement Physics Section Head

M. J. Saltmarsh, Confinement Projects Section Head

D. L. Akers[1]
J. L. Alvarez Rivas[2]
H. Attaya[3]
T. D. Bagwell[4]
F. W. Baity[5]
E. E. Bartlett[6]
D. B. Batchelor[7]
L. R. Baylor[8]
K. Behringer[9]
J. D. Bell[10]
R. D. Benson[8]
E. T. Blair[10]
S. K. Borowski[11]
J. Botija[2]
D. E. Brashears[8]
C. Bridgman[12]
A. Y. Broverman[8]
R. L. Brown[13]
W. E. Bryan[8]
C. E. Bush[7]
W. D. Cain[8]
J. L. Cantrell[10]
A. Carnevali[14]
B. A. Carreras[7]
W. H. Casson[14]
K. K. Chipley[8]
R. E. Clausing[15]
R. J. Colchin
M. J. Cole[8]
K. A. Connor[16]
T. B. Cook[17]
W. K. Cooper[8]
D. L. Coppenger[4]
G. R. Dyer
P. H. Edmonds
O. C. Eldridge
L. C. Emerson[15]
R. Engelstad[3]
A. C. England
J. W. Forseman[8]
R. A. Fortner[1]
R. H. Fowler[10]
R. D. Foskett[8]
W. A. Gabbard
M. D. Galloway[18]
W. L. Gardner[5]
J. C. Glowienka
R. C. Goldfinger[10]
D. Goodall[19]
J. E. Goyer[16]
D. E. Greenwood[10]
J. Guasp[2]
A. D. Guttery[1]
G. A. Hallock[16]
E. L. Halstead[6]
W. R. Hamilton[11]
J. H. Harris
D. E. Hastings[7]
D. I. Hatch[4]
L. Heatherly[15]
T. C. Hender[7]
G. H. Henkel
R. L. Hickok[16]
R. E. Hill[8]
D. L. Hillis
J. T. Hogan[7]
J. W. Holliwell[14]
W. A. Houlberg[7]
H. C. Howe[7]
D. P. Hutchinson[20]
R. C. Isler
W. C. Jennings[16]
T. C. Jernigan
O. V. Jett[1]
R. L. Johnson[8]
L. M. Jordan[21]
E. Källne[9]
S. S. Kalsi[11]
K. L. Kannan[10]
R. R. Kindsfather
P. W. King
J. Lacatski[14]
R. A. Langley
V. D. Latham[4]
E. A. Lazarus
V. D. Lee[11]
B. I. Leinart[14]
U. P. Lickliter[8]
A. Lopez[2]
D. C. Lousteau[11]
J. N. Luton, Jr.[13]
V. E. Lynch[10]
J. F. Lyon
C. H. Ma[20]
R. Martin[2]
L. A. Massengill
J. B. Mathew[16]
J. A. Mayhall[8]
T. J. McManamy[8]
M. M. Menon[5]
P. K. Mioduszewski
J. F. Monday[8]
J. A. Moore[8]
P. Morgan[9]
R. N. Morris[10]
J. K. Munro, Jr.[10]
M. Murakami
G. H. Neilson
B. E. Nelson[8]
V. K. Paré[22]
N. Peacock[19]
Y-K. M. Peng[11]
A. Perea[2]
A. Perez Navarro[2]
J. L. Ping[8]
L. A. Pollard[1]
A. Pueblas[2]
D. A. Rasmussen
T. F. Rayburn
W. J. Redmond
R. K. Richards
J. A. Rome[7]
S. D. Scott[23]
J. J. Schmidt[8]
J. Sheffield[24]
W. D. Shipley[8]
D. J. Sigmar[7]
J. E. Simpkins
M. L. Simpson[14]
K. Sonnenberg[9]
C. R. Stewart[10]
K. A. Stewart[7]
D. J. Strickler[10]
P. Stott[19]
I. N. Sviatoslavsky[3]
A. Tanga[9]
D. J. Taylor[8]
C. E. Thomas
C. K. Thomas[21]
M. B. Thompson[1]
P. B. Thompson[8]
C. C. Tsai[5]
K. Tschersich[25]
N. A. Uckan
L. M. Vinyard[8]
J. von Seggern[25]
M. A. Vornehm[1]
J. E. Warwick[8]
J. Watkins[26]
D. J. Webster[8]
J. A. White[8]
T. L. White[5]
J. B. Whitley[26]
J. C. Whitson[10]
R. M. Wieland[10,24]
J. B. Wilgen
D. E. Williamson[8]
W. R. Wing
A. L. Wintenberg
A. J. Wootton
W. L. Wright[8]
R. B. Wysor[8]
J. L. Yarber
K. E. Yokoyama[27]
R. A. Zuhr[17]

---

1. Section secretary.
2. Junta de Energia Nuclear, Madrid, Spain.
3. Nuclear Engineering Department, University of Wisconsin, Madison.
4. Y-12 Maintenance Division.
5. Plasma Technology Section.
6. Purchasing Division, Martin Marietta Energy Systems, Inc.
7. Plasma Theory Section.
8. Engineering Division, Martin Marietta Energy Systems, Inc.
9. JET Joint Undertaking, Abingdon, Oxfordshire, England.
10. Computing and Telecommunications Division, Martin Marietta Energy Systems, Inc.
11. Fusion Engineering Design Center.
12. Grumman Aerospace Corporation, Bethpage, N.Y.
13. Magnetics and Superconductivity Section.
14. The University of Tennessee, Knoxville.
15. Metals and Ceramics Division.
16. Rensselaer Polytechnic Institute, Troy, N.Y.
17. Solid State Division.
18. Auburn University, Auburn, Ala.
19. Culham Laboratory, Abingdon, Oxfordshire, England.
20. Physics Division.
21. Management Services Section.
22. Instrumentation and Controls Division.
23. Now at Princeton Plasma Physics Laboratory, Princeton, N.J.
24. Associate division director.
25. Kernforschungsanlage Jülich GmbH, Jülich, Federal Republic of Germany.
26. Sandia National Laboratories, Albuquerque, N.Mex.
27. Now at TRW, Inc., Redondo Beach, Calif.

CONTENTS

SUMMARY OF ACTIVITIES 1-5

1.1 THE ISX-B EXPERIMENTAL PROGRAM 1-5

1.1.1 Confinement Studies 1-5

1.1.1.1 Abstract of "Balanced Beam Injection on ISX-B" 1-5

1.1.1.2 Abstract of "Confinement of Beam-Heated Plasmas in ISX-B" 1-6

1.1.1.3 Abstract of "Confinement in Beam-Heated Plasmas: The Effects of Low-Z Impurities" 1-7

1.1.1.4 Abstract of "The Effects of Varying Wall Conditions, Minor and Major Radius on Confinement Properties in ISX-B" 1-7

1.1.1.5 MHD fluctuations in ISX-B 1-8

1.1.2 Measurements of Plasma Potential—Abstracts 1-10

1.1.2.1 *Investigation of the Electric Field Structure in Neutral Beam Heated ISX-B Plasmas* 1-10

1.1.2.2 "The Space Potential Distribution in ISX-B" 1-11

1.1.3 Particle and Impurity Control 1-11

1.1.3.1 Particle and impurity control with pump limiters 1-11

1.1.3.2 Impurity control and hydrogen pumping with chromium gettering in ISX-B 1-14

1.1.4 Abstract of "An Experimental Investigation of the Plasma Properties of the Edge Region of the ISX-B Tokamak Using Multiple Langmuir Probes" 1-16

1.1.5 The Joint JET-ISX Beryllium Limiter Experiment—Physics Results 1-17

1.1.6 ISX-B Operations and Technology 1-24

1.1.7 ISX-B Data System 1-25

1.2 THE ATF PROGRAM 1-27

1.2.1 Introduction 1-27

1.2.2 Physics Studies 1-27

1.2.3 Construction 1-30

1.2.3.1 Coils 1-31

1.2.3.2 Vacuum vessel 1-34

1.2.3.3 Support structure 1-36

1.2.3.4 Assembly sequence 1-36

1.2.4 Facility Preparation 1-38

1.2.4.1 Project management 1-39

1.2.4.2 Site preparation 1-39

1.2.4.3 Magnetic field power supplies 1-39

1.2.4.4 Heating systems 1-40

1.3 ADVANCED PROJECTS 1-41
1.3.1 ATF Extended Performance 1-41
1.3.2 The ATF-II 1-43
1.3.2.1 ATFSR studies 1-43
1.3.2.2 Low-aspect-ratio torsatron studies 1-45
1.3.2.3 Engineering assessments of Symmotron coils 1-46
1.3.3 The Spherical Torus Experiment 1-48
1.4 THE ORNL-JEN COLLABORATION ON TJ-II 1-50
1.4.1 Low-Aspect-Ratio Torsatrons 1-51
1.4.2 Helical-Axis Configurations 1-51
1.4.3 Engineering Design Studies 1-57
1.5 THE ORNL-PPPL COLLABORATION ON TFTR 1-57
REFERENCES 1-59

1. TOROIDAL CONFINEMENT EXPERIMENTS

Summary of Activities

The Impurity Study Experiment (ISX-B) operated through August 1984. The program funded by the Department of Energy was pursued through March and concentrated on several studies of confinement, on measurements of plasma potential (in collaboration with Rensselaer Polytechnic Institute), and on tests of pump limiters and chromium gettering. (Studies with pellet injection fueling in ISX-B are described in Chap. 6 of this report.) The remainder of the operating time was devoted to a test of a beryllium limiter, done under a work-for-others arrangement with the Joint European Torus Undertaking. These efforts are described in Sect. 1.1.

The program directed toward operation of the Advanced Toroidal Facility (ATF) torsatron in October 1986 continued to move smoothly, as described in Sect. 1.2. The physics issues are better defined and still encouraging, the construction project is on schedule and at cost with most major contracts let, and much detailing of the required facility preparations has been done.

Considerable work has been done on advanced projects. The rationale for extending the performance of ATF into the long-pulse/steady-state regime has been developed, and the additional work required to achieve this extended performance has been scoped. Studies have also been made toward definition of a next-generation ATF, the ATF-II, a factor of 2 to 3 scaleup of the current project. Work on conceptual design of a Spherical Torus Experiment has also been initiated. Section 1.3 contains details of these efforts.

Section personnel have participated in two other significant collaborations. The work to define a toroidal confinement experiment for the Junta de Energia Nuclear (JEN) in Madrid, performed jointly by ORNL and JEN, has focused on a flexible heliac. This work is described in Sect. 1.4. Staff members from ORNL who are collaborating with Princeton Plasma Physics Laboratory on the Tokamak Fusion Test Reactor are making significant contributions to the research efforts there, as described in Sect. 1.5.

1.1 THE ISX-B EXPERIMENTAL PROGRAM

1.1.1 Confinement Studies

1.1.1.1 Abstract of "Balanced Beam Injection on ISX-B"[1]

A. J. Wootton, J. D. Bell, C. E. Bush, A. Carnevali, B. A. Carreras, J. L. Dunlap, P. H. Edmonds, O. C. Eldridge, A. C. England, W. L. Gardner, G. A. Hallock, R. L. Hickok, H. C. Howe, D. P. Hutchinson, R. C. Isler, W. C. Jennings, K. L. Kannan, R. R. Kindsfather, R. A. Langley, E. A. Lazarus, C. H. Ma,

J. Mathew, M. Murakami, J. K. Munro, Jr., G. H. Neilson, V. K. Paré,
S. D. Scott, D. J. Sigmar, C. E. Thomas, R. M. Wieland, W. R. Wing,
and K. E. Yokoyama

Opposed-beam injection experiments, in which the momentum and power inputs are controlled independently, are described. This has facilitated a study of the effect of momentum sources on plasma properties. The momentum input is distinguished by a toroidal rotation velocity and a radial electric field. The global confinement properties of momentum, particles, and energy have been determined as the beam direction (with respect to the plasma current) is changed from co-injection through balanced injection to counter-injection. Global energy confinement times are unaffected by changing the momentum source, and thus by both toroidal rotation velocity and radial electric fields, in a gettered vacuum vessel. The deterioration of confinement with increasing beam power, previously observed with co-injection, is still present with balanced injection. An examination of radial profiles of plasma parameters shows the dominant loss to be electron conduction with both co-injection and balanced injection. Although global energy confinement is unchanged, large differences in particle behavior, for both working gas and impurities, have been observed as the momentum is changed. These observations suggest a link between rotation, electric fields, and particle confinement.

1.1.1.2 Abstract of "Confinement of Beam-Heated Plasmas in ISX-B"[2]

M. Murakami, P. H. Edmonds, G. A. Hallock, R. C. Isler, E. A. Lazarus, G. H. Neilson,
A. J. Wootton, J. D. Bell, C. E. Bush, A. Carnevali, B. A. Carreras, J. L. Dunlap,
A. C. England, W. L. Gardner, R. L. Hickok, H. C. Howe, D. P. Hutchinson,
W. C. Jennings, R. R. Kindsfather, R. A. Langley, C. H. Ma, J. Mathew,
P. K. Mioduszewski, J. K. Munro, Jr., V. K. Paré, M. J. Saltmarsh,
S. D. Scott, D. J. Sigmar, M. L. Simpson, C. E. Thomas, R. M. Wieland,
W. R. Wing, and K. E. Yokoyama

Confinement studies on the Impurity Study Experiment (ISX-B) have been directed at understanding the mechanisms governing the confinement in neutral-beam-heated plasmas. These studies have focused on two main areas: (1) the effects of toroidal plasma rotation and electric field on confinement and (2) confinement improvement with deliberate introduction of some low-Z impurities ("Z-mode"). In the first studies, the momentum input was controlled independently of the energy input using opposing injection systems. Measurements of the space potential using a heavy-ion beam probe (HIBP) showed that, as the injection direction is changed from counter-injection to balanced injection to co-injection, the *negative* potential well becomes shallower, as expected from the momentum balance, based on the observed changes in toroidal plasma rotation. The particle confinement of both bulk ions and impurities is correlated with beam directivity, potential, and rotation velocity. However, both global and electron energy confinement are unaffected by changing the momentum input. The Z-mode studies have shown that the deliberate introduction of recycling low-Z impurities (whether externally injected or intrinsic) improves global energy confinement times (τ_E^*) by a factor of up to 1.8 over those predicted by the standard ISX-B scaling, which was developed from and accurately represents τ_E^* in clean,

gettered discharges. Additional benefits of the impurity injection are improved particle confinement, increased ion heating efficiency, and reduced limiter heat flux. The improvement in τ_E^* is correlated with a reduction of the high-frequency (50- to 250-kHz) magnetic fluctuation $\tilde{B}_\theta/B_\theta$ without changing the fluctuations $\tilde{n}_e/n_e$. The confinement time improvement, which increases linearly with $\bar{n}_e$, results primarily from reduction of the electron thermal diffusivity (χ_e). The reduction of χ_e is consistent with the prediction of a resistive ballooning mode theory, which includes diamagnetic effects.

1.1.1.3 Abstract of "Confinement in Beam-Heated Plasmas: The Effects of Low-Z Impurities"[3]

E. A. Lazarus, J. D. Bell, C. E. Bush, A. Carnevali, B. A. Carreras, W. H. Casson, J. L. Dunlap, P. H. Edmonds, A. C. England, W. L. Gardner, G. A. Hallock, J. T. Hogan, H. C. Howe, D. P. Hutchinson, R. R. Kindsfather, R. C. Isler, R. A. Langley, C. H. Ma, J. Mathew, P. K. Mioduszewski, M. Murakami, G. H. Neilson, V. K. Paré, D. J. Sigmar, C. E. Thomas, R. M. Wieland, J. B. Wilgen, W. R. Wing, A. J. Wootton, and K. E. Yokoyama

Confinement studies on ISX-B in beam-heated plasmas contaminated with small quantities of low-Z impurities are reported. Experimental results on the correlation of particle and energy confinement are presented. A linear relationship of energy confinement and plasma density is observed. As density is increased further, this effect saturates and energy confinement becomes independent of electron density. The experiments have been extended to higher beam power, resulting in an expansion of the ISX-B operating space. Impurities other than neon (carbon and silicon) have been tried and do not produce an enhancement in confinement. Edge cooling by the introduction of impurities has been demonstrated. The change in confinement has been shown to be correlated with changes in the normalized poloidal field fluctuation level ($\tilde{B}_\theta/B_\theta$) but not with the density fluctuation level ($\tilde{n}_e/n_e$). The experimental results are compared with models of drift-wave and resistive ballooning turbulence, and an explanation is offered for the difference between the results with recycling and nonrecycling impurities.

1.1.1.4 Abstract of "The Effects of Varying Wall Conditions, Major and Minor Radius on Confinement Properties in ISX-B"[4]

A. J. Wootton, C. E. Bush, P. H. Edmonds, E. A. Lazarus, C. H. Ma, M. Murakami, and G. H. Neilson

The ISX-B data base from which the energy confinement time scaling $\tau_E \propto I_p^{3/2} P_b^{-2/3}$ was derived for neutral-beam-heated discharges has been enlarged. Now included are results obtained using a nongettered vacuum vessel and different minor and major radii. Energy confinement times improve, and a density dependence is introduced, if gettering is not employed. There is an associated increase in impurity radiation. A comparison of confinement properties obtained using two minor radii ($\sim$19 cm and the usual $\sim$26 cm) has been made. The correlation between radiation level and confinement is always found. No dependence of energy confinement on minor radius is found. The confinement

changes associated with wall conditions and radiation levels can be reproduced using a gettered vessel and small plasma position displacements. In particular, outward radial displacements toward a limiter at the outer equator improve confinement. In this case, any radiation increase is small.

1.1.1.5 MHD fluctuations in ISX-B

J. D. Bell, J. L. Dunlap, V. K. Paré, and A. J. Wootton

Studies of magnetohydrodynamic (MHD) fluctuations in beam-heated plasmas have been continued, using an array of 12 high-frequency Mirnov coils distributed poloidally and toroidally on the outside wall. Previous observations have shown that the amplitudes of the ($m = 1$, $n = 1$) mode and its harmonics are not correlated with confinement.[5] However, the frequency spectrum of signals from the high-frequency coils also includes, in addition to the peaks from the low-m, low-n modes, a continuous component that extends at least to our maximum analysis frequency of 250 kHz. We find that the amplitude of this component does appear to be correlated with confinement.

As an example, Fig. 1.1 shows the frequency spectrum of $\tilde{B}_\theta/B_\theta$ for otherwise similar beam-heated plasmas with and without neon injection. In ISX-B, neon injection has been found to enhance confinement significantly;[6] as can be seen in Fig. 1.1, it also reduces the

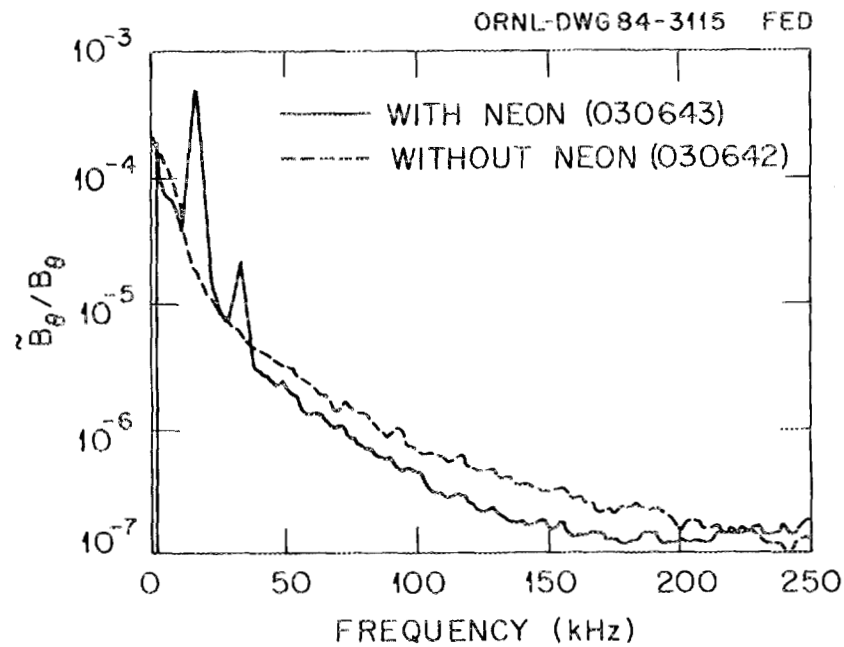

Fig. 1.1. Frequency spectrum of poloidal field fluctuations, normalized to average poloidal field, from beam-heated plasmas with and without injection. ($B_T = 1.23$ T, $I_p = 155$ kA, $\bar{n}_e \approx 5 \times 10^{19}$ m^{-3}, $P_b \approx 950$ kW.)

amplitude of the continuous spectrum. It may also be noted that confinement improves even though the power spectral density of the ($m = 1$, $n = 1$) mode and its harmonics increases.

The shape of the continuous spectrum is quite similar for most plasmas; thus, the level of the fluctuations producing it can be characterized by integrating the spectrum over a suitably chosen fixed frequency range. This operation has been done in two ways: (1) by recording the signal amplitude from a band-pass filter with a center frequency of 150 kHz, and (2) by numerically integrating from 100 to 250 kHz the spectra obtained by Fourier transform analysis of digitized waveforms. The two methods give similar correlations with confinement. The correlation obtained with method 1 is illustrated in Figs. 1.2 and 1.3, which are "scatter plots" of the fluctuation level against magnetically measured energy confinement time τ_E^* in scans of plasma current and of neutral beam injection power.

For a global rotating mode such as the ($m = 1$, $n = 1$), the mode structure can be determined from the phase shifts between signals from poloidally and toroidally displaced detectors, and one expects the signals from all detectors to be highly coherent. For the continuous part of the spectrum observed in the Mirnov coil signals, the phase shift is always nearly zero when there is enough coherence to permit measuring it, and the coherence falls rapidly with increasing detector separation. The decrease of coherence with poloidal

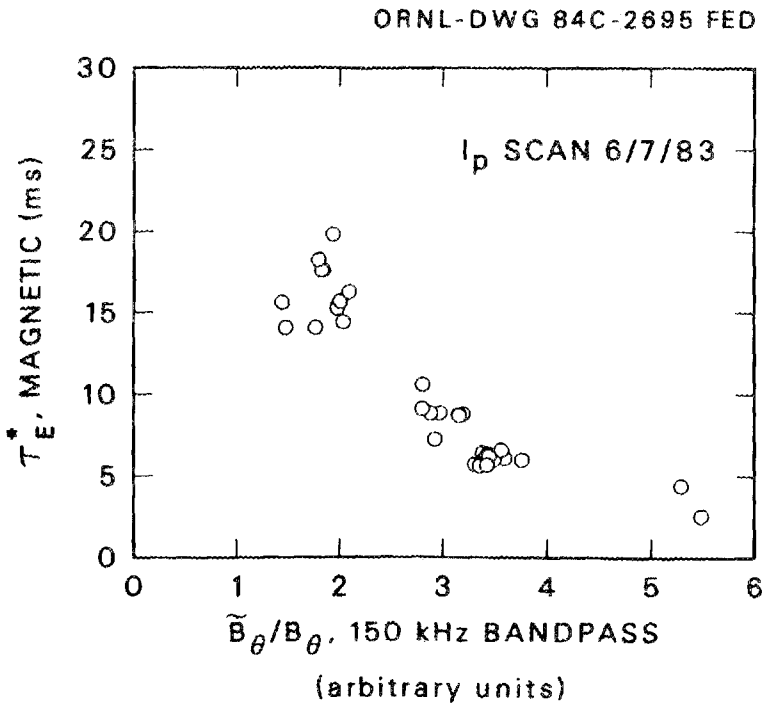

Fig. 1.2. Correlation of energy confinement time and fluctuation level in scan of plasma current. ($B_T = 1.37$ T, $I_p =$ 80, 116, 163, and 190 kA, $\bar{n}_e = 3.0$–4.0×10^{19} m^{-3}, $P_b =$ 0.9 MW.)

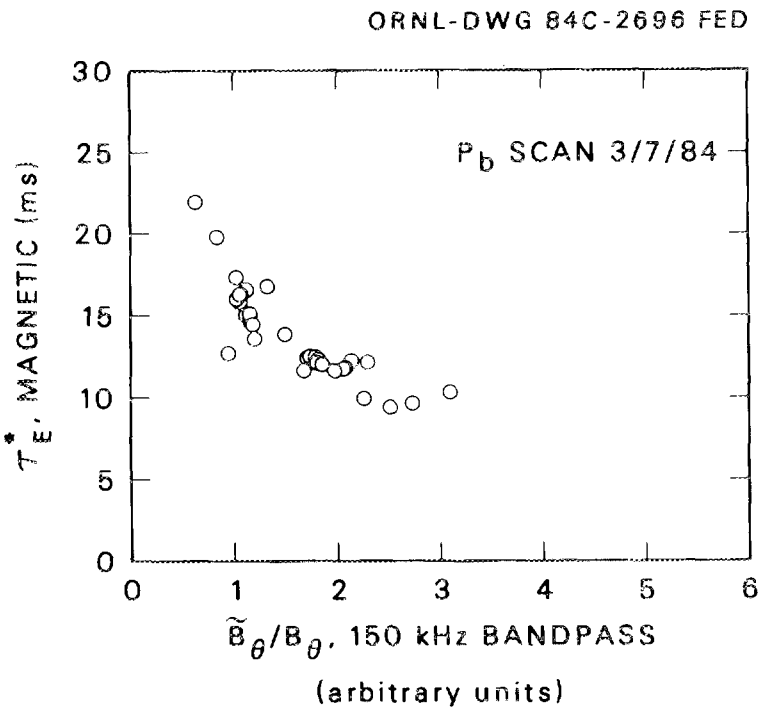

Fig. 1.3. Correlation of energy confinement time and fluctuation level in scan of neutral beam injection power. (B_T = 1.37 T, I_p = 170 kA, $\bar{n}_e$ = 3.8–4.0 × 10^{19} m^{-3}, P_b = 1.6, 0.85, and 0.32 MW.)

separation is especially fast and leads to the conclusion that the observed magnetic fluctuations must occur in the outermost few centimeters of the plasma.

1.1.2 Measurements of Plasma Potential—Abstracts

1.1.2.1 *Investigation of the Electric Field Structure in Neutral Beam Heated ISX-B Plasmas*[7]

J. Mathew

Plasma potentials have been measured for the first time in neutral-beam-heated tokamak discharges. Radial potential profiles have been obtained for co-injection, counter-injection, and balanced-injection discharges as well as for ohmically heated plasmas in the ISX-B tokamak. Within experimental uncertainties, the measured values of potential are consistent with calculations based on radial momentum balance using experimental values of rotation velocities, density, and ion temperature.

The measurements were made using an HIBP, with typical plasma conditions of $I_p \approx$ 150 kA, $B_T \approx$ 12.3 kG, $\bar{n}_e \approx 4 \times 10^{13}$ cm^{-3}, and $P_b \approx$ 0.9 MW. A negative potential

well depth of about 1.0 kV was observed in ohmically heated plasmas and increased somewhat for balanced injection. Counter-injection resulted in a significantly larger well depth of approximately 3–4 kV, while co-injection showed an outward-pointing electric field in the plasma interior. In ohmically heated plasmas the potential was constant in time, but significant time variations in potential were observed in neutral-beam-heated discharges. Potentials in ohmic plasmas showed both a density and a plasma current dependence.

There was an observed improvement in the particle confinement times of both ions and impurities with counter-injection as compared with co-injection. Inclusion of momentum sources and drags in the momentum equation leads to a component of the radial particle flux proportional to the radial electric field that is qualitatively capable of explaining the observed improvement.

1.1.2.2 "The Space Potential Distribution in ISX-B"[8]

G. A. Hallock, J. Mathew, W. C. Jennings, R. L. Hickok, A. J. Wootton, and R. C. Isler

Plasma potentials have been measured for the first time in neutral-beam-heated tokamak discharges. Radial profiles have been obtained for co-injection, counter-injection, and balanced injection and for plasmas with ohmic heating only. The measured potentials are consistent with that inferred from radial momentum balance using the measured toroidal rotation velocities. They are also qualitatively consistent with the strong dependence of impurity transport on the direction of beam injection.

1.1.3 Particle and Impurity Control

1.1.3.1 Particle and impurity control with pump limiters

P. K. Mioduszewski, C. E. Bush, L. C. Emerson, P. H. Edmonds, H. C. Howe, R. C. Isler, R. A. Langley, E. A. Lazarus, C. H. Ma, M. Murakami, G. H. Neilson, J. E. Simpkins, A. J. Wootton, and K. E. Yokoyama

The pump limiter experiments on ISX-B were primarily designed to demonstrate particle exhaust and density control with mechanical limiters. The experimental arrangement was described in detail in the 1982 annual report.[9] Two modules were installed in ISX-B, one in the top and one in the bottom of one toroidal sector of the tokamak. The limiter heads consisted of graphite coated with titanium carbide (TiC); the rest of the structure was made of stainless steel. Both limiters had a "pill-box" shape with a mushroom-shaped top. For the March 1984 run, the bottom limiter design was changed by extending the limiter throat length from 4 to 10 cm and by collecting particles only from the ion drift side. The two limiter designs are shown in Fig. 1.4. Experiments were performed in ohmically heated plasmas and in beam-heated plasmas. The pressure buildup in the limiter cavities is shown in Fig. 1.5 as a function of line density in the scrapeoff layer. The nonlinear pressure rise in the long-throat limiter indicates plasma effects that seem to be strongly dependent on the limiter geometry.

When the Zr-Al getters in the pump limiter cavities were activated, the limiter pressures dropped by a factor of 2–3 due to the pumping. At the same time, the line-averaged plasma density decreased if the gas flow rate was held constant. A maximum density

ORNL-DWG 84-2908AR FED

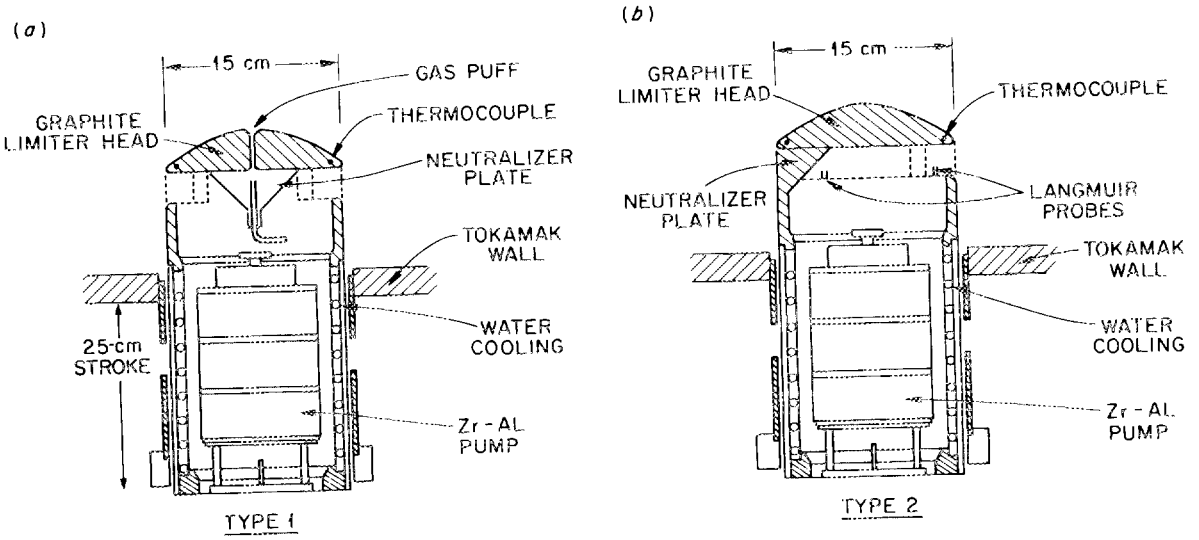

Fig. 1.4. The two designs of the ISX-B pump limiter modules.

ORNL-DWG 84-2448R FED

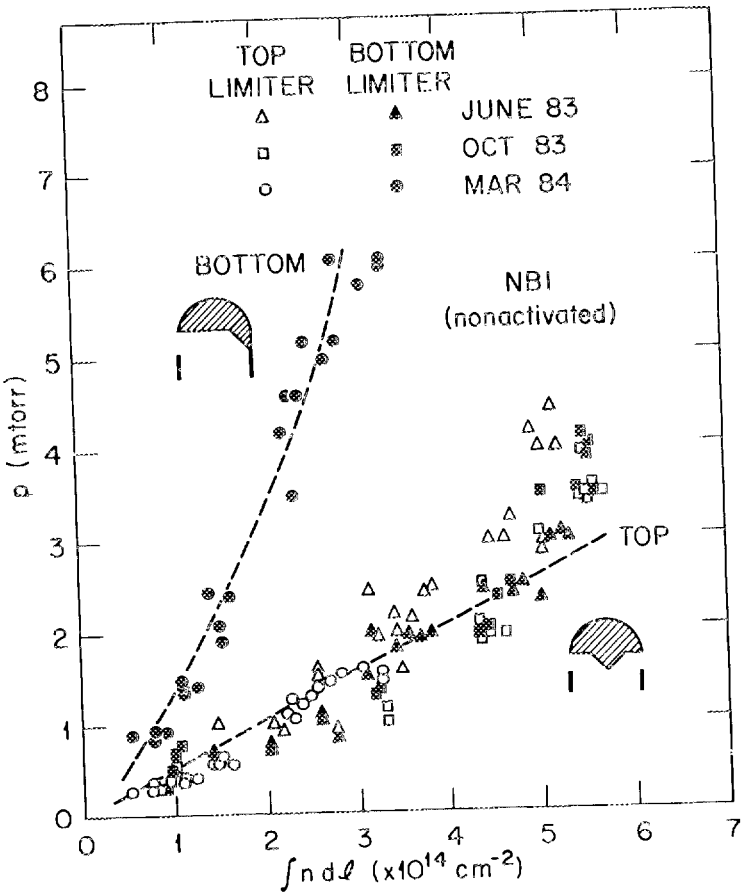

Fig. 1.5. Pressure buildup in the limiter cavities as a function of line density in the scrapeoff layer for beam-heated discharges.

decrease of a factor of 2 was observed in ohmically heated discharges with elongated plasmas. Typical density traces with and without pumping, with plasma parameters of I_p = 116 kA, B_T = 1.4 T, and P_b = 1 MW, are shown in Fig. 1.6. Exhaust rates up to 4 torr·L/s were observed, and the exhausted flux over the total flux in the scrapeoff layer was determined to be 5–8%.

Preliminary experiments on impurity (nitrogen) injection indicated that the total radiation was slightly reduced when the pump limiters were activated. Spectroscopy data show that the central nitrogen radiation is not much affected, but the edge radiation is strongly reduced by the pump limiters.

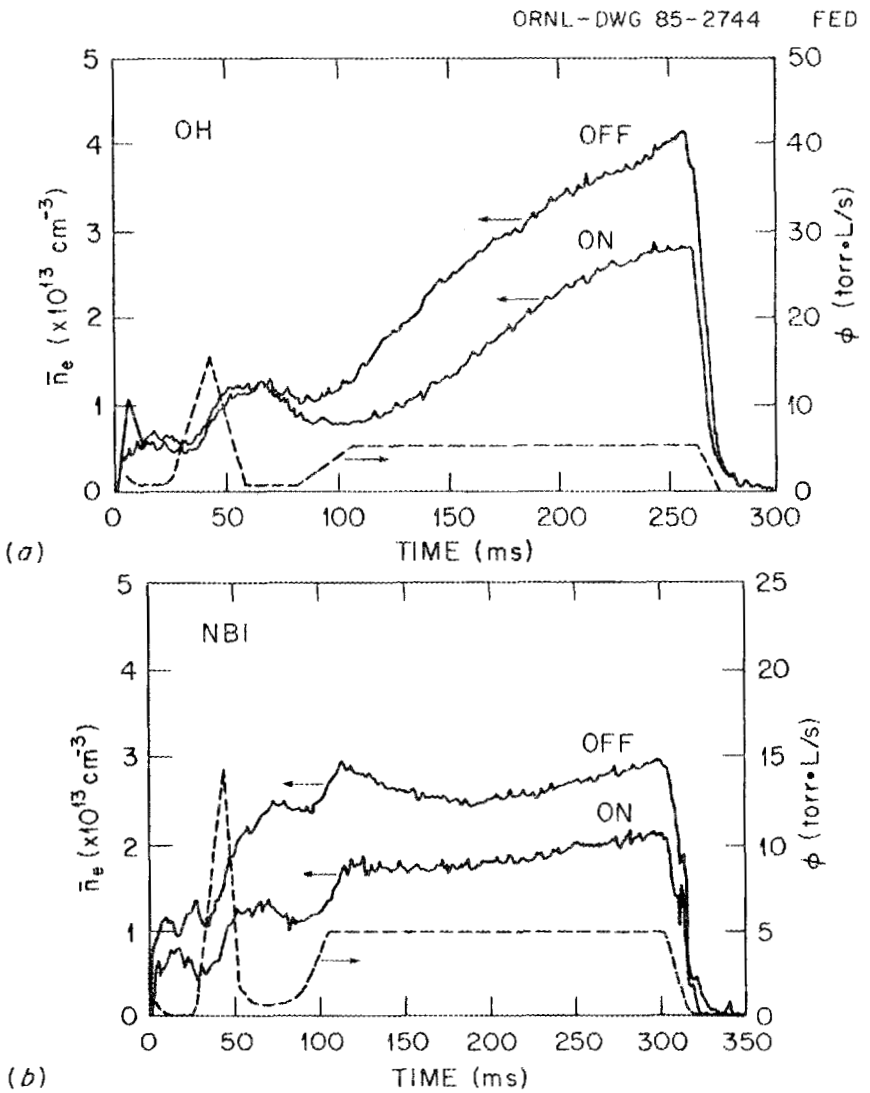

Fig. 1.6. Plasma density before and after activation of the limiter pumps at constant gas flow rate for (a) ohmically heated and (b) beam-heated discharges.

1.1.3.2 Impurity control and hydrogen pumping with chromium gettering in ISX-B[10]

P. K. Mioduszewski, J. E. Simpkins, P. H. Edmonds, W. A. Gabbard, R. C. Isler, E. A. Lazarus, C. H. Ma, M. Murakami, and A. J. Wootton

Chromium gettering allows impurity control without increased hydrogen flow rates and hydrogen retention in the wall. This makes it compatible with tritium operation.

To test chromium gettering in ISX-B, two getter sources, separated toroidally by about 180°, were installed in the torus. The sublimation rate was chosen to be 0.1 g/h for each source. A typical getter cycle lasted for 30 min. This procedure was identical to the usual titanium getter cycle in ISX-B to facilitate comparison between chromium and titanium. The gettered area in the torus is estimated to be 70% with a film thickness of 1–10 monolayers and about 5% with a coverage of 10–100 monolayers. From an operational viewpoint, chromium gettering was very convenient. While titanium sources must be outgassed and conditioned, sometimes for several hours, outgassing of the chromium balls was negligible. Only 5 min into the getter cycle, all impurity gases (H_2O, N_2, CO, etc.) in the residual gas were reduced by factors of 3–5, and after a full getter cycle of 30 min, all such impurities were reduced by almost an order of magnitude.

After chromium gettering, the total radiation from the plasma was strongly reduced. The content of individual impurities—as measured spectroscopically—was reduced by factors of 3–5. Figure 1.7 shows the total radiated power from the plasma, normalized to line-averaged density, before and after chromium gettering. In addition to a reduction of

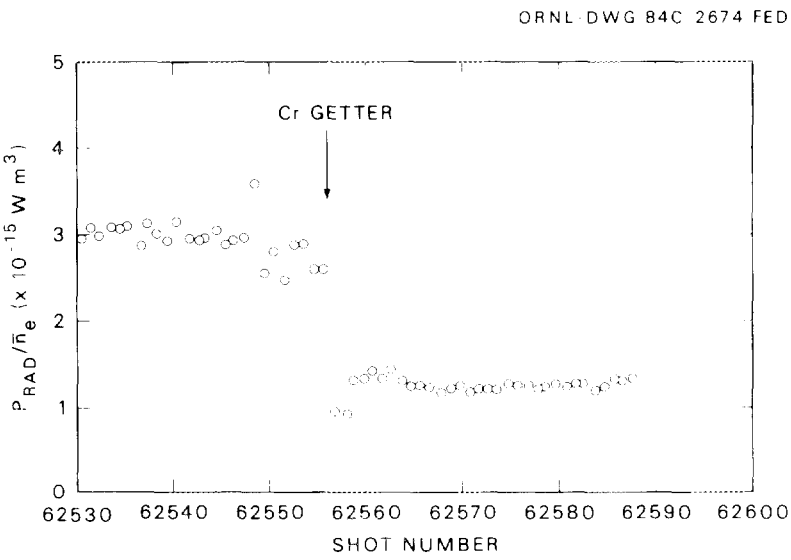

Fig. 1.7. Total radiated power from the plasma, normalized to line-averaged density, as a function of shot number before and after chromium gettering. (B = 1.4 T, I_p = 114 kA, $\bar{n}_e = 4 \times 10^{13}$ cm^{-3}, P_b = 1 MW, q_ϕ = 3.)

the total radiated power from the plasma, the discharges display high reproducibility after gettering. The normalized radiated power was monitored for up to 50 discharges after the getter cycle, and no exhaustion of the impurity pumping capability was observed.

Titanium gettering entails large pumping speeds and capacities for hydrogen species. To obtain reproducible discharges without tedious adjustments of the gas puff between shots, a procedure called "ungettering" has been established in ISX-B. It involves puffing a large amount of hydrogen into the torus to saturate the titanium, thus reducing the hydrogen pumping speed to a tolerably small value. This procedure does not affect the impurity pumping capability, because hydrogen on the getter surface is continually replaced by the more reactive gases like oxygen. In contrast to this behavior, chromium gettering does not significantly change the pumping speed or capacity of the walls for hydrogen isotopes. To demonstrate this, Fig. 1.8 shows the line-averaged density, normalized to the gas flow rate, as a function of shot number before and after gettering. It appears that the required gas flow rate for a given density is affected for only two shots after the getter cycle, and in subsequent discharges the effect becomes negligible. The same effect is observed if we merely interrupt tokamak operation for about 30 min. It is assumed that this increased gas flow rate is necessary to establish an equilibrium wall loading. In comparing individual shots before and after chromium gettering, the same line-averaged density is obtained for a given gas flow rate. After titanium gettering, on the other hand, gas flow rates must be increased by factors of 2–3 to maintain a given density.

Finally, it is worth mentioning that the operating space increased significantly after chromium gettering. A maximum line-averaged density of 1.6×10^{14} cm^{-3} was achieved. As indicated in the Hugill diagram in Fig. 1.9, this is the highest density observed in

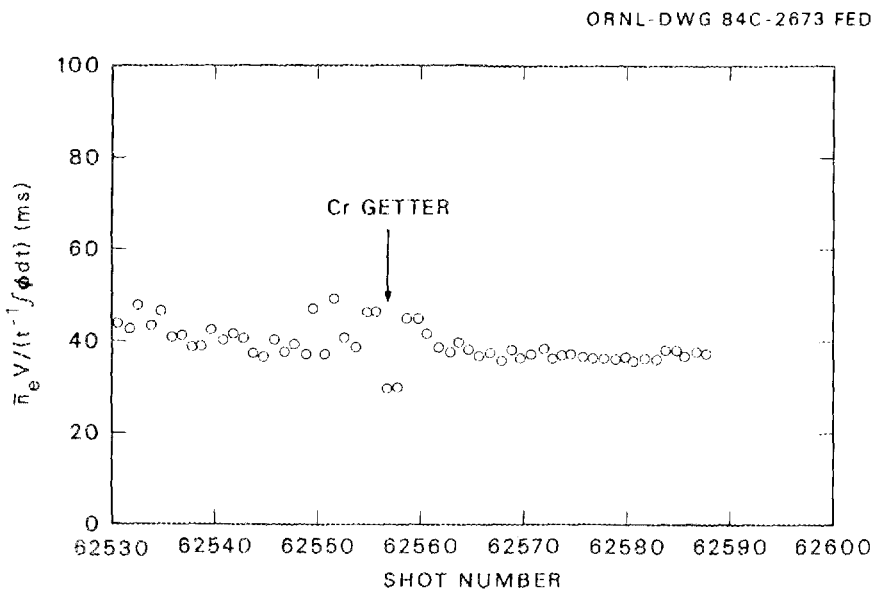

Fig. 1.8. Line-averaged density, normalized to gas flow (ϕ is the gas flow rate), as a function of shot number before and after chromium gettering.

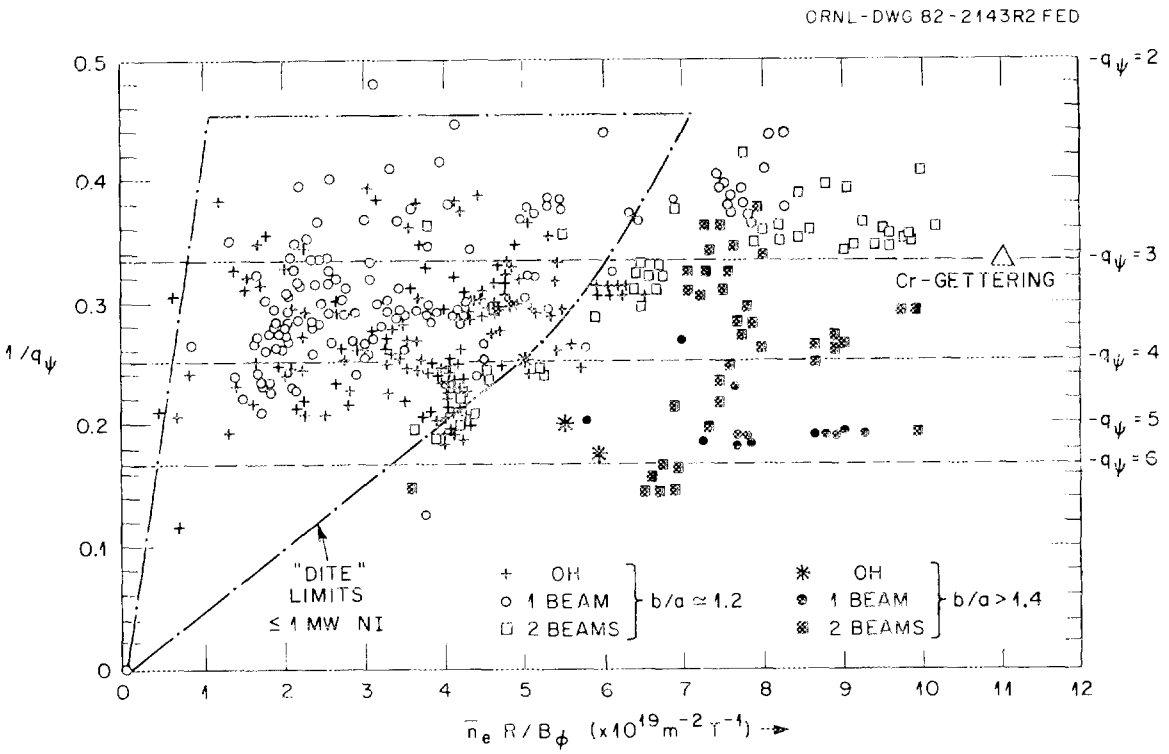

Fig. 1.9. Operating space in ISX-B with gettered torus. The main data base was obtained with titanium gettering [A. J. Wootton et al., "Gettering in ISX-B," *J. Nucl. Mater.* 111 & 112, 479–84 (1982)]; only the maximum density obtained with chromium gettering is shown. ("1 beam" corresponds to an injected power $P_b \simeq 1$ MW.)

ISX-B. It corresponds to a Murakami parameter of 11 at $q_\psi = 3$. Thus, the expansion of the operating space after chromium gettering is similar to that after titanium gettering without the disadvantage of increased gas flow.

Chromium gettering has been proved to be an efficient method of surface pumping in tokamaks. The impurity control capabilities are excellent and comparable to those of titanium. The hydrogen uptake is reduced to monolayer quantities on the surface. The expansion of the operating space is similar to that seen with titanium without the disadvantage of strongly increased hydrogen fluxes. Possible applications of chromium gettering include impurity control in contemporary tokamaks, surface pumping in short-pulse devices that burn deuterium-tritium (D-T) to minimize tritium inventory, and wall conditioning of future large machines before operation.

1.1.4 Abstract of "An Experimental Investigation of the Plasma Properties of the Edge Region of the ISX-B Tokamak Using Langmuir Probes"[11]

K. E. Yokoyama

The method of decomposing the Fourier components of the double-probe characteristic has been extended to include higher-order terms in the expansion parameter $V_{applied}/T_e$

and finite circuit resistance. The system uses a 10-kHz driving voltage, which, together with analog filtering of the current, allows measurements of electron temperature (2 eV < T_e < 40 eV) and electron density (3×10^9 cm^{-3} < n_e < 2×10^{13} cm^{-3}). Electron density calculations include corrections for magnetic field effects, probe potential, and finite sheath thickness. Fluctuation levels can be deduced from the frequency structure between the harmonics of the driving frequency. It has proven necessary to correct for these fluctuation levels in the calculation of both T_e and n_e. Diffusion coefficients are estimated from the decay lengths measured behind the limiter face, taking into account fluxes perpendicular to the wall and fluxes parallel to the limiter.

Experimental results obtained on ISX-B show that there are no significant temperature gradients along the field lines. However, variations of up to 50% are seen in the electron density, which may be due to the local recycling effects. Changes in local edge parameters when neutral beam heating is initiated are evident. In particular, the results show that the density decay lengths increase dramatically during the beam-heated phase of the discharge, implying an increase in particle diffusion. The direction of beam injection plays a minor role in determining particle confinement, especially if the recycling at the limiter surface changes with beam direction. Parameters in the scrapeoff vary linearly with the central line-averaged electron density, showing some evidence of saturation in the parallel particle flux at high densities. Parameters measured at the limiter demonstrate the effects of plasma plugging. Differences between high and low energy confinement regimes are also evident at the plasma edge. Measurements made during fueling studies with the pumped limiter are used to determine qualitatively the exhaust efficiency of the limiter. Finally, data taken during pellet injection experiments help to determine the role of fast-ion ablation in the scrapeoff layer in beam-heated discharges.

1.1.5 The Joint JET-ISX Beryllium Limiter Experiment—Physics Results

P. K. Mioduszewski, P. H. Edmonds, K. Behringer, C. E. Bush, A. Carnevali,
R. E. Clausing, T. B. Cook, A. C. England, L. C. Emerson, D. Goodall,
L. Heatherly, D. P. Hutchinson, R. C. Isler, E. Källne, P. W. King,
R. R. Kindsfather, R. A. Langley, E. A. Lazarus, C. H. Ma,
P. Morgan, M. Murakami, G. H. Neilson, N. Peacock,
J. E. Simpkins, J. von Seggern, P. Stott, K. Sonnenberg,
A. Tanga, C. E. Thomas, K. Tschersich, J. Watkins,
J. B. Whitley, A. J. Wootton, K. E. Yokoyama, and R. A. Zuhr

The beryllium limiter experiment, a collaboration between the Joint European Torus (JET) and ORNL, was performed under contract with the JET Undertaking. The objectives of the experiment were (1) to study the performance of beryllium as a limiter material, (2) to investigate the plasma characteristics with a beryllium limiter, and (3) to gain experience with handling beryllium in a tokamak environment.

The experiment was specified for a deuterium fluence of about 10^{22} ions/cm^2 to the limiter. This corresponded to 3000 beam-heated discharges with a single beam line at 0.8 MW. The limiter test was designed for a power flux of 2.5 kW/cm^2 for 0.2 s of neutral beam injection (NBI). The corresponding surface temperature rise was 600°C per discharge. The base temperature of the limiter was kept between 200 and 300°C at all

times to improve the ductility of the beryllium, which is very low at room temperature and improves strongly at elevated temperatures.

The experimental arrangement of the beryllium limiter in the tokamak is shown in Fig. 1.10. The top rail limiter consisted of a movable stainless steel structure with 12 individual beryllium tiles. The inset of Fig. 1.10 shows a diagonal view of a single tile; every other tile was slotted to relieve surface stresses. The figure also shows the visible spectrometer viewing the limiter. A photograph of the limiter after installation in the tokamak is shown in Fig. 1.11.

To evaluate the performance of the limiter, we distinguish three different regimes of operation:

1. No melting of the limiter surface. This was the case for ohmically heated discharges and for discharges with NBI at low currents.
2. Strong limiter melting with melt layer formation and material loss by melted droplets. This happened during discharges with NBI at high currents.
3. Limiter melting and evaporation only at hot spots, which were due to the surface roughness. This happened during discharges with NBI at low current after the surface morphology was drastically changed by heavy melting.

The power deposition at the limiter turned out to be a sensitive function of the plasma current. For ohmically heated plasmas this was expected, because the total input power increased with plasma current. For beam-heated discharges, however, the input power was dominated by the beam power, and a change in plasma current by 50% affected the total

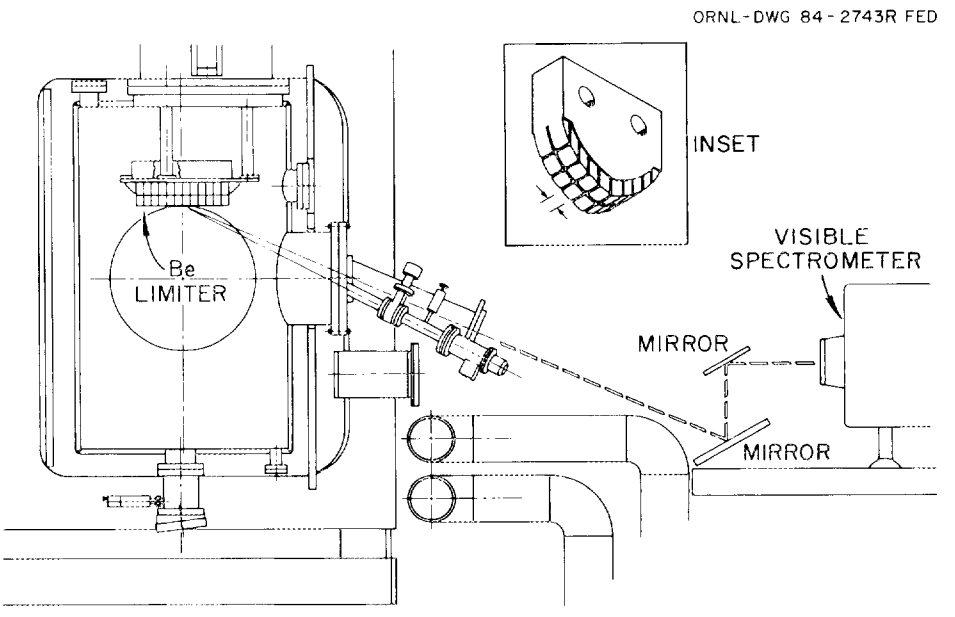

Fig. 1.10. Experimental arrangement of the beryllium limiter in ISX-B.

ORNL-PHOTO 6908-85

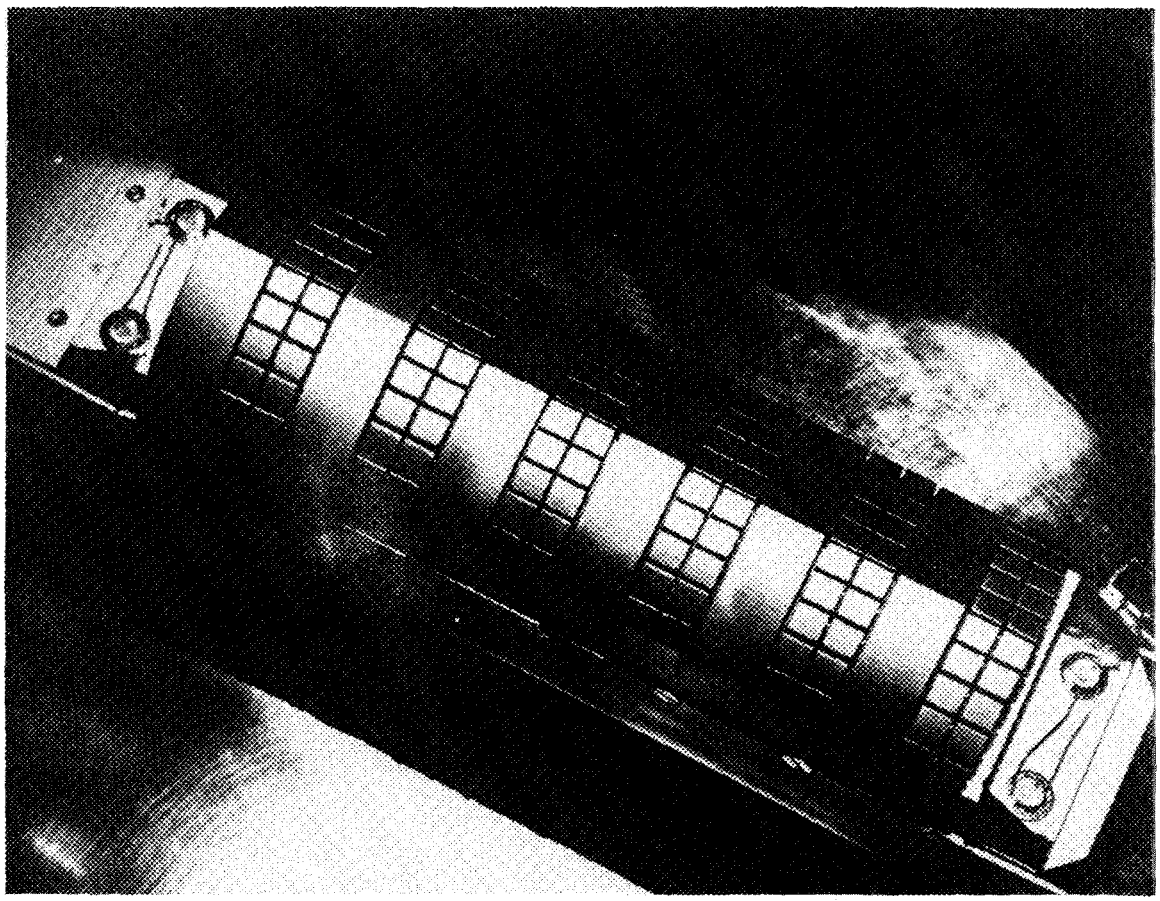

Fig. 1.11. The beryllium limiter installed in ISX-B.

input power by less than 10%. Even for beam-heated discharges with approximately constant input power, the limiter power increased strongly with plasma current. This effect allowed us to control the limiter power using only the plasma current and to keep the total input power constant.

Energy deposition at the limiter and decay lengths of the power flux in the scrapeoff layer were measured with a thermocouple array installed in the beryllium tiles. Typical temperature distributions across the limiter under various plasma conditions are shown in Fig. 1.12. A bulk temperature rise of 10°C corresponded to a peak power flux of about 2.5 kW/cm^2 and a surface temperature rise of 600°C. The labels "ug" and "g" refer to data obtained during "ungettered" and "gettered" discharges, respectively. The gettering here is self-gettering by evaporated and redeposited beryllium.

The decay length of the power flux was a function of plasma current. For 115 kA, it was about 1.2 cm for ohmically heated discharges and 1.5 cm for beam-heated discharges.

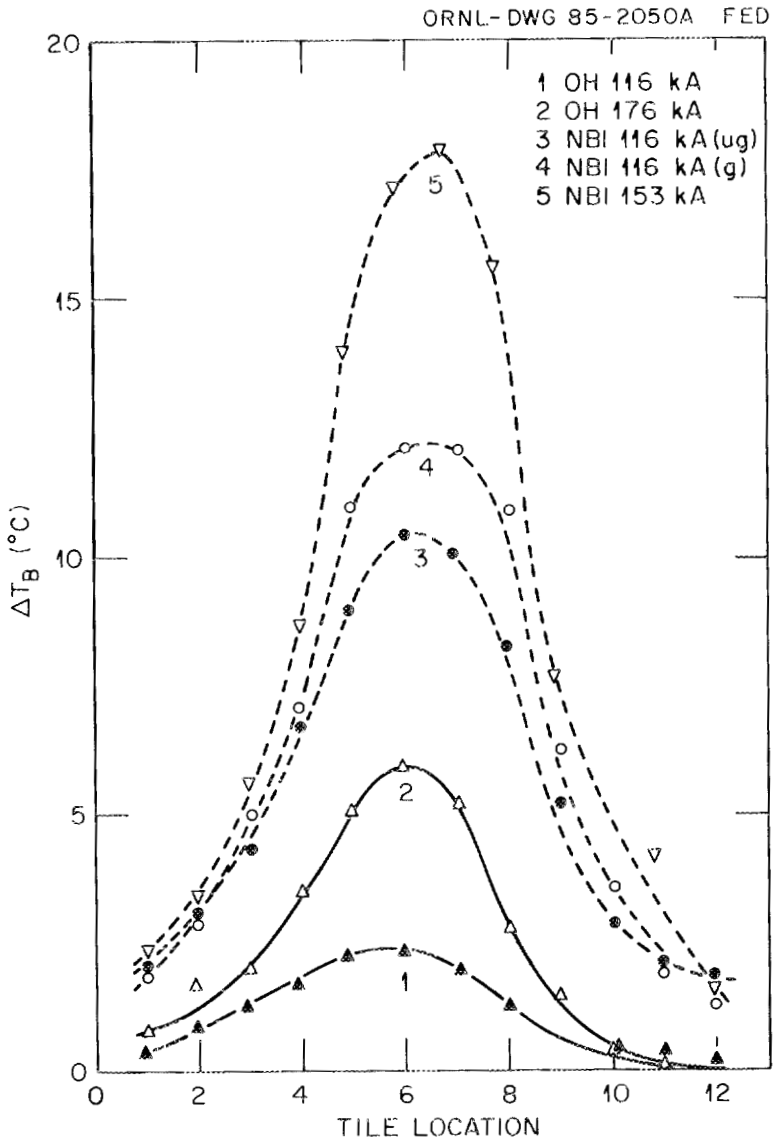

Fig. 1.12. Bulk temperature rise per shot across the limiter for various plasma conditions.

As illustrated in Fig. 1.12, the heat flux to the limiter increased strongly with plasma current. At I_p = 153 kA in beam-heated plasmas, the peak power flux was 4.5 kW/cm^2. At this heat flux, the surface temperature rise was 1000°C. After extended operation, the bulk temperature was around 300°C, so that a peak surface temperature of 1300°C was reached, exceeding the melting point of 1283°C. The limiter was intentionally operated at these high heat fluxes for several hundred shots to induce melting and subsequent gettering of the vacuum vessel with limiter material.

After characterization of the operating space and the impurity content under various conditions, an extended test was conducted to expose the limiter to a deuterium fluence of 10^{22} ions/cm^2. About 2500 shots were fired at low plasma current (116 kA), an injected neutral beam power of 0.8 MW, and a nominal power flux of about 2.5 kW/cm^2 to the limiter. Due to the high surface roughness induced by melting during high-current operation, melting and evaporation still occurred at protrusions and solidified droplets. This caused enough evaporation to continuously getter the vacuum vessel with limiter material throughout the fluence test. Figure 1.13 is a photograph of the limiter surface after the experiment. Although the surface was heavily damaged, the performance was as good as with the new limiter, with the added feature that the surface roughness caused the irreversible getter effect.

In the premelting phase the plasma was dominated by the light impurities oxygen, carbon, and nitrogen, at concentrations of about 1% each. The value of Z_{eff} under these conditions was about 3. The beryllium content in the plasma was 0.1%. With high-current operation and limiter evaporation, the beryllium content in the plasma increased to about 6%. The light impurities were effectively gettered, and the total radiation decreased by more than 50%. Figure 1.14 shows the oxygen and beryllium radiation before and after gettering. In the third phase of operation (i.e., evaporation at hot spots only), the beryllium content decreased by a factor of about 2, but the impurities were still effectively gettered.

The plasma performance in ohmically heated discharges was comparable to the performance with TiC-coated limiters in ISX-B. For beam-heated plasmas, the three phases

ORNL-PHOTO 6536-85

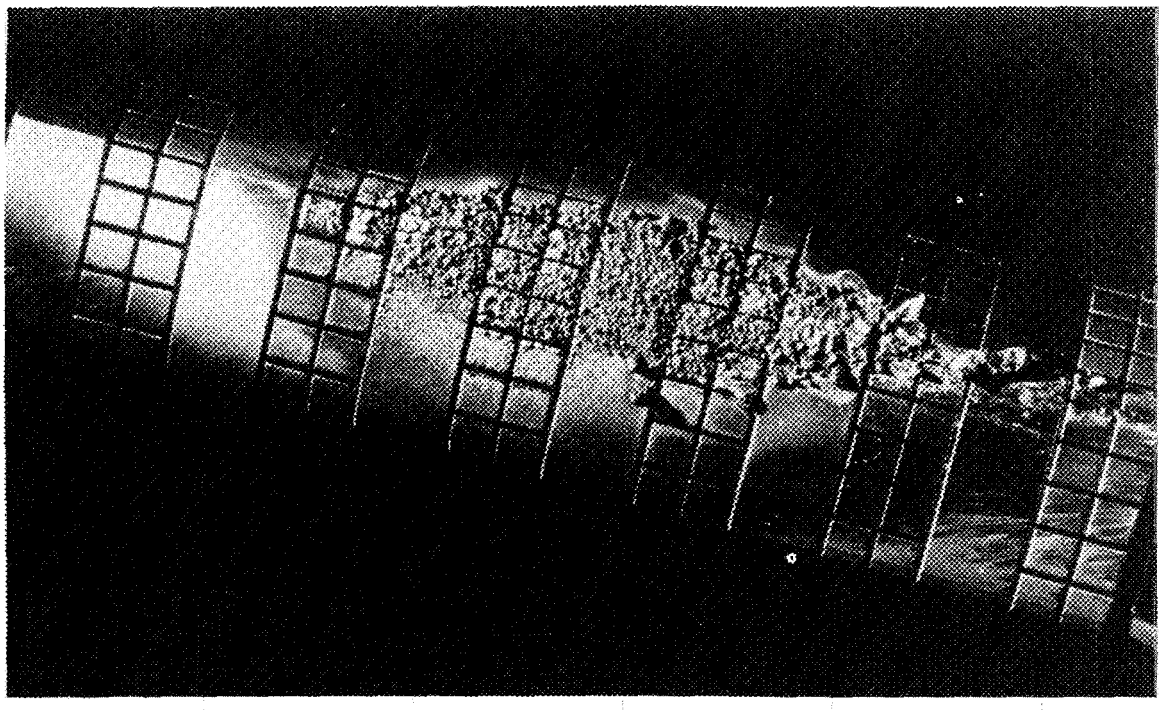

Fig. 1.13. The limiter surface after the experiment.

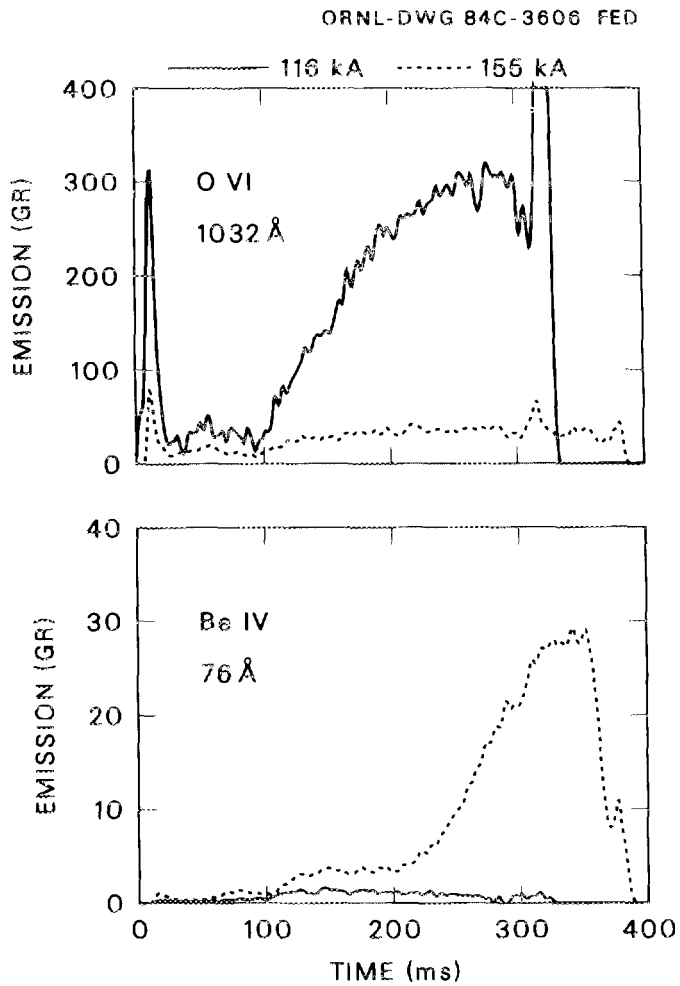

Fig. 1.14. Radiation of oxygen and beryllium before (solid line) and after (dashed line) self-gettering.

of operation must be distinguished again. With injected power to 0.82 MW and low plasma current (117 kA), the power to the limiter was about 2.2 kW/cm^2. At this power flux the plasma performance was comparable to previous data obtained with TiC limiters. The plasma radiation was dominated by light impurities from the wall.

At high plasma currents (150 kA), power fluxes of 4–5 kW/cm^2 were measured at the limiter, leading to surface melting. With limiter melting during every shot, plasma operation was possible but not very reproducible. The radiated power decreased from about 300 kW to 150 kW at a constant input power of 1 MW. Maximum densities were 9×10^{13} cm^{-3}, and energy confinement agreed with the phenomenological ISX scaling found for gettered discharges: $\tau_E^{\mathrm{ISX}} = 0.005 I_p^{3/2} P_b^{-2/3}$.

In the third phase of operation, with average power fluxes below 2.5 kW/cm^2 but with beryllium gettering by evaporation at hot spots, plasma operation was quite reproducible. The beryllium content was still about 2%, and low radiation indicated gettering.

Under these conditions about 2500 reproducible shots were fired (fluence test). At a plasma current of 116 kA, with well-gettered walls, a maximum density of 1.3×10^{14} cm^{-3} was achieved. Confinement was according to ISX scaling with gettering. Cooling of the plasma edge by impurity injection was demonstrated by puffing about 1% neon into gettered discharges. This reduced the energy to the limiter from 86 to 56 kJ, as shown in Fig. 1.15. The beryllium flux from the limiter was reduced correspondingly.

The beryllium limiter test has shown that beryllium is a suitable limiter material. The extremely low Z makes contributions to the plasma radiation negligible, even at high concentrations. The thermomechanical properties are good. A potential disadvantage is beryllium's low melting point (compared to graphite), because power excursions, for example in disruptions, cannot be totally avoided. However, the fluence test on ISX-B has shown that even with a heavily damaged limiter, thousands of reproducible discharges can be performed.

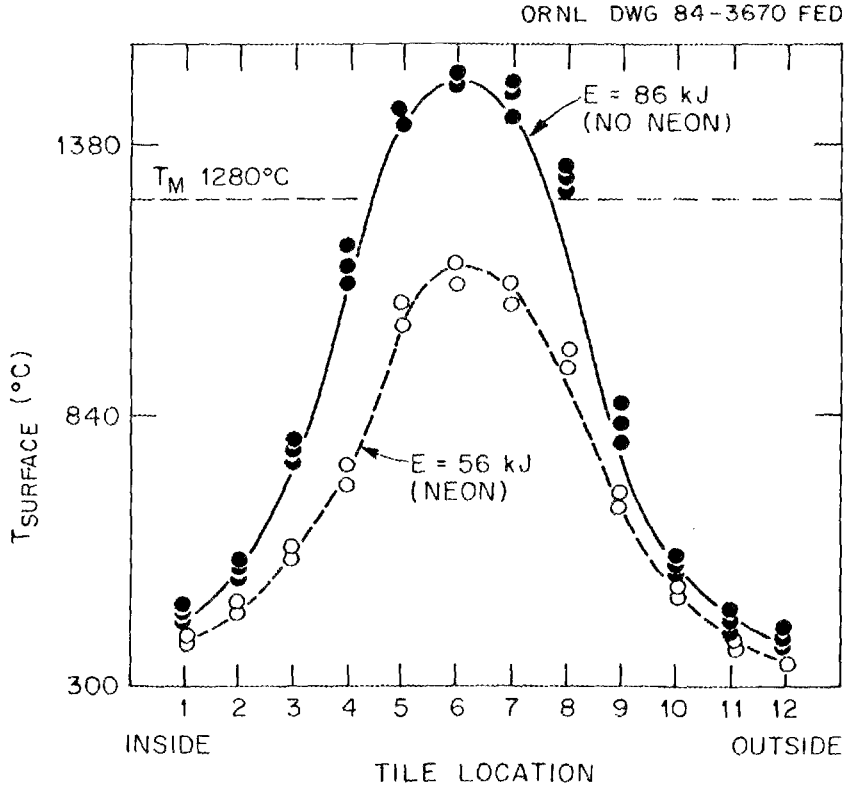

Fig. 1.15. Energy deposition at the limiter with and without neon injection.

1.1.6 ISX-B Operations and Technology

P. H. Edmonds, G. R. Dyer, A. C. England, W. A. Gabbard, W. L. Gardner,
M. M. Menon, J. A. Moore, C. C. Tsai, T. F. Rayburn, W. J. Redmond,
J. L. Yarber, L. A. Massengill, V. D. Latham, D. Hatch, T. D. Bagwell,
D. L. Coppenger, E. T. Blair, D. E. Greenwood, W. R. Wing,
C. R. Stewart, D. J. Webster, R. B. Wysor, J. E. Warwick,
U. P. Lickliter, J. J. Schmidt, and J. L. Ping

The first three months of ISX-B operation in 1984 were devoted to the Department of Energy (DOE) program. The tokamak was then shut down for two months while the modifications and installation necessary for the beryllium limiter experiment were completed. This experiment was completed in three months, and in August 1984 the tokamak was shut down for decontamination and disassembly.

The major emphasis of the year, and the final experiment on ISX-B, was the beryllium limiter experiment, which consisted of the design and construction of a beryllium limiter and the operation of the facility to evaluate the limiter's effects. These are described in refs. 12–14. Figure 1.16 shows the time history of the beryllium limiter experiment in the

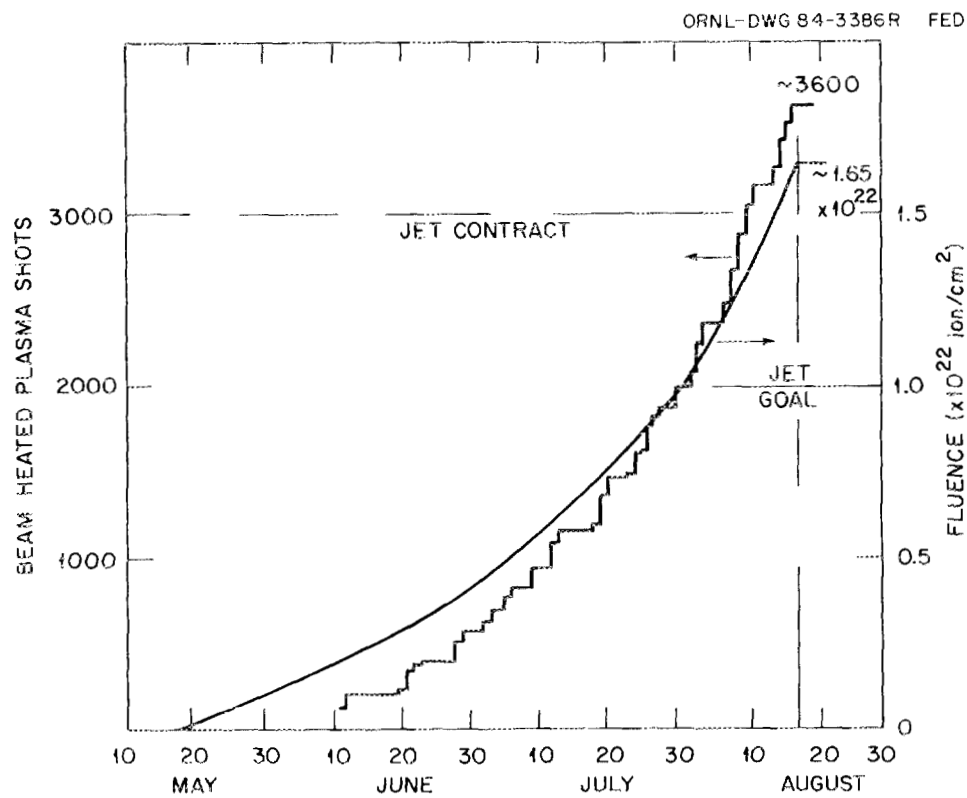

Fig. 1.16. Time history of the beryllium limiter experiment, including a histogram of the number of beam-heated shots and an estimate of the accumulated fluence to the limiter.

form of a histogram of the number of beam-heated shots. It includes an estimate of the accumulated hydrogen fluence to the limiter. The fluence is calculated from Thomson scattering measurements of the edge plasma, using the relationship

$$nv_{\parallel} = 0.4n_e\sqrt{kT_e/m_i}$$

where the symbols have the conventional meanings.[15] Because of the health and environmental hazards associated with the use of beryllium, a safety analysis report, including operating safety requirements, was written.[16]

On completion of the experiment, the device was progressively disassembled and tested for beryllium contamination. Components were classified into one of three categories.

The first category consisted of material that was known or suspected to be heavily contaminated, such as the main vacuum vessel, the pumping manifold, and certain diagnostics. Also included were components that showed some contamination or were suspected of being contaminated and that were not identified as having any future use, such as the Thomson scattering ducts and the liner ventilation system with its instrumentation. All components in this category were disposed of by burial in the Y-12 toxic waste site.

The second category consisted of items that showed contamination or were expected to be contaminated but were of considerable value and might be reusable. Typical members of this category were the isolation gate valves for the beam lines and diagnostics. These were double bagged, identified as contaminated, and stored. If they are proposed for reuse, the cost of decontamination will be compared with replacement cost and schedule.

The third category consisted of items that showed no sign of beryllium contamination and were not in line of sight of the discharge. For this category, "no sign of contamination" implies less than 0.01 μg of beryllium per sample wipe, taken over as large an exposed area as practical. These items will be carefully rechecked for beryllium contamination using damp or acidic wipes and, if no contamination is observed, thoroughly flushed with distilled water and returned to open storage for reuse. This category includes all the turbopumps and associated vacuum plumbing, the beam lines, and external diagnostics such as charge exchange and spectroscopy.

1.1.7 The ISX-B Data System

W. R. Wing, J. D. Bell, E. T. Blair, D. E. Greenwood, K. L. Kannan, and K. A. Stewart

Data system highlights from 1984 include the following:

- Complete conversion of the remaining parts of the PDP-11–based data system to the VAX-based system (including a VAX implementation of the lightpen-driven operations display).
- Implementation of an on-line data compression system that reduces the volume of data transmitted to the PDP-10 (and the time required to transmit it) by a factor of 2–4.
- Routine use of the VAX-based waveform generation system to drive the gas feed and plasma position control.

- Installation of network access port (NAP) hardware on VAX1 to allow this machine to function as a User Service Center host on the National Magnetic Fusion Energy Computing Center network (MFEnet).
- Installation of a QMS laser printer with software to support printing of integrated text and graphics.
- Installation of an HSC-50 disk-cluster controller. This forms the beginning of the disk farm necessary to support data handling for ATF.

Since it was clear at the beginning of the year that 1984 was going to be the last year for ISX operation, new development was minimized. However, a number of ongoing projects were completed, allowing the conversion of the data system from PDP-11s to a VAX-based system. The result was that the data system was able to support the beryllium limiter experiment in a unified, self-consistent way with a very low level of attention and a very high level of reliability.

The largest single conversion project was rewriting the operations display system. The operations display consists of a Sension display driver (a high-resolution, refreshed-vector, display system that interacts with users through a lightpen) and the associated software. This system was originally implemented on the PDP-11s in FORTRAN. In order to provide better support for the elaborate data structures necessary, it was decided to rewrite the software in PASCAL for the VAX implementation. This task was completed in early 1984 and shelved to await the rest of the conversion.

In early spring, the conversion was complete except for one key element: on-line data compression software to reduce the data transmission time to the PDP-10. Without this reduction, it would have required more than one shot-cycle time to transmit a data set for a normal shot, and data transmission would not have been able to keep up with machine operation. Just as this data compression software was completed, but before there was time for proper testing, the PDP-11 system failed. A week's efforts by Y-12 and Digital Equipment Corporation (DEC) field service failed to repair the problem (which was located in the dual-access disk controller). In an effort to minimize lost operating time, a decision was made to proceed immediately with the VAX conversion. The complete switchover was made in less than a day. No data were lost, operation continued, and the PDP-11 system was decommissioned. With this change, the data system became completely VAX-based, and the problems associated with trying to provide maintenance for two operating systems disappeared.

A system developed in 1983, the waveform generating system, which received some use in 1983 for driving the gas feed, was expanded in 1984 and became central to routine operation. The system consisted of a set of CAMAC arbitrary-waveform generators and software to drive them. The software provides "waveform editing" (with both graphical and numerical user input), a waveform "data base" of previously used waveforms, and the ability to scale the waveform generator's output range. The number of channels of output was expanded in 1984 from one to four. These channels were used for driving the gas feed, an impurity feed, and the plasma position and plasma current power supplies. The net result of all this work was that the operations group was able to support the beryllium limiter experiments with a smaller operating staff (two people) than had ever run ISX before. The VAX system allowed automated operation to an extent never previously possible.

Three final items of interest concern the installation of hardware. First, NAP hardware was installed on VAX1. This hardware allows the VAX to function as an MFEnet host (its node name is ATF); in addition, it provides a parallel path between Oak Ridge and the MFEnet and allows the Oak Ridge personnel on temporary assignment in Princeton to have much better access to the Fusion Energy Division VAX systems, where many of the codes and data they need are located. Second, late in the year a QMS 1200 laser printer was installed with software to support production of high-quality integrated text and graphics. Third, an HSC-50 (disk-cluster controller) was installed along with the first 2.5 gigabytes of disk storage. This forms the first installment of the disk farm that will represent the ultimate storage point for ATF data.

1.2 THE ATF PROGRAM

1.2.1 Introduction

The long-term goal of the Advanced Toroidal Facility (ATF) program at ORNL is to improve the toroidal confinement concept by demonstrating the principles of high-beta, steady-state operation in toroidal geometry and by searching for an optimum toroidal magnetic confinement system. In the near term (1987–1988), the ATF experiment will study access to the high-beta, second stability region and transport at low collisionality in the presence of large field ripple and electric fields. These studies will cover a wide range of magnetic configurations, including a variety of plasma cross sections, nonplanar (helical) magnetic axis, and stellarator features for stellarator-tokamak hybridization. The activities described in this section are all aimed at preparing for ATF operation in October 1986.

Collaborative activities with other stellarator groups increased in preparation for ATF operation. This year ORNL hosted a U.S.–Japan Stellarator/Heliotron Workshop on experimental planning, actively participated in the research programs at the Kyoto University Plasma Physics Laboratory[17] and the Max-Planck-Institut für Plasmaphysik by means of extended foreign research assignments, and supported torsatron research at the University of Wisconsin.

1.2.2 Physics Studies

D. B. Batchelor, B. A. Carreras, K. A. Connor, R. H. Fowler, J. C. Glowienka, R. C. Goldfinger, J. E. Goyer, J. H. Harris, D. E. Hastings, T. C. Hender, R. L. Hickok, W. A. Houlberg, J. F. Lyon, R. N. Morris, J. K. Munro, Jr., J. A. Rome, and T. L. White

ATF physics studies in 1984 concentrated on those areas needed to prepare for ATF operation rather than on development of the ATF concept.

Magnetic field calculations emphasized determination of allowable error fields and field line following for pump limiter/divertor studies. Low-order resonant field perturbations of $\sim 10^{-3}$ and random field perturbations of $\sim 10^{-2}$ can cause magnetic island formation and serious deterioration of vacuum magnetic surfaces; thus, potential field perturbations due to magnetic shielding on diagnostics and ion sources, beam-bending magnets, high-current bus bars, and magnetic permeability (μ) variations in the helical field (HF) coil T-sections and in the structural shell were evaluated.

Magnetic field line calculations were done to estimate the connection length and characteristic decay length in the scrapeoff layer that are needed for pump limiter/divertor design. The connection length is the total path length of a field line between the last closed flux surface and the wall. This parameter determines the number of limiters or divertor targets. In tokamaks, the magnetic field structure outside the last closed flux surface is such that the connection length corresponds to many toroidal revolutions. Hence, it is sufficient to have a limiter at one toroidal or poloidal location to intercept the total diffusive particle and energy flux crossing the plasma boundary. For ATF, calculations of field lines indicate connection lengths of several toroidal revolutions within the first few centimeters outside the last closed flux surface. This is illustrated in Fig. 1.17, where the length of a field line before it intersects the wall is plotted vs distance Z above the plasma magnetic center at a toroidal location with vertical ports. The last closed flux surface is at Z = 0.39 m. The length at Z = 0.47 m, 8 cm into the scrapeoff layer, is ~40 m, corresponding to three toroidal revolutions. Thus, within a few centimeters outside the plasma boundary, the scrapeoff layer in ATF is similar to that in a tokamak. If this proves to be the case, it will be possible to use pump limiter configurations that are very similar to those tested in tokamaks.

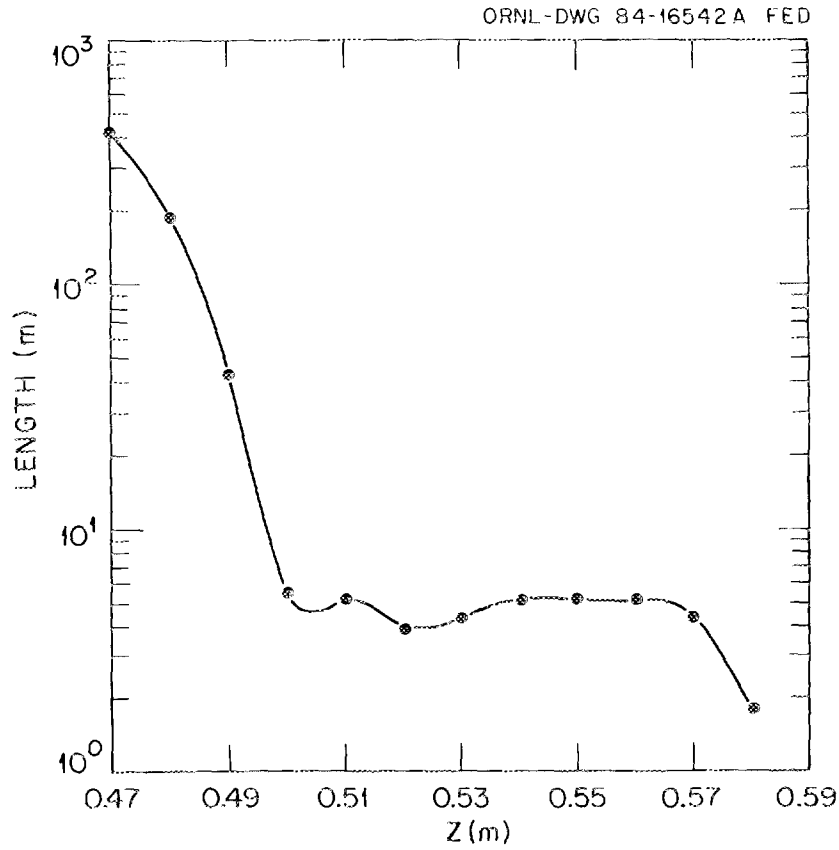

Fig. 1.17. ATF field line connection length vs vertical height Z in the ϕ = 0° plane. The last closed magnetic surface is at Z = 0.39 m.

A geometrical optics code was used to calculate ordinary-mode (O-mode) fundamental electron cyclotron ray propagation and absorption in ATF. Rays are propagated in a beam simulating the anticipated antenna design with the trajectories displayed in real space. A histogram is calculated for each beam showing fractional power absorption, via fundamental electron cyclotron heating (ECH), as a function of the toroidal magnetic flux. A simple, analytical model for magnetic field and flux is used to simulate the vacuum condition expected in ATF. We trace O-mode rays (polarization $\mathbf{E} \parallel \mathbf{B}$ for perpendicular propagation) with plasma and wave parameters assumed to be typical for ATF operation (f_{ECH} = 53.2 GHz, T_e = 500 eV, $n_e = 10^{13}$ cm^{-3}, $|\mathbf{B}_0| \sim 1.9$ T). Calculations are also done for a range of values of $|\mathbf{B}_0|$ to test the sensitivity to changes in the coil currents. Significant absorption (up to 100% of incident wave power) occurs with an optimally placed and oriented beam (FWHM = 3°). This situation occurs when the resonance is at the saddle point of the magnetic field and the beam passes through this region. However, these results are quite sensitive to antenna placement, orientation, and magnetic field (or, equivalently, wave frequency). Based on these calculations, it is argued that an optimum strategy is to launch the O-mode waves from the high-field side in the $\phi = 0°$ plane. This should be done using a gyrotron with a frequency lower than that associated with the maximum anticipated field at the saddle point.

Monte Carlo calculations of neutral beam power deposition in the plasma, on the vacuum vessel walls, and on apertures along the beam path have been made for different beam line positions. For a beam divergence of 1.3° and a peak plasma density of 4×10^{13} cm^{-3}, $F \approx 82\%$ of the power is deposited inside the plasma. A small amount ($\approx$6%) hits outside the large horizontal port, and $\approx$8% hits the helical coil trough just inside the port, where local wall power densities can exceed 200 W/cm^2. The remainder ($\approx$4%) is shinethrough. If larger apertures are used to stop beam impacts on the wall inside the port, then the power deposited in the plasma drops to $\approx$70%. Reducing the beam divergence to 1° completely stops the beam from hitting the inside wall or port.

Calculations of HIBP orbits are being done for ATF to determine whether a beam can be brought from a distance ($\sim$5 m) through a spatially varying magnetic field so that a useful grid map of the plasma potential can be formed. A number of primary beam injection conditions, when injecting vertically upward through a port, have been found to yield useful secondary beam detection grids. None of the injection conditions are fully optimized in terms of exit port utilization and maximum plasma profile scanned. Even without optimization, it appears that most of the plasma can be scanned along a single detector line during one shot. Future work might focus on the use of two detectors, rather than one. The two-detector system would add redundancy and flexibility and would relax the requirement that one detector be capable of scanning the entire plasma cross section. Calculations were made of primary beam attenuation by electron-impact ionization along the trajectory inside the plasma, assuming a 30-cm-radius plasma that was radially and toroidally uniform. The plasma had an electron temperature that varied from 600 eV to 5 keV and a constant density of 6×10^{13} cm^{-3}. The probing beam is a 200-keV cesium beam. The primary beam attenuation varied from 10^{-2} to 10^{-6} as a function of path length in the plasma and as a function of plasma conditions. These are worst-case numbers because of the crude assumptions made for the plasma geometry. The numbers would yield secondary signal levels of around 20 nA. This signal level was found to be adequate for HIBP measurements in ISX-B.

1.2.3 Construction

E. E. Bartlett, L. R. Baylor, R. D. Benson, D. E. Brashears, C. Bridgman, A. Y. Broverman, R. L. Brown, W. E. Bryan, W. D. Cain, K. K. Chipley, M. J. Cole, W. K. Cooper, D. L. Coppenger, P. H. Edmonds, J. W. Forseman, W. A. Gabbard, E. L. Halstead, J. H. Harris, G. H. Henkel, T. C. Jernigan, R. L. Johnson, L. M. Jordan, V. E. Lynch, J. F. Lyon, J. A. Mayhall, J. F. Monday, G. H. Neilson, B. E. Nelson, J. A. Rome, M. J. Saltmarsh, W. D. Shipley, D. J. Taylor, C. K. Thomas, P. B. Thompson, L. M. Vinyard, J. E. Warwick, J. A. White, J. C. Whitson, D. E. Williamson, W. L. Wright, and R. B. Wysor

As shown in Fig. 1.18, the ATF device consists of a set of HF coils, a set of poloidal field (PF) coils, an exterior shell structure to support the coils, and a thin, helically contoured vacuum vessel inside the coils. The ATF will use the existing facilities of the ISX-B tokamak: power supply, cooling, diagnostic, data acquisition, control, and heating systems. The ATF device parameters are listed in Table 1.1.

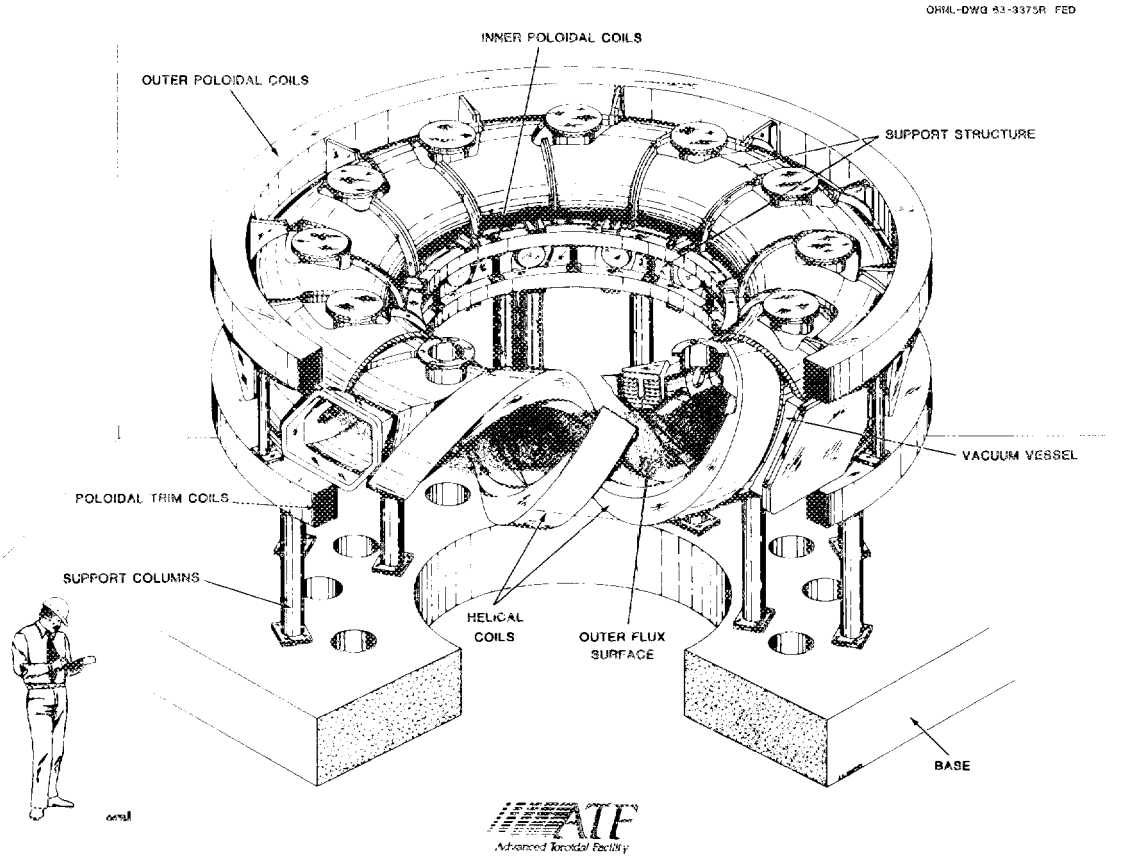

Fig. 1.18. Artist's conception of ATF.

Table 1.1. ATF device parameters

Major radius R_0, m	2.10
Average plasma minor radius $\langle a \rangle$, m	0.30
Average HF coil minor radius a_c, m	0.46
Toroidal field on axis B_0, T	2.0 (for 5 s) 1.0 (continuous)
Ion and electron temperature ($T_i = T_e$), keV	1–2
Plasma density $\langle n \rangle$, cm^{-3}	$(1–10) \times 10^{13}$
Average plasma beta β, %	4–8

1.2.3.1 Coils

The electrical characteristics of the different coil sets are summarized in Table 1.2. The HF set consists of a pair of coils that forms an ($\ell = 2$, $m = 12$) torsatron helix. The coils must be constructed so that the current winding law is within 1 mm of the theoretical winding law. In other stellarators, similar accuracies have been achieved by winding the HF conductor into an accurately machined groove on a toroidal vacuum vessel. Such a procedure requires serial production of the vessel and coils. In ATF, the HF coil will be made in 24 segments with joints in the equatorial plane of the machine. This permits parallel production of the coils and vacuum vessel. Each coil segment consists of 14 insulated copper conductors mounted on a structural steel brace with a T-shaped cross section (see Fig. 1.19). Each conductor is made from plate and contains a cooling-water tube brazed into a milled groove. The conductors are rough-formed to shape; then a complete set of conductors is clamped into a precision die and stress-relieved to achieve the final form tolerance. The stainless steel T-piece is cast to shape to fit in its tolerance window and is then machined to provide accurate location points for mounting the conductors

Table 1.2. Major coil characteristics

Coil set	Current per coil (MA·turns)	Current per turn (kA)	Current density (A/cm^2)	Voltage per coil set (V)	
				Peak	Flattop
HF	1.750	125.0	3350	1250	500
VF inner	0.263	16.4	2540	650	121
VF outer					
Main	0.375	125.0	2600	1250	63
Trim	0.159	15.9	2420	650	166

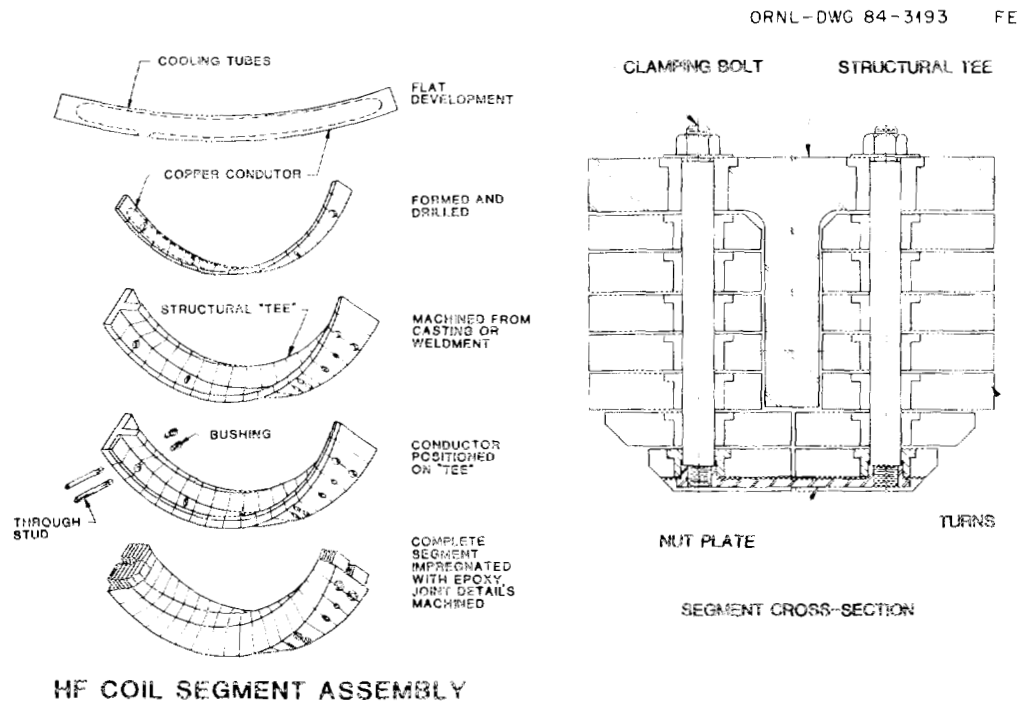

Fig. 1.19. Segmented helical coil concept.

and assembling the coil. These components are tested to see that they fit within the tolerance windows using a coordinate measuring machine with an accuracy of ~0.01 mm. This machine is also used to check the completed segment. Following assembly, the segment is potted in epoxy resin. Components for a full-scale prototype segment have been built by the Chicago Bridge and Iron Company (CBI) in Birmingham, Alabama. Fabrication of parts for the helical coil segments has begun at CBI. The structural T-pieces were cast by Esco Corporation in Portland, Oregon. Final delivery is scheduled for May 1986.

A critical design issue is the demountable joint. Many designs were tested, and a few met all the initial requirements for both pulsed and steady-state operation. The selected joint concept is a simple lap geometry for each turn with bolts through the entire segment stack, which is made up during HF coil assembly (see Fig. 1.20).

The lap configuration is composed of a half-lap machined tab at the end of each turn of a coil segment that mates with corresponding half-laps when upper and lower segments are joined during the HF coil assembly process. The tabs on each turn are machined while the copper is still in a flat development stage. A typical joint end is shown in Fig. 1.21. Precise control of each tab's position in the segment stack, including the holes for the through-bolts, is accomplished using tooling fixtures at the initial forming stage and again during segment assembly.

Field assembly of these HF coil joints is based on optical alignment to a particular joint control hole on each segment end. Tab misalignments (nonparallel surfaces) are

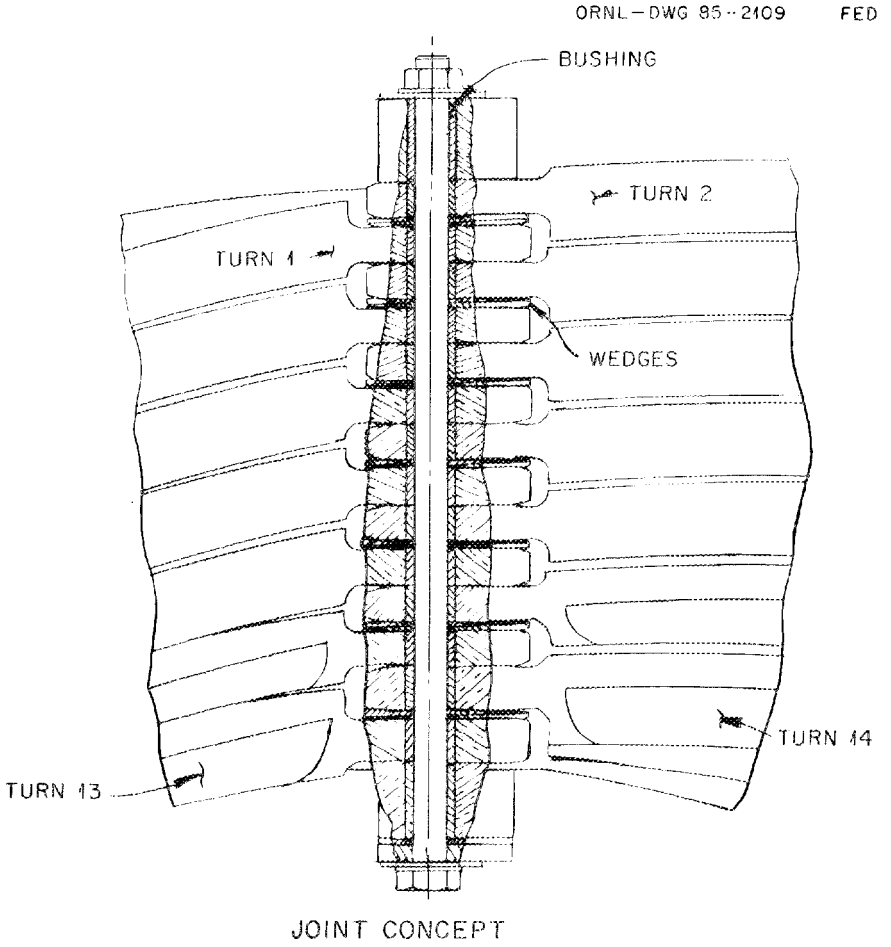

Fig. 1.20. View of lap joint joining helical coil segments.

corrected by assembly forces as the upper and lower segments are engaged. Tests of actual joint ends have been conducted and verify this characteristic. Once aligned, tapered G-10 insulating wedges are installed between turns to fill the gap and provide a solid block for through-bolt load transfer to each turn.

The through-bolts are a sliding fit to match honed G-10 bushings in each joint tab hole. The bolts are actually studs that engage a floating nut plate located at the innermost turn joint. The studs are tensioned and the load is secured by a nut applied to the outer end of the stack to provide joint contact pressure. Preliminary tests of joint resistances through the stack showed that all joints had a measured resistance less than the required 1 $\mu\Omega$.

Thermal-electric tests have also been made on joint specimens to verify cooling capability and margins relative to the hot spot temperature limit of 150°C. These specimens were half-width turns to match the required current density to available power supply limits. Actual tests were possible up to about 0.7 of the rated joint current density. Extrapolation, verified by tests of an appropriate copper specimen, was then used to analytically

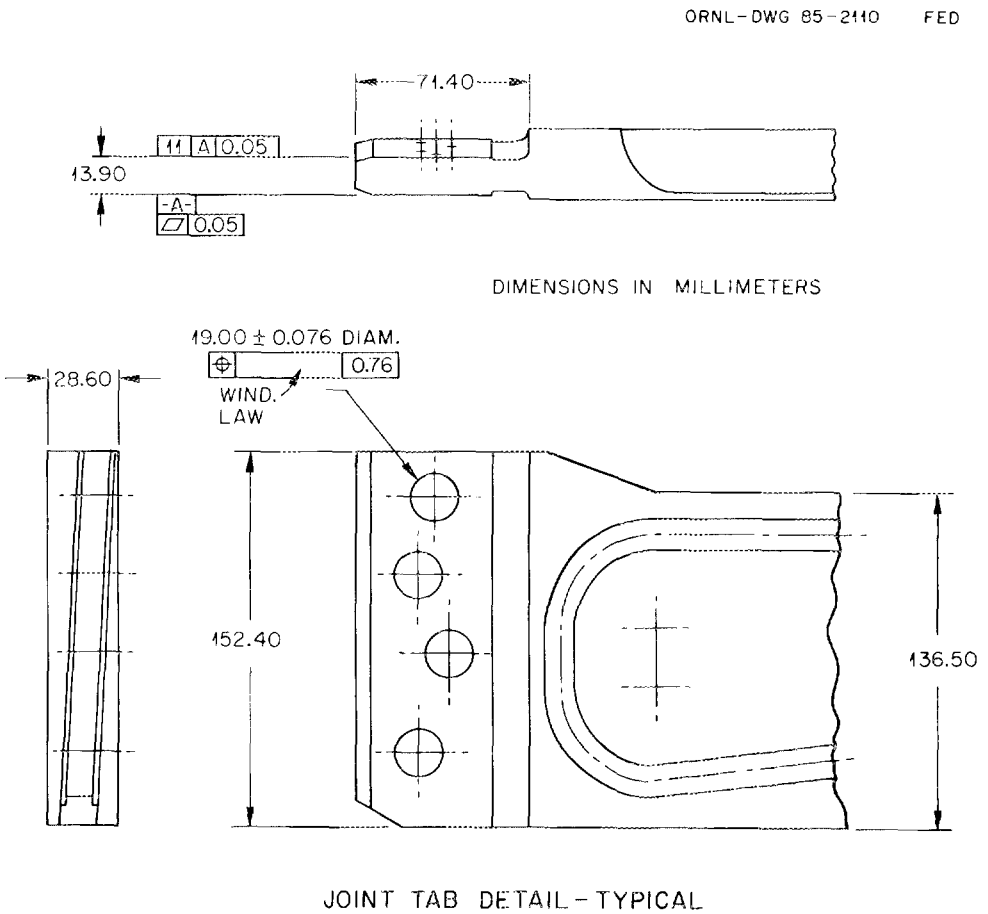

Fig. 1.21. Detail of lap joint for a single turn of the helical coils.

predict peak temperatures for the joint configurations. Two joints were evaluated since the inner and outer turns differ slightly. The results of these tests, summarized in Fig. 1.22, show that adequate cooling can be provided for all joint configurations.

The major joint parameters are summarized in Tables 1.3 and 1.4, where the differences between the inner and outer turns can be seen. Geometry constraints required the inner turns to be slightly thicker, narrower, and clamped by only three bolts.

The PF coils are of a more conventional design and use a wound, square-section, hollow copper conductor that is insulated with glass cloth and epoxy impregnated. They are being manufactured by the Princeton Plasma Physics Laboratory. Final delivery of the vertical field (VF) coils is scheduled for August 1985.

1.2.3.2 Vacuum vessel

The vacuum vessel is a stainless steel shell that fits closely to the inner bore and side walls of the HF coil, as shown in Fig. 1.23. The vessel is relieved in the area above and

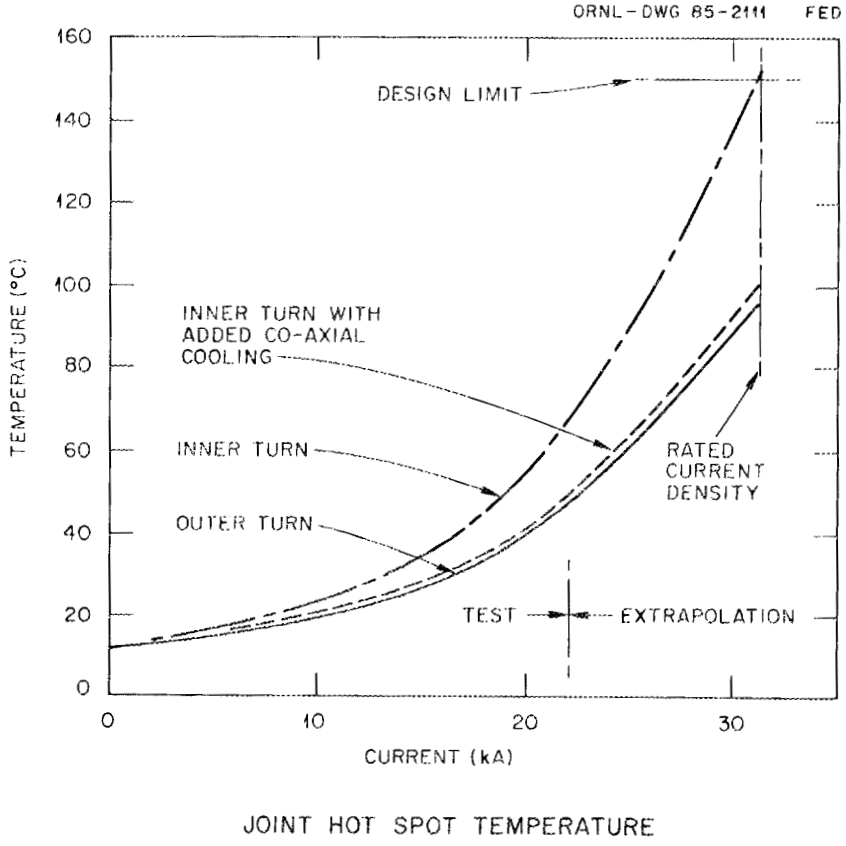

Fig. 1.22. Peak temperature in a half-size coil joint as a function of current.

Table 1.3. ATF coil joint design limits

OFHC copper	11,000 psi = endurance limit
	25,000 psi = 100,000 cycles
G-10 bushing	20,000 psi = $1/3S_{ult}$
G-10 insulation	20,000 psi = $1/3S_{ult}$
A286 bolts	200,000 psi = S_{ult}
	100,000 ± 30,000 = 100,000 cycles

Table 1.4. ATF coil joint parameters

	Outer	Inner
Dimensions, cm^2		
Joint cross sections		
Full copper turn	39.0	41.0
Full tab	19.6	18.07
Tear-out	54.2	51.7
Tab tension	10.2	14.9
Contact area	63.6	46.0
Current density, A/cm^2 (at 125 kA)		
Turns	3205	3048
Joint tab	6378	6918
Contact area	1965	2717
Current per bolt, kA	31	42

below the HF coil joint to allow clearance for installation and assembly of the segments. Twelve large ports on the outside (0.9 by 0.60 m), inside (0.15-m diam), top (0.4 by 0.4 m), and bottom (0.4 by 0.4 m) provide access for diagnostics, fueling, and heating systems. The wall thickness is 6.4 mm. Metallic seals on the port flanges permit the vessel to operate at 150°C for cleaning. For steady-state operation, cooling panels will be mounted on the inside of the vacuum vessel to remove heat from the plasma. Fabrication of the vacuum vessel has begun at Pittsburgh–Des Moines Steel Company in Pittsburgh. Delivery is scheduled for December 1985.

1.2.3.3 Support structure

The principal loads on the HF coils are due to thermal and magnetic forces that lead to radially outward hoop loads and overturning loads. The principal loads on the PF coils include a radial hoop force and the vertical force of interaction with the other coils. The structure consists of a toroidal shell, composed of identical upper and lower shell panels made from stainless steel castings and intermediate panels machined from rolled stainless steel plate. The panels are joined by bolts, and the entire shell is tied to the HF coil segments by additional special bolted fasteners. Westinghouse Electric Corporation in Pensacola, Florida, is fabricating the structural shell. Delivery is scheduled for August 1985.

1.2.3.4 Assembly sequence

The assembly sequence is shown in Fig. 1.24. First, the lower shell is assembled and aligned. Next, the lower halves of the HF segments are installed and positioned accurately

ORNL-DWG 85-2762 FED

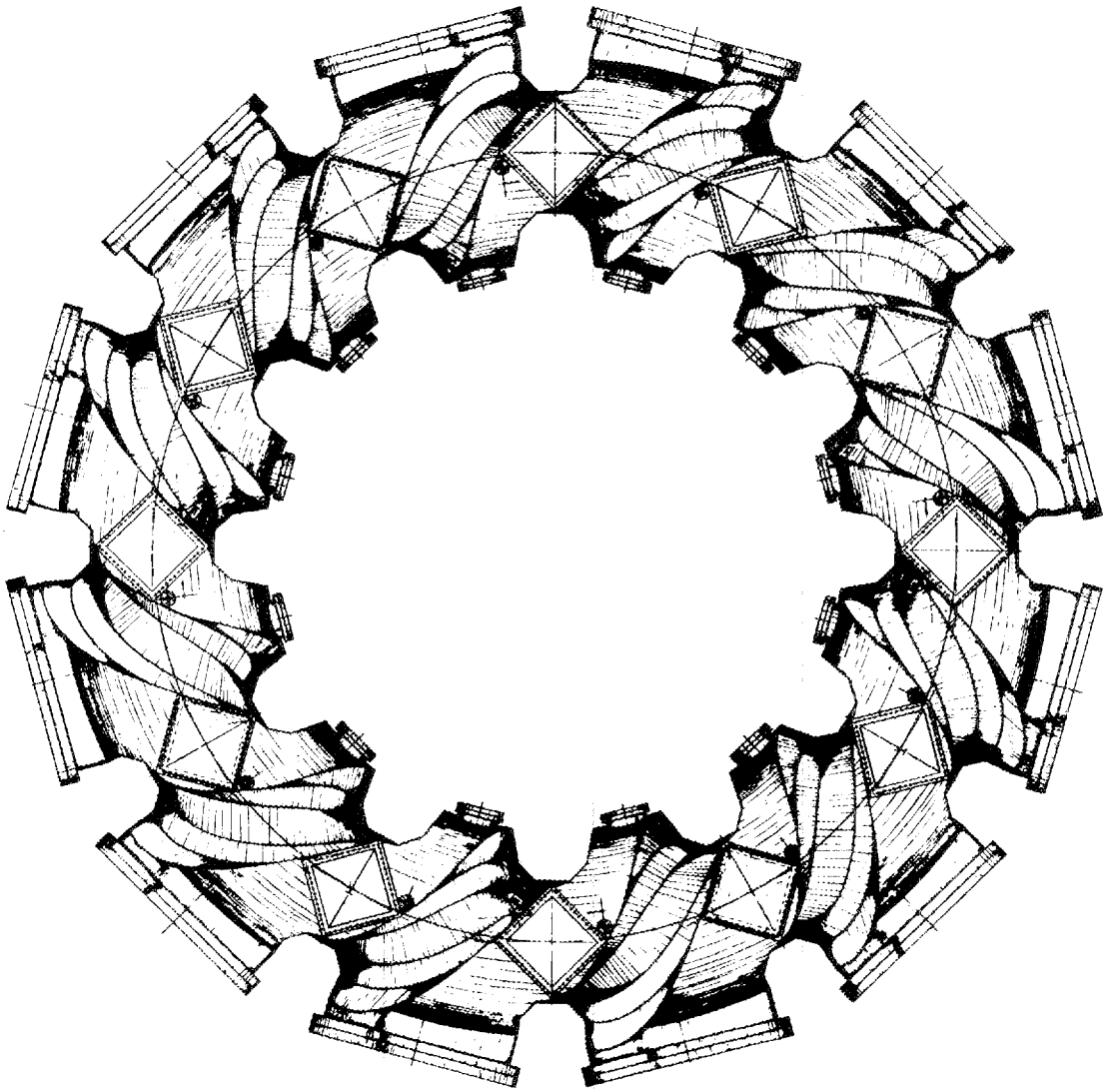

Fig. 1.23. Top view of the ATF vacuum vessel, showing diagnostic ports and grooves for the helical coils.

with an optical alignment system. The vacuum vessel is then lowered into place. Next, the upper HF segments are attached. The intermediate shell panels and the upper panels are mounted. Finally, the PF coils are mounted and aligned.

Assembly of ATF will begin in August 1985 after delivery of the lower half of the structural shell and the lower VF coils. Completion of ATF will be paced by delivery of components for the 24th helical coil segment in May 1986. Assembly is scheduled to be complete in September 1986, and initial operation should begin in October 1986 after pre-operational testing.

ORNL-DWG 83-4057 FED

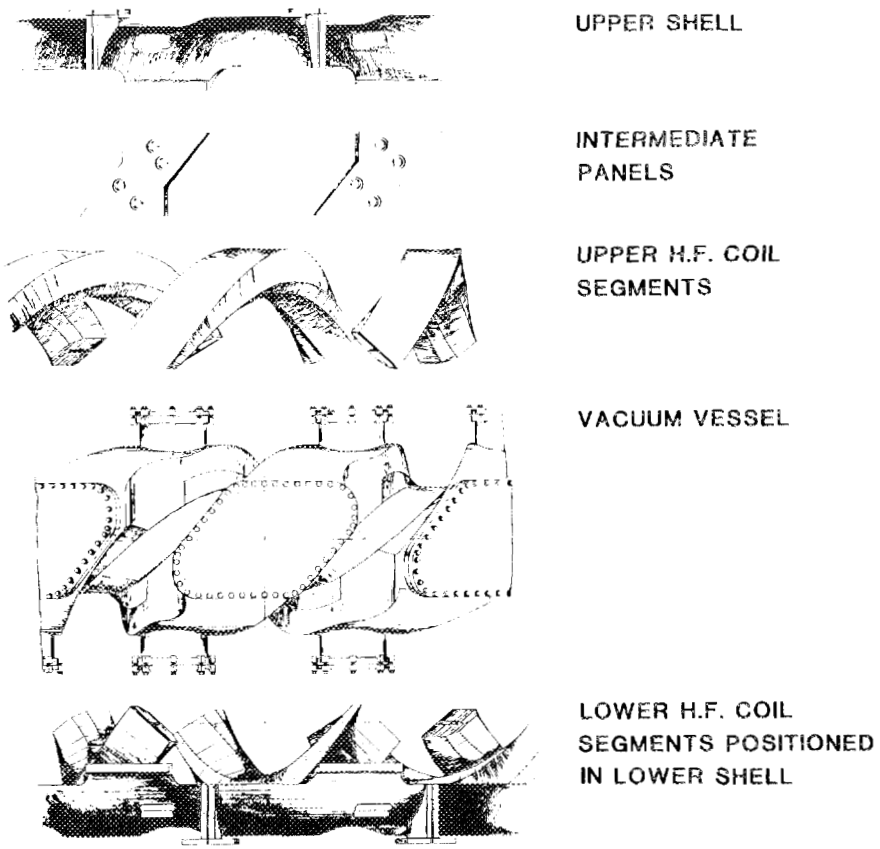

Fig. 1.24. Assembly concept.

1.2.4 Facility Preparations

F. W. Baity, G. R. Dyer, P. H. Edmonds, R. D. Foskett, W. A. Gabbard, M. M. Menon, G. H. Neilson, M. J. Saltmarsh, T. L. White, W. R. Wing, and W. L. Wright

Facility preparations for ATF include removal of the ISX-B tokamak, clearance of the site, and any necessary modification, upgrading, or replacement of facility subsystems, including the magnetic field power supplies, the vacuum system, the neutral beam lines, the instrumentation and controls, the data acquisition system, the diagnostics, the discharge cleaning system, and the site itself. They also include work required to adapt and implement ECH and ion cyclotron range of frequencies (ICRF) heating systems originally planned for use in the ELMO Bumpy Torus (EBT) program.

1.2.4.1 Project management

Organization and planning of the facility modification project was undertaken and completed. A project team was assembled, and a work breakdown structure was developed. The major task areas are:

1. magnetic field power supplies (HF, VF);
2. vacuum vessel support systems (vacuum, discharge cleaning, gas puff, bakeout systems, etc.);
3. site preparation (removal of ISX-B, facility layout, utilities, etc.);
4. instrumentation and controls (status monitors, shot sequencing, interlocks, grounding, cabling, subsystem interfaces, etc.);
5. data handling (computers, computer peripherals, CAMAC equipment, etc., for support of diagnostics, analysis, and operations);
6. machine diagnostics (coil voltage and current sensors, 2-mm interferometer, magnetic sensors, electron beam, television camera, survey spectrometer, bolometric monitor, etc.);
7. physics diagnostics [Thomson scattering, HIBP, charge exchange, spectroscopy, soft X-ray arrays, far-infrared (FIR) interferometer, etc.]; and
8. heating systems (ECH, ICRF, NBI).

Significant progress was made in some of these areas.

1.2.4.2 Site preparation

The ISX-B tokamak was removed from its enclosure. Diagnostics, neutral beam lines, instrumentation, controls, and some ISX-B components [e.g., the toroidal field (TF) coils] were removed, crated, and stored for future use. The device enclosure and control room are being completely cleared; other areas are being or will be cleared as required.

1.2.4.3 Magnetic field power supplies

Power supply requirements for ATF were assessed and compared with the capabilities of existing equipment. The HF power supply, formerly used with the ISX-B TF coils, will need a major upgrade because of the higher voltages and pulse lengths required for ATF. This supply consists of eight transformer-rectifier modules, housed in a separate building adjacent to the main confinement research facility. The transformers will be replaced with units having ~5 times the continuous power rating and ~1.25 times the voltage of the existing units; the silicon-controlled rectifiers (SCRs) will be replaced with higher-capacity components as well. The upgraded supply will also be compatible, with modest reconfiguration, with eventual steady-state operation of ATF at half field (1 T). The steady-state and pulsed configurations are illustrated in Fig. 1.25. The modularity, building, primary power system, and output buswork of the existing supply will be retained.

The power supply assessment indicated no need for major modifications to the transformer-rectifier supplies to be used with the VF windings. Some testing and modification of the low-power circuitry, instrumentation, controls, and interlocks are required.

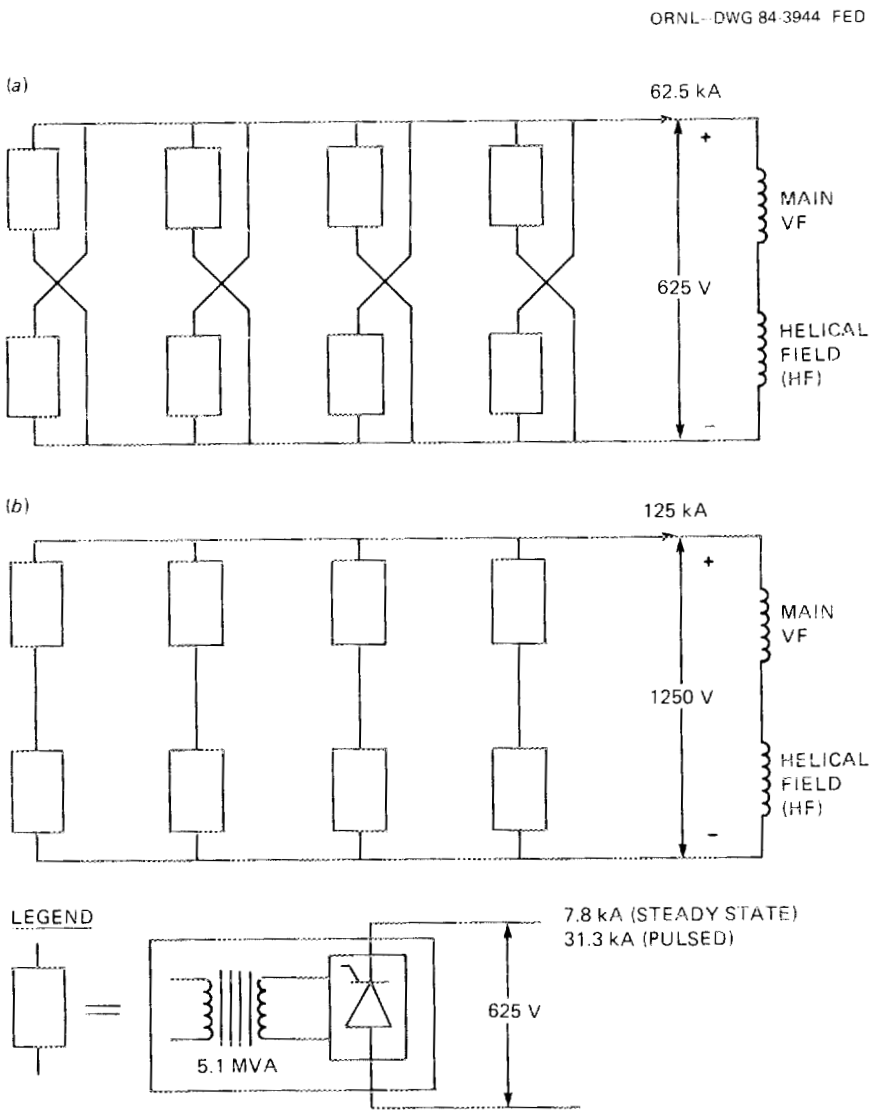

Fig. 1.25. HF power supply configured for (a) steady-state and (b) pulsed operation.

1.2.4.4 Heating systems

The three 1.5-MW, 0.3-s neutral beam lines from ISX-B were evaluated for use on ATF. Some modifications will be necessary; these include the addition of magnetic shielding in the ion source and neutralizer areas, the installation of limiting apertures to protect the ATF vessel walls, and the fabrication of new support stands. Major preventive maintenance of the high-voltage power supplies was also determined to be necessary.

The ECH gyrotron power supply was installed, and all the relevant qualification tests required for ATF gyrotron operation were performed, using a resistive high-voltage dummy load. In every case, the supply meets or exceeds those specifications that are important for

ATF operation. Procurement of 53.2-GHz gyrotrons and a superconducting gyrotron magnet system for ATF was inititated. A theoretical ray tracing study of ECH wave propagation in ATF showed that a narrowly directed, linearly polarized, O-mode launch is required to deposit most of the ECH power near the magnetic axis and thereby to couple to the best-confined electrons. A quasi-optical, mode-controlled ECH transmission system was chosen as the most cost-effective and lowest-risk approach to meeting these requirements, in both pulsed and steady-state operation of ATF. Cold testing of ECH components requires a source of 53.2-GHz signal with high mode purity. Such capability has been established in a laboratory setup, in which more than 95% of the power is produced in the TE^{o}_{02} mode.

The emphasis in the ICRF area was on the preparation of the three U.S. Navy surplus AN/FRT-86 HF band transmitters. One is fully operational at 100 kW cw, requiring only routine maintenance. A second unit has been modified from the standard Class AB operation to Class C, in order to boost its power output to 200 kW cw. This unit was operated at a power level of 130 kW and frequencies up to 16 MHz, with some oscillation problems. However, the work is proceeding satisfactorily toward the targeted April 1985 completion date. The third transmitter is in need of complete refurbishment. A full parts inventory was conducted, and replacement parts were ordered.

1.3 ADVANCED PROJECTS

1.3.1 ATF Extended Performance

F. W. Baity, B. A. Carreras, K. K. Chipley, R. L. Johnson, J. F. Lyon, M. M. Menon, P. K. Mioduszewski, J. F. Monday, G. H. Neilson, M. J. Saltmarsh, J. Sheffield, P. B. Thompson, and T. L. White

The long-term goal of the ATF program is to improve the toroidal confinement concept by demonstrating the principles of high-beta, steady-state operation in toroidal geometry and by searching for an optimum toroidal magnetic confinement system. The base ATF program, covering the first two to three years, will make significant contributions in these areas, but further essential contributions will be possible only when the full potential of ATF is realized.

The high-beta capability of ATF derives from its direct access to the second stability region with $\langle\beta\rangle \gtrsim 8\%$. To realize this full capability requires high power ($\gtrsim$5 MW) for long pulses (several skin times or $\approx$15–30 s). The base ATF will have three ISX-B beam lines (4.5-MW, 40-kV H^0 neutral beam injectors for 0.3-s pulses) and power supplies for 5-s pulsed fields.

The steady-state capability of ATF arises from the steady-state coil systems and from the fact that no plasma current is required to maintain the magnetic confinement geometry. However, the ATF vacuum vessel is uncooled, so the wall energy deposition is limited to 1.5 MJ per pulse every 5 min or to 150 MJ per day before the 150°C vacuum vessel temperature limit is exceeded. The study of long-pulse physics issues and of ultra-long-pulse plasma-wall interactions and the development of necessary plasma technology components (limiters, targets, fueling, heating systems) require, at a minimum, cooled panels inside the vacuum vessel and cooled limiters and targets. This operation requires edge

power densities of ~20 W/cm² (average) and ~400 W/cm² (peak) for times (many minutes) that make inertial cooling untenable, so active cooling must be employed. This requires a continuous cooling capability of 1–5 MW for hours (roughly half on the vacuum vessel and the remainder on limiters).

The flexibility that allows the study of a wide range of toroidal magnetic configurations in ATF arises from versatile coil sets (three PF coil sets and two helical windings) that can be independently powered and from the ability to accommodate (at a later time) TF coils for stellarator-tokamak hybrid studies. The base ATF can drive a modest plasma current ($I_p \lesssim 40$ kA) using a small fraction of the 12 V·s in the ATF coil sets before an $\iota = 1$ condition exists in the main part of the plasma. However, a definitive test of stellarator-tokamak hybrid issues would require the addition of 0.5-T TF coils and lower hybrid current drive (LHCD) for high-current ($\lesssim$200-kA), long-pulse capability. The other requirements for a stellarator-tokamak hybrid demonstration are the same as for stellarator high-beta operation (high heating power for long pulses and the ability to remove this high average power from the vacuum vessel and limiters).

All future ATF missions require, at a minimum, longer-pulse operation at moderate duty factor with adequate heating and cooling. Since ATF has been designed for steady-state operation and some components of the base program are already steady state, it is cost-effective to go directly to full steady-state capability at moderate power levels ($\lesssim$1 MW) in the next phase of the program, rather than to an intermediate (5- to 15-s) pulse length. This approach makes the most effective use of ATF in the short term and maximizes flexibility for future missions in the longer term.

Long-pulse to steady-state operation is needed for a number of reasons. An adequate test of high beta and possibly the demonstration of access to the second stability regime require long-pulse operation. Controlled access to the second stability region may require pulses long enough to permit detailed control of plasma profiles and shaping and relaxation of induced plasma currents. Pulses on the order of a few skin times may be necessary to demonstrate the achievement of a high-beta equilibrium. On ATF these times are ~15–30 s.

Tokamak experiments show that the bulk plasma behavior is affected by edge conditions (e.g., H-mode, Z-mode, and ELMs). Thus, equilibrium may not be reached until the entire system equilibrates. The time scale for plasma-wall interactions to come into equilibrium is measured in minutes rather than in seconds, as observed in laboratory simulations, in a wide range of analyses, from tokamak experience, and from observations on EBT-Scale (EBT-S).

There are additional important benefits from true steady-state operation. Steady fields reduce the thermal and mechanical stress associated with pulsed operation and greatly extend the integrated lifetime of the ATF coils (80 h pulsed vs 8000 h steady state). The long integrated exposure of walls and in-vessel components allows effective collection of a data base for plasma-materials interactions and permits component lifetime tests.

Five major items are needed to extend the performance of ATF: (1) in-vessel cooling panels to handle (eventually) 2.5 MW of steady-state power (the present limit is 1.5 MW every 5 min or 7.5 kW average); (2) additional steady-state rf heating capability at $\gtrsim$1 MW and actively cooled antennas; (3) actively cooled pump limiters/divertors and steady-state pumping; (4) power supply upgrades for steady-state operation at 1 T; and (5)

upgrade of the cooling water facility from 33 to 40 MW. It is planned to implement these improvements as time and budgets permit. The most critical item is the addition of actively cooled panels inside the vacuum vessel, which would remove the constraint of 1.5 MJ per 5 min but requires about six months of downtime for installation.

1.3.2 The ATF-II

H. Attaya, J. L. Cantrell, B. A. Carreras, R. Engelstad, J. H. Harris, T. C. Hender, W. A. Houlberg, J. T. Lacatski, J. F. Lyon, J. A. Rome, I. N. Sviatoslavsky, and N. A. Uckan

The stellarator magnetic configuration has a number of distinct advantages for an eventual fusion reactor: (1) it is the only reactor concept that can maintain an ignited, steady-state fusion plasma without external power input to the plasma; (2) it does not require driven currents in the plasma and does not suffer from plasma disruptions; (3) plasma startup is on existing "vacuum" magnetic surfaces; (4) it does not have pulsed thermal or magnetic loads; and (5) it allows access to a high-beta, second stability regime at moderate aspect ratio.

A necessary prerequisite for a reactor would be the physics and technology demonstration of stellarator reactor feasibility—a steady-state, high-beta plasma with good confinement and particle/impurity control properties at reactor-relevant parameters (density, temperature, beta, etc.) in hydrogen or deuterium. Extension to full D-T operation would be a further step. This would be the mission of ATF-II, a large, next-generation stellarator facility. ATF-II would be a factor of 2 to 3 scaleup of ATF (R = 4–6 m, a = 0.6–1.0 m, and B = 3–5 T). It would use superconducting coils and high-power rf or neutral beam heating and would operate steady state at high beta in the mid-1990s. The optimum magnetic configuration for high beta with good confinement will be based on results from the base and extended-performance ATF programs and from foreign stellarators (Heliotron-E, Wendelstein VII-AS, and TJ-II).

Present studies aimed at better defining the ATF-II include studies of a compact stellarator reactor based on ATF, the ATF Stellarator Reactor (ATFSR); further reduction of the aspect ratio for torsatrons; and the engineering feasibility of symmetric modular torsatron (Symmotron) coils and torsatron coils with joints.

1.3.2.1 ATFSR studies

In principle, steady-state operation should lead to a smaller, economical reactor concept. The key issues addressed by the ATFSR study[18] were the adequacy of confinement in a torsatron for a small reactor, the parameters governing confinement, and the extent to which these parameters can be addressed in ATF. For this study, the ATF machine parameters were scaled up to give a 1-m plasma radius. The parameters of the ATFSR and ATF, with a possible range for ATF-II, are given in Table 1.5.

Confinement analyses were carried out using the one-dimensional (1-D) WHIST transport code assuming D-T plasmas and a Gaussian power deposition profile appropriate to ion cyclotron heating (ICH) or neutral beam injection. The effects of a radial electric field on confinement were studied using the Shaing-Houlberg model[19,20] for the dominant

Table 1.5. Parameters of ATF-based torsatrons
$\iota(0) = 0.35$, $\iota(a) = 0.9$

	ATF	ATFSR	ATF-II
Major radius, m	2.1	7	4–6
Average minor radius, m	0.3	1	0.6–1
Field on axis, T	2	5	3–5
Number of field periods	12	12	10–12

particle and heat fluxes due to helically trapped particles in the presence of a radial electric field. The model joins the $1/\nu$ transport scaling in the intermediate collisionality regime to the ν transport scaling in the low collisionality regime through a resonant transition regime where the $\mathbf{E} \times \mathbf{B}$ and $\mathbf{B} \times \nabla B$ poloidal drifts cancel. Axisymmetric neoclassical (Hinton-Hazeltine) tokamak transport is also added to this stellarator ripple-produced neoclassical transport.

Figure 1.26(a) shows the results obtained with neoclassical losses for a fixed value of $\xi = e\phi/T = 2$. Here ignition does not occur, but a high-Q, driven plasma ($Q \sim 15$) is produced. For example, 20-MW auxiliary heating at $\langle n_e \rangle = 6.5 \times 10^{19}$ m^{-3} produces 300 MW of fusion power at $\langle \beta \rangle = 5.5\%$ and $\langle T \rangle = 22$ keV, and 40-MW auxiliary heating at $\langle n_e \rangle = 9.5 \times 10^{19}$ m^{-3} produces 600 MW of fusion power at $\langle \beta \rangle = 8\%$ and $\langle T \rangle = 22$ keV. Increasing ξ above 3 does produce ignition. Figure 1.26(b) shows the results obtained with neoclassical losses for a fixed value of $\xi = e\phi/T = 4$. Here ignition (the zero input power contour) occurs at a nearly constant value of $\langle T \rangle = 21.5$–23 keV over a wide range of densities and, in particular, can occur at very low values of density and beta. The ignited power output is 300 MW at $\langle n_e \rangle = 7 \times 10^{19}$ m^{-3} and $\langle \beta \rangle = 6\%$ and is 600 MW at $\langle n_e \rangle = 1 \times 10^{20}$ m^{-3} and $\langle \beta \rangle = 9\%$.

The addition of anomalous (Alcator scaling) losses prevents ignition at very low values of density and beta. At higher densities, the neoclassical stellarator losses still dominate. This is shown in Fig. 1.26(c) for a fixed value of $\xi = e\phi/T = 4$. Ignition occurs for $\langle n_e \rangle \geqslant 6.5 \times 10^{19}$ m^{-3} at $\langle T \rangle > 25$ keV and an output power of $\approx$300 MW. Operation at $\langle n_e \rangle = 1 \times 10^{20}$ m^{-3} yields 600 MW of output power and $\langle \beta \rangle \approx 8\%$.

Calculations were also made of transport due to a self-consistent radial electric field, determined by equating the electron and ion particle fluxes from the Shaing-Houlberg transport model. The net result is a large ($\sim$5–8) increase in losses in the transition region, where the $\mathbf{E} \times \mathbf{B}$ and $\mathbf{B} \times \nabla B$ poloidal drifts cancel and the potential changes sign from $\phi < 0$ at high collisionality to $\phi > 0$ at lower collisionality. This transition region approximately follows the locus of minima in the constant input power curves on the right-hand side of Fig. 1.26(c). Reactor operation will generally be in the $\phi > 0$ regime, so efficient means (ECH, control of direct particle losses) must be found for forcing this transition. In addition, neoclassical impurity fluxes in the $\phi > 0$ regime are outward and should provide a natural means of cleansing the plasma. The radial electric field is expected to play a similar role in ATF, where experiments to measure and control the potential and to develop an understanding of stellarator transport in the low-collisionality regime will be important.

ORNL-DWG 85-2745 FED

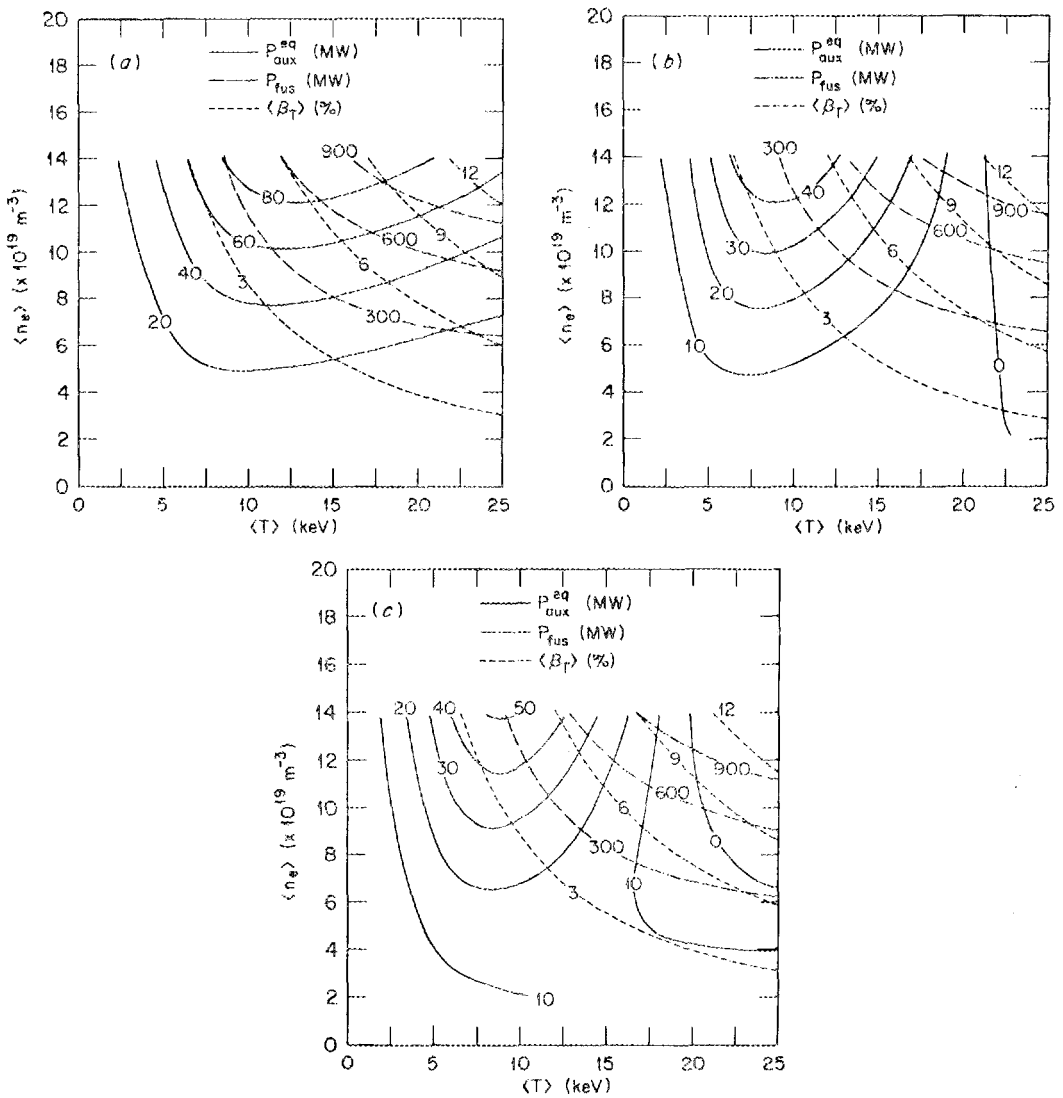

Fig. 1.26. Constant heating power (MW), solid curves; constant fusion power produced (MW), long-dashed curves; and volume-averaged beta (%), short-dashed curves, in the $\langle n_e\rangle$-$\langle T\rangle$ plane. (Here $\langle n_e\rangle$ and $\langle T\rangle$ are the volume-averaged density and temperature, respectively.) (a) Neoclassical transport with fixed $\xi = e\phi/T = 2$. (b) Neoclassical transport with fixed $\xi = e\phi/T = 4$. (c) Neoclassical and anomalous transport with fixed $= e\phi/T = 4$.

1.3.2.2 Low-aspect-ratio torsatron studies

The ATFSR discussed in Sect. 1.3.2.1 is based on ATF with a plasma aspect ratio of 7. Further gains could be made if the plasma aspect ratio could be reduced to $\lesssim 5$. The advantages would be a more compact reactor and a cost reduction in the ATF-II. The difficulty in finding a good torsatron configuration at low aspect ratio ($A = R/a$) arises from

the scaling β(equilibrium) $\sim \iota^2/A$ and $\iota \sim A$; hence $\beta \sim A$. Also, as A decreases, the high-beta, second stability region disappears and $\iota(0)$ drops to the point where the magnetic axis becomes bifurcated and central confinement is expected to deteriorate.

An interesting magnetic configuration was found in the TJ-II studies (Sect. 1.4.1) by increasing the triangularity of the torus for the $\ell = 2$ winding law as the aspect ratio was decreased. An $\ell = 2$ winding on a torus with a triangular cross section and $R/a < 5$ had the same gross magnetic configuration properties as an $\ell = 2$ winding on a torus with a circular cross section and $R/a = 7$ (ATF). It is difficult to have the $\iota = 0.5$ surface fall within the magnetic well in this case, but inclusion of higher-order terms in the stellarator expansion indicates that this configuration may have good high-beta properties.

1.3.2.3 Engineering assessments of Symmotron coils

The superconducting HF coils for a torsatron reactor or for ATF-II are too large to be single units. Practical coils would have to be modular—either jointed segments of a helical coil spanning 360° toroidally or separate, toroidally localized coils in a toroidal set that forms the desired magnetic configuration. The engineering feasibility of the latter modular (Symmotron) coil approach is being investigated through a subcontract with I. N. Sviatoslavsky and co-workers at the University of Wisconsin. The study entails determination of the engineering limits of such Symmotron coil aspects as stress, coil deflection, current density, bend radii, degree of twist, and ratio of field on axis to that on the conductor. The results will feed back into the next iteration in the evolution of Symmotron coils for ATF-II. Study of the feasibility of demountable joints in superconducting HF coils for ATF-II is planned at a later time.

The magnetic code EFFI is used to determine forces, moments, and magnetic fields. This information is then used in the NASTRAN finite-element stress analysis code to determine the stresses in the conductor and in the coil casing. Coil parameters and the location and extent of coil supports are iterated until acceptable stress levels are obtained with practical bend radii and twist in the coils. In the structural analysis, no credit is taken for the load-carrying capability of the conductor, so that forces and moments are reacted by the coil case alone. The maximum stress allowed is 500 MPa for 300-series stainless steel at 4.2 K.

A side view of the Symmotron reactor case studied is shown in Fig. 1.27, and the relevant parameters are given in Table 1.6. Figure 1.28 shows the results of a NASTRAN stress calculation using 104 elements along the coil length for a Symmotron example with a coil cross-sectional area of 1 m^2 and a 0.3-m-thick coil case. Acceptable stress levels were obtained with a current density of 1.5 kA/cm^2. Similar calculations for a 2-T, ATF-sized Symmotron with a coil cross section of 0.18 by 0.18 m and a 0.13-m-thick coil casing gave acceptable stress levels for a current density of 5.5 kA/cm^2. In the ATF case, the toroidally directed windbacks were on the inside, instead of on the outside as in the reactor case.

Although these studies are preliminary, some design guidelines can be inferred. Return legs on the outside appear to be better from a structural point of view, and convex segments are better than straight or concave ones. A larger number of coils reduces the circumferential span in the unsupported region and reduces the stress in that region. Bends in

ORNL-DWG 85-2746 FED

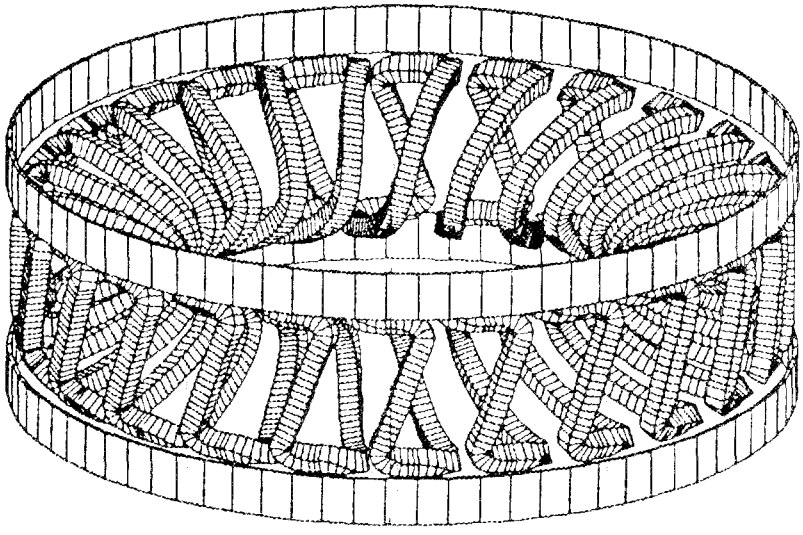

Fig. 1.27. Side view of Symmotron reactor with 24 identical, nonrotated twisted coils and 2 compensation (VF) coils to cancel the effect of the toroidal windbacks in the Symmotron coils.

Table 1.6. Coil parameters for Symmotron reactor study

Major radius, m	16
Minor radius, m	4
Number of Symmotron coils	24
Current in Symmotron coils, MA	15
Field on axis, T	4.5
Radius of VF coils, m	20.7
Vertical location of VF coils, m	±5.6
Number of VF coils	2
Current in VF coils, MA	6

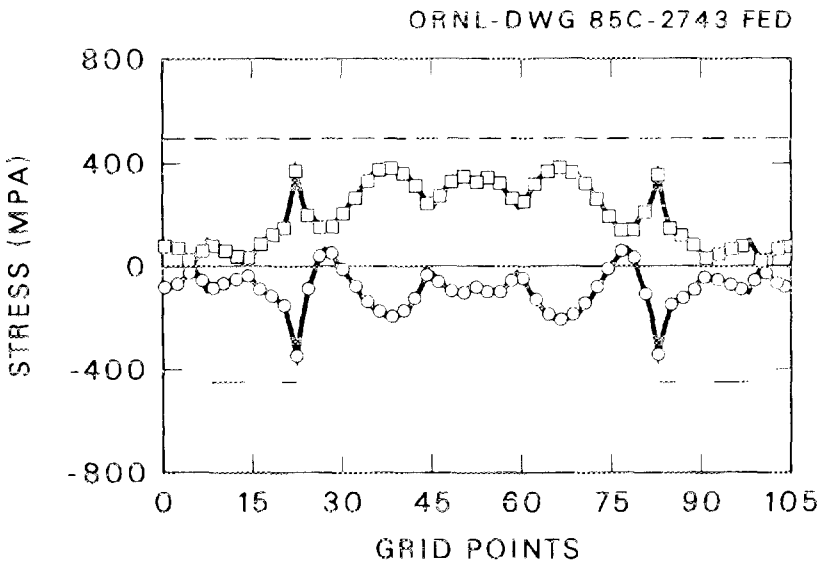

Fig. 1.28. Stress in the Symmotron reactor coil along the coil length. The short horizontal bars indicate the support areas; the dashed line shows the 500-MPa limit. The top curve shows the maximum tensile stress and the bottom curve the maximum compressive stress.

the return legs are limited by the need to fit a coil case around the bend. The proximity of a compensating coil to the return leg is limited by coil case thickness and not by forces.

1.3.3 The Spherical Torus Experiment

E. A. Lazarus, T. J. McManamy, W. L. Wright, S. K. Borowski, R. L. Brown, R. H. Fowler, W. R. Hamilton, R. E. Hill, S. S. Kalsi, V. D. Lee, D. C. Lousteau, J. N. Luton, Jr., G. H. Neilson, Y-K. M. Peng, D. J. Strickler, and C. C. Tsai

Conceptual design studies have started for a proposed new tokamak, the Spherical Torus Experiment (STX).[21] The design parameters are listed in Table 1.7.

The mission of STX will be to test beta limits and confinement in a tokamak with very low aspect ratio in the regime where auxiliary heating power dominates ohmic power. A significant aspect of this exploration will be the achievement of high plasma current density at low toroidal field. The device will study high-beta plasmas, which are highly paramagnetic ($B_0 \sim 1.7B_0^{ext}$). The high fraction of trapped particles allows a test of neoclassical ion transport in a new regime. Eventually, the device will offer the opportunity to study current maintenance by flux pumping and transition between the highly paramagnetic spherical torus plasma and the reversed-field pinch (RFP) and spheromak plasmas.

The critical issues in tokamak research include plasma beta, energy confinement, and steady-state operation, which are crucial to the feasibility of an ignition experiment at a

Table 1.7. STX design parameters

Aspect ratio A	1.67
Major radius R_0, m	0.45
Minor radius a_0, m	0.27
Elongation κ	2
Toroidal field B_T, T	0.5
Plasma current I_p, MA	0.9
Beam power P_b, MW	1
Impurity control system	Limiter or expanded-boundary divertor

viable cost and to the economy of future fusion reactors. The spherical torus offers a potential solution to these challenges by virtue of its very low aspect ratio ($A < 2$), natural elongation ($\kappa \sim 2$), strong paramagnetism ($B_T/B_T^{ext} \sim 1.7$), modest fields ($B_p \sim B_T$), and a number of other attractive features in comparison with a conventional tokamak ($A \gtrsim 3$).

Several conventional experiments (ISX-B, the Princeton Large Torus, the Poloidal Divertor Experiment, Doublet-III, ASDEX) have studied energy confinement and beta limits over the past several years, achieving relatively good consensus. The energy confinement is found to increase with increasing plasma current and plasma size, to decrease with increasing auxiliary heating power, and to decrease as the beta limit is approached. The uncertainty in confinement scaling as depicted by neo-Alcator and Mirnov scaling represents only a factor of 2–3 difference in confinement time in conventional tokamaks. In STX, with modest size and field ($R = 45$ cm, $B_T^{ext} = 5$ kG) and large current (I_p up to 900 kA), the two scaling laws give very different predictions (5 ms vs 125 ms, respectively). Thus, STX will serve to resolve these confinement uncertainties.

The limit to achievable beta is experimentally found to scale as I/aB, and theoretical stability analysis demonstrates this same scaling. This beta scaling predicts a beta above 20% in the STX when B_T^{ext} is used. However, the strong paramagnetism in the spherical torus, which gives $B_T/B_T^{ext} \simeq 1.7$ at the plasma axis in STX, introduces an uncertainty of the same factor in the beta limit and the achievable plasma pressure ($\propto B_T/B_T^{ext}$). The STX with significant neutral beam heating will be effective in clarifying this issue.

Assuming neo-Alcator confinement scaling, the Murakami density limit, and beta-limited pressure and using the total B_0 value (including paramagnetism), the aspect ratio scaling of $n\tau T$ for $1.5 < A < 3.3$ is approximately $(1 + 133/A^{4.1})$. If there are no shaping field coils, the benefits of low aspect ratio will be even more extreme. A test of such a dramatically beneficial scaling is needed.

The modest toroidal field, which is comparable to the poloidal field in STX, makes it an effective vehicle for testing oscillating-flux current drive, which has been recently proposed in the highly paramagnetic RFP and spheromak plasmas. Initial assessments have

indicated that a 10% oscillation of B_T and B_p at about 100 Hz would be required to test this process in the STX. The power supply required for this test is estimated to be modest over time scales of about 200 ms, although detailed assessments are needed to determine the best approach.

The strong paramagnetism makes the spherical torus similar to an RFP or a spheromak in that the B_T and B_p distributions are similar in the plasma core. Because of the relatively modest B_T^{ext} in STX, it is feasible to rapidly decrease B_T^{ext} after the spherical torus configuration is established, without dramatically disturbing the plasma core. The linked conductor (inner TF coil legs) will contribute to stabilizing the resulting RFP- or spheromak-like plasma. This will afford an opportunity to study the transition between these two regimes of plasma configuration.

1.4 THE ORNL-JEN COLLABORATION ON TJ-II

J. L. Alvarez Rivas, J. Botija, J. L. Cantrell, B. A. Carreras, K. K. Chipley, J. P. Guasp, J. H. Harris, T. C. Hender, T. C. Jernigan, A. Lopez, V. E. Lynch, J. F. Lyon, R. Martin, R. N. Morris, B. E. Nelson, A. Perea, A. Perez Navarro, A. Pueblas, and J. A. Rome

The Junta de Energia Nuclear (JEN) and ORNL are collaborating on the design of an advanced toroidal experiment, TJ-II,[22] to be built at the JEN laboratory in Madrid, Spain. The joint design study is funded by a grant from the U.S.-Spain Committee on Cooperation in Science and Technology. Funds for construction of TJ-II itself ($15 million) are detailed in the National Fusion Plan for Spain.

TJ-II is intended to serve as the focal point of the Spanish fusion program and to have strong participation from Spanish industry. TJ-II should have fusion-relevant plasma parameters and contribute to the search for an optimum magnetic configuration for an eventual fusion reactor. Experimental flexibility and the ability to make a significant contribution to the physics understanding of toroidally confined plasmas are important factors in selection of the TJ-II design concept. In addition, TJ-II should be a significant element in the European program and should complement the existing world fusion program. These considerations led to the choice of the stellarator area as that most appropriate for the TJ-II device.

A wide range of stellarator configurations has been studied in the search for the best magnetic configuration for TJ-II. Three new configurations that are interesting in themselves are also potential candidates for TJ-II: a low-aspect-ratio torsatron with a triangular toroidal cross section, a modular (Symmotron) version of this configuration, and a new flexible helical-axis configuration ("flexible heliac"). These configurations are discussed in this section.

The timetable for the TJ-II project calls for selection of the TJ-II configuration in May 1985, completion of the preconceptual design studies by August 1985, programmatic review of the TJ-II proposal in September 1985, final engineering design during 1986, construction during 1987 and 1988, and start of operation by December 1988.

1.4.1 Low-Aspect-Ratio Torsatrons

Low-aspect-ratio torsatrons ($R/a \lesssim 5$) offer a larger plasma radius for a given facility cost and eventually may lead to a more compact stellarator reactor. (Here R is the major radius and a is the average plasma radius.) Present stellarators are characterized by aspect ratios considerably larger than those of their tokamak relatives: in ATF, $R/a = 7$; in Heliotron-E, $R/a = 11$; and in Wendelstein VII-A, $R/a = 20$.

The TJ-II studies of low-aspect-ratio torsatrons examined the effects of coil aspect ratio, number of field periods, shape of the toroidal cross section for the windings, poloidal modulation of the winding law, and additional poloidal coils. The configurations studied were those with windings characterized by $\ell = 1$, $\ell = 2$, $\ell = 3$, $(\ell = 1) + (\ell = 2)$, and $(\ell = 2) + (\ell = 3)$. The criteria used in the optimization process were $R/a \lesssim 5$, $\iota(a)$ close to 1, moderate shear $\{[\iota(0) - \iota(a)]/\iota(a) \lesssim 0.3\}$, a magnetic well, and low-order rational surfaces within the well.

An interesting magnetic configuration was found by increasing the triangularity of the toroidal cross section for the $\ell = 2$ winding law as the aspect ratio was decreased. The best configuration had a 9-field-period, $\ell = 2$ winding on a torus with a triangular cross section and $R/a < 5$ but with the same magnetic configuration properties as an $\ell = 2$ winding on a torus with circular cross section and $R/a \approx 7$ (ATF). Figure 1.29 shows the vacuum field calculations for this case.

A modular version of this configuration was also found using Symmotron coils. This technique features a single modular coil for each field period that incorporates the torsatron helical arcs and toroidally directed windbacks to form a modular coil plus an opposing toroidal coil to compensate for the windbacks.

Other torsatron configurations studied were not as interesting. Although the $\ell = 1$ configurations had a large radius for the last closed flux surface, they had a low $\iota(a)$ and a marginal magnetic well with several low-order resonant surfaces outside the magnetic well. The $\ell = 3$ configurations had low ι values that produced doublet-type magnetic surfaces (bifurcated magnetic axis). An $\ell = 2$ component was added to these configurations to increase the ι value and to produce a magnetic well. However, the combinations $(\ell = 1) + (\ell = 2)$ and $(\ell = 2) + (\ell = 3)$ produced no better results than the single-ℓ-number configurations because the mixed symmetry of the combined systems caused a major deterioration of the outer magnetic surfaces, resulting in a drastically reduced average plasma radius.

1.4.2 Helical-Axis Configurations

Toroidal magnetic configurations with a helical magnetic axis offer the possibility of broad magnetic wells, which lead to increased MHD stability, and higher rotational transform, which leads to a smaller magnetic axis shift with increasing beta and hence a higher equilibrium beta limit. The ATF can produce helical-axis configurations by reduced current in one of its two helical windings, but these configurations are not optimized since ATF was designed to access the high-beta, second stability region in circular-axis configurations. Several approaches[22] to optimization of helical-axis configurations were investigated, including cycloidal stellarators, geodesic stellarators, the helicon, and the heliac.

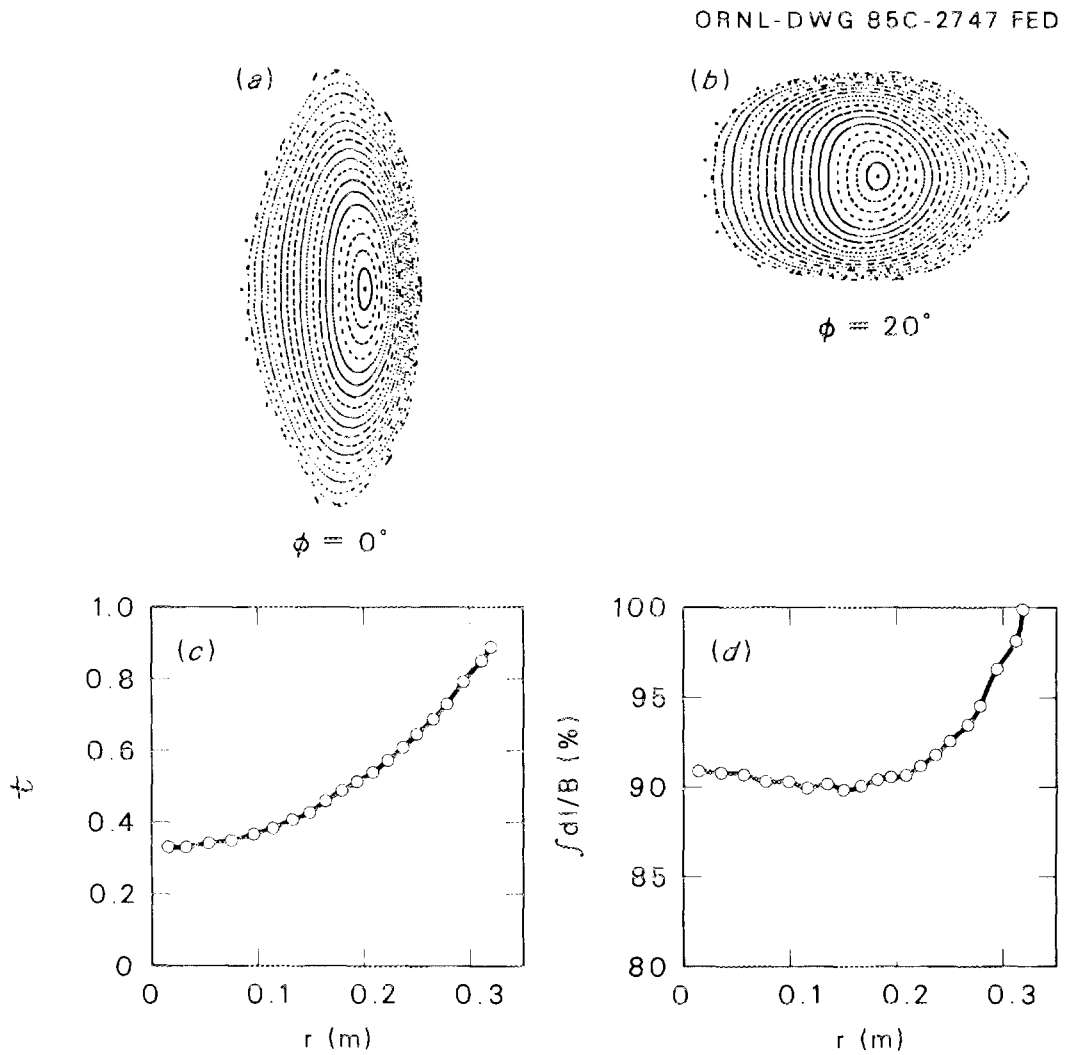

Fig. 1.29. Vacuum magnetic field line calculations for a torsatron with R = 1.5 m, ℓ = 2, and m = 9 wound on a triangular cross-section torus. (a) Flux surfaces at ϕ = 0°. (b) Flux surfaces at ϕ = 20°, halfway through a field period. (c) Rotational transform profile. (d) $V' = \int d\ell/B$ profile showing a small magnetic well.

The most interesting of the helical-axis configurations is the heliac[23-25] coil arrangement, which features a set of TF coils with centers that follow a helical path around a large, linked circular coil. This configuration is very attractive, at least in the straight helically symmetric limit, in that it offers the potential for very high beta operation ($\langle\beta\rangle \sim$ 25%). At finite aspect ratio, the main theoretical concern is a possible equilibrium beta limitation due to island formation and breakup of magnetic surfaces caused by low-m rational surfaces either inside or not far outside the plasma boundary. Flux surfaces for low-aspect-ratio heliacs are destroyed via the generation of resonant harmonics by nonlinear beating of the toroidal shift and the vacuum helical field. The amplitude of these

resonant components increases as beta increases. It is difficult to find a heliac configuration that has no dangerous low-m rational surfaces in or near the plasma because of the small but nonzero shear in the rotational transform profile. Even if the vacuum magnetic configuration is optimized, the modifications produced by plasma pressure effects move the configuration away from the optimum. A better approach is to build flexibility into the magnetic configuration, permitting a broad experimental optimization rather than a point theoretical optimization.

A good configuration has been found[26] that has high versatility, low plasma aspect ratio ($R/a \sim 6.5$), and good control of the magnetic configuration properties through the addition of an $\ell = 1$ helical winding to the central, linked circular coil. The coil currents can be chosen to give an ι/m profile that is nearly constant at a value of 0.38, thereby avoiding the most dangerous low-m rational surfaces. The resulting coil configuration is shown in Fig. 1.30. It has four field periods with eight TF coils per period and two central conductors. The TF coil aspect ratio (R/r_c) is 4, where $R = 1$ m, and the radius of the helical path of the TF coil centers is $0.7r_c$. The central $\ell = 1$ helical winding is in phase with the helical path followed by the centers of the encircling TF coils. The bean-shaped magnetic surfaces produced rotate around the central conductors as the magnetic axis follows a path similar to that of the TF coil centers. The indentation of the bean is always close to the $\ell = 1$ winding. The role of the $\ell = 1$ conductor in shaping the

ORNL-DWG 84-3803A FED

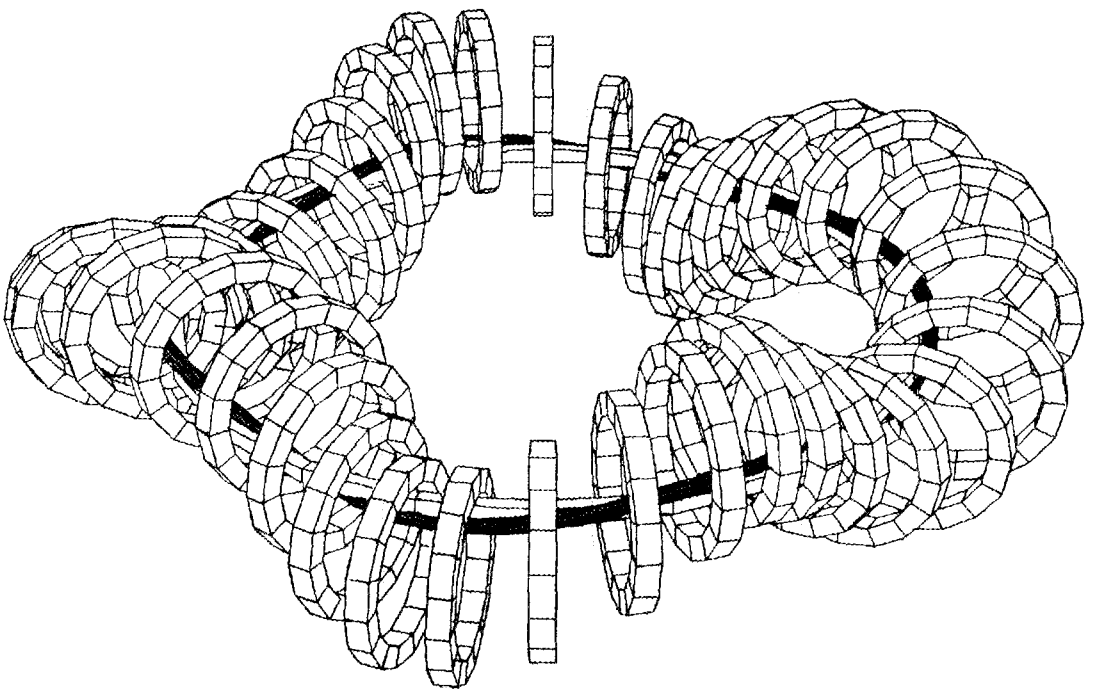

Fig. 1.30. Coil set for a flexible heliac showing the $\ell = 1$ helical winding (shaded) around the circular central conductor and the helically encircling TF coils.

predominantly helically symmetric plasma is similar to that played by the circular VF coil sets in shaping the predominantly axisymmetric ATF plasma.

This "flexible heliac" configuration has a number of significant advantages over the usual heliac configuration. First, similar magnetic configurations can be produced with less total current in the two central conductors than is required with a single circular conductor. Second, a deeper magnetic well can be achieved. Third, the shear can be easily controlled, and a nearly shearless configuration can be obtained, as shown in Fig. 1.31. Finally, the rotational transform can be varied over a wide range, as shown in Fig. 1.32.

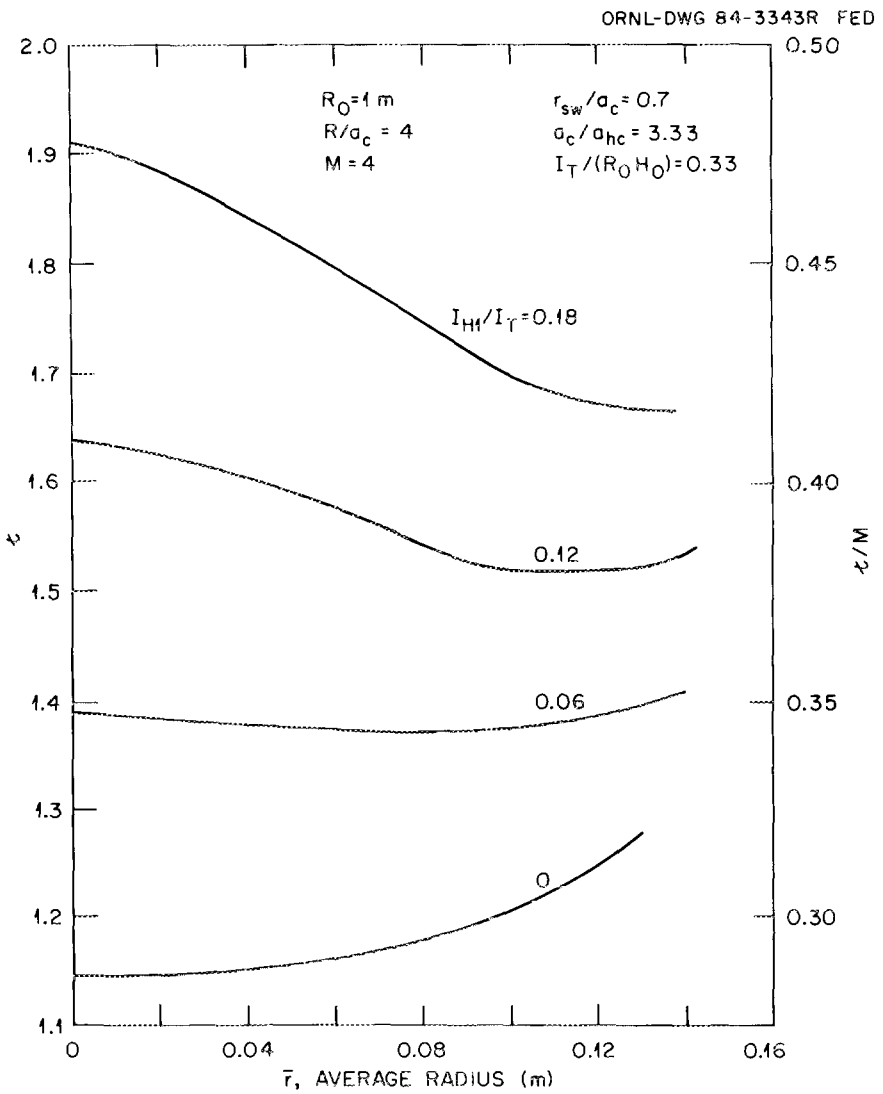

Fig. 1.31. Variable shear introduced in the rotational transform profile by changing the fraction of the helical current component in the total current of the two central conductors.

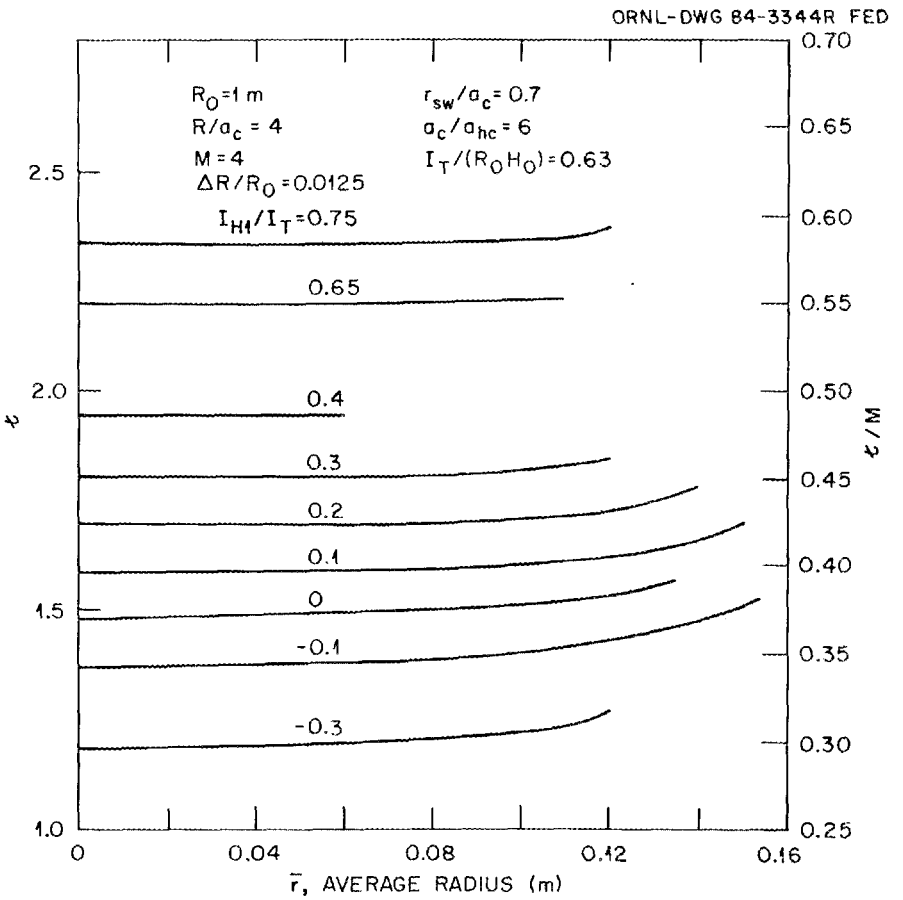

Fig. 1.32. Variation of rotational transform value for nearly shearless profiles, caused by changes in the fraction of the helical current component in the total current of the two central conductors. The total central current is a factor of ~2 larger with respect to the TF coil currents than that in Fig. 1.31.

Examples of the bean-shaped flux surfaces produced are shown in Fig. 1.33. The variations shown in Figs. 1.31–1.33 were produced by changing the ratio of the currents in the circular and $\ell = 1$ conductors. Additional flexibility can be introduced by varying the ratio of the total current in the central conductors to the current in the encircling TF coils.

In principle, additional improvements to the configuration can be made, such as toroidally modulating the current in the TF coils to reduce the toroidal shift and hence the breakup of the magnetic surfaces. Current modulation of the form $I_{TF} = I_0(1 + C \cos M\phi)$ has been studied, where ϕ is the toroidal angle, M is the number of field periods, and C is a measure of the amplitude of the spatial current modulation. The dominant effect is to alter the ($m = 0$, $n = M$) component of the magnetic field. The nonlinear beating of this component with the ($m = 1$, $n = M$) component in turn modifies the (m

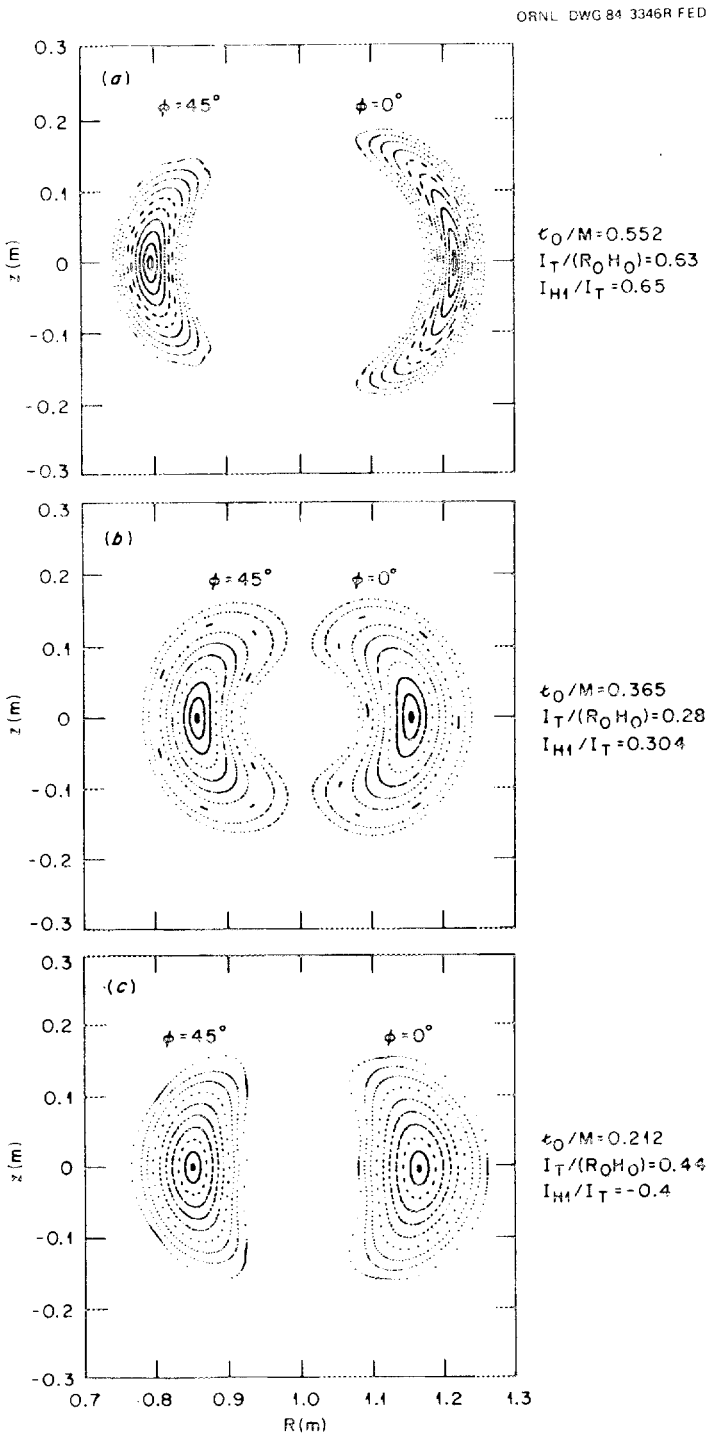

Fig. 1.33. Vacuum flux surfaces at the beginning (0°) and halfway through (45°) a field period for flexible heliac configurations with different ι_0/M.

$= 1, n = 0$) component on which the toroidal shift strongly depends. However, at the low coil aspect ratio ($R/r_c \sim 4$) appropriate to an experimental device, this nonlinear effect is small compared with the dominant toroidal effect due to the $1/R$ dependence of the toroidal field. It requires much higher coil aspect ratio ($R/r_c \sim 20$) before a significant reduction of the toroidal shift occurs. Nevertheless, such a current modulation would permit modification of the magnetic field ripple and study of its effect on confinement.

1.4.3 Engineering Design Studies

Of the magnetic configurations discussed above, the flexible heliac seems the most appropriate for further design studies. Despite its promise, the heliac configuration has not been explored experimentally, since it is a relatively new configuration. A small-scale test, the SHEILA experiment, is being pursued at Australian National University in Canberra. In addition, the design problems associated with low-aspect-ratio torsatrons are better understood through the ATF design process.

The reference case chosen for the TJ-II engineering design studies has four field periods with eight TF coils per period. The relevant device parameters are: major radius $R = 1.5$ m; average plasma radius $a = 0.23$ m for the nominal current setting; magnetic field $= 1$ T; pulse length $= 0.5$ s; TF coil radius $= 0.40$ m; swing radius of TF coil centers about the central circular conductor $= 0.26$ m; distance between the centers of the central circular conductor and the $\ell = 1$ helical winding $= 0.07$ m; TF coil current $=$ 210 kA (each); and total central [circular + ($\ell = 1$)] conductor current $= 600$ kA.

The magnetic forces on the TF coils are in a direction to reduce the swing radius of the TF coil centers. In the reference design, these forces are transmitted to an outside cylindrical vacuum vessel with a rectangular cross section. The VF coils are mounted outside the vacuum vessel. Design studies in progress are concentrating on details of the central conductor geometry, support of the TF coil forces, and geometry of the vacuum vessel.

1.5 THE ORNL-PPPL COLLABORATION ON TFTR

J. D. Bell, C. E. Bush, R. J. Colchin, J. L. Dunlap, L. C. Emerson, A. C. England, W. A. Gabbard, D. L. Hillis, D. P. Hutchinson, R. R. Kindsfather, R. A. Langley, C. H. Ma, M. Murakami, V. K. Paré, D. A. Rasmussen, R. K. Richards, J. E. Simpkins, and S. D. Scott

The working visits of ORNL staff to Princeton Plasma Physics Laboratory (PPPL), described in the previous annual report,[27] were continued as a means of integrating these persons into the research activities of the Tokamak Fusion Test Reactor (TFTR). Relocation to the Princeton area began in the summer as the operation of ISX-B drew to a close. By the end of the year, 12 ORNL staff members were on assignment to Princeton. Others were involved essentially full-time on TFTR activities but divided their time between ORNL and PPPL. Still others were making short visits to PPPL in response to specific needs for their assistance.

The involvement of ORNL staff includes detailed analyses and program planning, MHD instability studies, radiated power measurements, data base development, neutron diagnostics, spectroscopy and spectroscopic instrumentation, soft X-ray instrumentation,

electron cyclotron emission (ECE) diagnostics, Thomson scattering diagnostics, charge-exchange diagnostics, cleanup studies, chromium gettering, FIR diagnostics, 1-mm interferometry, and surface materials analyses. Positive contributions have been made in all of these areas. Particularly significant contributions have been made to confinement studies for full-bore, neutral-beam-heated plasmas; to chromium gettering experiments; and to development and implementation of the multichannel FIR interferometer/polarimeter.

REFERENCES

1. A. J. Wootton et al., "Balanced Beam Injection on ISX-B," p. 69 in *Heating in Toroidal Plasmas: Proceedings of the Fourth International Symposium, Rome, March 1984*, vol. 1, ed. H. Knoepfel and M. Sindoni, International School of Plasma Physics and ENEA, Varenna, Italy, 1984.

2. M. Murakami et al., "Confinement of Beam-Heated Plasmas in ISX-B," in *Proceedings of the 10th International Conference on Plasma Physics and Controlled Nuclear Fusion Research (London 1984)*, Int. Atomic Energy Agency, Vienna, in press.

3. E. A. Lazarus et al., "Confinement in Beam-Heated Plasmas: The Effects of Low-Z Impurities," *Nucl. Fusion* **25**, 171 (1985).

4. A. J. Wootton et al., "The Effects of Varying Wall Conditions, Minor and Major Radius on Confinement Properties in ISX-B," *Nucl. Fusion*, accepted for publication (1985).

5. J. L. Dunlap et al., "Magnetohydrodynamic Instability with Neutral Beam Heating in the ISX-B Tokamak," *Phys. Rev. Lett.* **48**, 538 (1982).

6. E. A. Lazarus et al., "Confinement Improvement in Beam-Heated ISX-B Discharges with Low-*Z* Impurity Injection," *J. Nucl. Mater.* **121**, 61 (1984).

7. J. Mathew, *Investigation of the Electric Field Structure in Neutral Beam Heated ISX-B Plasmas*, Ph.D. thesis, Rensselaer Polytechnic Institute, Troy, N.Y., 1984.

8. G. A. Hallock et al., "The Space Potential Distribution in ISX-B," *Phys. Rev. Lett.*, accepted for publication (1985).

9. P. K. Mioduszewski et al., "Pumped Limiter Studies," pp. 51–52 in *Fusion Energy Division Annual Progress Report for Period Ending December 31, 1982*, ORNL-5919, Union Carbide Corp. Nuclear Div., Oak Ridge Natl. Lab., November 1983.

10. This work is also described by P. Mioduszewski et al. in "Studies on Impurity Control and Hydrogen Pumping with Chromium Gettering in ISX-B," *J. Nucl. Mater.* **128 & 129**, 884 (1984).

11. K. E. Yokoyama, "An Experimental Investigation of the Plasma Properties of the Edge Region of the ISX-B Tokamak Using Multiple Langmuir Probes," master's thesis, the University of Tennessee, Knoxville, August 1984.

12. P. H. Edmonds et al., "The ISX-JET Beryllium Limiter Experiment," *J. Nucl. Mater.* **128 & 129**, 422 (1984).

13. P. H. Edmonds, R. D. Watson, and M. F. Smith, "Design and Fabrication of a Beryllium Limiter for ISX-B," presented at the 13th Symposium on Fusion Technology, Varese, Italy, Sept. 24–28, 1984; to be published in the proceedings.

14. P. H. Edmonds et al., "Technical Aspects of the Joint JET–ISX-B Beryllium Limiter Experiment," *J. Vac. Sci. Technol.*, accepted for publication (1985).

15. M. F. A. Harrison et al., *Tokamak Fusion Reactor Exhaust*, CLM-R211, United Kingdom Atomic Energy Authority, Culham Lab., Abingdon, England, 1981.

16. P. H. Edmonds, *The JET–ISX-B Beryllium Limiter Experiment Safety Analysis Report and Operational Safety Requirements*, ORNL/TM-9512, to be published at Oak Ridge National Laboratory.

17. J. H. Harris et al., "Magnetohydrodynamic Activity in High-β, Currentless Plasmas in Heliotron-E," *Phys. Rev. Lett.* **53**, 2242 (1984).

18. J. Lacatski, "Plasma Engineering Analysis of a Small Torsatron Reactor," master's thesis, the University of Tennessee, Knoxville, 1985.

19. K. C. Shaing, "Stability of the Radial Electric Field in a Nonaxisymmetric Torus," *Phys. Fluids* **27**, 1567 (1984).

20. K. C. Shaing et al., "The Radial Electric Field in a Non-Axisymmetric Torus," in *Proceedings of the 10th International Conference on Plasma Physics and Controlled Nuclear Fusion Research (London 1984)*, Int. Atomic Energy Agency, Vienna, in press.

21. Y-K. M. Peng, *Spherical Torus, Compact Fusion at Low Field*, ORNL/FEDC-84/7, Oak Ridge Natl. Lab., December 1984.

22. A. Perez Navarro, "Configuration Studies for the TJ-II Device," p. 563 in *Proceedings of the 5th IAEA Technical Committee Meeting on Confinement and Heating in Stellarators (Schloss Ringberg 1984)*, vol. 2, EUR 9618 EN, Commission of the European Communities, Brussels, 1984.

23. A. H. Boozer et al., "Two High-Beta Toroidal Configurations: A Stellarator and a Tokamak-Torsatron Hybrid," p. 129 in *Proceedings of the 9th International Conference on Plasma Physics and Controlled Nuclear Fusion Research (Baltimore 1982)*, vol. 3, Int. Atomic Energy, Agency, Vienna, 1983.

24. H. P. Furth et al., "Stabilization by Shear and Negative V''," p. 103 in *Proceedings of the Conference on Plasma Physics and Controlled Nuclear Fusion Research (1965)*, vol. 1, Int. Atomic Energy Agency, Vienna, 1966.

25. S. Yoshikawa, "Design of a Helical Axis Stellarator," *Nucl. Fusion* **23**, 667 (1983).

26. J. H. Harris et al., *A Flexible Heliac Configuration*, ORNL/TM-9504, to be published at Oak Ridge National Laboratory.

27. J. L. Dunlap, "TFTR Collaboration," pp. 2-41–2-42 in *Fusion Energy Division Annual Progress Report for Period Ending December 31, 1983*, ORNL-6015, Oak Ridge Natl. Lab., 1984.

Chapter 2

EBT Research and Development

L. A. Berry, EBT Program Manager

D. W. Swain, EBT-S Program Manager
H. C. McCurdy, EBT-P Program Manager
N. A. Uckan, Advanced Configurations Program Manager

S. L. Ackerman[1]
W. B. Ard[2]
F. W. Baity
J. K. Ballou[3]
D. B. Batchelor[4]
D. D. Bates[5]
D. B. Bible[5]
F. M. Bieniosek[2]
T. S. Bigelow
R. A. Brown[6]
W. E. Bryan[6]
N. B. Bryson[7]
R. D. Burris[8]
K. H. Carpenter[9]
W. H. Casson[10]
G. L. Chen[11]
J. A. Cobble
R. J. Colchin
K. A. Connor[12]
R. A. Dandl[13]
R. J. Dannenmueller[2]
W. A. Davis
R. J. DeBellis[2]
R. D. Donaldson
O. C. Eldridge
G. Federoff[2]
J. C. Glowienka
R. C. Goldfinger[8]
J. R. Goyer[12]
O. E. Hankins[14]
G. R. Haste
D. E. Hastings[4]
C. L. Hedrick[4]
R. L. Hickok[12]
D. L. Hillis
S. Hiroe
H. F. Imster[2]
E. F. Jaeger[4]
O. V. Jett[7]
R. E. Juhala[2]
H. D. Kimrey
D. K. Lee[8]
R. L. Livesey
J. W. Lue[3]
R. V. Lunsford[6]
R. Mahon[15]
J. B. Mankin[8]
J. C. McGill[7]
M. W. McGuffin
T. J. McManamy[6]
C. W. Nestor, Jr.[8]
D. R. Overbey[4]
L. W. Owen[8]
T. L. Owens[2]
B. G. Peterson[8]
J. H. Pfannmuller[2]
T. J. Poteat[2]
K. W. Prince[2]
B. H. Quon[16]
D. A. Rasmussen
M. A. Reedy[7]
R. K. Richards
C. R. Schaich
C. E. Schmid[8]
R. J. Schmidt[2]
S. S. Shen[3]
L. Solensten[12]
D. A. Spong[4]
G. R. Sullivan
T. Uckan
R. J. Warwick[6]
T. L. White
J. B. Wilgen
C. T Wilson[6]
R. E. Wintenberg[5]
W. L. Wright[6]
R. B. Wysor[6]
V. E. Yun[15]

---

1. General Dynamics Convair Division, San Diego.
2. McDonnell Douglas Astronautics Co., St. Louis.
3. Magnetics and Superconductivity Section.
4. Plasma Theory Section.
5. Instrumentation and Controls Division.
6. Engineering Division, Martin Marietta Energy Systems, Inc.
7. Section secretary.
8. Computing and Telecommunications Division, Martin Marietta Energy Systems, Inc.
9. University of Missouri, Rolla.
10. The University of Tennessee, Knoxville.
11. Plasma Technology Section.
12. Rensselaer Polytechnic Institute, Troy, N.Y.
13. Applied Microwave Plasma Concepts, Inc., Encinitas, Calif.
14. North Carolina State University, Raleigh.
15. University of Maryland, College Park.
16. JAYCOR, San Diego.

CONTENTS

SUMMARY OF ACTIVITIES 2-5

2.1 EBT RESEARCH 2-5

2.1.1 The Electron Distribution Function in EBT 2-5

2.1.2 Recent Soft X-Ray Measurements on EBT 2-12

2.1.3 Abstract of *Thomson Scattering on ELMO Bumpy Torus* 2-15

2.1.4 Abstract of "Electron Temperature Measurements From Induced Toroidal Current in ELMO Bumpy Torus–Scale" 2-15

2.1.5 Abstract of *Electron Confinement in the ELMO Bumpy Torus Without the Influence of Hot Electron Rings—The Ring Killer Experiment* 2-16

2.1.6 Abstract of *An Experimental Determination of the Hot Electron Ring Geometry in EBT-S and Its Implications for Bumpy Torus Stability* 2-17

2.1.7 Diamagnetic Measurements and Data Analysis 2-17

2.1.8 Abstract of *High-Field Launch Electron Cyclotron Heating Experiments in the ELMO Bumpy Torus* 2-18

2.1.9 Fundamental and Second-Harmonic Resonance Polarized Microwave Absorption and Heating Measurements on EBT 2-19

2.1.10 Abstract of *Multiple-Frequency Electron Cyclotron Heating of Hot Electron Rings in the ELMO Bumpy Torus* 2-22

2.1.11 Abstract of "The EBT-S 28-GHz, 200-kW, cw Mixed-Mode Quasi-Optical Plasma Heating System" 2-22

2.1.12 Abstract of "Mixed-Mode Distribution Systems for High Average Power Electron Cyclotron Heating" 2-22

2.1.13 Summary of "Performance of 28 GHz, 200 kW, cw, Gyrotron Oscillators on the ELMO Bumpy Torus-Scale (EBT-S) Experiment" 2-23

2.1.14 EBT Ion Cyclotron Heating 2-23

2.1.15 Abstract of "Ion Heating in the Range of High Ion Cyclotron Harmonics on EBT" 2-24

2.1.16 FIR Scattering Measurements of Density Fluctuations and Ion Waves 2-24

2.1.17 Abstract of "EBT Plasma Potential Measurements" 2-28

2.1.18 Summary of "Experimental Study of Equilibrium in the ELMO Bumpy Torus" 2-29

2.1.19 Abstract of *Measurements of Temperature and Density on the ELMO Bumpy Torus Using a Heavy Ion Beam Probe* 2-29

2.1.20 Summary of "Effect of Fluctuations on Confinement in ELMO Bumpy Torus" 2-30

2.1.21 Power Flow in EBT 2-31

2.1.22 Abstract of "Inherent Magnetic Field Error Measurements in ELMO Bumpy Torus" 2-31

2.1.23 Abstract of "Direct Reading Fast Microwave Interferometer for EBT" 2-31
2.1.24 Pulsed Experiments in the Collisional Electron Regime 2-31
2.1.25 Dynamic Measurements of Electron Energy Confinement 2-32
2.1.26 A Comparative Measurement of the Particle Confinement Time in EBT 2-34
2.1.27 H_α Laser Fluorescence Measurements of Neutral Hydrogen Densities 2-37
2.1.28 Abstract of *Monte Carlo Neutral Density Calculations for ELMO Bumpy Torus* 2-41
2.1.29 The Absolute Calibration of All 24 Ion Gages on EBT 2-43
2.2 EBT-P PROJECT 2-44
2.2.1 Introduction 2-44
2.2.2 EBT-P/RFTF Magnet Development 2-44
2.2.3 Project Closeout 2-45
2.3 EBT ADVANCED CONCEPTS 2-45
2.3.1 Innovative Bumpy Torus Configurations: Trend to Smaller EBT Reactor Systems 2-45
2.3.2 Abstract of *ELMO Bumpy Square* 2-48
2.3.3 Assessment of Magnet Field Asymmetries in EBS 2-49
2.3.4 Magnetics Calculations for an EBS 2-51
2.3.5 Abstract of *An EBT Reactor Systems Analysis and Cost Code: Description and User's Guide (Version 1)* 2-51
REFERENCES 2-52

2. EBT RESEARCH AND DEVELOPMENT

Summary of Activities

During the latter part of 1983, our understanding of experimental results from ELMO Bumpy Torus–Scale (EBT-S) suggested that the performance of the circular bumpy torus configuration was probably limited by three separate but related effects: (1) the velocity-space region where particles are best heated is close to the region where confinement is poorest, resulting in poor electron cyclotron heating efficiency; (2) the strong dispersion in drift orbits from asymmetric ambipolar drift surfaces further degrades confinement; and (3) the resulting ring heating efficiency is low, thus preventing the formation of high-beta rings that should provide strong stabilization from reversed $\int d\ell/B$. The 1984 research program substantially increased our confidence in these conclusions.

In parallel with the physics program, a preliminary design and associated costs and schedules were developed for converting EBT-S to a square configuration called ELMO Bumpy Square (EBS). This conversion could be accomplished in 18 months at a cost of less than $5 million. Based on the understanding gained from EBT, physics evaluation of the square predicts an order of magnitude increase in $n\tau$ to over 10^{10} $cm^{-3}\cdot s$. In addition, an evaluation of this configuration using the criteria established by the generic reactor study (see Chap. 11 of this report) suggests that EBS could be developed into a reactor having a mass utilization competitive with optimistic estimates for other fusion reactor candidates.

These favorable technical developments were not sufficient to sustain 1985 funding of the EBS program in the face of the reductions in the national program. As a result, the program was phased down. Staff members were reassigned to minimize the disruption associated with program termination. An effort to reduce proposed construction and operating costs of EBS and to continue examining the physics and reactor rationale of the program will continue into 1985 with the intent of obtaining 1986 funding.

2.1 EBT RESEARCH

2.1.1 The Electron Distribution Function in EBT

D. W. Swain, J. A. Cobble, D. L. Hillis, R. K. Richards, and T. Uckan

2.1.1.1 Introduction

Results from new and improved diagnostics and theoretical models have indicated a new model for the electron behavior in the ELMO Bumpy Torus (EBT).[1,2] The diagnostics include a significantly improved Thomson scattering apparatus, which has radial scanning

capability, and a new measurement of electron temperature using the spectroscopic ratio between two aluminum ion lines observed in the plasma. In addition, diagnostics that can observe the high-magnetic-field throat region of the plasma have allowed us to measure the density and temperature in that region for the first time. In conjunction with midplane measurements, these measurements provide information on the isotropy (or lack thereof) of the electron distribution function. We discuss the characteristics of the electron distribution function inside the rings (near the center of the plasma) for energies $\leq$ 2 keV. The rings, which have energies of several hundred kiloelectron volts, are relatively decoupled from the power balance of the bulk electrons; results from recent ring experiments are reported elsewhere.

Analysis of the new results indicates that the structure of the electron distribution function is as follows. (1) The distribution is non-Maxwellian and consists of a two-component plasma. There is a cold component ($n_c \leq 0.7 \times 10^{12}$ cm^{-3}, $T_c \leq 100$ eV) and a warm component with a density 10% to 30% of the total electron density and a temperature in the range of 200 to 800 eV. (2) The cold component is collisional and relatively isotropic, while the warm component is collisionless and anisotropic. The majority of the warm component is mirror trapped, and only a small percentage passes through the coil throat region. We believe that the non-Maxwellian nature is caused by the electron cyclotron heating (ECH) and will be present to some extent in other ECH plasmas.

2.1.1.2 Measurements in the cavity midplane

The results of temperature measurements by the three T_e diagnostics are shown in Fig. 2.1 as a function of neutral gas pressure p_0 under typical operating conditions for a nominal 28-GHz microwave power of $P_\mu = 150$ kW. The characteristics of the measurements indicated in this example are those generally observed; the soft X-ray T_e determination is substantially higher than that of the Thomson scattering, with the aluminum line ratio technique yielding an intermediate value. The difference among the techniques cannot be reconciled by accounting for statistical or known possible systematic errors (i.e., the errors bars of the measurements do not overlap).

The soft X-ray technique[3] is the one in use for the longest time on EBT. Due to the response of the detector, photons with energies < 400 eV are not detected, so that the dominant contribution to the analyzed bremsstrahlung is from electrons with energies in the 400- to 2000-eV range. Thus, the "temperature" measured by this diagnostic is determined by the characteristics of relatively high energy electrons in the plasma.

In contrast, measurements of electron temperature using the Thomson scattering techniques[4] are done by fitting a Gaussian function to the spectrum of the scattered photons and determining the electron temperature from the width of that function. In this case, the determined electron temperature is dominated by the low-energy electrons, because more photons are scattered from the low-energy electrons (so the statistical uncertainties in these numbers are smaller) than from the high-energy electrons.

The aluminum line ratio diagnostic[5] is a method of measuring the electron temperature that uses radiation resulting from inner-shell ionization of aluminum ions. Due to the energy dependence of the two cross sections involved, the response of this technique to different electron energy components is fairly uniform (i.e., the weighting function for T_e determination is relatively constant regardless of energy for this diagnostic).

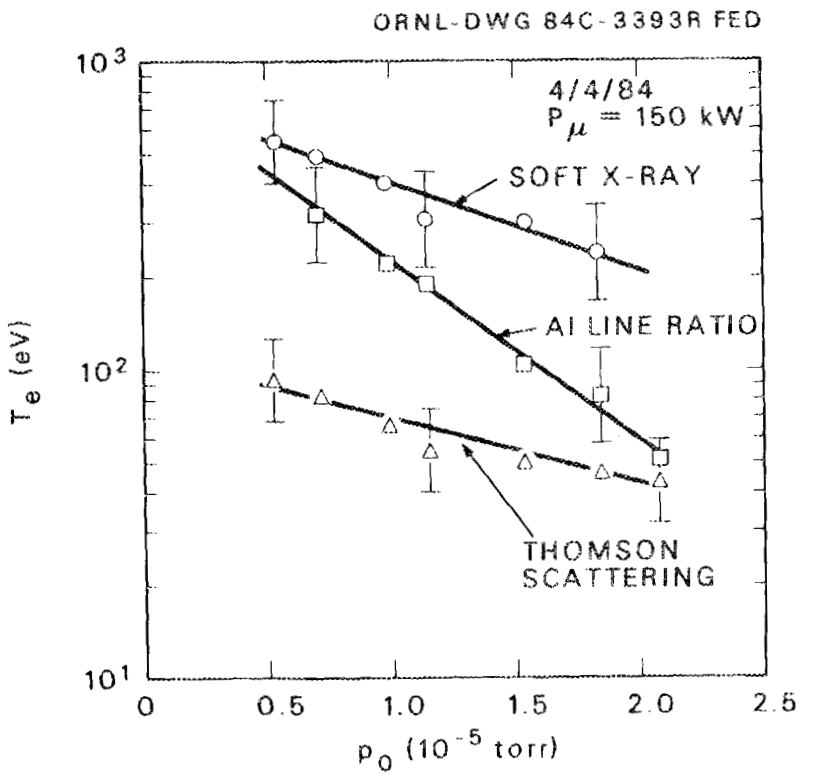

Fig. 2.1. Electron temperature determined from three diagnostics: soft X-ray, aluminum line ratio, and Thomson scattering vs neutral gas pressure for P_μ = 150 kW. Typical error bars are shown.

This is illustrated in Fig. 2.2, which plots the calculated intensity ratio of the two ion lines vs average electron temperature. The solid line shows the intensity ratio expected for a standard single-component (i.e., Maxwellian) plasma. The dashed line indicates the expected intensity ratio for a two-component plasma distribution function of the form

$$f(E) \sim (n_c/T_c^{1/2})\exp(-E/T_c) + (n_w/T_w^{1/2})\exp(-E/T_w) \ , \tag{1.1}$$

where n_c and T_c are the density and temperature of the cold component and n_w and T_w are the density and temperature of the warm component, respectively. The average electron temperature for this case is defined as

$$T_{avg} = (n_w T_w + n_c T_c)/n_e \ , \tag{1.2}$$

where $n_e = n_w + n_c$ is the total electron density. For the two-component case shown, the ratio of warm to cold density has been chosen to equal one and $T_w/T_c = 2$. As can be seen from the figure, a given value of intensity ratio will yield approximately the same average temperature for both cases.

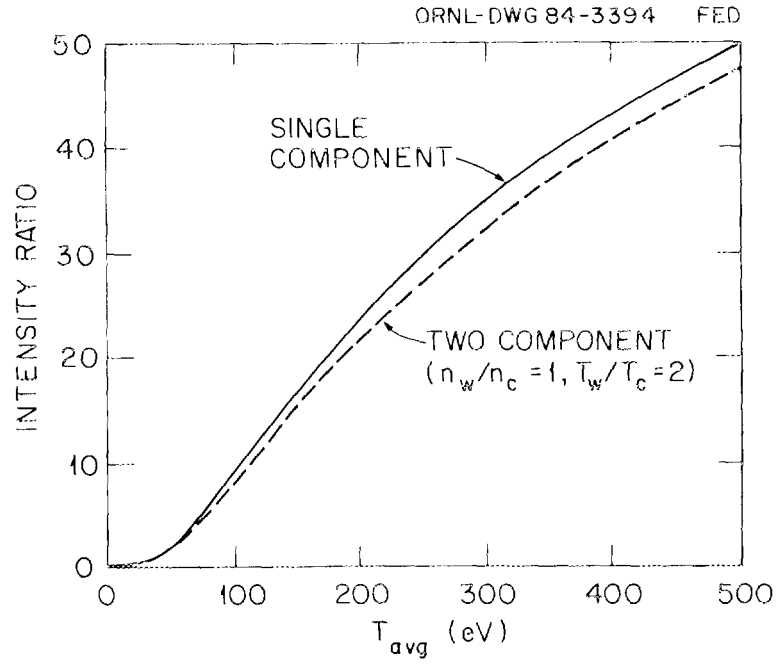

Fig. 2.2. Calculated intensity of two Al III lines vs T_{avg} for a simple Maxwellian distribution function (solid line) and a two-component distribution function (dashed line).

From these results, it appears that the Thomson scattering measurements will be dominated by the relatively cold electrons, the soft X-ray bremsstrahlung measurement will be dominated by the high-energy electrons, and the aluminum line ratio measurement will indicate the "average temperature" of almost the entire distribution function. It is clear that the assumption of a non-Maxwellian distribution, with a cold bulk component and a higher-energy warm tail component, could qualitatively explain the difference in the "temperature" measurements illustrated in Fig. 2.1. Since it has long been known that the entire distribution function in EBT is non-Maxwellian, as indicated by the presence of the high-energy ring electrons, it is not very surprising that the distribution function at energies below 2 keV would be non-Maxwellian in the presence of ECH.

Recent improvements in the Thomson scattering system sensitivity, data analysis capabilities, and radial scanning ability have been described elsewhere.[4] Results from the improved system indicate the possibility of the presence of a high-energy warm tail component on the relatively cold bulk plasma. A typical spectrum of number of photons per channel vs $\Delta\lambda^2$ (which is proportional to the energy of the scattering electron) is shown in Fig. 2.3. The ordinate is the total number of photons scattered in each channel summed over ten laser shots. Background plasma light has already been subtracted. The dashed line indicates the best fit for a single-component Maxwellian distribution function. For this case ($F_w = 0$), the calculated electron temperature is $T_c = 93$ eV, and the normalized value of $\chi^2 = 7.5$. The solid line is a weighted least-squares fit to the same data point using a

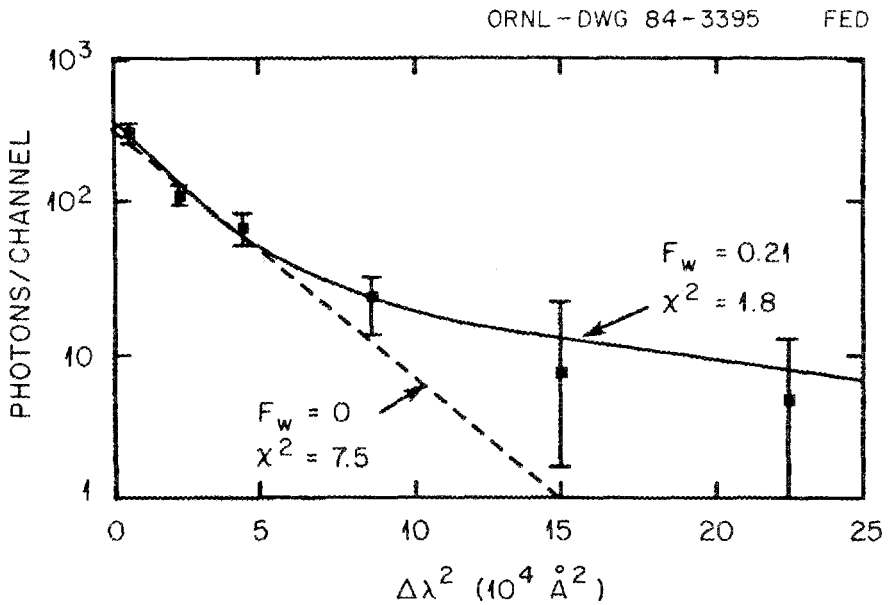

Fig. 2.3. The number of photons collected in each of six polychrometer channels vs $\Delta\lambda^2$, where $\Delta\lambda$ is the average shift of the collected light from the incident laser light. Data are summed over ten laser shots. Error bars shown are calculated statistical errors only and do not include possible systematic errors.

two-component distribution function in which the three parameters n_c, T_c, and n_w are treated as independent variables and varied to minimize χ^2. The value of T_w is specified to equal the measured soft X-ray temperature (~500 eV) for this case. For this case, the "best fit" of the parameters is $T_c = 66$ eV and $F_w = 0.21$, resulting in a normalized $\chi^2 = 1.8$. We conclude from the Thomson scattering analysis that the presence of a two-component distribution function with $F_w \leqslant 0.3$ is easily consistent with the Thomson scattering data. However, comparable cold and warm density components appear to be unlikely, since $F_w \simeq 0.5$ results in χ^2 values larger than the single-component assumption.

In addition to temperature information, density measurements may be obtained from the soft X-ray results. As with Thomson scattering, density measurements are more uncertain, since they require an absolute calibration of the detection and collimation system and a measurement of impurity species concentration in the plasma, whereas the temperature measurements depend only on the relative shape of the measured spectrum. Using the theory of free-free bremsstrahlung from a hydrogenic plasma,[3] the direct analysis of the soft X-ray data provides a chord-integrated measurement of the quantity

$$I_w = \int Z^2(x) n_w(x) n_i(x)\, dx \quad ,$$

where Z is the average ionization of the ions, n_w is the density of the electrons observed by the soft X-ray diagnostic, and n_i is the ion density. For EBT, impurity measurements[6,7]

indicate that Z is very close to unity (i.e., there are few impurities in the plasma). Dividing I_w by the interferometer measurement yields a quantity $\langle Z^2 n_w \rangle = \int Z^2 n_w n_e dx / \int n_e \, dx$. Dividing by the central electron density (obtained from radial scanning microwave interferometer data) yields an approximate measurement of the ratio of warm to total electron density. The result is shown by the solid curve in Fig. 2.4. These results indicate a warm density that is $\leq$30% the cold density from mid–T-mode (corresponding to a pressure of 1.0×10^{-5} torr) and higher pressures. For low T-mode, the calculated data points indicate that the fractional warm component increases dramatically and (according to the measurement) exceeds unity. The explanation of this physically untenable result is not clear. Two possible explanations are that (1) the impurity levels are increasing as the T-M transition is approached, thereby causing the soft X-ray bremsstrahlung signal to increase, or (2) the effects of increased fluctuations, ring dumps, and intermittent high-energy ions observed at lower neutral gas pressures invalidate the basic assumption used in the analysis of the soft X-ray data of a steady-state time-independent plasma.

A second, relatively simple estimate of the ratio of warm to total electron density can be made using only the temperature measurements of the three diagnostics under certain simplifying assumptions. If we assume that (1) the simple two-component plasma model is valid, (2) the soft X-ray diagnostic measures the warm temperature, (3) the Thomson scattering diagnostic measures the cold temperature, and (4) the aluminum line ratio

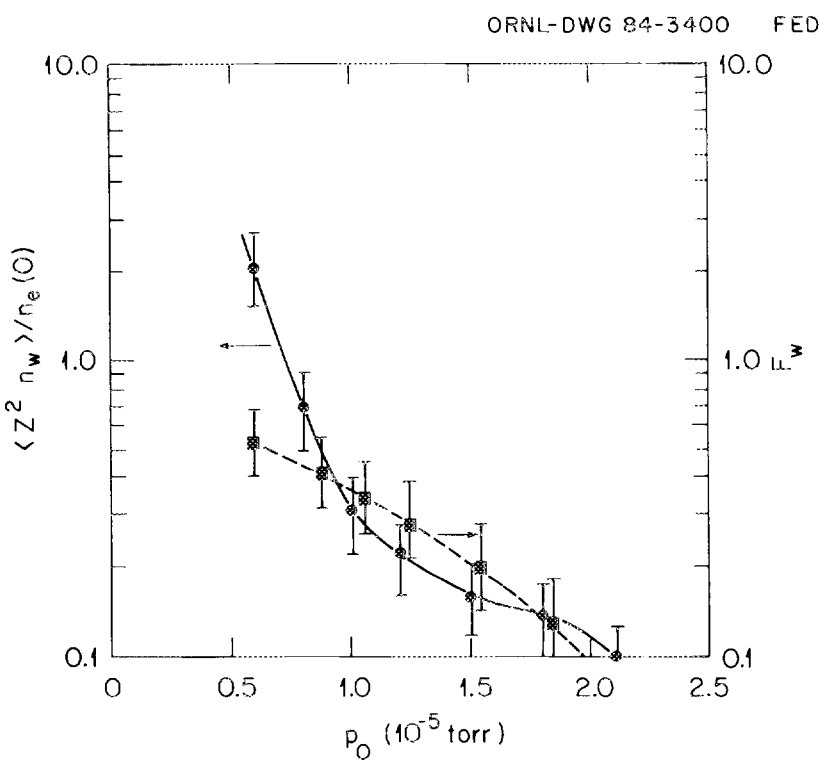

Fig. 2.4. $\langle Z^2 n_w \rangle / n_e(0)$ **determined from X-ray and interferometer measurements, and** $F_w = n_w / n_e$ **from** T_e **measurements.**

measures the density-weighted average temperature, then a simple expression can be derived for $F_w = n_w/(n_w + n_c) = (T_{avg} - T_c)/(T_w - T_c)$. The calculated value of F_w is shown by the dashed line in Fig. 2.4. We see that there is fairly good agreement between this estimate and the estimate obtained from the density ratio measurements except at lowest p_0 values (near the T-M transition).

2.1.1.3 Throat-midplane comparisons

The installation of new magnetic field coils with diagnostic ports embedded in the coils allows access to the high-field coil throat region. In this section, we present line-integrated measurements in the coil throat using a microwave interferometer and a soft X-ray detector and compare these measurements with comparable midplane results discussed in the previous section.

Curve A in Fig. 2.5 is the ratio of the average throat and average midplane electron densities measured by microwave interferometers. A measured density ratio close to unity is consistent with the assumption of an almost isotropic electron distribution function and the assumption (commonly made in EBT theoretical analysis) that the electrostatic potential does not vary along a magnetic field line.

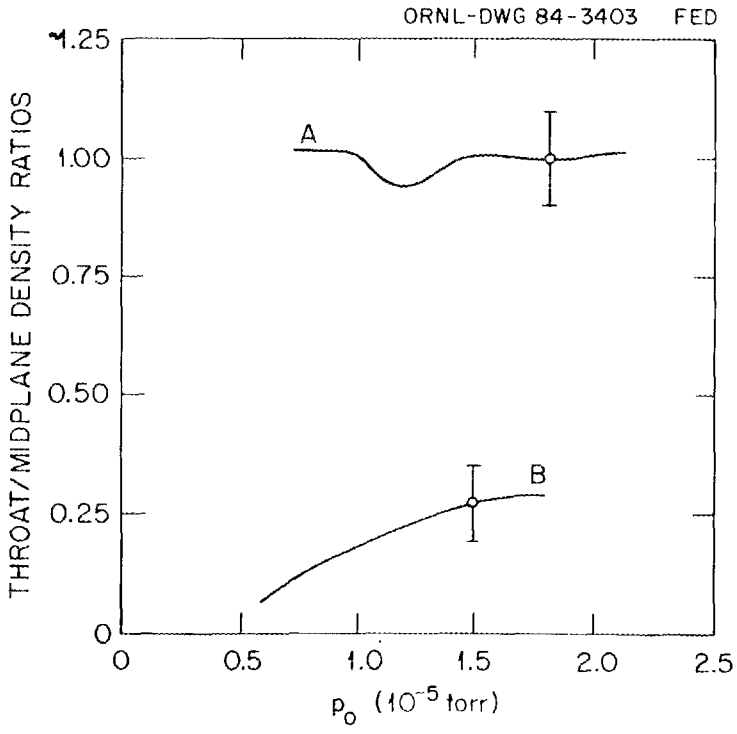

Fig. 2.5. Ratios of throat to midplane electron densities as measured by microwave interferometers (curve A) and soft X-ray detectors (curve B).

In contrast, the ratio $\langle Z^2 n_w \rangle_{thr} / \langle Z^2 n_w \rangle_{mid}$ measured by the soft X-ray diagnostic is substantially less than one, as shown by curve B in Fig. 2.5. The decrease in this ratio as the pressure is decreased indicates an increasing anisotropy of the warm component, with an increasing fraction of the warm electrons being mirror trapped. This is in qualitative agreement with ECH calculations by Batchelor et al.[8]

2.1.1.4 Discussion and conclusions

We have presented a new picture of the electron distribution function in EBT. Based on new and improved diagnostic measurements, recent advances in ECH theory, and a new model for power balance based on the ECH work, a non-Maxwellian distribution function with a high-energy tail appears to be a plausible and convincing explanation that reconciles previously inconsistent measurements of electron temperature.

New measurements of plasma properties in the coil throat region indicate that the warm component is anisotropic and that the anisotropy increases as the tail becomes less collisional. This is in qualitative agreement with the model of electrons gaining in perpendicular energy (i.e., $v_\perp$ increasing) due to heating at the fundamental resonance and thereby becoming mirror trapped.

2.1.2 Recent Soft X-Ray Measurements on EBT

D. L. Hillis, O. E. Hankins, and D. W. Swain

Electron temperature T_e and electron density n_e measurements on ELMO Bumpy Torus–Scale (EBT-S) have been possible only on the plasma components that could be viewed through diagnostic ports found on the cavity midplane. New "split mirror" coils installed on EBT-S have allowed diagnostic access to the high-field coil throat region.

A soft X-ray diagnostic was installed on one of the split mirror diagnostic ports to provide both T_e and n_e measurements of the plasma component present in the mirror throat. This diagnostic measured the soft X-ray energy distribution (0.4–6.5 keV) on EBT-S using an 80-mm^2 "windowless" Si(Li) detector.

Shown in Fig. 2.6 is a comparison of the electron temperature, as measured with the soft X-ray detection systems on EBT, in the cavity midplane and in the mirror throat region. The data of Fig. 2.6 were acquired during typical EBT-S operation with $P_\mu \approx$ 150 kW at 28 GHz and a midplane magnetic field of 0.72 T. It is also found that n_e(throat) $\approx 0.10 n_e$(midplane). At high collisionality (i.e., higher pressure points) the throat and midplane temperatures are about equal. As the pressure is lowered (and the collisionality decreases), both temperatures increase. However, the temperature of the trapped particles in the midplane increases more than that of the passing particles in the coil throat. This is in qualitative agreement with a model in which the trapped particles have absorbed more of the microwave heating energy than the passing particles.

An independent experiment, the three-cavity turnoff experiment, has confirmed that the warm tail is largely mirror-trapped and is driven by ECH at the fundamental resonance zones in the cavity of observation. The experimental setup and soft X-ray spectra are shown in Fig. 2.7. The conventional theory of ECH in EBT, based on ray tracing

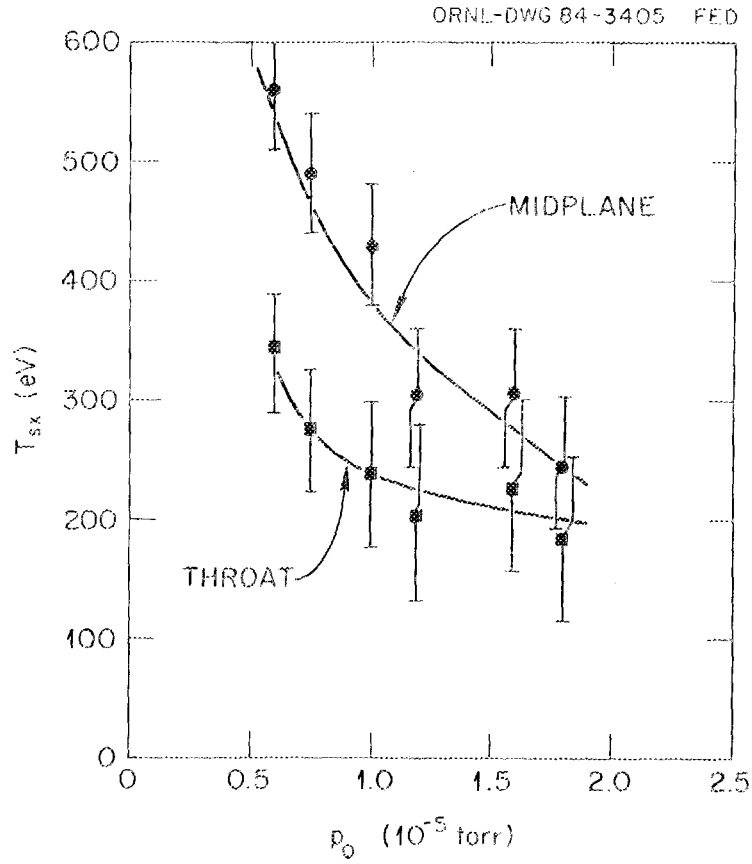

Fig. 2.6. Soft X-ray temperature measurement in the cavity midplane and throat vs neutral pressure for P_μ = 150 kW.

simulations and Monte Carlo calculations, indicates that microwave power injected into a cavity in the midplane (as shown in the figure) is absorbed largely at the four fundamental resonance zones nearest the cavity. Thus, with cavities 1, 2, 4, and 5 driven and cavity 3 undriven, as in Fig. 2.7(a), the resonance zones illustrated by the solid curves will receive almost 100% of their usual power, whereas those shown by the dashed lines will absorb about 50% of the power they would normally get if cavity 3 were driven. The resulting raw soft X-ray spectrum from a detector on the midplane of cavity 3 is shown at the bottom of Fig. 2.7(a). The spectrum shows the low-energy component ($E \leqslant 1200$ eV), from which the temperature is usually determined (after normalization); the aluminum K_α line at $E \approx 1500$ eV; and the high-energy continuum ($E \geqslant 2000$ eV) generated by the weak remnant of the relativistic electron ring in cavity 3. If cavity 3 is driven by ECH, the ring signal increases by about a factor of 10, making analysis of the resulting soft X-ray spectrum very difficult.

Figure 2.7(b) illustrates the results of the three-cavity turnoff experiment, in which cavities 2, 3, and 4 are not heated. In this case, almost no power gets to the fundamental

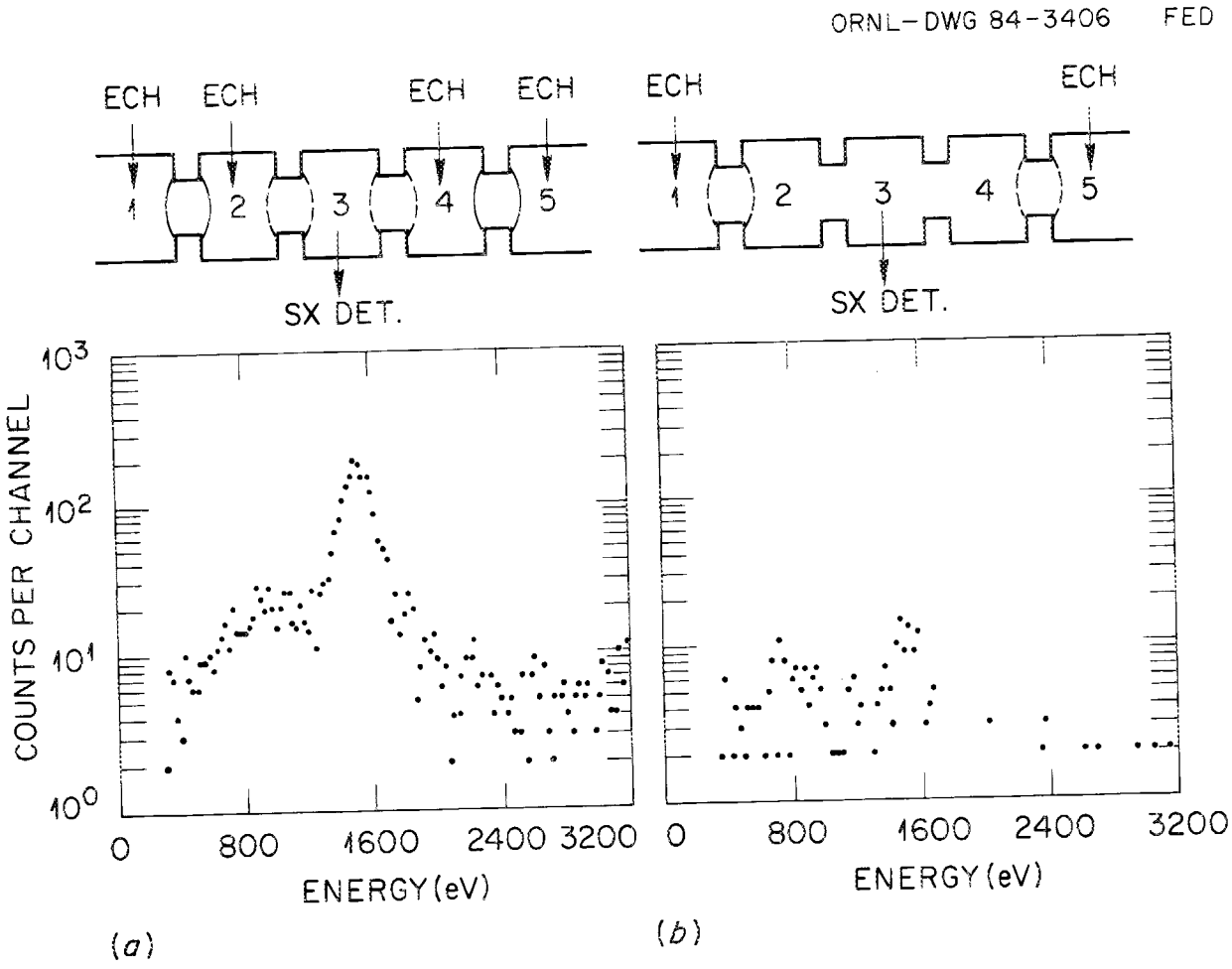

Fig. 2.7. Experimental setup and soft X-ray spectra for the three-cavity turnoff experiments. (a) Normal soft X-ray mode (cavity 3 only unheated). (b) Three-cavity turnoff mode (cavities 2, 3, and 4 unheated).

resonance zones in cavity 3, and the resulting soft X-ray spectrum is shown. Although the low number of counts and large statistical uncertainty make detailed quantitative comparisons between the two spectra difficult, the number of counts in the 300- to 1200-eV range for case (b) is down by a factor of 3.7 from case (a), while the counts in the K_α peak (which requires an electron energy of $\geqslant$1500 eV for excitation) are down by a factor of 13.

Plasma properties (density, temperature, and potential profile) generally change less than 10% during this experiment in cavities that remain heated, and the Thomson scattering T_e measurement and the neutral aluminum density (inferred from spectroscopy) in cavity 3 are relatively unchanged. This indicates that the warm tail component has decreased significantly and that the mechanism for creating the tail is most likely heating at the fundamental resonance zones.

2.1.3 Abstract of *Thomson Scattering on ELMO Bumpy Torus*[9]

J. A. Cobble

Below 10^{12}-cm^{-3} density, a Thomson scattering experiment is an exacting task. Aside from the low signal level, the core plasma in this instance is bathed in high-energy X rays, surrounded by a glowing molecular surface plasma, and heated steady state by microwaves. This means that the noise level from radiation is high, and the environment is extremely harsh—so harsh that much effort is required to overcome system damage. In spite of this, the EBT system has proven itself capable of providing reliable n_e and T_e measurements at densities as low as 2×10^{11} cm^{-3}. Radial scans across 20 cm of the plasma diameter have been obtained on a routine basis, and the resulting information has been a great help in understanding confinement in the EBT plasma. The bulk electron properties are revealed as flat profiles of n_e and T_e with density ranging from 0.5 to 2.0×10^{12} cm^{-3} and temperature decreasing from 100 to 20 eV as pressure in the discharge is increased at constant power. Evidence is presented for a suprathermal tail, which amounts to about 10% of the electron distribution at low pressures. The validity of this conclusion is supported by two independent sensitivity calibrations.

2.1.4 Abstract of "Electron Temperature Measurements from Induced Toroidal Current in ELMO Bumpy Torus–Scale"[10]

T. Uckan

We have carried out measurements on EBT-S to estimate the electron temperature of the toroidal plasma by inducing a small (~2-A), fluctuating (5-Hz) ac toroidal current. The modulating frequency used is low enough to minimize the effects of cavity skin time (~100 ms) and plasma inductance. We have calculated the temperature from the measured values of the current obtained by use of the Rogowski loop at various fill pressures at 100 kW with 28-GHz operation. The electron temperature has been estimated to be around 80–90 eV with an error of about 10% to 25% in the low T-mode, which is in good agreement with the Thomson scattering measurements (Fig. 2.8).

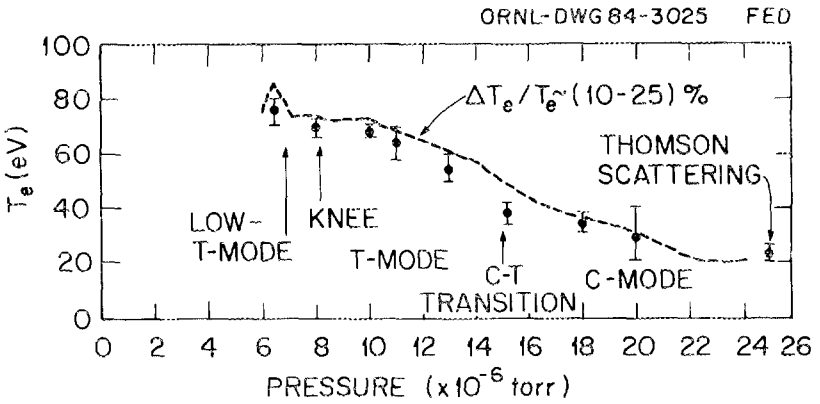

Fig. 2.8. The estimated toroidal plasma temperature (dashed line) from the measured induced toroidal currents, together with the Thomson scattering measurements of temperatures in EBT-S at 100 kW of 28-GHz operation.

2.1.5 Abstract of *Electron Confinement in the ELMO Bumpy Torus Without the Influence of Hot Electron Rings—The Ring Killer Experiment*[11]

D. L. Hillis, J. B. Wilgen, J. A. Cobble, W. A. Davis, S. Hiroe, D. A. Rasmussen, R. K. Richards, T. Uckan, E. F. Jaeger, O. E. Hankins, J. R. Goyer, and L. Solensten

The EBT normally has an energetic electron ring in each of its 24 mirror sectors. The original intention of using this hot electron population was to provide an average local minimum in the magnetic field (through its diamagnetism) to stabilize the simple interchange and flute modes, which otherwise are theoretically inherent in a closed-field-line bumpy torus. To study the confinement properties of a bumpy torus without the influence of hot electron rings, a water-cooled stainless steel limiter in each mirror sector was extended into the plasma to the ring location, and this eliminated the hot electron ring population. These limiters were aptly named "ring killers." Electron temperature, density, space potential, and plasma fluctuations have been measured during the ring killer experiment and are compared to standard EBT operation. The results of these experiments indicate that the hot electron rings in EBT do enhance the core plasma properties of EBT and do, in fact, reduce plasma fluctuations; however, these improvements are not large in magnitude. These measurements and recent theoretical models suggest that simple interchange/flute modes are stabilized, or fluctuation levels reduced, well before that condition is obtained for average minimum-B stabilization. Several possible mechanisms for this stabilization are discussed.

2.1.6 Abstract of *An Experimental Determination of the Hot Electron Ring Geometry in EBT-S and its Implications for Bumpy Torus Stability*[12]

D. L. Hillis, J. B. Wilgen, T. S. Bigelow, E. F. Jaeger, O. E. Hankins, and R. Juhala

The hot electron rings of the EBT are formed by microwaves resonant at the second-harmonic electron cyclotron frequency and have an electron temperature of 350 to 500 keV. The purpose of these hot electron rings is to provide (through their diamagnetism) a local minimum in the magnetic field and, thereby, stabilize the simple interchange and flute modes, which are inherent in a closed-field-line bumpy torus. To evaluate the electron energy density of the EBT rings and determine if enough stored energy is present to provide a local minimum in the magnetic field, a detailed understanding of the spatial distribution of the rings is imperative. The purpose of this paper is to measure for the first time the ring thickness for typical EBT operating conditions and investigate its implications for bumpy torus stability. The spatial location and radial profile of the hot electron ring are measured with a unique ballistic metal-ball pellet injector, which injects small 3.2-mm-diam stainless steel balls into the EBT ring plasma. To obtain the hot electron ring profile, the thick-target bremsstrahlung, synchrotron radiation, and ring stored energy are measured during passage of the metal ball through the hot electron ring. From these measurements, the radial extent (or ring thickness) is about 5 to 7 cm full width at half-maximum for typical EBT-S operation, which is much larger than previously expected. These measurements and recent theoretical modeling of the EBT plasma indicate that the hot electron ring's stored energy may not be sufficient to produce a local minimum in the magnetic field.

2.1.7 Diamagnetic Measurements and Data Analysis

K. H. Carpenter and R. F. Steimle*

Theoretical and experimental studies of the diamagnetism of the EBT electron rings have contributed to a better understanding of ring energy and geometry. The primary experimental effort during 1984 was the taking of data using the UMR Hall effect diamagnetic diagnostic instrument with the probes mounted along the horizontal midplane at the large major radius position of an EBT cavity.[13] Analysis of these data has confirmed earlier indications of an electron ring component near the cavity wall.

A "vacuum field model" for the electron rings has been formulated. It is based on the magnetohydrodynamic (MHD) equilibrium code pressure function but uses the vacuum field rather than the self-consistent field as the independent variable. This model produces a ring of more realistic geometry than the current sheet model in previous use. The diamagnetic fields produced by the model agree with those produced by the current sheet model for locations outside the EBT cavity, but the vacuum field model also produces fields that should be usable as ring simulations for locations inside the cavity.

The diamagnetic diagnostics, along with the other ring diagnostic experiments on EBT, have led to a consistent description of ring geometry. In EBT-S operation, a typical ring would be about 15 cm in mean radius with a thickness in the radial direction of 6 or 7 cm. It would have a toroidal extent of 10 to 12 cm and be centered in the EBT cavity

except for an offset of 1 to 2 cm toward the small major radius location. The ring would also have a small component of diamagnetism extending to near the cavity wall.

*University of Missouri, Rolla.

2.1.8 Abstract of *High-Field Launch Electron Cyclotron Heating Experiments in the ELMO Bumpy Torus*[14]

D. A. Rasmussen, D. B. Batchelor, D. W. Swain, T. L. White, H. D. Kimrey, T. S. Bigelow, J. A. Cobble, R. C. Goldfinger, D. L. Hillis, R. K. Richards, T. Uckan, J. B. Wilgen, and O. E. Hankins

The midplane microwave heating system in EBT was supplemented with power launched from the high-field side of the fundamental resonance by an antenna in the magnet coil throat (Figs. 2.9 and 2.10). Up to 43 kW of polarized [extraordinary (X) mode], 28-GHz power was successfully launched with one antenna. Measurements were made of changes in the core and hot electron ring plasma parameters when throat-launch power was added. In sharp contrast to initial expectations, the bulk core plasma parameters were degraded while the ring parameters in the launch cavity were improved. These results are explained in light of a modified picture of ECH in EBT. A picture of localized microwave absorption and particle losses is supported by additional measurements.

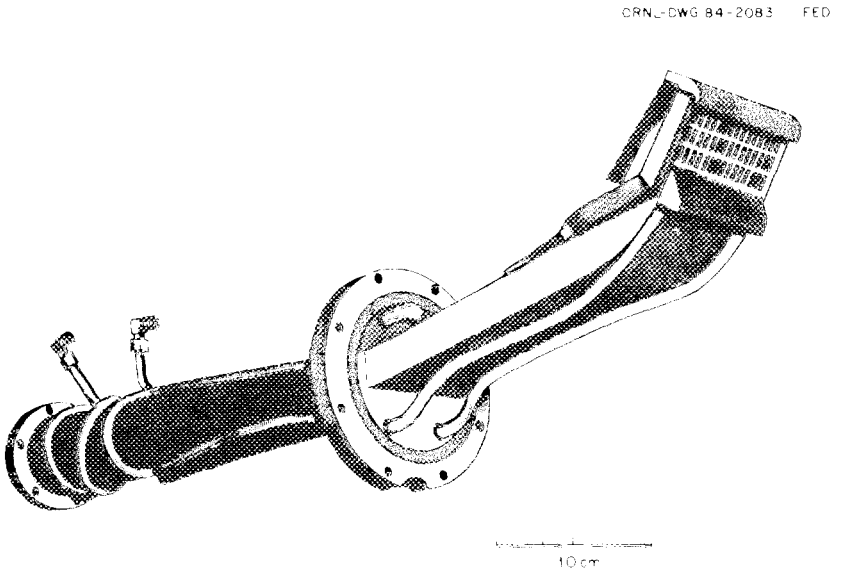

Fig. 2.9. Throat-launching antenna structure with rectangular polarizing grid.

ORNL-DWG 83-2446A FED

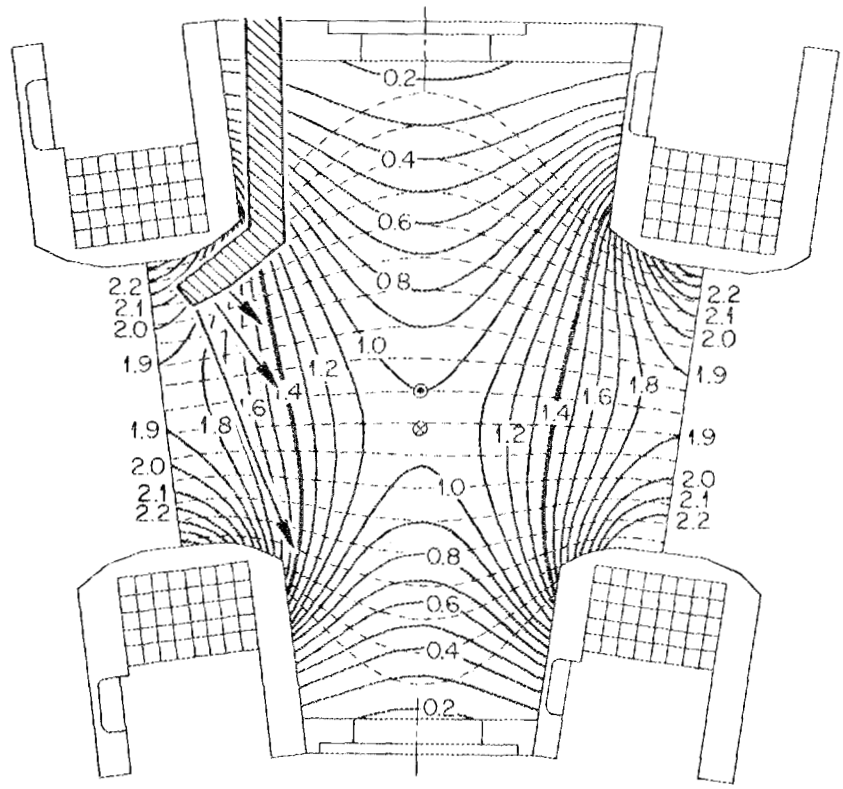

Fig. 2.10. High-field, polarized X-mode launcher snaked through the fundamental resonance.

2.1.9 Summary of "Fundamental and 2nd Harmonic Resonance Polarized Microwave Absorption and Heating Measurements on EBT"[15]

T. S. Bigelow, D. A. Rasmussen, and D. B. Batchelor

Absorption measurements were made with a lower-power polarized microwave test wave that was set up to travel through the fundamental electron cyclotron resonance zone in the initial EBT configuration (EBT-I). The polarization generated and received could be varied to any sense of linear or elliptical, which enabled the absorption to be measured vs polarization. The wave was launched from the high-magnetic-field side of the resonance zone and would cross the resonance layer at an angle of 140° (line of sight) to the local magnetic field B_0 as shown in Fig. 2.11. Since a fairly large receiving antenna was used, the effects of wall reflections and multipath were minimized due to the high directivity.

Results of the measurements indicate that the polarization of maximum absorption (X mode) is a left-hand elliptical wave with an axial ration (E_{max}/E_{min}) of 5 dB. Absorption

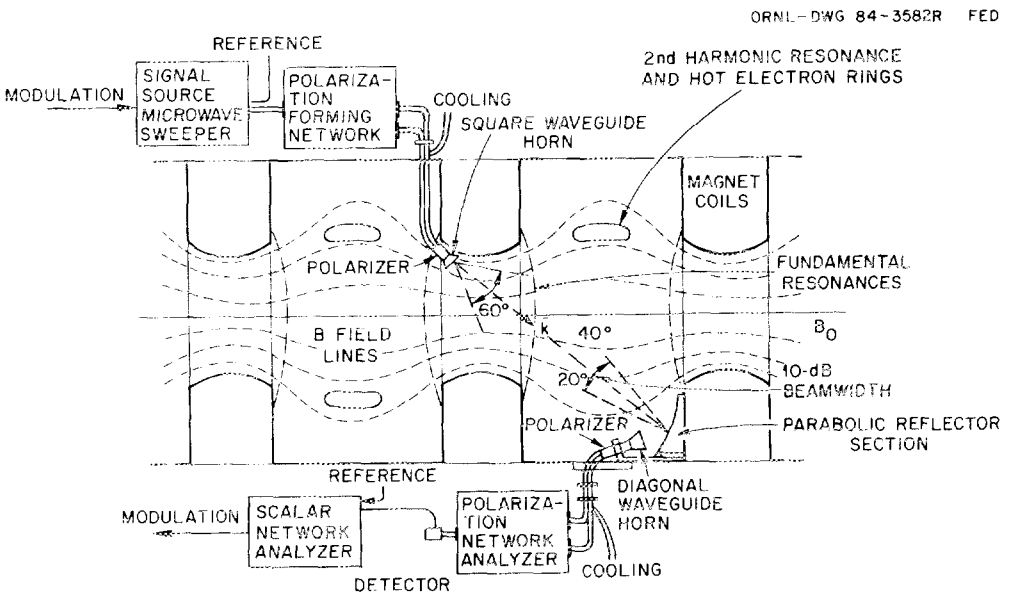

Fig. 2.11. Experimental setup for polarized microwave absorption tests.

of 25 dB was typical at normal machine operating parameters. Absorption of the other characteristic wave [ordinary (O) mode] was typically 1 dB or less (compared to the no-plasma reference). Rotation of the angle of the polarization ellipse relative to B_0 produces a measurable change in the X-mode absorption. If the plasma density is varied by changing the 18-GHz ECH power from off to 40 kW, the X-mode absorption increases rapidly up to around 10 kW and then levels off, as shown in Fig. 2.12.

These measurements can be compared with simple ray tracing calculations to check for agreement. Calculations were performed for standard EBT-I plasma density and temperature and show that an X-mode ray emanating from the source location that intersects the receiving antenna would actually cross the resonance zone slightly below the EBT centerline shown in Fig. 2.11. The angle between the ray and B_0 at the intersection is 125°. Using the Appleton-Hartree dispersion relation to obtain the X-mode wave polarization for this angle gives an axial ration of 5.1 dB, which agrees well with the 5 dB measured for the maximum absorption. (The line-of-sight angle of 140° gives 2.5 dB.) These results are very encouraging both for the accuracy of the test setup and for the ray tracing theory.

The transmitting waveguide antenna used in the polarized absorption study was modified to operate at high power by adding extra cooling lines and changing the phase shifter. The antenna could handle up to 3 kW cw at 18 GHz, except for the two vacuum windows, which caused problems. It was possible to operate at 1 kW into the plasma for extended periods, and some data were collected. The 18-GHz ECH power was obtained by borrowing power from another cavity on EBT. The power could be switched between throat launch and normal feed using a ferrite switch.

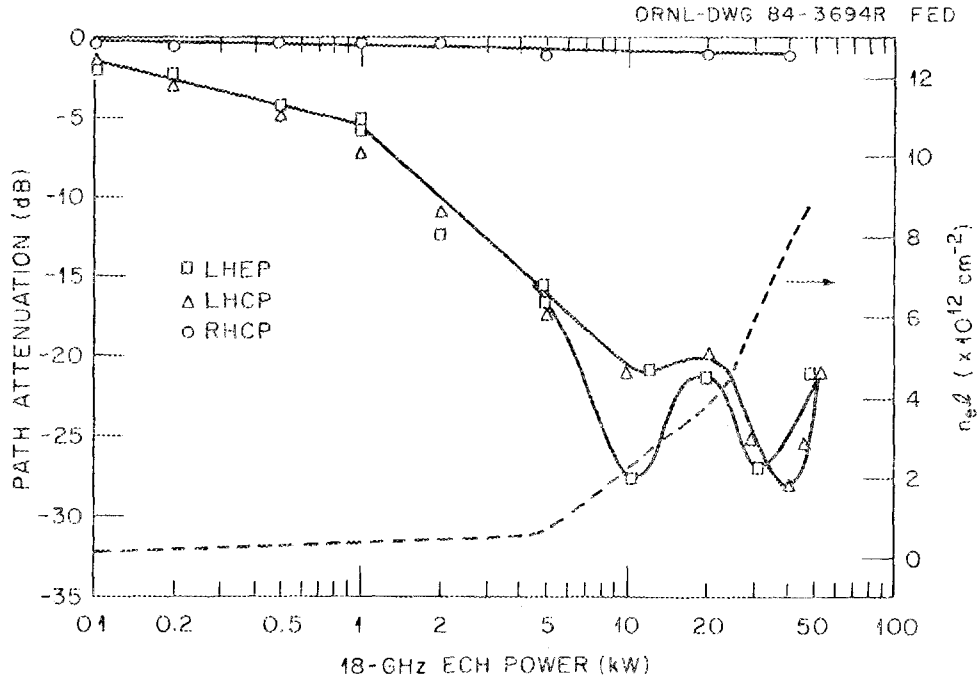

Fig. 2.12. Path attenuation and line density vs 18-GHz power.

As before, any sense of polarization could be generated, and the system could be operated while scanning polarization. In this experiment, the launcher was mounted facing into a cavity on EBT where an aluminum line ratio temperature diagnostic was located (N3). Also, $W_\perp$ coils were available to look for changes in hot electron ring energy. With this launch point, the angle between the wave k vector and B_0 was 40°, so X mode is RHEP.

Data for 1-kW throat launch operation with 40-kW normal ECH power indicate that, although most of the power is absorbed by the core plasma fundamental resonance, with the proper polarization, a significant portion of the power still is lost to the ring in the launch cavity. Presumably, this occurs due to poorly confined medium-energy electrons feeding straight into the ring. These higher-energy electrons are heated preferentially due to Doppler shift in their resonance frequency.

This effect is supported by observing that the ring stored energy $W_\perp$ for the launch cavity does not change significantly when the polarization is scanned between highly absorbed X mode and poorly absorbed O mode. The experiment would have been more meaningful at higher launch power.

2.1.10 Abstract of "Multiple-Frequency Electron Cyclotron Heating of Hot Electron Rings in the ELMO Bumpy Torus"[16]

D. A. Rasmussen, T. S. Bigelow, D. B. Batchelor, D. L. Hillis, G. R. Haste, B. H. Quon, and O. E. Hankins

The use of multiple-frequency microwave power for ECH significantly increased the ring stored energy in the SM-1 simple mirror device. Multiple-frequency ECH (MFECH) was used on EBT in an effort to increase its hot electron beta. No substantial improvement in the ring parameters was observed in a series of two-frequency ECH experiments, with frequency separations up to 90 MHz, in contrast to the dramatic improvement found in the axisymmetric SM-1 experiment. The toroidal canting of the EBT mirror sectors introduces asymmetries that destroy the superadiabatic behavior of the energetic electrons, reduce microwave heating efficiency, and produce additional ring losses. These effects qualitatively explain the different multiple-frequency heating results obtained in EBT and SM-1.

2.1.11 Abstract of "The EBT-S 28-GHz 200-kW, cw Mixed-Mode Quasi-Optical Plasma Heating System"[17]

T. L. White, H. D. Kimrey, T. S. Bigelow, D. D. Bates, and H. O. Eason*

The EBT-S 28-GHz, 200-kW, cw, plasma heating system consists of a gyrotron oscillator, an oversized waveguide two-bend transmission system, and a quasi-optical, mixed-mode microwave distribution manifold that feeds microwave power to the 24 plasma loads of the EBT-S fusion experiment. Balancing power to the 24 loads was achieved by adjusting the areas at 24 coupling irises. System performance is easily measured using system calorimetry. The distribution manifold mixed-mode power transmission, reflection, and loss coefficients are 89%, 6%, and 5%, respectively. The overall system efficiency (plasma power/gyrotron power) is 80%, but with some modifications to the distribution manifold, we believe the ultimate efficiency can approach 90%. The system reliability is outstanding, with a world's record of 1×10^5 kWh of 28-GHz energy delivered to the EBT-S device with well over 1×10^3 operating hours.

*Deceased.

2.1.12 Abstract of "Mixed-Mode Distribution Systems for High Average Power Electron Cyclotron Heating"[18]

T. L. White, H. D. Kimrey, and T. S. Bigelow

The EBT-S experiment consists of 24 simple magnetic mirrors joined end-to-end to form a torus of closed magnetic field lines. In this paper, we first describe an 80% efficient, mixed-mode, unpolarized heating system that couples 28-GHz microwave power to the midplane of the 24 EBT-S cavities. The system consists of two radiused bends feeding a quasi-optical, mixed-mode toroidal distribution manifold. Balancing power to the 24 cavities is determined by detailed computer ray tracing. A second 28-GHz ECH system using

a polarized grid high-field launcher is described. The launcher penetrates the fundamental ECH resonant surface without a vacuum window with no observable breakdown up to 1 kW/cm^2 (source limited) with 24 kW delivered to the plasma. This system uses the same mixed-mode output as the first system but polarizes the launcher power by using a grid of WR 42 apertures. The efficiency of this system is 32% but can be improved by feeding multiple launchers from a separate distribution manifold.

2.1.13 Summary of "Performance of 28 GHz, 200 kW, cw, Gyrotron Oscillators on the ELMO Bumpy Torus-Scale (EBT-S) Experiments"[19]

H. D. Kimrey, T. L. White, and T. S. Bigelow

VGA-8000 28-GHz, 200 kW, cw gyrotrons have been heating the EBT-S experiment for the past five years. During this time techniques have been developed for accessing the gyrotron high-efficiency regime. A world's record, 54% total efficiency, has been achieved. Details of the operating space are presented, including experimentally determined limits of the TE_{02}^{O} mode caused by competition from neighboring modes. We have found that the simple cavity oscillator can operate stably in the "hysteresis" region, where operating space is theoretically shared by more than one mode. Access to this regime has only been achieved by first initiating oscillation in the proper mode and then lowering the cavity magnetic field. Techniques have been developed for pulsing at high average power necessary for studying various EBT-S plasma formation and decay times. A technique has also been successfully tested for operating two gyrotrons from common beam and gun supplies, thereby making possible substantial cost savings in designing cw ECH power systems. Finally, second-harmonic gyrotron emission from commercially available pulse gyrotrons, first identified at Massachusetts Institute of Technology (MIT) in the TE_{43}^{O} mode, has been verified at ORNL on the cw model and operated to 30 kW cw.

2.1.14 EBT Ion Cyclotron Heating

F. W. Baity and T. L. Owens

Large increases in the plasma density on the Nagoya Bumpy Torus (NBT-1M) at the Institute for Plasma Physics, Nagoya, Japan, were observed during pulsed ion cyclotron heating (ICH) using a so-called "Nagoya Type III" antenna in conjunction with gas puffing. With about 200 kW of ICH power, average density values of 1.0×10^{13} cm^{-3} were measured. Several attempts were made to reproduce these results on EBT-S with an antenna of similar design. No reproducible density increase was ever observed on EBT.

A Type III antenna differs from the normal loop antennas used for fast-wave and slow-wave ICH in that it is oriented such that the loop is parallel to the toroidal magnetic field lines. Two different designs were tried on EBT-S: one that was completely unshielded and passed through the throat of one of the toroidal field (TF) magnets, the other with the same shape and orientation but with solid shields between the feedthroughs and the mirror throat region, so that the only exposed portion of the antenna radiating element was the portion located in the magnet bore. A full parameter scan was made of magnetic field, ambient neutral pressure (operating mode), gas puff timing, and ICH frequency in trying to find the proper operating conditions.

The antenna loading resistance on EBT-S was about one order of magnitude greater than that on NBT-1M, even for the antenna with the surface shields. For the completely unshielded antenna, the loading was several times greater still. This difference in loading is probably the key to understanding the discrepancy. One major difference between EBT-S and NBT-1M is the volume occupied by the surface plasma. NBT-1M was designed with a slightly lower magnetic mirror ratio and with a vacuum wall much closer to the toroidal plasma, thus reducing the volume available for the surface plasma. It is suspected that the higher loading measured on EBT-S is due, at least in part, to increased surface plasma loading.

A second difference between the two machines is the vacuum wall material. The NBT-1M vacuum vessel is entirely stainless steel, and the EBT-S vacuum vessel is constructed of aluminum. These two materials presumably exhibit significantly different particle recycling, which may also account for the disparate results.

The two antennas used on EBT-S were constructed of copper and suffered sufficient damage from sputtering to result in a loss of coolant into the vacuum vessel. The copper sputtering probably accounts for the irreproducible results on EBT.

The results on NBT-1M, while spectacular in the magnitude of the observed density increase, did not indicate any increase in energy confinement time, however, as no increase in ion or electron temperatures was observed upon application of the ICH using the type III antennas. On EBT, no change in core plasma temperatures was observed, either. Thus, it is suspected that most of the ICH on EBT went directly to poorly confined or completely unconfined surface plasma.

2.1.15 Abstract of "Ion Heating in the Range of High Ion Cyclotron Harmonics on EBT"[20]

T. L. Owens, F. W. Baity, and W. A. Davis

Wave heating of ions is obtained in EBT experiments when 18 GHz $\geqslant \omega\Omega_1 \geqslant$ 3 GHz. Absorption of wave energy in the plasma center is demonstrated. The fast magnetosonic wave is observed on electrostatically shielded loop probes placed at the edge of the plasma, but it is shown that the fast wave cannot directly heat the ions in EBT. The experiments suggest, however, that the waves that do produce the ion heating are coupled to the fast wave. The possibility that the heating is due to excitation of electrostatic waves is investigated theoretically.

2.1.16 FIR Scattering Measurements of Density Fluctuations and Ion Waves

W. H. Casson and J. B. Wilgen

A considerable portion of the final experimental effort on EBT was directed toward measuring the density fluctuations and ion wave characteristics by the scattering of far-infrared (FIR) radiation. The FIR source laser operated at 447 μm and was supplemented with a 2-mm klystron option. Scattered signals were observed using a homodyne receiver with an antenna beam that scanned the plasma spatially along the central horizontal diameter of cavity W6. The fluctuation level could be recorded for three different angles for

each spatial location. Measurements were made of the frequency spectrum, spatial dependence, angular distribution, and integrated scattered power for a wide range of machine operations.[21]

In order to evaluate the scattered signal amplitude, a measurement of the system losses and detection efficiency was made using a plastic Bragg cell to simulate the plasma. The scattering of laser radiation from acoustic waves in plastic is reasonably well understood. Simultaneous measurement of the scattered and transmitted power of HeNe laser radiation and of the FIR scattered signal allowed calculation of the scattered FIR power, which could be compared with the signal detected by the receiver system. The ratio of the scattered intensity to the incident intensity is given by

$$\frac{I_{\text{diff}}}{I_{\text{inc}}} = \sin^2(K/\sqrt{2\lambda}) \ ,$$

where λ is the wavelength and K is a constant that depends on the acoustic intensity, the interaction volume, and the physical characteristics of the plastic. This constant is assumed to be independent of the wavelength and intensity of the incident radiation. A typical measurement of the scattering of HeNe laser radiation is shown in Fig. 2.13. The central peak is the transmitted beam, and the sidebands are the scattered signals corresponding to Stokes and anti-Stokes light. Calibration measurements were made at both 447 μm and 2 mm.

Measurements with the 2-mm klystron were the most successful, although spatial and wave number resolution were not as good as with the shorter wavelength. Figure 2.14 shows the change in scattered signal at the cavity center vs gage pressure during the operation of EBT-I. The same basic trend was observed at all spatial locations, although the level of fluctuations differed considerably and depended strongly on the scattering angle. The change in fluctuation level vs the central magnetic field strength is shown in Fig. 2.15.

Measurements were also made during pulsed operation of the machine and during ICH. In Fig. 2.16 the recorded signal is shown vs spatial position for ICH-driven waves observed with the shorter wavelength beam probe. The signal was processed by a high-frequency lock-in amplifier in sync with the source signal for the ICH transmitter. Different ICH frequencies were used, as were various machine conditions. Although signals were recorded, they were small and usually could not be reproduced. The scanning of the magnetic field during otherwise steady-state conditions showed marked changes in the scattered signal (Fig. 2.17) that could be reliably reproduced for a given set of machine conditions. This could be a sign that the signals are dependent upon the location of the ICH resonance zones.

Comparison of these data with information obtained using Langmuir probes and magnetic probes should provide information about how well measurements with the mechanical probe method on this type of plasma device relate to plasma core properties. A complete analysis of the information obtained is in progress.

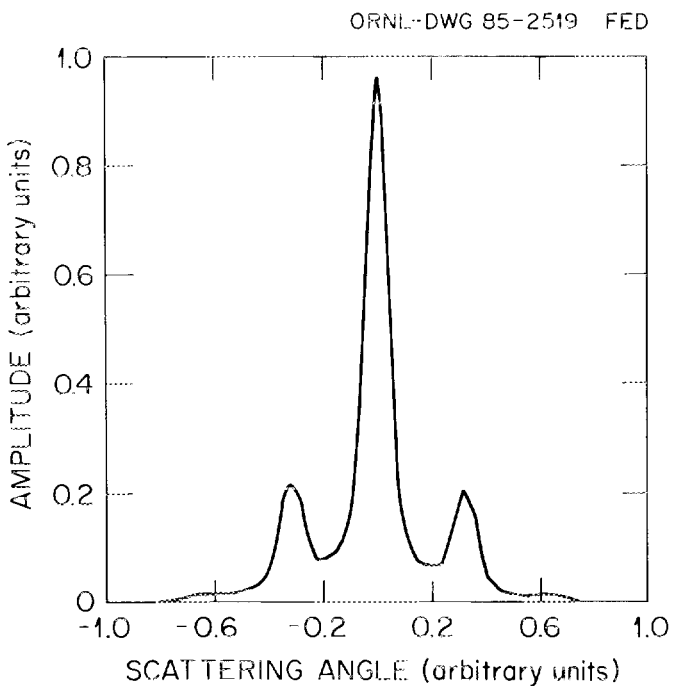

Fig. 2.13. Results of Bragg scattering of HeNe light in a plastic acoustic cell. Central peak is the zero-order or transmitted beam. On each side are the first-order signals, and outside those are the weak second-order peaks.

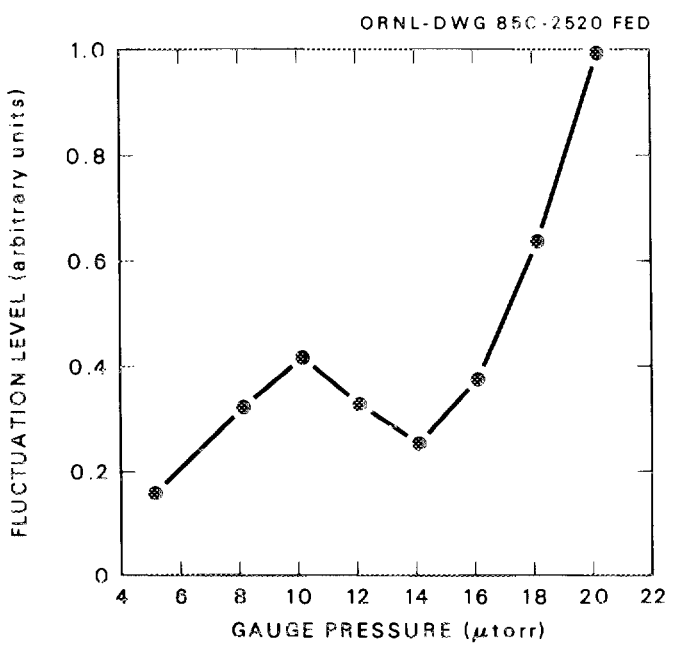

Fig. 2.14. Change in fluctuation level at the cavity center with changing neutral pressure during normal EBT-I conditions, as detected by 2-mm scattering.

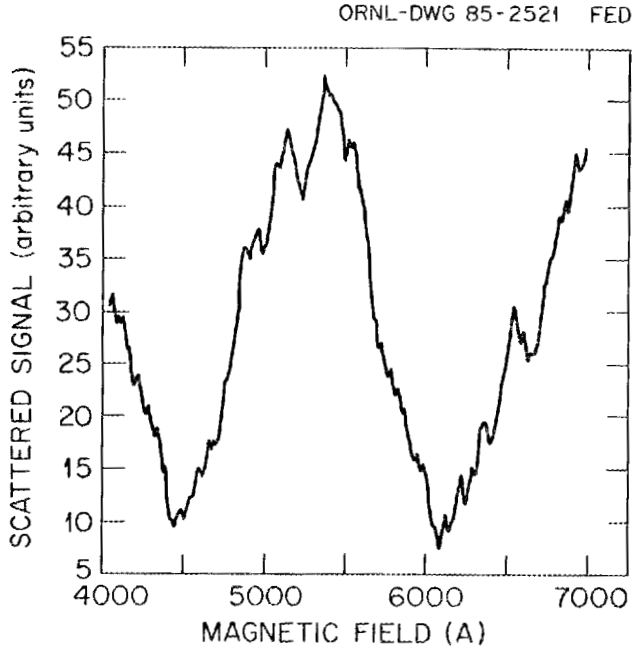

Fig. 2.15. Signal level of FIR scattering from cavity center vs magnetic field strength during pulsed (10-kHz) EBT-I operation at p_0 = 16 μtorr.

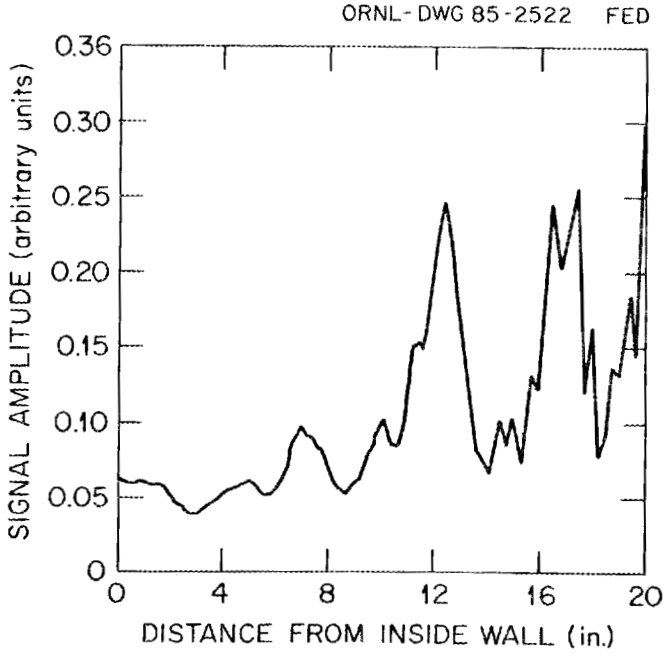

Fig. 2.16. Scattered signal vs spatial location during ICH heating with 43 kW of 15-MHz input power to an EBT-I plasma at 20-μtorr neutral pressure, resulting from FIR (447-μm) scattering.

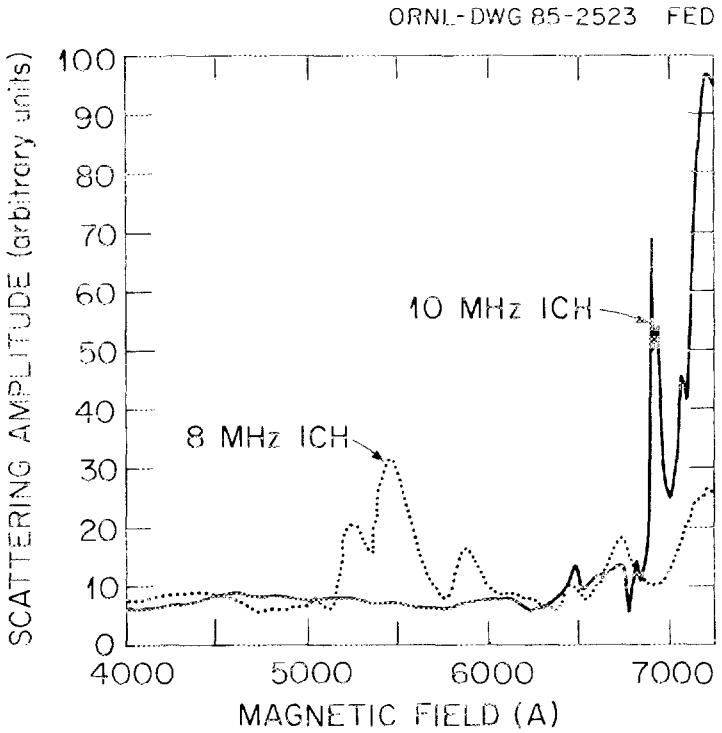

Fig. 2.17. Difference in scattered signal from the cavity center vs magnetic field for 10-MHz (solid line) and 8-MHz (dotted line) ICH in FR mode at 16 μtorr, showing the difference as detected by FIR scattering.

2.1.17 Abstract of "EBT Plasma Potential Measurements"[22]

L. Solensten, J. R. Goyer, K. A. Connor, and R. L. Hickok

The EBT heavy-ion beam probe has been used to measure the two-dimensional (2-D) structure of the steady-state potential in EBT. Data have been acquired in the cavity midplane between adjacent mirror coils for a wide range of machine conditions. For example, a scan of potential vs pressure in EBT-I (B = 0.5 T, ECH at 18 GHz) revealed two distinct topologies. At low pressures (T-mode) the potential is characterized by a central region of nested closed contours indicative of good confinement. The potential at high pressure is dominated by roughly diagonal contours leading to an $\mathbf{E} \times \mathbf{B}$ drift directed vertically upward and radially outward. The potential changes smoothly from one structure to the other over a narrow pressure range around the minimum in the line-integrated electron density which defines the C-T transition point.[23]

2.1.18 Summary of "Experimental Study of Equilibrium in the ELMO Bumpy Torus"[24]

S. Hiroe, J. A. Cobble, R. J. Colchin, G. L. Chen, K. A. Connor, J. R. Goyer, and L. Solensten

The equilibrium in EBT has been studied. The potential structure in the C-mode represents a typical nonequilibrium structure. At the T-C transition, closed potential contours start to form. High-energy tail electrons are necessary for the formation of closed potential contours.

Theory predicts the inward shift of the potential contours from an electrostatic equilibrium point of view. Experiments seem to be qualitatively in agreement with the theoretical predictions but disagree quantitatively. The most serious disagreement is that the bulk plasma parameters do not depend much on whether the nested potential contours are in the plasma or not. The electrostatic beta limit has been examined. Because of the reasons given previously, it is very difficult to find the electrostatic beta limit in the present EBT. The MHD equilibrium has also been discussed, and it was found that the necessary inward shift to sustain the plasma in equilibrium is too large, compared with the inward shift of the experimental pressure profile.

It has been suggested that the electrostatic force balance is necessary to cancel the toroidal expansion force. When excess charge accumulates inside the plasma, the conducting wall surrounding the plasma induces an image charge and consequently forms an effective external electric field. This force balances the toroidal expansion force (nT/R). A simple estimate is in good agreement with observations.

When an instability with a long wavelength penetrates from outside to inside across the hot electron ring location, the closed potential contours are deformed. This deformation is corrected by the stabilization of the long-wavelength instability.

It is worth noting that we have not taken into account the effects of the hot electrons because the hot electron beta value in present ECH devices is about 5% to 10%, as measured by Zeeman splitting of a lithium line. This is not strong enough to reverse $\oint d\ell/B$, but we do not know whether it is reasonable to neglect its effect. The equilibrium under the reverse $\oint d\ell/B$ system may not be the same as observed in this paper, and it would be interesting to study such a new configuration.

2.1.19 Abstract of "Measurements of Temperature and Density on the ELMO Bumpy Torus Using a Heavy Ion Beam Probe"[25]

J. R. Goyer

Two-dimensional electron temperature and density data have been obtained in the midplane of EBT through the use of a heavy-ion beam probe. These data have been used to determine under what conditions an equilibrium configuration is present. Under those conditions, the data were averaged, using confidence-weighting, along the equilibrium contours and reduced to one-dimensional (1-D) format.

The 1-D data were then compared to theoretical predictions for stability. It was found that in the stable mode of EBT operations, the T-mode, the acquired data indicated stability due to a hollow temperature profile. As the unstable operating mode of EBT was approached, the temperature profile became less hollow, until the marginal stability profile

was reached. The agreement between theory and experiment on this point was very good, allowing for typical measurement errors.

To understand the significance of this, one must understand the underlying principle of operation of EBT: that the hot electron rings modify the magnetic geometry to provide stability. Recent data have indicated that the rings are too weak to provide the necessary magnetic modification, leaving stability (and the close relation of it to ring formation) an unanswered question. This thesis attempts to answer that question.

In addition, the data are used to obtain an indirect measure of the energy confinement time in EBT, and, with the results of other diagnostics, a possible operational scenario is developed.

2.1.20 Summary of "Effect of Fluctuations on Confinement in ELMO Bumpy Torus"[26]

S. Hiroe, J. A. Cobble, J. C. Glowienka, D. L. Hillis, G. L. Chen, A. M. El Nadi,*
J. R. Goyer, L. Solensten, W. H. Casson, O. E. Hankins, and B. H. Quon

We have discussed experimentally whether the plasma parameters obey the neoclassical transport or the anomalous transport. The experiment indicates that the plasma is anomalous rather than neoclassical because plasma parameters do not scale with $(E/T_e)^2$ but correlate well with the percentage density fluctuation level. The stability condition is satisfied with the criterion of $\delta(\ln P_e U^\gamma) > 0$ for the flute mode.

We found the plasma stored energy density $(3/2 n_e T_e)$ for the cold component to be restricted between the values

$$4.5 \times 10^{13}\ \mathrm{eV/cm^3} < 3/2\, nT < 9 \times 10^{13}\ \mathrm{eV/cm^3}\ .$$

The lower limit does not depend on the heating power and results from the nonequilibrium or instabilities associated with the low-frequency broadband fluctuations. The upper limit is phenomenologically related to the hot electron instabilities. However, it is not clear that it results from the instabilities. The upper limit has a heating power dependence.

We found that there is an attractive pressure region where the electron density increases with the electron temperature. This implies that the stabilization of the hot electron modes is an important issue to improve the plasma parameters in this type of the confinement system.

---

*Cairo University, Giza, Egypt.

2.1.21 Power Flow in ELMO Bumpy Torus

S. Hiroe, J. R. Goyer, L. Solensten, and B. H. Quon

In discussing the power flow in EBT, we note that $(60 \pm 5)\%$ of the gyrotron output power is related to plasma transport, and 80% of this power is lost convectively. This convection results from the open potential contours (mainly on the surface plasma), the elimination of $\nabla \mathbf{B}$ and $\mathbf{E} \times \mathbf{B}$ drift near the annulus, and the horizontal electric field. The horizontal electric field is never eliminated in the present experiment and may be related to the equilibrium. Thus, 20% of the transport power can travel around the torus. However, this power correlates well with the percentage fluctuation level. When the error field $\delta B/B$ becomes larger than 2×10^{-4}, the energy loss due to the error field is comparable with the convection, so the effect from the field error is not significant in the present machine.

The global confinement time in the nonequilibrium C-mode is about 100 μs. It is 100 to 200 μs in the T-mode. Even if the contribution from the warm part of the electron distributions is counted, the energy confinement time is still less than 300 μs.

2.1.22 Abstract of "Inherent Magnetic Field Error Measurements in ELMO Bumpy Torus"[27]

T. Uckan

The inherent magnetic field error and its radial distribution in the closed-field-line device of EBT have been measured with an electron beam probe. It is found that the field error is almost radially uniform and is about $\Delta B \leqslant 4$ G at an average field of $B \simeq 7.2$ kG. This yields $\Delta B/B \simeq 5 \times 10^{-4}$, which is large enough to open the confined drift surfaces of the toroidally circulating electrons as a result of field-error-dominated large radial shifts. By using two pairs of correction coils (loops) around the device, this inherent field error has been successfully reduced to a level of 10^{-4} or less.

2.1.23 Abstract of "Direct Reading Fast Microwave Interferometer for EBT"[28]

T. Uckan

A simple and inexpensive 4-mm, direct reading, fast (rise time $\sim$ 100 μs) microwave interferometer is described. The system is particularly useful for density measurements on EBT during pulsed operation.

2.1.24 Pulsed Experiments in the Collisional Electron Regime

F. M. Bieniosek, J. B. Wilgen, R. K. Richards, J. A. Cobble, D. L. Hillis, S. Hiroe, T. Uckan, and T. L. White

Experiments have been performed on the EBT-S device to study plasma parameters and transient response under the collisional electron regime $\nu_c/\nu_d > 1$ in the presence of the slowly decaying hot electron ring. Under these conditions, the electron distribution function is more nearly Maxwellian, and the plasma transport may be dominated by effects different from those in the steady-state T-mode. These experiments are performed

by various combinations of gas puffs lasting several milliseconds and rapid switching of the 28-GHz microwave power between two levels. During these experiments, time evolution of the electron energy distribution was measured by Thomson scattering, Al III line ratio techniques, and soft X-ray measurements. Time evolution of the spatial electron distribution was measured by microwave interferometers in the midplane and throat.

The primary goal of these experiments was to determine whether, with the existing EBT-S device, substantially improved performance could be obtained by operating in the collisional regime to reduce direct particle losses. Little evidence of improvement was found in the experiments. In spite of average ring beta $\langle\beta\rangle \approx 8\%$ (the 100-kW experiments), the ratio of stored core energy (as determined by Thomson scattering) to microwave power input is comparable during a gas puff to the steady-state C-mode and is no better than before the gas puff. A rapid turndown in power level provides a convenient method to study the collisional regime; however, the difference between performance in the high-power and in the low-power states is small.[29]

2.1.25 Dynamic Measurements of Electron Energy Confinement

J. B. Wilgen, R. K. Richards, D. L. Hillis, J. A. Cobble, and T. L. White

The purpose of these measurements is to determine confinement properties from the dynamic response of the plasma and thereby to establish a second independent method for measuring the electron energy confinement time and for investigating mechanisms of electron energy transport in EBT.[30] The appeal of this approach is that it does not require accurate knowledge of either the heating rate or the energy content of the plasma, both of which must be well known for the usual steady-state determination of the energy confinement time.

Two methods of measurement have been explored. In the first, the ECH power is pulse modulated to examine the plasma response to a step function in the heating rate. In the second, a sinusoidal perturbation is superimposed on the ECH power, allowing measurement of the transfer function of plasma parameters (i.e., amplitude and phase) as a function of modulation frequency.

For the step function response, the ECH power is pulse modulated with an amplitude ranging from 5% for small modulation to 80% for large-amplitude modulation. The plasma response (primarily the electron energy) is monitored with an array of diagnostics, including Thomson scattering to measure the temperature and density of the bulk electrons, soft X-ray measurements to monitor the energetic electron tail, a spectroscopic aluminum impurity line ratio technique that is sensitive to the mean electron energy, and a microwave interferometer to measure the line-averaged electron density. Under the assumption that the profile does not change significantly, the temporal behavior of the total (volume-integrated) electron energy content of both bulk and tail components can be inferred from these measurements.

The Thomson scattering and interferometer data show that the electron temperature dominates the response of the core plasma, tracking changes in the ECH power in a manner consistent with roughly constant electron energy confinement. Changes in electron density are smaller by an order of magnitude. The electron temperature, as shown by the Thomson scattering data (Fig. 2.18), responds very quickly to each step discontinuity in

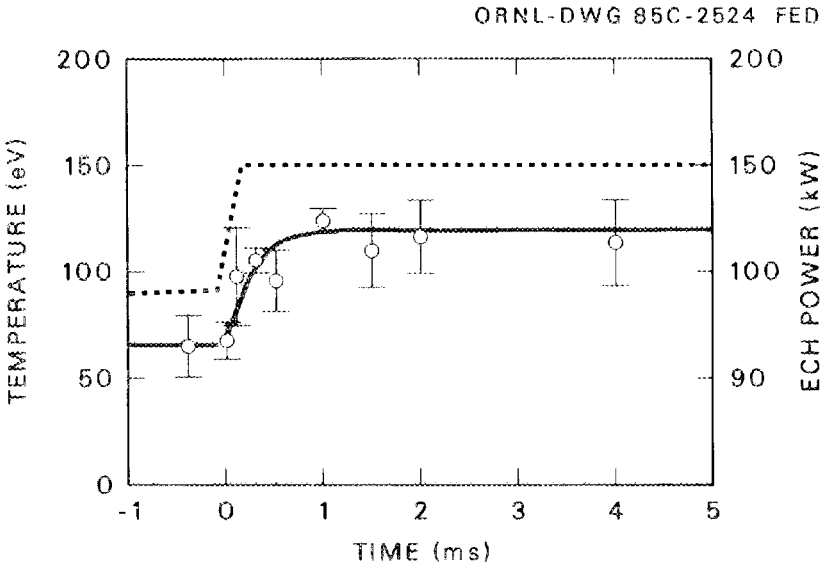

Fig. 2.18. Thomson scattering data showing the response of the bulk electron temperature following a step increase in the ECH power from 90 to 150 kW.

the heating rate, showing an e-folding equilibration time of roughly 0.3 ms, after the finite switching time of the ECH power is taken into account.

The response of the electron tail, as evidenced by the soft X-ray measurements, is quite different, showing large excursions in both the density and the temperature of the tail component. For example, a 40% modulation in the heating rate results in a factor of four change in the tail density and a factor of two change in the tail temperature. The time evolution of the density and temperature waveforms can be quite complex, with the temperature waveform showing a time delay and a tendency to overshoot. However, the density-temperature product is nearly exponential in shape, and it is consistent with an e-folding time in the range from 0.6 to 1.4 ms. The aluminum line ratio measurement, which is sensitive to the mean electron energy, gives a result that is intermediate between these two cases.

For measurements of the transfer function of the plasma, only the aluminum line ratio temperature data are available. A 5% sinusoidal amplitude modulation is superimposed on the ECH power with a frequency in the range from 10 Hz to 2 kHz. Once again, the dominant plasma response is in the electron temperature. For T-mode operation, the amplitude of the electron temperature response is very large, exceeding 30%, and shows only a modest rolloff in amplitude for modulation frequencies above 400 Hz (Fig. 2.19). The phase lag of the temperature waveform, relative to the ECH power waveform, shows an unexpectedly large phase shift of almost 400° as the modulation frequency is increased from 10 Hz to 1 kHz. In comparison, the amplitude of the density response is smaller by

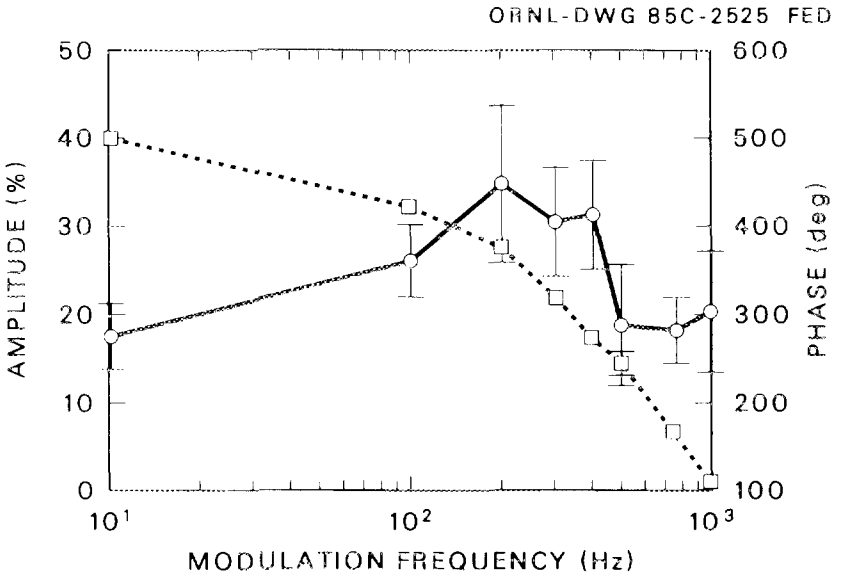

Fig. 2.19. Amplitude (circles) and phase (crosses) of the electron temperature perturbation as a function of modulation frequency.

an order of magnitude. However, the measured phase lag is very similar to the temperature data. Above 200 Hz, the phase shift data are suggestive of a time delay of ~0.8 ms. Taking this into account, the transfer function data are consistent with an electron energy confinement time of <0.5 ms.

When EBT is operated at higher neutral gas pressure (C-mode), where the electron tail is not observed, then the experimental results more nearly correspond to the simple solutions of the electron energy balance equation expected for a single-component plasma with constant confinement. For example, the amplitude of the temperature waveform is greatly reduced and comparable to the 5% amplitude of the ECH power waveform.

2.1.26 A Comparative Measurement of the Particle Confinement Time in EBT

R. K. Richards and J. C. Glowienka

The neutral density and the particle confinement time in EBT-S have been determined by two different techniques. These involve a spectroscopic measurement and a fast-ion decay measurement from a diagnostic neutral beam. The results from these measurements are displayed in Figs. 2.20, 2.21, and 2.22. Both diagnostics exhibit a strong dependence of the particle confinement time on the fill gas pressure but only a weak dependence on the heating power. Although both diagnostics exhibit identical trends for the particle confinement time, the results differ by a factor of 2 to 3.

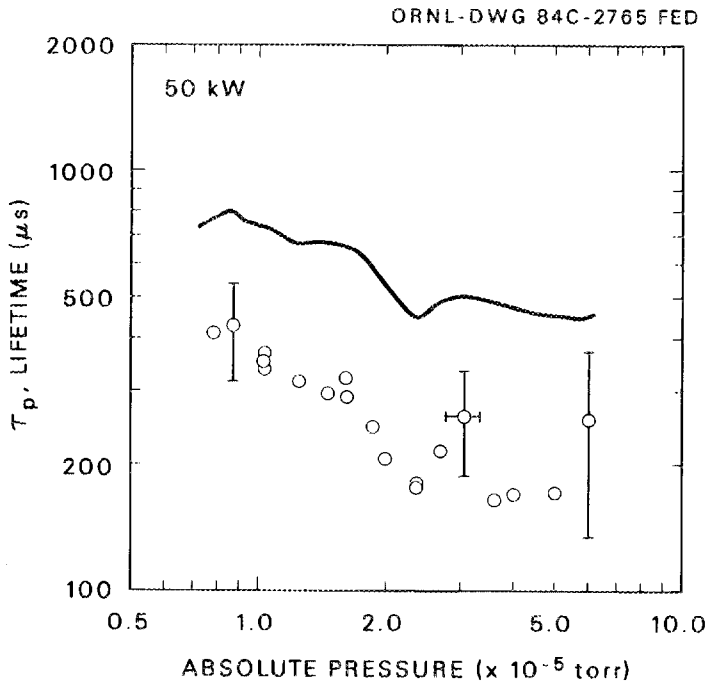

Fig. 2.20. The variation of the particle confinement time τ_p as a function of fill gas pressure with a constant microwave heating power P_μ = 50 kW. The open circles represent results from the fast-ion decay measurements, and the solid curve is from spectroscopic measurements.

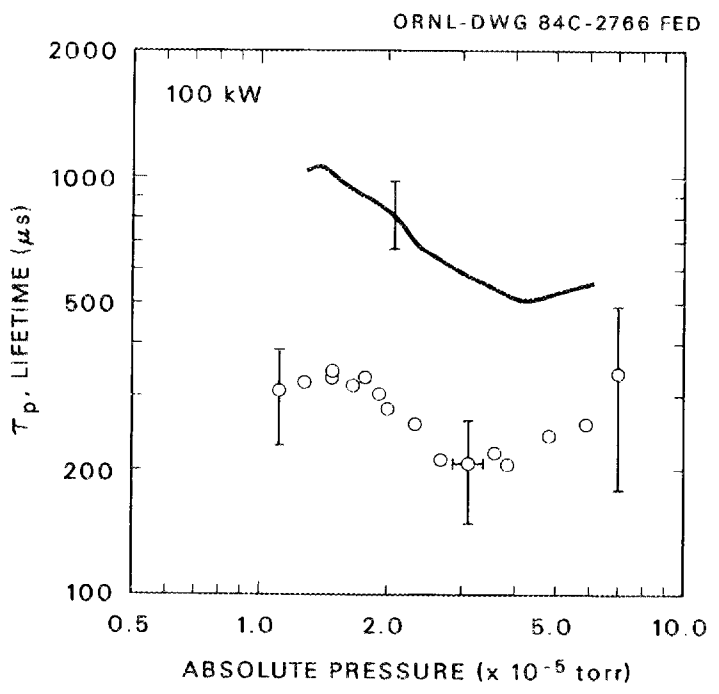

Fig. 2.21. Variation of τ_p as in Fig. 2.20 for P_μ = 100 kW.

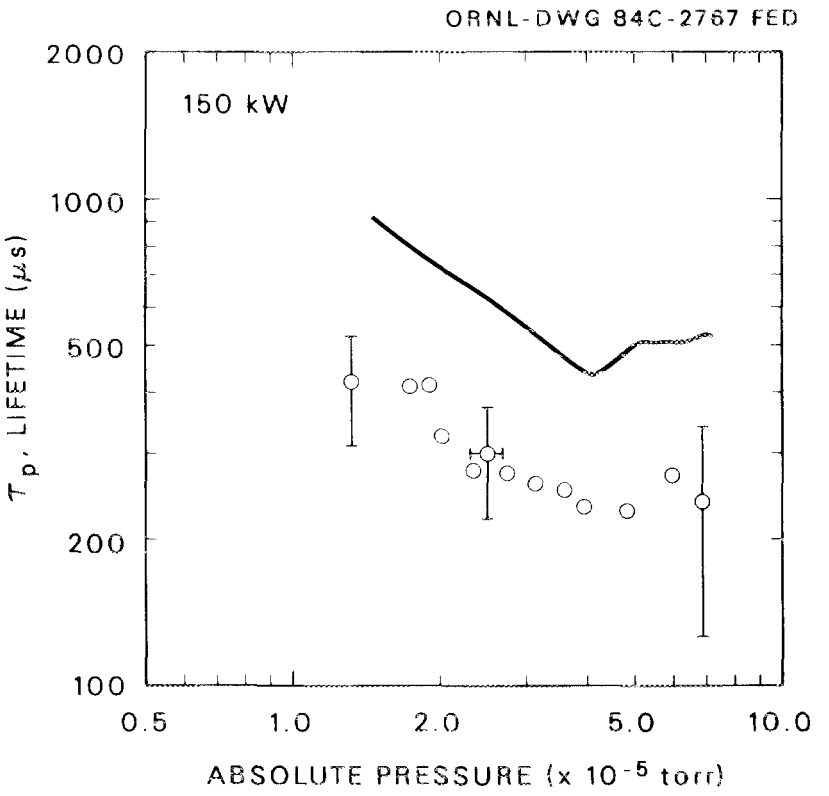

Fig. 2.22. Variation of τ_p as in Fig. 2.20 for P_μ = 150 kW.

The neutral density is related to the particle confinement τ_p by

$$\sum_j n_j s_j = \frac{1}{\tau_p} ,$$

where n_j is the neutral density of atomic and molecular hydrogen and s_j is the respective ionization rate. Each of the diagnostics measures a property of the neutral density to determine the particle confinement time. In the spectroscopic measurement, the photon emissions from atomic and molecular hydrogen are measured separately to determine the individual densities; then these are combined for calculating the particle confinement time. In the fast-ion decay diagnostic, fast ions are created in the plasma with a diagnostic neutral beam. The decay rate of these fast ions on the background neutral population, both atomic and molecular, is then measured to estimate the neutral density.

The observed variation of τ_p with fill gas pressure and microwave power can be expected from the parameters of electron density and electron temperature in EBT. For $n_e\ell \sim (1\text{–}3) \times 10^{13}$ cm^{-2}, the molecular neutrals are strongly attenuated, but the atomic

Franck-Condon neutrals are only weakly attenuated. Therefore, the neutral density will vary roughly as the fill gas pressure and the particle confinement time as the inverse of the fill gas pressure. At very high fill gas pressure, the electron temperature decreases to a point at which the ionization rate of the neutrals is reduced, and the particle confinement time can increase with increasing fill gas pressure.

The variation of the particle confinement time with microwave power can be understood by the dependence of the electron density. In EBT the electron density increases slowly with microwave power; since the neutrals are only slightly attenuated, the particle confinement can only be expected to show a weak increase with increasing power.

2.1.27 H_α Laser Fluorescence Measurements of Neutral Hydrogen Densities

R. Mahon

2.1.27.1 Experiment details

A schematic of the H_α fluorescence experiment is shown in Fig. 2.23. The flashlamp-pumped dye laser used for this experiment was a Candela SLL-66 coaxially pumped system. Using a sulforhodamine 640 dye dissolved in methanol, the laser produced ~80 mJ at 6563 Å in a 200-ns pulse. With a 25-μm, air-spaced etalon, the full-width, half-intensity bandwidth was 0.75 Å; with a 10-μm etalon, the bandwidth was 3 Å, as measured with a 1-m Jarrell-Ash spectrograph. Two 6563-Å mirrors were used to steer the laser beam through a hole in the lead wall and through the median plane of the W5 cavity on EBT. A Suprasil lens with a 70-cm focal length was used to focus the light at the 6-in.-long, 0.375-in.-diam, microwave absorber; otherwise, the laser power in the interaction zone was significantly reduced, and the light reflected off the microwave absorber walls, producing

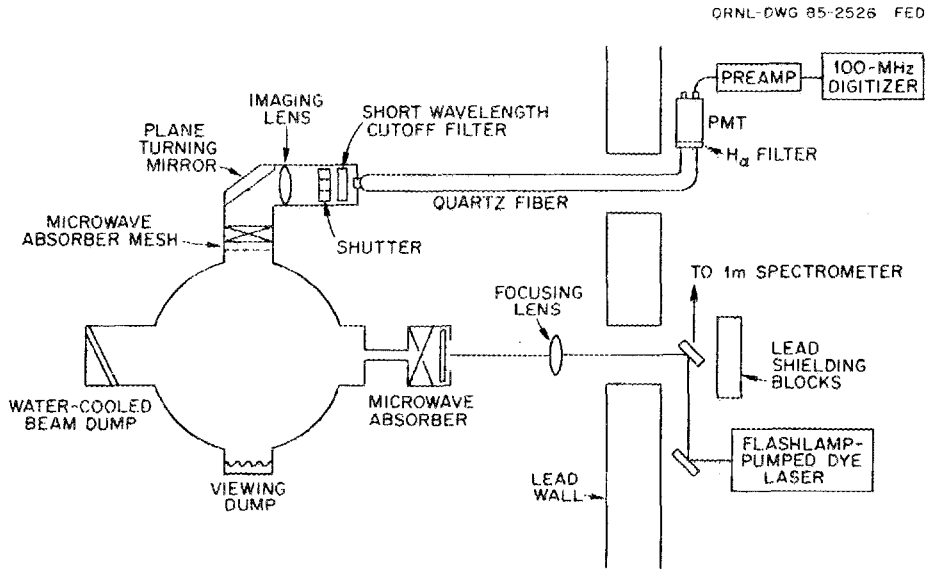

Fig. 2.23. Schematic diagram for the H_α scattering experiment performed on EBT.

unacceptably large stray light levels. With this focusing arrangement, the beam was 7 mm in diameter in the center of EBT, and approximately 40% of the energy from the dye laser transited the cavity.

The blackened horn that we originally tried as a beam dump proved inadequate in attenuating the direct laser beam. A dramatic decrease in stray light level, of one to two orders of magnitude, was observed when the water-cooled, Brewster-angled, blue glass beam dump was transferred from the Thomson scattering experiment. A plane 10-cm-diam turning mirror, followed by a 7-cm-diam Suprasil lens with a focal length of 20 cm at an object distance of 73 cm, imaged a 1-cm-diam section from the center of EBT onto a quartz fiber optics bundle placed 27.5 cm from the lens. Between the lens and the fiber were installed a 10-ms shutter and a short-wavelength cutoff filter that only transmits wavelengths longer than 6400 Å. The quartz fiber bundle was long enough to transport the scattered signal out beyond the lead wall. The entrance to the fibers is circular, and they exit through a 1- by 11-mm slit. The light exits at $f/7.7$ and is incident on an 80-Å bandpass filter with 51% peak transmission. We could not use a more narrow (5-Å) bandpass filter that was available without adding more elements to the system to provide a region of collimated light. Extreme rays of the $f/7.7$ beam see the central transmission peak shifted by 26 Å, which creates the need for a much broader bandpass filter in this case. The filter was placed against the exiting fibers, and a Hamamatsu R928 photomultiplier (with a photocathode area of 8 by 24 mm, well in excess of the exiting beam size) came directly after the filter. We originally tried to use a GaAs R636 photomultiplier tube (PMT) with a 12% quantum efficiency at 6563 Å. However, the photocathode degraded after just a few days of use, and the mean anode current of the R636 is only 1μA. Hence, we changed to a general multialkali PMT (R928) with a 6% quantum efficiency and a potential 0.1-mA anode current. This, together with the 10-ms shutter (which had to be installed inside the lead enclosure, just in front of the fiber entrance), cut the ambient H_α plasma radiation to an acceptable level. Even so, the anode current had to be regularly checked when EBT was operating at high pressures and high microwave powers to ensure linearity of the PMT. For instance, our data recorded at 100 kW of 28-GHz power were taken with just 450 V on the PMT so that radiation observed during the 10-ms shutter exposure time did not saturate the PMT when EBT was operated at pressures of up to 40 μtorr of H_2.

The essential part of the amplification in the detection system was a Hewlett-Packard, non-dc-coupled, 100$\times$ amplifier. This unit observed only signals between 1 kHz and 150 MHz and so did not amplify the constant-level, 10-ms, plasma background H_α pulse. The scattered signals were subsequently processed by a 100-MHz Transiac digitizer, in which consecutive shots could be stored and later averaged, thereby improving the signal statistics.

Whenever the machine was run in D_2, as opposed to H_2, there was a deleterious effect on the stray light level due to sputtering of aluminum from the walls. Centimeter-sized aluminum flakes were deposited in the viewing dump, partially blocked the 0.375-in.-diam microwave absorber, and coated the input quartz window.

Our original aim of illuminating a 1-cm^3 volume in the center of EBT was dictated by the size of the quartz fiber bundles available for our use and by the minimum object distance at which we could place the Suprasil collection lens so as to maximize the collection

solid angle. However, because of the 0.375-in.-diam by 6-in.-long microwave absorber at the entrance port, we had to focus the laser beam to a beam waist just in front of the entrance window to minimize the stray light produced as the beam passed through the microwave absorber. With this configuration, the spot size was measured as a function of distance and gave a beam radius of 0.35 cm at the center of EBT. If the focusing lens was moved back in order to increase this central spot size, the stray light level was observed to rise rapidly. Hence, we were irradiating only 50% of the volume imaged at the fibers, which ideally would have been matched.

2.1.27.2 Data analysis

In analyzing the H_α fluorescence data, we made extensive use of Gohil's computations of the hydrogen level populations, which are based on a standard collisional-radiative model.[31] The change in population of the $n = 3$ level, ΔN_3^L, when irradiated with a saturating power level H_α laser, is also computed in this model. Gohil and Burgess[31] give results for tokamak plasmas with $T_e = 100$ eV and 1 keV and $n_e > 5 \times 10^{12}$ cm^{-3}. For conditions relevant to EBT (5 eV $< T_e < 100$ eV and 5×10^{11} cm$^{-3} < n_e > 3 \times 10^{12}$ cm^{-3}), Gohil provided the detailed values of N_2^0, N_3^0, N_3^L, and ΔN_3^L needed to derive neutral density values from our H_α scattered signals. At present, the code does not include level-populating processes involving direct molecular hydrogen dissociation into excited levels. These processes are important in tokamak wall regions and in the EBT plasma, especially at low microwave powers, and could account for some of the observed discrepancies among the various neutral density measurements made on EBT. We hope to incorporate the molecular populating processes more systematically in the future. Figures 2.24 and 2.25 show our derived values of neutral density vs the absolute pressure (equal to twice the ion gage reading) when EBT-I was operating with 40 kW of 18-GHz microwave power. We plot results from the scattered H_α data and from the background H_α data taken at the same time. The background data give a mean density that is a factor of 2 to 3 lower than the spatially resolved fluorescence data would indicate. These data were taken before the fire, when we had not done Rayleigh scattering, so the calibration was done by assuming the manufacturer's values for the transmission of the H_α filter (51%) and for the quantum efficiency of the PMT (6%) and by measuring the gain of the PMT (1.2×10^4) using a standard source. Also, the fiber bundle was measured to have a transmission of 55% and the microwave mesh an 85% throughput. The fluorescence signal F_N is given by

$$F_N = \eta A_{32} V_F \frac{\Delta\Omega}{4\pi} \int_0^{\tau_L} [N_3(t,r) - N_3(0,r)]\, dt \ ,$$

with the fluorescence volume $V_F = 0.385$ cm^3, $\Delta\Omega = 7.2 \times 10^{-3}$ sr, $A_{32} = 4.4 \times 10^7$ s^{-1}, and the efficiency $\eta = 1.3 \times 10^{-2}$. For a PMT gain $G = 1.2 \times 10^4$ and using a further 100× amplifier, the signal into the digitizer is given by

$$V_F = 1.21 \times 10^{-9}\, \Delta N_3^L$$

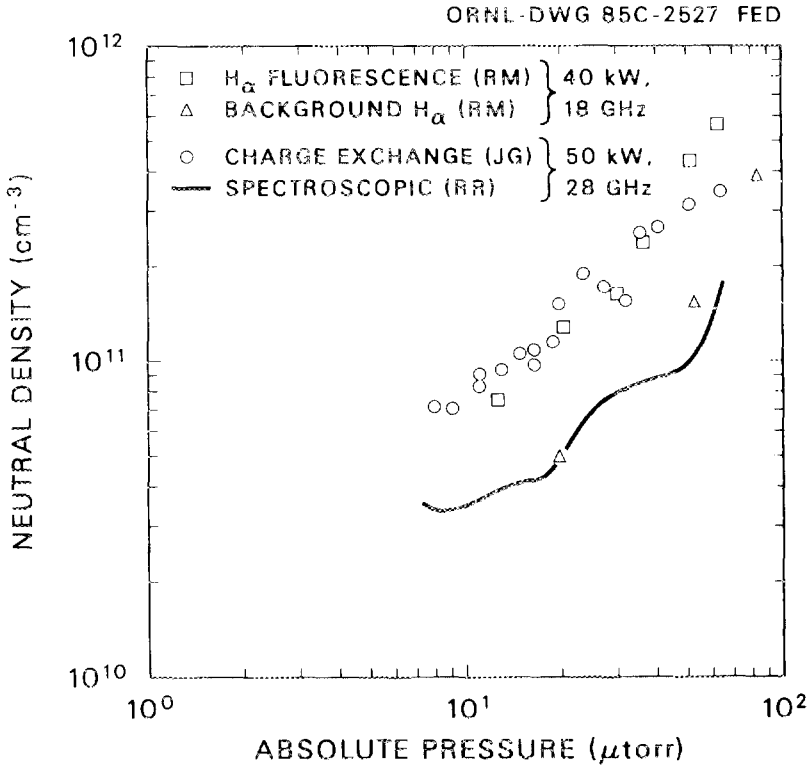

Fig. 2.24. Neutral atomic densities as determined by H_α fluorescence in the center of EBT (open squares), by H_α background measurements (open triangles), by diagnostic neutral beams (open circles), and by H_α spectroscopic measurements (solid line).

(in volts). Thus, by measuring the fluorescence voltage signal we derive ΔN_3^L, from which, knowing n_e and T_e from Thomson scattering data, we can determine the neutral density from Gohil's computations.

Figures 2.26 and 2.27 show the density measurements made when EBT-S was operating at 100 kW of 28-GHz microwave power. Figure 2.26 shows the neutral atomic density measured by the H_α fluorescence technique compared with the diagnostic neutral beam measurements, which include molecular as well as atomic neutrals, and the H_α spectroscopic neutral density of R. K. Richards. The latter estimates the molecular contribution to be one-third of the total density, regardless of plasma conditions. Figure 2.27 shows the same H_α fluorescence data compared with just the atomic neutral density as determined by H_α spectroscopy. Note that the abscissa of Fig. 2.27 is ion gage pressure and not absolute pressure as in Figs. 2.24–2.26. For the 28-GHz data we had Rayleigh scattering data with which to calibrate. The Rayleigh scattered signal R_N is related to the fluorescence signal F_N by

$$\frac{F_N}{R_N} = \frac{\Delta N_3^L A_{32} \Upsilon_L (\pi R^2)}{N_L N_{N_2} \sigma_R} ,$$

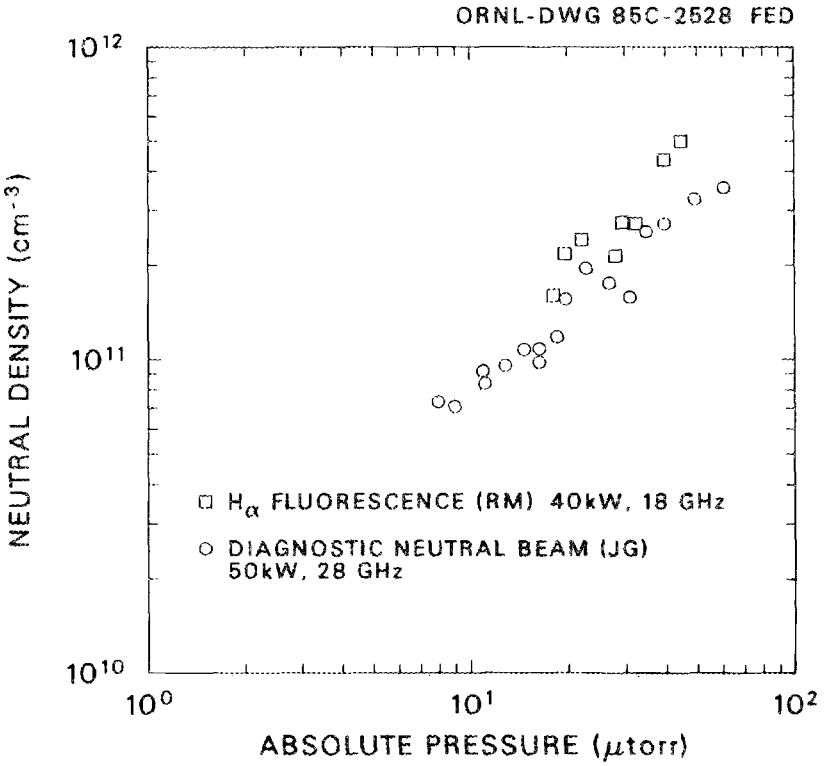

Fig. 2.25. Neutral atomic density determined by H_α fluorescence scattering (open squares) and neutral density measurements from charge-exchange measurements (open circles) made by J. C. Glowienka.

where N_L is the number of photons in the laser and is given by $N_L = (3.304 \times 10^{18})E$, with E the laser energy in joules. Since the laser is unpolarized, only $N_L/2$ photons contribute to the Rayleigh scattered signal in the observed direction. N_{N_2} is the number density of nitrogen at which the Rayleigh scattered signal R_N (minus stray light level) is measured, and $\sigma_R = 2.16 \times 10^{-27}\,cm^2$ is the Rayleigh scattering cross section at 6563 Å. We also had to take into account the fact that the laser bandwidth was 2.5 Å as measured with a 1-m Czerny-Turner spectrograph with a 0.25-Å resolution, whereas the Doppler width for the 4-eV neutrals is only 1.1 Å.

2.1.28 Abstract of *Monte Carlo Neutral Density Calculations for ELMO Bumpy Torus*[32]

W. A. Davis and R. J. Colchin

The steady-state nature of the EBT plasma implies that the neutral density inside the plasma volume will determine the particle confinement time. This paper describes a Monte Carlo calculation of three-dimensional (3-D) atomic and molecular neutral density profiles in EBT. The calculation has been done using various models for neutral source points, for

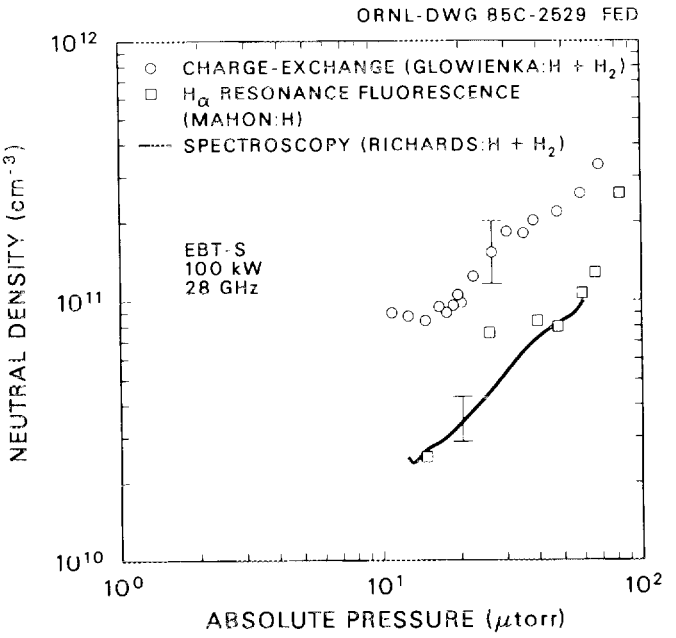

Fig. 2.26. Neutral atomic hydrogen densities deduced from H_α fluorescence scattering measurements in the center of EBT (open squares), neutral densities measured by a diagnostic neutral beam (open circles), and neutral densities measured by spectroscopic methods (solid line).

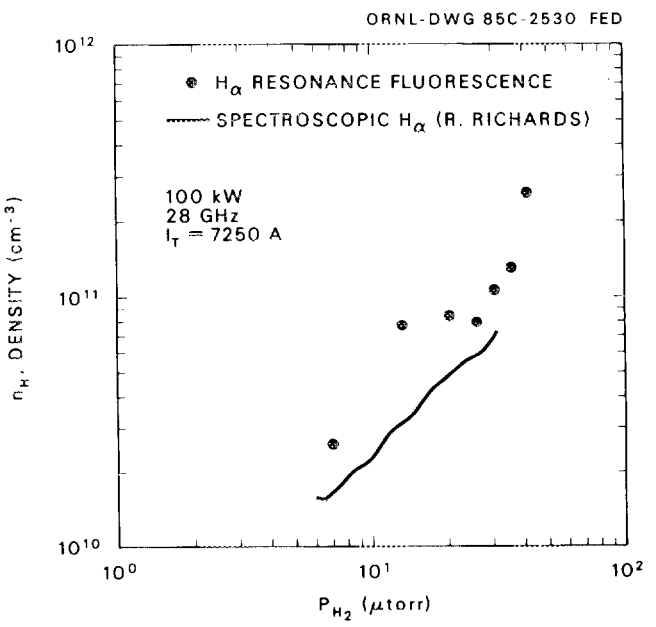

Fig. 2.27. Neutral atomic hydrogen densities as measured by H_α fluorescence from the center of EBT (open circles) and H_α spectroscopic, line-of-sight measurements (solid line).

launching schemes, for plasma profiles, and for plasma densities and temperatures. Calculated results are compared with experimental observations—principally spectroscopic measurements—both for guidance in normalization and for overall consistency checks. Implications of the predicted neutral profiles for the fast-ion decay measurement of neutral densities are also addressed.

2.1.29 The Absolute Calibration of All 24 Ion Gages on EBT

J. C. Glowienka

The ion gages on EBT were calibrated absolutely to an accuracy of ±10% by means of a spinning rotor friction gage and a simple computer code. The background cavity pressure is the most frequently changed experimental variable on EBT; yet, until recently, the absolute calibration had not been done. Absolute gage calibration was done in 1983 for a single ion gage on cavity E1 of EBT on which the neutral density diagnostic [the single-aperture reflex arc (SARA) diagnostic neutral beam system] had been mounted. Prior to absolute calibration, estimates of molecular gas density from the ion gage were lower, by a factor of 2 to 3, than estimates made from the neutral density diagnostic. With absolute calibration, the agreement between the two techniques was well within the error bars of ±10%.

The motivation to calibrate the remaining gages came from what appeared to be aperiodic and puzzling changes in the known EBT operating window as a function of background pressure. The absolute calibration was extended to all the other gages by assuming that the EBT vessel pressure was constant toroidally with no external gas feed. A dynamic test of this assumption was made by valving off all pumping and documenting, by means of a computer data acquisition system, the pressure rise as a function of time. The calibration factors relative to the absolutely calibrated gage did not vary (to within the stated accuracy of ±10%) irrespective of the time during the pressure rise.

With this calibration, in particular for gage S4 that controls the gas flow into EBT, the puzzling nature of the abrupt change in operating parameters became apparent. The changes were caused by technicians performing undocumented "leveling" of all ion gages prior to leak hunting. In this procedure, all pumping is valved off and the gages are adjusted to read the same. Fortunately, the absolute calibration of the E1 gage had been done before and after the leveling operations, with the result that the abrupt changes in operating space as monitored by gage S4 were directly related to the technicians' activities.

In summary, all 24 vacuum gages on EBT have been and can be repeatedly absolutely calibrated to ±10%. An apparent shift of EBT operating space has been explained by a gage decalibration procedure employed to aid leak hunting.

2.2 EBT-P PROJECT

H. C. McCurdy, R. A. Brown, J. W. Luc, T. J. McManamy, S. S. Shen, and C. T. Wilson

2.2.1 Introduction

The EBT Proof-of-Principle (EBT-P) project was authorized as a proof-of-principle experiment for the EBT concept. The objectives were to extend the data base for the concept, to resolve the main scientific and technology issues and, thus, to provide a definitive answer to the question of whether the concept merited continued development. Responsibility for management of the EBT-P project was assigned by the Department of Energy (DOE) to ORNL with the understanding that industry would have a major role. Project definition studies were performed in 1979 by ORNL and independently by four industrial teams. A reference design was then selected that included design features from all of the studies. Following a competitive selection process, McDonnell Douglas Astronautics Company (MDAC) was chosen in September 1980 as the primary industrial participant to design and build the EBT-P in the Oak Ridge Valley Industrial Park. The baseline cost estimate was $86 million for the device and $59 million for related technical support; scheduled completion was September 1985.

The preliminary (Title I) design was completed, and detailed design started in 1982. However, because of budget constraints and a less favorable assessment of physics performance, a phasedown of project activities was initiated in May 1983. As part of the phasedown effort, the three EBT-P development magnets were to be completed and tested to qualify them for use in the Radio-Frequency Test Facility (RFTF) being constructed at ORNL. All other technical support tasks and the EBT-P design effort were brought to an orderly halt in 1983.

2.2.2 EBT-P/RFTF Magnet Development

The EBT-P superconducting magnet development program was a joint effort by ORNL, MDAC, and General Dynamics Convair Division (GD/C) to create the technical basis for detailed design and fabrication of the EBT-P mirror magnets. As planned, the program included three development magnets, one of which was to be a prototype for the EBT-P device.

Following curtailment of the project, the EBT-P magnet development effort was refocused to aim directly at completing and testing the development magnets for use in the RFTF (see Sect. 6.3.2). The test facility will use two of the magnets, and the third will be a spare.

Two-magnet tests of development magnets D1 and D2 were completed successfully in April 1984. The magnets were energized three times to 1200 A, producing a peak field of 5.1 T at the conductor and an out-of-plane mechanical load of 73,000 lb on each magnet, which is considerably higher than the mechanical loading expected in RFTF service. Measured strains were in good agreement with predictions, and the magnets operated stably throughout the tests. The results are encouraging with respect to suitability of the magnets for RFTF; however, magnet D1 developed a small vacuum leak between the liquid helium and vacuum regions and must be repaired before use in RFTF.

Similar two-magnet tests of magnets D2 and D3 were completed successfully in June 1984. The magnets were operated at 1200 A, producing a 5.1-T peak field and a 73,000-lb out-of-plane force, for nearly one hour. As in the previous tests, there was no training; the measured strains agreed well with predictions and the heat leaks were close to expected values.

All significant objectives of the magnet development program were met. Magnets D2 and D3 are now considered qualified for the proposed use in the RFTF. Magnet D1 also performed adequately except for an internal vacuum leak that is believed to be repairable. The excellent operation of magnet D3, which was constructed entirely by GD/C as part of the cooperative effort among ORNL, MDAC, and GD/C, is convincing evidence of a successful technology transfer from ORNL to industry.

2.2.3 Project Closeout

All work authorized in the project phasedown was completed in September 1984, and direction was received from DOE to terminate the EBT-P project. A closeout plan was approved by DOE and is being implemented.

2.3 EBT ADVANCED CONCEPTS

N. A. Uckan

As part of the phasing down of the EBT program, the EBT Advanced Concepts activities were brought to completion during the middle of 1984. A conceptual design and associated costs and schedules were completed and documented for the ELMO Bumpy Square (EBS),[33] a reconfiguration of the present EBT-S device from a torus into a square with stronger magnetic fields in the corners (Fig. 2.28). An estimated time for this reconfiguration was 18 months at a cost of less than $5 million. An effort to reduce this cost and further examination of the physics of EBS and its reactor rationale will continue in 1985 within the Plasma Theory Section.

2.3.1 Innovative Bumpy Torus Configurations: Trend to Smaller EBT Reactor Systems

N. A. Uckan

Several aspects of the EBT concept make it an attractive fusion reactor concept. These include steady-state operation; simple, noninterlocking coil geometry; modularity; ease of maintenance; and accessibility. For a simple bumpy torus, however, the need to improve confinement characteristics and use the magnetic fields efficiently has led to large reactors with high power output, despite various aspect ratio enhancement schemes suggested to reduce the device size. During the past two years, attempts have been made to realize the advantages of EBT without using size as a scaling factor. A number of innovative magnetic configurations have been developed to improve the basic bumpy torus concept. The confinement, heating, and stability properties of these new configurations are better than those of a conventional EBT but do not require an increase in size (i.e., aspect ratio). The EBS, one of these new configurations, uses hot electron rings (formed by ECH) in bumpy straight sections on the sides to provide MHD stability (as in EBT), with high-field

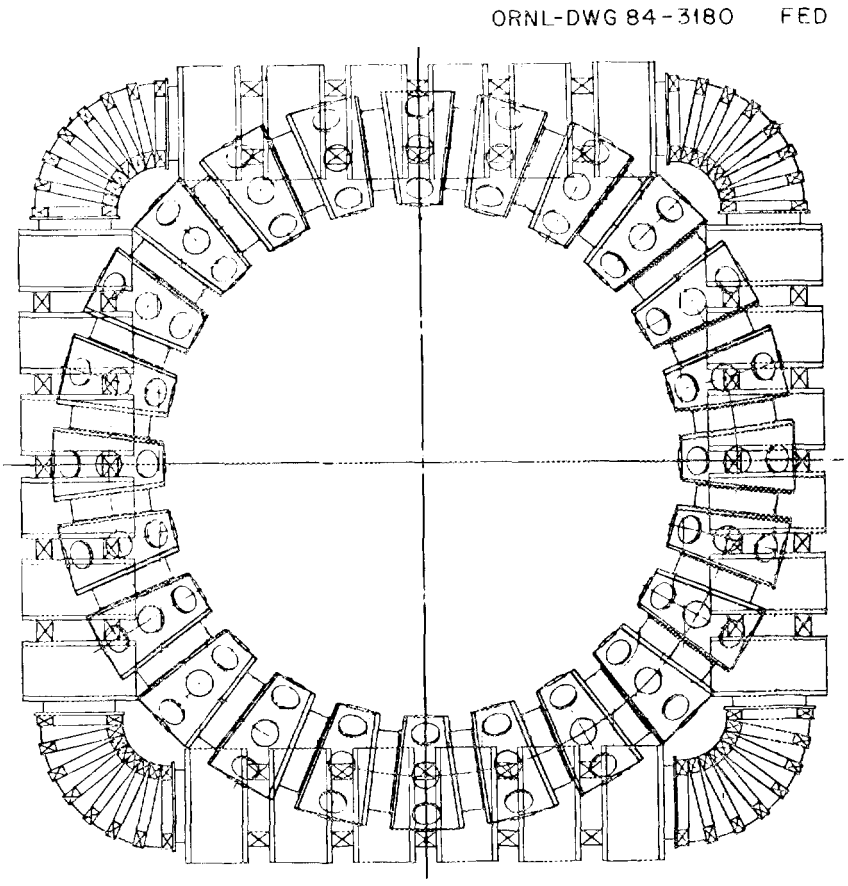

Fig. 2.28. EBT-S and EBS reference configurations.

corners to minimize the toroidal effects and thus improve particle confinement. Bumpiness of the field provides the equilibrium and drift surface closure. Reactor projections for EBS show that it may be substantially smaller (a factor of 2 to 4) than past EBT designs. The continuing trend to smaller EBT reactor systems is summarized in Fig. 2.29.

The underlying physical constraint that has severely limited the performance of present experiments (EBT-S and Nagoya Bumpy Torus) has been associated with poor single-particle confinement; that is, large drift-orbit-induced losses. This results from toroidal effects inherent in these devices that result in substantial direct particle losses, inefficient heating geometry, less-than-optimal ring formation, and asymmetric equipotential surfaces. Novel magnetic configurations have been studied in attempts to minimize the toroidal effects through innovative coil design and arrangement (as in the Andreoletti torus, known as EBTEC), through localizing the toroidal effects in regions of high magnetic field (as in EBS), or through hybridization of the bumpy torus and the stellarator [as in the twisted racetrack (TRT), ELMO Snakey Torus, and others]. The EBS is particularly attractive because of its intrinsic desirability as a reactor configuration (Fig. 2.28) and its ability to resolve critical EBT issues for near-term investigation.

ORNL-DWG 84-2300 FED

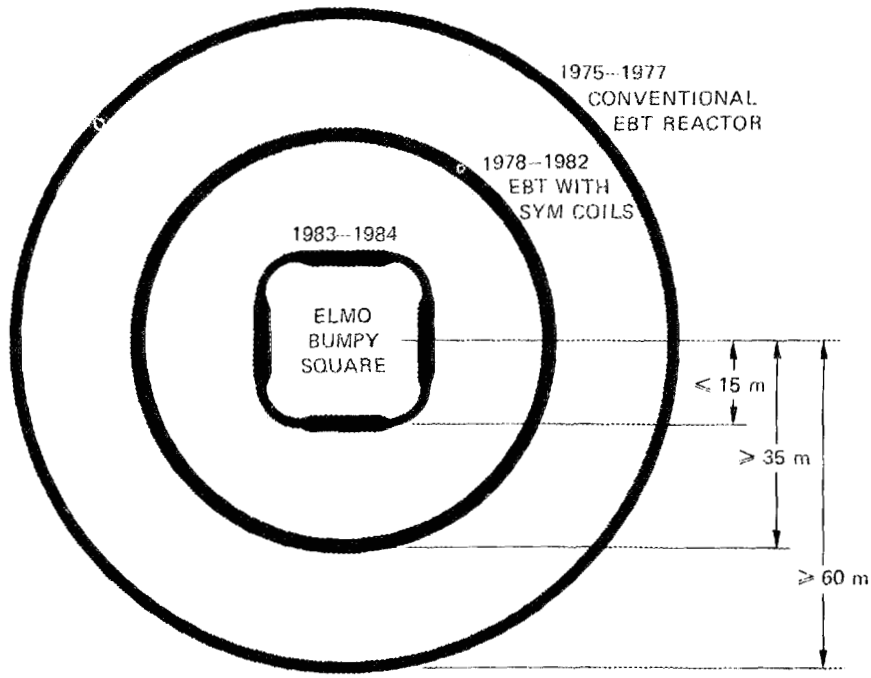

Fig. 2.29. Trend to smaller EBT reactor systems exploited by EBT-S.

Detailed calculations in the areas of magnetics, transport, equilibrium, stability, and heating have yielded the following results:

- The configurations (EBS, TRT, EBTEC, etc.) with nearly concentric drift orbits and greatly reduced velocity-space loss regions have better use of magnetic volume, significantly reduced direct particle losses, more symmetric potential surfaces, and increased microwave heating efficiency.
- In configurations with nearly axisymmetric fields (EBS, TRT), high-beta, hot electron rings will be much more easily formed with reasonable ECH power, and the rings will be well centered, with little or none of the radial broadening that occurs in a conventional EBT. This should make it easier to form an average magnetic well and thus to have strong MHD stabilization at high toroidal core plasma pressures and pressure gradients.
- In configurations with high-field corners (EBS), both the equilibrium surface shifts ($\xi \sim M_G^{-3/2}$) and confinement time ($\tau \sim M_G^2$) improve with the global mirror ratio M_G, which is defined as B_{max}(corners)/B_{min}(sides). In addition, Monte Carlo calculations indicate an order-of-magnitude increase in diffusion lifetimes associated with symmetric potentials, which are expected in EBS.

- Fokker-Planck calculations show that configurations (such as EBS) in which the heating zone is well separated from the direct particle loss zone and in which there is a large geometric separation between the fundamental and second-harmonic resonance surfaces of ECH have much lower ECH-driven losses through unconfined orbits (5- to 10-fold reduction from EBT) and much higher heating efficiency.

These improvements in magnetics, confinement, heating, and equilibrium lead to smaller reactor sizes. The EBS, along with several of the other new concepts, shows a reduction in size by a factor of 2 to 4, to a major radius of about 15 m, compared with values of 30 to 60 m for earlier devices (Fig. 2.29).

A 15-m-radius EBS configuration was evaluated using the criteria established by the generic reactor study (see Chap. 11 of this report). The results suggest that EBS can be developed into an attractive reactor with a mass utlization competitive with that of other attractive fusion reactor candidates.

2.3.2 Abstract of *ELMO Bumpy Square*[33]

N. A. Uckan, C. L. Hedrick, D. A. Spong, T. Uckan, L. A. Berry, L. W. Owen, D. K. Lee, W. E. Bryan, T. J. McManamy, P. B. Thompson,* and W. L. Wright

The EBS is formed by four linear arrays of simple magnetic mirrors linked by four high-field toroidal solenoids (corners). The EBS configuration offers a number of distinct advantages over a conventional EBT with respect to particle confinement, heating, transport, ring production, and stability. In EBS the particle drift orbits are nearly concentric for trapped and passing particles. The velocity-space loss region for transitional particles (near the boundary between trapped and passing zones) at high energy is greatly reduced, leading to improved volume utilization, significantly reduced direct particle losses, and increased microwave heating efficiency. The combination of nearly concentric particle drift orbits and small radial displacements in the high-field corners gives an order of magnitude reduction in neoclassical diffusive losses. The orbits of the deeply trapped particles ($v_\parallel/v = 0$) and core plasma pressure surfaces ($\oint d\ell/B$ contours) almost coincide and are centered on the minor axis. Because there is no shift, hot electron rings will be exceedingly well centered in EBS. For the same anisotropy ($v_\perp/v_\parallel$) in EBS, there should be little or none of the radial broadening of the ring that occurs in EBT. This should make it easier to form an average magnetic well in EBS than in EBT. Detailed calculations in the areas of equilibrium and stability indicate that equilibria exist (shifts are smaller in a square configuration than in a torus), and the stability limits (especially those associated with the corners) are no more restrictive than those studied for a conventional EBT. Conceptual design of the EBS, involving the modification and reconfiguration of the present EBT facility, has been completed. Reactor projections for EBS indicate the possibility of a substantial reduction in reactor physical size (a factor of 2 to 3) as compared to past EBT designs.

---

*Engineering Division, Martin Marietta Energy Systems, Inc.

2.3.3 Assessment of Magnetic Field Asymmetries in EBS

T. Uckan and N. A. Uckan

Two separate and independent field asymmetries exist in EBS. The first is associated with the small perturbations in the magnetic fields known as field errors and is caused by coil misalignments during installation, imperfect coil windings, proximity of magnetic materials, etc. The second is due to the magnetic field ripple in the high-field toroidal solenoids (corners), which is produced by the finite number of coils. In general, these two sources of asymmetry introduce enhanced transport losses (in addition to other effects) in the system, although they affect different classes of particles. Toroidally passing (circulating) particles ($v_\parallel/v \sim 1$) are influenced by the field errors, and trapped particles ($v_\parallel/v \sim 0$) in the corners are influenced by the field ripple.

The EBS geometry consists of linear segments of simple mirrors that are linked by sections of high-field toroidal solenoids, as shown in Fig. 2.30. The toroidal effects are localized in the corners. An ideal EBS has the same characteristics as an ideal EBT: a closed-field-line configuration with zero rotational transform and no toroidal current. This

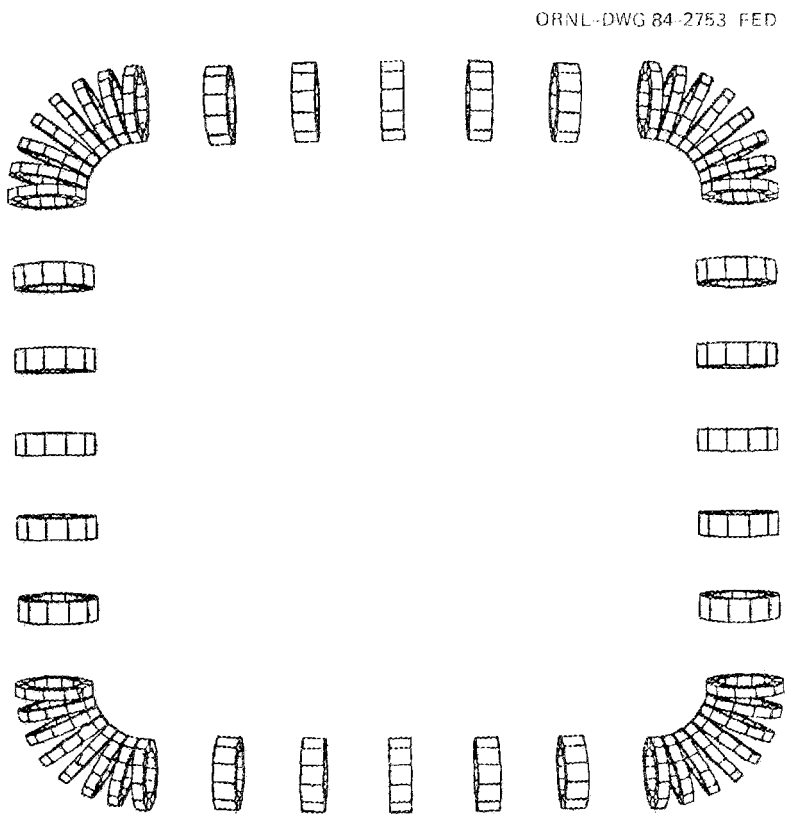

Fig. 2.30. Geometry of an EBS configuration (top view of coil arrangement).

current-free equilibrium configuration is very sensitive to the system magnetic field asymmetries (field errors). If these field errors are large enough, they can cause field lines to spiral out of the confinement volume (enhanced losses), thus degrading confinement.

We have estimated the maximum tolerable field error $\delta B/B$ and the corresponding constraint on coil alignment. Numerical calculations of field errors due to single-coil misalignments indicate that field line closure is most sensitive to angular misalignments ($\Delta\theta$ and $\Delta\phi$). Errors in absolute spatial positions have very little (if any) effect. A misalignment of 1° in one coil orientation causes an error $\delta B/B \sim 10^{-4}$, whereas a misalignment of 1 cm in one coil location yields $\delta B/B \sim 10^{-6}$–10^{-7}. Statistical analysis of errors from N coils (where $N = N_s + N_c$, with N_s the number of coils in straight sections and N_c the number of coils in curved sections), assuming that errors in all N coil alignments are randomly distributed in a Gaussian fashion, is in reasonable agreement with the numerical calculations. We define a critical error field $(\delta B/B)_{crit}$ such that if $\delta B/B > (\delta B/B)_{crit}$ the drift surfaces of toroidally passing particles become open. From the requirement of closed drift surfaces, we find $\delta B/B < (\delta B/B)_{crit} \sim \rho/\langle R_c \rangle$, where ρ is the Larmor radius and $\rho/\langle R_c \rangle$ is the average magnetic radius of curvature around the torus. For an experimental-size device, the required $(\delta B/B)_{crit} \sim (1\text{–}3) \times 10^{-4}$, and for a reactorlike device, $(\delta B/B)_{crit} \lesssim 10^{-5}$.

Next we consider the effect of toroidal field ripple (due to the discrete coils in the high-field corners) on transport. In the presence of ripple, there is a new class of so-called locally trapped particles in the corners. These particles oscillate (are trapped) in the field minimum (local magnetic well) between coils (those coils that produce the toroidal solenoid field in the corners) that are localized in the toroidal direction and experience a unidirectional toroidal drift that leads to the ripple-enhanced diffusion. Especially in the low collisionality (ν/Ω) regime, ripple-induced losses could lead to significant increases in diffusion and thermal conductivity and may be the determining factor in transport of particles and energy. We have calculated the enhanced transport coefficients associated with the ripple-induced drifts and compared them with the EBT neoclassical diffusion coefficients to determine the allowable range for field ripple magnitude. For neoclassical losses to dominate (or for ripple losses to be negligible), ripple-induced losses from the toroidal solenoid sections should be smaller than the neoclassical losses from the straight sections. In simplest form, the diffusion coefficient associated with ripple is $D^\delta \sim \delta^{3/2} v_d^2/\nu$, where

$$\delta = \frac{(B_{max} - B_{min})}{(B_{max} + B_{min})} \simeq \left(\frac{\Delta B}{B_0}\right)_{corner}$$

is the ripple well depth, v_d is the toroidal drift velocity, and ν is the 90° collision frequency. The neoclassical diffusion coefficient (in the collisionless regime) for EBT is $D^{NC} \sim \nu(v_d/\Omega)^2$, where Ω is the precessional drift frequency. For $D^\delta < D^{NC}$, we find $\delta < (\nu/\Omega)^{4/3}$. For $\nu/\Omega \sim 0.1$, representative of existing experiments, the magnitude of the ripple well depth should be only a few percent to prevent ripple losses from dominating. For very low collision frequencies ($\nu/\Omega \sim 0.01$, representative of reactorlike plasmas), δ must be <0.5%. These estimates for ripple magnitude are somewhat pessimistic because we have

neglected (1) the effect of poloidal variation in ripple magnitude and (2) the influence of the ambipolar electric field, both of which play important roles.

2.3.4 Magnetics Calculations for an EBS

R. T. Santoro, N. A. Uckan, and R. J. Schmitt*

Calculations have been carried out to determine the vacuum magnetic parameters, the forces, and the usefulness of trim coils in an EBS. A configuration with five mirror coils on each side and eight coils in each toroidal solenoid corner was studied. Favorable magnetic fields are achieved in this device. An on-axis mirror ratio of 1.9, a global mirror ratio of 3.6, and excellent centering of plasma pressure contours are achieved. Particle losses are minimal (<5%). The magnetic forces acting between coils are comparable with those encountered in the EBT-I/S magnet configuration. Circular trim coils were found to be suitable for restoring hot electron ring locations that are displaced when the coil currents are varied to perform magnetic studies or to assess the effects of the global mirror ratio on EBS.

---

*McDonnell Douglas Astronautics Company, St. Louis.

2.3.5 Abstract of *An EBT Reactor Systems Analysis and Cost Code: Description and User's Guide (Version 1)*[34]

R. T. Santoro*, N. A. Uckan, J. M. Barnes,† and D. E. Driemeyer‡

An EBT reactor systems analysis and cost code that incorporates the most recent advances in EBT physics has been written. The code determines a set of reactors that fall within an allowed operating window determined from the coupling of ring and core plasma properties and the self-consistent treatment of the coupled ring-core stability and power balance requirements. The essential elements of the systems analysis and cost code are described, along with the calculational sequences leading to the specification of the reactor options and their associated costs. The input parameters, the constraints imposed upon them, and the operating range over which the code provides valid results are discussed. A sample problem and the interpretation of the results are also presented.

---

*Engineering Physics and Mathematics Division.
†Computing and Telecommunications Division, Martin Marietta Energy Systems, Inc.
‡McDonnell Douglas Astronautics Co., St. Louis.

REFERENCES

1. L. A. Berry et al., "Recent Advances in Confinement and Heating Physics on EBT-S," in *Proceedings of the 10th International Conference on Plasma Physics and Controlled Nuclear Fusion Research (London, 1984)*, Int. Atomic Energy Agency, Vienna, in press, 1985.

2. D. W. Swain et al., "The Electron Distribution Function in ELMO Bumpy Torus," *Phys. Fluids*, accepted for publication (1985).

3. D. L. Hillis, G. R. Haste, and L. A. Berry, "Electron Confinement Studies on the EBT-S Bumpy Torus Experiment Using Soft X-Ray Techniques," *Phys. Fluids* **26**, 820–9 (1983).

4. J. A. Cobble and L. Bighel, "Thomson Scattering Diagnostic for a Low-Density, High-Temperature, Steady-State Plasma," *Rev. Sci. Instrum.* **53**, 436 (1982); J. A. Cobble, "Thomson Scattering at Plasma Densities Below 10^{12} cm^{-3}," *Rev. Sci. Instrum.* **56**, 73–76 (1985).

5. R. K. Richards, "Analysis of EBT Plasmas and Confinement Including Electron Temperature Measurements from Inner Shell Ionization," p. 42 in *Proceedings of the 4th Topical Conference on Atomic Processes in High-Temperature Plasmas (Princeton, N.J., 1983)*.

6. N. H. Lazar et al., "Spatial Distribution of Impurities and H Neutrals in ELMO Bumpy Torus (EBT)," *Nucl. Fusion* **19**, 571–82 (1979).

7. E. Dullni et al., "Measurement of the Density and Velocity Distribution of Sputtered Al in EBT-S by Laser-Induced Fluorescence," *J. Nucl. Mater.* **111 & 112**, 61–66 (1982).

8. D. B. Batchelor for the EBT Experimental Group and EBT Theory Group, "Comparison of Electron Cyclotron Heating Theory and Experiment in EBT," p. 779 in *Heating in Toroidal Plasmas: Proceedings of the Fourth International Symposium, Rome, March 1984*, ed. H. Knoepfel and E. Sindoni, vol. II, International School of Plasma Physics and ENEA, Varenna, Italy, 1984.

9. J. A. Cobble, *Thomson Scattering on ELMO Bumpy Torus*, ORNL/TM-9471, Oak Ridge Natl. Lab., December 1984.

10. T. Uckan, "Electron Temperature Measurements from Induced Toroidal Current in ELMO Bumpy Torus-Scale," *Rev. Sci. Instrum.* **56**, 250–4 (1985).

11. D. L. Hillis et al., *Electron Confinement in the ELMO Bumpy Torus Without the Influence of Hot Electron Rings—The Ring Killer Experiment*, ORNL/TM-9475, Oak Ridge Natl. Lab., 1985; also submitted to *Phys. Fluids*.

12. D. L. Hillis et al., *An Experimental Determination of the Hot Electron Ring Geometry in EBT-S and Its Implications for Bumpy Torus Stability*, ORNL/TM-9494, Oak Ridge Natl. Lab., 1985; also submitted to *Phys. Fluids*.

13. K. H. Carpenter and R. F. Steimle, *Research Support for Plasma Diagnostics on ELMO Bumpy Torus: Diamagnetic Measurements and Data Analysis, and Development of Ring Models for Realistic Representations of Fields Near the Plasma*, ORNL/Sub-7676/5, Oak Ridge Natl. Lab., October 1984.

14. D. A. Rasmussen et al., *High Field Launch ECH Experiments in EBT*, ORNL/TM-9399, Oak Ridge Natl. Lab., 1985; also submitted to *Phys. Fluids*.

15. T. S. Bigelow, D. A. Rasmussen, and D. B. Batchelor, "Fundamental and 2nd Harmonic Resonance Polarized Microwave Absorption Measurements on EBT," *Bull. Am. Phys. Soc.* **29**, 1428 (1984).

16. D. A. Rasmussen et al., *Multiple-Frequency Electron Cyclotron Heating of Hot Electron Rings in EBT-I*, ORNL/TM-9372, Oak Ridge Natl. Lab., 1985; also submitted to *Phys. Fluids.*

17. T. L. White et al., "The EBT-S 28-GHz, 200-kW, cw, Mixed-Mode Quasi-Optical Plasma Heating System," *Int. J. Infrared Millimeter Waves* **5**, 1129–52 (1984).

18. T. L. White, H. D. Kimrey, and T. S. Bigelow, "Mixed-Mode Distribution Systems for High Average Power Electron Cyclotron Heating," p. 1444 in *Heating in Toroidal Plasmas: Proceedings of the Fourth International Symposium, Rome, March 1984*, ed. H. Knoepfel and E. Sindoni, vol. II, International School of Plasma Physics and ENEA, Varenna, Italy, 1984.

19. H. D. Kimrey, T. L. White, and T. S. Bigelow, "Performance of 28-GHz, 200-kW, cw, Gyrotron Oscillators on the ELMO Bumpy Torus-Scale (EBT-S) Experiment," *Bull. Am. Phys. Soc.* **29**, 1256 (1984).

20. T. L. Owens, F. W. Baity, and W. A. Davis, "Ion Heating in the Range of High Ion Cyclotron Harmonics on EBT," *Nucl. Fusion* **24**, 1561–72 (1984).

21. W. H. Casson et al., "Far-Infrared Laser Diagnostic on EBT and Extreme Far-Forward Laser Scattering on ISX," in *Proceedings of the 5th Topical Conference on High Temperature Plasma Diagnostics (Tahoe City, Calif., 1984)*; W. H. Casson, Ph.D. thesis, The University of Tennessee, Knoxville.

22. L. Solensten et al., "EBT Plasma Potential Measurements," *Bull. Am. Phys. Soc.* **29**, 1418 (1984).

23. L. Solensten, Ph.D. thesis, Rensselaer Polytechnic Institute, Troy, N.Y., 1985.

24. S. Hiroe et al., "Experimental Study of Electrostatic Equilibrium in EBT," to be submitted to *Phys. Fluids.*

25. J. R. Goyer, *Measurements of Temperature and Density on the ELMO Bumpy Torus Using a Heavy Ion Beam Probe*, Ph.D. thesis, Rensselaer Polytechnic Institute, Troy, N.Y., 1984.

26. S. Hiroe et al., "Effect of Fluctuation and Potential on EBT Confinement," *Bull. Am. Phys. Soc.* **29**, 1234 (1984); to be submitted to *Phys. Fluids.*

27. T. Uckan, "Inherent Magnetic Field Error Measurements in ELMO Bumpy Torus," *Rev. Sci. Instrum.* **56**, 90–93 (1985).

28. T. Uckan, "Direct Reading Fast Microwave Interferometer for ELMO Bumpy Torus," *Rev. Sci. Instrum.* **55**, 1874 (1984).

29. F. M. Bieniosek, W. B. Ard, and J. F. Pipkins, "EBT-S Experiments," in *ELMO Bumpy Torus Physics: Final Report*, MDC E2805, McDonnell Douglas Astronautics Co., St. Louis, August 1984.

30. J. B. Wilgen et al., "EBT Electron Energy Confinement Experiments," in *Proceedings of the 1984 International Conference on Plasma Physics (Lausanne, Switzerland).*

31. P. Gohil and D. Burgess, "A Comparison Between Laser Induced Fluorescence at Balmer-Alpha and at Lyman-Alpha for the Measurement of Neutral Hydrogen Densities in Magnetically Contained Fusion Plasmas," *Plasma Phys.* **25**, 1149 (1983).

32. W. A. Davis and R. J. Colchin, *Monte Carlo Neutral Density Calculations for ELMO Bumpy Torus*, ORNL/TM-9502, to be published at Oak Ridge National Laboratory.

33. N. A. Uckan et al., *ELMO Bumpy Square*, ORNL-9110, Oak Ridge Natl. Lab., 1984.

34. R. T. Santoro et al., *An EBT Reactor Systems Analysis and Cost Code: Description and User's Guide (Version 1)*, ORNL/TM-9026, Oak Ridge Natl. Lab., 1984.

Chapter 3

Atomic Physics and Plasma Diagnostics Development

R. A. Phaneuf,[1] Program Manager

P. M. Bakshi[2]	J. W. Hale[1]	C. R. Mahon[12]
C. F. Barnett[1]	C. C. Havener[8]	E. W. McDaniel[11]
C. A. Bennett[3]	T. G. Heil[9]	R. H. McKnight[13]
C. Bottcher[1]	A. M. Howald[8]	F. W. Meyer[1]
D. H. Crandall[4]	H. T. Hunter[1]	T. J. Morgan[14]
N. G. Demas[5]	D. P. Hutchinson[1]	F. M. Ownby[15]
H. B. Gilbody[6]	R. K. Janev[10]	M. S. Pindzola[16]
D. C. Gregory[1]	M. I. Kirkpatrick[1]	P. A. Staats[1]
D. C. Griffin[7]	K. O. Legg[11]	E. W. Thomas[11]
P. M. Griffin[1]	C. H. Ma[1]	K. L. Vander Sluis[1]

---

1. Physics Division.
2. Consultant, Boston College, Boston, Mass.
3. Oak Ridge Associated Universities Faculty Research Participant, University of North Carolina, Asheville.
4. Present address: Office of Fusion Energy, U.S. Department of Energy, Washington, D.C.
5. Oak Ridge Associated Universities Faculty Research Participant, Tennessee Technological University, Cookeville.
6. Consultant, Queen's University, Belfast, Northern Ireland.
7. Research subcontract, Rollins College, Winter Park, Fla.
8. Oak Ridge Associated Universities postdoctoral research associate.
9. Collaborator, University of Georgia, Athens.
10. Consultant, Institute of Physics, Belgrade, Yugoslavia.
11. Consultant, Georgia Institute of Technology, Atlanta.
12. Student participant, University of Virginia, Charlottesville.
13. Consultant, National Bureau of Standards, Gaithersburg, Md.
14. Consultant, Wesleyan University, Middletown, Conn.
15. Program secretary.
16. Research subcontract, Auburn University, Auburn, Ala.

CONTENTS

SUMMARY OF ACTIVITIES 3-5
3.1 EXPERIMENTAL ATOMIC COLLISIONS 3-6
3.1.1 ECR Multicharged Ion Source 3-6
3.1.2 Electron-Capture Cross-Section Measurements 3-10
3.1.3 Ion-Atom Merged-Beams Experiment 3-13
3.1.4 Electron-Impact Ionization of Multicharged Metallic Ions 3-15
3.1.5 Single, Double, and Triple Electron-Impact Ionization of Xe^{6+} 3-17
3.1.6 New Electron-Ion Crossed-Beams Apparatus 3-21
3.1.7 Radiometric Standard for the Extreme Ultraviolet 3-22
3.2 ATOMIC THEORY 3-25
3.2.1 Low-Energy Charge Exchange 3-25
3.2.2 Code Development for Electron-Ion Scattering 3-27
3.2.3 Direct and Indirect Ionization of Transition Metal Ions 3-28
3.2.4 Dielectronic Recombination in the Lithium Isoelectronic Sequence 3-28
3.2.5 The Effect of Electric Fields on Dielectronic Recombination in Ions of the Lithium and Sodium Isoelectronic Sequences 3-30
3.3 CONTROLLED FUSION ATOMIC DATA CENTER 3-33
3.4 PLASMA DIAGNOSTICS DEVELOPMENT 3-34
3.4.1 Multichannel Polarimetry Using Faraday Rotation 3-34
3.4.2 Diagnostics Development Center 3-37
3.4.3 Feasibility of Alpha Particle Diagnostics by CO_2 Laser Thomson Scattering 3-39
REFERENCES 3-46

3. ATOMIC PHYSICS AND PLASMA DIAGNOSTICS DEVELOPMENT

Summary of Activities

The activities within this program are divided between atomic collisions research and plasma diagnostics development. The majority of this research is supported through the ORNL Fusion Program but is carried out within the Physics Division.

The experimental atomic collisions research focuses on inelastic processes that are important in determining the energy balance and impurity transport in high-temperature plasmas and in diagnostic measurements. This activity is not directed toward a particular fusion device but concentrates rather on developing a better basic understanding of collision processes involving highly ionized atoms at the relatively low kinetic energies that are characteristic of fusion plasmas. During the past year, the majority of this research has concerned inelastic collisions of multiply charged ions with both electrons and neutral atoms. Strong interaction with the theoretical atomic physics activities has guided the selection of experiments and has provided new challenges for theory. Significant progress has been made in our understanding of electron-impact ionization of ions and particularly of the important role of indirect ionization mechanisms. The characterization of electron capture by partially stripped ions at low energies remains a difficult theoretical problem, and our experiments have provided a basis for the evaluation of various approximations. Experiments have continued to address the lower kinetic energies that are appropriate to the edge or scrapeoff plasma. A new electron cyclotron resonance source of low-energy, highly charged ions has been implemented during this period for atomic collision experiments. This facility has expanded our experimental capabilities to considerably more highly ionized systems than have been previously accessible to us. The ability to extend our measurements along isoelectronic and isoionic sequences will permit tests of various scaling laws and will challenge the limits of our understanding of atomic collision processes. The atomic physics group also operates the Controlled Fusion Atomic Data Center, which searches and categorizes publications on atomic collisions and prepares and distributes bibliographies and compilations of recommended atomic data to the fusion research community.

The plasma diagnostics program has concentrated on the development of optically pumped, continuous-wave, far-infrared laser systems during the past year. In addition to density measurements via interferometry, Faraday rotation of the polarization of submillimeter-wavelength laser radiation has been developed as a probe of plasma magnetic fields. Full simultaneous five-channel operation of the interferometer/polarimeter system on the Impurity Study Experiment was achieved during the period. The diagnostic has routinely yielded time-dependent plasma density profiles from the multichordal interferometric data and has demonstrated the potential for determining the spatial current distribution in a tokamak from chordal magnetic field data. During this reporting period, a

study of the feasibility of pulsed CO_2 laser Thomson scattering as a diagnostic for fusion-produced alpha particles in ignited plasmas was completed, and work on the development of this diagnostic was initiated. The Diagnostics Development Center has continued to identify and evaluate both the need and the potential for particular new plasma diagnostics and to participate in selecting them and initiating their development in universities and industry. A subcontract was awarded to develop a diagnostic for the measurement of static and time-varying electric fields in plasmas.

3.1 EXPERIMENTAL ATOMIC COLLISIONS

3.1.1 ECR Multicharged Ion Source

F. W. Meyer and J. W. Hale

Construction and installation of the electron cyclotron resonance (ECR) multicharged ion source was completed on schedule early in FY 1984. Although the ECR ion source was designed for operation at 10.6 GHz, initial source testing was carried out at 2.45 GHz in order to gain experience in source operation before the 10.6-GHz microwave amplifier was delivered in June 1984.

During the initial testing phase at 2.45 GHz, X-ray measurements of the bremsstrahlung spectrum produced by the source provided evidence of ECR heating of electrons. A calibrated Si-Li X-ray detector indicated electron energies up to 160 keV. Following construction and installation of the beam line and charge analyzer in March 1984, source performance could be assessed more directly by measuring charge-state distributions of extracted beams. Even at the lower microwave frequency, fully stripped carbon beams were obtained; these were used to initiate the first planned experiment involving the new source, total cross-section measurements of electron capture by fully stripped light ions incident on atomic hydrogen. Operation of the source at its design frequency of 10.6 GHz started on schedule in June 1984. Since that time, efforts toward source optimization have been carried out in parallel with the cross-section measurements.

The salient features of the ECR ion source, shown in Fig. 3.1, are summarized in Table 3.1. The source consists of two stages and is quite similar in size to MINIMAFIOS.[1] The first stage, which supplies plasma to the second stage to facilitate startup, is operated in overdense mode.[2] A helical slow-wave launcher[3] is used to inject 2.45-GHz microwaves into the first stage, which is located in an axial magnetic field of 5 to 7 kG. Plasma density is controlled by the microwave power level and gas pressure, which varies in the range from 10^{-3} to 10^{-4} torr. Since microwave absorption in the first stage is nonresonant, the magnetic field can be tuned to optimize second-stage performance. The second stage is separated from the first stage by two stages of differential pumping, which is sufficient to maintain low pressure (10^{-6} torr) in the second stage during source operation.

ORNL-PHOTO 8247-84

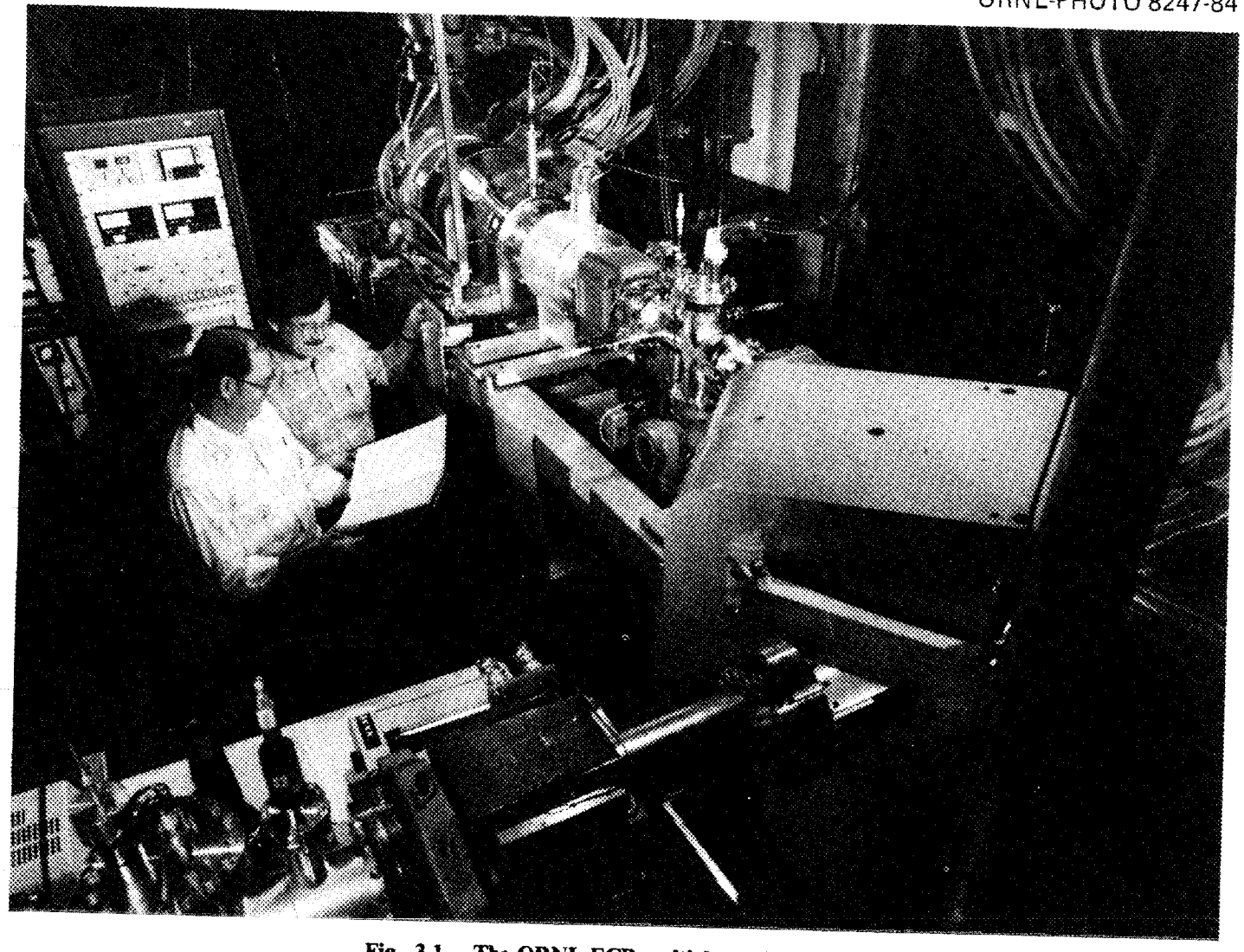

Fig. 3.1. The ORNL ECR multicharged ion source.

Table 3.1. ORNL ECR source parameters

Microwaves	
First-stage 2.45-GHz power, W (300 W max)	50–200
Second-stage 10.6-GHz power, W (2200 W max)	20–800
Magnetic fields	
Mirror ratio	1.6
Hexapole field at vacuum wall, T	0.4
Field in extraction plane, T	0.45
Field in first stage, T	0.5–0.7
Total solenoid power, kW	60
Vacuum (operating condition)	
First-stage pressure, torr	$(1–10) \times 10^{-4}$
Second-stage pressure, torr (1×10^{-7}-torr base)	$(1–6) \times 10^{-6}$
Extraction, torr	1×10^{-7}
Beam line pressure, torr (2×10^{-9}-torr base)	2×10^{-8}
Dimensions	
Solenoid ID, cm	18
Solenoid OD, cm	40
Hexapole ID, cm	9.5
Hexapole length, cm	33
Vacuum wall ID (second stage), cm	8.6
Anode aperture, cm	0.5
Extraction aperture, cm	0.8
Extraction gap, cm	2.6

In the second stage, electrons confined in a minimum-*B* configuration are heated by resonant absorption of 10.6-GHz microwaves that are injected radially immediately following the differential pumping section. The minimum-*B* configuration is produced by the superposition of an axial mirror field and a radial hexapole field. Three conventional water-cooled solenoids are used to establish the axial magnetic field.[4] The hexapole field is produced by a compact assembly[4,5] of $SmCo_5$ permanent magnets positioned around the cylindrical vacuum wall of the second stage. The permanent magnet assembly is cooled by

water circulation through the voids created between cylindrical vacuum wall and the duodecagon defined by the placement of the $SmCo_5$ bars.

In the mechanical design, care was taken to ensure ease of assembly and access. The source divides into three sections, each of which is separately supported by, and can be rolled freely on, precision tracks. The three solenoidal field coils are supported by a similar track structure and can be moved freely about to expose otherwise inaccessible source parts during source disassembly or to change the axial mirror ratio in the second stage while the source is fully assembled.

Ion extraction is accomplished by a three-element extraction electrode, the first two elements of which can be biased independently for ion focusing and prevention of electron backstreaming. The positions of the anode and the extraction electrode and the size of the extraction gap itself can be varied by the use of shims. An electrostatic unipotential lens operated in "accel" mode[6] images the extracted beam onto the entrance slit of a stigmatic 90° magnetic charge analyzer having a 40-cm radius of curvature. The entrance slit assembly is located about 100 cm downstream of the source anode; object and image distances for the 90° magnet are 80 cm. Retractable Faraday cups located immediately after the entrance and exit slits are used to measure total extracted beam currents and charge-selected beam intensities, respectively. Both entrance and exit slit assemblies feature independently adjustable horizontal and vertical slit jaws, to which current can be measured. An electrostatic quadrupole lens located downstream of the exit slits can be used to transport the charge-selected beam to experiments requiring maximum beam intensities.

Before the 10.6-GHz microwave system was delivered, the ECR ion source was operated at an interim frequency of 2.45 GHz. In order to maintain roughly the same ratio of hexapole to axial magnetic field strength at the lower frequency, only 6 of the 12 $SmCo_5$ bars were used, reducing the strength of the hexapole by a factor of 2. An additional 25% decrease in hexapole strength was obtained by shimming out the bars to their maximum radius, determined by adequate clearance to the solenoidal field windings.

Operation of the source at the lower frequency was far from optimum, due mainly to poor coupling between the second-stage plasma and the 2.45-GHz microwaves. Due to their longer wavelength, only a few modes propagated in the second-stage cavity; microwave absorption seemed to occur preferentially on the microwave injection side of the second stage, which is furthest removed from the extraction region. Even in this mode, the high-charge-state capability of the new source significantly exceeded that of the ORNL PIG ion source. Figure 3.2 shows a typical charge-state distribution for argon source gas obtained at this frequency. For light-ion production, beams up to fully stripped ^{13}C (10^{-14} A) and up to H-like O (10^{-12} A) were produced at the lower frequency.

Significant improvement in source performance was obtained, as expected, after installation of the 10.6-GHz microwave system, in terms of both total extracted beam intensity and mean charge state of the extracted beams. Microwave absorption increased dramatically, as evidenced by very low reflected power (typically less than 10%) during source operation. Optimum charge-state distributions were obtained for a second-stage mirror ratio of about 1.6, significantly below the 2.1 mirror ratio attainable at maximum second-stage field coil separation. Figure 3.3 shows a measured charge-state distribution obtained for argon with the source operating at 10.6 GHz. As noted by other workers,[7,8] an admixture of O_2 was found to significantly increase the argon high-charge-state output of the

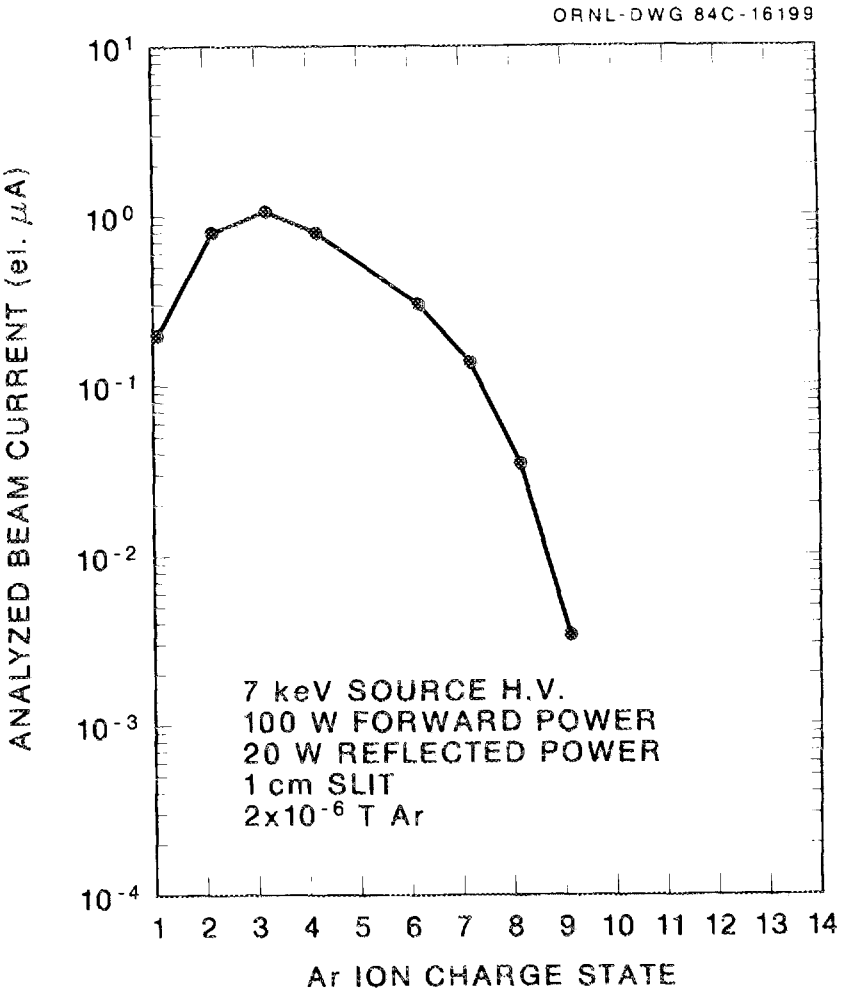

Fig. 3.2. Argon charge-state distribution from ECR ion source for 2.45-GHz operation.

source. Production of light-ion beams has yet to be optimized. So far, ^{13}C, ^{15}N, ^{18}O, ^{19}F, and ^{22}Ne beams have been obtained, with intensities varying from a few microamperes for charge states up to and including He-like ions, about 0.1–1 μA for H-like ions, and 1–50 nA for fully stripped ions.

3.1.2 Electron-Capture Cross-Section Measurements

F. W. Meyer, C. C. Havener, A. M. Howald, and R. A. Phaneuf

Measurements of total electron-capture cross sections for fully stripped and H-like C, N, O, F, and Ne ions incident on H and H_2 have been performed in the energy range from 0.2 to 10 keV/amu using ion beams produced by the new ECR multicharged ion source.

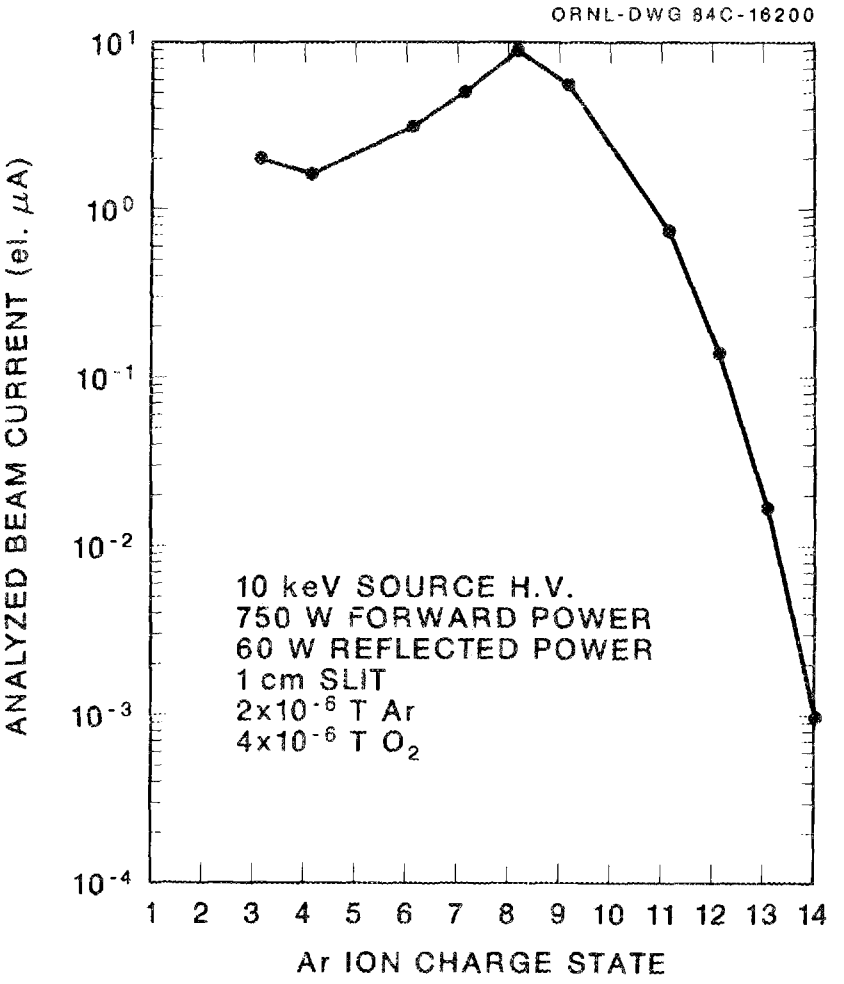

Fig. 3.3. Argon charge-state distribution from ECR ion source for 10.6-GHz operation.

While straightforward experimentally, these measurements are of significant current interest from both a basic and an applied scientific perspective; they also provide a convenient mechanism for exploring the range of operating parameters and capabilities of the new source.

The experiment employed the ORNL atomic hydrogen gas target, a directly heated tungsten tube in which molecular hydrogen is thermally dissociated. A collimation section preceding the target limited the magnetically charge-analyzed incident beam to a divergence of ± 1.7 mrad and a cross section of 1 mm inside the target. Immediately downstream of the collision target cell, charge analysis occurred in an electrostatic parallel-plate analyzer. A single channel electron multiplier (CEM) operated in pulse-counting mode was employed for particle detection. The electron-capture-signal and primary beams were measured alternately for a preselected number of cycles under computer control; the total

electron-capture cross sections were deduced from the fraction of ions that capture an electron at a known (calibrated) target thickness.

Figure 3.4 shows typical experimental electron-capture cross-section results obtained for fully stripped and H-like oxygen ions incident on atomic and molecular hydrogen. The

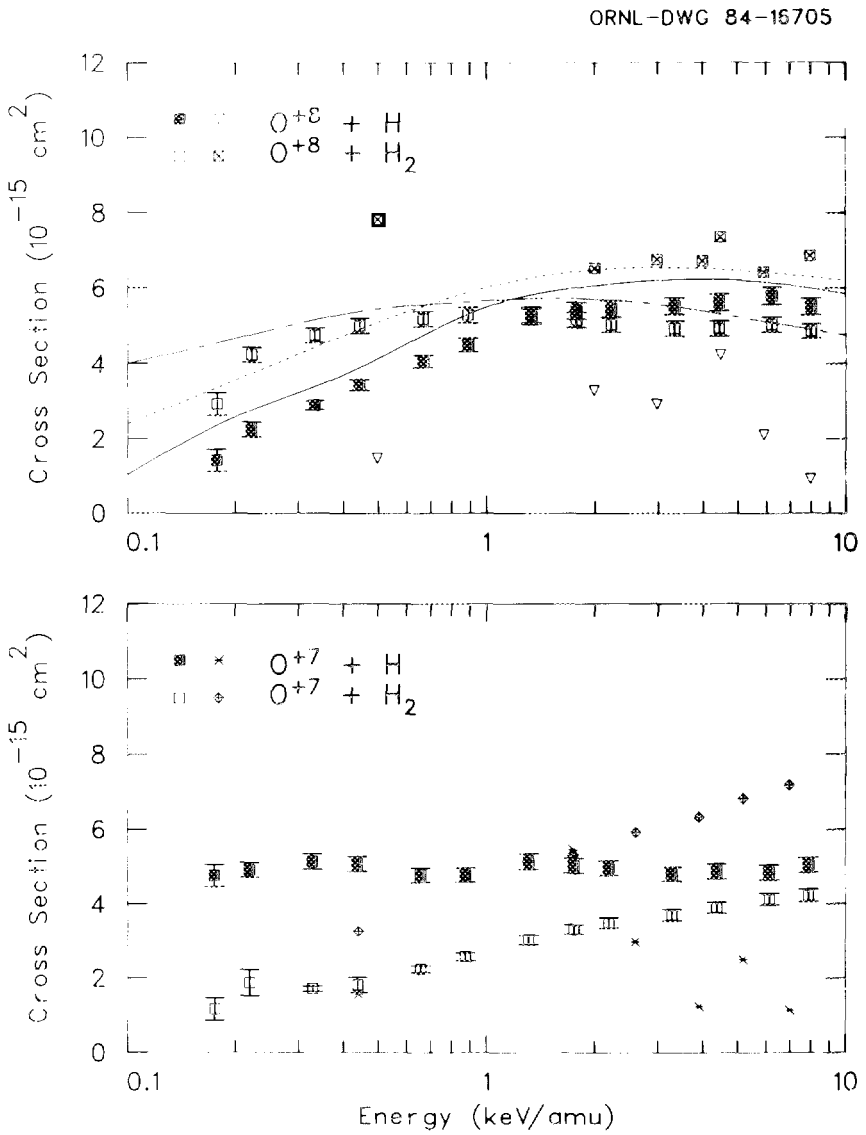

Fig. 3.4. Total electron-capture cross sections for O^{8+} and O^{7+} incident on H and H_2 vs energy. Solid and open squares: present results; solid line: AO calculation by Fritsch and Lin (ref. 9); dashed line: MO calculation by Shipsey et al. (ref. 10); chain-dashed curve: multichannel Landau Zener calculation by Janev et al. (ref. 12); data points without error bars: measurements by Panov et al. (ref. 13). Theoretical calculations are for O^{8+} + H collisions.

error bars shown reflect random uncertainty in terms of reproducibility of the measurements at two standard deviations. Systematic uncertainties are estimated to be ±9% for both the H and H_2 cross sections. Present results are compared to theoretical predictions[9-12] and to measurements of Panov et al.[13]

In the case of the fully stripped carbon, nitrogen, and oxygen projectiles incident on hydrogen, the present measurements can be compared to theoretical calculations. Very good agreement is found between the present results for C^{6+}, N^{7+}, and O^{8+} incident on hydrogen and the close-coupling calculations of Fritsch and Lin[9] employing a modified atomic-orbital (AO) expansion. While these results fall systematically below the AO calculations, the discrepancy is less than 20% at energies above 1.5 keV/amu and approaches 40% at the lowest energies measured. For C^{6+} and O^{8+} incident on hydrogen, close-coupling calculations by Green et al.[10] and Shipsey et al.,[11] respectively, employing a molecular-orbital (MO) expansion are also in reasonable accord with the present results. The MO results lie systematically above the AO calculations by about 10% above 1.0 keV/amu and by as much as 40% at 0.2 keV/amu.

An interesting comparison can be made between the total electron-capture cross sections for fully stripped projectiles of nuclear charge Z and those for H-like projectiles of nuclear charge $Z + 1$. It is observed that the cross sections for the pairs of ions C^{6+} and N^{6+}, N^{7+} and O^{7+}, O^{8+} and F^{8+}, and F^{9+} and Ne^{9+} are nearly identical over the entire energy range covered, indicating that the projectile charge is the prime determinant of the total electron-capture cross section for these highly stripped systems. This finding is consistent with the theoretical results[10,11] that, for the fully stripped ions, electron capture occurs preferentially into high n level ($n \geqslant 4$). The presence of a tightly bound electron in the ionic core should have only a minimal effect on the behavior of the electronic wave function of these highly excited states. The interesting question of how many electrons can be added to the core before an effect *is* observed in terms of the total electron-capture cross section will be addressed in future experiments.

3.1.3 Ion-Atom Merged-Beams Experiment

C. C. Havener, H. F. Krause,* and R. A. Phaneuf

An ion-atom merged-beams experiment[14] has been developed to measure the total electron-capture cross sections for collisions of multicharged ions with hydrogen at energies in the range 1–500 eV/amu. Our aim is to extend to lower energies previous measurements made at ORNL using a pulsed laser source.[15] At such low energies, theoretical models remain essentially untested. In some multiply ionized systems, an orbiting mechanism is predicted to give very large electron-capture cross sections with a $1/v$ velocity dependence.

The current arrangement of the apparatus is shown in Fig. 3.5. A 2- to 5-kV, mass-analyzed beam of H^- from a duoplasmatron ion source passes through the optical cavity of a 1.06-μm, Nd:YAG laser, where up to 1 kW of circulating intracavity power is maintained. Up to 1% photodetachment has been achieved, producing a collimated flux of up to 2×10^{12} H^0 per second. The undetached H^- beam is electrostatically separated from the neutrals and collected in a differentially pumped beam dump. The apparatus has been operated on line using the ORNL PIG multicharged ion source, which has produced a

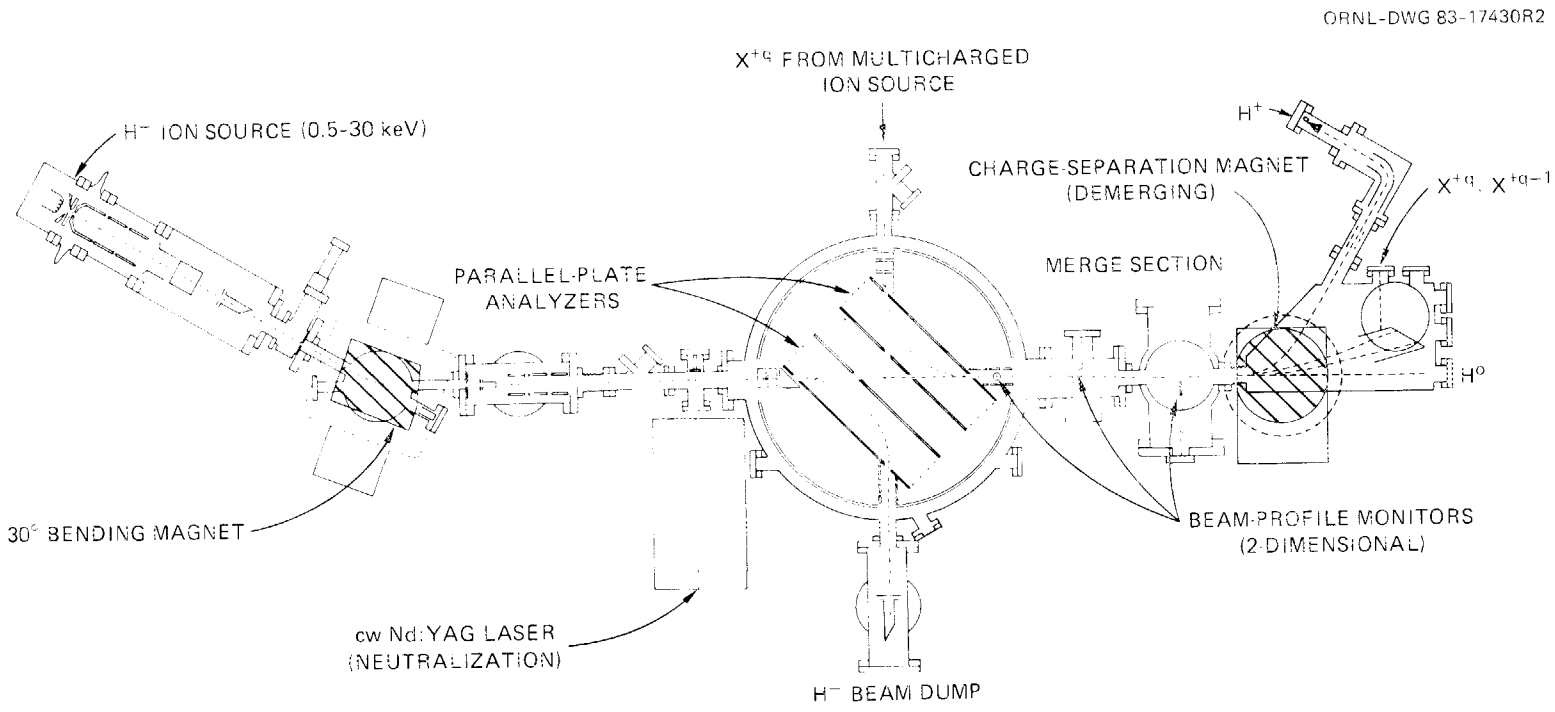

Fig. 3.5. Schematic of the ion-atom merged-beams apparatus.

highly collimated 200-nA beam of N^{3+} at 30 keV. This N^{3+} beam has been successfully merged with the H^0 beam in the 70-cm ultrahigh vacuum merge path ($p = 5 \times 10^{-10}$ torr). A two-dimensional scan of the spatial beam overlap at one position in the merge path is generated by a commercial rotating-wire beam profile monitor. Additional scans at different positions along the merged path must be made before the spatial overlap over the entire merged section can be accurately quantified. The ions are then magnetically demerged, separating the H^+ from the N^{3+}, the N^{2+}, and the neutrals. Signals in the H^+ detector resulting from the beam-beam interaction have been observed above background by modulating both the N^{3+} and H^0 beams. These beam-beam signals are only about 10 Hz, compared to 8 kHz due to the H^0 being stripped on background gas and 1 kHz due to photons emerging from the N^{q+} Faraday cup.

Modifications that are under way are expected to significantly improve the signal-to-noise ratio. The gas load from the duoplasmatron ion source will be further decoupled, reducing the pressure in the merge path, and therefore the 8-kHz background signal due to stripping, by at least a factor of 2. The H^+ signal beam will be focused and electrostatically deflected out of the plane of magnetic dispersion, ensuring detection of all of the signal and eliminating the 1-kHz background due to photons produced in the multicharged ion cup. With this decoupling of the H^+ detector from the photon background, only the N^{3+} beam need be chopped to separate the signal from the background, thereby halving the time required to acquire reasonable statistics. Within a few months these modifications will be complete, and the apparatus will be ready for more definitive cross-section measurements.

---

*Physics Division.

3.1.4 Electron-Impact Ionization of Multicharged Metallic Ions: Cu^{2+}, Cu^{3+}, Ni^{3+}, Sb^{3+}

D. C. Gregory and A. M. Howald

The present study is part of our continuing effort to provide accurate cross-section data for metallic ions of interest in controlled thermonuclear fusion research.

Details of the electron-ion crossed-beams apparatus have been published.[16,17] Ion beams were obtained from the ORNL PIG multicharged ion source. All measurements are independently absolute, and a typical absolute uncertainty at good confidence level (equivalent to two standard deviations for statistical uncertainties) near the peak cross section is $\pm 8\%$. Typical relative uncertainties (due mainly to signal-counting statistics) are shown in the figures.

The cross section for ionization of Cu^{2+} (Fig. 3.6) is typical of the measurements for copper and nickel reported here. The data are compared to predictions of the three-parameter Lotz semiempirical formula[18] and distorted-wave calculations.[19] The latter provide a reasonable prediction for the single-ionization cross sections for Cu^{2+}, Cu^{3+}, and Ni^{3+}. In each case, the Lotz prediction for total ionization is somewhat higher than the measurement, even taking into account the expected effects of multiple ionization. At high

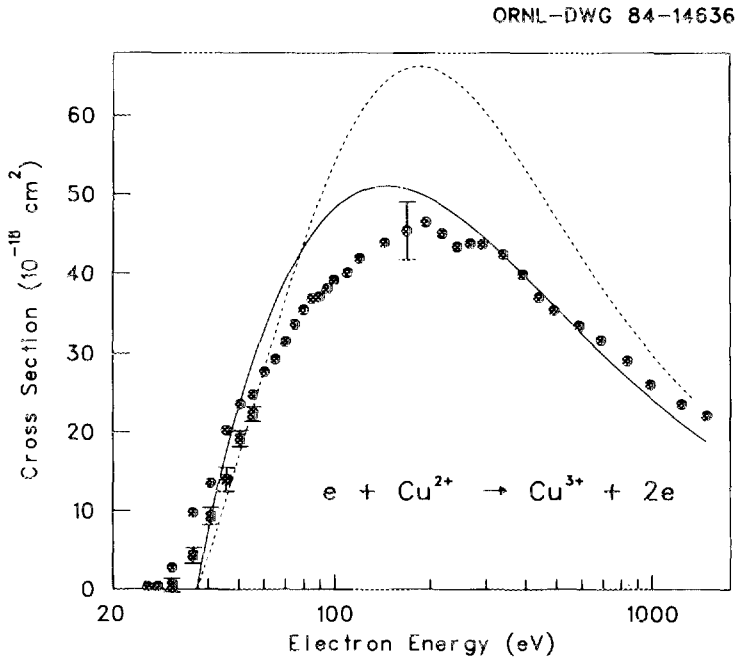

Fig. 3.6. Electron-impact ionization of Cu^{2+}. The circles and squares present near-threshold data with ion beams having different metastable ion content. A typical absolute uncertainty at good confidence level is plotted near 200 eV. The theoretical predictions are from the three-parameter Lotz formula for 3*d* ionization (dashed curve: ref. 18) and the distorted-wave calculations of Pindzola et al. (ref. 19).

energies, the two calculations converge with the data in each case. In the Cu^{2+} measurements, a significant contribution to the cross section is observed below the ground-state ionization threshold due to the presence of metastable ions in the beam. In fact, significantly different metastable contents were observed from day to day, and near-threshold measurements for two ground-state/metastable ratios are plotted. In general, for ionization of Cu^{2+}, Cu^{3+}, and Ni^{3+}, we conclude that distorted-wave direct ionization calculations give a reasonably accurate representation of single ionization. No large indirect ionization contributions are observed. The three-parameter Lotz formula, although not as reliable as distorted-wave calculations, is observed to be well within its predicted factor-of-2 accuracy in each case.

In contrast to the preceding examples, electron-impact ionization of Sb^{3+} has a considerable contribution from indirect effects (Fig. 3.7). The indirect ionization, contributing up to 45×10^{-18} cm^2 to the total cross section, is mainly due to non-dipole-allowed excitation of inner-shell electrons to autoionizing states. The cross section for this type of transition increases abruptly to a maximum at or just above its threshold energy but has a much faster falloff with increasing energy ($\sigma \propto 1/E$) than does direct ionization ($\sigma \propto \ln E/E$), so that its signature is a "hump" superimposed on the direct cross-section curve.

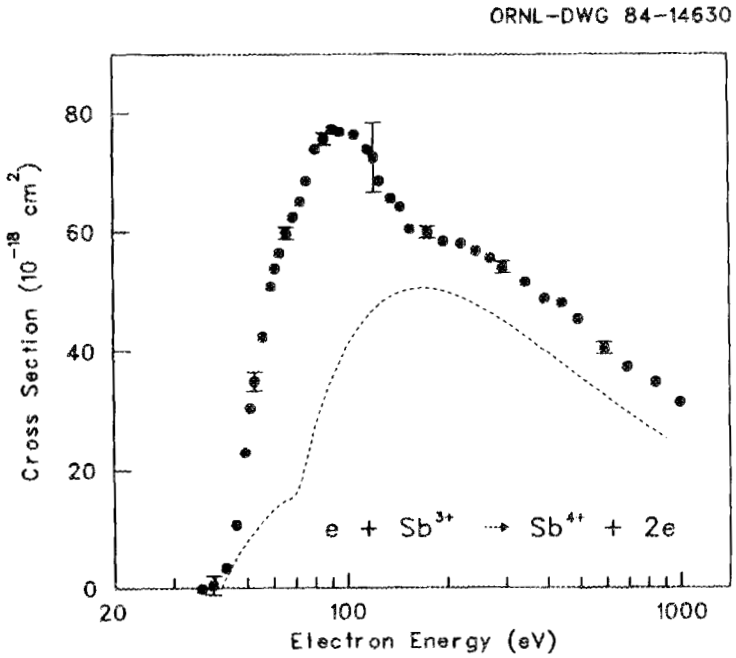

Fig. 3.7. Electron-impact ionization of Sb^{3+}. Typical relative uncertainties are plotted, and the absolute uncertainty at good confidence level is shown near 100 eV. The dashed curve is from the Lotz formula for 4*d* and 5*s* ionization (ref. 18).

This measurement was undertaken as a check of detailed distorted-wave, indirect-ionization calculations that predicted the observed feature.[20] Good agreement is found with the calculations and predictions of that study.

The examples discussed illustrate two goals of our current research efforts. First, selected measurements are made to provide specific data requested by the fusion community for electron-impact ionization of multicharged ions. Second, cooperative studies involving experiment and detailed calculations provide our best means of understanding the relative importance of the many possible mechanisms that can lead to ionization by electron impact.

3.1.5 Single, Double, and Triple Electron-Impact Ionization of Xe^{6+}

A. M. Howald, D. C. Gregory, D. H. Crandall, and R. A. Phaneuf

Electron-impact ionization of xenon ions has been studied previously at ORNL from several different perspectives. Experimentally, the ORNL PIG ion source and the electron-ion crossed-beams apparatus have been used to study single ionization of xenon ions from Xe^{2+} to Xe^{6+} (ref. 21) and Sb^{3+} (ref. 22), which is isoelectronic with Xe^{6+}. The xenon isonuclear sequence and the In^{+}, Sb^{3+}, Xe^{6+} isoelectronic sequence have also been studied theoretically,[20,21] and comparisons have been made with experiment.

During the past year, electron-impact ionization of Xe^{6+} was studied from yet another point of view. Measurements were made of the cross sections for double and triple ionization of this ion. The processes are

$$e + Xe^{6+} \rightarrow Xe^{8+} + 3e$$

and

$$e + Xe^{6+} \rightarrow Xe^{9+} + 4e \ ,$$

and the cross sections are denoted by σ_{68} and σ_{69}, respectively.

The results of these measurements are shown in Figs. 3.8 and 3.9, with the previously measured cross section[23] for single ionization of Xe^{6+} (denoted by σ_{67}) shown in Fig. 3.10 for comparison. The peak of σ_{67} is roughly an order of magnitude larger than the peak of σ_{68}, which in turn is roughly an order of magnitude larger than the peak of σ_{69}. As expected, the successive ionization thresholds increase along this sequence.

The dashed line in Fig. 3.10 is an estimate of the cross section for direct single ionization of Xe^{6+} from the semiempirical formula of Lotz. The actual cross section is much

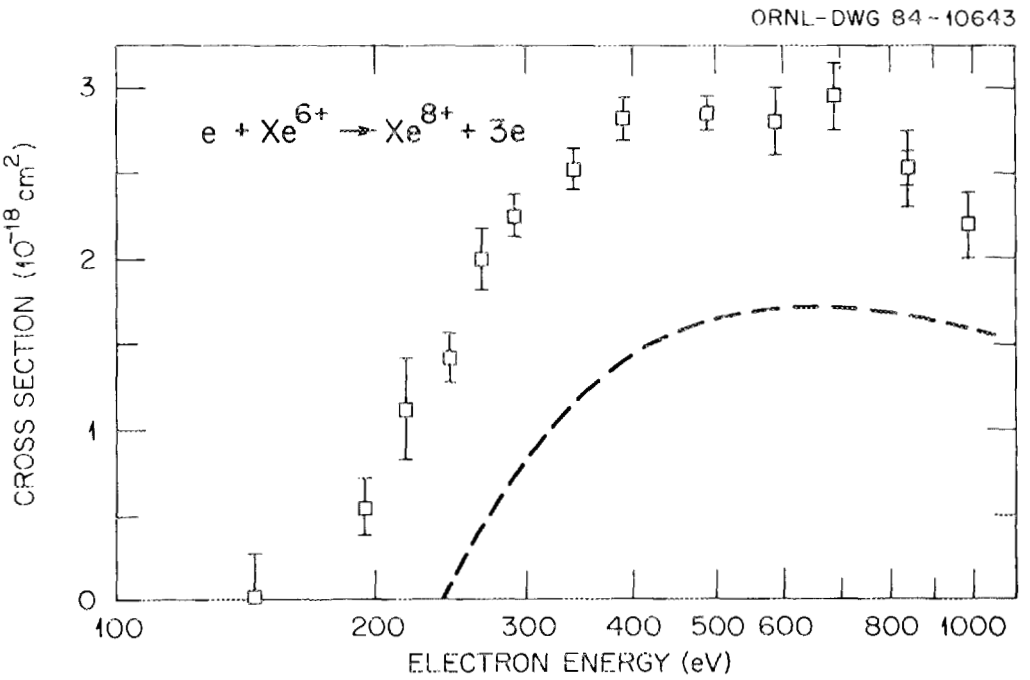

Fig. 3.8. Double ionization of Xe^{6+} by electron impact. The dashed line is the Lotz formula estimate for direct single ionization of an inner-shell $4p$ or $4s$ electron.

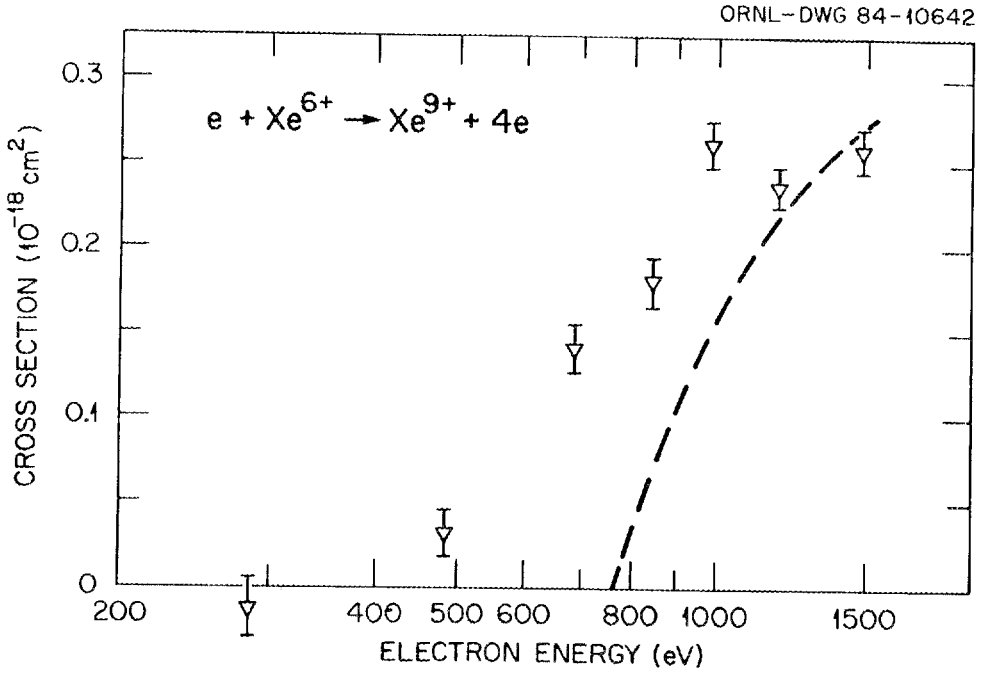

Fig. 3.9. Triple ionization of Xe^{6+} by electron impact. The dashed line is the Lotz formula estimate for direct single ionization of an inner-shell $3d$ electron.

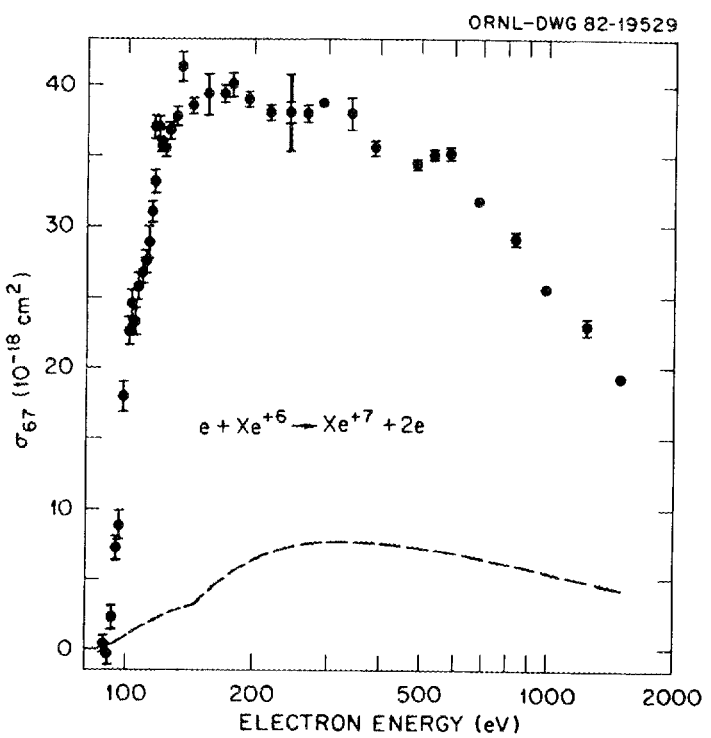

Fig. 3.10. Measured cross section for single ionization of Xe^{6+} by electron impact. The dashed line is the Lotz formula estimate for direct ionization of an outer-shell $4s$ electron.

larger as the result of ionization by mechanisms other than direct ionization, especially electron-impact excitation of an inner-shell electron followed by autoionization.

Single direct ionization of an inner-shell electron of Xe^{6+} can also lead to production of Xe^{8+} or Xe^{9+} if the Xe^{7+} is produced in a multiply excited autoionizing level. For example, collision of an electron with Xe^{6+} ($4p^6 4d^{10} 5s^2$) can remove an inner-shell $4p$ electron to form Xe^{7+} ($4p^5 4d^{10} 5s^2$), which can subsequently autoionize to form Xe^{8+} ($4p^6 4d^{10}$). A number of calculated energy levels of various ionization stages of xenon are shown in Fig. 3.11, along with some autoionizing transitions.[24]

In Fig. 3.8 the dashed line is the sum of the Lotz estimates for direct single ionization of Xe^{6+} $4p$ and $4s$ electrons. The resulting Xe^{7+} ions are in autoionizing levels. Hence (assuming a branching ratio near unity for autoionization vs radiative stabilization), this

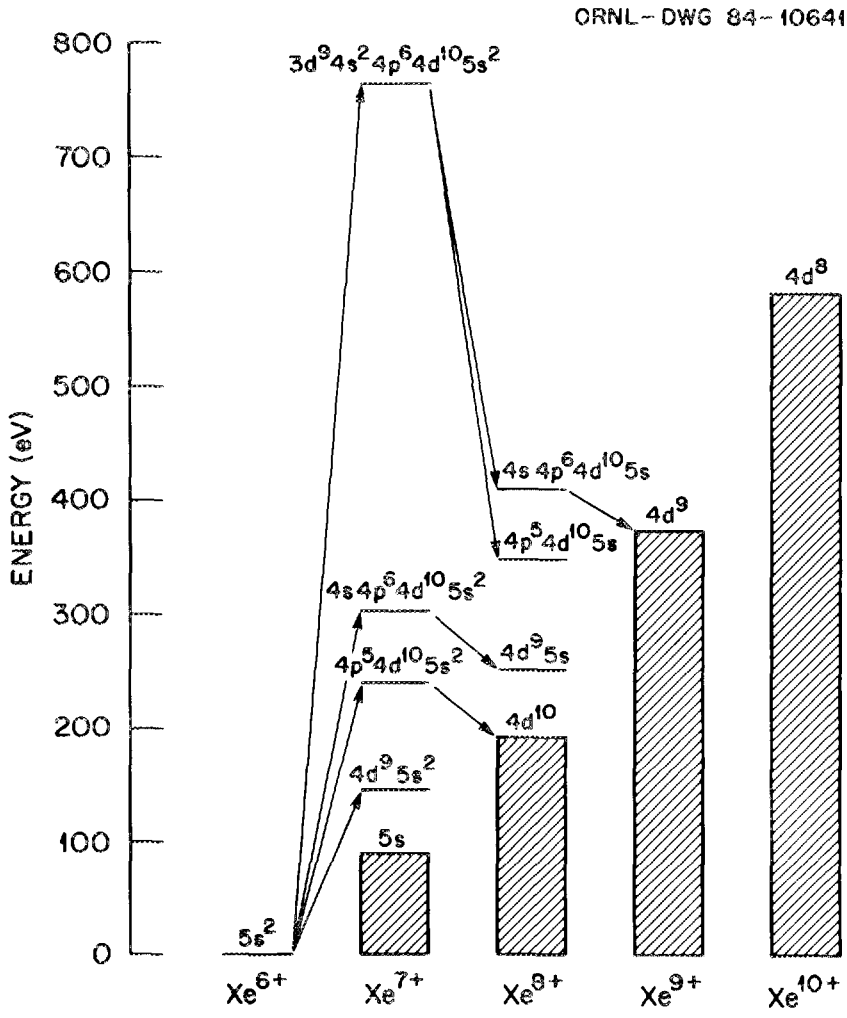

Fig. 3.11. Calculated energy levels (from ref. 24) of xenon ions, showing some electron-impact and autoionizing transitions.

gives an estimate of the *double*-ionization cross section due to the process of single direct ionization followed by autoionization. Similarly, the dashed line in Fig. 3.9 is the Lotz estimate for single direct removal of a $3d$ electron from Xe^{6+}. In this case the resulting excited Xe^{7+} has sufficient potential energy to doubly autoionize to form Xe^{9+}.

The double-ionization cross section (Fig. 3.8) calculated for this mechanism is similar in magnitude to the measured cross section (within a factor of 2) but has a threshold value higher than the experimentally observed ionization onset. For triple ionization (Fig. 3.9), the Lotz estimate of the cross section for the mechanism of single direct ionization followed by double autoionization also has the correct magnitude and has a predicted threshold that is higher than observed.

Other higher-order mechanisms must be responsible for the observed nonzero cross sections below 240 eV and 760 eV in Figs. 3.8 and 3.9, respectively. There are at least four possibilities: direct multiple ionization; electron-impact excitation, followed by double or triple autoionization; direct single ionization, accompanied by the simultaneous excitation of a second electron; or multiple excitation in a single collision, followed by autoionization. Direct multiple ionization of Xe^{6+} is expected from the classical binary encounter approximation (BEA) model to be of negligible importance. The other three processes have not been studied in detail and are not yet well understood. Our experimental results offer intriguing evidence that one or more of these processes can play a significant role in electron-impact multiple ionization of multiply charged ions.

3.1.6 New Electron-Ion Crossed-Beams Apparatus

D. C. Gregory and F. W. Meyer

Since 1977, electron-impact ionization cross-section measurements have been completed at ORNL for some 44 different ions with initial charges ranging from 2+ through 6+ and spanning the periodic table from boron to tantalum.[16,17] These total cross-section measurements for single, double, and triple ionization have all used the ORNL PIG ion source and crossed ion-electron beams apparatus.[24,25] With the completion of the new ORNL ECR ion source, our capabilities for producing multicharged ion beams now extend to considerably higher ionization stages. Since some aspects of the existing apparatus are inadequate for operation with more highly charged ions, the experiment has been redesigned.

Electrostatic separation of ion beams by charge state is difficult to achieve. In a crossed-beams ionization experiment, as little as 1 part in 10^8 crosstalk between exit channels produces an intolerable background level, and separation becomes progressively more difficult as the charge increases and the ratio of initial to final charge approaches unity. In addition, low-noise electrostatic analyzers must usually be mechanically modified for each charge ratio under study. To overcome both of these difficulties, a magnetic spectrometer is being constructed for product charge-state analysis.

The modified apparatus is shown in Fig. 3.12. The ion beam optics and ultrahigh vacuum system will remain much the same as in the present arrangement through the interaction volume in the center of the electron gun. The combined beam, containing the primary ions and further ionized signal ions, then enters a double-focusing analyzing magnet, which disperses the beam components by charge state. Signal ions are deflected

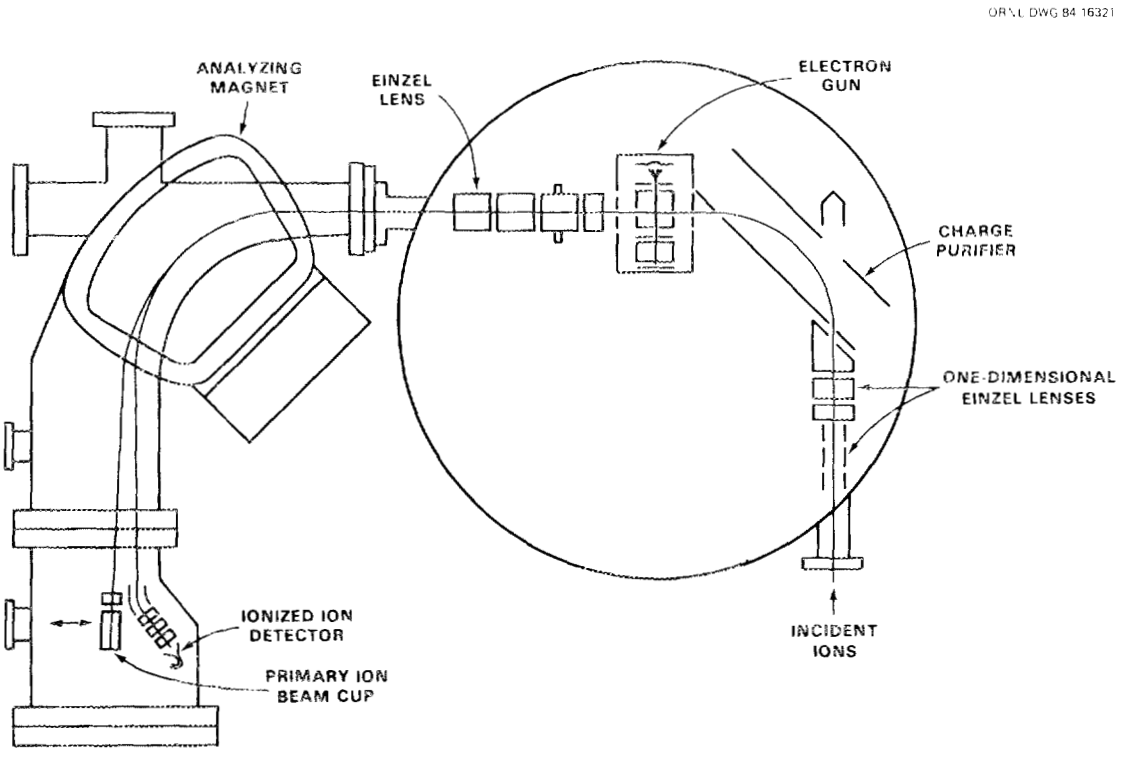

Fig. 3.12. New electron-ion crossed-beams apparatus with post-collision charge analyzer magnet. Measurements will include single and multiple ionization of a wide range of highly ionized ($6 \leq q \leq 15$) target ions.

through 90° and focused into a CEM. The ion optics are designed so that the crossed-beams interaction region is imaged onto the signal detector with unit magnification. The primary ion beam is trapped in one of two movable, guarded Faraday cups, depending on the ratio of initial to final charge for that particular experiment. Deflection plates and einzel lenses are provided as diagnostic tools, both in the main interaction chamber and immediately before the signal ion detector.

The apparatus is designed to allow measurements of initial-to-final charge-state ratios from 4/5 to 15/16. Initial tests of the completed apparatus are planned for early 1985. The next phase in the development of the crossed-beams apparatus will involve redesign or replacement of the existing magnetically confined electron gun to extend the available range for reliable measurements to electron energies greater than 1.5 keV.

3.1.7 Radiometric Standard for the Extreme Ultraviolet

P. M. Griffin, C. C. Havener, and J. W. Johnson*

A light source using bremsstrahlung and transition radiation[27,28] generated by kiloelectron-volt electron impact on metals is being investigated. This low-power, compact,

simple lamp has potential as a secondary-standard radiometric source for the soft X-ray (SXR) and extreme ultraviolet (EUV) spectral region. Its spectral radiance is characterized by a few easily measurable and controllable electrical, mechanical, and chemical parameters.

The essential elements of the lamp are the straight edge of an ohmically heated, 0.12-mm-thick, tungsten cathode and a flat metal anode. A well-defined thin sheath of kiloelectron-volt electrons is electrostatically drawn from the hot edge of the cathode located ~0.18 mm from and perpendicular to the anode target. At the intersection of the flat sheath of impinging electrons and the flat anode, a 6-mm-long, narrow, luminous line is generated.

An example of spectrometric measurements of radiation generated by the prototype source is shown in Fig. 3.13. It should be noted that at each spectrometer setting,

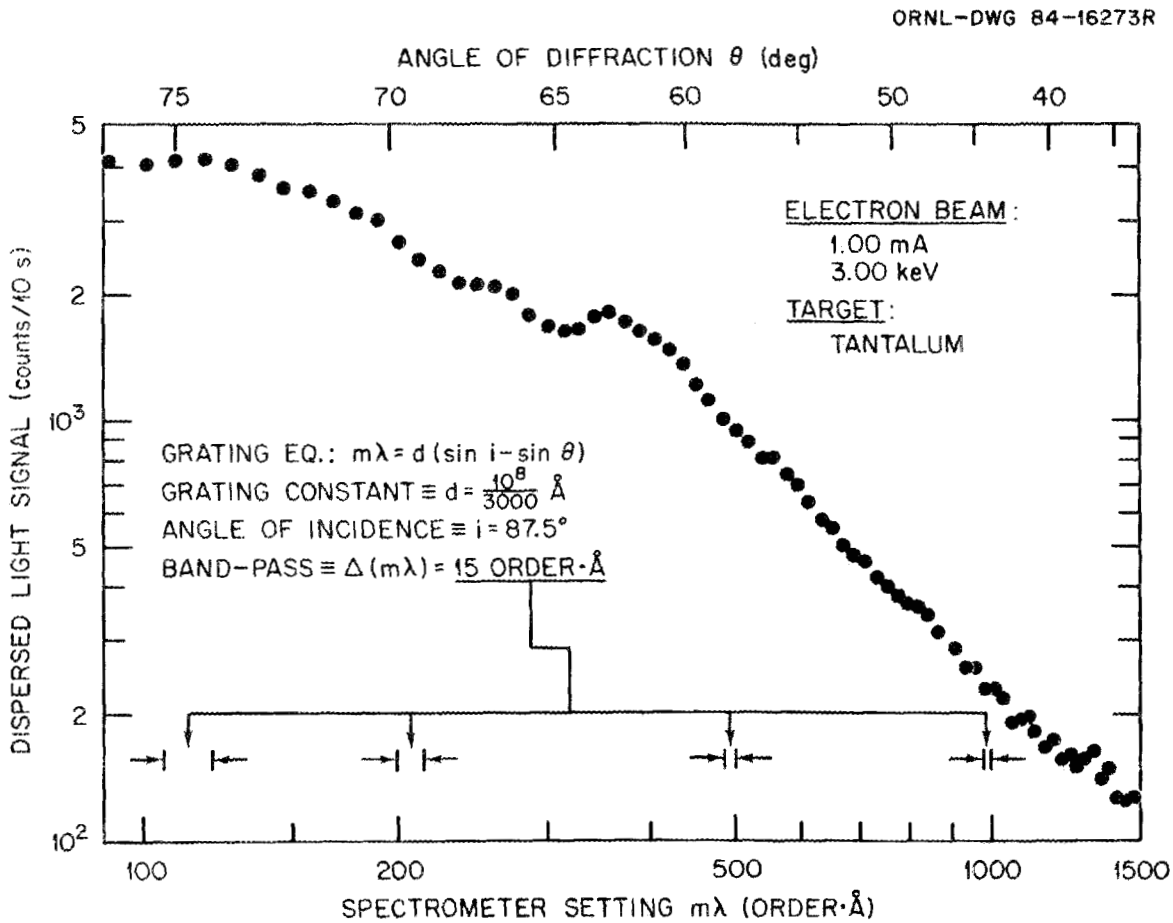

Fig. 3.13. Spectrometric measurement of the SXR and EUV light generated by 1.00 mA of 3.00-keV electrons incident on a tantalum target in the prototype radiometric source. Data are from a stepwise scan with a 2.2-m, grazing-incidence spectrometer. The dispersed light was detected with a ZnO-TiO_2 ceramic CEM. The spectrometer entrance slit subtended a 0.005-sr solid angle at the source.

corresponding to a given value of $m\lambda$, several discrete portions of the output spectrum are simultaneously sampled. The emissions from wavelength intervals $(\Delta m\lambda/n)$ Å wide, centered at wavelengths (m/n) Å, contribute to the measured signal at that setting. Relatively high spectral order numbers n must be considered because, for high-Z metals, bremsstrahlung and transition radiation intensities vary as λ^{-3} and λ^{-2}, respectively. The number of spectral orders observed is limited by the product of the short-wavelength cutoffs of the grating and detector efficiencies. The undulations in the data in Fig. 3.13 are accounted for in terms of the dropping-out rate of the highest integral spectral orders in proceeding to smaller values of $m\lambda$.

As this source is operated, bremsstrahlung, generated as the penetrating electrons are decelerated or deflected below the surface of the target, is the principal light-emitting mechanism for the continuum at wavelengths less than ~450 Å. Of particular interest is the lamp's scalable emission in the overlapping SXR and EUV spectral regions, as displayed in Fig. 3.14. The spectrometer was set to simultaneously sample the emissions from 7.5-, 3.8-, and 2.5-Å intervals in the continuum observed at 90, 45, and 30 Å, respectively. As expected, according to the theory of bremsstrahlung, the combined signals scale with electron current at four representative electron energies. The utility of this lamp as a practical standard is indicated by the fact that statistically acceptable data were obtained with only 10-s integration times and electron beam powers of only 2 to 15 W.

At wavelengths longer than ~450 Å, transition radiation should be the dominant light-emitting mechanism in the lamp. Phenomenologically, this radiation is a consequence of the collapse of the dipole field, produced by the approaching electron and its positive image charge in the metallic target, as the electron "transits" through the vacuum-target interface. The Fourier transform of the resulting electromagnetic pulse is a "white" frequency spectrum. The optical constants of whatever material exists at the surface characterize this radiation, rather than the bulk properties of the target. A reproducible surface is self-maintained if the source is operated at an adequate electron-beam areal power density.,

Investigations of the transition radiation component of the lamp's emission have been hampered by the overlapping of high spectral orders of shorter-wavelength bremsstrahlung. Solutions to this problem are being sought through the use of combinations of thin metal-foil spectral filters, which effect appropriate transmission "windows."

An improved model of the source and vacuum system has been designed and built and should permit operation at electron energies greater than 10 keV. This will permit generation of transition radiation of much longer wavelength. In addition, with the resulting greater electron penetration depths, the bremsstrahlung will be completely absorbed before it can emerge from within the target to proceed to the spectrometer. This technique will permit, where applicable, less complicated procedures for studies of the transition radiation component of the lamp's emissions.

---

*Physics Division.

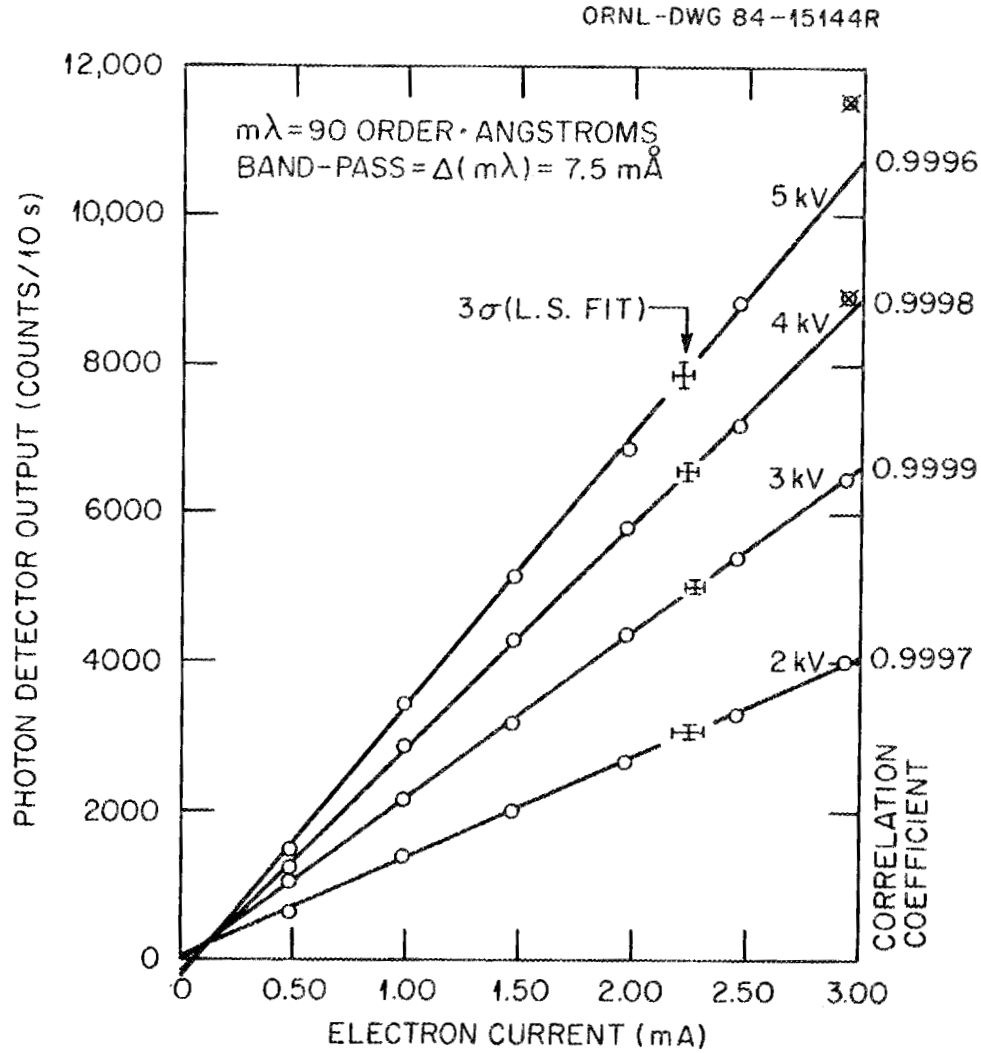

Fig. 3.14. Dependence of bremsstrahlung signal strength on electron beam current for accelerating voltages of 2.00, 3.00, 4.00, and 5.00 kV. The least-squares fits of the signals with current had standard deviations of 32, 31, 49, and 61 counts per 10 s, respectively. The highest current measurements at 4.00 and 5.00 kV were excluded in the fits because their deviations were greater than the 3σ error bars shown for each line.

3.2 ATOMIC THEORY

3.2.1 Low-Energy Charge Exchange

C. Bottcher and T. G. Heil

We have continued our studies of electron capture from hydrogen atoms by highly stripped ions using expansions in one-electron molecular eigenstates and a fully quantal description of the nuclear motion.[29] When the adiabatic potential energy functions and

coupling matrix elements have been calculated, we can solve the resulting coupled equations with some facility, using fully vectorized programs developed for the Cray-1 and Cray-1S.

In the past year, we have moved on to study more highly ionized projectiles, notably the 8+ isoelectronic sequence. Some results on O^{8+} and Ar^{8+} are shown in Fig. 3.15. We hope to study several members of this sequence with larger basis sets in order to make comparison with measurements in progress using the new ECR ion source.[30]

Since we now routinely include π states in our basis sets, we have found a number of cases where σ-π couplings affect the charge capture cross section by more than 30%. Figure 3.16 shows results for C^{4+} and O^{6+} projectiles. In the case of C^{4+} the disagreement with experiments[15,31] appears to have worsened, a situation that merits further study.

We are also pursuing the more fundamental objective of a very accurate calculation on B^{5+} + H, in which translation factors are included by matching to moving orbitals on some boundary. This matching requires an expansion in about 40 molecular eigenstates, for which we have now assembled the coupling matrix elements.

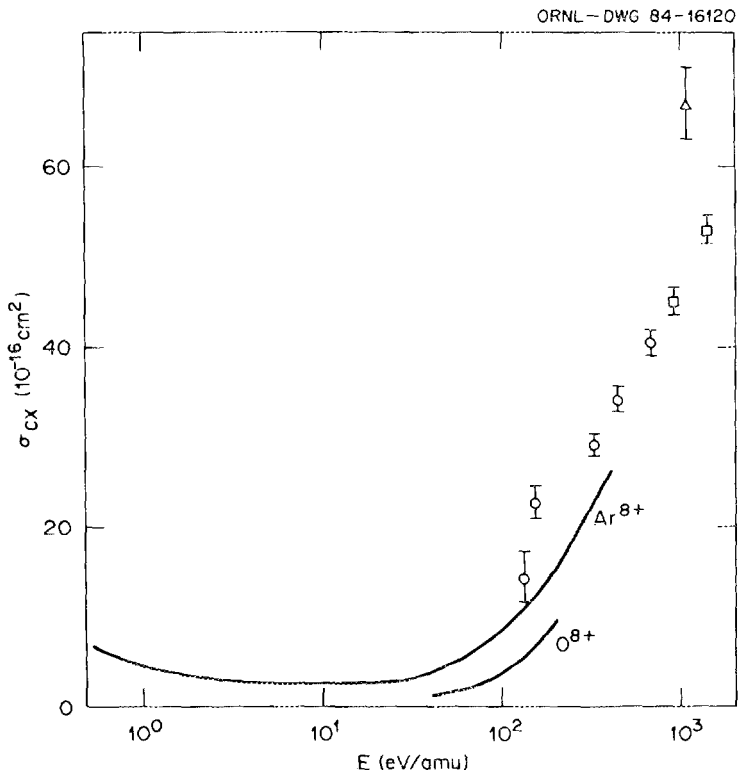

Fig. 3.15. Charge-exchange cross sections for multicharged ions on hydrogen atoms. Full lines: calculated with a basis of three σ states; open circles: measurement of ref. 30 on O^{8+}; open triangles: measurement of ref. 31 on Ar^{8+}.

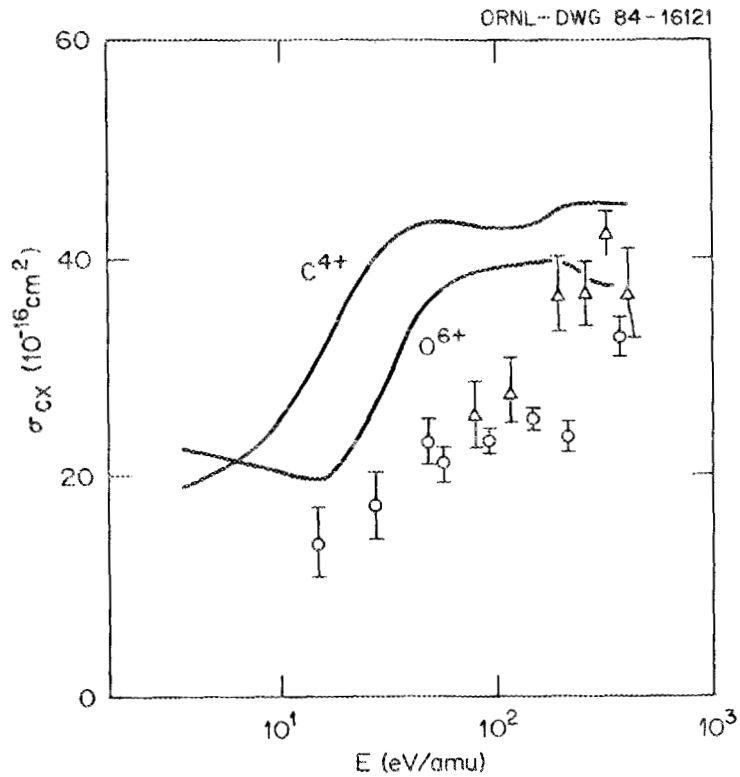

Fig. 3.16. Charge-exchange cross sections for multicharged ions on hydrogen atoms. Solid lines: calculated with a basis of three σ and three π states; open circles: measurements of ref. 32 on C^{4+}; open triangles: measurements of ref. 32 on O^{6+}.

3.2.2 Code Development for Electron-Ion Scattering

C. Bottcher, D. C. Griffin, and M. S. Pindzola

Between 1980 and 1983 we developed a program package to calculate distorted-wave excitation cross sections with intermediate coupling wave functions based on a single configuration of Hartree-Fock orbitals. The structure eigenvectors and radiative branching ratios (for autoionizing states) are obtained from the Los Alamos atomic structure package developed by R. W. Cowan.

In the past year we have added codes to calculate direct ionization and dielectronic recombination. These codes are still based on Hartree-Fock orbitals for bound states and distorted waves for continuum states, but they use "configuration-averaged" approximations in the structure calculations. They are well suited to surveys of, for example, isoelectronic sequences, and we can study in more detail individual cases in which a breakdown of the approximations is suspected.

At the same time, a major effort has been devoted to extending the excitation code to handle configuration-interaction wave functions that describe effects omitted by single-configuration Hartree-Fock theory—in particular, coupling between almost degenerate

configurations in the Hartree-Fock sea (e.g., $3s^2 3p^2, 3p^4, 3p^2 3d^2$) and pair excitations out of the sea ($3d^{10}, 3d^8 4f^2$). The process of checking these new codes is almost complete, and application to transition metal ions will be made in the near future.

We have been able for some time to perform close-coupling calculations, but progress on the complex targets we are interested in has been hindered by the lack of an efficient angular momentum algebra package in other groups as well as ours. This defect has been remedied by adapting our distorted-wave algebra package, and pilot calculations are in progress.

Particular applications of these codes are described in Sects. 3.2.3–3.2.5.

3.2.3 Direct and Indirect Ionization of Transition Metal Ions

M. S. Pindzola, D. C. Griffin, and C. Bottcher

During the past year we completed a survey of experimental and theoretical electron-impact ionization cross sections for transition metal ions in low stages of ionization. The atomic ions Ti^+, Ti^{2+}, Ti^{3+}, Fe^+, Fe^{2+}, Fe^{3+}, Fe^{4+}, Ni^+, Ni^{2+}, Ni^{3+}, Cu^+, Cu^{2+}, and Cu^{3+} were examined using electron-ion crossed-beams measurements and distorted-wave theory. In Fig. 3.17 we compare a single-configuration, level-to-level, distorted-wave calculation with experiment for Ti^{2+} (ref. 19). The theory predicts a rapid change in the cross section for 30 to 35 eV, followed by a 10-eV plateau and then further jumps in the cross section around 45 eV. On a smaller scale, the experimental measurements follow the same pattern. We believe that inclusion of configuration-interaction effects in the distorted-wave excitation calculations for Ti^{2+} will lower the cross section and thus improve the agreement between theory and experiment. In Fig. 3.18, we present the results of a single-configuration, level-to-level, distorted-wave calculation for Fe^{4+} (no experiment has yet been performed in this case). From our survey work, we expect that the total cross-section results and the direct cross-section results will bracket experiment. In order for our predictions to be more precise, configuration-interaction effects in Fe^{4+} will need to be included not only in the indirect excitation process but in the direct ionization calculation as well.

3.2.4 Dielectronic Recombination in the Lithium Isoelectronic Sequence

D. C. Griffin, M. S. Pindzola, and C. Bottcher

We have applied our recently developed distorted-wave code for dielectronic recombination to calculate the cross sections associated with the $2s$–$2p$ transition in the Li-like ions B^{2+}, C^{3+}, and O^{5+} (ref. 32). We have compared calculated cross sections to selected configurations of the type $2pnl$ in pure L-S coupling, in intermediate coupling, and in a configuration-averaged approximation. The most precise (intermediate coupling) results tend to be 50% higher than L-S coupling but agree fairly well with configuration-averaged results.

The explanation can be seen if we write the process, for example in B^{2+}, as

$$e(k'l') + B^{2+}(1s^2 2s) \rightleftarrows B^+(1s^2 2pnl, L) \rightarrow B^+(1s^2 2snl) + h\nu \ . \tag{3.1}$$

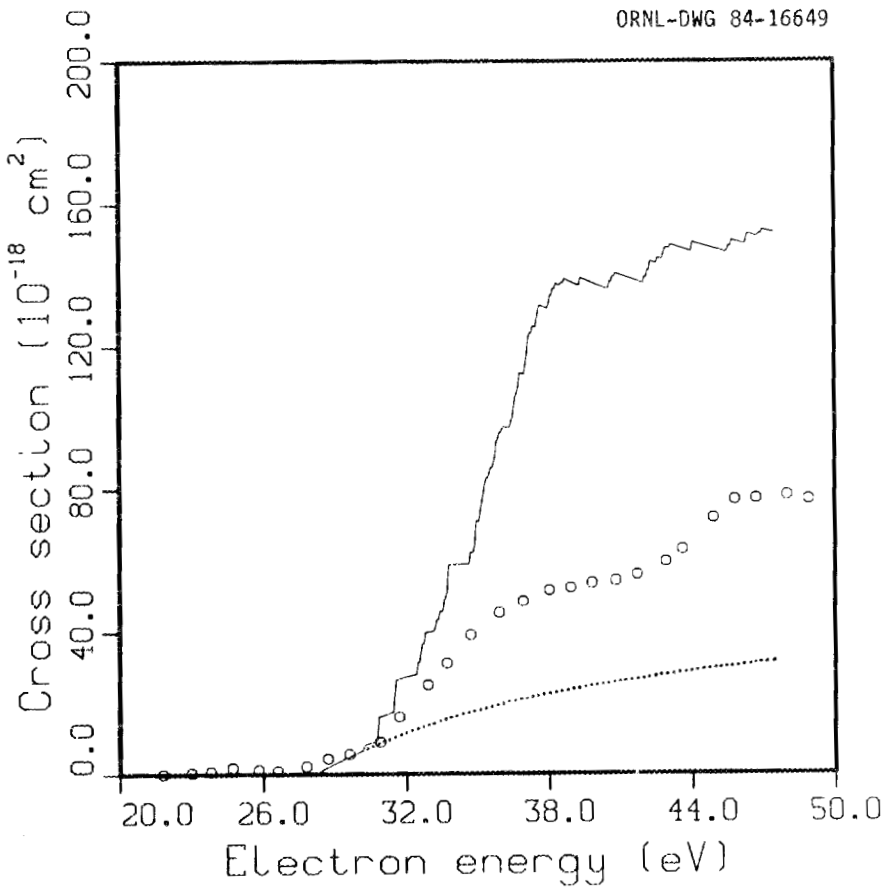

Fig. 3.17. Comparison of theory and experiment for electron-impact ionization of Ti^{2+}. Dotted line: direct ionization; solid line: sum of direct and excitation-autoionization; open circles: measurements of ref. 19.

In pure L-S coupling the total angular momentum $L = l \pm 1 = l'$, while in intermediate coupling the spin-orbit interaction mixes $L = l = l' \pm 1$. The former states typically have autoionizing rates 10^3 to 10^5 times the radiative rate, so that if the latter are mixed to the extent of 1 part in 10^3, they will contribute equally to the cross section.

The interpretation of experiments[33] on dielectronic recombination is presently in a state of flux. However, we note that measurements seem to be much larger than early theoretical predictions suggested and that the effect of spin-orbit interactions and external fields is usually to enhance the calculated cross section.

The sensitivity of comparisons with experiment[33] to assumptions about experimental conditions is illustrated in Fig. 3.19, which shows the predicted cross section for B^{2+} as a function of experimental energy resolution and the variation with the field ionization cutoff.

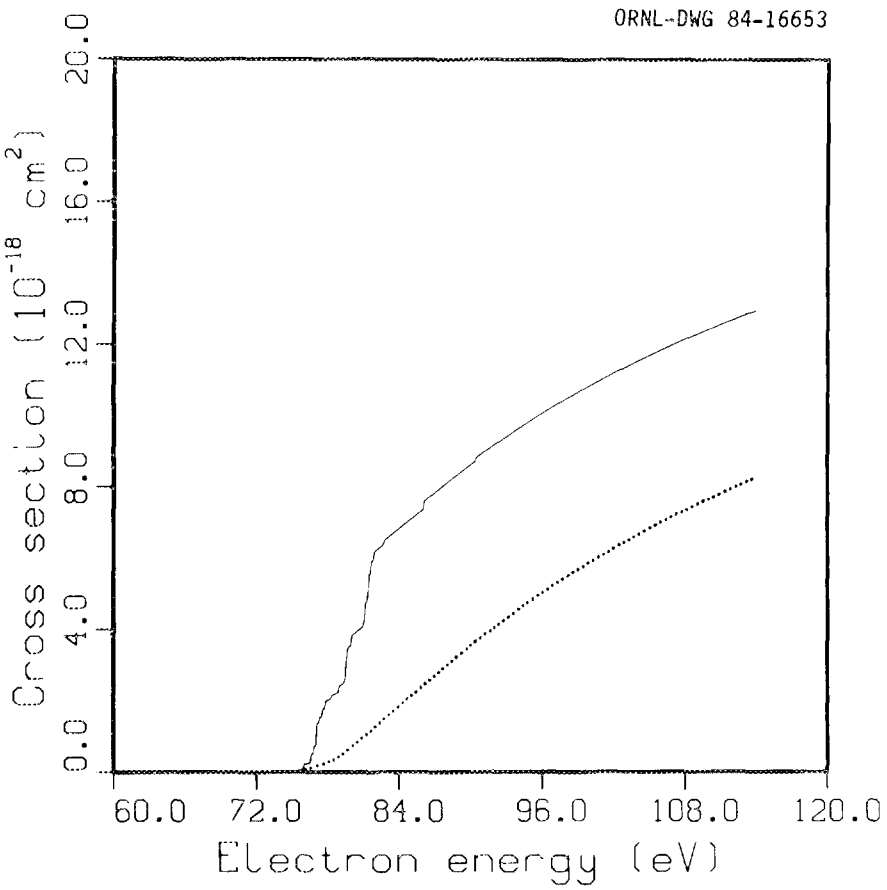

Fig. 3.18. Predictions for electron-impact ionization of Fe^{4+}. Dotted line: direct ionization; solid line: sum of direct ionization and excitation-ionization.

3.2.5 The Effect of Electric Fields on Dielectronic Recombination in Ions of the Lithium and Sodium Isoelectronic Sequences

D. C. Griffin, M. S. Pindzola, and C. Bottcher

Dielectronic recombination (DR) is particularly sensitive to the presence of external electric fields. Such fields can cause a redistribution of angular momentum among the doubly excited, resonant, Rydberg states that, in turn, increases the number of states for which the rate of resonant recombination is appreciable. We have just completed a systematic study of the field enhancement of dielectronic recombination in the lithium and sodium isoelectronic sequences. In particular, we have applied the linear Stark approximation to examine these field effects for the dielectronic recombination transitions associated with the $2s \rightarrow 2p$ excitation in the Li-like ions B^{2+}, C^{3+}, O^{5+}, and Fe^{23+} and the $3s \rightarrow 3p$ excitation in the Na-like ions Mg^{+}, S^{5+}, Cl^{6+}, and Fe^{15+}.

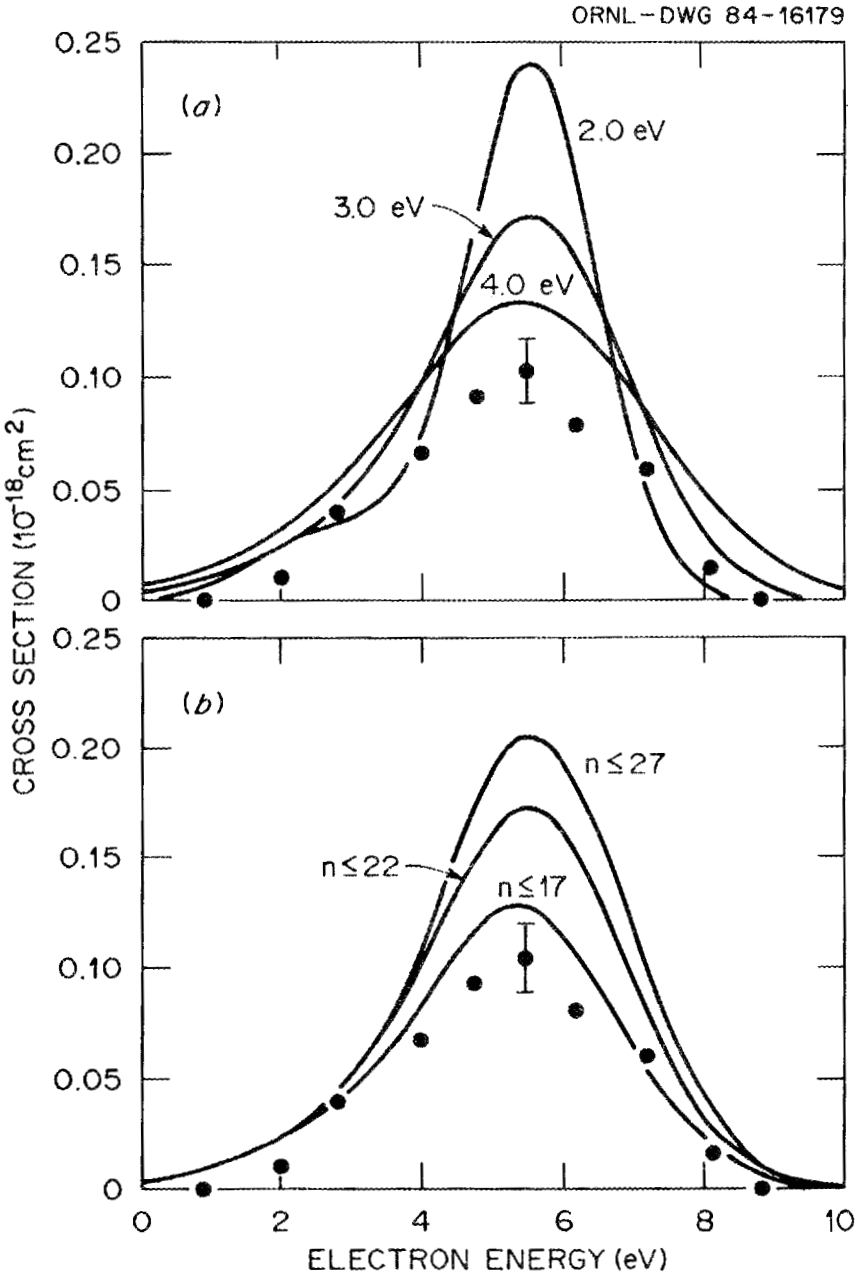

Fig. 3.19. Predicted cross section for dielectronic recombination of B^{2+}. (a) Variation of predicted cross section with electronic energy spread. (b) Variation with analyzer field cutoff in principal quantum number *n*. Solid circles are measurements from ref. 33.

Although this technique does not allow determination of field mixing as a function of electric field strength, it does provide physical insight into the nature of field effects in dielectronic recombination and allows study of important trends in the maximum field enhancement of the DR cross section as a function of ionization stage. We find that the magnitude of the field enhancement decreases as we move up an isoelectronic sequence and is on the order of two or three in highly ionized systems. Furthermore, we show that DR transitions through doubly excited states near threshold can produce large narrow peaks in the cross section at low energies, which are especially prominent in high stages of ionization and are not affected by electric fields. An especially striking example of this effect is provided by the DR cross section for Fe^{23+}, shown in Fig. 3.20 as a function of electron energy. In this plot, the narrow resonances associated with recombination transitions through the doubly excited configurations $2pnl$ are convoluted with a 3.0-eV Gaussian to simulate an experimental electron energy spread. The field enhancement in the high-energy peak is approximately 2.3. The prominent low-energy peak is due to transitions through the resonant states for which the principal quantum of the Rydberg electron is $n = 12$.

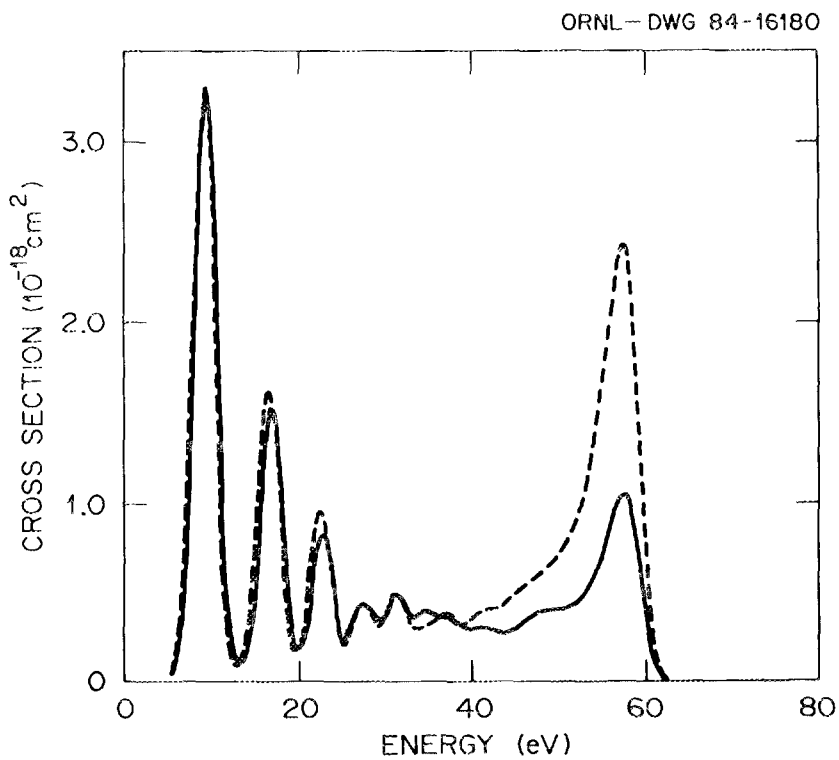

Fig. 3.20. Predicted dielectronic recombination cross section of Fe^{23+} convoluted into a 3-eV Gaussian electron energy distribution. The solid and dashed lines pertain to the cross sections with and without an external electric field.

3.3 CONTROLLED FUSION ATOMIC DATA CENTER

C. F. Barnett, H. B. Gilbody, D. C. Gregory, P. M. Griffin, C. C. Havener, A. M. Howald, H. T. Hunter, R. K. Janev, M. I. Kirkpatrick, C. R. Mahon, E. W. McDaniel, R. H. McKnight, F. W. Meyer, T. J. Morgan, R. A. Phaneuf, M. S. Pindzola, and E. W. Thomas

The data center continues to maintain a current annotated bibliography of atomic and molecular collision processes of interest in fusion research. During the 24-year history of the data center, we have consistently been one to two years behind in entering current references into our data base. This year, references have been entered directly into our computer file every three months, and within a few months we anticipate a monthly input. A universal data storage and retrieval system, INQUIRE, has been implemented by M. Wright of the Computing and Telecommunications Division, Martin Marietta Energy Systems, Inc. Bibliographical information can now be retrieved on line using ten different search elements. At present, three outside users are experimenting with retrieval using telecommunications lines to determine the feasibility of extending the data base to a larger group of outside users. Over the years, as computer technology has advanced, we have used several different storage and retrieval programs, with the result that we are now able to conduct on-line searches only of references entered since 1978. Efforts are being made to convert the various earlier bibliographic formats to one compatible with the INQUIRE format.

Cooperative efforts have continued with the Atomic Data Center for Fusion at the Institute of Plasma Physics (IPP), Nagoya, Japan; the Atomic and Nuclear Data Center of the Japan Atomic Energy Research Institute (JAERI), Tokai-mura, Japan; and the International Atomic Energy Agency (IAEA) Atomic Data Center, Vienna, Austria. During this reporting period, an agreement was reached that the ORNL bibliography would serve as the major input to these centers. ORNL will provide computer tapes every three months. Our staff continues to meet with and advise the IAEA data center staff on their activities. To increase the accuracy and efficiency of extracting numerical data from the literature, we have purchased a digitizer tablet and a small stand-alone computer with telecommunications capabilities. The required software has been written and implemented to perform the following steps: (1) digitize numerical data and store them on floppy disk; (2) concatenate individual data sets for a given process into one set for comparison and evaluation; (3) redigitize the recommended cross-section curve; (4) calculate Maxwellian reaction rate coefficients from cross-section data; (5) provide a seven-parameter fit to rate coefficients as a function of temperature; and (6) prepare computer-generated curves of recommended data and data tables for publication. Interfacing the center's computer with the central PDP-10 permits steps 4–6 to be completed.

During the present reporting period, a decision has been made to update and expand vols. 1 and 2 of the present compilation, *Atomic Data for Controlled Fusion* (ORNL-5206 and ORNL-5207), to a new series with five or more volumes. Previously, the compilations contained only graphs and data tables of recommended numerical data. Future volumes will add tables and graphs of reaction rate coefficients for interactions of beam-Maxwellian or Maxwellian-Maxwellian distributions. Progress has been made on the first

volume, *Heavy Particle Collisions*, which will be done in-house. An interagency agreement with J. Gallagher of the data center at the Joint Institute of Laboratory Astrophysics, Boulder, Colo., has been initiated to compile cross-section data for vol. 2, *Electron Collisions*. Reaction rate coefficient tables and graphs will be generated by the ORNL data center staff. Volume 3 of the series, *Collision of Atomic Particles with Surfaces*, has been completed and is now in the final stages of review before publication. Particle interaction with surfaces is still an inexact science and many of the data are qualitative. The fourth volume, *Spectroscopic Data for Iron*, has been compiled by W. Wiese and his colleagues at the National Bureau of Standards. We have received the compilation, except for one chapter on atomic energy levels, which awaits computer reformatting for compatibility prior to publication. Work has been initiated on vol. 5, *Collisions of Carbon and Oxygen Ions with Electrons, H, H_2, and He*, by R. A. Phaneuf of the ORNL Data Center, R. K. Janev of the Institute of Physics–Belgrade, and M. S. Pindzola of Auburn University. Data have been compiled from the literature, digitized, and evaluated, and cross sections have been recommended for electron capture by C^{q+} and O^{q+} ions from atomic hydrogen and helium. The anticipated completion date of these five volumes is December 1985. Additional volumes are planned for collisions of other impurity ions present in high-temperature fusion plasmas.

3.4 PLASMA DIAGNOSTICS DEVELOPMENT

3.4.1 Multichannel Polarimetry Using Faraday Rotation

C. H. Ma, D. P. Hutchinson, and P. A. Staats

Simultaneous measurements of electron density and Faraday rotation on all five channels of the far-infrared (FIR) interferometer/polarimeter system on the Impurity Study Experiment (ISX-B) tokamak have been achieved. The achievement is due mainly to two major improvements to the detectors and the Faraday modulator of the previous system: (1) the helium-cooled Putley detectors have been replaced by high-responsivity Schottky diodes, and (2) a novel technique is used to improve the performance of the polarization modulator. The use of the Schottky diodes in the present system has not only increased the detection sensitivity but also eliminated the need for a wire-grid analyzer for polarization determination. The previous Faraday modulator used an air-core coil, with a ferrite disk mounted in the center of the coil. The modulation frequency was limited to 3–5 kHz due to the high inductance and large stray capacitance of the 600-turn coil. In the present system, the multiple-turn coil has been replaced by a single-turn copper coil, which acts as the secondary of a radio-frequency (rf) transformer. A modulation frequency of 92 kHz has been achieved by using a series-resonant circuit for the primary winding. The increase of the modulation frequency has not only greatly improved the time resolution of the polarimeter but also reduced the rf coupling between the modulator and the detection circuit.

A schematic diagram of the modified interferometer/polarimeter system is shown in Fig. 3.21. Briefly, the system consists of a pair of cw 447-μm iodomethane lasers, optically pumped by separate CO_2 lasers. The FIR cavities are tuned so that the two FIR lasers oscillate at frequencies differing by $\Delta f \sim 1$ MHz. The linearly polarized beam of the

ORNL-DWG 82-3419R FED

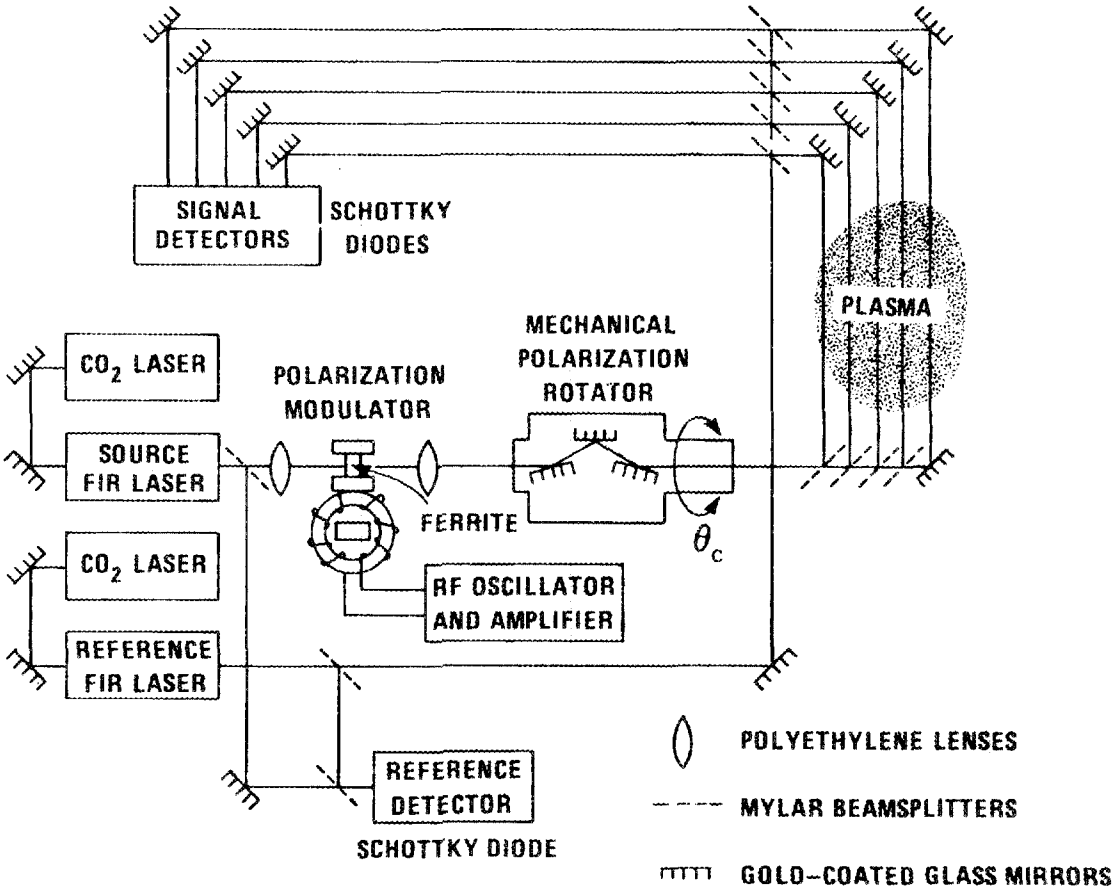

Fig. 3.21. Schematic of the multichord FIR interferometer/polarimeter system for simultaneous measurements of line-averaged electron density and Faraday rotation in an ISX-B tokamak plasma.

source laser is passed through a ferrite polarization modulator and a mechanical polarization rotator into the dielectric waveguide and is then divided into five beams that are projected through the plasma. Emerging from the plasma chamber, each beam again enters a waveguide and is directed onto a signal detector. Part of the beam from the reference laser is mixed first in a reference detector with a portion of the source laser, which is split off before passage through the modulator, and the remainder is guided to the signal detector to mix with the plasma-probing beam. Schottky diodes are used for all detectors. The output of the reference detector is a sinusoid at frequency Δf and is used as reference signal for phase detection. The output of each signal detector is filtered, amplified, and fed into a digital phase-detection circuit to extract the phase shift due to plasma density. An envelope detection circuit demodulates the phase-modulated signal and provides a sinusoidal signal at the modulation frequency with amplitude proportional to $J_1(\theta_m)\sin(\theta)$, where θ_m is the

amplitude of the modulation angle and θ is the sum of the rotation angles due to the mechanical polarization rotator θ_c and the Faraday rotation in plasma θ_p; $J_1(\theta_m)$ is the Bessel function of the first kind with order one. This signal is synchronously detected by a lock-in amplifier, yielding an output voltage $V_{out} = V_0 \sin(\theta)$. The calibration constant V_0 can be obtained by setting the mechanical polarization rotator at a few degrees ($\leqslant 4°$) and measuring the value of V_{out} without plasma in the chamber. The voltage V_0 as determined by this technique calibrates the polarimeter in a manner that does not require the absolute knowledge of laser power, detector responsivity, modulation angle, or any system losses.

The system has been routinely employed to study ohmically heated and neutral-beam-heated plasma discharges in ISX-B for over a year. The standard deviation of the output of the interferometer of a constant phase shift is less than 5×10^{-2} fringe. Since one fringe corresponds to a line-averaged density of 9.2×10^{12} cm^{-3}, density variations as small as 4.6×10^{11} cm^{-3} can be measured. The polarimeter shows a sensitivity on the order of 1 mrad and a time resolution of 1 ms. Figure 3.22 shows the time-resolved traces of (a) Faraday rotation and (b) line-averaged electron density of a typical tokamak plasma discharge. A neutral hydrogen beam of approximately 1 MW was injected into the plasma 70 ms after the initiation of the plasma discharge. The position of each channel, relative to the center of the tokamak vacuum chamber, is indicated in the inset. The negative Faraday rotation on the central channel (channel 2) is due to the outward shift of the plasma centroid. The fast response of the system is demonstrated in Fig. 3.23. During this plasma discharge, a solid hydrogen pellet was injected into the plasma at approximately 204 ms. The pellet caused an abrupt density increase of $\sim 1.4 \times 10^{13}$ cm^{-3} and a change in Faraday rotation of $\sim 0.15°$ on the central channel. The changes of density and Faraday rotation occur during a period of approximately 400 μs. The time delay (≈ 3 ms) between two curves is due to the resistance-capacitance (R-C) constant of the lock-in amplifier (1 ms). It is believed that this is the first simultaneous measurement of electron density and Faraday rotation in pellet-injected discharges. Data analysis codes are under development to reconstruct the asymmetric spatial profiles of electron density and plasma current from the line-averaged chordal measurements.

We have continued to support the implementation of the FIR diagnostics on the Texas Tokamak (TEXT) at the University of Texas in Austin. T. Price has simultaneously measured both density and Faraday rotation on all six channels of the TEXT system. Although the system is not completely calibrated, the Faraday signals have the proper polarity on all six channels and roughly the proper magnitude.

C. H. Ma has been engaged in development of the FIR polarimeter for the Tokamak Fusion Test Reactor (TFTR) at Princeton Plasma Physics Laboratory. Experiments have been conducted to determine the performance characteristics of the polarimeter. A signal-to-noise ratio of 20 dB has been achieved for a simulated Faraday rotation angle of 5° with 4 mW of laser power. An analysis has also been carried out to identify some possible problems in the measurements and to establish the calibration procedure for the system.

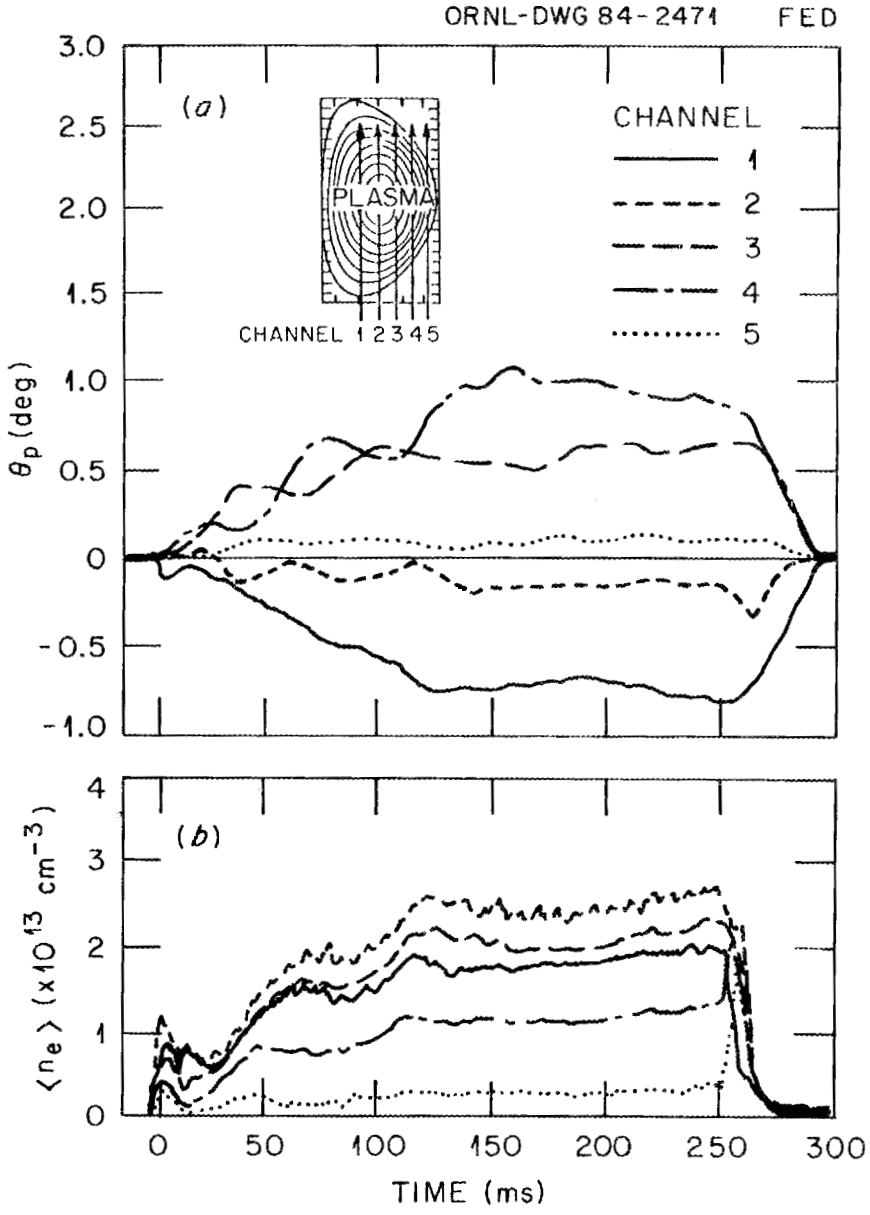

Fig. 3.22. Time variation of (a) Faraday rotation and (b) line-averaged electron density, measured by the multichord FIR interferometer/polarimeter system on ISX-B.

3.4.2 Diagnostics Development Center

C. F. Barnett, E. W. Thomas, K. O. Legg, and P. Bakshi

A collaborative effort has been initiated to determine the feasibility of measuring plasma edge turbulence and electric fields in magnetically confined plasmas. Fast-response

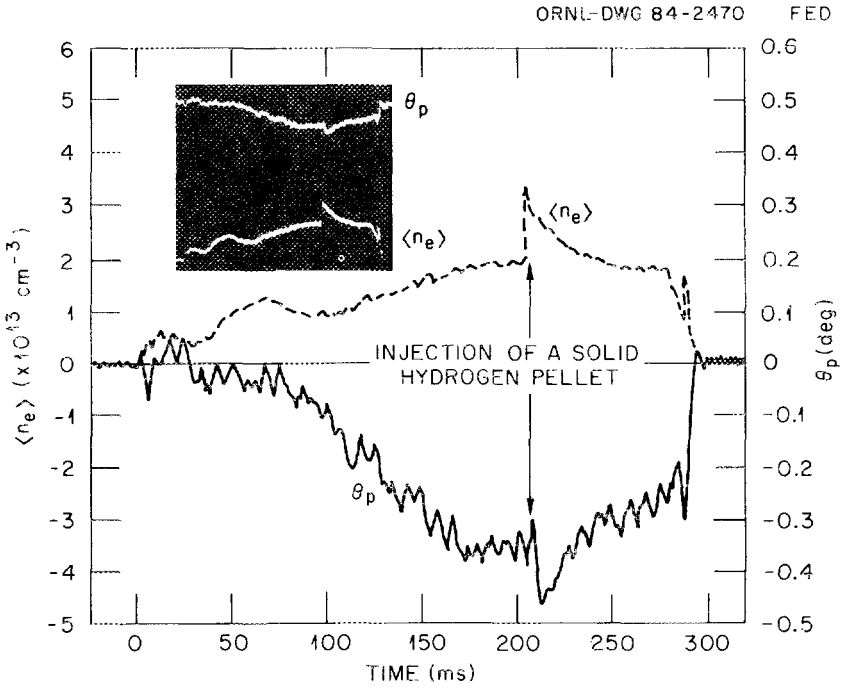

Fig. 3.23. Typical display of time variation of line electron density and Faraday rotation signal on central channel of the FIR interferometer/polarimeter system. The abrupt changes of the line density and Faraday rotation are caused by the injection of a solid hydrogen pellet 204 ms after the beginning of the discharge.

diode arrays with H_α filters have been constructed to observe time correlations of H_α emission from adjacent locations in the plasma edge, using techniques developed by Zweben et al.[34] The first series of measurements will establish the physical extent of coherent emission regions, both poloidally and toroidally. The second series will include the replacement of the H_α filter with a monochromator. By imaging a poloidal strip of the plasma on a vertical entrance slit and placing the diode array in the vertical detector plane, we can determine the electric field from the Stark-broadened profiles or shifts of the H_α line. Since the conventional analysis of the Stark effect in plasmas is in terms of the static Holtsmark field, it is necessary to include the line shape and the shifts due to quasi-static and high-frequency fields. Modeling of the line shape for different magnitudes and frequencies for these fields has been completed. In addition, the analysis indicates that by determining the polarization of the H_δ line the direction of the driving electric field can be determined. Two eight-diode arrays have been fabricated and tested with their associated amplifiers, circuitry, and signal recording. Computer programs are being written for cross-correlation analysis. Initial tests will be performed using a rapidly pulsed proton beam in H_2 gas, after which the apparatus will be moved to TEXT.

To measure the ion temperature in a high-temperature deuterium-deuterium (D-D) plasma, we have proposed to make use of the oxygen total neutron cross section, which has a deep resonance at about 2.35 MeV (ref. 35). At low plasma temperatures, the 2.45-MeV

D-D neutron spectrum is narrow. As the plasma temperature increases, kinetic broadening increases the width of the neutron distribution, with the low-energy tail spilling over into the oxygen resonance. By measuring the attenuation of the neutrons through a liquid oxygen cell, the plasma ion temperature can be obtained if the ions have a Maxwellian velocity distribution. Preliminary calculations[36] had shown the experiment to be feasible for a 2-keV plasma ion temperature using an available liquid oxygen cell. More precise calculations by Alsmiller et al.[37] for a global neutron source from a 6-keV D-D plasma indicated that the overall efficiency of the neutron detector at the rear of the absorption cell would be 4×10^{-11} counts per source neutron. This can be compared to a source strength on the ISX-B tokamak of 2×10^{10} neutrons/s or approximately 0.16 counts per discharge at the rear detector. Since the calculations are believed to be accurate to within 20%, the technique does not appear to be feasible.

High-speed (4000-ft/s) framing camera studies have been completed on TEXT during stable and turbulent operation. Photographs were taken at three viewing ports: perpendicular to the plasma at the limiter port, longitudinal to the plasma viewing the inside of the toroidal limiter, and perpendicular to the plasma 180° from the limiter. Semiquantitative data from the films were obtained by visual observation and frame-by-frame scanning with an optical densitometer. The observations are summarized as follows.

- Striations or particle density channels were always present at the beginning or end of the discharge and during turbulent operation.
- During stable periods of operation, no fluctuations were observed.
- Spallation of macroparticles or molten pieces of metal was observed during the formation of the discharge, at disruption or with unstable operation, and at the end of the discharge.
- Macroparticles were observed 180° from the limiter, apparently coming from the wall.
- Particles coming from the wall or limiter usually flowed in the direction of the plasma current, with a luminous plume extending in front of and behind the particles.

A low-energy cesium neutral particle analyzer[38] has been lent to the University of Wisconsin to measure tokamak plasma ion temperature. In recalibrating the conversion and detection efficiency of the analyzer, we found that the sensitivities of two of the channel multipliers were a factor of 2 to 5 less than the other two. The electrostatic analyzer is being rebuilt and the multipliers are being replaced. These changes in calibration demonstrate the need for periodic recalibration of analyzers after several months of operation.

3.4.3 Feasibility of Alpha Particle Diagnostics by CO_2 Laser Thomson Scattering

D. P. Hutchinson, K. L. Vander Sluis, J. Sheffield,* and D. J. Sigmar*

Introduction

The behavior of alpha particles in an ignited fusion plasma is of considerable importance in fusion research, because it is the energy transferred to the deuterium-tritium (D-T) plasma from the energetic alphas that will sustain the plasma temperature. Several methods have been proposed to measure the density and the velocity distribution of the alphas.[39-42] Among the suggested techniques are the use of charge-exchange reactions of

the alphas with high-energy neutral diagnostic beams,[39-41] the scattering of FIR radiation,[41] and the detection of alphas that escape from the plasma.[41,42] We have evaluated a method that uses the scattering of a high-power CO_2 laser by the Debye sphere of electrons associated with each alpha particle to determine both the density and the velocity distribution of these energetic fusion products.

Scattered power spectrum

The incident radiation at the wave number $\vec{k}_i$ and frequency ω_i is scattered and Doppler shifted by electrons in the plasma to the scattered wave number $\vec{k}_s$ and frequency ω_s. The radiation of a particular $\vec{k}_s$ and ω_s reaching the detector comes from a periodic distribution of electrons in the plasma with wave number $\vec{k} = \vec{k}_s - \vec{k}_i$ and frequency $\omega = \omega_s - \omega_i$. The ions are massive and scatter relatively little of the incident radiation. However, when $|\vec{k}| > \lambda_D$, the Debye length, radiation is scattered from the electrons that are a Debye shield on each ion. For the conditions used in this diagnostic, the shift in frequency corresponds to the Doppler shift caused by the ion thermal speed $v_i = \omega/k_i$ and the electron thermal speed $v_e = \omega/k$. The scattered power P_s in the frequency range $\omega \rightarrow \omega + d\omega$ and solid angle $d\Omega$ from a length L of the incident beam of electromagnetic radiation is given by Sheffield:[43]

$$P_s(\vec{R},\omega)d\Omega\, d\omega = P_i r_0^2 n_e L\, d\Omega\, \frac{d\omega}{2\pi}\, Q(\vec{k},\omega) \ , \tag{3.2}$$

where

$$Q(\vec{k},\omega) = \frac{2\pi}{k}\left|1 - \frac{G_e}{\epsilon}\right|^2 f_e(\omega/k) + \frac{2\pi}{k}\left|\frac{G_e}{\epsilon}\right|^2 \sum_Z Z f_i(\omega/k)$$

and it is assumed that the scattered frequency shift $\omega << \omega_i$. The electron and ion velocity distribution functions are $f_e(\omega/k)$ and $f_i(\omega/k)$, respectively; r_0^2 is the Thomson cross section, 7.95×10^{-26} cm^2; n_e is the electron density; P_i is the incident laser power; and G_e is the electron susceptibility.

We assume that the electron and bulk ion velocity distributions of the plasma are Maxwellian and that the bulk plasma is made up of isotopes of hydrogen ($Z = 1$). The high-energy spectrum of the alphas is assumed to be isotropically distributed in velocity space, and $f_\alpha(v_\alpha) = \text{const}$ for $v < v_{\alpha 0}$, the velocity of a 3.5-MeV alpha particle. Above v_α the alpha distribution function is zero. Also, we ignore kinetic broadening of the alpha velocity distribution due to the finite energy of the interacting D-T ions.

In order to determine the range of scattering angles and frequencies over which more detailed calculations should be performed, we first place simplifying constraints upon the scattered spectrum: (1) consider only phase velocities near $\omega/k = v_\alpha$ and (2) pick a region where the alpha particle scattering and electron scattering are equal. Assuming a laser with a 10.6-μm wavelength, this corresponds to a scattering angle $\theta = 0.70°$. The signal

received from the electron scattering for $v_e > v_\alpha$ will be used to calibrate the alpha-scattered signal, so that for known n_e and T_e we may determine n_α.

Based on this simplified calculation, the scattering geometry depicted in Fig. 3.24 was chosen. The scattered signal is assumed to emerge from the plasma device through an annular window centered on the input laser beam. The viewing window has an angular span from 0.5° to 1.0°. A plot of the total scattered spectrum expected from a TFTR-like

ORNL-DWG 84C-13863

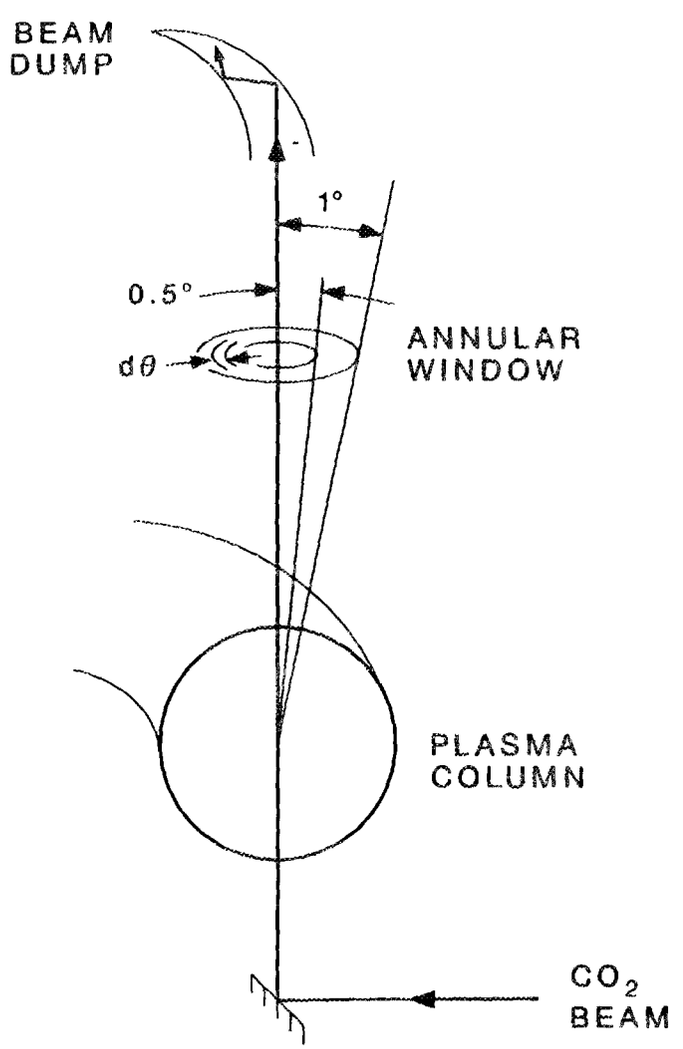

Fig. 3.24. The scattering geometry for the proposed CO_2 laser Thomson scattering diagnostic, chosen to accommodate the small scattering angle necessary to measure the alpha particle velocity distribution.

plasma as a function of scattered frequency shift, based on the geometry depicted in Fig. 3.24, is shown in Fig. 3.25. This calculation assumes a flat alpha particle velocity distribution and indicates that alpha-particle-produced scattering is dominant over a range of scattered frequencies from 6 to 22 GHz. Figure 3.26 depicts a calculation of the composite spectrum as a function of frequency (in watts of scattered power per unit frequency) for scattering frequencies δf from 0.1 to 25 GHz about the line center of the incident laser for three simple velocity distributions. The distributions modeled are (1) $f_\alpha(v) \simeq 1/v$, (2) $f_\alpha(v) \simeq$ const, and (3) $f_\alpha(v) \simeq v$. The amplitude of the distributions was normalized to the value n_α/v_α at v_α. The first distribution, proportional to $1/v$, would represent a buildup of particles toward zero velocity, assuming little or no diffusion in real space; the second assumes a model based on calculations of TFTR-like[44] plasmas that predict a flat alpha

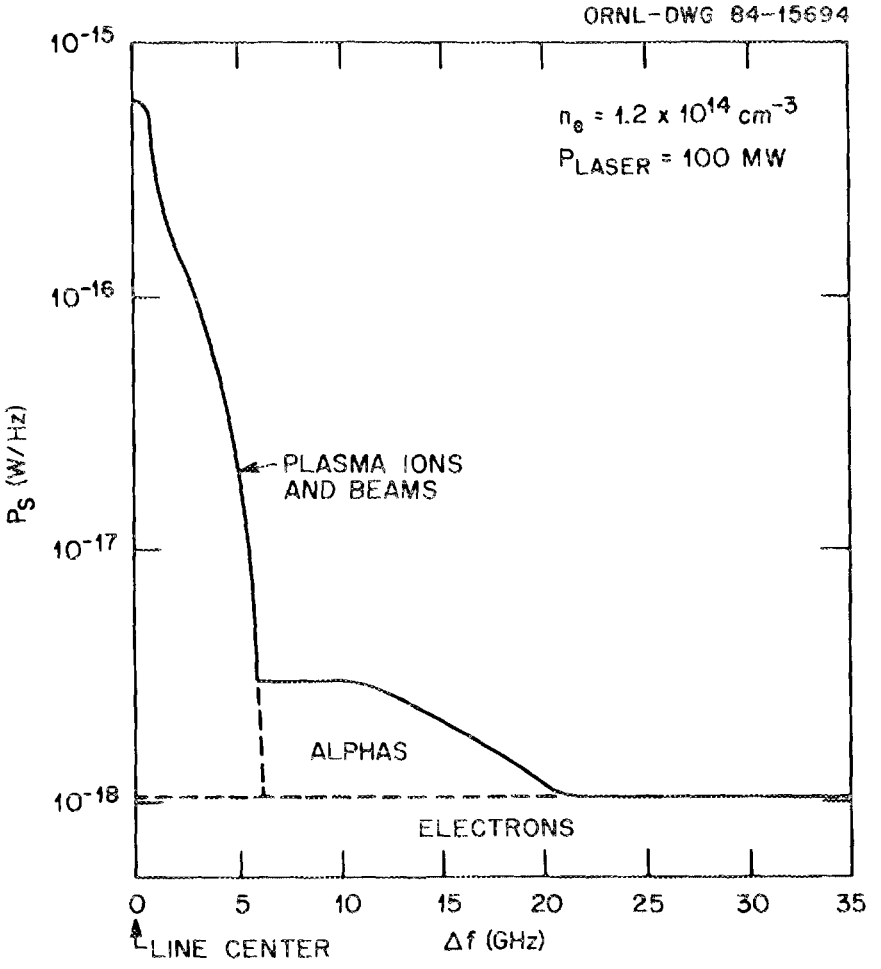

Fig. 3.25. The total scattered spectrum from a TFTR-like plasma calculated from Eq. (3.1), shown as a function of scattered frequency shift.

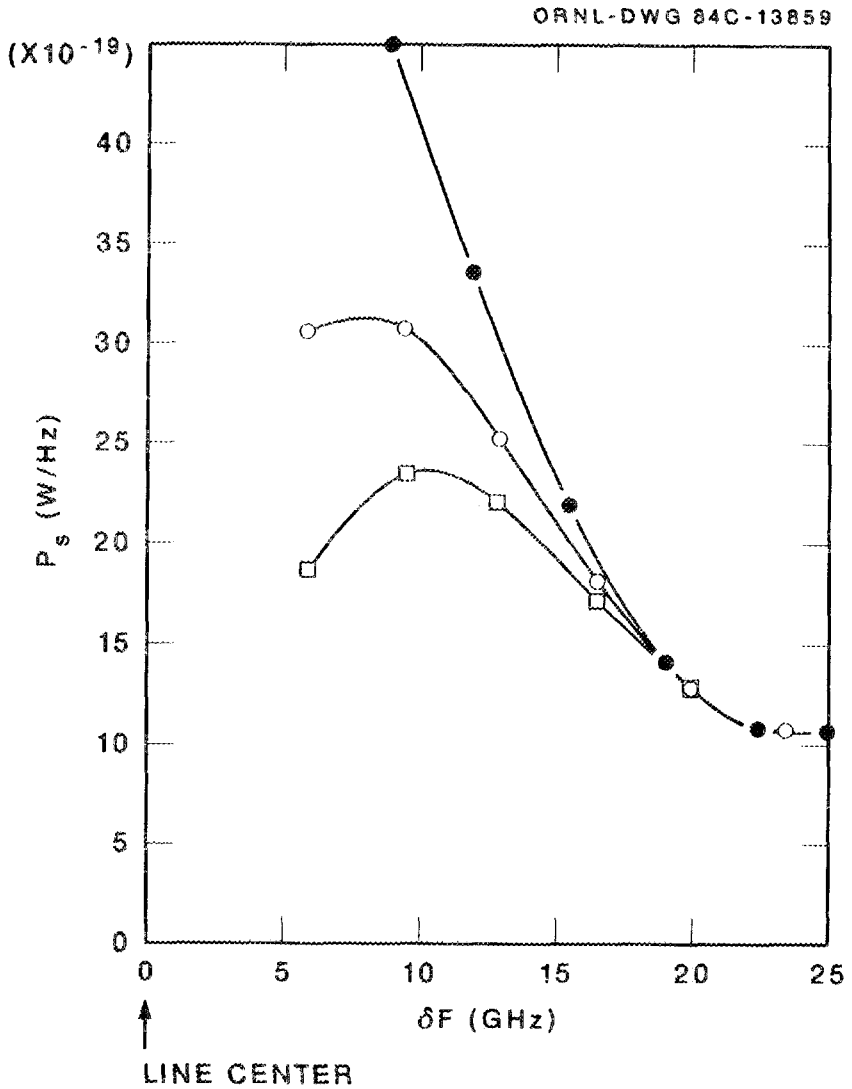

Fig. 3.26. The scattered power vs the shifted frequency δf is plotted for three simple alpha particle distributions. The alpha particle distribution proportional to 1/v is represented by the open circles, the $f(v)$ = constant distribution by the open squares, and the distribution proportional to v by the closed circles. The electron density assumed for these calculations is 1.2×10^{14} cm^{-3}.

velocity distribution; and the third distribution, proportional to v, could result if alpha particles were lost during the slowing-down process. These distributions are not assumed to accurately model a true plasma case but were chosen to investigate the sensitivity of the proposed diagnostic technique to changes in the alpha particle velocity distribution. Figure 3.26 shows the scattered power plotted for scattering frequencies greater than 6 GHz, the approximate frequency at which the scattering from the injected beam components goes to zero. The composite scattered power from the electrons is constant over

this range and has a value of approximately 1.05×10^{-17} W/Hz. The $1/f$ portion of the scattered spectrum from 10 to 20 GHz is due to averaging over the window. The scattering from the alpha particles is two to three times the scattering from the electrons over this frequency range.

Detection system

The scattered power from the alpha particles covers the frequency range from 6 to ≈20 GHz on either side of the 10.6-μm line of the CO_2 laser, which has a center frequency of approximately 28,306 GHz. The frequency resolution required is too high to use a grating for dispersion, as in a conventional Thomson scattering measurement, and too small to use a Fabry-Perot interferometer. Also, the noise level of a liquid-nitrogen-cooled HgCdTe detector operating in the video mode is too high to allow measurement of this power level. If we assume a required frequency resolution of 6 GHz, the video noise-equivalent-power $(NEP)_v$ of this detector is on the order of 5×10^{-8} W (ref. 45). In Fig. 3.27 the bar graph shows the scattered power, integrated over a 6-GHz bandwidth, plotted as a function of the frequency of a number of channels centered on the frequencies 7, 11, 17, and 53 GHz from the center of the laser line. (The reason for this channel selection is stated later.) The power level observed by the detectors varies from approximately 2×10^{-9} W to 1×10^{-8} W, resulting in a signal-to-noise ratio (S/N) of 0.02 to 0.1. This (S/N) is clearly unacceptable. By using these detectors as mixers in a heterodyne mode, the $(NEP)_v$ reduces to 1×10^{-19} W/Hz (ref. 45), resulting in a detector noise power of 2×10^{-10} W over a 6-GHz bandwidth. This detector noise level translates into an input signal-to-noise ratio $(S/N)_i$ of 3–16 for a 100-MW CO_2 laser. The postdetection signal-to-noise ratio $(S/N)_{pd}$ for a heterodyne receiver is primarily determined by the postdetection averaging time and the input detector bandwidth. Assuming that the signal is averaged over a laser pulse width of 1 μs from a detector with a bandwidth of 6 GHz, $(S/N)_{pd}$ will be improved by a factor $\sqrt{B\tau + 1}$, where B = predetection bandwidth = 6 GHz and τ = laser pulse width = 1 μs,

$$(S/N)_{pd} = \frac{(S/N)_i}{(S/N)_i + 1} \sqrt{B\tau + 1} = 77.5 \ , \tag{3.3}$$

so that a system (S/N) of approximately 75 will be achieved.

In order to convert the system to heterodyne detection, a series of CO_2 laser local oscillators must be found with frequencies that differ from the incident laser frequency by only a few gigahertz. A CO_2 rotational line spacing of 53 GHz occurs in the vicinity of the highest-gain transition, the 10P20 line. Fortunately, a number of cw lasers are available within the required frequency range. We have constructed lasers operating on the first sequence bands of CO_2 and N_2O that produce power levels of several watts, far more than the 1- to 2-mW local oscillator requirement of the HgCdTe detectors.[46] It is expected that other useful local oscillator frequencies will become available when isotopic CO_2 lasers are considered.

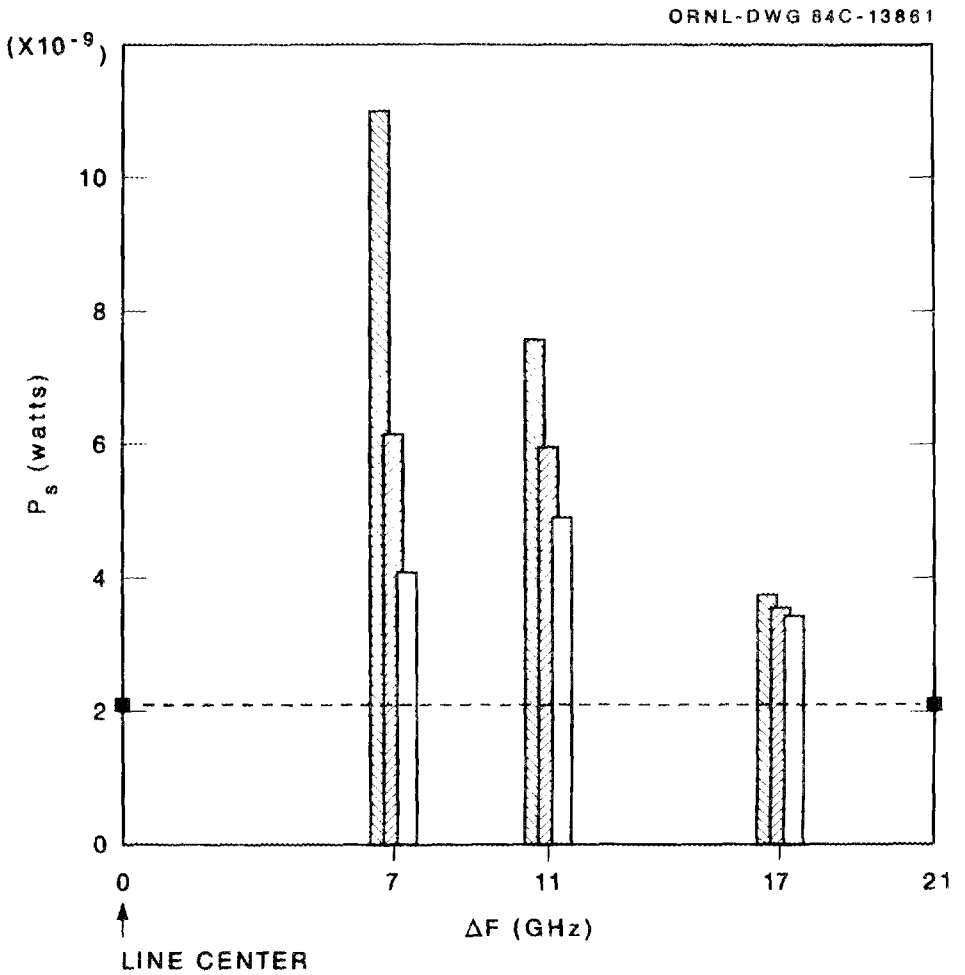

Fig. 3.27. The scattered power integrated over a 2-GHz bandwidth is plotted as a function of the shifted frequency of a number of channels centered on the frequencies 7, 11, and 17 GHz from the center of the incident laser line. The channel at 53 GHz, which observes only the electrons, is shown as a dotted line. The $1/v$ distribution is represented by the bars slanted down to the right, the $f(v)$ = constant distribution by the bars slanted up to the right, and the $f(v) = v$ distribution by the open bars.

Testing and calibration

A very interesting and attractive feature of the proposed alpha particle diagnostic is that a simpler scattering experiment may be conducted on a nonignited plasma device to determine the feasibility of the measurement. Referring to Fig. 3.26, since the scattered power due to the alpha particles is roughly equal to the small-angle Thomson scattering measurement of the electron scattering in the absence of alpha particles, the sensitivity of the diagnostic may be determined. In fact, since the electron density and temperature will be known from other diagnostics, an absolute calibration is possible. Also, because a detector observing frequencies shifted 53 GHz from line center will see only scattering from the electrons, even in a burning plasma with alphas present, the experiment will be self-calibrating for every measurement.

REFERENCES

1. R. Geller, B. Jacquot, and C. Jacquot, "ECR Sources for Single and Multiply Charged Ion Production," p. 187 in *Proceedings of the 7th International Symposium on Ion Sources and Ion Assisted Technology (ISIAT Kyoto)*, Institute of Electrical Engineers of Japan, Tokyo, 1983.

2. G. Lisitano, M. Fontanesi, and E. Sindoni, "Nonresonant Absorption of Electromagnetic Waves in a High-Density Plasma," *Appl. Phys. Lett.* **16**, 122 (1970).

3. D. P. Grubb and T. Lovell, "Conical Slow-Wave Antenna as a Plasma Source," *Rev. Sci. Instrum.* **49**, 77 (1978).

4. *Physics Division Progress Report for Period Ending September 30, 1983*, ORNL-6004, Union Carbide Corp. Nuclear Div., Oak Ridge Natl. Lab., December 1983.

5. K. Halbach, "Design of Permanent Multipole Magnets with Oriented Rare Earth Cobalt Material," *Nucl. Instrum. Methods* **169**, 1 (1980).

6. Operation in decel mode is not possible in the present application due to the favorable conditions for Penning discharge produced by the combination of ion source magnetic fringe field and lens electrostatic field.

7. H.-G. Mathews, H. Beuscher, R. Fiedler, and W. Krauss-Vogt, "Pre-ISIS2—A Two-Stage ECR Source for Highly-Stripped Light Heavy Ions," in *Institut für Kernphysik Annual Report 1983*, Kernforschungsanlage Jülich GmBH, Jülich, Federal Republic of Germany, 1983.

8. D. J. Clark, Y. Jongen, and C. M. Lyneis, "Progress on the LBL ECR Heavy Ion Source," *IEEE Trans. Nucl. Sci.*, accepted for publication (1985).

9. W. Fritsch and C. D. Lin, "Atomic-Orbital-Expansion Studies of Electron Transfer in Bare-Nucleus Z ($Z = 2, 4$–8) Hydrogen Atom Collisions," *Phys. Rev. A* **29**, 3039 (1984).

10. T. A. Green, E. J. Shipsey, and J. C. Browne, "Modified Method of Perturbed Stationary States. IV. Electron-Capture Cross Sections for the Reaction $C^{6+} + H(1s) \rightarrow C^{5+}(n,l) + H^+$," *Phys. Rev. A* **25**, 1364 (1982).

11. E. J. Shipsey, T. A. Green, and J. C. Browne, "Modified Method of Perturbed Stationary States. V. Electron-Capture Cross Sections for the Reaction $O^{8+} + H(1s) \rightarrow O^{7+}(n, l) + H^+$," *Phys. Rev. A* **27**, 821 (1983).

12. R. K. Janev, D. S. Belic, and B. H. Brandsen, "Total and Partial Cross Sections for Electron Capture in Collisions of Hydrogen Atoms with Fully Stripped Ions," *Phys. Rev. A* **28**, 1293 (1983).

13. M. N. Panov, A. A. Basalev, and K. O. Lozhkin, "Interaction of Fully Stripped, Hydrogenlike and Heliumlike C, N, O, Ne, and Ar Ions with H and He Atoms and H_2 Molecules," *Phys. Scr.* **T3**, 124 (1983).

14. This project is supported by the Division of Chemical Sciences of the Office of Basic Energy Sciences, U.S. Department of Energy.

15. R. A. Phaneuf et al., "Electron Capture in Low-Energy Collisions of C^{q+} and O^{q+} with H and H_2," *Phys. Rev. A* **26**, 1892 (1982).

16. D. H. Crandall, R. A. Phaneuf, and D. C. Gregory, *Electron Impact Ionization of Multicharged Ions*, ORNL/TM-7020, Union Carbide Corp. Nuclear Div., Oak Ridge Natl. Lab., September 1979.

17. D. C. Gregory, D. H. Crandall, R. A. Phaneuf, A. M. Howald, G. H. Dunn, R. A. Falk, D. W. Mueller, and T. J. Morgan, *Electron Impact Ionization of Multicharged Ions at ORNL, 1980–1984*, ORNL/TM-9501, Oak Ridge Natl. Lab., April 1985.

18. W. Lotz, "Electron-Impact Ionization Cross Sections and Ionization Rate Coefficients for Atoms and Ions from Scandium to Zinc," *Z. Phys.* **220**, 466 (1969).

19. M. S. Pindzola, D. C. Griffin, C. Bottcher, D. C. Gregory, A. M. Howald, R. A. Phaneuf, D. H. Crandall, G. H. Dunn, D. W. Mueller, and T. J. Morgan, *Survey of Experimental and Theoretical Electron-Impact Ionization Cross Sections for Transition Metal Ions in Low Stages of Ionization*, ORNL/TM-9436, Oak Ridge Natl. Lab., March 1985.

20. M. S. Pindzola, D. C. Griffin, and C. Bottcher, "Electron-Impact Excitation-Autoionization in the Cadmium Isoelectronic Sequence: A Case of Target Term Dependence in Scattering Theory," *Phys. Rev. A* **27**, 2331–7 (1983).

21. D. C. Griffin, C. Bottcher, M. S. Pindzola, S. M. Younger, D. C. Gregory, and D. H. Crandall, "Electron-Impact Ionization in the Xenon Isonuclear Sequence," *Phys. Rev. A.* **29**, 1729–41 (1984).

22. D. C. Gregory and A. M. Howald, unpublished data, March 27, 1985.

23. D. C. Gregory and D. H. Crandall, "Measurement of the Cross Section for Electron Impact Ionization of Xe^{6+} Ions," *Phys. Rev. A* **27**, 2338–41 (1983).

24. M. S. Pindzola, Auburn University, Auburn, Ala., personal communication, 1984.

25. D. C. Gregory, P. F. Dittner, and D. H. Crandall, "Absolute Cross-Section Measurements for Electron-Impact Ionization of Triply Charged Inert Gas Ions: Ne^{3+}, Ar^{3+}, Kr^{3+}, and Xe^{3+}," *Phys. Rev. A* **27**, 724–36 (1983); D. H. Crandall et al., "Absolute Cross-Section Measurements for Electron-Impact Ionization of Na-Like Ions—Mg^{+}, Al^{2+}, and Si^{3+}," *Phys. Rev. A* **25**, 143 (1982).

26. P. O. Taylor, K. T. Dolder, W. E. Kauppila, and G. H. Dunn, "Measurement of Spiraling in a Magnetically Confined Electron Beam for Use in Collision Studies," *Rev. Sci. Instrum.* **45**, 538 (1975).

27. I. Frank and W. Ginzburg, "Radiation of a Uniformly Moving Electron Due to Its Transition from One Medium to Another," *J. Phys. (Moscow)* **9**, 363 (1945).

28. H. Boersch and G. Sauerbrey, "Transition Radiation, Bremsstrahlung, and Plasma Radiation," p. 386 in *Proceedings of the International Colloquium on Optical Properties and Electronic Structure of Metals and Alloys*, ed. F. Abelès, North-Holland Publishing Co., Amsterdam, 1966.

29. C. Bottcher and T. G. Heil, "Low-Energy Charge Exchange from Hydrogen Atoms by Few-Electron Ions," *Chem. Phys. Lett.* **86**, 506 (1982).

30. F. W. Meyer et al., Sects. 3.1.1 and 3.1.2 of this report.

31. D. H. Crandall et al., "Electron Capture by Heavy Multicharged Ions from Atomic Hydrogen at Low Velocities," *Phys. Rev. A* **22**, 379 (1980).

32. D. C. Griffin, M. S. Pindzola, and C. Bottcher, "Distorted-Wave Calculations of Dielectronic Recombination Cross Sections in the Li Isoelectronic Sequence," *Phys. Rev. A* **31**, 568–75 (1985).

33. P. F. Dittner et al., "Cross Sections for Dielectronic Recombination of B^{2+} and C^{3+} via 2s → 2p Excitation," *Phys. Rev. Lett.* **51**, 31–34 (1983).

34. S. J. Zweben, J. McChesney, and R. W. Gould, "Optical Imaging of Edge Turbulence in the Caltech Tokamak," *Nucl. Fusion* **23**, 825 (1983).

35. P. H. Stelson and C. F. Barnett, "Plasma Ion Temperature Measured by Neutron Transmission Through Liquid Oxygen," *Bull. Am. Phys. Soc.* **23**, 882 (1978).

36. C. H. Johnson et al., "Measurement of the 2.35-MeV Window in O + n," in *Nuclear Cross Sections for Technology*, Special Technical Publication 594, U.S. Department of Commerce, Bur. Standards, 1980.

37. R. G. Alsmiller, Jr., et al., *Background Calculations for the Measurement of the Ion Temperature in a Deuterium Plasma*, ORNL/TM-9230, Oak Ridge Natl. Lab., July 1984.

38. D. M. Thomas, "Low Energy Neutral Particle Spectrometer," p. 266 in *Physics Division Annual Progress Report*, ORNL-6004, Union Carbide Corp. Nuclear Div., Oak Ridge Natl. Lab., December 1983.

39. D. E. Post et al., "Techniques for Measuring the Alpha-Particle Distribution in Magnetically Confined Plasmas," *J. Fusion Energy* **1**, 129–42 (1981).

40. U. Schumacher and E. Springmann, *Some Considerations Concerning Fusion Alpha Particle Diagnostics*, IPP 1/215, Max-Planck-Institut für Plasmaphysik, Garching, Federal Republic of Germany, April 1983.

41. K. N. Sato and M. Sasao, "Alpha Particle Diagnostics for the R-Project," p. 51 in *Annual Review, April 1981–March 1982*, Institute of Plasma Physics, Nagoya University, Nagoya, Japan, 1982.

42. G. Gerdin and B. W. Wehring, *Technical Progress Report on the TFTR Alpha Extraction and Measurement Project*, DOE/ER/53197-1, U.S. Department of Energy, September 1983.

43. J. Sheffield, *Plasma Scattering of Electromagnetic Radiation*, Academic Press, New York, 1975.

44. W. Houlberg, Oak Ridge National Laboratory, personal communication, 1984.

45. Catalog, Santa Barbara Research, 1983, p. 6.

46. B. J. Peyton et al., "High-Sensitivity Receiver for Infrared Laser Communications," *IEEE J. Quantum Electronics* **QE-8**, 252 (1972).

Chapter 4

Plasma Theory

R. A. Dory, Section Head

D. E. Arnurius[1]	P. H. Diamond[5]	W. A. Houlberg	K. C. Shaing
S. E. Attenberger[1]	R. H. Fowler[1]	H. C. Howe	D. J. Sigmar
D. B. Batchelor	J. P. Freidberg[6]	J. V. Hughes	D. A. Spong
C. O. Beasley, Jr.	L. Garcia	E. F. Jaeger	W. M. Stacey, Jr.[9]
E. T. Blair[1]	R. C. Goldfinger[1]	K. L. Kannan[1]	C. R. Stewart, Jr.
R. D. Burris[1]	W. H. Gray[7]	H. E. Ketterer	K. A. Stewart
J. D. Callen[2]	D. E. Greenwood[1]	D. K. Lee[1]	D. J. Tate[4]
J. L. Cantrell[1]	J. H. Harris[8]	V. E. Lynch[1]	J. S. Tolliver[1]
B. A. Carreras	D. E. Hastings	J. F. Lyon[8]	W. I. van Rij[1]
L. A. Charlton[1]	C. L. Hedrick	J. B. Mankin[1]	G. M. Warren[4]
G. L. Chen[3]	T. C. Hender	K. Molvig[6]	H. Weitzner[10]
D. N. Clark[1]	H. R. Hicks[1]	R. N. Morris[1]	J. C. Whitson[1]
W. A. Cooper	S. P. Hirshman	D. R. Overbey	J. W. Wooten
J. F. Cox[4]	J. T. Hogan	L. W. Owen[1]	G. B. Wootton
E. C. Crume, Jr.	J. A. Holmes[1]	J. A. Rome	K. G. Young

1. Computing and Telecommunications Division, Martin Marietta Energy Systems, Inc.
2. The University of Wisconsin, Madison.
3. Plasma Technology Section.
4. Section secretary.
5. Institute for Fusion Studies, University of Texas, Austin.
6. Massachusetts Institute of Technology, Cambridge.
7. Magnetics and Superconductivity Section.
8. Toroidal Confinement Physics Section.
9. Georgia Institute of Technology, Atlanta.
10. Courant Institute of Mathematical Sciences, New York University, New York.

CONTENTS

SUMMARY OF ACTIVITIES 4-9

4.1 MHD EQUILIBRIUM, STABILITY,AND TURBULENCE 4-9

4.1.1 Stellarators—Abstracts 4-11

4.1.1.1 "MHD Equilibrium and Stability for Stellarator/Torsatron Configurations" 4-11

4.1.1.2 "MHD Equilibrium and Stability for Stellarator Configurations" 4-12

4.1.1.3 "Zero-Current, High Beta Stellarator Equilibria with Rotational Transform Profile Control" 4-14

4.1.1.4 "Generic Ballooning in Anisotropic Pressure Toroids" 4-14

4.1.1.5 "Helically Symmetric Magnetohydrodynamic Plasma Equilibrium" 4-14

4.1.1.6 "Stability Calculations for High-Beta Torsatrons" 4-15

4.1.1.7 "Equilibrium Studies for Helical Axis Stellarators" 4-15

4.1.1.8 "Equilibrium Studies for Helical Axis Stellarators" 4-15

4.1.1.9 "Equilibrium Calculations for Helical Axis Stellarators" 4-15

4.1.1.10 "Equilibrium Studies in Helical Axis Stellarators" 4-16

4.1.1.11 "The Calculation of Stellarator Equilibria in Vacuum Flux Surface Coordinates" 4-16

4.1.1.12 "Comparison of 3-D Moments and Finite Difference Inverse MHD Equilibrium Codes" 4-16

4.1.1.13 "Optimized Fourier Representations for Three-Dimensional Magnetic Surfaces" 4-17

4.1.1.14 "A Convergent Spectral Representation for Three-Dimensional Inverse MHD Equilibria" 4-17

4.1.1.15 "Comparison of 3D MHD Inverse Coordinates Codes" 4-17

4.1.1.16 "Free Boundary Stellarator Expansion MHD Equilibrium and Stability Calculations" 4-18

4.1.1.17 "Stellarator Expansion Studies of a High Beta Torsatron" 4-18

4.1.1.18 "Free Boundary Equilibrium and Stability of a Moderate Aspect Ratio Torsatron Using the Stellarator Expansion" 4-19

4.1.1.19 "Resistive Ballooning in Plasma Confinement Schemes with a Coordinate of Symmetry" 4-19

4.1.1.20 *Accelerated Convergence of the Steepest Descent Method for Magnetohydrodynamic Equilibria* 4-19

4.1.2 Tokamaks and Reversed-Field Pinches—Abstracts 4-20

4.1.2.1 "The Effects of Toroidicity on Resistive MHD Instabilities in the RFP" 4-20

4.1.2.2 "Fully Toroidal Nonlinear MHD Calculations Without Ordering Assumptions" 4-20

4.1.2.3 "Incompressible MHD Modes in Toroidal Geometry" 4-20
4.1.2.4 "Calculations in Toroidal Geometry with Full MHD Equations" 4-21
4.1.2.5 "Centrifugal Force Effects from Toroidal Rotation on Incompressible Resistive Ballooning" 4-21
4.1.2.6 "Resistive Ballooning Modes in Toroidally Rotating Tokamak Plasmas" 4-21
4.1.2.7 "Suppression of Spectral Pollution by Angle Renormalization" 4-21
4.1.2.8 *Magnetic Fluctuations, Field Reversal Maintenance, and Anomalous Thermal Transport in the Reversed Field Pinch* 4-22
4.1.2.9 *Theory of Resistivity-Gradient-Driven Turbulence* 4-22
4.1.2.10 "Nonlinear Evolution of Microtearing Modes" 4-22
4.1.2.11 *The Reliability of Initial Value MHD Calculations of Tokamak Disruptions* 4-23
4.1.2.12 *Nonlinear Interaction of Tearing Modes: A Comparison Between the Tokamak and the Reversed Field Pinch Configuration* 4-23
4.1.2.13 "Inverse Mapping Algorithm for Moments Formulation of MHD Equilibria" 4-24
4.1.2.14 "The Spectrum of the MHD and Kinetic Alfvén Waves in a Cylindrical Tokamak" 4-24
4.1.2.15 "Role of Multiple Helicity Nonlinear Interaction of Tearing Modes in Dynamo and Anomalous Thermal Transport in the Reversed Field Pinch" 4-25
4.1.2.16 "Spectrum of Rippling Mode Turbulence" 4-25
4.1.2.17 "Investigation into the Structure of Saturated Magnetic Islands in a Poloidal Divertor Tokamak" 4-26
4.1.2.18 "MHD Equilibrium Studies of a Poloidal Divertor Tokamak Using the Chodura-Schlüter Method" 4-26
4.1.3 EBS and EBT Devices—Abstracts 4-27
4.1.3.1 "Magnetic Equilibria for Square and Circular EBTs" 4-27
4.1.3.2 "Magnetic Equilibrium and Single Particle Orbits in EBS" 4-27
4.1.3.3 "Ballooning Modes in the ELMO Bumpy Square Configuration Using the Generalized Kinetic Energy Principle" 4-28
4.1.3.4 "Electrostatic Confinement in a Bumpy Torus" 4-28
4.1.3.5 "Electrostatic Confinement in a Bumpy Torus with Hot Electron Rings" 4-29
4.1.3.6 "The Magnetohydrodynamic Equilibria in a Bumpy Torus with Toroidal Current" 4-29
4.2 TRANSPORT KINETICS: KINETIC THEORY 4-30
4.2.1 Ambipolar Potential—Abstracts 4-31

4.2.1.1 "Development of a Differential Equation for the Ambipolar Electric Field in a Bumpy Torus in the Low Collision Frequency Limit" 4-31
4.2.1.2 "A Differential Equation for the Ambipolar Electric Field in a Multiple-Helicity Torsatron" 4-32
4.2.1.3 "The Ambipolar Electric Field in Stellarators" 4-32
4.2.1.4 "Calculation of the Self-Consistent Electric Field in Toroidal Nonaxisymmetric Devices" 4-32
4.2.1.5 "Azimuthal Electric Fields and Ambipolarity in a Multiple Helicity Torsatron" 4-32
4.2.1.6 "Noise-Induced Transition of the Radial Electric Field in a Nonaxisymmetric Torus" 4-33
4.2.1.7 "Stability of the Radial Electric Field in a Nonaxisymmetric Torus" 4-33
4.2.1.8 "The Radial Electric Field in a Nonaxisymmetric Torus" 4-33
4.2.1.9 "The Radial Electric Field in a Stellarator" 4-35
4.2.2 Transport Coefficients—Abstracts 4-37
4.2.2.1 "Stochastic Particle Diffusion in Velocity Space for a Bumpy Torus" 4-37
4.2.2.2 "Monte Carlo Studies of Transport in Stellarators" 4-37
4.2.2.3 "Transport Associated with the Collisionless Detrapping/Retrapping of Orbits in a Nonaxisymmetric Torus II" 4-37
4.2.2.4 "Collisionless Neoclassical Nonresonant Transport in Bumpy Tori" 4-38
4.2.2.5 "Neoclassical Transport in a Bumpy Closed Field Line Device in the Collisional, Small Electric Field Regime" 4-38
4.2.2.6 "Superbanana Plateau Regime Transport in a Multiple-Helicity Torsatron and a Bumpy Torus" 4-38
4.2.2.7 "Non-Local Transport in Tokamaks" 4-39
4.2.2.8 "Monte Carlo Estimates of Transport Rates in EBT with Asymmetric Potential Profiles" 4-39
4.2.2.9 "Bounce-Averaged Monte Carlo Calculations for Stellarators" 4-40
4.2.2.10 "Enhanced Neoclassical Diffusion of Nonresonant Particles in a Bumpy Torus" 4-40
4.2.3 Extensions to MHD—Abstracts 4-40
4.2.3.1 "A Pressure-Gradient-Driven Tokamak 'Neoclassical MHD' Instability in the Banana-Plateau Collisionality Regime" 4-40
4.2.3.2 "Resistive MHD-Like Equations in the Banana-Plateau Collisionality Regime" 4-41

4.2.3.3 "A Kinetic Approach to a New Pressure Gradient Driven Tokamak Instability" 4-41
4.2.4 Microstability and Turbulence—Abstracts 4-41
4.2.4.1 "Drift Waves Destabilized by Pellet Injection" 4-41
4.2.4.2 "Effect of Coulomb Collisions on Universal Mode Stability" 4-42
4.2.4.3 *Theory and Calculation of Finite Beta Drift Wave Turbulence* 4-42
4.2.4.4 "Influence of Ideal Ballooning Modes on Confinement Scaling at High β" 4-42
4.3 RF HEATING AND CURRENT DRIVE 4-43
4.3.1 Abstract of "Propagation and Absorption of Electromagnetic Waves in Fully Relativistic Plasmas" 4-43
4.3.2 Abstract of "Strong Damping of Electron Cyclotron Waves in Nearly Parallel Stratified Plasmas" 4-44
4.3.3 Abstract of "Fokker-Planck Calculations of Core Plasma Heating by ECRH in EBT" 4-44
4.3.4 Abstract of "Fokker-Planck Modeling of Electron Cyclotron Heating and Direct Particle Loss in EBT and ELMO Bumpy Square" 4-45
4.3.5 Abstract of "Propagation and Absorption of Electron Cyclotron Waves in ATF" 4-45
4.3.6 Abstract of "R-F and Microwave Induced Losses" 4-45
4.3.7 Abstract of "Microwave-Induced Neoclassical Transport" 4-46
4.3.8 Abstract of "Full Wave Treatment of Wave Propagation in a Three-Dimensional Cavity Containing Cold Plasma" 4-46
4.3.9 Abstract of "A Numerical Model for Examining Noninductive Current Drive Scenarios in Ignition Tokamaks" 4-47
4.3.10 Abstract of "Second Harmonic Electron Cyclotron Heating" 4-47
4.3.11 Abstract of "Absorption, Reflection, and Mode Coupling at the Second Cyclotron Resonance in a Weakly Relativistic, Inhomogeneous Plasma" 4-48
4.4 CONFINEMENT OPTIMIZATION AND IMPROVEMENT 4-48
4.4.1 Abstract of "The Flexible Heliac" 4-52
4.4.2 Abstract of "Approximate Flux Conserving Stellarator" 4-52
4.4.3 Abstract of "Study of ATF-1 Torsatron Configurations Using the NYU Code BETA" 4-52
4.4.4 Abstract of "$\ell=1/\ell=2$ Torsatron Hybrids" 4-53
4.5 PLASMA MODELING, BURN ANALYSIS, IMPURITIES, AND PELLETS 4-53
4.5.1 Abstract of "Intersections of a Trajectory with Tokamak or Stellarator Flux Surfaces" 4-55
4.5.2 Abstract of "Efficient Mapping Algorithms Between Flux Coordinates and Real-Space Coordinates for Toroidal Plasmas" 4-55
4.5.3 Abstract of "Effects of Momentum Input and Sonic Flow on Impurity Transport in Tokamaks" 4-56

4.5.4 Abstract of "Theory and Simulations of the Electrostatic Potential in Neutral-Beam-Driven Tokamaks and Effects on Impurity Transport" 4-56
4.5.5 Abstract of "Beam-Induced Current Effects on Stellarator Transform" 4-57
4.5.6 Abstract of "Current Generation in Stellarators" 4-57
4.5.7 Abstract of "Rotation and Impurity Flow Reversal in Tokamak Plasmas with Neutral Beam Injection" 4-58
4.5.8 Abstract of *Rotation and Impurity Transport in a Tokamak with Directed Neutral Beam Injection* 4-58
4.5.9 Abstract of "Long Pulse Evolution of Elongated, Rippled High-Beta Tokamaks" 4-59
4.6 ALPHA PARTICLE PHYSICS 4-59
4.6.1 Abstract of "Effects of Trapped Alpha Particles on Ballooning Modes" 4-60
4.6.2 Abstract of "Effects of α-Particles on CO_2 Laser Scattering From a Fusion Plasma" 4-61
4.7 EXPERIMENT INTERPRETATION 4-61
4.7.1 Tokamak Interpretation—Abstracts 4-63
4.7.1.1 "Equilibrium Modeling of ISX-B Tokamak Discharges" 4-63
4.7.1.2 "Simulation of Impurity Transport in the ISX-B Tokamak with Directed Neutral Beam Heating" 4-63
4.7.1.3 "Anomalous Pellet Ablation in ISX-B Discharges" 4-64
4.7.1.4 "Toroidal Flow Analysis of ISX-B Density and Temperature Profiles" 4-64
4.7.1.5 "Particle Confinement in ISX-B" 4-65
4.7.1.6 "Neutral Beam Driven Impurity Flow Reversal in PLT and ISX-B" 4-65
4.7.1.7 "Limiting β Investigations at Low Collisionality" 4-65
4.7.2 EBT Interpretation—Abstracts 4-66
4.7.2.1 "Core Plasma Heating in EBT-S and the Effect of Strongly Damped Cyclotron Waves" 4-66
4.7.2.2 "Comparison of Electron Cyclotron Heating Theory and Experiment in EBT" 4-66
4.7.2.3 "Coupled Transport and Heating in EBT and EBS" 4-67
4.7.2.4 "Magnetic Well Depth in EBT and Sensitivity to Hot Electron Ring Geometry" 4-69
4.7.2.5 "Finite $k_{\parallel}$ High Frequency Fluctuations in EBT" 4-70
4.8 COMPUTING SUPPORT 4-70
4.8.1 USC Operations 4-70
4.8.2 Experimental Support 4-71
4.8.2.1 Support of experiments 4-71
4.8.2.2 Repeating pellet injector stand-alone control system 4-72
4.8.2.3 Large Coil Program data acquisition system 4-72
4.8.2.4 RFTF experiment support 4-73
REFERENCES 4-74

4. PLASMA THEORY

Summary of Activities

The plasma theory effort concentrates on *toroidal* confinement theory. The goals of toroidal confinement theory are to understand, improve, and optimize the confinement of plasmas for fusion reactors. To achieve these goals, it is necessary to develop new theories and validate them with experiments. The approach is to identify critical problems and then to integrate the necessary plasma physics disciplines to solve them. Our fundamental areas of research are (1) equilibrium, stability, and turbulence; (2) transport kinetics; and (3) rf heating and current drive. These feed basic results into the integrating efforts, (4) confinement optimization, (5) plasma modeling, and (6) alpha particle physics, which in turn drive the primary application area, (7) experiment interpretation. This approach maximizes internal collaboration while keeping a sharp focus on key issues. Collaboration with ORNL experimental groups, with university groups, and at the international level is strongly emphasized.

Key results in the last year include definitions of ways to increase flexibility and improve confinement for the Advanced Toroidal Facility (ATF) device; invention of the flexible heliac concept; improved understanding of confinement in the Impurity Study Experiment (ISX-B) tokamak; improved understanding of electron cyclotron heating and confinement in ELMO Bumpy Torus (EBT); development of an improved bumpy system, ELMO Bumpy Square (EBS); and successful application of pellet models to the Tokamak Fusion Test Reactor (TFTR) and the Doublet III (DIII) tokamak.

This past year's work is summarized in more detail in the sections on fundamental areas of research, Sects. 4.1, 4.2, and 4.3; in the sections on the integrating efforts, Sects. 4.4, 4.5, and 4.6; and in the section on experimental interpretation, Sect. 4.7. Computing support activities are summarized in Sect. 4.8.

4.1 MHD EQUILIBRIUM, STABILITY, AND TURBULENCE

The magnetohydrodynamic (MHD) equilibrium, stability, and turbulence effort is characterized by the use of analytic and numerical fluid models to study the behavior of magnetically confined plasmas. Equilibrium properties and linear and nonlinear stability properties are analyzed, and calculations are made of nonlinearly evolved fluctuation levels and their consequences for particle and heat transport. Research is carried out on two strongly interconnected levels. First, fundamental physics research is performed, generally using simplified geometry, to unveil some of the basic mechanisms underlying plasma behavior. This work establishes a sound basis for theoretical developments. The theoretical

developments are then applied to specific devices, providing the basic physics understanding and tools for configuration optimization and for plasma modeling.

In the area of equilibrium theory, new techniques that provide for more efficient calculations and better physics understanding were developed in the past year. A new stellarator expansion applicable to planar, as well as helical-axis, configurations was developed. It gives results that compare very favorably with three-dimensional (3-D) calculations. A spectral representation for 3-D inverse MHD equilibria was also developed; it possesses superior convergence properties in mode number space. Free boundary and 3-D equilibrium calculations were made for the Advanced Toroidal Facility (ATF) configuration to verify the existence of a flux-controlled path to high beta. Heliac equilibria were studied intensively. The equilibria were examined for sensitivity to the presence of nearby resonances. The possibility of improving equilibrium quality was investigated through calculations in which parameters such as aspect ratio, number of field periods, and toroidal current modulation were varied. In addition, equilibrium calculations were made for the High-Beta Q Machine (HBQM) at the University of Washington and for the Tokapole device at the University of Wisconsin. The calculations were made in collaboration with groups at these universities, who are using them for experimental comparisons.

In the area of linear stability theory, the 3-D ballooning mode equation was extended to treat resistive instabilities and anisotropic plasmas. The stability of ATF to external modes was studied, and the instability boundaries to be explored experimentally were mapped. Stability properties of the optimized equilibria for low-aspect-ratio torsatrons were determined. The effect of the toroidal field on the MHD stability of the Heliotron-E device was analyzed. It was found that the added toroidal field makes the rotational transform close to the ATF vacuum transform and raises the value of the critical beta. Also, a study was made of the effects of toroidicity on resistive instabilities of reversed-field pinch (RFP) devices. The effects are very weak for tearing modes, but they modify the g mode stability properties.

A combination of analytic and computational work in the areas of nonlinear stability theory and turbulence brought to light two new connections between MHD phenomena and anomalous transport. First, a new turbulent stabilization mechanism for rippling modes was discovered. This discovery permits the development of an analytic theory that predicts the saturation levels for the fluctuations and the consequent diffusion coefficients. Also, a saturation mechanism for tearing modes in RFP devices was uncovered. With this mechanism, the present theories of tokamak disruptions and of field reversal maintenance can be unified.

The physics studies discussed above require continual development and evolution of efficient codes and numerical techniques. In the past year, a new 3-D equilibrium code, MOMCON, based on the optimized Fourier representation of the equilibrium, was originated. The linear FAR code was adapted to treat stellarators and RFP configurations, and a nonlinear version was developed and tested. Several significant new computational algorithms were developed. A zero-current equilibrium algorithm was incorporated into the 3-D equilibrium codes NEAR and ORMEC. Implicit-explicit hybrid schemes that have increased the efficiency of nonlinear calculations were developed. Also, a fully implicit scheme for the full MHD linear equations was devised that is very stable, allows calculations of modes that are not the most unstable ones, and reduces the computational time considerably.

The following abstracts of work performed in this effort are organized by device type rather than by area because many of them report on work covering more than one area.

4.1.1 Stellarators—Abstracts

4.1.1.1 "MHD Equilibrium and Stability for Stellarator/Torsatron Configurations"[1]

B. A. Carreras, J. L. Cantrell, L. A. Charlton, W. A. Cooper, L. Garcia, J. H. Harris,
T. C. Hender, H. R. Hicks, J. A. Holmes, J. A. Rome,
and V. E. Lynch

The MHD studies at ORNL have mainly concentrated in two areas: the improvement of the understanding of high-beta torsatrons through the concept of flux conservation and the study of helical-axis configurations. In this paper we will describe the results obtained in both areas.

I. The flux-conserving path to high beta. The concept of a flux-conserving tokamak has been a very useful one to understand the access to a high-beta regime for tokamaks. It has also been useful as an experimental guide in achieving such a regime. The stellarator, being a steady-state device, will, in general, not follow the flux-conserving path in the simple way that tokamaks do. After the fast heating process, which conserves flux, the rotational transform profile will evolve due to resistive diffusion, and the equilibrium will become a zero-current equilibrium. By changing the shape of the poloidal field during the evolution it is, in principle, possible to maintain the rotational transform profile while the equilibrium tends to the zero-current limit. We have investigated this for the particular case of the ATF device. In this case, using the vertical field (VF) coil system, an approximate flux-conserving path to high beta can be followed. In Fig. 4.1, an approximate flux-conserving sequence of equilibria is shown. The figure shows that an increase in ellipticity and triangularity is required. The strong "bean" shaping of the flux surfaces is apparent. Following this equilibrium sequence, it is possible to access the second stability regime even with broad pressure profiles, avoiding the free boundary instability found by Rewoldt and Johnson. These studies have been made using the stellarator expansion for the equilibrium and stability calculations. From the condition of zero current in each flux surface and the equilibrium equation, the following relations can be derived:

$$\iota(\rho) = -\frac{1}{\rho F}\left(\int_0^{2\pi} d\Theta\, g^{\rho\rho}\right)^{-1} \int_0^{2\pi} d\Theta \left[g^{\rho\rho}\frac{\partial(\overline{\gamma}_v + \psi_0)}{\partial\rho} + \frac{g^{\rho\theta}}{\rho}\frac{\partial(\overline{\gamma}_v + \psi_0)}{\partial\Theta}\right],$$

$$\frac{dF}{d\rho}\left(F + \int_0^{2\pi} d\Theta\, F^*\right) = \frac{\beta_0}{2}\frac{dp}{d\rho}\int_0^{2\pi} d\Theta\, R^2 .$$

Here ψ_v is the vacuum-field-averaged poloidal flux function due to the helical fields only, and ψ_0 is the poloidal flux function due to the vertical field system. The coordinates ρ, Θ are straight field line coordinates, and $F^* = -R^2\langle(\vec{\nabla}\tilde{\phi})^2\rangle/F$. From these equations ψ_0 can be calculated by a multipolar expansion in Θ when the ι profile is prescribed. For a given system of coils, at best, only an approximate solution can be obtained. The flexibility of the ATF VF coil system permits such an approximate solution (Fig. 4.1).

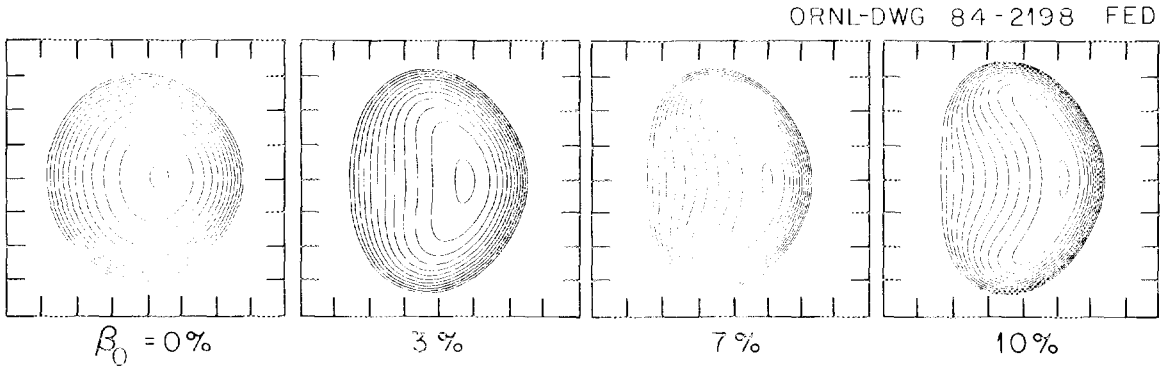

Fig. 4.1. Approximate flux-conserving path to high beta.

II. Helical-axis configurations. In the large-aspect-ratio limit, stellarator configurations with helical axes have attractive stability features. To study such configurations, the 3-D code NEAR and a generalized averaging method have been used. The averaged method is based on an ordering similar to that of Greene and Johnson, but the averaging is performed in a vacuum flux coordinate system. In this coordinate system the averaging technique has a more direct physical interpretation than in real space and provides, in a natural way, a trivial extension to helical-axis configurations. In this way the equilibrium problem is reduced to solving a two-dimensional (2-D) Grad-Shafranov type of equation. By using the ordering, the helically varying part of the equilibrium equations may be reduced to a Poisson-type equation for the toroidal field fluctuations. By computing these helical corrections to the average equilibrium solution we are able to study configurations that have toroidally dominated shifts but with significant helical distortions (e.g., small-aspect-ratio heliacs). This method has been applied to the ATF helical-axis configuration and to heliac-type configurations. The results of the equilibrium calculation show good agreement with numerical results using 3-D codes (Figs. 4.2 and 4.3).

4.1.1.2 "MHD Equilibrium and Stability for Stellarator Configurations"[2]

B. A. Carreras, J. L. Cantrell, L. A. Charlton, L. Garcia, J. H. Harris, T. C. Hender, H. R. Hicks, J. A. Holmes, and V. E. Lynch

The stellarator equilibrium and stability studies presented in this paper are focused on improving the understanding of high-beta torsatrons through the concept of flux control and the extension of the stellarator expansion to helical-axis configurations.

The torsatron VF coil system can be programmed to control the rotational transform profile at high beta by modifying the plasma shape while keeping the ι at the magnetic axis fixed. This technique is potentially very useful, because if the external fields are not changed as beta is increased, zero-net-current equilibrium sequences show significant deformation of the rotational transform profile. A progressive elongation of the flux surfaces with increasing beta is required to maintain constant ι_0. The flux-controlled equilibrium path also has the favorable property of reduced finite-beta axis shift relative to

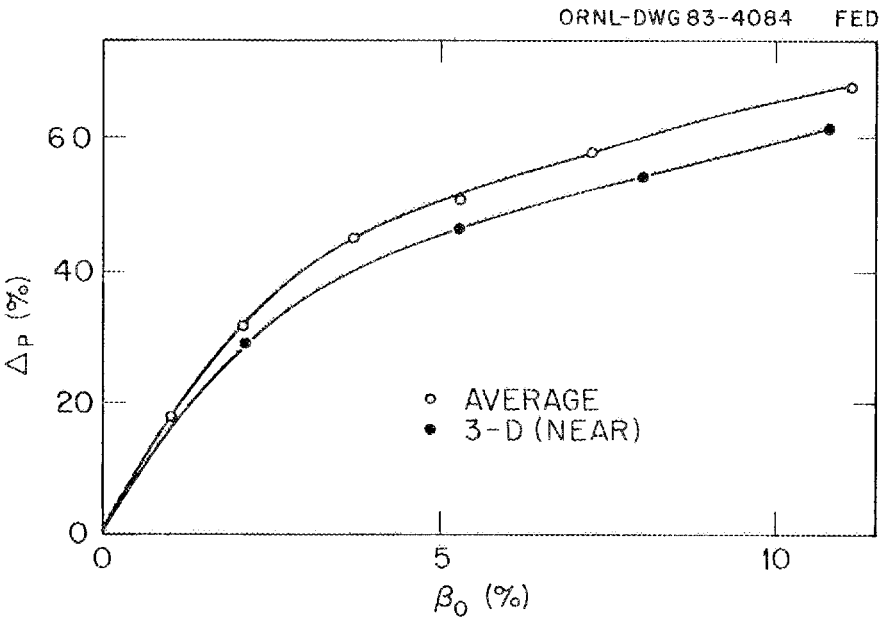

Fig. 4.2. Magnetic axis shift for the ATF helical-axis configuration.

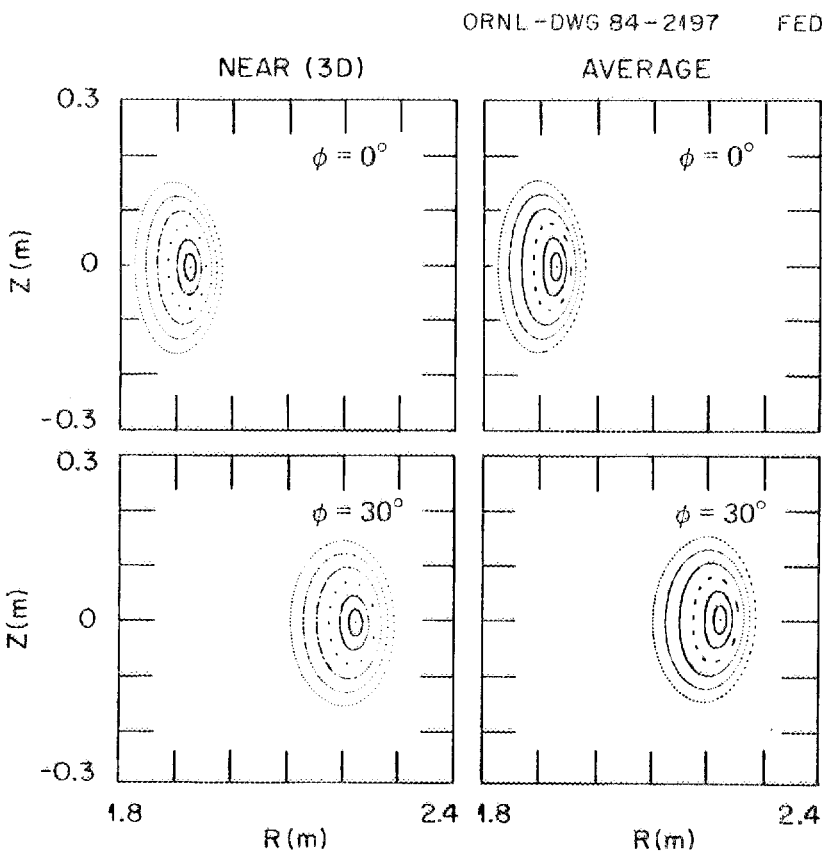

Fig. 4.3. Magnetic surfaces for the ATF helical-axis configuration, $\beta_0 = 5\%$.

that of the fixed-configuration equilibrium sequence. This decrease can be understood as a consequence of a reduction in the Pfirsch-Schlüter currents with increasing elongation of the magnetic surfaces.

The stellarator expansion technique can be generalized to helical-axis configurations by performing the expansion in a vacuum flux coordinate system. To leading order, the averaged equilibrium equations yield a Grad-Shafranov–type equation for the average flux. Also to leading order, the toroidally varying part of the equilibrium equation reduces to a Poisson-type equation. In this way, the 3-D equilibrium problem has been reduced to two second-order equations. Good equilibria have been found for the helical-axis ATF for central beta up to 10%.

4.1.1.3 "Zero-Current, High Beta Stellarator Equilibria with Rotational Transform Profile Control"[3]

B. A. Carreras, H. R. Hicks, J. A. Holmes, V. E. Lynch, and G. H. Neilson*

High-beta, zero-current equilibria for a stellarator device are calculated using the averaging method. It is found that, by shaping the vertical field, the rotational transform can be controlled in an approximate way as beta is increased. At the same time, the Pfirsch-Schlüter currents are reduced—with no modification of the magnetic well. This permits access to the high-beta regime with more favorable rotational transform profiles. Results are presented for the ATF device.

---

*Confinement Projects Section.

4.1.1.4 "Generic Ballooning in Anisotropic Pressure Toroids"[4]

W. A. Cooper

The ballooning mode equation for 3-D toroidal configurations with anisotropic plasma pressure is derived from the Kruskal-Oberman energy principle. The Mercier criterion is evaluated for nonaxisymmetric systems with shear (stellarators).

4.1.1.5 "Helically Symmetric Magnetohydrodynamic Plasma Equilibrium"[5]

W. A. Cooper and M. C. Depassier*

A variety of plasma confinement configurations can be very adequately modeled by assuming that the MHD equilibrium properties satisfy helical symmetry. Using asymptotic expansion techniques, we solve the helically symmetric equilibrium equation. Analogous solutions have been obtained previously only for axisymmetric devices. We calculate the plasma beta value, the q profile, and the plasma current. We also discuss how flux-conserving and zero-current sequences can be obtained with this model.

---

*Pontificia Universidad Católica de Chile, Santiago, Chile.

4.1.1.6 "Stability Calculations for High-Beta Torsatrons"[6]

L. Garcia, B. A. Carreras, L. A. Charlton, H. R. Hicks, and J. A. Holmes

In a previous work we have studied stability properties of torsatrons using a reduced set of MHD equations that includes the averaged effect of the external magnetic field. Kovrizhnykh and Shchepetov obtain the averaged MHD equations without expansion in the inverse aspect ratio. We use this system of averaged equations to study stability properties of low-aspect-ratio torsatrons. The numerical code FAR has been modified to include the averaged effect of the magnetic field. Keeping only the terms which enter in the reduced set of equations, we get similar results for moderate aspect ratio. The effect of the finite-aspect-ratio terms is, in general, stabilizing.

4.1.1.7 "Equilibrium Studies for Helical Axis Stellarators"[7]

T. C. Hender

The equilibrium properties of helical-axis stellarators are studied with the 3-D NEAR code and an average method (2-D). For the helical-axis ATF, which has a toroidally dominated shift, the average method and NEAR code equilibria agree well. The equilibrium properties of a wide range of heliacs have also been studied. Heliacs are typified by low shear and thus are very sensitive to resonant or nearly resonant perturbations. It is found that if the vacuum heliac configuration contains, or has nearby, low-order rational surfaces, then gross distortions to equilibrium may result. These effects are particularly pronounced at low aspect ratio, where the toroidal and helical shifts are well coupled to the resonant or nearly resonant harmonics. Vacuum configurations which avoid low-order resonances have improved equilibria. Also, lowering the toroidal effects by increasing aspect ratio and number of field periods proportionately improves the equilibria by reducing the coupling effects to resonant harmonics.

4.1.1.8 "Equilibrium Studies for Helical Axis Stellarators"[8]

T. C. Hender, J. L. Cantrell, B. A. Carreras, J. H. Harris, and J. A. Rome

The equilibrium properties of helical-axis stellarator configurations have been studied with the 3-D NEAR code and by an average method. Two sequences of heliac configurations with a given ratio of number of field periods to aspect ratio have been studied. Heliacs with a relatively small aspect ratio and number of field periods, which have a toroidally dominated shift, are found to have a low equilibrium beta limit. More favorable results are found at larger aspect ratio and field periods. The effects on the equilibria of modulating the currents in the toroidal field (TF) coils and by winding the TF coil axis as a geodesic on a torus are being studied.

4.1.1.9 "Equilibrium Calculations for Helical Axis Stellarators"[9]

T. C. Hender and B. A. Carreras

An average method based on a vacuum flux coodinate system is presented. This average method permits the study of helical-axis stellarators with toroidally dominated shifts.

An ordering is introduced, and to lowest order the toroidally averaged equilibrium equations are reduced to a Grad-Shafranov equation. Also to lowest order, a Poisson-type equation is obtained for the toroidally varying corrections to the equilibrium. By including these corrections, systems that are toroidally dominated, but with significant helical distortion to the equilibrium, may be studied. Numerical solutions of the average method equations are shown to agree well with 3-D calculations.

4.1.1.10 "Equilibrium Studies in Helical Axis Stellarators"[10]

T. C. Hender, B. A. Carreras, L. Garcia, J. H. Harris, J. A. Rome, J. L. Cantrell, and V. E. Lynch

The equilibrium properties of helical-axis stellarators are studied with a 3-D equilibrium code and with an average method (2-D). The helical-axis ATF is shown to have a toroidally dominated equilibrium shift and good equilibria up to at least 10% peak beta. Low-aspect-ratio heliacs, with relatively large toroidal shifts, are shown to have low equilibrium beta limits (~5%). Increasing the aspect ratio and number of field periods proportionally is found to improve the equilibrium beta limit. Alternatively, increasing the number of field periods at fixed aspect ratio, which raises ι and lowers the toroidal shift, improves the equilibrium beta limit.

4.1.1.11 "The Calculation of Stellarator Equilibria in Vacuum Flux Surface Coordinates"[11]

T. C. Hender, B. A. Carreras, L. Garcia, J. A. Rome, and V. E. Lynch

Details are given of a 3-D stellarator equilibrium code NEAR. This code uses a set of vacuum flux coordinates as an Eulerian basis for the equilibrium calculations. This coordinate system provides an economical representation of the complex geometry associated with stellarators. The equilibrium equations are solved by an energy minimization technique employing a conjugate gradient iteration scheme. The results of extensive numerical convergence studies are presented. Also, comparisons with existing codes are made to benchmark the NEAR code.

4.1.1.12 "Comparison of 3-D Moments and Finite Difference Inverse MHD Equilibrium Codes"[12]

S. P. Hirshman and J. T. Hogan

To facilitate the development of 3-D plasma transport simulations, we have undertaken a comparative evaluation of the Bauer-Betancourt-Garabedian equilibrium code, which solves $\mathbf{J} \times \mathbf{B} - \nabla P = 0$ for nested magnetic surfaces using finite differences, and the 3-D moments code (MOMS3D), which uses a Fourier expansion technique. The version of the Bauer-Betancourt-Garabedian code we have used is that described in *A Computational Method in Plasma Physics*. The method underlying the algorithms in the moments code is given by Hirshman and Whitson [Phys. Fluids **26**, 3553–68 (1983)]. Several fixed-boundary configurations, including heliotron, ATF, and heliac, have been analyzed to assess the following equilibrium properties: (1) convergence rates (with mesh

size) of the magnetic axis and general magnetic surface shapes, (2) magnetic well depth $dV/d\Phi$ (measuring interchange stability), (3) inductance and other geometric surface-averaged coefficients relevant to transport processes, and (4) approximate CPU time required to achieve a given level of force residual.

4.1.1.13 "Optimized Fourier Representations for Three-Dimensional Magnetic Surfaces"[13]

S. P. Hirshman and H. K. Meier*

The selection of an optimal parametric angle θ describing a closed magnetic flux surface is considered with regard to accelerating the convergence rate of the Fourier series for the Cartesian coordinates $x(\theta,\phi) \equiv R - R_0$ and $y(\theta,\phi) \equiv Z - Z_0$. Geometric criteria are developed based on the Hamiltonian invariants of Keplerian orbits. These criteria relate the rate of curve traversal (tangential speed) to the curvature (normal acceleration) so as to provide increased angular resolution in regions of largest curvature. They are, however, limited to either convex or starlike domains and do not provide rapid convergence for complex domains with alternating convex and concave regions. A generally applicable constraint criterion, based directly on minimizing the width of the x and y Fourier spectra, is also derived. A variational principle is given for implementing these constraints numerically. Application to the representation of 3-D magnetic flux surfaces is discussed.

---

*Computing and Telecommunications Division, Martin Marietta Energy Systems, Inc.

4.1.1.14 "A Convergent Spectral Representation for Three-Dimensional Inverse MHD Equilibria"[14]

S. P. Hirshman and H. Weitzner

By rearranging terms in a polar representation for the cylindrical spatial coordinates (R,ϕ,Z), a renormalized Fourier series moment expansion is obtained that possesses superior convergence properties in mode number space. This convergent spectral representation also determines a unique poloidal angle and thus resolves the underdetermined structure of previous moment expansions. A conformal mapping technique is used to demonstrate the existence and uniqueness of the new representation.

4.1.1.15 "Comparison of 3D MHD Inverse Coordinates Codes"[15]

J. T. Hogan and S. P. Hirshman

We have compared results of the Oak Ridge Moments Equilibrium Code ORMEC with those of the Bauer-Betancourt-Garabedian finite difference code BETA. The comparison involved these cases: heliotron vacuum and finite beta, "ATF" (simplified boundary) vacuum and finite beta, and Wendelstein VIIA vacuum. We have compared values extrapolated to zero grid size. The highest-resolution cases employ the Bauer-Betancourt-Garabedian zero-current algorithm, while cases with cruder grid are given the iota profile corresponding to this case. Parameters chosen for comparison include the shift Δ, elongation, helical-axis amplitude, axial pressure, and minimum energy E_f. Typical results are given in Table 4.1.

Table 4.1. Comparison of 3-D MHD inverse-coordinates codes

	ORMEC			BETA		
Case	Grid	Δ	E_f	Grid	Δ	E_f
ATF vacuum	30^{-1}	0.192	6.62739	30^{-3}	0.204	6.63299
ATF beta	30^{-1}	0.143	6.79159	30^{-3}	0.417	6.79676
Wendelstein VIIA	30^{-1}	0.012	45.1148	30^{-3}	0.011	45.11449

4.1.1.16 "Free Boundary Stellarator Expansion MHD Equilibrium and Stability Calculations"[16]

J. A. Holmes, B. A. Carreras, L. A. Charlton, H. R. Hicks, and V. E. Lynch

We study free boundary MHD equilibrium and stability of stellarators using the stellarator expansion to reduce the equilibrium calculation to a 2-D one. Fixed boundary equilibria calculated using this model have been demonstrated to be in good agreement with 3-D equilibrium calculations. Stellarator expansion Mercier and low-n stability calculations have also been performed on a wide range of fixed boundary equilibria.

To address the free boundary stability problem we use a version of the PEST code modified to include stellarator expansion terms. Detailed comparisons between the results of the fixed boundary and free boundary calculations will be presented. In particular, using the fixed boundary approach, it has been shown that vertical field shaping is important for accessing high-beta, net-current-free, stable configurations. It is, therefore, crucial to study the effect of vertical field shaping as a path to high beta using a free boundary equilibrium and stability model. Specific applications to the ATF device will be presented.

4.1.1.17 "Stellarator Expansion Studies of a High Beta Torsatron"[17]

J. A. Holmes, B. A. Carreras, L. A. Charlton, H. R. Hicks, and V. E. Lynch

The VF coil system in ATF is shown to be sufficiently versatile to provide equilibrium paths to high beta with favorable equilibrium and stability properties. In particular, using the stellarator expansion, it is shown that, through proper shaping of the magnetic fields, flux-controlled paths to high beta can be found with the following characteristics: the rotational transform profile deviations from the vacuum are small; the Pfirsch-Schlüter currents and magnetic axis shifts are reduced in comparison with those obtained at similar beta using the vacuum VF coil currents; there is no loss of magnetic well accompanying the reductions in Pfirsch-Schlüter currents and magnetic axis shifts; and the stability of the flux-controlled equilibria to global modes is enhanced by an improvement in the relationship between the rotational transform and the magnetic well. Initial investigation of the free boundary equilibrium and stability of ATF also reveals stability to global modes.

4.1.1.18 "Free Boundary Equilibrium and Stability of a Moderate Aspect Ratio Torsatron Using the Stellarator Expansion"[18]

J. A. Holmes, B. A. Carreras, L. A. Charlton, and V. E. Lynch

The ATF device is being designed to access high beta through a combination of magnetic shear and well. In order to find stable paths it is desirable to control the equilibrium properties as beta is increased. The VF coil system of ATF is being designed to provide this control. To carry out this study, a stellarator expansion version of the PEST equilibrium and stability code is used. The results of the free boundary calculations show that, through the use of the VF coil system, it is possible to access high-beta, stable equilibria in a "flux-controlled" manner. That is, sequences of stable, $\langle J_\zeta \rangle_\psi = 0$ equilibria are calculated in which, through plasma shaping, the variations in the rotational transform profile, the magnetic axis shift, and the magnetic well are controlled as beta is increased.

4.1.1.19 "Resistive Ballooning in Plasma Confinement Schemes with a Coordinate of Symmetry"[19]

M. C. Depassier* and W. A. Cooper

We have derived the resistive ballooning mode equation for systems having a coordinate of symmetry from the linearized incompressible resistive MHD equations. As an application we consider the stability of an approximate analytic solution to the MHD equilibrium equation found by asymptotic methods. We compare the ideal and resistive stability for zero-current and for flux-conserving equilibria.

---

*Pontificia Universidad Católica de Chile, Santiago, Chile.

4.1.1.20 *Accelerated Convergence of the Steepest Descent Method for Magnetohydrodynamic Equilibria*[20]

C. R. Handy* and S. P. Hirshman

Iterative schemes based on the method of steepest descent have recently been used to obtain MHD equilibria. Such schemes generate asymptotic geometric vector sequences whose convergence rate can be improved through the use of the ϵ algorithm. The application of this nonlinear recursive technique to stiff systems is discussed. In principle, the ϵ algorithm is capable of yielding quadratic convergence and therefore represents an attractive alternative to other quadratic convergence schemes requiring Jacobian matrix inversion. Because the damped MHD equations have eigenvalues with negative real parts (in the neighborhood of a stable equilibrium), the ϵ algorithm will generally be stable. Concern for residual monotonic sequences leads to consideration of alternative methods for implementing the algorithm.

---

*Department of Physics, Atlanta University, Atlanta.

4.1.2 Tokamaks and Reversed-Field Pinches—Abstracts

4.1.2.1 "The Effects of Toroidicity on Resistive MHD Instabilities in the RFP"[21]

B. A. Carreras, T. C. Hender, L. A. Charlton, J. A. Holmes

The turbulence generated by resistive MHD instabilities in the RFP has been linked to transport and maintenance in the configuration. To study the linear effects of toroidicity, the FAR code has been used. FAR solves the linear incompressible resistive MHD equations in toroidal geometry with no aspect ratio assumptions. Finite-beta numerical equilibria are used as inputs for the computations. For the tearing mode it is found that toroidicity has little effect for aspect ratios greater than 4 at zero beta. For tighter aspect ratios, the effects are stabilizing. For g modes, because of the finite-beta equilibrium shift and differences in the q profile, the effects of toroidicity are significant at slightly higher aspect ratios.

4.1.2.2 "Fully Toroidal Nonlinear MHD Calculations Without Ordering Assumptions"[22]

L. A. Charlton, B. A. Carreras, L. Garcia, J. A. Holmes, H. R. Hicks, and V. E. Lynch

Experimental results which indicated that, at high beam power, the internal kink mode could play an important role in tokamak discharges motivated, in part, linear calculations using the incompressible approximation, since the internal kink cannot be studied with the reduced model. The linear work not only used a formalism which relaxed the ordering assumptions used in the reduced equations but also used highly efficient implicit numerical techniques. These techniques also allowed modes which were not the most unstable to be studied. This work has now been extended to include the nonlinear terms. Comparison with other nonlinear codes and additional results will be presented.

4.1.2.3 "Incompressible MHD Modes in Toroidal Geometry"[23]

L. A. Charlton, B. A. Carreras, H. R. Hicks, J. A. Holmes, and V. E. Lynch

The use of a nonlinear resistive MHD model valid in the large-aspect-ratio limit has been successful in interpreting low-frequency MHD activity in high-beta tokamak plasmas with low-power injection. Recent experimental results indicate that at high injection power the internal kink mode could play an important role. Since this instability cannot be studied with the reduced MHD model, a study was conducted using the full MHD equations in the incompressible limit. The computer code FAR was constructed using these equations. A sequence of equilibria with differing beta values was studied for stability to linear $n = 1$ modes. At low beta, the usual tearing modes of the reduced theory are visible. At intermediate betas ($1\% \leq \beta_0 \leq 15\%$, where β_0 is the value of beta at the magnetic axis) the anticipated ideal internal kink modes are seen. Ideal internal kink means (1) the mode structure is identical to the classical kink but is confined inside the $q = 1.0$ surface and (2) the structure of the mode is basically unchanged when the resistivity is taken to zero. At values of β_0 above 15%, results identical to those from the reduced equations are recovered when modes with a resistive ballooning structure are unstable. The existence of a region at high β_0 where any deleterious effects due to the ideal internal kink may be avoided confirms results found using an analytic theory and results from an ideal study.

Modes with higher toroidal wave number are now being investigated. Details of the above and calculational methods will be presented.

4.1.2.4 "Calculations in Toroidal Geometry with Full MHD Equations"[24]

L. A. Charlton, B. A. Carreras, J. A. Holmes, H. R. Hicks, and V. E. Lynch

An incompressible, fully toroidal formalism has been developed which uses the full MHD equations. This formalism has been used to construct a computer code which uses an implicit algorithm to time-advance the unknown quantities. The algorithm is shown to allow extremely rapid convergence (usually in one time step) and can be used to study modes which are not the most unstable. Calculations have been done for $n = 1$ tokamak modes which show a second stability region for the ideal internal kink mode.

4.1.2.5 "Centrifugal Force Effects from Toroidal Rotation on Incompressible Resistive Ballooning"[25]

W. A. Cooper

The incompressible resistive ballooning mode equation that retains the effects of the centrifugal force due to toroidal plasma rotation is derived. In the small rotation velocity limit, the static results are recovered. For large rotation velocity, the mode scales linearly with resistivity and is driven by the interaction of the curvature and the centrifugal force with the radial pressure and mass density gradients, respectively.

4.1.2.6 "Resistive Ballooning Modes in Toroidally Rotating Tokamak Plasmas"[26]

W. A. Cooper

A ballooning mode equation is derived from the linearized incompressible resistive MHD equations employing the eikonal representation. To obtain this equation, we ignore the velocity-shear-driven, Kelvin-Helmholtz instabilities but retain the centrifugal force as a source of energy. The resulting second-order ordinary differential equation is applicable to arbitrary axisymmetric toroidal geometry. We analyze the large-aspect-ratio limit with model circular flux surface equilibria and use the two-length scale expansion in the electrostatic approximation to describe the modes. For small rotation velocity, we recover the static plasma result: the growth rate γ is proportional to $\eta^{1/3}$ (η = resistivity). When the toroidal rotation frequency exceeds the growth rate, γ scales linearly with η. The modes are driven by the interaction of the pressure and mass density gradients normal to the flux surface with the geodesic components of the curvature and the centrifugal force, respectively.

4.1.2.7 "Suppression of Spectral Pollution by Angle Renormalization"[27]

W. A. Cooper and S. P. Hirshman

It has been previously conjectured that the Fourier spectra of the cylindrical coordinates (R,Z) describing MHD equilibria (inverse mapping) can be significantly compressed

by an appropriate choice for the poloidal angle θ. By considering mappings of the form $\theta_* = \theta + \lambda(\theta,\phi)$, where λ is a periodic function of (θ,ϕ) and θ_* is the poloidal flux coordinate for which $\vec{B} \cdot \nabla\theta_* / \vec{B} \cdot \nabla\phi = \iota(\rho)$, the respective spectra in the θ_* and θ representations can be related by a formula corresponding to spatial frequency modulation of R_θ and Z_θ, with a modulation index equal to λ. Thus, for $|\lambda| \rightarrow 1$, broadening (pollution) of the θ_* spectra occurs. Examples which depict the spectral effects of increasing beta (plasma shift) and shaping of the plasma boundary are considered. In two dimensions, the diagnostic $\partial(R^2/\sqrt{g})/\partial\theta_* = 0$ is used to check our results.

4.1.2.8 *Magnetic Fluctuations, Field Reversal Maintenance, and Anomalous Thermal Transport in the Reversed Field Pinch*[28]

P. H. Diamond, Z. G. An,* M. N. Rosenbluth,* B. A. Carreras, T. C. Hender, and J. A. Holmes

A theory of magnetic fluctuations, field reversal maintenance (dynamo activity), and anomalous thermal transport in the RFP is proposed. Nonlinear generation of the coupling to $m \geqslant 2$ modes is advanced as an $m = 1$ tearing mode saturation mechanism. The mechanism by which nonlinear $m = 1$ modes sustain the toroidal magnetic field is elucidated. The predicted fluctuation levels are consistent with those required for maintaining the B_z configuration. Heat transport is estimated using stochastic magnetic field diffusion arguments.

---

*Institute for Fusion Studies, University of Texas, Austin.

4.1.2.9 *Theory of Resistivity-Gradient-Driven Turbulence*[29]

L. Garcia, B. A. Carreras, P. H. Diamond, and J. D. Callen

A theory of the nonlinear evolution and saturation of resistivity-driven turbulence, which evolves from linear rippling instabilities, is presented. The nonlinear saturation mechanism is identified both analytically and numerically. Saturation occurs when the turbulent diffusion of the resistivity is large enough so that dissipation due to parallel electron thermal conduction balances the nonlinearly modified, resistivity-gradient-driving term. The levels of potential, resistivity, and density fluctuations at saturation are calculated. A combination of computational modeling and analytic treatment is used in this investigation.

4.1.2.10 "Nonlinear Evolution of Microtearing Modes"[30]

L. Garcia, B. A. Carreras, and H. R. Hicks

It has been shown that corrections of Braginskii fluid equations of order ω/ν_e introduce a new term in the Ohm's law proportional to the time derivative of the thermal force. This term can produce an instability driven by the free energy stored in the electron temperature gradient. The modes are strongly localized around the singular surface and could be identified as microtearing. We have calculated the linear stability properties of these modes in cylindrical and slab geometry, and they compare favorably with the analytical

dispersion relation. We are presently investigating the nonlinear saturation in the single-helicity approximation as a first step to study nonlinear interaction of modes of different helicities and breaking of magnetic surfaces.

4.1.2.11 *The Reliability of Initial Value MHD Calculations of Tokamak Disruptions*[31]

H. R. Hicks, B. A. Carreras, L. Garcia, and J. A. Holmes

We have proposed the nonlinear coupling of resistive tearing modes as the mechanism for some tokamak disruptions. This is based primarily on initial-value resistive MHD calculations performed with a finite-difference grid in minor radius and Fourier series expansion in the poloidal and toroidal angles. The calculations show that, for certain q profiles, the nonlinear interaction of tearing modes of different helicities leads to the rapid destabilization of other modes. The resulting effects and the time scale are consistent with the tokamak disruption.

Recently Eastwood and Hopcraft have disputed this basic numerical result. Using a copy of our code (RSF) they claim to have shown that "numerical effects play a significant role. Computational results based on RSF and related codes must be regarded as suspect until independently confirmed." However, it is shown here that it is their result that is incorrect, because even though the true solution enters a turbulent phase, they use only 11 Fourier modes to represent 2 space dimensions. The 11-mode result is qualitatively different from results obtained with more modes, and one cannot derive from it conclusions about the reliability of numerically converged results. Moreover, the energy conservation test, as performed by Eastwood and Hopcraft, is neither a necessary nor a sufficient condition for convergence.

We go beyond refuting their specific claim, however, and consider each source of numerical error in turn. It has been widely recognized that this type of calculation pushes the numerical techniques near their limits. Therefore we (and other authors) have been especially careful to verify that the results are reliable by routinely carrying out tests that refute the conclusions of Eastwood and Hopcraft. In addition to convergence studies, the same results are produced with four different integration schemes that include both mostly implicit and mostly explicit schemes, finite-difference methods, and spectral methods. The results we have published, and in particular the basic nonlinear mode coupling mechanism of the tokamak disruption, are reliable and survive the appropriate numerical tests.

4.1.2.12 *Nonlinear Interaction of Tearing Modes: A Comparison Between the Tokamak and the Reversed Field Pinch Configuration*[32]

J. A. Holmes, B. A. Carreras, T. C. Hender, H. R. Hicks, V. E. Lynch, Z. G. An,* and P. H. Diamond

The multiple-helicity nonlinear interaction of resistive tearing modes is compared for the tokamak and RFP configurations using the MHD equations. Unlike the case of the tokamak disruption, for which this interaction is destabilizing when islands overlap, the nonlinear coupling of the dominant helicities is shown to be a stabilizing influence in the RFP. The behavior of the coupled instabilities in the two configurations can be understood as a consequence of the stability properties of the nonlinearly driven modes. In the case of

the tokamak disruption, quasi-linear effects linearly destabilize the dominant driven mode, which then feeds energy to the driving mode. For the RFP, the driven modes remain stable, acting as a brake on the growth of the dominant instabilities. Furthermore, for the RFP configuration numerical results indicate that nonlinear coupling of different helicities results in noticeably more rapid saturation of the dominant instabilities than was observed in single-helicity studies.

---

*Institute for Fusion Studies, University of Texas, Austin.

4.1.2.13 "Inverse Mapping Algorithm for Moments Formulation of MHD Equilibria"[33]

W. A. Houlberg, S. P. Hirshman, and S. E. Attenberger

Toroidal MHD equilibria calculated from moments expansions generate Fourier series in the poloidal and toroidal (in three dimensions) angles and a coupled set of differential equations in the radial coordinate for the expansion coefficients. Numerical solutions for the inverse equilibria $[R(\rho,\theta,\phi),\ Z(\rho,\theta,\phi)]$ are therefore continuous in the angle coordinates and discrete only in the radial coordinate, thus requiring interpolation only in the ρ coordinate. When ϕ is the real toroidal coordinate, the inverse $[\rho(R,Z),\ \theta(R,Z)]$ in either two or three dimensions is easily and efficiently calculated by the iterative scheme

$$\rho_{n+1} = \rho_n + [Z_\theta^n(R_n - R) - R_\theta^n(Z_n - Z)]/g_n \ ,$$

$$\theta_{n+1} = \theta_n - [Z_\rho^n(R_n - R) - R_\rho^n(Z_n - Z)]/g_n \ ,$$

where

$$g_n \equiv R_\theta^n Z_\rho^n - R_\rho^n Z_\theta^n$$

is the Jacobian of the transformation from (R,Z) to (ρ,θ) and the subscripts ρ and θ designate derivatives with respect to those coordinates. Examples of using the scheme in tracking segmented chords through flux coordinate space will be given. The method is useful for interpretation of diagnostics on experiments and as a geometry package for neutral particle transport, rf ray tracing, etc., in noncircular and/or nonaxisymmetric plasmas.

4.1.2.14 "The Spectrum of the MHD and Kinetic Alfvén Waves in a Cylindrical Tokamak"[34]

W. I. van Rij, G. Vahala,* and D. J. Sigmar

The ideal MHD Hain-Lüst equation yields the well-known continuum of shear Alfvén waves defined by $\omega_A^2|_{\min} \leqslant \omega^2 \leqslant \omega_A^2|_{\max}$, $\omega_A^2 = k_\parallel^2 v_A^2 (k_\parallel \neq 0)$. This second-order differential equation also possesses discrete spectra for $\omega^2 < \omega_A^2|_{\min}$, recently investigated by

Appert et al. We find for a cylindrical tokamak that the discrete modes vanish if $\partial/\partial r\ (k_\parallel^2)$ is positive or in the presence of a flat density profile. As the toroidal mode number ℓ decreases, the accumulation point moves down from $\omega_A^2|_{\min}$. Transformation to a Schrödinger-like equation makes the existence and disappearance of these states particularly transparent. In the region above the continuum $\omega^2 > \omega_A^2|_{\max}$, the normal (negative-gradient) density profile forbids the existence of a discrete spectrum from the second-order MHD equation.

The lowest-order finite gyroradius correction to the ideal MHD equation yields a fourth-order radial differential equation which removes the Alfvén continuum, and a discrete spectrum appears. Where second-order equation discrete states do exist, the fourth-order equation perturbs them, raising the eigenvalues and removing the accumulation point.

In the frequency regime $\omega^2 > \omega_A^2|_{\max}$ we find that when the second-order equation has no discrete states the fourth-order equation permits them, with the eigenvalues ω_n^2 increasing with the radial quantum number n. WKB predictions of high eigenvalues ($\omega_n^2 > \omega_A^2|_{\max}$) agree with the numerical calculations.

---

*College of William and Mary, Williamsburg, Va.

4.1.2.15 "Role of Multiple Helicity Nonlinear Interaction of Tearing Modes in Dynamo and Anomalous Thermal Transport in the Reversed Field Pinch"[35]

Z. G. An,* P. H. Diamond, R. D. Hazeltine,* J. N. Leboeuf,* M. N. Rosenbluth,* R. D. Sydora,* T. Tajima,* B. A. Carreras, L. Garcia, T. C. Hender, H. R. Hicks, J. A. Holmes, V. E. Lynch, and H. R. Strauss†

A theory of magnetic fluctuation dynamics, the dynamo mechanism, and anomalous thermal transport in the RFP is presented. Nonlinear generation of the coupling to $m \geqslant 2$ modes is advanced as an $m = 1$ tearing mode saturation mechanism. The processes by which $m = 1$ tearing modes sustain the magnetic configuration and stabilize themselves by lowering the safety factor on axis $q(0)$ are elucidated. The nonlinear dynamics of resistive interchange modes are discussed. Stochastic magnetic field transport arguments are used to estimate anomalous thermal conductivity and confinement scaling.

---

*Institute for Fusion Studies, University of Texas, Austin.

†New York University, New York.

4.1.2.16 "Spectrum of Rippling Mode Turbulence"[36]

P. W. Terry,* K. C. Shaing, P. H. Diamond, B. A. Carreras, and L. Garcia

The turbulence of temperature-gradient-driven electrostatic rippling modes is investigated analytically and numerically. We consider the saturated state where the electrostatic

potential and resistivity perturbations are shifted radially outward from equilibrium positions and effectively decouple from the current perturbation. The mode width is determined from the balance of thermal conductivity with the nonlinear $\mathbf{E} \times \mathbf{B}$ convection of resistivity. Thermal conductivity provides the sink for nonlinearly transferred energy input by the temperature gradient. The rippling mode is investigated as a possible candidate for edge fluctuations. The two-point resistivity correlation is solved and evaluated for several Reynolds numbers. Incoherent emission driven by the relaxation of the temperature gradient is treated, and enhanced fluctuation levels for $e\phi/T_e$ and $\hat{\eta}/\eta_0$ are obtained. The wave number spectrum is calculated and transport estimates are reported.

---

*Institute for Fusion Studies, University of Texas, Austin.

4.1.2.17 "Investigation into the Structure of Saturated Magnetic Islands in a Poloidal Divertor Tokamak"[37]

E. Uchimoto,* J. D. Callen, L. Garcia, and B. A. Carreras

A computer code is being developed to numerically advance the 3-D resistive magnetohydrofriction (MHF) equations in a poloidal-divertor-configuration tokamak. This is a natural extension of the 2-D resistive MHF code that finds axisymmetric MHD equilibria in such a device. The primary objective of the new code is to find a nonaxisymmetric lower energy state with saturated magnetic islands and to understand low-q discharges in the Wisconsin Tokapole II. In order to handle the divertor separatrix, the equations are written in a finite-difference form in two Cartesian components in a poloidal plane. They are, however, Fourier analyzed in the toroidal direction to facilitate an efficient representation of the island structure. Time advancement is explicit.

---

*University of Wisconsin, Madison.

4.1.2.18 "MHD Equilibrium Studies of a Poloidal Divertor Tokamak Using the Chodura-Schlüter Method"[38]

E. Uchimoto,* J. D. Callen, L. Garcia, and B. A. Carreras

The Wisconsin Tokapole II is a poloidal-divertor-configuration tokamak with a considerable amount of plasma residing outside the separatrix. To help us understand resistive MHD instabilities in such a geometry, a numerical code has been developed to find MHD equilibria in a Tokapole-type device including plasma pressure outside the separatrix. The code employs the basic features of the Chodura-Schlüter method for an axisymmetric plasma in which a set of 2-D MHF equations is numerically advanced to relax the plasma into an equilibrium configuration. This method is advantageous over the standard Grad-Shafranov approach in that the multivaluedness of the pressure p and poloidal current I

functions with respect to the poloidal flux need be considered only in the initialization procedure. In addition to the fictitious friction force, a small resistivity is introduced to suppress numerical instabilities of the toroidal current density that tend to make the code numerically unstable. A small viscosity is also added to smooth ripples in the pressure. A parameter survey is conducted to investigate the effects of the divertor position and the plasma outside the separatrix on equilibrium.

---

*University of Wisconsin, Madison.

4.1.3 EBS and EBT Devices—Abstracts

4.1.3.1 "Magnetic Equilibria for Square and Circular EBTs"[39]

C. L. Hedrick and L. W. Owen

For closed magnetic field line devices, scalar pressure MHD implies that the pressure surfaces are the same as surfaces of constant $\oint d\ell/B$. This relation can also be developed from the drift kinetic equation. Here we contrast this result with that obtained from the bounce-averaged drift kinetic equation. We consider a collisionality regime such that the collision frequency is much less than the bounce frequency but comparable (within an order of magnitude) to the poloidal precession frequency. Under these circumstances it is reasonable to assume that scattering causes the distribution function to be approximately isotropic and that J is not conserved on a drift time scale. This assumption allows us to make a direct comparison to the MHD results, which would not be possible for lower collisionality where the distribution function would be anisotropic and approximately a function of ϵ, μ, and J. Our motivation for discussing this collisionality regime lies in its possible application to the initial EBT (EBT-I) and EBT-Scale (EBT-S) and Nagoya Bumpy Torus (NBT-IM) experiments, as well as to configurations projected for the near future such as the ELMO Bumpy Square (EBS).

4.1.3.2 "Magnetic Equilibrium and Single Particle Orbits in EBS"[40]

C. L. Hedrick and L. W. Owen

The EBS consists of four bumpy cylinders connected by four high-field "corners." Here we compare the magnetic equilibrium properties of an EBS with those of EBT-I/S. We also give a qualitative discussion of single-particle drift orbits which provides further insight into the detailed numerical calculations.

The standard theory of closed-line (and mirror) equilibria is sketched using both MHD and drift kinetic formalisms. The drift kinetic approach provides a more direct connection to the fact that pressure surfaces for isotropic distribution functions are "average drift surfaces" (surfaces of constant $\oint d\ell/B$). An analytic calculation of the pressure surfaces shows that they are circular in cross section (and constant along field lines)—in agreement with numerical results. As in the EBT-I/S case, these circles are shifted inward by toroidal effects. Unlike EBT-I/S, the toroidal effects for EBS are concentrated in the

high-B corners, and the shift shows an additional dependence on B_{corner} (or global mirror ratio). It is this dependence on global mirror ratio which is exploited to reduce the pressure surface shift (average drift surface), as well as the shift of passing and transitional particles.

The drift behavior of trapped, passing, and transitional particles is usually obtained using bounce-averaged equations. Here we justify this procedure and discuss the motion on the shorter (local drift) time scale—either one of which may be used to gain qualitative insights into the behavior of single particles—and hence insights into collective effects such as transport and heating.

4.1.3.3 "Ballooning Modes in the ELMO Bumpy Square Configuration Using the Generalized Kinetic Energy Principle"[41]

D. A. Spong, C. L. Hedrick, and J. W. Van Dam*

In the bumpy square configuration, toroidal curvature is localized in the corner sections rather than uniformly distributed, as is the case in the existing circular EBT configuration. This feature, coupled with the fact that the magnetic field is higher in the corner sections, results in a number of distinct advantages with respect to particle confinement, heating, and transport. It might be expected, however, that ballooning modes should have some tendency to concentrate in the corner sections—especially along the outer field lines where the curvature and pressure gradients are unfavorable. Here we examine the stability of such a configuration using a ballooning mode equation derived from the generalized kinetic energy principle. The side and corner sections of the square are treated with a piecewise constant approximation and matched at a transition boundary to obtain the stability condition. This retains the ring-core coupling and yields both the low β_c diamagnetic well stabilization condition and a high β_c stability limit analogous to the Van Dam-Lee-Nelson β_c limit. Due to the high magnetic field in the corners and the relatively weak curvature there ($\approx 1/2$ of the curvature in the bumpy sections), this upper β_c limit is not significantly changed from that which would be present in the conventional circular bumpy torus configuration.

---

*Institute for Fusion Studies, University of Texas, Austin.

4.1.3.4 "Electrostatic Confinement in a Bumpy Torus"[42]

A. M. El Nadi*

In a closed-field-line device such as a bumpy torus, the combined $\mathbf{E} \times \mathbf{B}$ and ∇B drifts lead to charge separation that is balanced by the ion polarization drift. In this work, we determine self-consistent potential and density profiles and the condition for electric island formation.

---

*Giza University, Cairo, Egypt.

4.1.3.5 "Electrostatic Confinement in a Bumpy Torus with Hot Electron Rings"[43]

A. M. El Nadi*

We have analyzed the equilibrium of a bumpy torus in the presence of an ambipolar potential. Previous work neglecting the effects of the potential showed that the pressure P is a function of $U = \int d\ell/B$. A different picture emerges when the charge-independent $\mathbf{E} \times \mathbf{B}$ poloidal drift is no longer negligible in comparison with the magnetic precession. Charge separation would then result generally if an ion polarization drift did not arise. The drift kinetic equation can be used in the collisionless constant temperature limit to show that $P = g(e\phi/T_e + \ln U)/U$, where g is an arbitrary function, ϕ is the electrostatic potential, e is the magnitude of the electron charge, and T_e is the electron temperature. Besides, the quasi-neutrality condition turns out to be equivalent to solving the equation $\nabla \cdot \mathbf{D} = \rho_f$, where $\mathbf{D}$ is the displacement vector in the high-plasma-density limit and ρ is the net charge obtained using the drift kinetic equation, excluding only the ion polarization. To ensure quasi-neutrality in the hot electron ring region, we assume that the outermost equipotential coincides with the ring boundary. The solution to the above partial differential equation (PDE) shows an asymmetry in the potential, caused by the toroidal magnetic curvature, which forms a pressure-dependent electrostatic dipole along the major radius (analogous to the Pfirsch-Schlüter current in a tokamak). Formation of potential islands occurs when $(T_e + T_i)$ exceeds $2ML_nR\Omega^2$, where M is the ion mass, L_n is the density scale length, R is the major radius, and Ω is the $\mathbf{E} \times \mathbf{B}$ precession frequency. Because of its effect on equilibrium, it is obvious that taking the ion polarization into account should have important effects on both the stability and the radial transport of the toroidal plasma.

---

*Giza University, Cairo, Egypt.

4.1.3.6 "The Magnetohydrodynamic Equilibria in a Bumpy Torus with Toroidal Current"[44]

R. E. Juhala* and S. P. Hirshman

The EBT is a large-aspect-ratio device which provides good access to the plasma, thus facilitating reactor maintenance and the introduction of external heating sources. However, questions of plasma stability, stringent requirements on field line closure, and serious particle transport losses due to dispersion in the particle drift orbits remain unresolved. Several ideas for enhancing the aspect ratio have been put forth with potentially significant improvements. Some of these retain the closed-field-line configuration with corresponding tight tolerances on coil alignment, and others require a nonplanar minor axis, compounding the problem of high mechanical stresses in reactor-scale devices.

These issues may be corrected by driving a modest (by tokamak standards) toroidal current in EBT, thereby providing magnetic flux surfaces with rotational transform and shear. This may offer a way to retain the simplicity of a planar, circular torus and possibly reduce the size of an EBT reactor by requiring fewer sectors.

Plasma stability and transport are largely unexplored for a current-driven EBT. In the present work, 3-D MHD equilibria are determined using an energy principle to obtain the

solution of the force balance equation for nested magnetic flux surfaces. Equilibrium states are found for a range of plasma beta and rotational transform and compared for three circular coil configurations—tokamak, EBT-S, and EBT with a split-wedge TF coil—all with the same aspect ratio and plasma volume.

In EBT a convergent solution is not obtained for very low rotational transform ($\iota \ll 1$). High transform, $\iota \sim 1$, can be obtained with a toroidal current of 40 kA. In this case, equilibrium states are obtained as the plasma begins to form a magnetic well. Also, there appears to be stability against kink modes for $\iota \gtrsim 1$. This may be due to the local minimum-B regions, present in each magnetic aperture, preventing displacement of the magnetic axis and inhibiting the growth of these modes. By contrast, no convergence is found in the tokamak for $\iota \lesssim 1$.

The effect of the hot electron ring diamagnetism has not yet been included. However, based on the EBT experiment, one would expect the ring to stabilize the surface plasma against flute modes. It is expected that imposing the required equilibrium fields will influence the rings. These encouraging results invite further exploration of this concept and may justify an experiment on EBT-S.

---

*McDonnell Douglas Astronautics Co., St. Louis.

4.2 TRANSPORT KINETICS: KINETIC THEORY

The transport kinetics effort integrates topics that cross the boundaries of the traditional subcategories of theoretical plasma physics: equilibrium, orbits, stability, heating, and transport. While an immediate goal is to provide theories and codes that permit direct comparison with current and near-term experiments, another goal is to provide the background and insights necessary for understanding and predicting the behavior of longer-term experiments.

The electric field plays an essential role in plasma confinement for nonaxisymmetric systems, and the experience acquired in EBT research has proved very useful. The analysis of the radial electric field was extended in several areas. Differential equations for the electric field were developed to treat different collisionality regimes in a number of devices. The stability of the radial electric field was considered from a thermodynamic point of view. A potential called the generalized heat production rate was defined. This new point of view improved the understanding of radial electric fields in nonaxisymmetric magnetic configurations. The stellarator version of the WHIST code, which is used for predicting ATF performance and for analyzing Heliotron-E data, was upgraded by the development of a package that not only solves the algebraic equation for the electric field but also checks the roots for stability and reliably tracks their evolution in time. Detailed studies with this code, using both algebraic and diffusive models to find self-consistent solutions for the electric field, have shown that large loss regions can be healed with modest radial fields.

The poloidal electric field was determined in various regimes for stellarators, and most of this analytic work was incorporated in the stellarator version of the WHIST code. A multifluid treatment of the non-Maxwellian electron distribution function was developed to

obtain the poloidal electric field in bumpy tori. The first results have been compared with measurements done in EBT, and good agreement was found.

Neoclassical diffusion coefficients for stellarators with a radial electric field have also been calculated. These coefficients have been benchmarked with the guiding-center Monte Carlo code at ORNL and at the Max-Planck-Institut für Plasmaphysik, Garching, Federal Republic of Germany. In regimes where the theory applies and the Monte Carlo calculations are valid, agreement is good. The bounce-averaged Monte Carlo code has been benchmarked against the guiding-center Monte Carlo code. Agreement is good for transport due to helically trapped particles. Better models for non–helically trapped particles are being developed. For example, an improved expression for the adiabatic invariant associated with non–helically trapped particles in stellarators was suggested based on experience with EBT. A simple physical picture for describing the behavior of transitional particles was advanced.

An anomalous transport model for the edge of torsatron/heliotron devices has been developed. It is based on g-mode turbulence generated in the region with $V'' > 0$ and incorporates the effect of poloidal rotation to couple to the radial electric field effects. Various scalings in stellarators and rippled tokamaks were analyzed and clarified. This led to an improved understanding of the transport associated with collisionless trapping/detrapping orbits in stellarators and tokamaks.

The integration of neoclassical theory with anomalous transport mechanisms is being developed, and the results can have a strong impact on the overall picture of stellarator transport. In this area, stability and transport formalisms were combined to develop resistive-MHD–like equations in the banana-plateau collisionality regime using both kinetic and fluid approaches.

Including the effects of orbit renormalization, a detailed evaluation of the microstability of electrostatic and electromagnetic drift waves was accomplished using a time-dependent, nonlinear Vlasov code.

4.2.1 Ambipolar Potential—Abstracts

4.2.1.1 "Development of a Differential Equation for the Ambipolar Electric Field in a Bumpy Torus in the Low Collision Frequency Limit"[45]

D. E. Hastings

In a bumpy torus the radial electric field is determined by the constraint of ambipolarity. If both species are dominated by nonresonant diffusion, then the ambipolarity relationship as it is usually formulated is algebraic in the electric field. The solutions of this algebraic equation may have a discontinuous first derivative of the electric field. The unphysical situation arises from the neglect of the finite orbit deviation from the pressure surface. If the fluxes are calculated to higher order in the inverse aspect ratio, a second-order differential equation for the electric field is obtained that will give a continuous first derivative for the electric field.

4.2.1.2 "A Differential Equation for the Ambipolar Electric Field in a Multiple-Helicity Torsatron"[46]

D. E. Hastings

In a torsatron, the ambipolar electric field is obtained by equating the ion and electron fluxes. This formulation, when solved simultaneously with the density and temperature rate equations, gives continuous electric fields but may lead to the radial derivative of the electric field being discontinuous. This unphysical situation arises from the neglect of the finite orbit deviation from the flux surfaces. If the fluxes are calculated to higher order in inverse aspect ratio to include the finite orbit deviation, then a second-order differential equation is obtained that will give a continuous first derivative for the electric field.

4.2.1.3 "The Ambipolar Electric Field in Stellarators"[47]

D. E. Hastings, W. A. Houlberg, and K. C. Shaing

In a 3-D device like a stellarator, the ambipolar electric field must be determined self-consistently from the ambipolarity constraint and can have a significant effect on the transport through the diffusion coefficients. A differential and an algebraic formulation for the electric field are solved along with the density and temperature equations. The results are compared, and in both cases multiple electric field solutions can exist with bifurcations occurring between different solutions. It is shown that heating of the electrons encourages bifurcation to the more favorable positive electric field root.

4.2.1.4 "Calculation of the Self-Consistent Electric Field in Toroidal Nonaxisymmetric Devices"[48]

D. E. Hastings and T. Kamimura*

In a toroidal nonaxisymmetric plasma, the radial electric field is determined by the constraint that the radial ion and electron fluxes be equal. This ambipolarity relationship is, in general, a nonlinear algebraic equation for the electric field that can have multiple solutions. An algorithm is proposed here to solve this equation and obtain a spatially continuous, temporarily stable solution. For definiteness, this is applied to a bumpy torus, and it is shown that there exists a boundary in the density, electron temperature, and ion temperature space across which the potential changes abruptly from a spatial hill to a spatial well.

---

*Institute for Plasma Physics, Nagoya University, Nagoya, Japan.

4.2.1.5 "Azimuthal Electric Fields and Ambipolarity in a Multiple Helicity Torsatron"[49]

D. E. Hastings and K. C. Shaing

In a torsatron there are multiple solutions to the ambipolarity relationship for the electric field. If the plasma attempts to change from one solution to another spatially, then

it typically has a small electric field over some region of space. Over this region, the self-consistent poloidal electric field can be important and lead to potential islands. If the plasma is in the superbanana-plateau regime, then slow resonant particles limit the rate of change of the electric field and, hence, give a minimum width for the spatial zone where the plasma is changing roots of the ambipolarity relationship.

4.2.1.6 "Noise-Induced Transition of the Radial Electric Field in a Nonaxisymmetric Torus"[50]

K. C. Shaing

The effect of external noise on the transition of the radial electric field is studied. Depending on the size of the fluctuations, the transition of the radial electric field can either exhibit hysteresis or choose the path for which the thermodynamic potential (generalized heat production rate) $\dot{S}_l$ is an absolute minimum. Fluctuations other than the radial electric field are also studied.

4.2.1.7 "Stability of the Radial Electric Field in a Nonaxisymmetric Torus"[51]

K. C. Shaing

The stability of the radial electric field in a nonaxisymmetric torus is discussed from the thermodynamic point of view. It is found that for both radially local and nonlocal models, the stable radial electric field is at the minimum of the generalized heat production rate. A similarity between the local model and the liquid-gas phase transition is pointed out.

4.2.1.8 "The Radial Electric Field in a Nonaxisymmetric Torus"[52]

K. C. Shaing, R. H. Fowler, D. E. Hastings, W. A. Houlberg, E. F. Jaeger, J. F. Lyon, J. A. Rome, and J. S. Tolliver

The effects of radial electric fields have been studied for a wide range of nonaxisymmetric tori (e.g., rippled tokamak, stellarator, and EBT). For these devices the particle fluxes are not intrinsically ambipolar, and a radial electric field E_r develops to ensure quasi-neutrality. Such effects on plasma transport have been studied in four areas: (1) analytic expressions for particle and heat fluxes and comparisons with calculations by others, (2) Monte Carlo simulations of transport scaling, (3) transport code simulations for existing and proposed devices, and (4) analytic understanding of the stability of an E_r value and the probability of transitions between allowed values for E_r.

Because of a stellarator's complicated orbits and the strong effect of E_r on these orbits, a Monte Carlo code was used to benchmark the theoretically derived transport expressions. Figure 4.4 shows the data points for Monte Carlo calculations of the diffusion coefficient in a model $\ell = 1$ stellarator. For small values of E_r, the Monte Carlo results agree closely with the predictions of theory. But, when E_r is increased (with either sign), the value of D rapidly decreases to a residual level which is roughly the axisymmetric neoclassical value with ν_{ei} replaced by ν_{ii} and m_e replaced by m_i. This asymptotic level is caused by nonconservation of momentum by the Monte Carlo test particles and the

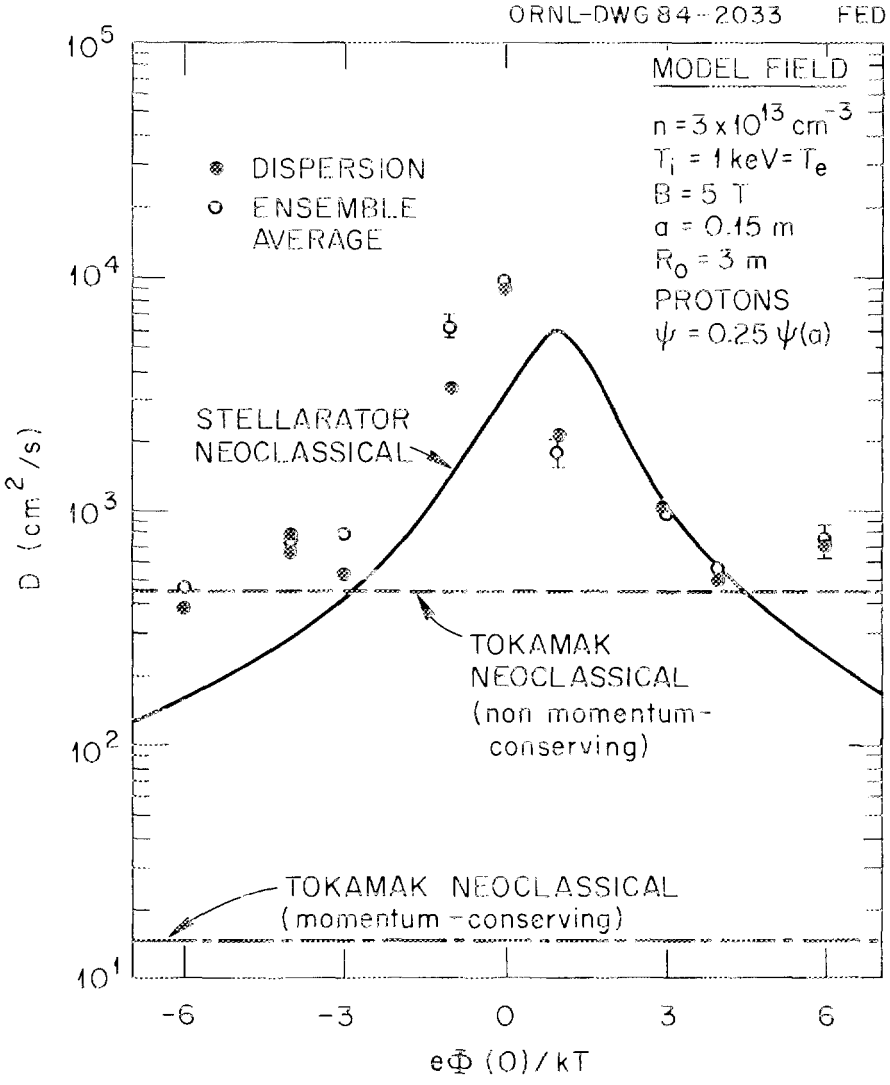

Fig. 4.4. The effect of a radial electric field on transport in a model $\ell = 1$ stellarator with $\phi(\psi) = \phi(0)(1 - \psi)$.

resulting flux generated by like-particle collisions. Similar results pertain when we follow test particles in the correct ATF magnetic field, which has a richer harmonic content. A similar Monte Carlo code for EBT with a bounce-averaged collision operator has been developed. Since the flux analogous to that of the axisymmetric tokamak part (i.e., the parallel-friction-driven flux) is much smaller than the flux induced by the bounce-averaged drift orbits, the problem mentioned above does not occur for EBT. In this case the Monte Carlo results agree with the theoretical results in the limit where the theory is valid: large aspect ratio, large E_r, and small radius.

Earlier work obtained an algebraic equation for E_r from the ambipolarity condition. However, an algebraic equation can yield multiple roots, some of which are unstable. In

addition, that formulation was local in space, so that unphysical, discontinuous E_r profiles could be obtained. This motivated the development of a new differential equation to describe E_r. The model equation employed to determine E_r is

$$\frac{d\Phi'}{dt} = \frac{4\pi\left|\vec{\nabla}\psi\right|^{-2}}{1 + c^2/V_A^2} \sum_a \langle e_a \vec{\Gamma}_a \cdot \vec{\nabla}\psi \rangle + \frac{1}{V'} \frac{\partial}{\partial\psi}\left[V' D_E \frac{\partial\Phi'}{\partial\psi}\right] , \tag{4.1}$$

where $E_r = -\Phi'|\nabla\psi|$ and D_E is a diffusion coefficient for E_r. Ambipolarity at steady state is still preserved in Eq. (4.1), since the diffusion term in Eq. (4.1) is the higher-order particle flux in the ordering of $\Delta r/r_n$, where Δr is the size of the particle orbit and r_n is the radial scale length. The physical origin for the diffusion term is the radial coupling of adjacent flux surfaces due to the finite size of the particle orbits. Around the position where E_r changes sign, this diffusion term guarantees a smooth profile for the electric field. The results of simulations for existing stellarators, ATF, and EBT, using Eq. (4.1) coupled with the transport equation, will be discussed. Equation (4.1) is similar to the dynamic equation for a first-order phase transition problem; for example, the liquid-gas phase transition. Here the thermodynamic potential $\dot{S}_n$ from which the steady state of Eq. (4.1) can be derived by minimization is given by $\dot{S}_n = \int dV\,[\dot{S}_l + D_E(\Phi'')^2/2]$. In $\dot{S}_n$,

$$\dot{S}_l = -4\pi[|\vec{\nabla}\psi|^2(1 + c^2/V_A^2)]^{-1} \int^{\Phi'} d\Phi' \sum_a e_a \langle \vec{\Gamma}_a \cdot \vec{\nabla}\psi \rangle$$

is a local thermodynamic potential from which the nondiffusive term on the right-hand side of Eq. (4.1) can be derived as $\partial\dot{S}_l/\partial\Phi'$. A typical example of the local potential $\dot{S}_l$ for a stellarator is shown in Fig. 4.5. The stable roots correspond to the local minima of $\dot{S}_l$. The discontinuous transition of Φ' from one local minimum to the other implies that it is a first-order phase transition. Furthermore, around the critical point where $\partial\dot{S}_l/\partial\Phi' = \partial^2\dot{S}_l/\partial\Phi'^2 = \partial^3\dot{S}_l/\partial\Phi'^3 = 0$, the fluctuations of E_r are enhanced and are well correlated, similar to those in a liquid-gas transition.

4.2.1.9 "The Radial Electric Field in a Stellarator"[53]

K. C. Shaing, R. H. Fowler, D. E. Hastings, W. A. Houlberg, E. F. Jaeger, J. F. Lyon, J. A. Rome, J. S. Tolliver, and J. D. Callen

In a stellarator, the particle fluxes are not intrinsically ambipolar, and a radial electric field E_r develops to ensure quasi-neutrality. The radial electric field is important to the confinement of a stellarator. In the presence of a strong E_r, the particles execute a fast $\mathbf{E} \times \mathbf{B}$ poloidal rotation that reduces the size of the particle orbits and therefore improves the confinement. Both analytic calculations and Monte Carlo simulations have shown that the diffusion coefficients decrease as the value of the radial electric field increases in the

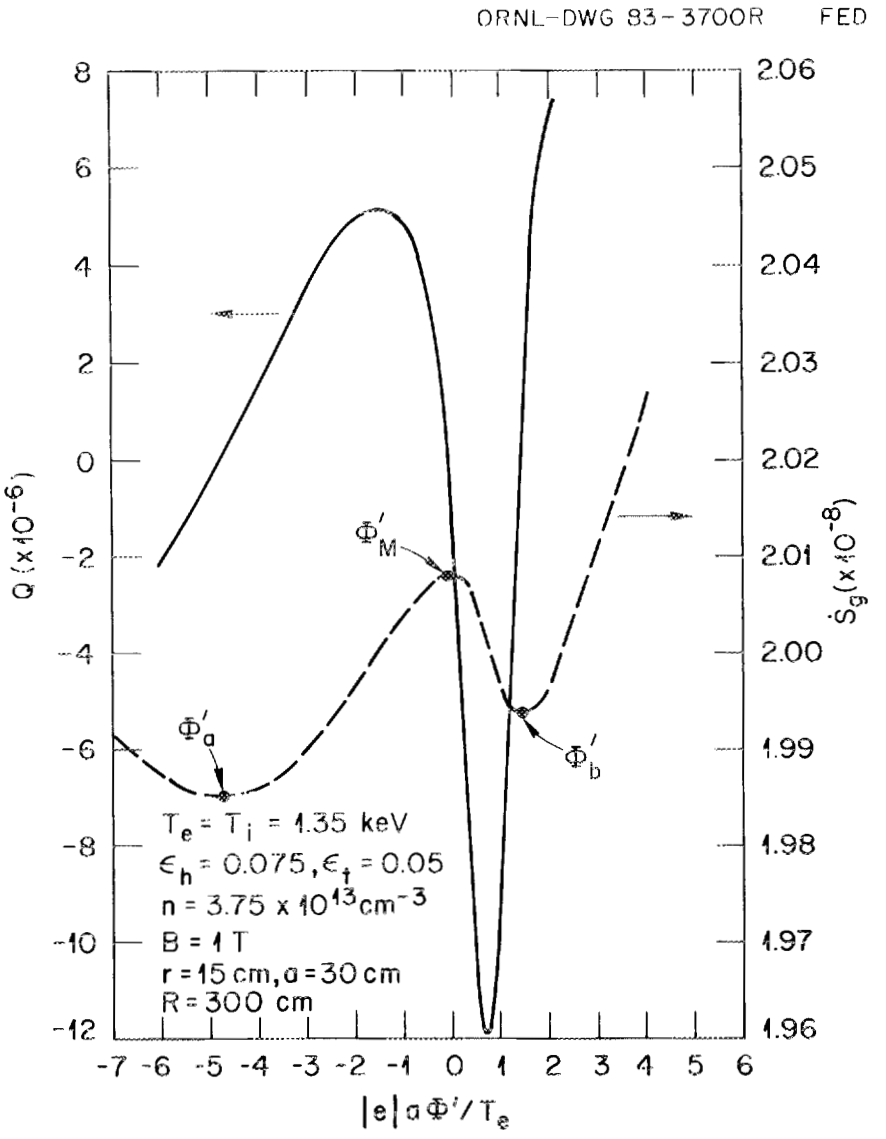

Fig. 4.5. The functions $Q = |e|(\Gamma_e - \Gamma_i)$ and $\dot{S}_g = \dot{S}_A(1 + c^2/V_A^2)$ vs $|e|a\phi'/T_e$, showing two stable states. The profiles for the density, temperature, and ϵ_h are parabolic.

low collisionality regime. The value of E_r needs to be determined self-consistently from the transport equations. An evolution equation for E_r is developed from neoclassical transport theory. Two models for E_r have been considered. One is a radially local model obtained by balancing the electron and ion particle fluxes. In the radially nonlocal model, besides the usual particle fluxes driven by the linear gradients of density, temperature, and electric potential, a higher-order particle flux due to the finite size of the particle drift orbits is included. The stability of E_r is studied by defining a thermodynamic-like potential. A

stable value of E_r is at a minimum of this potential. The transport simulation results from these two models with the ATF-like parameters show reasonable confinement time and plasma beta.

4.2.2 Transport Coefficients—Abstracts

4.2.2.1 "Stochastic Particle Diffusion in Velocity Space for a Bumpy Torus"[54]

G. L. Chen, L. W. Owen, D. B. Batchelor, and C. L. Hedrick

Nonadiabatic changes of the magnetic moment μ in EBT-S have been studied both analytically and numerically. Simple forms of $\Delta\mu$ and the gyrophase change $\Delta\theta$ were obtained, permitting the changes in these quantities to be studied using an iteration mapping. The mapping results show stochastic behavior for particles having high energy and low initial μ. Otherwise, superadiabatic motion appears. The stochastic diffusion coefficient for the variation of μ was measured numerically by mapping and was also calculated from quasi-linear theory. The results are shown to agree well in the stochastic region. For high-energy particles, the diffusion in μ due to nonadiabaticity can be comparable to collisional diffusion when stochastic motion occurs in EBT-S.

4.2.2.2 "Monte Carlo Studies of Transport in Stellarators"[55]

R. H. Fowler, J. A. Rome, and J. F. Lyon

Transport is studied in toroidal geometry by integrating the guiding-center equations in magnetic coordinates and simulating collisions with a Monte Carlo collision operator. The effects of the ambipolar electric field on diffusion losses are determined for model magnetic fields and the correct magnetic field of the ATF stellarator. Comparisons are made of the computed diffusion coefficients and the theoretically predicted values.

4.2.2.3 "Transport Associated with the Collisionless Detrapping/Retrapping of Orbits in a Nonaxisymmetric Torus II"[56]

R. H. Fowler, J. A. Rome, and K. C. Shaing

In a previous paper, we discussed heuristically the transport scaling associated with the collisionless detrapping/retrapping orbits in a nonaxisymmetric torus. It is found that the transport scaling depends on the retrapping possibility of the toroidally trapped particles in a time scale of the order of ω_E^{-1}, where ω_E is the $\mathbf{E} \times \mathbf{B}$ poloidal drift frequency. (Here we adopt the strong electric field ordering, i.e., $\omega_E > \omega_{\nabla B}$, the ∇B drift frequency.) Now we develop a kinetic method to calculate the transport coefficients in a stellarator with an even retrapping probability distribution in the pitch-angle space. This method is a generalization of that developed in ORNL/TM-8773. The solution we obtain is continuous in both pitch-angle and configuration space. It is found that if the probability distribution is localized around the trapping/retrapping boundary, the Kovrizhnykh scaling is obtained. On the other hand, if it is a uniform distribution, the Galeev and Sagdeev scaling prevails. Our approach can treat an arbitrary probability distribution; therefore, it represents a generalization of those two scalings. It is also found that the Galeev and Sagdeev scaling is strictly valid only in the limit of $\epsilon_h \gg \epsilon_t$. In case of $\epsilon_h \sim \epsilon_t$ and order of unity, correction is required. With slight modifications this method is also applicable to a rippled tokamak.

4.2.2.4 "Collisionless Neoclassical Nonresonant Transport in Bumpy Tori"[57]

D. E. Hastings

Neoclassical diffusion coefficients for a bumpy torus were first computed by Kovrizhnykh. He showed that for low collisionalities the transport rates scaled with collisionality. However, he ignored many important effects, and recent theoretical work in the collisionless limit indicates that substantial modifications need to be made to his diffusion coefficients. First, in a closed-field-line device the pressure surfaces can deviate substantially from the $|B|$ surfaces and, in addition, can have some ellipticity. It is found that the effect of ellipticity enters in the same way as in a tokamak, while the shift of the pressure surfaces modifies the radial drift and, hence, the diffusion coefficients. Second, in a bumpy torus there can be a significant poloidal electric field, which enhances the radial drift and therefore the transport rates. This can be calculated self-consistently from the requirement of first-order quasi-neutrality. Third, when a realistic magnetic geometry is used in bounce averaging the differential collision operator, particles near the trapped/passing boundary make a larger contribution to the transport than indicated in Kovrizhnykh's work. In particular, it is found that for collisionalities close to one, a collisional boundary layer forms across the trapped/passing boundary, and this leads to diffusion coefficients scaling with the square root of collisionality. For lower collisionalities, the effect of collisionless detrapping is important, and this leads to transport rates scaling with collisionality but with the inverse aspect ratio rather than its square. When these results are generalized to a multiple-ion-species plasma, it is found that energy coupling between the different ion species can produce significant modifications of the diffusion coefficients. The new diffusion coefficients with all these effects included have been confirmed with the use of a Monte Carlo code developed for bumpy tori. Finally, the use of these transport rates in one-and-one-half-dimensional (1½-D) radial transport codes indicates much lower lifetimes than obtained with the Kovrizhnykh coefficients. The lifetimes now obtained are within a factor of 2 of the experimentally observed numbers.

4.2.2.5 "Neoclassical Transport in a Bumpy Closed Field Line Device in the Collisional, Small Electric Field Regime"[58]

D. E. Hastings

Neoclassical diffusion coefficients are obtained in the collisional, small-electric-field regime for any bumpy closed-field-line device. A variational principle is used, and energy scattering is included in the collisional operator.

4.2.2.6 "Superbanana Plateau Regime Transport in a Multiple-Helicity Torsatron and a Bumpy Torus"[59]

D. E. Hastings and K. C. Shaing

An analytic expression for the neoclassical flux valid in both a multiple-helicity torsatron and a bumpy torus in the superbanana-plateau regime is obtained. The expression is valid for arbitrary values of Φ', the radial electric field, $\partial\epsilon_H/\partial_r$ with ϵ_H the effective helical

modulation or bumpiness, and $\partial\epsilon_T/\partial_r$ with ϵ_T the effective toroidal modulation. When small mirror force terms are included in the flux, then a nonlinear first-order ordinary differential equation (ODE) in Φ' is obtained from the ambipolarity relationship.

4.2.2.7 "Non-Local Transport in Tokamaks"[60]

J. A. Rome and R. H. Fowler

Monte Carlo codes can be used to account for the effects of large orbits and loss regions if their results are interpreted in a nonlocal manner. In a tokamak, because of axisymmetry, the orbits equations can be integrated by using three constants of motion (COMs): the energy ϵ, the magnetic moment μ, and the toroidal canonical angular momentum P_ϕ. Even a large collisionless orbit is just a point in COM space. When collisions are introduced, the motion of an individual particle in COM space resembles a random-walk process, and the collisionless motion of the particle can be separated from its collisional motion. The variables used for the calculation are ψ, ϵ, μ, and P_ϕ. In this space, the Jacobian is $(v_d \cdot \nabla\psi)^{-1}$, which is just the fraction of time spent at any point along the orbit. The topology of this space is examined to determine the locus of allowed particle orbits and the loss region boundary. To calculate the density and flux, Monte Carlo particles are followed in real space by integrating the equation for $dv_\parallel/dt$. After each integration step, pitch-angle and energy scattering occur and the new COMs are calculated. The new values of ψ_{max} and ψ_{min} are calculated numerically to determine whether the orbit crossed the surface ψ for the first time. If it did so, the change in flux is given by the mapping of $(\Delta\psi)/(\Delta t)$ onto $(\Delta\psi_{max,min})/(\Delta t)$. The density can be obtained by integrating $f(\epsilon,\mu,P_\phi)$ over the portion of COM space containing those orbits which pass through the flux surface. The principal advantage of this method is that it separates the motion of the particles along their collisionless orbits from their collisional motion between orbits.

4.2.2.8 "Monte Carlo Estimates of Transport Rates in EBT with Asymmetric Potential Profiles"[61]

J. S. Tolliver and C. L. Hedrick

The ORNL bounce-averaged EBT Monte Carlo transport code has been used to study loss rates in EBT for three cases: (1) closed electrostatic potential contours which coincide with the alpha contours, (2) in-out asymmetric potential profiles producing crescent-shaped equipotential surfaces, and (3) asymmetric potential profiles with open equipotential contours (i.e., potential contours that intersect the "wall"). Since low-energy particles are strongly influenced by the $\mathbf{E} \times \mathbf{B}$ drift to roughly follow the potential contours, such asymmetric potential profiles can be a significant loss mechanism for such particles. This idea has been quantified with the Monte Carlo calculations to be presented. We will show results for the particle and energy confinement times for the three cases mentioned.

4.2.2.9 "Bounce-Averaged Monte Carlo Calculations for Stellarators"[62]

J. S. Tolliver and J. A. Rome

We have developed a bounce-averaged Monte Carlo code suitable for stellarator transport physics. By bounce averaging, we avoid the need to follow the detailed longitudinal motion of test particles and are able to use much larger time steps than are appropriate in guiding-center codes. The code runs considerably faster than a guiding-center code and can be economically used for electrons as well as ions. The code has been benchmarked against analytic theory for EBT, in which all particles conserve J and can be treated by bounce-averaging. In a stellarator, particles can become detrapped so that bounce-averaging no longer applies. We make the assumption that such particles stream along field lines until they (either collisionlessly or via collisions) become retrapped. Results will be presented using a model field for the ATF.

4.2.2.10 "Enhanced Neoclassical Diffusion of Nonresonant Particles in a Bumpy Torus"[63]

R. L. Miller,* C. S. Chang,* and D. K. Lee

Significantly enhanced neoclassical diffusion is found for the hot nonresonant species in an EBT device by considering the detailed pitch-angle scattering for the transition and passing particles. Due to the presence of transition particles (trapped-passing boundary), the drift kinetic equation has more pitch-angle structure in the vertical drift term than has previously been considered. Using a bounce-averaged, pitch-angle-scattering collision operator, this equation is solved numerically, and evidence of a plateau regime is sought. Initial calculations using a collision operator that was not bounce-averaged agree with the results of Kovrizhnykh in the collisional regime but yield diffusion coefficients as much as four times larger than those of Kovrizhnykh in the collisionless regime.

---

*Applied Microwave Plasmas, Inc., Encinitas, Calif.

4.2.3 Extensions to MHD—Abstracts

4.2.3.1 "A Pressure-Gradient-Driven Tokamak 'Neoclassical MHD' Instability in the Banana-Plateau Collisionality Regime"[64]

J. D. Callen and K. C. Shaing

The moment equation approach to neoclassical processes is used to derive the perturbed flows, currents, and resistive MHD-like equations for a tokamak plasma. The new features of the resultant "neoclassical MHD," which requires a multiple-length scale analysis for the parallel eigenfunction but is valid in the banana-plateau collisionality regime, are: (1) a global Ohm's law, which includes a viscosity-driven (bootstrap) current; (2) reduction of the curvature effects to their flux surface average; and (3) an increased polarization drift contribution with the B^{-2} replaced by B_θ^{-2}. An electrostatic eigenmode equation is determined from $\nabla \cdot \mathbf{J} = 0$. For the unstable eigenmodes the viscous damping

(μ_e) effects dominate (by $\epsilon^{-3/2}$) over the curvature effects, but the growth rates of the modes still scale somewhat like resistive-g or ballooning modes—$\gamma_\mu \tau_A \sim n^{2/3} S^{1/3} \beta^{2/3} (\mu_e/\nu_e)^{2/3}$.

4.2.3.2 "Resistive MHD-Like Equations in the Banana-Plateau Collisionality Regime"[65]

J. D. Callen and K. C. Shaing

We are continuing our work attempting to derive resistive MHD-like equations in a banana-plateau or long mean-free-path collisionality regime. The dominant physical feature arising in the banana-plateau regime is the viscous damping of the poloidal flow embodied in modes that are highly extended along the magnetic field but are radially well localized. In this paper we will discuss how this long mean-free-path, flow-damping mechanism couples the parallel and perpendicular (geodesic-curvature-driven) compressibility effects in the usual resistive MHD equations and thus should lead to a significant modification of the compressibility effects on resistive MHD instabilities.

4.2.3.3 "A Kinetic Approach to a New Pressure Gradient Driven Tokamak Instability"[66]

K. C. Shaing and J. D. Callen

A newly proposed low-frequency ($\nu \sim \omega_b \gg \omega$) tokamak resistive instability driven by the pressure gradient is extended to the high-frequency regime ($\omega_b \gtrsim \omega \gg \nu$). To obtain a dispersion relation in the high-frequency regime, a frequency-dependent parallel viscosity is calculated from the kinetic equation. It has the same form as that in the low-frequency limit except that the collision frequency ν is replaced by $\nu - ia\omega$, where a is a constant of the order of unity. With this parallel viscosity, a perturbed bootstrap current is calculated from the parallel force balance equation. The ion polarization term is a factor of $\sqrt{\epsilon}$ smaller than that in the low-frequency case. There are two modes. The ion mode has a real frequency ω_{*i} and a higher growth rate ($1/\epsilon$) than that of the electron mode, which has a real frequency ω_{*e}.

4.2.4 Microstability and Turbulence—Abstracts

4.2.4.1 "Drift Waves Destabilized by Pellet Injection"[67]

C. O. Beasley, Jr., K. Molvig,* and W. I. van Rij

Pellet injection can cause density and temperature profiles such that drift waves are destabilized in a tokamak. We present numerical calculations of the instability using profiles similar to those in Alcator-C. In the region of pellet injection, the density profile becomes locally inverted, leading to a negative $\eta_e \equiv d \ln T_e / d \ln n$. If the magnitude of η_e becomes sufficiently large, modes can be excited down to very low mode number and correspondingly large radial mode structure extending beyond the range of the density inversion into the center of the tokamak. Profiles, frequencies, and growth rates for these modes are given.

---

*Massachusetts Institute of Technology, Cambridge.

4.2.4.2 "Effect of Coulomb Collisions on Universal Mode Stability"[68]

C. O. Beasley, Jr., W. I. van Rij, and K. Molvig*

The effect of electron-ion Coulomb collisions on the universal mode is studied using a Fokker-Planck collision operator in the kinetic equation for the electron distribution $f_e(x,v_\parallel,t)$. The expected smoothing of the $v_\parallel$ structure of $\bar{f}_e$ is found, and the character of the mode is little changed when $\nu_{ei} \rightarrow \omega_*$. It is also confirmed that a collisionality on the order of that of present tokamaks is sufficient to provide for destabilization of the mode even in the absence of nonlinear orbit stochastic diffusion.

*Massachusetts Institute of Technology, Cambridge.

4.2.4.3 *Theory and Calculation of Finite Beta Drift Wave Turbulence*[69]

C. O. Beasley, Jr., W. I. van Rij, K. Molvig,* and J. P. Freidberg*

Using numerical techniques, we calculate eigenmodes of the nonlinear universal mode with finite beta in order to determine the scaling of the saturation level of the instability with beta. We use two different renormalizations in the calculations and find that, using the appropriate renormalization, we are able to recover Alcator density scaling, as originally found in analytic work by Molvig and Hirshman. We also find that the universal mode should be stable in ohmically heated tokamaks above a critical beta on the order of 0.02.

*Massachusetts Institute of Technology, Cambridge.

4.2.4.4 "Influence of Ideal Ballooning Modes on Confinement Scaling at High β"[70]

J. P. Freidberg* and D. J. Sigmar

Recently, Connor et al. proposed a simple model to explain the degradation in confinement time in auxiliary heated tokamaks. They suggested that confinement is described by International Tokamak Reactor (INTOR) scaling except in regions where the ideal ballooning mode stability criterion is violated. In these regions the pressure gradient is limited to the ideal MHD threshold value. In the present work, we extend their analysis to include finite Larmor radius (FLR) effects on the ballooning mode stability boundary. Our motivation is to ascertain whether the remarkably good agreement between their theory and the empirical scaling laws and Impurity Study Experiment (ISX-B) beta saturation prevails when a more realistic stability criterion is introduced. FLR effects enter the scaling relations in a rather complicated way, as well as altering the regions of plasma where ballooning modes can occur. FLR-modified confinement scaling results will be presented.

*Massachusetts Institute of Technology, Cambridge.

4.3 RF HEATING AND CURRENT DRIVE

The rf heating and current drive effort is aimed at developing fundamental theory as well as computational modeling capability for plasma wave generation, propagation, and absorption and plasma response in all fusion-relevant regimes (Alfvén, ion cyclotron, lower hybrid, and electron cyclotron). Application of the models to make detailed comparison with measurements provides insight into the experiments and feedback for further refinements in the theory.

Over the past year, the emphasis has shifted from bumpy tori toward tokamaks and stellarators. Nevertheless, much progress has been made in understanding the core heating in ELMO Bumpy Torus (EBT) and the role of the Doppler-shifted resonance, the microwave field profiles, and the confinement of the strongly heated particles. The Fokker-Planck code has been developed to the point that the effects have been demonstrated and qualitative agreement obtained with experiment. Furthermore, it was shown that pitch-angle scattering due to electron cyclotron heating (ECH) can have a large impact on neoclassical transport. While this was first demonstrated for the EBT configuration, there are possible implications for both tokamaks and stellarators.

The RAYS geometrical optics code has been modified to study wave heating in stellarator geometry. Various ECH strategies on ATF have been investigated to optimize wave absorption and heating profiles. Important sensitivities and constraints have been delineated. In addition, full-wave ion cyclotron resonance heating (ICRH) calculations have begun with the objective of studying wave propagation and absorption in stellarators and tokamaks. A 3-D wave code has been developed and tested in a uniform, bounded, cold plasma. Various reductions have been studied, including a 2-D version for nonuniform plasmas and a version employing special electromagnetic potentials.

Considerable effort has also gone into the basic physics of wave processes in plasmas. The basic physics of fundamental and second-harmonic cyclotron absorption and mode conversion in weakly relativistic plasmas has been investigated using a rigorous full-wave treatment. The physics of strongly cyclotron damped waves in nonuniform plasmas has been investigated with a kinetic, full-wave model. Also, further studies of wave propagation and absorption in highly relativistic plasmas have been carried out.

4.3.1 Abstract of "Propagation and Absorption of Electromagnetic Waves in Fully Relativistic Plasmas"[71]

D. B. Batchelor, R. C. Goldfinger, and H. Weitzner

The propagation and absorption of electromagnetic waves in a relativistic Maxwellian plasma are investigated by solving the uniform plasma dispersion relation. The Hermitian and the anti-Hermitian parts of the plasma conductivity tensor $\underset{\approx}{\sigma}$ are calculated relativistically. The Bessel functions occurring in $\underset{\approx}{\sigma}$ are not expanded, and many cyclotron harmonic terms are included at high temperatures. The dispersion relation is solved numerically for perpendicular propagation, $k_{\parallel} = 0$, where the relativistic effects are maximum and are not masked by Doppler broadening, which has been more thoroughly investigated. It is found that relativistic broadening has a substantial effect on wave dispersion, shifting the extraordinary (X) mode right-hand cutoff and the upper hybrid resonance to a higher magnetic

field with increasing temperature. Above a critical temperature the cutoff disappears entirely. There is a broad range of temperatures, 20 keV $\leq T_e \leq$ 500 keV, for which the wave number $k_\perp$ differs significantly from both the cold plasma value and the vacuum value. This has important implications for ray tracing in relativistic plasmas. Wave damping rates are calculated and compared to results from a previous formulation using the Poynting theorem, in which only the Hermitian part of $\underset{\approx}{\sigma}$ is calculated relativistically.

4.3.2 Abstract of "Strong Damping of Electron Cyclotron Waves in Nearly Parallel Stratified Plasmas"[72]

D. B. Batchelor, K. S. Riedel,* and H. Weitzner

In mirrorlike devices, where the magnetic gradient is along the direction of the magnetic field (parallel stratification), the right circularly polarized component of E is not suppressed, and very strong local damping of the extraordinary mode can occur. In such circumstances, the warm plasma dispersion relation predicts essentially total absorption of the wave with no reflection. However, because of the strong damping and the rapid spatial variations of k as the resonance is approached, one would not expect the usual geometrical optics theories to be valid. Adapting a calculation done by Weitzner for ICRH, we introduce two small parameters $\epsilon_1 = v_{th}\omega_{pe}/\omega c$ and $\epsilon_2 = \lambda/L \sim c/\omega_{pe}L$ and perform a boundary layer analysis in the resonance region which is matched asymptotically to the geometrical optics solution. The integrodifferential equations obtained in the resonance layer are solved numerically.

*New York University, New York.

4.3.3 Abstract of "Fokker-Planck Calculations of Core Plasma Heating by ECRH in EBT"[73]

G. L. Chen, D. B. Batchelor, and Y. Matsuda*

In the heating of the bulk plasma in EBT devices by fundamental electron cyclotron resonance heating (ECRH), we find the details of wave propagation, plasma heating, and transport of the deposited wave energy to be very tightly coupled. The Doppler shift couples the spatial structure of the wave electric field profile to the energy and pitch-angle structure of the distribution function. In turn, the radial drift and neoclassical step size of energetic particles in EBT are very pitch-angle dependent, with the result that large losses occur in the population of particles which actually absorb the wave energy. A 2-D Fokker-Planck code has been used to investigate core plasma heating, including a bounce-averaged quasi-linear heating operator and Coulomb collisions. An rf electric field profile is used which maintains consistency between the microwave power flux and the particle heating rate. We find that most of the rf power is absorbed by passing particles or energetic trapped particles that are transitional between trapped and passing and tend to be poorly confined in EBT-S.

*Lawrence Livermore National Laboratory, Livermore, Calif.

4.3.4 Abstract of "Fokker-Planck Modeling of Electron Cyclotron Heating and Direct Particle Loss in EBT and ELMO Bumpy Square"[74]

G. L. Chen, D. B. Batchelor, and Y. Matsuda*

The SMOKES 2-D Fokker-Planck code has been used to investigate core plasma heating at the fundamental cyclotron resonance including a bounce-averaged, quasi-linear fundamental ECH operator and Coulomb collisions. Heating depends very sensitively on details of the rf electric field profile. A profile is used which maintains consistency between the microwave power flux and the particle heating rate. Using this profile, we find that most of the rf power is absorbed by passing particles or energetic trapped particles that are transitional between trapped and passing and tend to be poorly confined in EBT-S. In order to model the direct loss of these transitional particles on open drift surfaces, we introduce a lossy region in velocity space with particle lifetime $\tau_D(\epsilon,\mu)$ = time for particles to drift out. We find that substantial power is lost directly. These processes show promise of explaining a number of experimental observations, including the presence of an energetic, anisotropic, locally produced electron tail. Because the transitional particles in an EBS device are removed in velocity space from the heating zone and because the lossy region associated with transitional particles is much narrower than in the bumpy torus, ECH in EBS should be much more efficient than in EBT-S.

*Lawrence Livermore National Laboratory, Livermore, Calif.

4.3.5 Abstract of "Propagation and Absorption of Electron Cyclotron Waves in ATF"[75]

R. C. Goldfinger, D. B. Batchelor, and S. P. Hirshman

The ORNL ray tracing code, RAYS, has been adapted to trace rays in the electron cyclotron frequency range for the ATF stellarator device to be built at ORNL. For the magnetic equilibrium model, a vacuum field is produced due to two filamentary helical windings and four VF coils. The flux surfaces [which define $n_e(\psi)$] are taken to be elliptical in a plane of constant ϕ (ϕ = toroidal angle) and to rotate about the minor axis with the helical windings. Work has begun on modifying RAYS to trace rays in a hybrid flux–Cartesian coordinate system. The Cartesian wave vector components (K_x, K_y, K_z) are integrated the conventional way in a fixed Cartesian system. The ray position, however, is expressed and integrated in the flux coordinate system, $\underset{\sim}{\alpha} = (\rho, \theta, \phi)$. The RAYS code can then make direct use of the moments method solutions of the 3-D MHD equilibrium equations, which are expressed in flux coordinates. This yields much simpler and more efficient ray tracing, since it is no longer necessary to perform the inversion from flux coordinates to real space [i.e., to invert $\underset{\sim}{\alpha}(\underset{\sim}{X})$ and obtain $\underset{\sim}{X}(\underset{\sim}{\alpha})$].

4.3.6 Abstract of "R-F and Microwave Induced Losses"[76]

C. L. Hedrick and E. F. Jaeger

The use of rf or microwave power to produce heating (or current drive) in toroidal devices also introduces additional losses. Here we consider losses similar to neoclassical losses

except that we consider wave-induced scattering in addition to Coulomb scattering. In many instances previous neoclassical results for transport coefficients can be extended simply by replacing the Coulomb collision frequency by a total scattering frequency. However, in many cases of practical interest, the suprathermal part of the distribution function (largely responsible for the losses) is distorted by the wave-induced losses as well as by the wave heating. In these cases it becomes necessary to solve for the distribution function itself rather than its moments [as is usually done in one-dimensional (1-D) transport]. For intermediate scattering rates (plateau and above) a reasonably simple procedure, very similar to standard neoclassical, can be followed.

4.3.7 Abstract of "Microwave-Induced Neoclassical Transport"[77]

E. F. Jaeger, C. L. Hedrick, and D. B. Batchelor

Microwave scattering in pitch angle is included in a simplified drift kinetic equation for electrons, assuming a Lorentz collision operator for pitch-angle scattering and moderate to high collisionality $\nu/\Omega \geqslant (r/R_T)^{3/2} \sim 0.03$. A simple estimate of the effect of microwave scattering on neoclassical transport in EBT geometry is obtained by assuming the lowest-order distribution function to be Maxwellian and treating energy as a parameter. Strong absorption of the microwaves near the Doppler-shifted resonance leads to relatively rapid pitch-angle scattering for high-energy particles ($1/2mv^2 > kT$) with large parallel velocity ($v_\parallel/v > 0.5$). This enhanced effective collisionality can increase thermal conductivity by as much as an order of magnitude, depending on the temperature of the assumed Maxwellian.

4.3.8 Abstract of "Full Wave Treatment of Wave Propagation in a Three-Dimensional Cavity Containing Cold Plasma"[78]

E. F. Jaeger, J. H. Whealton,* H. Weitzner, and D. B. Batchelor

For many laboratory plasmas in which low-frequency, long-wavelength rf fields are present, the geometrical optics assumptions are not valid, and a full-wave treatment of wave propagation is desirable. Recently, finite difference techniques have been applied to calculate electric field components and resonant frequencies in 3-D cavities in a vacuum. This involves solving Maxwell's equations with the constraint $\nabla \cdot \mathbf{E} = 0$. However, with the introduction of cold plasma in the cavity, the constraint $\nabla \cdot \mathbf{E} = 0$ is violated and the system of equations becomes highly degenerate, causing the vacuum technique to fail. We therefore reformulate the problem in terms of the electromagnetic potentials $\mathbf{A}$ and ϕ with Coulomb gauge $\nabla \cdot \mathbf{A} = 0$. This allows calculation of field component shapes and resonant frequencies for cavity modes in the presence of cold plasma.

---

*Plasma Technology Section.

4.3.9 Abstract of "A Numerical Model for Examining Noninductive Current Drive Scenarios in Ignition Tokamaks"[79]

S. K. Borowski,* Y-K. M. Peng,* and W. A. Houlberg

The processes involved in noninductive current drive (rampup, current maintenance, and transformer recharging) are examined for an ignition-size tokamak [e.g., the Toroidal Fusion Core Experiment (TFCX)] using an expanding-radius version of the WHIST tokamak transport code, which includes a simplified lower hybrid current drive (LHCD) model with assumed rf-driven current density profiles. The purpose of this study is to obtain information regarding the lower hybrid (LH) wave power and $n_{\parallel}(r,t)$ spectrum requirements necessary to support a specified $J_{rf}(r,t)$ as a function of the evolving plasma parameters $n_e(r,t)$, $T_e(r,t)$, etc., poloidal magnetic field $B_p(r,t)$, and programmed $I_{rf}(r,t)$. Substantial variation in the wave frequency and $n_{\parallel}$ spectrum is anticipated from adiabatic compression effects as the major radius is reduced in size to accommodate the minor radius expansion. The optimum rf-driven current density profiles for transformer recharging as well as the required recharging time in the presence of flux diffusion are investigated. Finally, a comparison of model results and Princeton Large Torus (PLT) current drive experimental data is presented.

---

*Fusion Engineering Design Center.

4.3.10 Abstract of "Second Harmonic Electron Cyclotron Heating"[80]

M. D. Carter,* D. B. Batchelor, and J. D. Callen

When electron particle orbits are trapped very near the second-harmonic cyclotron resonance, quasi-linear heating theory breaks down and nonlinear effects become important for particles with small $v_{\parallel}/v$. Numerical studies, as well as a multiple time scale analysis, demonstrate that when the change in the gyrofrequency due to the relativistic mass shift, $(\gamma - 1)\Omega_0$, is on the order of $\Omega_0|\mathbf{E}|/|\mathbf{B}_0|$, where $|\mathbf{E}|$ is the rf electric field strength of a perpendicularly propagating wave and $|\mathbf{B}_0|$ is the strength of the static magnetic field, nonlinear energy growth begins to saturate. This effect is important even for low-energy electrons ($\sim$20 eV), resulting in periodic motion with energy excursions on the order of 5 to 10 times ϵmc^2, where $\epsilon \equiv e|\mathbf{E}|/mc\omega = \Omega_0|\mathbf{E}|/\omega|\mathbf{B}_0|$. In EBT, such excursions are on the order of 100 to 200 eV on time scales several thousand times the gyroperiod. Small-angle Coulomb collisions and other phase-randomizing processes can cause net heating from this otherwise periodic nonlinear behavior. A Monte Carlo code has been used to determine the dependence of heating on collisionality and the possible effects on the electron distribution function. For highly collisional regimes, collisions annihilate the energy excursion behavior, while in very collisionless regimes, the randomizing process and the net heating efficiency are reduced. Analytic formulas are derived which describe the large energy excursions and their repetition time scale in a mildly relativistic limit. Utilizing these characteristics of the nonlinear energy excursions, estimates of the net heating rate

as a function of collisionality are made and compared with the Monte Carlo numerical results.

*University of Wisconsin, Madison.

4.3.11 Abstract of "Absorption, Reflection, and Mode Coupling at the Second Cyclotron Resonance in a Weakly Relativistic, Inhomogeneous Plasma"[81]

K. Imre,* H. Weitzner, and D. B. Batchelor

The relativistic linearized Vlasov equation is rescaled and solved in the boundary layer at the second electron cyclotron harmonic, where it is known that the geometrical optics approach breaks down for a perpendicularly stratified plasma with zero (or small) parallel refractive index. The full-wave equations valid in the boundary layer are then obtained by calculating the currents and substituting into the Maxwell equations, which yields a fourth-order differential equation for E. This equation is numerically integrated from the high-field side to the low-field side across the boundary layer. The asymptotic form of this equation, which corresponds to the nonrelativistic case, is solved by quadratures and expressed analytically in the high- and low-field sides. These solutions are numerically matched to the solutions of the weakly relativistic full-wave equation. The latter, which correspond to the incoming and outgoing extraordinary waves and quasi-electrostatic waves, are recombined to give the solutions of three physical problems, namely, X-mode incidence from either side and ordinary-mode (O-mode) incidence from the low-field side. In the outer region, treated by the standard geometrical optics, the appropriate Poynting theorem is derived, which enables one to calculate the fractional energy associated with the wave and the particles in a given mode. We have calculated the transmission, reflection, mode conversion, and absorption for the three problems mentioned above. The nonrelativistic case, which is expressed analytically, shows that the incident energy which is not transmitted is mode converted (or partially reflected in the low-field-side incidence), thus yielding zero absorption. The weakly relativistic treatment yields the fractional absorbed energy due to the broadening. The results are presented in terms of two parameters, namely $X = (\omega_p/\omega)^2$ and $\eta^2\tilde{L}$, where $\eta = v_e/c$ is the smallness parameter and $\tilde{L}$ is the characteristic scale length for the external field normalized to the free space wavelength. It is found that in general the absorption in the low-field-side incidence is higher due to the smaller mode conversion rate.

*New York University, New York.

4.4 CONFINEMENT OPTIMIZATION AND IMPROVEMENT

The confinement optimization and improvement effort integrates physics results from MHD equilibrium and stability, transport, and heating studies in order to devise ways of improving confinement in toroidal systems. Three main approaches are followed. The first

approach, optimization of magnetic fields to improve equilibrium and stability properties of the plasmas, is primarily directed toward designing new stellarator configurations. The basic tools used are vacuum magnetic field, orbit, and MHD codes. The optimization and the control of the electrostatic potential are pursued in order to improve transport properties. In general, such control will depend on the plasma heating mechanism. Because of the consequent beneficial impact on overall plasma confinement, much emphasis is also given to improvement of particle and impurity control at the plasma edge.

The other two approaches are followed to improve the performance of previously determined configurations such as ATF or EBS. However, the goals are not limited solely to finding improved configurations or regimes of improved confinement. Another very important goal is to provide ways of experimentally varying basic parameters that are thought to be crucial for plasma confinement so as to test applicability of the optimization concepts.

Attractive new stellarator configurations have been discovered, and old ones have been investigated in more detail. An important improvement was added to the basic ATF configuration when the flux-controlled torsatron concept was included in the ATF design. This idea permits practical access to the second stability regime through the control of the rotational transform and magnetic well.

With the flexible heliac concept we have transformed the basic heliac configuration into a practical and attractive experimental device. Studies of other heliac configurations had shown breakup of the flux surfaces at very low values of beta. We realized that this breakup could be avoided by carefully controlling the shear and transform to avoid rational surfaces within the plasma. Very low shear and a sufficiently irrational transform value are required. By introducing a helical hard core wrapped around the usual circular hard core, enough configurational flexibility is obtained to:

- keep very low shear,
- provide an optimum value for ι,
- introduce shear to cancel finite-beta effects,
- explore nonoptimum configurations to test theories, and
- obtain deep magnetic wells.

This concept is the basis for the design of the TJ-II device, to be built by the Junta de Energia Nuclear (JEN), Madrid, Spain. The design is being carried out as part of a collaboration between ORNL and JEN. The coil configuration is illustrated in Fig. 4.6, and some of the effects of the $\ell = 1$ hard-core winding are illustrated in Fig. 4.7.

A low-aspect-ratio, $\ell = 2$ torsatron ($A_c \sim 3$) was developed by applying triangular shaping of the cross section of the helical coils. This shaping permits edge transforms close to one and therefore maintains good equilibrium properties. A modular version of this configuration that uses Symmotron-type coils was also developed. The resulting design retained the good transform properties of the continuous version.

Hybrid configurations were explored, consisting primarily of $\ell = 1$ and $\ell = 2$ mixtures. It was hoped that these would combine the large flux surfaces and high transform of the $\ell = 1$ devices with the magnetic well of the $\ell = 2$ devices. Unfortunately, these hybrids seemed to combine the worst aspects of the two configurations, rather than the best. Similar studies were carried out for $\ell = 2$ and $\ell = 3$ mixed configurations.

ORNL-DWG 84-3803A FED

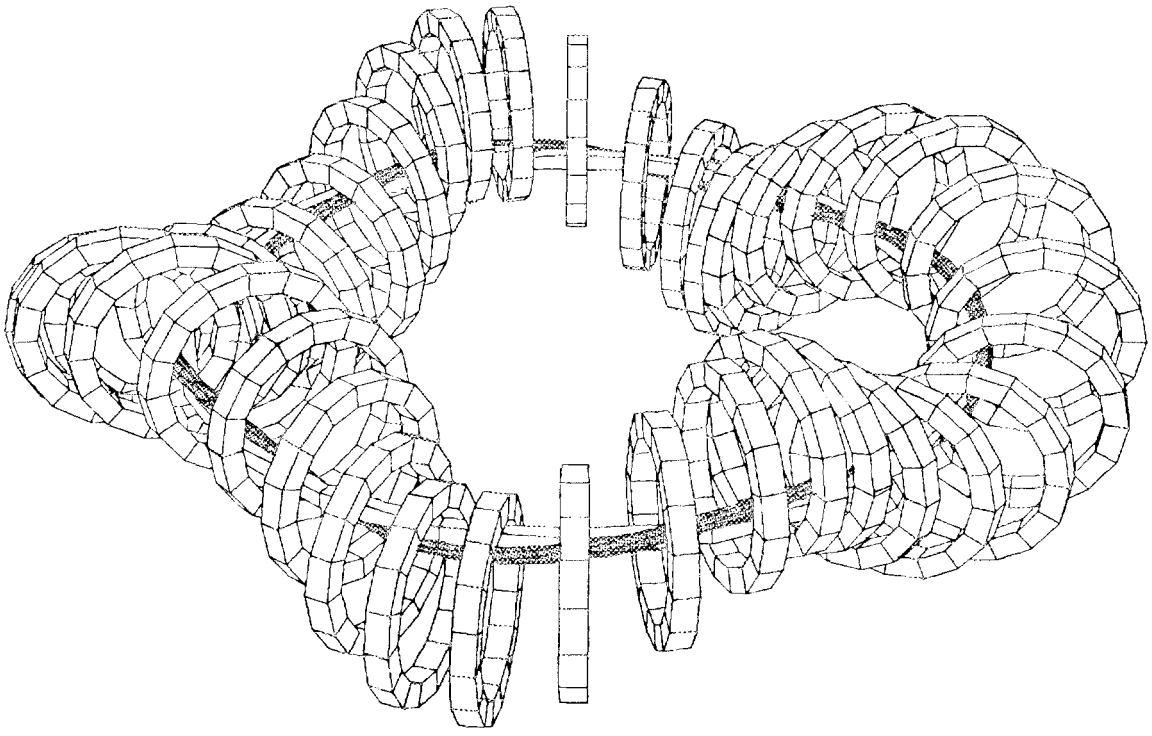

Fig. 4.6. Flexible heliac coil configuration with additional $\ell = 1$ hardcore winding shown shaded.

Optimization of the transport properties through the radial electric field in the EBS design can theoretically improve the confinement properties of EBT by an order of magnitude. This should overcome some of the basic limitations in the EBT-I/S experiments. This particular optimization procedure is a source of ideas for further improvements in tokamaks and stellarator devices.

The radial electric field has an important effect on the transport of impurities. If the plasma is on the electron root of the field equation, it may be possible to make the impurities exit the plasma. Startup scenarios that favor this choice of root have been studied. Also, the deterioration of electron confinement at the plasma center will change the electric field. By lowering the magnetic axis transform in ATF using the VF coils, sawtooth-type oscillations can be artificially stimulated. This is expected to help the control of impurities in ATF.

Confinement outside the last closed flux surface is strongly related to configuration optimization. Particle and impurity control must be applied in this region. Stellarators in general, and ATF in particular, may behave quite differently from tokamaks. In contrast to other stellarators, ATF has ergodic field line topology outside the last closed flux surface. This is believed to be due to the fact that the edge lies on the $q = 1$ surface. The helically trapped particles that were thought to be in the loss region are actually mirrored by the helical field (HF) coils and return to the plasma.

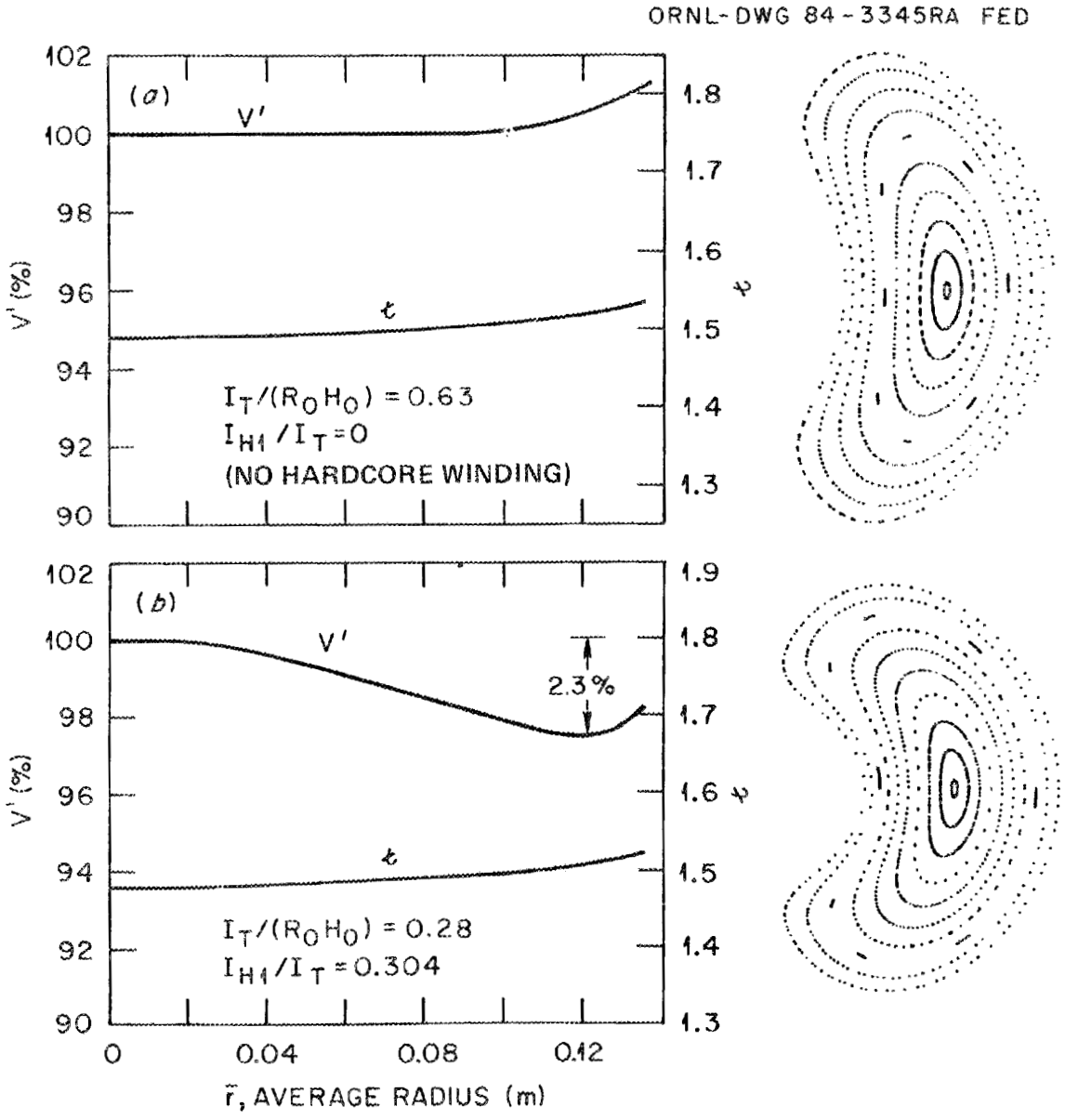

Fig. 4.7. Comparison of ι and V' profiles for $M = 4$, $R/a_c = 4$ heliacs with and without $\ell = 1$ hardcore winding. For this example, $R_0 = 1$ m, $r_{SW}/a_c = 0.7$, $a_c/a_{hc} = 6$, and $\Delta R/R_0 = 0.0125$.

Finally, major advances have been made in conjunction with the construction of the ATF coils. These make stellarators more attractive reactor candidates. Techniques have been devised to provide automated measurement for very complicated large parts with no reference surfaces. Using these techniques, the tolerance of molded stainless steel parts has been improved by an order of magnitude. In addition, application of the same techniques to five-axis milling machines reduces setup times dramatically, because parts can be machined in their own coordinate systems, rather than that of the machine.

4.4.1 Abstract of "The Flexible Heliac"[82]

B. A. Carreras, J. L. Cantrell, L. Garcia, J. H. Harris, T. C. Hender, and V. E. Lynch

The addition of an $\ell = 1$ helical winding to the heliac central conductor adds a significant degree of flexibility to the configuration by making it possible to control the rotational transform and shear. These effects are consistent with results for helically symmetric fields, but additional helical harmonics produced by toroidal coupling may also be important. Such control is essential for an experiment because the presence of low-m resonant surfaces in or near the plasma can cause breakup of the equilibrium magnetic surfaces. The use of an additional helical winding also permits reduction of the total central conductor current and deepens the magnetic well at low aspect ratio.

To further improve the equilibrium beta limits for low-aspect-ratio configurations, it is necessary to reduce the toroidal magnetic axis shift. Several ways to achieve this goal have been examined, including (1) an increase in the aspect ratio, (2) an increase in the number of field periods, (3) a reduction of the variation of $\int d\ell/B$ by a helical tilt of the coils, and (4) toroidal modulation of the coil currents. The results indicate that an increase in aspect ratio and number of field periods is the most effective means of improvement.

4.4.2 Abstract of "Approximate Flux Conserving Stellarator"[83]

B. A. Carreras, H. R. Hicks, J. A. Holmes, and V. E. Lynch

A steady-state stellarator equilibrium is usually assumed to have zero current inside each flux surface. In this limit, the rotational transform profile changes strongly with increasing beta. The transform at the magnetic axis increases with beta, while the transform at the edge decreases. This results in double-valued profiles even for moderate beta values ($\beta \geqslant 3\%$). Such profiles can be unstable. Therefore, it is desirable to control the transform profile in going to a high-beta regime. This can be achieved by conveniently shaping the poloidal magnetic field. Using the stellarator expansion, we calculate sequences of zero-current equilibria with approximately constant rotational transform profile. We also investigate the stability properties of these equilibria. We show that, for the ATF device, such equilibrium sequences can be obtained using the present VF coil system to shape the poloidal magnetic field. This mode of operation offers a better way of accessing the second stability regime.

4.4.3 Abstract of "Study of ATF-1 Torsatron Configurations Using the NYU Code BETA"[84]

H. R. Hicks, B. A. Carreras, and J. A. Holmes

Equilibrium and Mercier stability properties of various ATF-1 plasma configurations are analyzed using the 3-D, fixed boundary code BETA. The boundary shape is varied to study the effects of varying the VF coil currents. This allows control of the iota profile as beta is increased. This approach complements other techniques being used to study ATF-1.

4.4.4 Abstract of "$\ell=1/\ell=2$ Torsatron Hybrids"[85]

J. A. Rome

$\ell=1$ continuous helical torsatrons have large flux surfaces and significant rotational transforms but usually have a magnetic hill. $\ell=2$ continuous helical torsatrons have less transform and smaller surfaces but have a magnetic well. $\ell=1/\ell=2$ hybrids were created in two ways: (1) one of the two coils in an $\ell=2$ torsatron was moved toroidally until the configuration continuously approached an $\ell=1$ torsatron (when the coils coincided); (2) the winding law was modulated so that the two coils overlapped on either the inside or the outside ($\ell=1$) and were apart on the other ($\ell=2$) side. Cross-sectional shaping of the torus was tried. Unfortunately, these designs seem to combine the worst features of the $\ell=1$ and $\ell=2$ devices, rather than the best.

4.5 PLASMA MODELING, BURN ANALYSIS, IMPURITIES, AND PELLETS

Fluid transport simulation codes represent the widest range of contact between plasma theory and experimentally measured quantities. Because of this broad contact, these codes are used both to interpret experimental results in terms of theoretical models and to provide guidance for new experiments. The plasma transport modeling effort is therefore aimed at developing a comprehensive set of simulation models for application to both existing and planned toroidal devices. Heavy emphasis is placed on development of generalized models that can be applied to either axisymmetric or nonaxisymmetric plasmas. The range of application covers small experiments proposed to explore innovations in plasma physics, existing devices, and more advanced ignition devices. Continuity in the models and analysis codes, extending across the traditional boundaries of specific confinement concepts and plasma parameter regimes, is a very high priority, so that comparisons between various concepts and various parameter ranges within a given concept are more useful. In addition, the nature of experiments is such that substantial work in the ancillary areas of atomic and molecular physics, plasma-surface interactions, and solid pellet ablation modeling is required.

A set of efficient subroutines has been developed for using the solutions of 2-D and 3-D MHD equilibria in a large class of particle and energy source subroutines for transport modeling and analysis codes. These can be applied to a broad class of advanced tokamaks (bean-shaped and very low aspect ratio concepts) and helical devices (stellarators, torsatrons, and helical-axis concepts). Thus, it will be possible to use a common analysis to compare the relative advantages and disadvantages of the different types of devices. These subroutines have been used to provide the magnetic field needed in the ion cyclotron resonant frequency (ICRF) ray tracing codes by Hwang, used at Princeton Plasma Physics Laboratory (PPPL) for TFCX studies, and by Brambilla, used for studies of the Joint European Torus (JET), and in the ECH ray tracing code by Batchelor, used at ORNL for ISX-B studies; they are being considered for use in a fully 3-D, ICRF/ECH ray tracing code having general application in reactor studies.

A library of modular computer codes and subroutines is being developed with intercompatibility of physics units and input/output for transport analysis of toroidal plasmas. The

individual codes and subroutines can be used as stand-alone modules for model development and benchmarking or integrated into a complete transport code. Comprehensive diagnostics and error analyses are included, as are options for quality of graphics. Among the computer codes incorporated into the library are PELLET (pellet ablation physics), VMOMS (2-D axisymmetric MHD equilibrium), BOX-2D (geometry subroutines for arbitrary chords in an axisymmetric plasma), and a set of graphics subroutines. The chord-mapping subroutines have been incorporated into an analysis code that unfolds bremsstrahlung emission data from the Doublet III (DIII) pellet injection experiments to yield time-dependent density profiles for particle confinement studies. The subroutines have also been coupled into the JET transport code for comparison of calculated and measured chordal density and radiation signals.

Parametric studies of deuterium-tritium (D-T) ignition devices have been made using the WHIST code. For the TFCX device, ICRF heating, current drive scenarios, and ignition margins with various confinement models have been studied. Similar ignition margin studies are being performed for compact ($a \simeq 0.5$-m), high-field tokamak plasmas that may be candidates for international collaboration. Feasibility studies of high-Q or ignited steady-state stellarator/torsatron systems with 300–500 MW of fusion power indicate that such systems show promise of being attractive reactors. Maintenance of an electrostatic potential of $e\phi/kT \simeq 2$–4 appears to be a critical issue.

The previous collisional regime theory for plasma rotation and impurity transport in a tokamak plasma with strong, directed, neutral beam heating and strong rotation ($v_\phi \sim v_{th}$) was extended to the plateau regime. As in the collisional regime theory, an anomalous cross-field transport of toroidal momentum, such as is observed experimentally, is incorporated into the theory. The predicted impurity transport exhibits features in agreement with observations in ISX-B and PLT.

The collisional regime theory was reviewed, and it was determined that anomalous cross-field transport of momentum, even in the absence of beam heating, leads to a particle flux term directly proportional to the radial electric field. Beam heating, or other heating that introduces directed momentum into the plasma and impurities, modifies the electric field and thus the particle transport. It is expected that these results carry over into the plateau regime.

The treatment of the collisional regime theory in the IMPTAR code was upgraded, and further time-dependent simulations of the evolution of impurity profiles during directed neutral beam heating were carried out.

An atomic physics package for beryllium was developed for use in the analysis of the ISX-B beryllium limiter experiment, and a nitrogen package was developed for use in the analysis of the ISX-B pump limiter experiment.

Pellet ablation physics has been extended to neutral-beam-heated plasmas. Stopping cross sections for fast-beam ions and electrons in an ionized cloud have been added to the original neutral shielding model that was successfully used to model pellet injection into ohmic plasmas. The effect of cloud ionization in stopping electrons was shown to be minimal; for ions, the net reduction in ablation was substantial. To help explain anomalously large ablation in the scrapeoff region of beam-heated Poloidal Divertor Experiment (PDX) and ISX-B plasmas, model variations that included enhanced fast-ion ablation from a combination of large orbits and reduced cloud shielding were developed.

The upgraded ablation physics models were applied to pellet injection studies for the Tokamak Fusion Test Reactor (TFTR) and JET. The effect of uncertainties in the fast-ion ablation physics was examined and shown to be less critical than in smaller, intensely heated experiments. Pellet needs for both machines have been predicted in collaboration with the responsible local groups.

4.5.1 Abstract of "Intersections of a Trajectory with Tokamak or Stellarator Flux Surfaces"[86]

S. E. Attenberger and W. A. Houlberg

Many experimental and theoretical applications require finding the intersections of a ray or particle trajectory (specified in cylindrical or Cartesian coordinates) with a set of flux surfaces. We start with any unique transformation from flux coordinates to cylindrical coordinates (as from any moments method of solving for MHD equilibria). Both iterative and noniterative methods have been examined for accuracy, speed, and flexibility in solving the intersection problem. Application is made to fully 3-D plasmas.

4.5.2 Abstract of "Efficient Mapping Algorithms Between Flux Coordinates and Real-Space Coordinates for Toroidal Plasmas"[87]

S. E. Attenberger, W. A. Houlberg, and S. P. Hirshman

The evolution of plasma properties in toroidal plasmas which possess magnetic flux surfaces is most conveniently expressed in magnetic flux coordinates. However, Cartesian or cylindrical coordinate representation is more convenient for evaluating many particle and energy sources and for most plasma diagnostics. Computationally efficient algorithms are therefore desirable for mapping in both directions. We report here on one such set of algorithms. This work was motivated by rf heating applications in finite-beta, axisymmetric plasmas with noncircular cross sections. However, the methods employed here are applicable to a much broader class of problems and can even be extended to nonaxisymmetric plasmas.

A poloidal moments representation of magnetic flux surfaces in an axisymmetric plasma with up-down symmetry is of the form

$$R(\rho,\theta) = \sum_{n=0}^{\infty} R_n(\rho)\cos(n\theta) \ , \quad Z(\rho) = \sum_{n=1}^{\infty} Z_n(\rho)\sin(n\theta) \ ,$$

where ρ is the flux surface label, θ is a poloidal coordinate, R is measured from the major axis, and Z is measured from the midplane. The functions $R_n(\rho)$ and $Z_n(\rho)$ satisfy a set of coupled ODEs determined by poloidal integrals of the Grad-Shafranov equation. Typically, terms through $n = 2$ give an excellent representation of finite-beta plasmas with elongation and triangularity.

The inverse mapping may be done using a Newton's method iteration based on a Taylor expansion about the point (ρ_K,θ_K) at each Kth iteration. The convergence is rapid for typical axisymmetric equilibria. Using a tolerance of $0.001\rho_{max}$, about two to five iterations

are required, depending on the initial guess for (ρ,θ). On the Cray-1 this requires about 7×10^{-5} s, typically.

Once the flux surface coordinates are known, $n(\rho)$, $T(\rho)$, and $B(\rho,\theta)$ and its Cartesian components are easily found. There are two possible procedures for finding the gradients of these quantities: (1) a simple finite difference or (2) application of the chain rule to express the gradient in terms of the derivatives with respect to ρ and θ. Both methods require comparable execution time for computing the field gradients.

A separate but related problem is to find all intersections of a chord with an arbitrary set of flux surfaces—for example, those surfaces on which the plasma density and temperature are computed by a transport code. A ray through the plasma may be treated as a sequence of these chords laid end-to-end. An algorithm has been devised whereby the plasma is divided into quadrilateral bins whose corners are given by uniform steps in ρ and θ. Tracking the chord then becomes a simple noniterative procedure. In the present code the entire chord is assumed to lie in a ϕ = const plane. The extension to three dimensions will be the subject of future development.

4.5.3 Abstract of "Effects of Momentum Input and Sonic Flow on Impurity Transport in Tokamaks"[88]

E. C. Crume, Jr.

Experiments on beam-heated ISX-B plasmas indicate that co-injection reduces the accumulation of impurities in comparison with ohmically heated plasmas. Stacey and Sigmar have recently included the strong toroidal rotation induced by directed neutral beam heating in a self-consistent theory for particle flows within the flux surfaces, the radial electric field, and the radial particle transport in a tokamak plasma for both the collisional regime and a mixed regime in which the main plasma ions are in the plateau regime while the impurities remain in the collisional regime. We have implemented the collisional regime theory in our basic impurity transport simulation code IMPTAR and present simulation results for co-injected plasmas. These results differ qualitatively from our previous results in which rotation effects and all other momentum exchange effects were treated separately. That is, for a model plasma with ion densities and temperatures comparable to those in ISX-B, (1) simulations with the new theory show that co-injection can drive impurities out, in agreement with experiment, whereas (2) simulations with the rotation effect theory alone show that co-injection can drive impurities in, in contrast to experiment. Some attempt was made to account for the low collisionality of the plasma ions in these simulations, but the mixed regime theory must be implemented to adequately represent the actual plasma conditions.

4.5.4 Abstract of "Theory and Simulations of the Electrostatic Potential in Neutral-Beam-Driven Tokamaks and Effects on Impurity Transport"[89]

E. C. Crume, Jr.

The theory of the calculation of the electrostatic potential in tokamaks is reviewed, especially the recent analyses by Stacey and Sigmar, which take anomalous cross-field

momentum transport into account. In neutral-beam-heated tokamaks, impurity ions may reach sonic speeds and, as a consequence, develop poloidal density perturbations on the order of the inverse aspect ratio ϵ, rather than only on the order of the ratio δ of the poloidal gyroradius to the characteristic gradient scale length, as occurs when their speeds are subsonic. These poloidal density variations can influence the cross-field particle fluxes in several ways, some of which depend on the direction of injection with respect to the plasma current. Numerical simulations are presented to illustrate the evolution of the electrostatic potential and impurity transport for plasma conditions representative of ISX-B.

4.5.5 Abstract of "Beam-Induced Current Effects on Stellarator Transform"[90]

J. T. Hogan

Beam-induced currents should be produced in beam-heated stellarators with unidirectional or imperfectly balanced neutral beam injection. We have computed the expected magnitudes of the effects for "currentless" conditions in the Wendelstein VIIA (W-VIIA) and the Heliotron-E. The model employs semiempirical values of D and χ_e [$\sim(nT_e)^{-2/3}$ for Wendelstein VIIA and $\sim(\chi_e^{ALC} + \chi_e^{ripple})$ for Heliotron-E], classical transform evolution, and Monte Carlo beam deposition. The results for Heliotron-E are consistent with calculations using a lumped-parameter model. Significant contributions to local transform are found in both cases. Larger beam pulse lengths will enhance the effect, since high-T_e shielding effects are active on present time scales.

4.5.6 Abstract of "Current Generatioa in Stellarators"[91]

J. T. Hogan, L. Ibanez,* and H. Grad*

The "ideal" stellarator ($\langle \mathbf{J} \cdot \mathbf{B} \rangle = 0$ on each flux surface) requires special pressure and rotational transform profiles, and these profiles are not necessarily consistent with diffusion constraints. We have studied the generation of currents (in initially current-free stellarators) which arise from:

- finite pressure due to external heating;
- the classical "bootstrap" effect, related to toroidal/nonaxisymmetric geometry; or
- direct external current sources (e.g., LH or neutral beam heating).

We have thus extended the analytic results of Pustovitov.

The New York University (NYU) 3-D transport-equilibrium code (3DETC) has been used for these studies, with the following modifications.

- The one-fluid transport model incorporates ripple thermal diffusivity.
- Model profiles have been adopted for external heating (centrally peaked) and for recycling/radiation loss (increasing toward the edge).
- An external current source has been added.

While the transport model is relatively simple (one-fluid, model profiles), it fulfills the requirements of the "method of given pressure" proposed by Shafranov and co-workers, in which the evolution of rotational transform is studied with model assumptions about the

coevolving particle and energy balance. In addition, it provides a self-consistent 3-D geometry. The transform evolution equation is

$$\frac{\partial}{\partial t}\bigg|_{\chi} \nu = \frac{\partial}{\partial_{\chi}} \left\{ \eta_{\parallel} \left[\Delta \left(\frac{\partial \chi}{\partial V} \right)^2 \frac{\partial \nu}{\partial \chi} + A/(\partial \chi / \partial V) - \langle \mathbf{J}^s \cdot \mathbf{B} \rangle \right] \right\} ,$$

where A is a classical version of the bootstrap current, χ is toroidal flux, and $\mathbf{J}^s$ is the external current source.

We find that significant evolution of the rotational transform occurs on the skin time, stimulated by each of the mechanisms mentioned above. Configurations based on the ATF torsatron have been specifically chosen for study.

*New York University, New York.

4.5.7 Abstract of "Rotation and Impurity Flow Reversal in Tokamak Plasmas with Neutral Beam Injection"[92]

W. M. Stacey, Jr., A. W. Bailey,* and D. J. Sigmar

We have extended our previous collisional regime theory for rotation and impurity transport in a tokamak plasma with neutral beam injection and strong rotation ($v_\phi \sim v_{th}$) to the plateau regime, which accommodates the important case of the main ion species being nearly collisionless and the impurity species being collisional—the mixed regime. This extension required a kinetic theory solution for the unaveraged as well as for the averaged parallel viscous force $\mathbf{B} \cdot \nabla \cdot \pi$ with large rotation velocities and the incorporation of this viscous force into the fluid formalism. We allow for anomalous radial, viscous transfer of toroidal momentum, as indicated by experimental data. The theory provides a self-consistent formalism for calculating toroidal and poloidal rotation velocities, the radial particle fluxes, the radial electric field, and the poloidal variation of the impurity density over the flux surface.

The theory has been applied to interpret impurity injection experiments in ISX-B and PLT. We find a good correlation between the predicted impurity fluxes and the experimental observation of enhanced inward impurity fluxes with counter-injection and reduced inward or, for sufficiently large injected power, reversed (outward) impurity fluxes with co-injection.

*Georgia Institute of Technology, Atlanta.

4.5.8 Abstract of *Rotation and Impurity Transport in a Tokamak with Directed Neutral Beam Injection*[93]

W. M. Stacey, Jr., and D. J. Sigmar

We have extended our previous collisional regime theory for rotation and impurity transport in a tokamak plasma with strong, directed neutral beam injection and strong

rotation ($v_\phi \sim v_{th}$) to the plateau regime. We present a kinetic theory derivation of the parallel viscous force in the strong rotation ordering and a self-consistent formalism for calculating ion and impurity rotation velocities and radial transport fluxes, as well as the radial electric field and the poloidal variation of the impurity density, upon which the former strongly depend. Calculations for model problems representative of ISX-B and PLT are presented. The predicted impurity transport exhibits features in agreement with experimental observation.

4.5.9 Abstract of "Long Pulse Evolution of Elongated, Rippled High-Beta Tokamaks"[94]

L. Ibanez,* H. Grad,* A. Bayliss,* and J. T. Hogan

We have studied the long-pulse evolution of high-beta tokamaks with the NYU 3-D transport-equilibrium code (3DETC). The code embodies Grad's alternating dimension algorithm for transport in nonaxisymmetric configurations. The classical one-fluid, anisotropic transport model has been extended by adding models for energy sources (centrally peaked) and recycling/radiation loss (increasing toward the boundary). Ripple-plateau thermal conductivity has been added to the classical thermal loss processes to couple the 3-D and 1-D effects more closely.

Using parameters chosen to model the proposed Alcator-DCT device, we have examined the existence of high-beta (5%), highly elongated (40%), and triangulated (20%) configurations which have been produced by rapid heating. We have studied ripple values typically quoted for Alcator-DCT and configurations having much higher ripple (10%). After strong and rapid heating (reaching $\beta = 4\%$ with $\tau_{heating} << \tau_{skin}$), we find the expected flux-conserving tokamak (FCT) phase, but with accelerated flux diffusion at the edge from the ripple diffusivity. Following the FCT phase, the q profile relaxes by resistive diffusion with steadily decreasing shear. After a core skin time, only a 20 to 30% variation of q from the core to the edge remains. There is also some shrinkage of the highly elongated configurations.

Using the diagnostic island solver reported earlier, we have also searched for the effects of the interaction of large-scale islands ($m = 2$) with the high ripple region near the plasma edge.

---

*New York University, New York.

4.6 ALPHA PARTICLE PHYSICS

The alpha particle physics effort, which started with multi-energy-group modeling of alpha energy relaxation and spatial diffusion, has now expanded to include not only Fokker-Planck equation extensions of the previous effort, but also investigations of both kinetic MHD and purely kinetic alpha particle instabilities and theoretical support for important alpha diagnostics.

A Fokker-Planck equation for the alpha particle distribution function, $f_\alpha(E,r,t)$, was solved to examine the consequences of anomalous cross-field alpha diffusion and

anomalous energy relaxation. Such effects influence the attainable burn parameters in the nT (Lawson) diagram. It was shown that $D_\alpha \geqslant 10^5$ cm^2/s will prevent ignition in a device of INTOR dimensions.

The effects of the alpha particles that are created when tritium pellets are injected into neutral-beam-heated deuterium plasmas in TFTR were also studied using combined Fokker-Planck and transport modeling.

A gyrokinetic description of hot species effects on high-n ballooning modes has been developed. It is valid for mode frequencies of the same order as the hot species drift frequency and has been applied in the deeply trapped limit to alpha populations in tokamaks. Detailed numerical solutions have been carried out for TFTR parameters near breakeven. The results indicate that if the alphas are sufficiently well confined to form a slowing-down distribution of mean energy within 100 times the background temperature, then resonant interaction with the alpha precessional drift occurs, degrading ballooning stability boundaries and closing off access to the second stability regime.

Since the alpha velocity at 3.5 MeV approaches the electron thermal velocity, coherent Thomson scattering by the Debye shielding cloud surrounding the alphas becomes measurable. Using numerical techniques, calculations were started of the scattering function $S(\kappa,\omega)$ for light scattering from alpha particles, including the effect of the magnetic field and the sensitivity of the scattered signal on the orientation with respect to $\mathbf{B}$. The approach continues to look promising for application to fusing plasmas.

4.6.1 Abstract of "Effects of Trapped Alpha Particles on Ballooning Modes"[95]

D. A. Spong, D. J. Sigmar, K. T. Tsang,* W. A. Cooper, and D. E. Hastings

Using the gyrokinetic formalism of Catto et al., we solve the coupled integrodifferential equations of the kinetic ballooning mode problem in a tokamak reactor plasma, including the frequency regime of the toroidal precession drift resonance. Two types of approximations have been considered to simplify these equations. First, model hot species distribution functions which result in tractable velocity space integrals have been used, leading to a single integrodifferential equation along a field line. Second, approximations which reduce the configuration space dependence of the hot species, but still retain the resonant nature of the velocity integrals, can be shown to lead to a single, inhomogeneous, ODE eigenmode equation. Both analytic and numerical solution techniques will be employed in solving these equations for the case of a slowing-down alpha distribution in a tokamak reactor.

*Science Applications International Corp., Boulder, Colo.

4.6.2 Abstract of "Effects of α-Particles on CO_2 Laser Scattering From a Fusion Plasma"[96]

L. Vahala,* G. Vahala,* and D. J. Sigmar

Since it is crucial to understand the spatial, velocity space, and temporal effects of alpha particles on the bulk plasma, we investigate the possibility of using CO_2 laser scattering from a fusion plasma to determine the alpha particle distribution function. The scattered power is dependent on the scattering function $S_{\kappa,\omega}$. S is dominated by the fluctuating electron density which, for coherent scattering, is calculated by the Rostoker test particle picture. The kinetic shear Alfvén wave is destabilized by the alpha particles. A resonance in the associated dispersion relation will lead to a large contribution to the scattered signal, increasing significantly the intrinsically small signal-to-noise ratio. We investigate the scattering cross section and the parameter regimes in which the alpha particle contribution to the Alfvén fluctuation is detectable.

*College of William and Mary, Williamsburg, Va.

4.7 EXPERIMENT INTERPRETATION

Preparations for ATF data interpretation and modeling have begun. Three levels of sophistication will be employed. At the most basic level, measurements of plasma temperature, density, and magnetic fields will be used to provide simple estimates of gross energy confinement time and plasma beta. This level of interpretation requires an equilibrium model for the plasma shape and position, so that point or line measurements may be converted to volume-integrated quantities. To this end, the 3-D inverse equilibrium solver has been refined and improved to the point that it is now a reliable computational tool. An efficient linear ray tracing and integrating subroutine has been developed to be used with it for calculating signals from diagnostics that make chordal measurements, such as the line-averaged density interferometer and soft x-ray detector arrays. A study has been done to determine the accuracy of measurement of the equilibrium using a line-of-sight diagnostic (such as a laser) as a function of the orientation of the viewing chord. Also, a preliminary study has been made of the accuracy of determining the magnetic beta and plasma currents from external magnetic loop signals as a function of loop placement. At the next level of interpretation, radial flows of heat, particles, current density, and toroidal momentum will be studied. At the most sophisticated level of interpretation, theoretical models for plasma transport will be used to attempt prediction of measured plasma parameters. At this level, the effect of a radial potential on plasma confinement and net toroidal currents driven by neutral beam heating may be studied.

In the past year, work on tokamak experiment interpretation has been carried out in collaboration with the ISX-B experimental group and in association with the teams working with DIII [GA Technologies, Inc. (GA) and Japan Atomic Energy Research Institute (JAERI)], the Poloidal Beam Experiment (PBX), and TFTR. The Z-mode confinement improvement on ISX-B with profile modifications has been shown to be consistent with predictions of the Carreras-Diamond resistive ballooning theory when diamagnetic drift

stabilization effects are included. In addition, Monte Carlo modeling of the depth of neon penetration in ISX-B Z-mode discharges has shown that the density profile modifications of the magnitude required for diamagnetic drift stabilization are consistent with the probable density and mean energy of limiter-reflected neon. It has also been found that cross-field particle diffusivities in the scrapeoff region correlate with measured edge density, temperature, and potential fluctuation levels in ISX-B.

The pellet ablation models discussed in Sect. 4.5 were used to interpret data from ISX-B, DIII, and PBX. Although the magnitude of the apparent pellet mass loss in the scrapeoff regions of ISX-B and PBX could be explained using the qualitative edge model, there was not enough experimental information on fast-ion populations in the edge region to yield detailed confirmation of the model. The models for pellet ablation during intense beam heating were used in a detailed analysis of DIII results for beam powers up to 4.5 MW. This analysis showed the importance of the fast-ion flux in determining the depth of penetration, and the observed depth has been bracketed. Enhanced ablation in the scrapeoff region was not observed, which is in agreement with the qualitative edge model.

The 2-D version of the Oak Ridge Moments Equilibrium Code (ORMEC) has been integrated with the PPPL TRANSP analysis code in a joint ORNL/PPPL project. The coupled codes have been used to model TFTR compression experiments and to analyze PBX data. ORMEC is particularly well suited to treating the many moment amplitudes required to describe the complex bean-shaped PBX plasma.

The Stacey-Sigmar theory for impurity transport in plasmas with intense beam heating (see Sect. 4.5) has been used in simulations of ISX-B and PLT plasma experiments to see whether the differences in observed impurity behavior between co- and counter-injection are explained by it. When observed ISX-B toroidal rotation velocities are used in the time-dependent IMPTAR simulations, qualitative agreement is found for a reasonable choice of the empirical anomalous cross-field momentum diffusion coefficient. However, for conclusive comparisons using IMPTAR, a more complete description of that anomalous diffusion is needed. The Georgia Tech group headed by Stacey, on the other hand, finds more conclusive agreement with ISX-B and PLT data from their simulations.

Considerable progress in understanding the various aspects of EBT operation was made in the past year. The insights gained from heating calculations, which spanned this and the previous year, were supplemented with a 2-D, multiple-fluid theory based on insights gained from experiment. This theory has been carried to the point that the asymmetry in the electrostatic potential can be calculated analytically. The analytic formulas are in reasonable agreement with experimental observations from EBT-I/S and predict a reduction of several orders of magnitude in the asymmetry for EBS. Further Monte Carlo calculations have substantiated the previous preliminary estimate of a degradation of one to two orders of magnitude in the lifetime due to the asymmetry in the electrostatic potential in EBT. The 2-D, multiple-fluid theory, which combines elements of equilibrium, transport, and heating, is of general interest for other magnetic configurations, especially in high-temperature, low-collisionality regimes of operation.

4.7.1 Tokamak Interpretation—Abstracts

4.7.1.1 "Equilibrium Modeling of ISX-B Tokamak Discharges"[97]

L. A. Charlton, R. M. Wieland,* and G. H. Neilson†

Poloidal magnetic measurements of the multipole moments of the toroidal current density and of the external multipole fields provide information on the current profile in ISX-B. This can be used to prescribe a form for the current profile which produces an equilibrium consistent with profile measurements, magnetic data, and the $q = 1$ surface. This procedure has been applied satisfactorily in a number of cases, several of which are presented here.

---

*Formerly with Computing and Telecommunications Division, Martin Marietta Energy Systems, Inc. Present address: Princeton Plasma Physics Laboratory, Princeton, N.J.
†Toroidal Confinement Physics Section.

4.7.1.2 "Simulation of Impurity Transport in the ISX-B Tokamak with Directed Neutral Beam Heating"[98]

E. C. Crume, Jr., and D. E. Arnurius

Experiments on beam-heated ISX-B and PLT plasmas indicate that counter-injection leads to enhanced accumulation of impurities and co-injection leads to reduced accumulation of impurities, relative to ohmically heated plasmas. Stacey and Sigmar have recently included the effects of the strong toroidal rotation induced by directed neutral beam heating in a self-consistent theory for particle flows within the flux surfaces, the radial electric field, and the radial particle transport in a tokamak plasma with directed neutral beam injection both in the collisional regime and in a mixed regime in which the main plasma ions are in the plateau regime while the impurities remain in the collisional regime.

We have implemented the collisional regime theory in our basic impurity transport simulation code, IMPTAR, and present here simulation results for both co-injected and counter-injected plasmas. These results are qualitatively similar to results reported previously for simulations in which the rotation effects and all other momentum exchange effects were treated separately. That is, for plasmas with ion density and temperature gradients comparable to those observed in ISX-B: (1) enhanced impurity accumulation is observed in simulations of counter-injected plasmas and (2) impurities are initially driven out of the plasma during co-injection, but after large rotation speeds are reached, there is a tendency for the impurities to be driven back into the plasma. Although some attempt was made to account for the low collisionality of the plasma ions in these simulations, implementation of the mixed regime theory is required to adequately represent the actual plasma conditions.

4.7.1.3 "Anomalous Pellet Ablation in ISX-B Discharges"[99]

H. C. Howe, D. Schuresko,* and W. A. Houlberg

Relatively large hydrogen pellets (radius = 0.8 mm) have been injected into beam-heated ISX-B discharges (P_{inj} = 1.7 MW). The observed plasma density increase due to the pellet ($\Delta\bar{n}_e = 5 \times 10^{13}$) was approximately 50% of the increase ($\Delta\bar{n}_e = 10^{14}$) predicted by the Milora-Foster pellet ablation model, including fast-ion ablation. The observed and predicted penetration depths agreed. To obtain agreement between the observed and predicted $\Delta\bar{n}_e$ while retaining the penetration depth agreement, it is necessary to assume that (1) only 50% of the pellet mass is deposited in the plasma and (2) fast ions do not ablate the pellet in the main plasma. The corresponding hypotheses for these two effects are (1) anomalously large pellet ablation outside the main plasma, perhaps due to fast ions on outwardly shifted drift orbits, and (2) complete attenuation of the fast ions in the main plasma by the small ionized fraction of the pellet-cloud density.

*Plasma Technology Section.

4.7.1.4 "Toroidal Flow Analysis of ISX-B Density and Temperature Profiles"[100]

R. M. Wieland,* E. A. Lazarus,† M. Murakami,† J. D. Bell,‡ W. A. Cooper,
S. P. Hirshman, and G. H. Neilson**

Near-tangential injection of up to 2 MW of neutral beam power into ISX-B plasmas results in toroidal flows measured spectroscopically to be $\sim 10^7$ cm/s. Using simple force balance arguments in a shape analysis of some Thomson scattering temperature (T_e) and density (n_e) profiles, we attribute the relative asymmetry of n_e with respect to the flux surface defined by T_e to centrifugal effects alone and extract an "effective" flow velocity profile for the bulk plasma. The ZORNOC confinement analysis code has been modified to explicitly include this flow in the MHD part of its operation, and the resulting calculations for the plasma shift, diamagnetism, and Shafranov Λ show good agreement with those same parameters determined from magnetic measurements.

*Formerly with Computing and Telecommunications Division, Martin Marietta Energy Systems, Inc. Present address: Princeton Plasma Physics Laboratory, Princeton, N.J.

†Toroidal Confinement Physics Section.

‡Computing and Telecommunications Division, Martin Marietta Energy Systems, Inc.

**Confinement Projects Section.

4.7.1.5 "Particle Confinement in ISX-B"[101]

K. E. Yokoyama,* H. C. Howe, D. P. Hutchinson,† R. C. Isler,‡ E. A. Lazarus,‡
C. H. Ma,† M. Murakami,‡ G. H. Neilson,** and A. J. Wootton†

Particle confinement in both ohmically heated and beam-heated tokamaks is studied. Global confinement is measured from known sources and densities. Recycling is monitored using D_α detectors around the machine. Langmuir probes are used in the scrapeoff layer to obtain density and temperature gradients both across and along the field lines, from which the perpendicular diffusion coefficient and particle confinement times are estimated. Results show increased edge diffusion following beam injection in the co-injected direction. If balanced injection or counter-injection is used, the diffusion coefficient is decreased. Outward radial displacements of the plasma column also decrease the diffusion coefficient. The different scrapeoff layer parameters produced are compared with the predictions of a 1-D transport code in which simple loss terms are included with various boundary conditions to simulate parallel flow to limiters.

---

*Formerly with Toroidal Confinement Physics Section. Present address: TRW, Inc., Redondo Beach, Calif.
†Physics Division.
‡Toroidal Confinement Physics Section.
**Confinement Projects Section.

4.7.1.6 "Neutral Beam Driven Impurity Flow Reversal in PLT and ISX-B"[102]

A. W. Bailey,* W. M. Stacey, Jr., and D. J. Sigmar

The Stacey-Sigmar formalism, extended to include time-dependent effects, is used to model experimentally observed impurity transport in PLT and ISX-B. Comparison is made with the PLT impurity fluxes determined by Eames from chordal radiation measurements. Experimental observations by Suckewer et al. are also modeled. The line radiation observed in ISX-B as a function of time from specific impurity lines is compared with the predicted line radiation.

---

*Georgia Institute of Technology, Atlanta.

4.7.1.7 "Limiting β Investigations at Low Collisionality"[103]

D. C. Robinson,* N. R. Ainsworth,* M. W. Alcock,* D. Atkinson,* P. R. Collins,*
A. N. Dellis,* T. Edlington,* A. Ferreira,† Q. Gao,‡ T. C. Hender, Z. Ma,‡
A. W. Morris,** M. O'Brien,* B. Parham,* A. C. Rivière,* D. F. H. Start,*
S. Takamura,†† and T. N. Todd*

Electron cyclotron heating has been employed at high power densities on TOSCA ($R/a \geqslant 3.5$, $R = 0.3$ m) and CLEO ($R/a = 7$, $R = 0.9$ m) to investigate the limiting beta value in tokamaks of differing aspect ratio. The influences of both q and a toroidal helical field were studied. The studies have been principally conducted at the second harmonic at

28 GHz and 60 GHz and with power levels of up to 200 kW. During the heating on both devices, the ratio of absorbed rf power to ohmic heating power can be >10, the electron temperature above 3 keV, and the collisionality such that $\nu_e^* \leq 0.01$. As the power is increased, beta saturates, indicating a decrease in confinement which is accompanied by an increase in the magnetic fluctuation level. Average beta values of 0.2% have been achieved in an $\ell = 3$ helical configuration in CLEO. Profile modification experiments show the suppression or enhancement of sawtooth activity and produce $m = 2$ activity which may lead to a disruption.

---

*UKAEA, Culham Laboratory, Abingdon, Oxfordshire, England.
†Comissão Nacional de Energie Nuclear, Brazil.
‡People's Republic of China.
**Balliol College, Oxford University.
††Nagoya University, Nagoya, Japan.

4.7.2 EBT Interpretation—Abstracts

4.7.2.1 "Core Plasma Heating in EBT-S and the Effect of Strongly Damped Cyclotron Waves"[104]

D. B. Batchelor

A much more satisfactory understanding of the core plasma in EBT-S has been obtained from recent improvements in diagnostics (Thomson scattering and heavy-ion potential probe, as well as interferometry and soft X-rays at the mirror throat) and from theoretical insights into the unique features of ECH in mirror geometry. The experiments indicate the presence of a cold, isotropic bulk component which is collisionally heated by an energetic (~0.5-keV), anisotropic, locally produced tail. This resolves a long-standing discrepancy between electron temperature measurements obtained from Thomson scattering vs soft X rays. The theory shows that the microwaves are very heavily damped before reaching the resonance layer and that, due to the Doppler effect, there is very strong coupling among the spatial structure of the wave fields, the velocity space structure of the distribution function, and the particle and energy confinement. The result is that wave power is most strongly absorbed by energetic passing or transitional particles whose confinement is poor. We will review the experimental data, describe the theory in simple physical terms, and present detailed Fokker-Planck modeling of the distribution function. We will also indicate how the net heating efficiency is expected to improve in the EBS and how similar effects are to be expected in other devices.

4.7.2.2 "Comparison of Electron Cyclotron Heating Theory and Experiment in EBT"[105]

D. B. Batchelor, the EBT Experimental Group, and the EBT Theory Group

The first objective of the program of ECH studies on EBT was to understand the gross features of microwave power flow and power deposition in each of the plasma components. This was accomplished by using ray tracing and by developing a zero-dimensional (0-D) wave-energy balance model that takes into account the many passes through the plasma

and essentially random reflections which a typical ray makes before being absorbed. We also present results of experiments that have been performed with microwave calorimeters, which are in good agreement with the power flow calculations for a wide variety of operating conditions.

Recent experiments have shown that the core plasma confinement is considerably more complicated than was previously indicated by the midplane soft X-ray measurements. Thomson scattering measurements indicate that the bulk of the core density (50 to 90%) is composed of a collisional isotropic core component with T_e = 70–120 eV. Also, other recent experiments (mirror throat soft X-ray, throat-launched microwave power, and power feed turnoff experiments) demonstrate that the T_e = 200–1200 eV component seen by the midplane soft X-ray diagnostic is in fact a collisionless, anisotropic hot tail.

A theoretical interpretation of these results is presented based on the close coupling between the spatial structure of wave fields and the velocity space structure of the distribution function.

4.7.2.3 "Coupled Transport and Heating in EBT and EBS"[186]

C. L. Hedrick, D. B. Batchelor, G. L. Chen, R. C. Goldfinger, D. E. Hastings,
E. F. Jaeger, D. K. Lee, L. W. Owen, D. A. Spong, J. S. Tolliver, N. Krall,*
S. Hamasaki,* and J. Sperling*

In EBT and EBT-like devices, hot electron rings form at the edge of the cooler background of a core plasma. As early as 1975 it was recognized that microwave heating, which plays such a significant role in electron dynamics, should be incorporated into transport models. Recent theoretical microwave heating and transport studies suggest that this may be necessary to describe existing experimental EBT devices. In particular, descriptions of the electron distribution as a sum of only two distributions (i.e., one for the core and one for the rings) seem inadequate to understand either the heating or the losses in any depth. Here we discuss the interplay of heating and transport from a kinetic standpoint and point out some of the possible phenomena associated with the microwave heating at the fundamental and second harmonic of the electron cyclotron frequency.

When considering microwave heating at the fundamental, it is important to include Doppler shifts ($\omega_\mu = \omega_{ce} - kv_\parallel$). When these Doppler shifts are taken into account in heat deposition calculations, it is found that virtually all the microwave energy can be absorbed by Doppler-shifted particles before the wave reaches the spatial point where B is such that $\omega_\mu = \omega_{ce}$. Thus the microwave field is highly nonuniform; omitting such nonuniformity can lead to gross overestimates of the power absorbed by a plasma.

In an EBT, this power is absorbed within 1 to 2 cm of the $\omega_\mu = \omega_{ce}$ surface on the high-field side. The onset of power absorption as a function of particle energy occurs first for passing particles since they have the largest Doppler shift ($kv_\parallel$). Since ECH produces perpendicular heating, this has the consequence that particles are scattered through and into regions of velocity with poorly centered drift orbits (transitional particles). This is an inefficient way to couple power to the plasma.

Because the scattering due to microwaves can be so large, it is necessary to distinguish at least three types of loss processes. The first two are resonant and nonresonant diffusive losses associated with scattering by both Coulomb collision (neoclassical) and microwaves

("microclassical"). The third process is direct losses due to scattering onto unconfined drift orbits—which has formal aspects similar to a mirror loss cone. The relative importance of these processes varies with conditions and is the subject of current research. It is interesting to note that they all are reduced by improved orbits such as would occur in the EBS (see Fig. 4.8). Because the drift orbits in the EBS are much better centered, and because the transitional region is much narrower in pitch angle and occurs at larger $v_{\parallel}/v$ than in EBT-S, all three processes are reduced in EBS.

Fokker-Planck calculations of the distribution functions in the presence of second-harmonic heating as a function of radius and energy have indicated that a population intermediate in energy to that of the core and ring plasmas will form. This population becomes increasingly localized in radius near the position of the second-harmonic resonance as energy is increased. Here we discuss the orbit, heating, and loss ideas which lead to the conclusion that this population could be controlling the ambipolar potential in present EBT devices. It is noteworthy that this population is predicted to be asymmetric because of high-energy particle orbit asymmetries. For devices such as the EBS, the high-energy orbits are much more symmetric and would lead to more symmetric ambipolar potentials. This in turn would lead to greatly reduced losses associated with the low-energy particles, which are strongly influenced by the ambipolar potential through $\mathbf{E} \times \mathbf{B}$ drifts.

Since part of the motivation for considering a bumpy square as an alternate to a bumpy torus comes from the simultaneous evidence in EBT-S of a substantial population

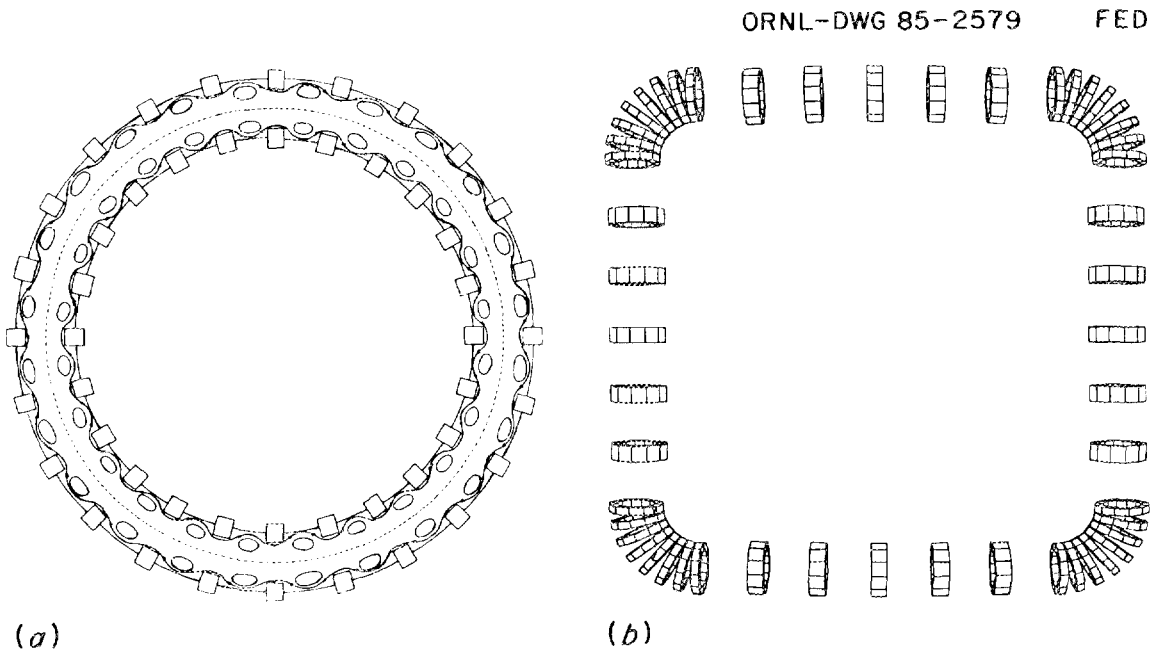

Fig. 4.8. Comparison of (a) the standard EBT and (b) the EBS configurations. The toroidal effects on particle drifts in the EBS are greatly reduced by increasing the ratio of the "corner" magnetic field to the bumpy field of the sides.

of hot electrons ($T \sim 2$–$3T_{bulk}$) and of a substantial energy loss channel [$\tau \sim 0.1$–0.3τ(neoclassical)], we have analyzed the formation and properties of energetic electron distributions, taking into account the radial structure of both heating geometry and particle drift surfaces.

The calculation is based on taking moments of spatially segregated, Fokker-Planck equations describing appropriate heating and loss processes. Results include the spatial structure, density, electron distribution, equivalent temperature, and anisotropy of the hot component and an estimate of the energy flow out of EBT due to this component (direct loss).

For the hot component, density accumulates by microwave pumping of cooler particles into the tail and is lost by scattering into the loss cone ($v_\perp \rightarrow v_\parallel$). Only a narrow slice of velocity space is populated by the hot component, because at $v_\perp < v_\parallel$ particles are lost rapidly, while for $v_\perp > 1.6v_\parallel$ their orbits no longer encounter the first-harmonic resonant heating surfaces and stop their runaway behavior. We calculate T_{tail} and find it consistent with soft X-ray temperature diagnostics. We calculate the density of this warm tail; again, the results are consistent. The energy loss is of order 50% through this channel.

*JAYCOR, San Diego.

4.7.2.4 "Magnetic Well Depth in EBT and Sensitivity to Hot Electron Ring Geometry"[107]

E. F. Jaeger, L. A. Berry,* C. L. Hedrick, and R. K. Richards†

We examine the possibility that diamagnetic currents in the hot electron rings in the EBT plasma are strong enough to reverse gradients in $\oint d\ell/B$, thereby providing gross MHD stability. Using a 2-D solution to the Grad-Shafranov equation with tensor pressure, we compute the electromotive force induced in a diamagnetic loop surrounding the EBT plasma. This allows direct comparison between calculated and measured diamagnetic loop signals for different values of perpendicular energy stored in the electron rings. Signals required for a local minimum in B and maximum in $\oint d\ell/B$ are found to be sensitive functions of ring width for which there is presently no direct measurement. However, theoretical arguments provide estimates for the hot electron gyrodiameter ($\sim$1.0 cm for 400 keV) and for the dispersion in guiding center drift orbits (<1 cm for the measured ring length of 10 cm). Thus, a ring with a width of 2 cm or 2 gyrodiameters (full-width at half-maximum) and length of 10 cm requires a diamagnetic loop signal of 443 mV ($W_\perp \sim 49$ J and $\beta_{\perp,max} \sim 0.45$) for a local maximum in $\oint d\ell/B$. To illustrate the sensitivity of this result to ring width, we note that a ring with a width of 1 gyrodiameter and length of 10 cm requires 193 mV ($W_\perp \sim 22.3$ J and $\beta_{\perp,max} \sim 0.35$), whereas a ring with a width of 0.75 gyrodiameter and length 10 cm requires only about 100 mV ($W_\perp \sim 10$ J and $\beta_{\perp,max} \sim 0.30$).

*Associate division director.
†Toroidal Confinement Physics Section.

4.7.2.5 "Finite $k_{\parallel}$ High Frequency Fluctuations in EBT"[108]

A. M. El Nadi,* J. C. Whitson, and S. Hiroe†

It is well known that the interaction of the hot electron precession in EBT with the high-frequency surface wave leads to a flute instability when the ratio of the hot electron density to the background ion density exceeds a certain threshold. This mechanism seems to explain the compressional instability observed at the T-M transition. By allowing for a finite component of the wave vector parallel to the magnetic field lines, we find that the above coupling occurs for any finite hot electron density and should then lead to an unstable spectrum characterized by the presence of poloidal and radial magnetic components. Recent measurements in EBT have verified that such a spectrum is actually present.

*Giza University, Cairo, Egypt.
†Toroidal Confinement Physics Section.

4.8 COMPUTING SUPPORT

J. W. Wooten

The computing support group provides the division with computing resources in two areas: operation of the User Service Center (USC) and development of the experimental data acquisition network. The USC provides (1) access to the large computing systems at the National Magnetic Fusion Energy Computing Center (NMFECC) at the Lawrence Livermore National Laboratory (LLNL) and (2) immediate analysis and storage of experimental data. The data-handling network supports the division's experimental efforts by providing a rapid, state-of-the-art means of acquiring and storing experimental data.

4.8.1 USC Operations

H. E. Ketterer, D. N. Clark, J. V. Hughes, and G. B. Wootton

The system's primary swapping area was moved from an RP04 drive to an RP07, resulting in improved performance. In addition, better separation was achieved between the system areas and the user areas by rearranging disk assignments. This resulted in better throughput and, along with some scheduler parameter refinements, improved user response time appreciably.

A QMS 1200 laser printer was obtained from TALARIS along with software for T_EX. The QMS printer is currently driven by a VAX 780 using a serial interface that will be replaced by a parallel interface during 1985.

The local graphics user service stations (GUSSes) have been upgraded to GUSS+'s. This provides more capabilities and speed for our users.

An Ethernet link has been installed that connects all VAXes. In addition, a DECnet link has been tested as a replacement for the FEDnet link with the Computing and Telecommunications Division (C&TD) systems at ORNL.

A network access point (NAP) has been installed for the ATF VAX. It is being used for testing network access from a local VAX.

4.8.2 Experimental Support

The Experimental Support group provides service to the experimental groups within the division, both individually and collectively. This section summarizes the activities of the support group during 1984. Other significant activities are reported within the chapters for the individual experimental groups.

Two important projects during 1984 improved communications among the divison VAXes. The first was the installation of Ethernet as the hardware basis for DECnet, the network by which the VAXes communicate with each other. (DECnet is also used between the VAXes and PDP-10 system, but different hardware is used.) Ethernet improves the reliability and availability of the network by allowing any VAX to communicate directly with any other VAX, independently of the state of other VAXes on the network. Ethernet also reduces the CPU load for communications.

The second project was the installation of an HSC-50 (cluster disk controller) and 2.5 gigabytes of disk storage. The HSC-50 and disks form the basis for a disk farm that will be shared by the three VAX 11/780s in the division (and any future large VAXes that may be obtained). When VMS version 4 is installed on the VAXes in 1985, those systems will share equal access to all disks, allowing users to have access to all of their files, regardless of which VAX they are using.

Another network-related project was the connection of VX1 to the NMFECC network using the MFE node name ATF. This provides a parallel path from Oak Ridge to the MFE network and provides better access to the FED VAX systems for Oak Ridge personnel who are temporarily assigned to PPPL.

A third hardware project was the installation of a QMS model 1200 laser printer on VX2. This printer should provide high-quality integrated text and graphics output.

4.8.2.1 Support of experiments

D. E. Greenwood, J. D. Bell,* E. T. Blair, K. L. Kannan, B. G. Peterson,* K. A. Stewart, and W. R. Wing†

New development was kept to a minimum since 1984 was the last year for ISX operation. However, several ongoing projects were completed. The most important was the replacement of the PDP-11–based data acquisition system with a VAX-based system. This conversion was made suddenly, in a few hours, when the PDP-11 system failed and neither Y-12 nor Digital Equipment Corporation (DEC) field service was able to repair the problem.

The largest conversion project was a rewrite of the operations system display code from PDP-11 FORTRAN to VAX PASCAL. This was done because the elaborate data structures necessary to support the display were more easily implemented in PASCAL. Also essential to the conversion was the installation of on-line data compression to reduce the

time required to transmit data from the VAX to the PDP-10. The result was a more reliable system that permitted faster access to acquired data (since it was possible to view and analyze data on the VAX rather than waiting for data to reach the PDP-10).

*Computing and Telecommunications Division, Martin Marietta Energy Systems, Inc.
†Toroidal Confinement Physics Section.

4.8.2.2 Repeating pellet injector stand-alone control system

R. D. Burris, L. R. Baylor,* D. E. Greenwood, and K. A. Stewart

A stand-alone control system, using an Allen-Bradley programmable logic controller (PLC) and a DEC VAX-11/730, was developed for the ORNL pneumatic pellet injectors. The system includes a color mimic panel for status display, a VT100 menu display for command and setpoint entry, and the PLC for the actual control of the device. Transient waveform digitization of several traces, with graphic display of the inputs, is performed on a second VT100.

This project was somewhat more than half complete at the end of 1984, with completion scheduled for February 15, 1985. The first device to use the injector is to be TFTR, with first pellet injection to occur before March 18, 1985.

*Engineering Division, Martin Marietta Energy Systems, Inc.

4.8.2.3 Large Coil Program data acquisition system

E. T. Blair, L. R. Baylor,* and D. E. Greenwood

It was decided to replace a portion of the existing DEC PDP-11/60–based data acquisition system with a VAX-based system using VX1. This decison was made because the 11/60 system lacks the computer power, memory resources, and on-line disk storage to adequately support a full coil test. The new system will use CAMAC hardware to interface to existing LSI-11/23 front-end data acquisition processors. The data and supporting data bases will be stored on an RA81 disk drive that is part of the VAX disk farm. Results of the experiment will be available to users in both printed and graphic form using terminals and a Versatec printer/plotter located in Bldg. 9204-1. The target time for the completed system is the third quarter of CY85.

The following steps were completed in 1984:

- A system design and interface document was prepared to describe the major software and hardware components of the VAX-based data system.
- All CAMAC support hardware, including a pair of 1-km fiberoptic cables, was purchased and tested.
- The data bases were extensively reworked and made accessible through Datatrieve (a DEC data management product), thus providing very sophisticated report generation capabilities. The data base utilities were rewritten to be more user-friendly.

- VERSAPLOT graphics software was installed on the VAX, and supporting library routines developed, to permit generation of graphic output using existing display routines.
- The existing data were moved to the VAX.

4.8.2.4 RFTF experiment support

J. B. Mankin

The Radio-Frequency Test Facility (RFTF) project will use an Allen-Bradley PLC-3 and associated communication equipment to monitor the device. A U.S. Data color graphics terminal will serve as the monitor display and as a touchscreen for input of system commands. Programs were developed to support the magnet pumping page and the magnet system status page.

REFERENCES

1. B. A. Carreras, J. L. Cantrell, L. A. Charlton, W. A. Cooper, L. Garcia, J. H. Harris, T. C. Hender, H. R. Hicks, J. A. Holmes, J. A. Rome, and V. E. Lynch, "MHD Equilibrium and Stability for Stellarator/Torsatron Configurations," in *Proceedings of the 10th International Conference on Plasma Physics and Controlled Nuclear Fusion Research (London 1984)*, Int. Atomic Energy Agency, Vienna, in press.

2. B. A. Carreras, J. L. Cantrell, L. A. Charlton, L. Garcia, J. H. Harris, T. C. Hender, H. R. Hicks, J. A. Holmes, and V. E. Lynch, "MHD Equilibrium and Stability for Stellarator Configurations," p. 317 in *5th International Workshop on Stellarators: IAEA Technical Committee Meeting on Plasma Confinement and Heating in Stellarators, September 24–28, 1984*, ed. F. Rau and G. G. Leotta, vol. I, EUR 9618 EN, Commission of the European Communities, Brussels, 1984.

3. B. A. Carreras, H. R. Hicks, J. A. Holmes, V. E. Lynch, and G. H. Neilson, "Zero-Current, High Beta Stellarator Equilibria with Rotational Transform Profile Control," *Nucl. Fusion* **24**, 1347 (1984); also published as ORNL/TM-9182, Oak Ridge Natl. Lab., 1984.

4. W. A. Cooper, "Generic Ballooning in Anisotropic Pressure Toroids," *Phys. Fluids* **28**, 754–6 (1985).

5. W. A. Cooper and M. C. Depassier, "Helically Symmetric Magnetohydrodynamic Plasma Equilibrium," pp. 82–85 in *Actas Cuarto Simposio Chileno de Fisica (Proceedings, Fourth Chilean Symposium of Physics)*, Universidad de Chile, Santiago, 1984.

6. L. Garcia, B. A. Carreras, L. A. Charlton, H. R. Hicks, and J. A. Holmes, "Stability Calculations for High-Beta Torsatrons," *Bull. Am. Phys. Soc.* **29**, 1272 (1984).

7. T. C. Hender, "Equilibrium Studies for Helical Axis Stellarators," invited talk, *Bull. Am. Phys. Soc.* **29**, 1287 (1984); see also T. C. Hender, J. L. Cantrell, B. A. Carreras, L. Garcia, J. H. Harris, H. R. Hicks, V. E. Lynch, and J. A. Rome, "Helical Axis Stellarator Equilibria," *Bull. Am. Phys. Soc.* **29**, 1373 (1984).

8. T. C. Hender, J. Cantrell, B. A. Carreras, J. H. Harris, and J. A. Rome, "Equilibrium Studies for Helical Axis Stellarators," presented at the Annual Conference on Theoretical Aspects of Controlled Nuclear Fusion (Sherwood Meeting 1984), Incline Village, Nev., Apr. 11–13, 1984.

9. T. C. Hender and B. A. Carreras, "Equilibrium Calculations for Helical Axis Stellarators," *Phys. Fluids* **27**, 2101 (1984); also published as ORNL/TM-9147, Oak Ridge Natl. Lab., April 1984.

10. T. C. Hender, B. A. Carreras, L. Garcia, J. H. Harris, J. A. Rome, J. L. Cantrell, and V. E. Lynch, "Equilibrium Studies in Helical Axis Stellarators," p. 21 in *Proceedings of the U.S.–Japan Workshop on 3-D MHD Studies*, ed. B. A. Carreras, CONF-840370, Oak Ridge Natl. Lab., 1984.

11. T. C. Hender, B. A. Carreras, L. Garcia, J. A. Rome, and V. E. Lynch, "The Calculation of Stellarator Equilibria in Vacuum Flux Surface Coordinates," *J. Comput. Phys.*, accepted for publication (1985).

12. S. P. Hirshman and J. T. Hogan, "Comparison of 3-D Moments and Finite Difference Inverse MHD Equilibrium Codes," presented at the Annual Conference on Theoretical Aspects of Controlled Nuclear Fusion (Sherwood Meeting 1984), Incline Village, Nev., Apr. 11–13, 1984.

13. S. P. Hirshman and H. K. Meier, "Optimized Fourier Representations for Three-Dimensional Magnetic Surfaces," *Phys. Fluids*, accepted for publication (1985); also published as ORNL/TM-9300, Oak Ridge Natl. Lab., 1984.

14. S. P. Hirshman and H. Weitzner, "A Convergent Spectral Representation for Three-Dimensional Inverse MHD Equilibria," *Phys. Fluids* **28**, 1207–9 (1985); also published as ORNL/TM-9302, Oak Ridge Natl. Lab., 1984.

15. J. T. Hogan and S. P. Hirshman, "Comparison of 3D MHD Inverse Coordinates Codes," *Bull. Am. Phys. Soc.* **29**, 1410 (1984).

16. J. A. Holmes, B. A. Carreras, L. A. Charlton, H. R. Hicks, and V. E. Lynch, "Free Boundary Stellarator Expansion MHD Equilibrium and Stability Calculations," presented at the Annual Conference on Theoretical Aspects of Controlled Nuclear Fusion (Sherwood Meeting 1984), Incline Village, Nev., Apr. 11–13, 1984.

17. J. A. Holmes, B. A. Carreras, L. A. Charlton, H. R. Hicks, and V. E. Lynch, "Stellarator Expansion Studies of a High Beta Torsatron," pp. 42–67 in *Proceedings of the U.S.–Japan Workshop on 3-D MHD Studies*, ed. B. A. Carreras, CONF-840370, Oak Ridge Natl. Lab., 1984.

18. J. A. Holmes, B. A. Carreras, L. A. Charlton, and V. E. Lynch, "Free Boundary Equilibrium and Stability of a Moderate Aspect Ratio Torsatron Using the Stellarator Expansion," presented at the Annual Meeting of the Division of Plasma Physics, American Physical Society, Boston, Oct. 29–Nov. 2, 1984 (postdeadline paper).

19. M. C. Depassier and W. A. Cooper, "Resistive Ballooning in Plasma Confinement Schemes with a Coordinate of Symmetry," pp. 86–88 in *Actas Cuarto Simposio Chileno de Fisica (Proceedings, Fourth Chilean Symposium of Physics)*, Universidad de Chile, Santiago, 1984.

20. C. R. Handy and S. P. Hirshman, *Accelerated Convergence of the Steepest Descent Method for Magnetohydrodynamic Equilibria*, ORNL/TM-9133, Oak Ridge Natl. Lab., 1984.

21. B. A. Carreras, T. C. Hender, L. A. Charlton, and J. A. Holmes, "The Effects of Toroidicity on Resistive MHD Instabilities in the RFP," *Bull. Am. Phys. Soc.* **29**, 1356 (1984).

22. L. A. Charlton, B. A. Carreras, L. Garcia, J. A. Holmes, H. R. Hicks, and V. E. Lynch, "Fully Toroidal Nonlinear MHD Calculations Without Ordering Assumptions," presented at the Annual Meeting of the Division of Plasma Physics, American Physical Society, Boston, Oct. 29–Nov. 2, 1984 (postdeadline paper).

23. L. A. Charlton, B. A. Carreras, H. R. Hicks, J. A. Holmes, and V. E. Lynch, "Incompressible MHD Modes in Toroidal Geometry," presented at the Annual Conference on Theoretical Aspects of Controlled Nuclear Fusion (Sherwood Meeting 1984), Incline Village, Nev., Apr. 11–13, 1984.

24. L. A. Charlton, B. A. Carreras, J. A. Holmes, H. R. Hicks, and V. E. Lynch, "Calculations in Toroidal Geometry with Full MHD Equations," pp. 174–91 in *Proceedings of the U.S.–Japan Workshop on MHD Studies*, ed. B. A. Carreras, CONF-840370, Oak Ridge Natl. Lab., 1984.

25. W. A. Cooper, "Centrifugal Force Effects from Toroidal Rotation on Incompressible Resistive Ballooning," *Plasma Phys. Controlled Fusion* **26**, 1351 (1984).

26. W. A. Cooper, "Resistive Ballooning Modes in Toroidally Rotating Tokamak Plasmas," *Bull. Am. Phys. Soc.* **29**, 1387 (1984).

27. W. A. Cooper and S. P. Hirshman, "Suppression of Spectral Pollution by Angle Renormalization," presented at the Annual Conference on Theoretical Aspects of Controlled Nuclear Fusion (Sherwood Meeting 1984), Incline Village, Nev., Apr. 11–13, 1984.

28. P. H. Diamond, Z. G. An, M. N. Rosenbluth, B. A. Carreras, T. C. Hender, and J. A. Holmes, *Magnetic Fluctuations, Field Reversal Maintenance, and Anomalous Thermal Transport in the Reversed Field Pinch*, ORNL/TM-9306, Oak Ridge Natl. Lab., November 1984. A summary of this material was presented at the Annual Conference on Theoretical Aspects of Controlled Nuclear Fusion (Sherwood Meeting 1984), Incline Village, Nev., Apr. 11–13, 1984.

29. L. Garcia, B. A. Carreras, P. H. Diamond, and J. D. Callen, *Theory of Resistivity-Gradient-Driven Turbulence*, IFSR-146, Institute for Fusion Studies, University of Texas, Austin, October 1984.

30. L. Garcia, B. A. Carreras, and H. R. Hicks, "Nonlinear Evolution of Microtearing Modes," presented at the Annual Conference on Theoretical Aspects of Controlled Nuclear Fusion (Sherwood Meeting 1984), Incline Village, Nev., Apr. 11–13, 1984.

31. H. R. Hicks, B. A. Carreras, L. Garcia, and J. A. Holmes, *The Reliability of Initial Value MHD Calculations of Tokamak Disruptions*, ORNL/TM-9127, Oak Ridge Natl. Lab., June 1984. A summary of this material was presented at the Annual Conference on Theoretical Aspects of Controlled Nuclear Fusion (Sherwood Meeting 1984), Incline Village, Nev., Apr. 11–13, 1984.

32. J. A. Holmes, B. A. Carreras, T. C. Hender, H. R. Hicks, V. E. Lynch, Z. G. An, and P. H. Diamond, "Nonlinear Interaction of Tearing Modes: A Comparison Between the Tokamak and the Reversed Field Pinch Configurations," *Phys. Fluids* **28**, 261–70 (1985); also published as ORNL/TM-9148, Oak Ridge Natl. Lab., April 1984.

33. W. A. Houlberg, S. P. Hirshman, and S. E. Attenberger, "Inverse Mapping Algorithm for Moments Formulation of MHD Equilibria," presented at the Annual Conference on Theoretical Aspects of Controlled Nuclear Fusion (Sherwood Meeting 1984), Incline Valley, Nev., Apr. 11–13, 1984.

34. W. I. van Rij, G. Vahala, and D. J. Sigmar, "The Spectrum of the MHD and Kinetic Alfvén Waves in a Cylindrical Tokamak," presented at the Annual Conference on Theoretical Aspects of Controlled Nuclear Fusion (Sherwood Meeting 1984), Incline Village, Nev., Apr. 11–13, 1984.

35. Z. G. An, P. H. Diamond, R. D. Hazeltine, J. N. Leboeuf, M. N. Rosenbluth, R. D. Sydora, T. Tajima, B. A. Carreras, L. Garcia, T. C. Hender, H. R. Hicks, J. A. Holmes, V. E. Lynch, and H. R. Strauss, "Role of Multiple Helicity Nonlinear Interaction of Tearing Modes in Dynamo and Anomalous Thermal Transport in the Reversed Field Pinch," in *Proceedings of the 10th International Conference on Plasma Physics and Controlled Nuclear Fusion Research (London 1984)*, Int. Atomic Energy Agency, Vienna, in press.

36. P. W. Terry, K. C. Shaing, P. H. Diamond, B. A. Carreras, and L. Garcia, "Spectrum of Rippling Mode Turbulence," *Bull. Am. Phys. Soc.* **29**, 1239 (1984).

37. E. Uchimoto, J. D. Callen, L. Garcia, and B. A. Carreras, "MHD Equilibrium Studies of a Poloidal Divertor Tokamak Using the Chodura-Schlüter Method," presented

at the Annual Conference on Theoretical Aspects of Controlled Nuclear Fusion (Sherwood Meeting 1984), Incline Valley, Nev., Apr. 11–13, 1984.

38. E. Uchimoto, J. D. Callen, L. Garcia, and B. A. Carreras, "Investigation into the Structure of Saturated Magnetic Islands in a Poloidal Divertor Tokamak," *Bull. Am. Phys. Soc.* **29**, 1376 (1984).

39. C. L. Hedrick and L. W. Owen, "Magnetic Equilibria for Square and Circular EBTs," pp. 126–37 in *Proceedings of the U.S.–Japan Workshop on 3-D MHD Studies*, ed. B. A. Carreras, CONF-840370, Oak Ridge Natl. Lab., 1984.

40. C. L. Hedrick and L. W. Owen, "Magnetic Equilibrium and Single Particle Orbits in EBS," presented at the Annual Conference on Theoretical Aspects of Controlled Nuclear Fusion (Sherwood Meeting 1984), Incline Valley, Nev., Apr. 11–13, 1984.

41. D. A. Spong, C. L. Hedrick, and J. W. Van Dam, "Ballooning Modes in the ELMO Bumpy Square Configuration Using the Generalized Kinetic Energy Principle," presented at the Annual Conference on Theoretical Aspects of Controlled Nuclear Fusion (Sherwood Meeting 1984), Incline Village, Nev., Apr. 11–13, 1984.

42. A. M. El Nadi, "Electrostatic Confinement in a Bumpy Torus," *Phys. Fluids* **28**, 878–82 (1985).

43. A. M. El Nadi, "Electrostatic Confinement in a Bumpy Torus with Hot Electron Rings," presented at the Annual Conference on Theoretical Aspects of Controlled Nuclear Fusion (Sherwood Meeting 1984), Incline Valley, Nev., Apr. 11–13, 1984.

44. R. E. Juhala and S. P. Hirshman, "The Magnetohydrodynamic Equilibria in a Bumpy Torus with Toroidal Current," p. 93 in *Conference Record—Abstracts, 1984 IEEE International Conference on Plasma Science, May 14–16, 1984, St. Louis, Missouri*, IEEE Publication No. 84CH1958-8, Institute Electrical and Electronics Engineers, New York, N.Y., 1984.

45. D. E. Hastings, "Development of a Differential Equation for the Ambipolar Electric Field in a Bumpy Torus in the Low Collision Frequency Limit," *Phys. Fluids* **27**, 2372 (1984).

46. D. E. Hastings, "A Differential Equation for the Ambipolar Electric Field in a Multiple-Helicity Torsatron," *Phys. Fluids* **28**, 334–7. A summary of this work was presented at the Annual Meeting of the Division of Plasma Physics, American Physical Society, Boston, Oct. 29–Nov. 2, 1984 [*Bull. Am. Phys. Soc.* **29**, 1272 (1984)].

47. D. E. Hastings, W. A. Houlberg, and K. C. Shaing, "The Ambipolar Electric Field in Stellarators," *Nucl. Fusion*, accepted for publication (1985).

48. D. E. Hastings and T. Kamimura, "Calculation of the Self-Consistent Electric Field in Toroidal Nonaxisymmetric Devices," *J. Comput. Phys.*, accepted for publication (1985).

49. D. E. Hastings and K. C. Shaing, "Azimuthal Electric Fields and Ambipolarity in A Multiple Helicity Torsatron," *Phys. Fluids*, accepted for publication (1985).

50. K. C. Shaing, "Noise-Induced Transition of the Radial Electric Field in a Nonaxisymmetric Torus," *Phys. Fluids* **27**, 1924–6 (1984).

51. K. C. Shaing, "Stability of the Radial Electric Field in a Nonaxisymmetric Torus," *Phys. Fluids* **27**, 1567 (1984). A summary of this work was presented at the Annual Conference on Theoretical Aspects of Controlled Nuclear Fusion (Sherwood Meeting 1984), Incline Village, Nev., Apr. 11–13, 1984.

52. K. C. Shaing, R. H. Fowler, D. E. Hastings, W. A. Houlberg, E. F. Jaeger, J. F. Lyon, J. A. Rome, and J. S. Tolliver, "The Radial Electric Field in a Nonaxisymmetric Torus," in *Proceedings of the 10th International Conference on Plasma Physics and Controlled Nuclear Fusion (London, 1984)*, Int. Atomic Energy Agency, Vienna, in press, 1985.

53. K. C. Shaing, R. H. Fowler, D. E. Hastings, W. A. Houlberg, E. F. Jaeger, J. F. Lyon, J. A. Rome, J. S. Tolliver, and J. D. Callen, "The Radial Electric Field in a Stellarator," p. 483 in *5th International Workshop on Stellarators: IAEA Technical Committee Meeting on Confinement and Heating in Stellarators, September 24–28, 1984*, ed. F. Rau and G. Leotta, vol. 2, EUR 9618 EN, Commission of the European Communities, Brussels, 1984.

54. G. L. Chen, L. W. Owen, D. B. Batchelor, and C. L. Hedrick, "Stochastic Particle Diffusion in Velocity Space for a Bumpy Torus," *Phys. Fluids*, **28**, 883–7 (1985).

55. R. H. Fowler, J. A. Rome, and J. F. Lyon, "Monte Carlo Studies of Transport in Stellarators," *Phys. Fluids* **28**, 338–44 (1985); also published as ORNL/TM-9193, Oak Ridge Natl. Lab., August 1984.

56. R. H. Fowler, J. A. Rome, and K. C. Shaing, "Transport Associated with the Collisionless Detrapping/Retrapping of Orbits in a Nonaxisymmetric Torus II," presented at the Annual Conference on Theoretical Aspects of Controlled Nuclear Fusion (Sherwood Meeting 1984), Incline Village, Nev., Apr. 11–13, 1984.

57. D. E. Hastings, "Collisionless Neoclassical Nonresonant Transport in Bumpy Tori," presented at the Annual Conference on Theoretical Aspects of Controlled Nuclear Fusion (Sherwood Meeting 1984), Incline Village, Nev., Apr. 11–13, 1984.

58. D. E. Hastings, "Neoclassical Transport in a Bumpy Closed Field Line Device in the Collisional, Small Electric Field Regime," *Phys. Fluids* **27**, 2115 (1984).

59. D. E. Hastings and K. C. Shaing, "Superbanana Plateau Regime Transport in a Multiple-Helicity Torsatron and a Bumpy Torus," *Phys. Fluids*, accepted for publication (1985).

60. J. A. Rome and R. H. Fowler, "Non-Local Transport in Tokamaks," presented at the Annual Conference on Theoretical Aspects of Controlled Nuclear Fusion (Sherwood Meeting 1984), Incline Village, Nev., Apr. 11–13, 1984.

61. J. S. Tolliver and C. L. Hedrick, "Monte Carlo Estimates of Transport Rates in EBT with Asymmetric Potential Profiles," presented at the Annual Conference on Theoretical Aspects of Controlled Nuclear Fusion (Sherwood Meeting 1984), Incline Village, Nev., Apr. 11–13, 1984.

62. J. S. Tolliver and J. A. Rome, "Bounce-Averaged Monte Carlo Calculations for Stellarators," *Bull. Am. Phys. Soc.* **29**, 1322 (1984).

63. R. L. Miller, C. S. Chang, and D. K. Lee, "Enhanced Neoclassical Diffusion of Nonresonant Particles in a Bumpy Torus," presented at the Annual Conference on Theoretical Aspects of Controlled Nuclear Fusion (Sherwood Meeting 1984), Incline Village, Nev., Apr. 11–13, 1984.

64. J. D. Callen and K. C. Shaing, "A Pressure-Gradient-Driven Tokamak 'Neoclassical MHD' Instability in the Banana-Plateau Collisionality Regime," *Bull. Am. Phys. Soc.* **29**, 1294 (1984).

65. J. D. Callen and K. C. Shaing, "Resistive MHD-Like Equations in the Banana-Plateau Collisionality Regime," presented at the Annual Conference on Theoretical Aspects of Controlled Nuclear Fusion (Sherwood Meeting 1984), Incline Village, Nev., Apr. 11–13, 1984.

66. K. C. Shaing and J. D. Callen, "A Kinetic Approach to a New Pressure Gradient Driven Tokamak Instability," *Bull. Am. Phys. Soc.* **29**, 1294 (1984).

67. C. O. Beasley, K. Molvig, and W. I. van Rij, "Drift Waves Destabilized by Pellet Injection," presented at the Annual Meeting of the Division of Plasma Physics, American Physical Society, Boston, Oct. 29–Nov. 2, 1984 (postdeadline paper).

68. C. O. Beasley, W. I. van Rij, and K. Molvig, "Effect of Coulomb Collisions on Universal Mode Stability," *Phys. Fluids* **28**, 271–4 (1985).

69. C. O. Beasley, W. I. van Rij, K. Molvig, and J. P. Freidberg, *Theory and Calculation of Finite Beta Drift Wave Turbulence*, ORNL/TM-9351, Oak Ridge Natl. Lab., 1984.

70. J. P. Freidberg and D. J. Sigmar, "Influence of Ideal Ballooning Modes on Confinement Scaling at High β," *Bull. Am. Phys. Soc.* **29**, 1370 (1984).

71. D. B. Batchelor, R. C. Goldfinger, and H. Weitzner, "Propagation and Absorption of Electromagnetic Waves in Fully Relativistic Plasmas," *Phys. Fluids* **27**, 2835–46 (1984). A summary of this work was presented by R. C. Goldfinger (paper 2Q21) at the Annual Conference on Theoretical Aspects of Controlled Nuclear Fusion (Sherwood Meeting 1984), Incline Village, Nev., Apr. 11–13, 1984.

72. D. B. Batchelor, K. S. Riedel, and H. Weitzner, "Strong Damping of Electron Cyclotron Waves in Nearly Parallel Stratified Plasmas," *Bull. Am. Phys. Soc.* **29**, 1311 (1984).

73. G. L. Chen, D. B. Batchelor, and Y. Matsuda, "Fokker-Planck Calculations of Core Plasma Heating by ECRH in EBT," *Bull. Am. Phys. Soc.* **29**, 1417 (1984).

74. G. L. Chen, D. B. Batchelor, and Y. Matsuda, "Fokker-Planck Modeling of Electron Cyclotron Heating and Direct Particle Loss in EBT and ELMO Bumpy Square," presented at the Annual Conference on Theoretical Aspects of Controlled Nuclear Fusion (Sherwood Meeting 1984), Incline Village, Nev., Apr. 11–13, 1984.

75. R. C. Goldfinger, D. B. Batchelor, and S. P. Hirshman, "Propagation and Absorption of Electron Cyclotron Waves in ATF," presented at the Annual Meeting of the Division of Plasma Physics, American Physical Society, Boston, Oct. 29–Nov. 2, 1984 (postdeadline paper).

76. C. L. Hedrick and E. F. Jaeger, "R-F and Microwave Induced Losses," *Bull. Am. Phys. Soc.* **29**, 1328 (1984).

77. E. F. Jaeger, C. L. Hedrick, and D. B. Batchelor, *Microwave-Induced Neoclassical Transport*, ORNL/TM-9331, Oak Ridge Natl. Lab., 1984. A summary of this material was presented at the Annual Conference on Theoretical Aspects of Controlled Nuclear Fusion (Sherwood Meeting 1984), Incline Village, Nev., Apr. 11–13, 1984.

78. E. F. Jaeger, J. H. Whealton, H. Weitzner, and D. B. Batchelor, "Full Wave Treatment of Wave Propagation in a Three-Dimensional Cavity Containing Cold Plasma," *Bull. Am. Phys. Soc.* **29**, 1401 (1984).

79. S. K. Borowski, Y-K. M. Peng, and W. A. Houlberg, "A Numerical Model for Examining Noninductive Current Drive Scenarios in Ignition Tokamaks," *Bull. Am. Phys. Soc.* **29**, 1215 (1984).

80. M. D. Carter, D. B. Batchelor, and J. D. Callen, "Second Harmonic Electron Cyclotron Heating," presented at the Annual Conference on Theoretical Aspects of Controlled Nuclear Fusion (Sherwood Meeting 1984), Incline Village, Nev., Apr. 11–13, 1984.

81. K. Imre, H. Weitzner, and D. B. Batchelor, "Absorption, Reflection, and Mode Coupling at the Second Cyclotron Resonance in a Weakly Relativistic, Inhomogeneous Plasma," presented at the Annual Conference on Theoretical Aspects of Controlled Nuclear Fusion (Sherwood Meeting 1984), Incline Village, Nev., Apr. 11–13, 1984.

82. B. A. Carreras, J. L. Cantrell, L. Garcia, J. H. Harris, T. C. Hender, and V. E. Lynch, "The Flexible Heliac," p. 317 in *5th International Workshop on Stellarators: IAEA Technical Meeting on Confinement and Heating in Stellarators, September 24–28, 1984*, ed. F. Rau and G. G. Leotta, vol. 2, EUR 9618 EN, Commission of the European Communities, Brussels, 1984.

83. B. A. Carreras, H. R. Hicks, J. A. Holmes, and V. E. Lynch, "Approximate Flux Conserving Stellarator," presented at the Annual Conference on Theoretical Aspects of Controlled Nuclear Fusion (Sherwood Meeting 1984), Incline Village, Nev., Apr. 11–13, 1984.

84. H. R. Hicks, B. A. Carreras, and J. A. Holmes, "Study of ATF-1 Torsatron Configurations Using the NYU Code BETA," presented at the Annual Meeting of the Division of Plasma Physics, American Physical Society, Boston, Oct. 29–Nov. 2, 1984 (postdeadline paper).

85. J. A. Rome, "$\ell=1/\ell=2$ Torsatron Hybrids," *Bull. Am. Phys. Soc.* **29**, 1271 (1984).

86. S. E. Attenberger and W. A. Houlberg, "Intersections of a Trajectory with Tokamak or Stellarator Flux Surfaces," presented at the Annual Meeting of the Division of Plasma Physics, American Physical Society, Boston, Oct. 29–Nov. 2, 1984 (postdeadline paper).

87. S. E. Attenberger, W. A. Houlberg, and S. P. Hirshman, "Efficient Mapping Algorithms Between Flux Coordinates and Real-Space Coordinates for Toroidal Plasmas," p. 121 in *Conference Record—Abstracts, 1984 IEEE International Conference on Plasma Science, May 14–16, 1984, St. Louis, Missouri*, IEEE Publication No. 84CH1958-8, Institute Electrical and Electronics Engineers, New York, N.Y., 1984.

88. E. C. Crume, "Effects of Momentum Input and Sonic Flow on Impurity Transport in Tokamaks," presented at the NATO Advanced Study Institute Programme, Val Morin, Quebec, Canada, Jul. 30–Aug. 11, 1984.

89. E. C. Crume, "Theory and Simulations of the Electrostatic Potential in Neutral-Beam-Driven Tokamaks and Effects on Impurity Transport," presented at the U.S./U.S.S.R. Topical Meeting on Plasma Rotation and Ambipolar Electric Fields, RF Heating, and Transport in Tokamaks, Kurchatov Institute, Moscow, Sept. 23–29, 1984.

90. J. T. Hogan, "Beam-Induced Current Effects on Stellarator Transform," *Bull. Am. Phys. Soc.* **29**, 1271 (1984).

91. J. T. Hogan, L. Ibanez, and H. Grad, "Current Generation in Stellarators," presented at the Annual Conference on Theoretical Aspects of Controlled Fusion (Sherwood Meeting 1984), Incline Village, Nev., Apr. 11–13, 1984.

92. W. M. Stacey, A. W. Bailey, and D. J. Sigmar, "Rotation and Impurity Flow Reversal in Tokamak Plasmas with Neutral Beam Injection," presented at the Annual

Conference on Theoretical Aspects of Controlled Fusion (Sherwood Meeting 1984), Incline Village, Nev., Apr. 11–13, 1984.

93. W. M. Stacey and D. J. Sigmar, *Rotation and Impurity Transport in a Tokamak with Directed Neutral Beam Injection*, GTFR-47, Georgia Institute of Technology, Atlanta, 1984.

94. L. Ibanez, H. Grad, A. Bayliss, and J. Hogan, "Long Pulse Evolution of Elongated, Rippled High-Beta Tokamaks," presented at the Annual Conference on Theoretical Aspects of Controlled Fusion (Sherwood Meeting 1984), Incline Village, Nev., Apr. 11–13, 1984.

95. D. A. Spong, D. J. Sigmar, K. T. Tsang, W. A. Cooper, and D. E. Hastings, "Effects of Trapped Alpha Particles on Ballooning Modes," *Bull. Am. Phys. Soc.* **29**, 1387 (1984).

96. L. Vahala, G. Vahala, and D. J. Sigmar, "Effects of α-Particles on CO_2 Laser Scattering From a Fusion Plasma," *Bull. Am. Phys. Soc.* **29**, 1310 (1984).

97. L. A. Charlton, R. M. Wieland, and G. H. Neilson, "Equilibrium Modeling of ISX-B Tokamak Discharges," *Phys. Fluids* **28**, 1738–42 (1984).

98. E. C. Crume, Jr., and D. E. Arnurius "Simulation of Impurity Transport in the ISX-B Tokamak with Directed Neutral Beam Heating," presented at the Annual Conference on Theoretical Aspects of Controlled Nuclear Fusion (Sherwood Meeting 1984), Incline Village, Nev., Apr. 11–13, 1984.

99. H. C. Howe, D. Schuresko, and W. A. Houlberg, "Anomalous Pellet Ablation in ISX-B Discharges," *Bull. Am. Phys. Soc.* **29**, 1425 (1984).

100. R. M. Wieland, E. A. Lazarus, M. Murakami, J. D. Bell, W. A. Cooper, S. P. Hirshman, and G. H. Neilson, "Toroidal Flow Analysis of ISX-B Density and Temperature Profiles," *Bull. Am. Phys. Soc.* **29**, 1425 (1984).

101. K. E. Yokoyama, H. C. Howe, D. P. Hutchinson, R. C. Isler, E. A. Lazarus, C. H. Ma, M. Murakami, G. H. Neilson, and A. J. Wootton, "Particle Confinement in ISX-B," *Bull. Am. Phys. Soc.* **29**, 1351 (1984).

102. A. W. Bailey, W. M. Stacey, Jr., and D. J. Sigmar, "Neutral Beam Driven Impurity Flow Reversal in PLT and ISX-B," *Bull. Am. Phys. Soc.* **29**, 1426 (1984).

103. D. C. Robinson, N. R. Ainsworth, M. W. Alcock, D. Atkinson, P. R. Collins, A. N. Dellis, T. Edlington, A. Ferreira, Q. Gao, T. C. Hender, Z. Ma, A. W. Morris, M. O'Brien, B. Parham, A. C. Riviere, D. F. H. Start, S. Takamura, and T. N. Todd, "Limiting β Investigations at Low Collisionality," in *Proceedings of the 10th International Conference on Plasma Physics and Controlled Nuclear Fusion Research (London 1984)*, Int. Atomic Energy Agency, Vienna, in press.

104. D. B. Batchelor, "Core Plasma Heating in EBT-S and the Effect of Strongly Damped Cyclotron Waves," invited paper, *Bull. Am. Phys. Soc.* **29**, 1287 (1984).

105. D. B. Batchelor, EBT Experimental Group, and EBT Theory Group, "Comparison of Electron Cyclotron Heating Theory and Experiment in EBT," p. 779 in *Heating in Toroidal Plasmas: Proceedings of the Fourth International Symposium, Rome, March 1984*, ed. H. Knoepfel and E. Sindoni, vol. II, International School of Plasma Physics and ENEA, Varenna, Italy, 1984.

106. C. L. Hedrick, D. B. Batchelor, G. L. Chen, R. C. Goldfinger, D. E. Hastings, E. F. Jaeger, D. K. Lee, L. W. Owen, D. A. Spong, J. S. Tolliver, "Coupled Transport and

Heating in EBT and EBS," in *Proceedings of the 10th International Conference on Plasma Physics and Controlled Nuclear Fusion Research (London 1984)*, Int. Atomic Energy Agency, Vienna, in press.

107. E. F. Jaeger, L. A. Berry, C. L. Hedrick, and R. K. Richards, "Magnetic Well Depth in EBT and Sensitivity to Hot Electron Ring Geometry," *Nucl. Fusion* **25**, 71 (1985); also published as ORNL/TM-9185, Oak Ridge Natl. Lab., 1984.

108. A. M. El Nadi, J. C. Whitson, and S. Hiroe, "Finite $k_{\parallel}$ High Frequency Fluctuations in EBT," *Bull. Am. Phys. Soc.* **29**, 1416 (1984).

Chapter 5

Plasma-Materials Interactions

P. K. Mioduszewski, Coordinator

J. B. Roberto[1] (Coordinator until August 1984)

R. E. Clausing[2]	D. L. Hillis	K. G. Tschersich[3]
T. B. Cook[1]	P. W. King	T. Uckan
L. C. Emerson[2]	R. A. Langley	J. von Seggern[3]
L. Heatherly[2]	J. E. Simpkins	R. A. Zuhr[1]

1. Solid State Division.
2. Metals and Ceramics Division.
3. Kernforschungsanlage Jülich GmbH, Jülich, Federal Republic of Germany.

CONTENTS

SUMMARY OF ACTIVITIES 5-5
5.1 SUMMARY OF "TIME-RESOLVED IMPURITY FLUXES IN THE TEXTOR PLASMA EDGE" 5-5
5.2 ABSTRACT OF "THE INFLUENCE OF IMPURITIES ON THE HIGH-TEMPERATURE SPUTTERING YIELD OF GRAPHITE" 5-8
5.3 IN SITU EROSION STUDIES WITH LASER FLUORESCENCE TECHNIQUES 5-10
5.4 WALL CONDITIONING AND CARBONIZATION FOR CONTROL OF IMPURITIES AND HYDROGEN RECYCLE 5-11
5.5 EXPERIMENTS ON IMPURITY AND PARTICLE CONTROL IN ISX-B 5-13
5.6 PLASMA-MATERIALS INTERACTION STUDIES DURING THE JET-ISX BERYLLIUM LIMITER EXPERIMENT 5-14
REFERENCES 5-19

5. PLASMA-MATERIALS INTERACTIONS

Summary of Activities

The Plasma-Materials Interactions Program addresses key research and technology issues related to the interaction of fusion plasmas with surrounding material surfaces. The goal of the base program is to understand the fundamental phenomena related to impurity control, erosion/redeposition of wall and limiter materials, recycling/retention of hydrogen isotopes, and particle handling. The ORNL program combines laboratory studies of basic processes and techniques with applications in fusion devices. Impurity control studies include the identification and evaluation of impurity sources as well as conditioning of wall and limiter materials to minimize impurity production. Over the past year, laboratory studies have concentrated on the influence of impurities on the high-temperature sputtering yield of graphite and on wall conditioning. Wall conditioning techniques like wall carbonization [on TEXTOR and the Joint European Torus (JET)] and chromium gettering [on the Impurity Study Experiment (ISX-B) and the Tokamak Fusion Test Reactor (TFTR)] have been proved to be very successful in reducing impurity radiation and improving plasma performance. Studies of the impurity fluxes in the edge plasma of the TEXTOR tokamak were continued in collaboration with Sandia National Laboratories and Kernforschungsanlage (KFA) Jülich. Time-resolved and in situ erosion studies have been performed at a reference limiter in ISX-B using laser fluorescence. Particle handling with pump limiters in beam-heated plasmas was demonstrated in ISX-B. During the second half of the past year, the work was focused on the JET-ISX beryllium limiter test. Studies included cleanup of the vacuum vessel with beryllium gettering, transport of wall material to the limiter, erosion/redeposition of limiter material, and deuterium retention in beryllium at high fluence (10^{22} ions/cm^2).

5.1 SUMMARY OF "TIME-RESOLVED IMPURITY FLUXES IN THE TEXTOR PLASMA EDGE"[1]

R. A. Zuhr and W. R. Wampler*

The internal configuration of the TEXTOR tokamak at Kernforschungsanlage (KFA) Jülich, Federal Republic of Germany, has been modified recently to include antennas for ion cyclotron resonance heating (ICRH) of the plasma. Passive deposition probe measurements of edge impurity fluxes were made for typical ohmic discharges with this new liner configuration. The time-resolved behavior of impurities in the edge was determined as a function of radius and limiter position using rotating probe techniques. All exposures were made for standard ohmically heated hydrogen discharges having the following parameters: toroidal field = 2 T, plasma current = 340 kA, line-averaged electron density = (2–3) $\times$ 10^{13} cm^{-3}, central electron temperature = 1–1.5 keV, and discharge length = 2.5 s. After

exposure, the samples were removed and transferred in air to a megaelectron volt accelerator facility, where Rutherford ion backscattering (RBS) was used to determine quantitatively the amounts of impurities retained on the samples. Present results are compared with previous measurements of edge fluxes made prior to modifications to the plasma-side liner of TEXTOR.

The amounts of impurity elements detected in the scrapeoff layer of TEXTOR at 2 and 5 cm behind the limiter radius are given in Table 5.1. The numerical values are the average fluxes retained in the electron drift direction for exposures that are time integrated over nondisruptive ohmic discharges. The most common element in the edge is seen to be oxygen, with maximum time-averaged fluxes on the order of 5×10^{15} $cm^{-2} \cdot s^{-1}$. The most abundant metallic elements are iron, chromium, and nickel. Lesser amounts of molybdenum, which is a component in one of the Inconel alloys used in TEXTOR, and traces of tungsten or tantalum are also observed. Titanium, the material from which the probe slits were made, is not detectable on the samples. The ratio of iron, chromium, and nickel found on the probes is approximately 8:2:1. Nickel, the major constituent of Inconel, is present in smaller amounts than either iron or chromium. Such a result indicates that the metallic impurities originate from stainless steel components, such as the limiters, rather than from the Inconel liner.

The time dependence of radial distributions in the electron drift direction for Fe + Cr + Ni, oxygen, and molybdenum is shown in Fig. 5.1. Here the retained flux is plotted as a function of the tokamak minor radius at four different times during the 2.5-s discharges. Data taken before (−0.5 s) and after (+3.0 s) the discharge indicate no measurable impurity deposition and are not included in the figure. Time resolution for these data is ±370 ms, so rapid fluctuations are not observed. On this time scale, it is clear that the radial distribution of impurities is a smoothly varying function of time. The shape of the distribution for each of the impurities remains essentially the same throughout the discharge. The observation that the impurity deposition rate does not increase during the discharge indicates that impurities are not accumulating in the edge as the discharge progresses. This is an important result and confirms data obtained in earlier TEXTOR discharges.[2]

Least-squares fits to the data and radial decay lengths derived from them are also included in Fig. 5.1. Fits are for $r > 48$ cm except for the transition metals at 2.3 s, where

Table 5.1. Time-averaged retained impurity fluxes in the electron drift direction for ohmic hydrogen discharges in TEXTOR

Probe radius (cm)	Distance behind limiter (cm)	Average flux ($cm^{-2} \cdot s^{-1}$)				
		O	Fe	Cr	Ni	Mo
47	2	5.8×10^{15}	2.8×10^{15}	7.8×10^{14}	3.4×10^{14}	2.4×10^{13}
50	5	4.9×10^{15}	1.0×10^{15}	2.7×10^{14}	1.2×10^{14}	1.1×10^{13}

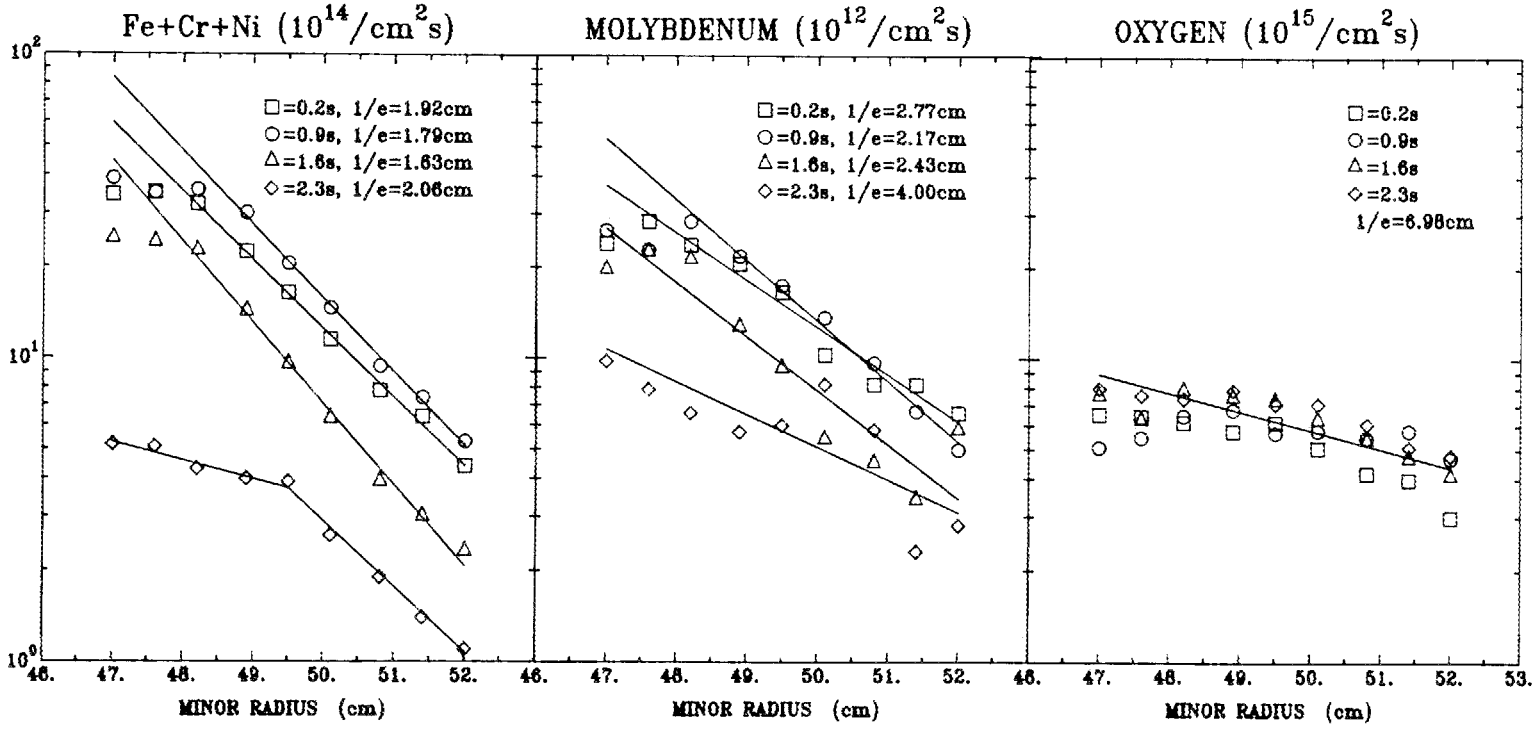

Fig. 5.1. Time evolution of the radial dependence of retained impurity fluxes for Fe + Cr + Ni, molybdenum, and oxygen. Data are for ohmic hydrogen discharges in the electron drift direction at 0.2 s (□), 0.9 s (○), 1.6 s (△), and 2.3 s (◇). Deposition before (−0.5 s) and after (+3.0 s) the discharge is essentially zero. Radial e-folding lengths (1/e) for $r > 48$ cm are shown.

separate curves are fitted above and below 49.5 cm. The time dependence of the decay lengths is included for the metals. The results for the most abundant metals in the edge, Fe + Cr + Ni, are shown on the graph to the left and indicate a decay length for $r >$ 48 cm that varies only slightly during the main portion of the discharge (1.85 ± 0.22 cm). The variation that does occur is consistent for all the metals and results in a shortening of the scrapeoff length by 10 to 20% during the most stable central portion of the discharge. This is an indication that the plasma is most tightly confined at these times. As the plasma begins to collapse (t = 2.3 s), the radial scrapeoff length increases and the flux retained on the probe decreases. The behavior of molybdenum is similar to that of Fe + Cr + Ni, although the measured decay length is somewhat longer (2.45 ± 0.3 cm). The change in the slope of the profiles that is observed for all the metals at r = 48–49 cm is believed to be due to the fixed inner limiter at r = 49 cm and to the limiting action of the newly installed rf antenna system, which is located 116° from the probe in the ion drift direction at a radius of 48.8 cm.

The results for oxygen deposition (Fig. 5.1, right) are in contrast to those achieved for the metals. The radial distributions are much flatter, the observed decay length is longer, and there is little variation with time during the discharge. In this case, because of the lack of time dependence, only a single decay length is fitted to all the data ($1/e$ = 6.98 cm). If the oxygen radial profiles have not been distorted by experimental complications in the measurement of oxygen deposition, these results suggest that the introduction mechanism or edge transport for oxygen must be different from that for the metals.

In comparison with measurements made prior to modification of the liner, several changes are observed. The radial dependence of the impurities now shows a clear decrease with distance behind the limiter that may have been smeared by plasma instability in earlier exposures. The previous increase in metallic fluxes near the liner is no longer observed, perhaps because of decreased contact between the plasma and the liner due to the limiting effect of the antenna installation. The deposited fluxes of oxygen are approximately the same, indicating a similar level of wall conditioning, but the flux of transition metals has increased by a factor of 2 to 3. The relative amounts of iron, chromium, and nickel have also changed. The relative amount of iron has increased, while that of nickel has decreased, indicating relatively less interaction between the plasma and the Inconel liner. In combination, these changes point toward a more stable plasma that is better confined by the limiters and interacts less strongly with the first wall.

---

*Sandia National Laboratories, Albuquerque, N. Mex.

5.2 ABSTRACT OF "THE INFLUENCE OF IMPURITIES ON THE HIGH-TEMPERATURE SPUTTERING YIELD OF GRAPHITE"[3]

J. Roth,* J. Bohdansky,* and J. B. Roberto

The influence of surface and bulk impurities on the chemically enhanced sputtering of graphite near 600°C and the radiation-enhanced sublimation of graphite above 1000°C has been investigated. Such investigations yield additional information on the mechanisms

of high-temperature erosion processes in graphite and may lead to procedures for minimizing the erosion rates. In particular, an understanding of the effect of simultaneous impurity fluxes on the enhanced erosion could be important in determining the usefulness of graphite as a high-temperature plasma-side material in fusion reactors.

The chemical sputtering yield for 500-eV hydrogen bombardment of graphite at 600°C was investigated at the Max-Planck-Institut high-current ion source for graphite samples with deposited layers of gold, iron, nickel, titanium, and molybdenum. For the gold, iron, and nickel films, clustering of the deposited films allowed high chemical sputtering (methane) yields despite average surface coverages of many monolayers. For the non-clustering titanium and molybdenum films, suppression of the chemical sputtering yield was approximately a factor of 2 with one monolayer coverage. Addition of bulk impurities (4 at. % Si) was most effective in suppressing the chemical sputtering of graphite.

The radiation-enhanced sublimation of graphite bombarded at 1520°C by 50-keV argon ions was investigated during simultaneous titanium evaporation onto the surface at the ion implantation facility in the Solid State Division. The titanium concentration in the near surface has a strong influence on the ion-enhanced sublimation yield, as shown in Fig. 5.2. Low concentrations of titanium initially increase the carbon yield, while concentrations above 10 at. % lead to a nearly complete suppression of the enhanced yield. The increase in carbon erosion at low titanium concentrations is attributed to the occupation of

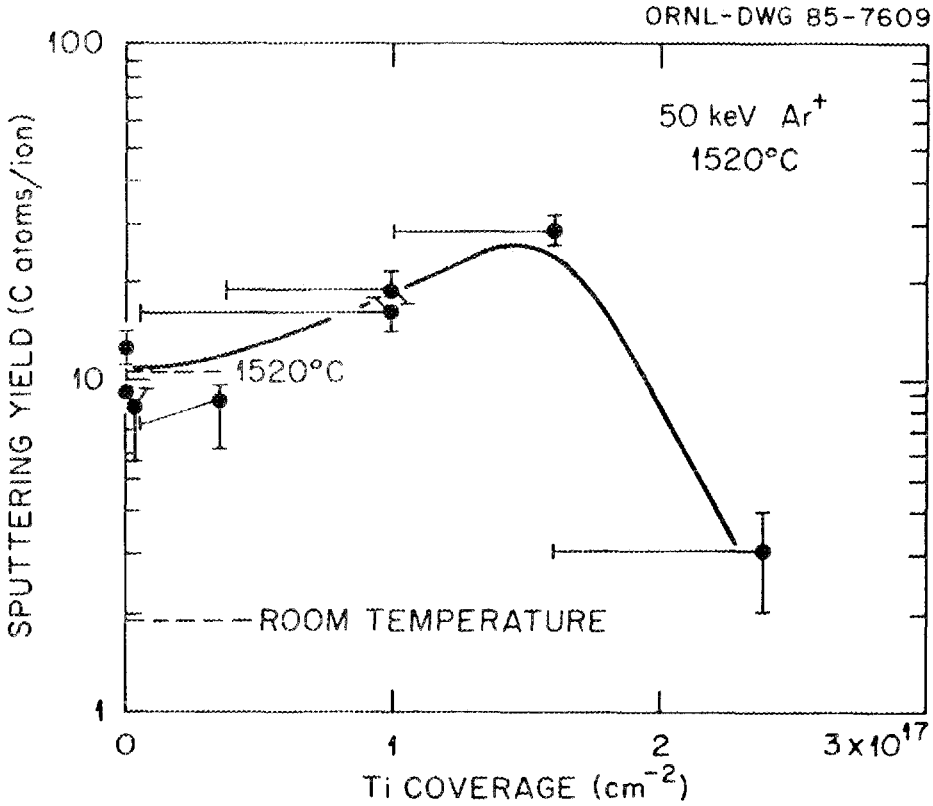

Fig. 5.2. Dependence of the enhanced sublimation yield on titanium coverage for 50-keV argon bombardment of graphite at 1520°C. For comparison, the room-temperature sputtering yield for graphite is shown, as is the sputtering yield of bulk TiC at 1520°C.

vacancies by titanium atoms, allowing additional carbon interstitials to diffuse to the surface and evaporate.

Overall, the results indicate that suppression of high-temperature erosion processes in graphite can occur for sufficiently high surface coverages and bulk concentrations of impurities. Furthermore, the effectiveness of bulk impurity concentrations in reducing erosion rates indicates that the chemical and radiation-enhanced erosion processes originate at depths beyond the surface layer.

*Max-Planck-Institut für Plasmaphysik, Garching bei München, Federal Republic of Germany.

5.3 IN SITU EROSION STUDIES WITH LASER FLUORESCENCE TECHNIQUES

P. W. King and T. B. Cook

Sputtering measurements at a reference limiter, initiated last year,[4] were continued. Studies were performed for both graphite coated with titanium carbide (TiC) and beryllium as the material of the main limiter. Experimental results (discussed in more detail elsewhere[5,6]) are summarized below.

For neutral-beam-heated plasmas with a beryllium rail limiter, titanium erosion rates from a reference limiter made of TiC-coated graphite are $\simeq 9 \times 10^{14}$ atoms/cm$^2 \cdot$s^{-1} at a midplane location about 10 cm outside the plasma boundary. The measured electron-impact ionization length is $\lesssim 0.3$ cm. When a small amount of neon is injected into the edge of the plasma, the measured Ti I radiation decreases by about a factor of 2 near the end of the tokamak discharge (see Fig. 5.3). This result is consistent with a model having decreased beryllium sputtering of the probe with the addition of neon.

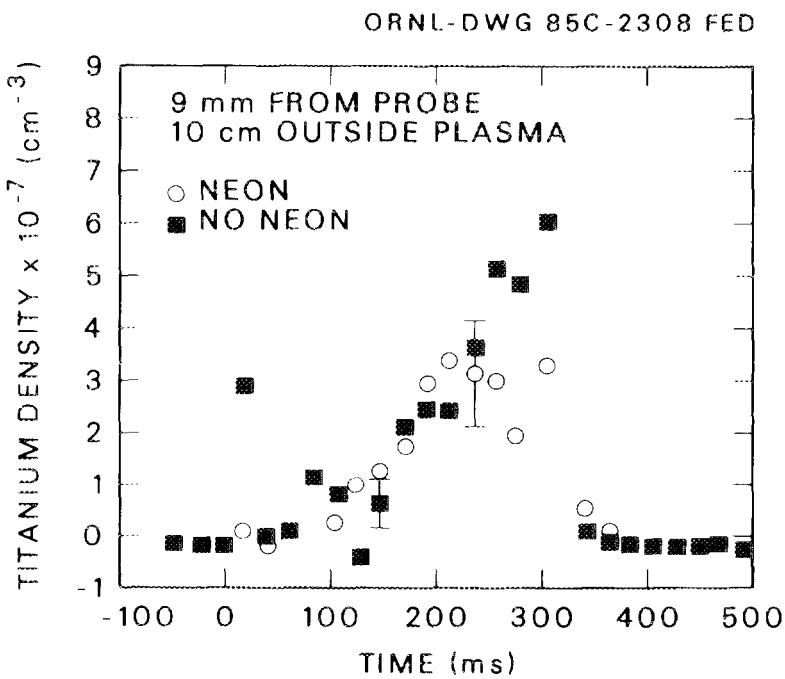

Fig. 5.3. Comparison of Ti I density for plasmas with neon injection vs plasmas without neon injection. Results suggest beryllium sputtering.

Electron-impact ionization lengths outside neutral-beam-heated plasmas with the TiC limiter are approximately the same as for the beryllium limiter case. For the TiC limiter case, the erosion rate for deuterium plasmas is three to four times higher than that for hydrogen plasmas. The erosion rate on the ion side is at least ten times greater than on the electron side, and the neutral metal density in the scrapeoff layer decreases with increasing $\bar{n}_e$ (see Fig. 5.4) and increases with neutral beam power (up to about 1 MW). The hydrogen vs deuterium and ion-side vs electron-side studies were done for Fe I erosion from a stainless steel reference limiter.

5.4 WALL CONDITIONING AND CARBONIZATION FOR CONTROL OF IMPURITIES AND HYDROGEN RECYCLE

R. E. Clausing and L. Heatherly

New ways are being found to control the recycling of impurities and hydrogen from the walls of fusion devices. Data from a laboratory simulator are being used and analyzed together with data from TEXTOR, the Joint European Torus (JET), and other tokamaks to learn how best to exploit and extend our understanding of the interaction between impurities on surfaces exposed to plasma conditioning. These data show that oxygen and carbon surface impurities are interrelated and can be manipulated by controlling the composition of the gas used for plasma surface conditioning.[7] Not only can oxygen be reduced to low levels, but also carbon (and other elements) can be either removed or deposited and reacted with the substrate. In the case of carbon deposits, a thin metal carbide layer can be formed or thicker deposits of elemental carbon can be made. Surface compositions can be reproduced easily and reversibly in a controlled way. Furthermore, these composition changes can alter the hydrogen recycling and plasma impurity levels by an order of magnitude or more.

The use of selected additions to the gas used in discharge cleaning permits the purposeful manipulation of surface compositions or deposits on the walls and limiters of fusion devices and makes possible the rapid and nearly complete elimination of oxygen and other impurities on the walls and in the plasmas of tokamaks. Carbon films deposited on surfaces affect not only hydrogen recycling but also hydrogen permeation and the hydrogen inventory in the wall. Many of these effects are incompletely understood and not well documented. The plasma-wall interaction simulator provides a convenient and efficient way to document the effects of the many variables involved and to develop and optimize techniques for use in larger devices.

In the simulator we have related gas composition to surface composition changes and resulting recycle behavior. Surface oxygen levels can be reduced from 30 to less than 3 at. % in 45 min of discharge cleaning. We have demonstrated the ease with which carbon can be deposited or removed rapidly and reproducibly and have shown that it displaces or reacts with other surface-active impurities to produce a clean carbon- or carbide-covered wall (depending on the conditions). Figure 5.5 shows the effectiveness of carbon in removing impurities from the walls of the simulator. Hydrogen recycle from these walls rapidly approaches unity, but there appear to be strong effects due to hydrogen inventories in the films, which in turn are influenced by the preparation and history of the film. Studies of these variables are continuing using isotope exchange and thermal desorption methods.

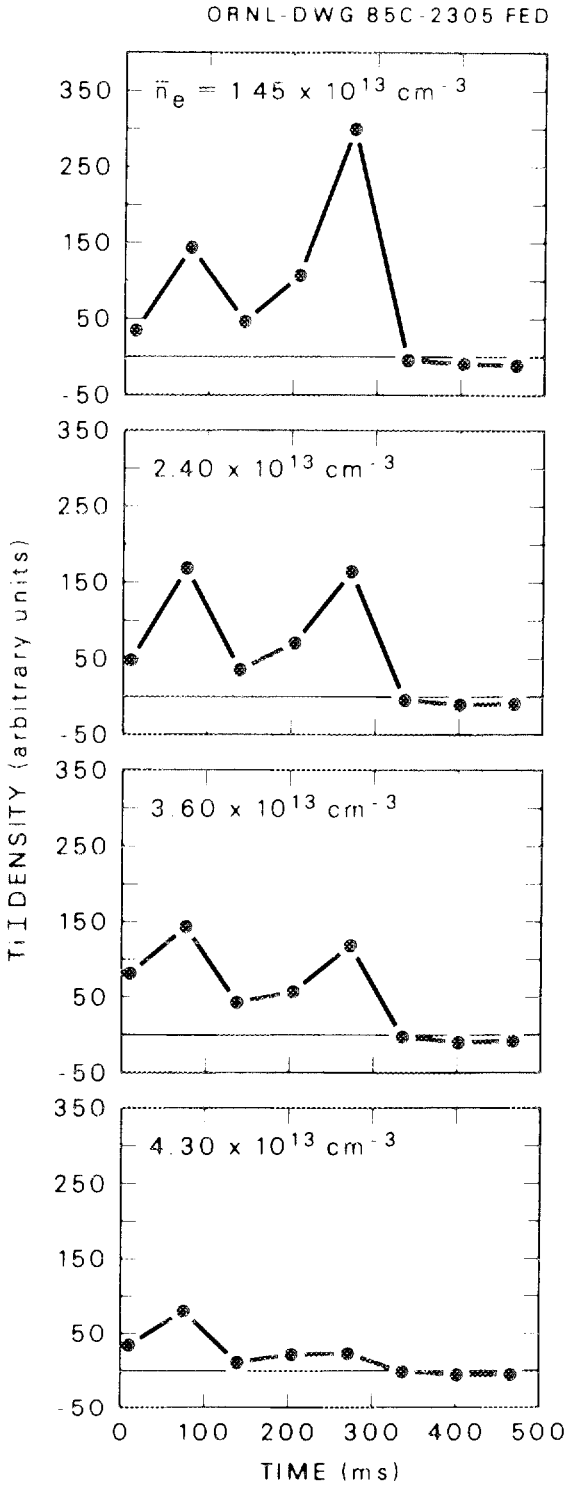

Fig. 5.4. $\bar{n}_e$ **scan.** Relative Ti I density is plotted vs time with line-averaged electron density as the parameter.

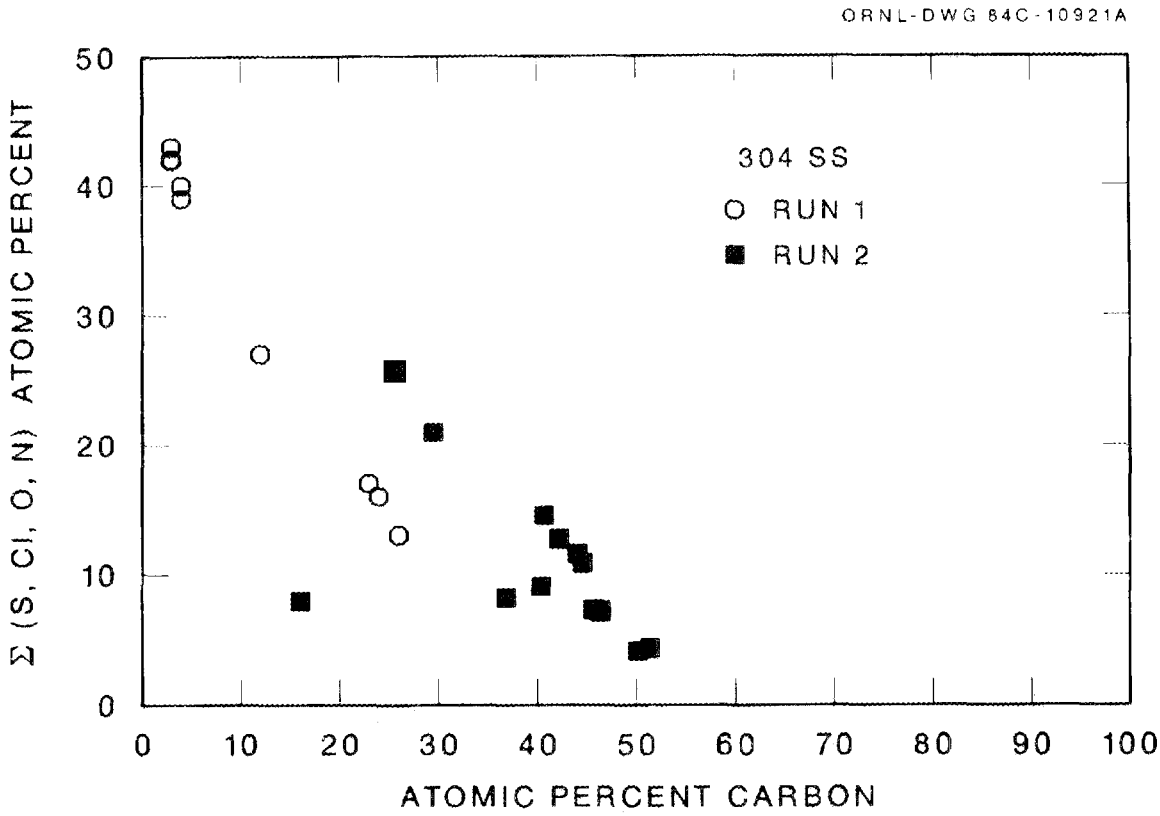

Fig. 5.5. The decrease in surface-active impurities as carbon is increased by adding methane to the glow discharge. The wall material is 304 stainless steel.

5.5 EXPERIMENTS ON IMPURITY AND PARTICLE CONTROL IN ISX-B

During 1984, the experimental program on the Impurity Study Experiment (ISX-B) tokamak emphasized studies on limiter materials and configurations, impurity control, and particle handling. These studies were performed with strong involvement and under coordination of the Plasma-Materials Interactions (PMI) group. The main efforts were (1) the ISX-JET beryllium limiter experiment, (2) the pump limiter experiment, and (3) the chromium gettering experiment. Details of these experiments, especially with respect to plasma operation, are described in Chap. 1 of this report. Chromium gettering, which has been shown to be an efficient technique of impurity control in tokamaks, was developed over the past years in the PMI program. The pump limiters on ISX-B, with which particle exhaust was successfully demonstrated, were built and tested as part of the PMI program. Finally, an important part of the beryllium limiter experiment was the material and surface studies described in Sect. 5.6.

5.6 PLASMA-MATERIALS INTERACTION STUDIES DURING THE BERYLLIUM LIMITER EXPERIMENT

R. E. Clausing, L. Heatherly, R. A. Langley, J. B. Roberto, R. A. Zuhr, J. von Seggern, and K. G. Tschersich

The beryllium limiter experiment provided a unique opportunity for certain kinds of plasma-materials studies. Studies reported here include those associated with the initial cleanup of the ISX-B machine after installation of the limiters, the transport of impurities and beryllium during the experiment, and the deposition of deuterium into the limiter and wall samples.

The initial cleanup, using 120-Hz discharge cleaning pulses, produced conditions suitable for normal ungettered tokamak discharges after one day. The wall composition (monitored through the use of a surface analysis station) showed the progress of cleaning and the transport of wall and limiter material from prior getter deposits as well as the transport of beryllium. Significant amounts of beryllium (but much less than a monolayer) were transported as neutral particles produced by sputtering during a typical overnight discharge cleaning cycle. This sputtered beryllium acted as a getter but was insufficient to alter machine performance.

The evaporation and transport of beryllium around ISX-B during the initial tokamak operation, with limiter loads within the design specifications, were small. A subsequent series of high-power shots, however, caused much melting and evaporation. From that time on, small hot spots formed on the limiter during each normal-power (fluence) shot, causing more beryllium to be evaporated, so that the machine operated in a gettered mode for the balance of the limiter test. Figures 1.11 and 1.13 in Chap. 1 show changes in the gross appearance of the limiter during the course of the tests. Figures 5.6 and 5.7 show the macroscopic appearance of the limiter surface after the tests. Note that many of the melt structures have been eroded or evaporated severely; most of the protrusions having exposed surfaces perpendicular to the power flux have bright shiny spots, indicative of repeated melting on every shot. These spots are the sources of the beryllium observed in the plasma and at the walls.

Depth profiles of deposits on samples exposed in the edge plasma during tokamak shots (see Fig. 5.8) show much thicker deposits on the surfaces oriented to intercept beryllium ions drifting along magnetic field lines than on those that would intercept neutral atoms in a direct line of sight. Thus, it appears that neutrals leaving the limiter during tokamak shots are ionized and either move around the machine along the magnetic field lines until they are redeposited on the limiter or diffuse into the main plasma. The deposits contain significant amounts of free beryllium metal, implying that much more beryllium is being deposited than is needed to getter oxygen. Beryllium oxide is quite stable, and earlier measurements indicate that, in these experiments, it does not contribute much oxygen to the main plasma.

Silicon and stainless steel collector samples were placed in a number of locations to determine the distribution and amounts of beryllium and deuterium deposited during the entire beryllium limiter experiment. The results are summarized in Fig. 5.9. The numbers in parentheses indicate beryllium deposits; the numbers in square brackets indicate deuterium levels retained after approximately two months. Note that the beryllium levels were

Y-12 PHOTO Y198947

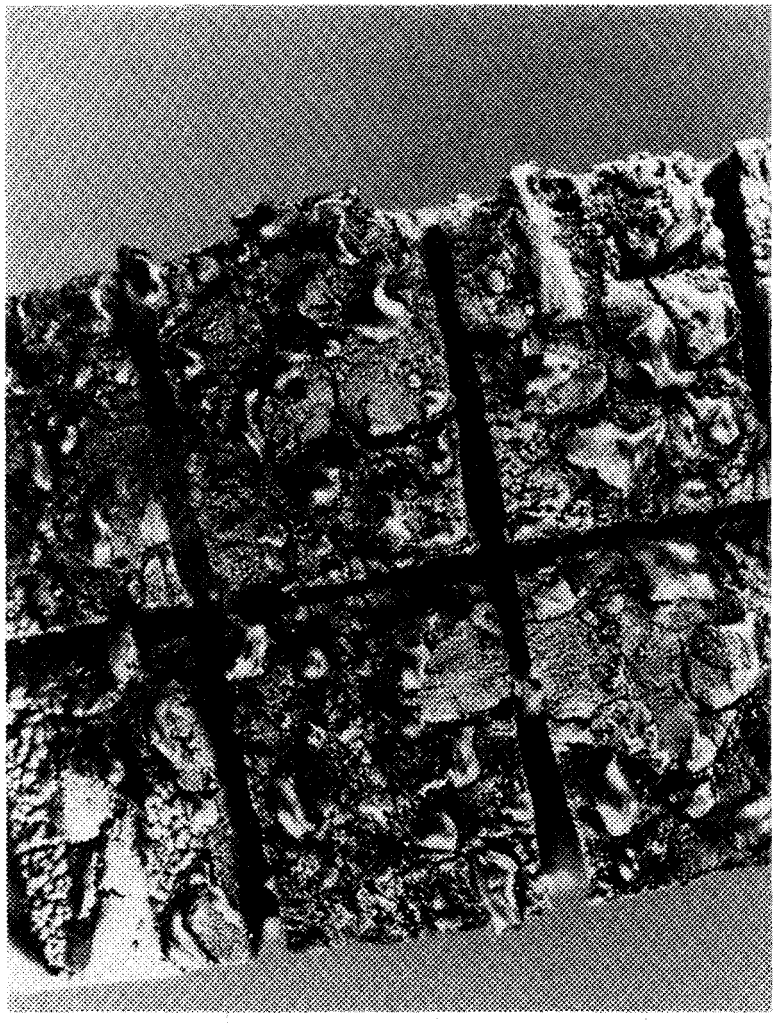

Fig. 5.6. Photomicrograph of the center part of limiter tile 8 showing the appearance of the melted and eroded surface. Magnification is 4×. Note the shiny areas on the protruding structures; these are indicative of repeated melting.

higher near the limiter but that considerable amounts were spread entirely around ISX-B. Also note that these deposits on the walls are orders of magnitude smaller than would have accumulated on the samples in the plasma edge as described above. Thus, we see that surfaces that intercept edge plasma will be much more heavily coated than wall surfaces. The retained deuterium decreases monotonically as a function of distance from the limiter in the direction of ion drift.

The limiter was carefully analyzed after the tests. Each segment was weighed to determine the amount of material lost. The center sections lost the most; some weight gains are noted on end sections. Overall, about 2 g of beryllium was lost from the limiter.

Y-12 PHOTO Y198945

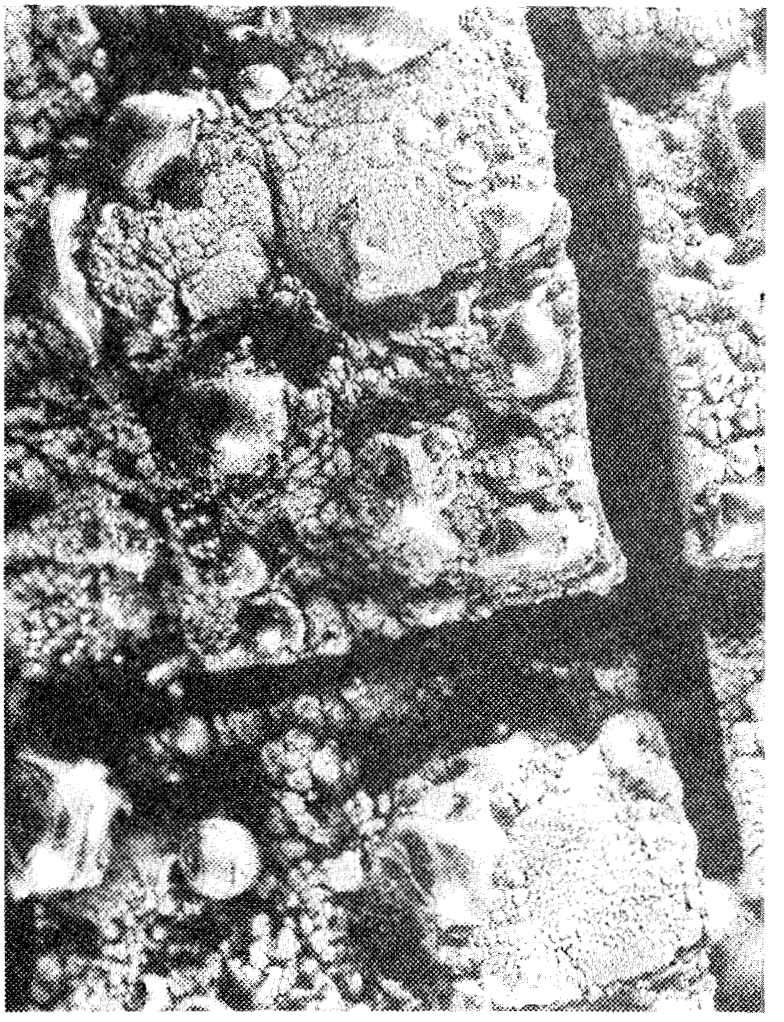

Fig. 5.7. A section of Fig. 5.6 with magnification 10×.

Accelerator-based techniques were used to measure the deposition of metallic impurities and deuterium into the limiter segments. The analysis provides total concentrations for the first few thousand atom layers. Further measurements will be required to be certain that diffusion to deeper layers has not occurred, but it appears that the values for deuterium are approaching saturation levels of about $(1–5) \times 10^{17}$ cm^{-2}. These values were measured about two months after the last plasma exposure. Concentrations of the transition metals iron, chromium, and nickel were $(0.5–10) \times 10^{16}$ cm^{-2}. A beryllium sample exposed in the edge plasma to 72 tokamak fluence shots (3.5×10^{19} ions/cm^2) retained $(6–9) \times 10^{16}$ deuterium atoms/cm^2 after two months.

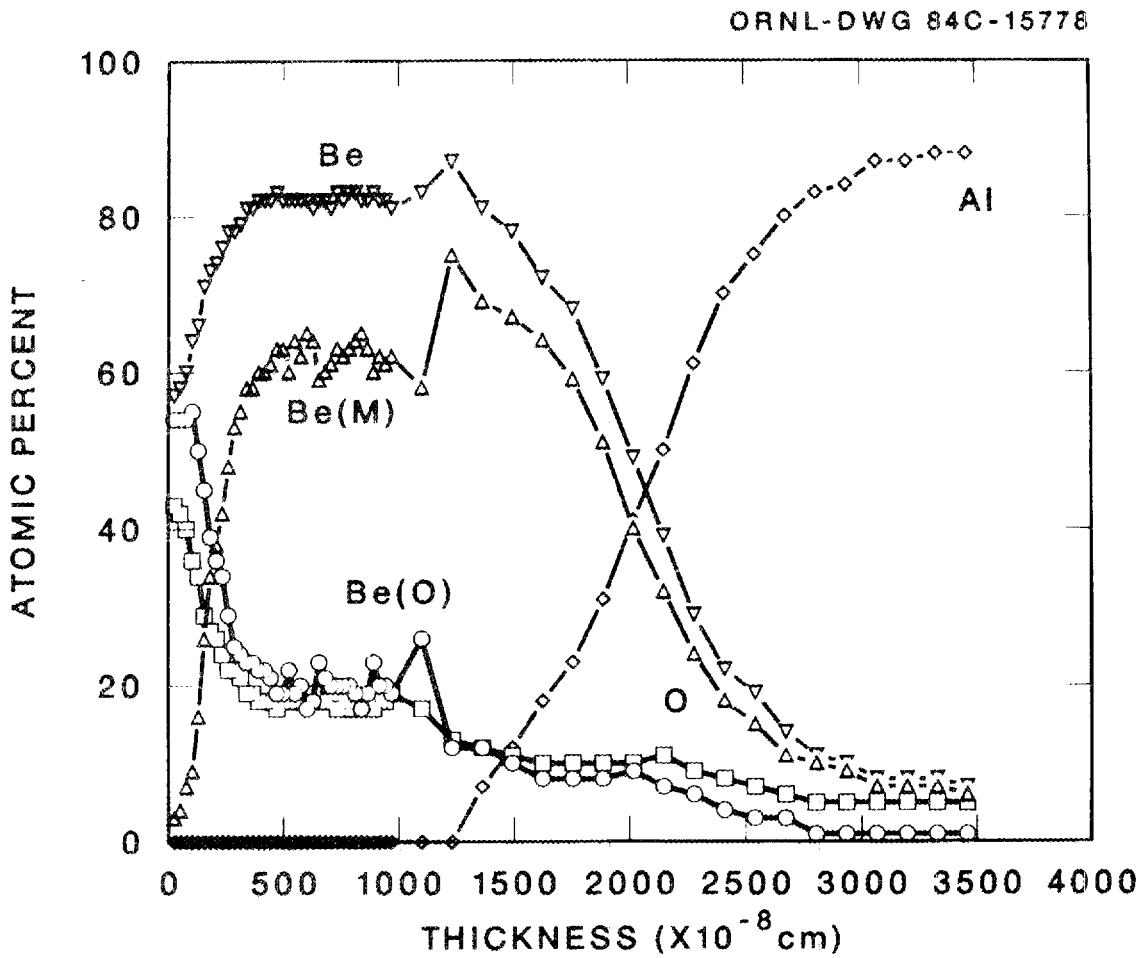

Fig. 5.8. Composition of the surface deposit on an aluminum cube as a function of depth. The cube was exposed to 138 fluence shots at a position 7 cm outside the plasma boundary in the midplane of sector 5. The data shown are for a surface perpendicular to the plasma flow. The film on the front face of the cube (facing the main plasma) was only about one-tenth as thick.

ORNL-DWG 85-7232A

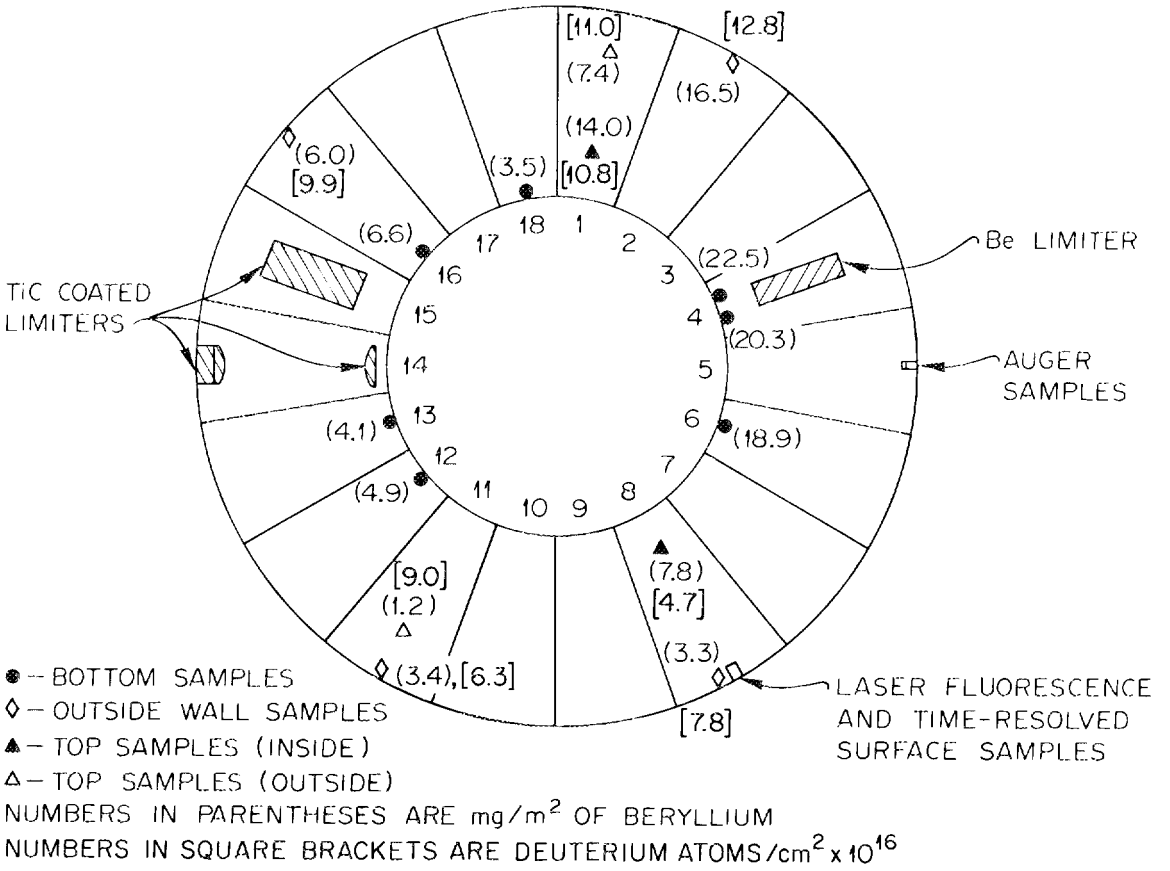

Fig. 5.9. Retention of beryllium and deuterium on long-term samples exposed in the ISX-B tokamak.

REFERENCES

1. R. A. Zuhr and W. R. Wampler, "Time-Resolved Impurity Fluxes in the TEXTOR Plasma Edge," *J. Vac. Sci. Technol.*, accepted for publication (1985).

2. R. A. Zuhr, "Impurity Measurements in the TEXTOR Plasma Edge Using Deposition Probe Techniques," *J. Nucl. Mater.* **122 & 123**, 1193 (1984).

3. J. Roth, J. Bohdansky, and J. B. Roberto, "The Influence of Impurities on the High-Temperature Sputtering Yield of Graphite," *J. Nucl. Mater.* **128 & 129**, 531 (1984).

4. P. W. King and T. B. Cook, "Erosion Measurements at Wall and Limiter-Like Positions in ISX-B using Laser-Induced Fluorescence," p. 5-5 in *Fusion Energy Division Annual Progress Report for Period Ending December 31, 1983*, ORNL-6015, Oak Ridge Natl. Lab., September 1984.

5. T. B. Cook et al., "Time-Resolved Erosion Measurements at a Reference Limiter in ISX-B using Laser-Induced Fluorescence," *J. Nucl. Mater.* **128 & 129**, 253–6 (1984).

6. P. W. King et al., *Time-Resolved Measurements at a Sputtering Target in the ISX-B Scrapeoff Layer using Laser-Induced Fluorescence*, ORNL/TM-9476, to be published at Oak Ridge National Laboratory.

7. R. E. Clausing and L. Heatherly, *J. Nucl. Mater.* **128 & 129**, 855 (1984).

Chapter 6

Plasma Technology

H. H. Haselton, Section Head

F. W. Baity, Jr.
G. C. Barber
D. D. Bates[1]
W. R. Becraft[2]
M. A. Bell[3]
T. S. Bigelow
R. A. Brown[4]
N. B. Bryson[5]
J. B. O. Caughman[6]
G. L. Chen
S. K. Combs
W. K. Dagenhart
J. J. Donaghy[7]
S. C. Forrester
C. A. Foster
C. R. Foust
W. L. Gardner
G. R. Haste, Jr.
P. P. Helton[5]
R. E. Hill[4]
D. J. Hoffman
P. A. Holliday[5]
G. G. Kelley[8]
H. D. Kimrey, Jr.
R. L. Livesey
R. V. Lunsford[4]
B. S. Maxon
K. L. Mays[5]
H. C. McCurdy
R. W. McGaffey[3]
T. J. McManamy[4]
M. M. Menon
S. L. Milora
J. A. Moeller[9]
J. A. Moore[4]
T. L. Owens[10]
K. W. Prince[10]
R. J. Raridon[3]
M. A. Reedy[5]
P. F. Rice[5]
P. M. Ryan
D. E. Schechter
D. D. Schuresko
F. Sluss, Jr.
D. O. Sparks
W. L. Stirling
D. W. Swain
P. B. Thompson[4]
C. C. Tsai
D. Tunison[11]
J. E. Warwick[4]
D. J. Webster[4]
J. H. Whealton
J. A. White[4]
T. L. White
C. L. Wilson[4]
D. H. Wooten[3]
J. W. Wooten[3]
R. E. Wright
W. L. Wright[4]
R. B. Wysor[4]

---

1. Instrumentation and Controls Division.
2. Formerly with General Electric Co., Schenectady, N.Y.; now with Grumman Aerospace Corp., Bethpage, N.Y.
3. Computing and Telecommunications Division, Martin Marietta Energy Systems, Inc.
4. Engineering Division, Martin Marietta Energy Systems, Inc.
5. Section secretary.
6. University of Illinois, Urbana.
7. Washington and Lee University, Lexington, Va.
8. Consultant.
9. Grumman Aerospace Corp., Bethpage, N.Y.
10. McDonnell Douglas Astronautics Co., St. Louis.
11. University of Kansas, Lawrence.

CONTENTS

SUMMARY OF ACTIVITIES 6-5
6.1 NEUTRAL BEAM HEATING 6-6
6.1.1 Positive-Ion, Long-Pulse Source Development 6-6
6.1.2 Negative-Ion Source Development—Abstract of "Intense Li^0 Beam Production with an ORNL SITEX Li^- Source" 6-7
6.1.3 Theoretical Ion Optics—Abstract of "New Accelerator Designs for Positive and Negative Ions" 6-9
6.2 PELLET FUELING 6-9
6.2.1 Pellet Injector Development 6-9
6.2.1.1 Mechanical injector 6-9
6.2.1.2 Pneumatic injector 6-9
6.2.1.3 Tritium pellet injector 6-10
6.2.2 Pellet Fueling Applications 6-16
6.2.2.1 Pellet injection in ISX-B 6-16
6.2.2.2 Pellet injection into ICRF-heated plasmas in PLT: preliminary results 6-17
6.2.2.3 Pellet injection in Doublet III 6-20
6.2.2.4 Pellet injection in TFTR 6-21
6.3 RF HEATING 6-22
6.3.1 National RF Research and Development Program 6-22
6.3.2 RF Development Technology 6-23
6.3.3 RF Theoretical Support 6-24
6.3.3.1 Theory of feedthroughs: wave transmission and voltage characteristics of high-power current feeds for ICRH 6-24
6.3.3.2 Multidimensional waveguide, cavity, and feedthrough calculations for the design of multimegawatt ICRH launchers 6-25
6.3.4 The ORNL RF Test Facility 6-30
6.3.4.1 Introduction 6-30
6.3.4.2 Status 6-32
6.4 GYROTRON DEVELOPMENT 6-33
REFERENCES 6-36

6. PLASMA TECHNOLOGY

Summary of Activities

The Plasma Technology Section continued its work in the areas of neutral beams, pellet fueling, rf heating, and gyrotron development.

Development and testing of the Advanced Positive Ion Source were successfully completed. Beam pulses at energies up to 80 keV, currents up to 48 A, and durations up to 30 s with hydrogen as the working gas were achieved at the Medium Energy Test Facility with a high degree of reliability. The source was further tested with deuterium as the working gas at the Neutral Beam Engineering Test Facility of the Lawrence Berkeley Laboratory, where its high atomic ion fraction and low beam divergence were confirmed. Two-dimensional (2-D) ion optics codes were used to design accelerator structures that will increase the available beam current density while maintaining low beamlet divergence for both positive- and negative-ion beams. A three-dimensional code that was developed allows design of an optimized cesium converter and accelerator geometry for a negative-ion source operating in an applied magnetic field.

Development and application of pellet injectors proceeded at a rapid pace in 1984. A mechanical centrifuge-type injector that can inject 1.3-mm-diam deuterium pellets at speeds of up to 800 m/s and repetition rates of up to 40 pellets/s was operated on the Doublet III tokamak at GA Technologies, Inc. An upgrade version has been designed to deliver pellets 1.5–3.5 mm in diameter at speeds of 1200 m/s and repetition rates of 30 pellets/s. The repeating pneumatic injector was extensively modified to produce 4-mm-diam pellets; velocities of 1600 m/s for deuterium pellets and 1900 m/s for hydrogen pellets were achieved. This system is scheduled to be shipped to Princeton Plasma Physics Laboratory (PPPL) in early 1985. The preliminary design phase of a tritium pellet injector, intended for use during the $Q = 1$ operation of the Tokamak Fusion Test Reactor experiment at PPPL, was concluded in 1984.

Both theoretical and experimental achievements were made in the area of component development for the application of rf heating of plasmas. ORNL continued in its role of lead laboratory for ion cyclotron resonant frequency (ICRF) heating component development. Progress was made in the development of a single-tube rf power source that will deliver over 2 MW of power in the frequency range from 40 to 80 MHz. The Plasma Technology Section is also coordinating the complementary ICRF research at other institutions. Antennas for ICRF heating have been built and tested, resulting in the improvement of our analytical models and the increase of the power-handling capability of such structures. Development of Faraday shields, structures designed to protect antennas from plasmas while providing proper electromagnetic wave polarization, proceeded in two directions. Experiments were conducted on the geometry of the shields to optimize rf power coupling to the plasma while providing suitable protection for the antenna. Testing of materials for

the shields was also carried out; the electrical, thermal, and mechanical properties of various materials and bonding techniques were ascertained by subjecting samples to high-heat-flux hydrogen ion beams. Improved current feedthroughs, which couple rf power through the wall of an experimental device, were successfully developed. Careful design, aided by a 2-D Poisson solver, resulted in feedthroughs with lower voltage standing-wave ratios, allowing more power to be transmitted. The Radio Frequency Test Facility, a simple magnetic mirror using superconducting magnets and microwave plasma production, was approved in 1984, and construction has started. This facility will provide the plasma environment necessary for testing high-power, steady-state rf heating components.

The contracts with Hughes Electron Dynamics Division and with Varian Associates to develop 60-GHz gyrotrons came to successful conclusions during 1984. A contract was let with Varian Associates for a gyrotron power source that will operate at 140 GHz; it will use two 100-kW cw tubes.

6.1 NEUTRAL BEAM HEATING

6.1.1 Positive-Ion, Long-Pulse Source Development

The Advanced Positive Ion Source (APIS) development was successfully completed this year. A brief summary of the work is included here; details are available in a recent publication.[1]

The long-pulse ion source, designed to deliver 80-keV hydrogen ion beams with low beamlet divergence ($\theta_{rms} = 0.26°$) at a current density of 0.19 $A \cdot cm^{-2}$, was operated to meet the design specifications. Hydrogen ion beam pulses of 40–48 A were extracted at beam energies of 77–80 keV and a pulse length of 30 s. The rectangular accelerator (13 by 43 cm) provided an effective emission surface of 250 cm^2, which translates to 47.5 A at the design current density. The beamlet divergence was estimated from beam profiles measured 370 cm downstream. After corrections were made for imperfect steering effects due to manufacturing errors and the effect of residual magnetic fields at the test facility, the beamlet divergence was found to be 0.3°, in agreement with the numerical design. Other characteristics measured were very low accelerator heat loadings (the sum of all four grid loadings was 0.7% of the extracted beam energy), high power transmission efficiency (>85%), and low gas flow (10–12 torr·L/s).

Apart from the excellent optical characteristics of the beam, an important feature of the ion source was its reliability and ruggedness during long-pulse operation. About 600 30-s-long pulses and thousands of multisecond pulses were extracted at a power level of around 3.2 MW. A sample from this test sequence is shown in Fig. 6.1. A simple electronic circuit was used to turn the beam back on after a time delay of 150 ms (limited by the circuit components) if a breakdown occurred during the 30-s pulse duration. A histogram illustrating the percentage of shots at full power vs the interrupt frequency is shown in Fig. 6.2. It shows that approximately one-third of the pulses have no interrupts at all, with the average number of interrupts during a 30-s pulse being only 1.5.

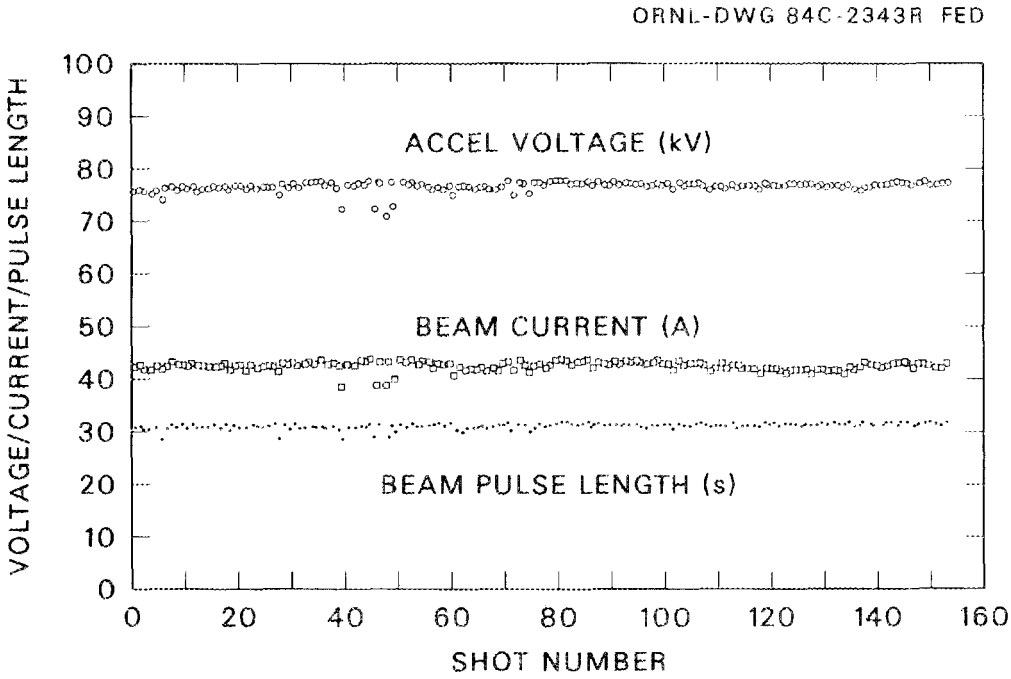

Fig. 6.1. Reliability plot showing the beam parameters vs shot sequence.

The ion source was also operated with deuterium as the working gas at the neutron-shielded Neutral Beam Engineering Test Facility, located at Lawrence Berkeley Laboratory. The optimum deuterium current at 80 keV was measured to be 33 A, in agreement with the inverse square-root scaling of current density with atomic mass. Using their optical mass analyzer (OMA), based on Doppler shift spectroscopy, the full-, half-, and third-energy species mix obtained was 76.6%:16.7%:6.6% from the blue-shifted spectrum and 80.4%:14.8%:5.8% from the red-shifted spectrum. The oxygen impurity was found to be below the sensitivity of the OMA (<0.1%).

In summary, a high-power (3.2-MW), quasi-steady-state ion source, with excellent optical characteristics (beamlet divergence of 0.3°) and high reliability has been developed for multisecond neutral beam injection applications.

6.1.2 Negative-Ion Source Development—Abstract of "Intense Li^0 Beam Production with an ORNL SITEX Li^- Source"[2]

W. K. Dagenhart and W. L. Stirling

H^- beams of 625 mA, 18 keV, and 9 s, as well as D^- beams, have been generated at a 10% duty cycle using the ORNL SITEX (surface ionization by transverse extraction) source.[3] In a similar manner we propose to produce intense Li^- beams for acceleration and neutralization to be used in a charge-exchange alpha particle diagnostic scheme for fusion reactors. Li^- ions would be generated by Cs^+ (generated in a reflex discharge) sputtering of lithium absorbed on the converter, which is biased −150 V with respect to the anode.

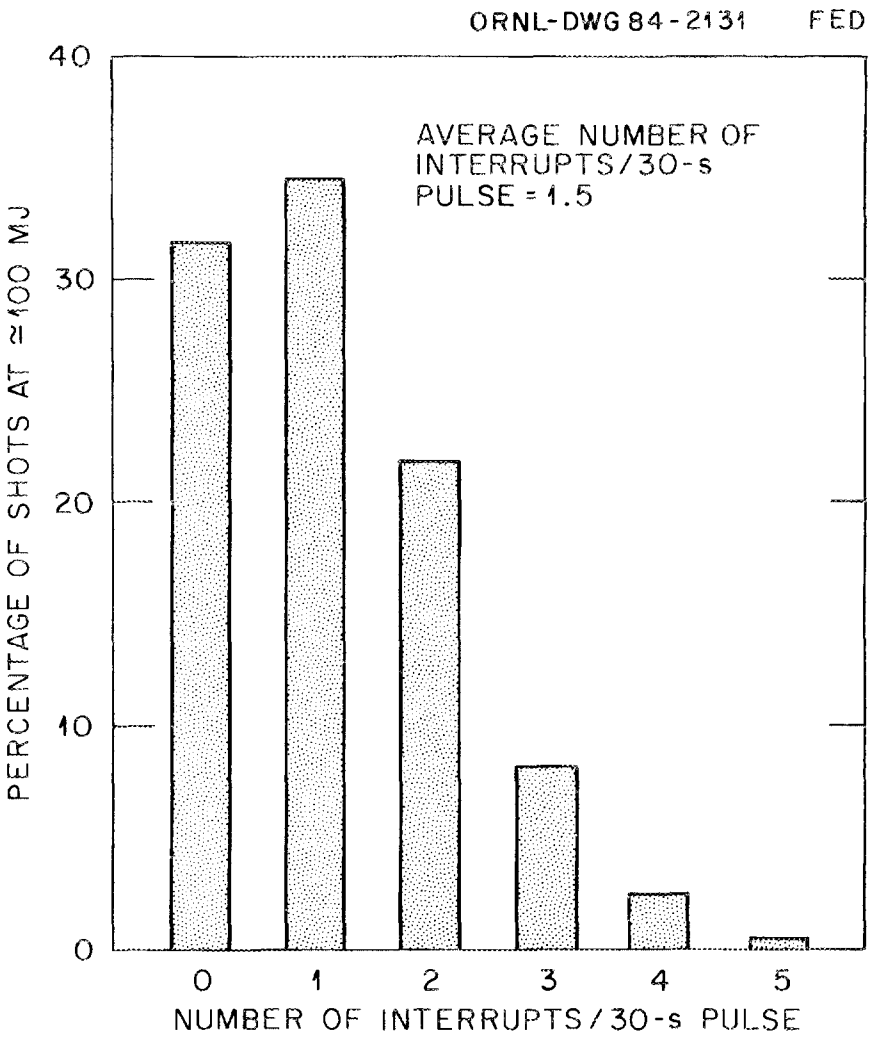

Fig. 6.2. Interrupt frequency vs percentage of shots at full power and pulse length.

The scaled extracted electron to Li^- current ratio would be <5%, with all extracted electrons being recovered at an energy of 0.1 of the first acceleration gap potential energy difference. The arc efficiency should scale to 5 kW of source power per ampere of Li^- beam. Direct-current acceleration with a multiple grid system will be used to 100 keV with a small angular divergence and an emittance suitable for injection into an RFQ-LINAC system for a final energy of ~15 MeV. We expect the Li^- output to scale to ~100 mA, which will be required for the next-generation tokamak alpha particle diagnostic.

6.1.3 Theoretical Ion Optics—Abstract of "New Accelerator Designs for Positive and Negative Ions"[4]

M. A. Bell, J. H. Whealton, R. E. Raridon, D. H. Wooten, and R. W. McGaffey

For positive ions extracted from a plasma, several two-dimensional (2-D) cylindrically symmetric designs are proposed using the ORNL ion optics code.[5,6] These designs ensure higher current density than that of ref. 7 with low divergence and are important for Tokamak Fusion Test Reactor (TFTR), Doublet III (DIII), and Tandem Mirror Fusion Test Facility applications. For negative ions using the configuration of the ORNL SITEX ion source, a 2-D design is proposed which yields much higher beam current and converter utilization than that of ref. 8.

6.2 PELLET FUELING

The focus of the ORNL development program in pellet fueling was on advancing the state of the art of pneumatic and centrifuge pellet injectors to higher velocity, larger pellet size, and steady-state operation, consistent with the pellet fueling needs of present and near-term confinement systems such as TFTR, Big Dee, and the Advanced Toroidal Facility (ATF). The appropriate vehicles for achieving these objectives are the ORNL repeating pneumatic injector (RPI) and the centrifuge upgrade facility presently under construction at ORNL.

6.2.1 Pellet Injector Development

6.2.1.1 Mechanical injector

A new version of the centrifuge injector, which was recently tested on DIII, was designed, and construction was initiated. This device is designed to be a primary fueling device for the large, long-pulse tokamaks now operating or under construction, such as TFTR, JT-60, Tore Supra, and Big Dee. The design parameters for this device are a pellet size of 1.5–3.5 mm, a speed of 1.2 km/s, and a repetition rate of 30 pellets/s for a pulse length of 30 s.

6.2.1.2 Pneumatic injector

The RPI has been modified extensively and tested over a broad range of operating parameters and geometrical configurations. A fast propellant valve compatible with high temperature and tritium operation was developed for use in TFTR. An injection-line shutter valve (conductance limiting) based on this design was incorporated in the TFTR system. A new vacuum housing for improved access to the gun cryostats was installed, and the manual control system was replaced by an automated, menu-driven system that uses a

VAX mainframe computer for data acquisition and display and an Allen-Bradley programmable logic controller for machine operation. A remotely operable and instrumented gas manifold system was incorporated to facilitate operations at TFTR.

The objective of the test program for the RPI was to demonstrate the production of 4-mm-diam pellets (in deuterium) at a 1500-m/s muzzle velocity. Gun barrel length optimization studies (Fig. 6.3) were completed for a nominal pellet diameter of 3.4 mm. Acceleration lengths of 20, 40, 60, 80, and 100 cm were tested. A broad optimum was found in the 60- to 100-cm range, and velocities as high as 1550 m/s were recorded at the maximum operating pressure of 93 bar. The tests of the 4-mm-diam pellet configuration (Fig. 6.4) were performed with an 80-cm-long gun barrel. The highest measured velocities were 1600 m/s with deuterium pellets and 1900 m/s with lighter hydrogen pellets. The injector was also operated in the repeating mode in this configuration. Repetition rates as high as 6 pellets/s for 2.5-s bursts in hydrogen and 5 pellets/s for 4-s bursts in deuterium were reached. The complete system, including the stand-alone controls package, is to be qualified at these parameters and then shipped to Princeton Plasma Physics Laboratory (PPPL) in March 1985.

6.2.1.3 Tritium pellet injector

The preliminary design phase of a tritium pellet injector (TPI) for TFTR was concluded in 1984. The injection system, which is scheduled for use during the $Q = 1$ operation of TFTR in 1988, features a pneumatic injector capable of delivering eight

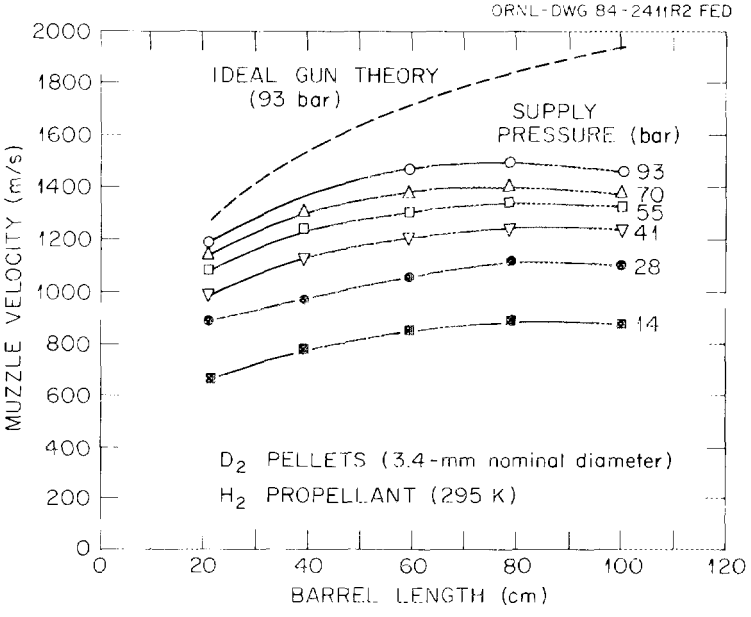

Fig. 6.3. Results of gun barrel length optimization studies, showing muzzle velocity vs barrel length. The results of the ideal gun theory are shown for comparison.

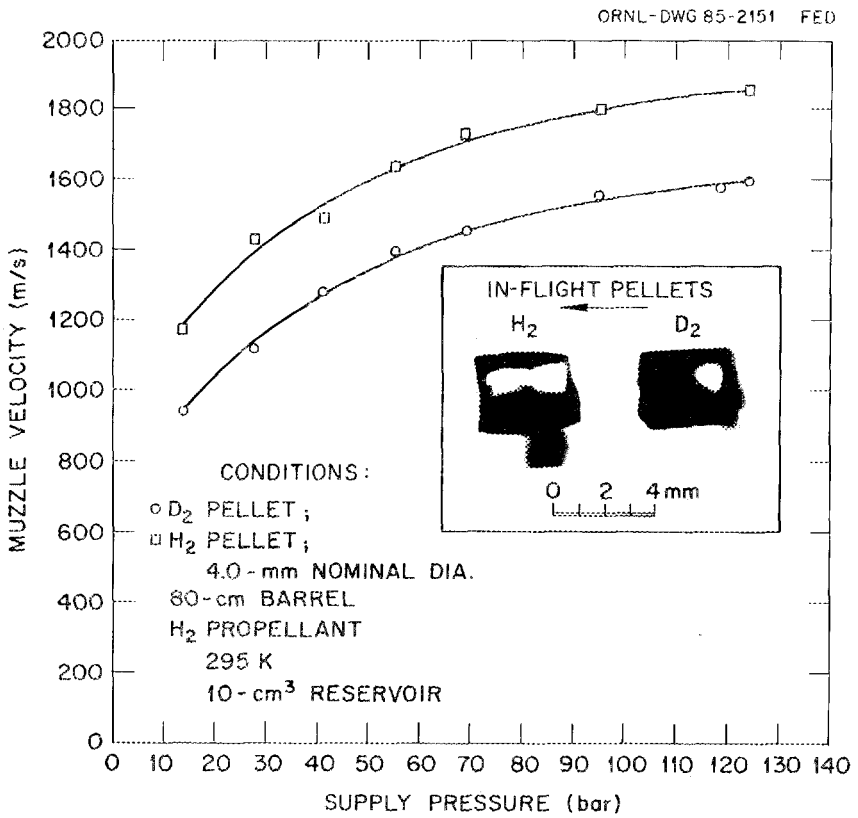

Fig. 6.4. Muzzle velocity vs supply pressure for 4-mm-diam hydrogen and deuterium pellets.

tritium [or deuterium-tritium (D-T)] pellets of variable size (up to 4 mm) and velocity (up to 1500 m/s). The gun design shown in Figs. 6.5 and 6.6 is based on the parameters achieved on the ORNL RPI (high-pressure H_2 propellant). The pellet feed mechanism features (1) a small-volume extruder to minimize the tritium inventory (less than 5000 Ci), (2) a He^3 separator to purify the T_2 gas feed, and (3) extraction of the tritium not used during a pulse.

The materials and components used in the pellet injector, injection line, and vacuum systems are compatible with tritium service and high neutron fluences. Secondary containment is provided by a large glovebox structure (see Fig. 6.7) equipped with maintenance ports for access to the injector components. Three separate TFTR gas cleanup systems (Fig. 6.8) provide for purification of the glovebox atmosphere and safe disposal of gaseous wastes from the pellet injector and vacuum systems.

ORNL-DWG 85-2859 FED

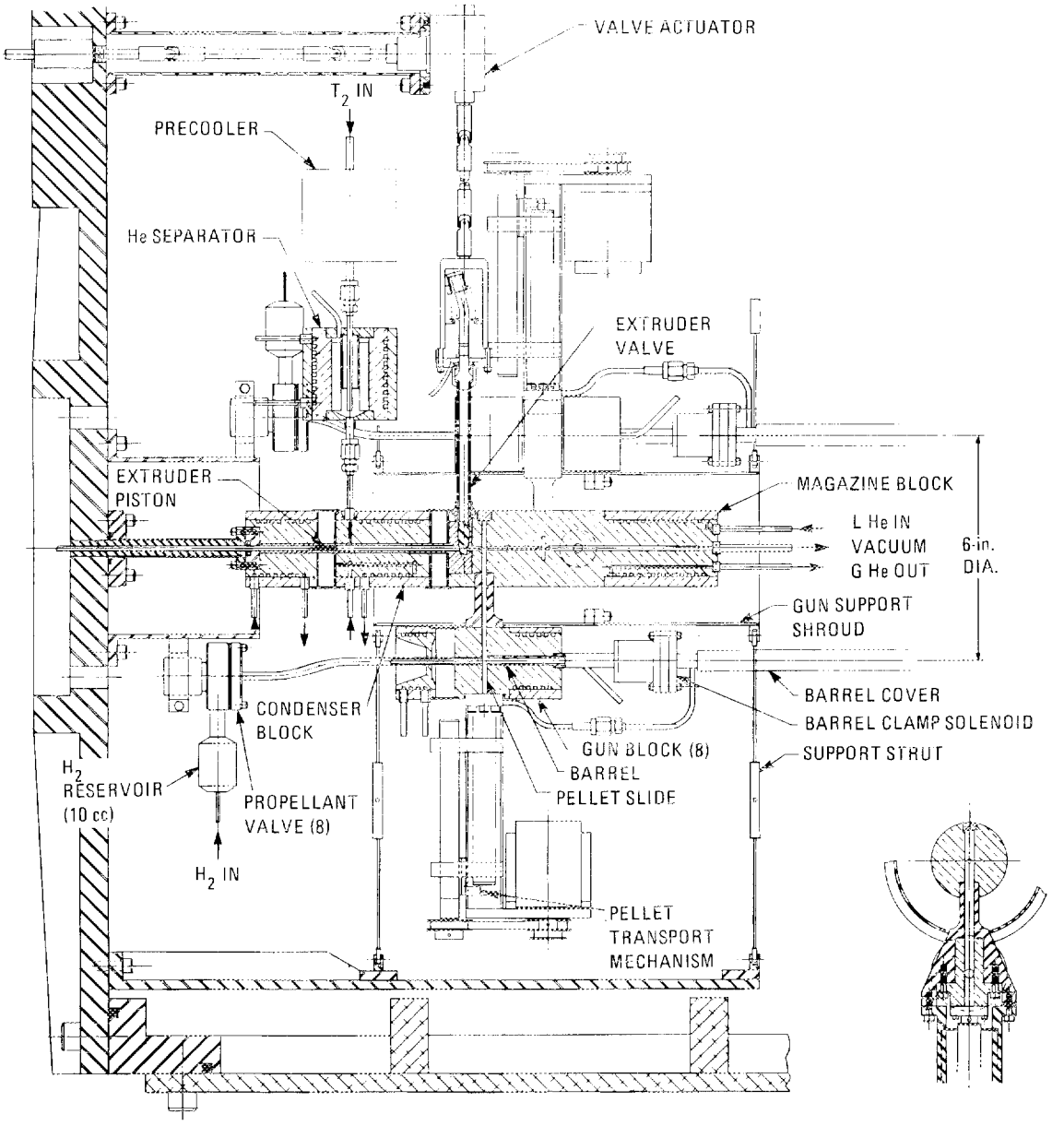

Fig. 6.5. Side view of TFTR tritium pellet injector, showing solid T_2 extruder, He^3 purifier, central magazine, and separate guns.

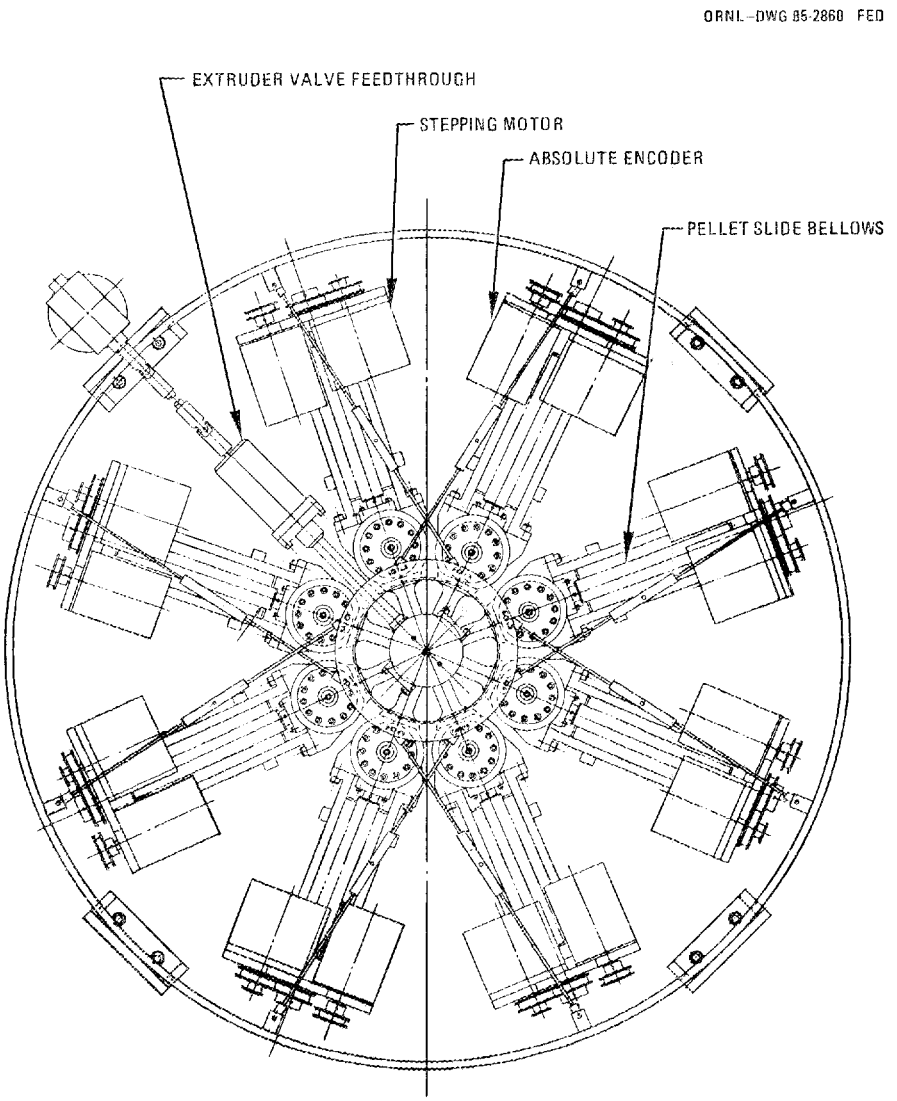

Fig. 6.6. Top view of TFTR tritium pellet injector.

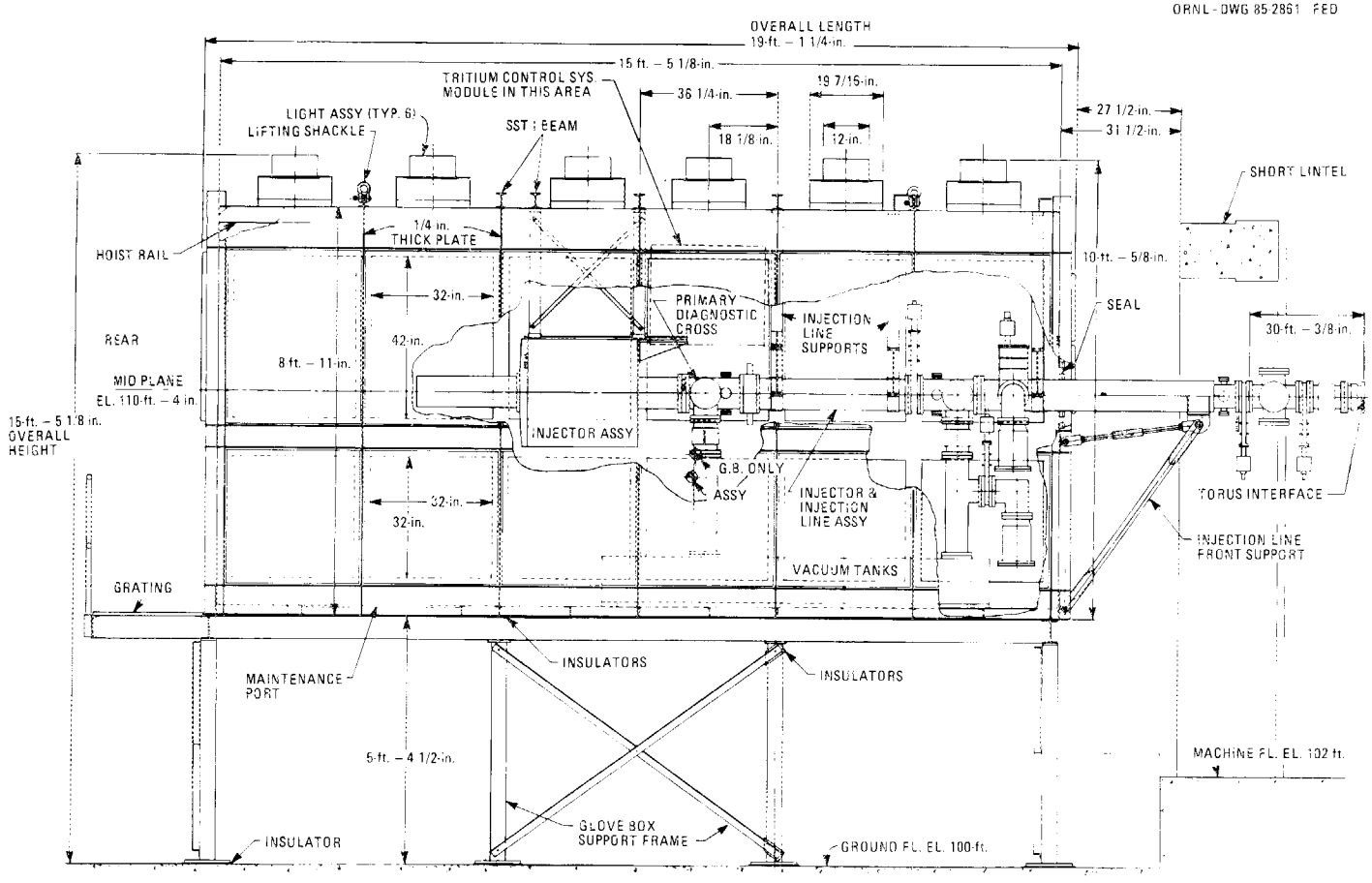

Fig. 6.7. Tritium pellet injection system, showing glovebox/support structure, pellet injector and injection line, and tritium-compatible vacuum systems.

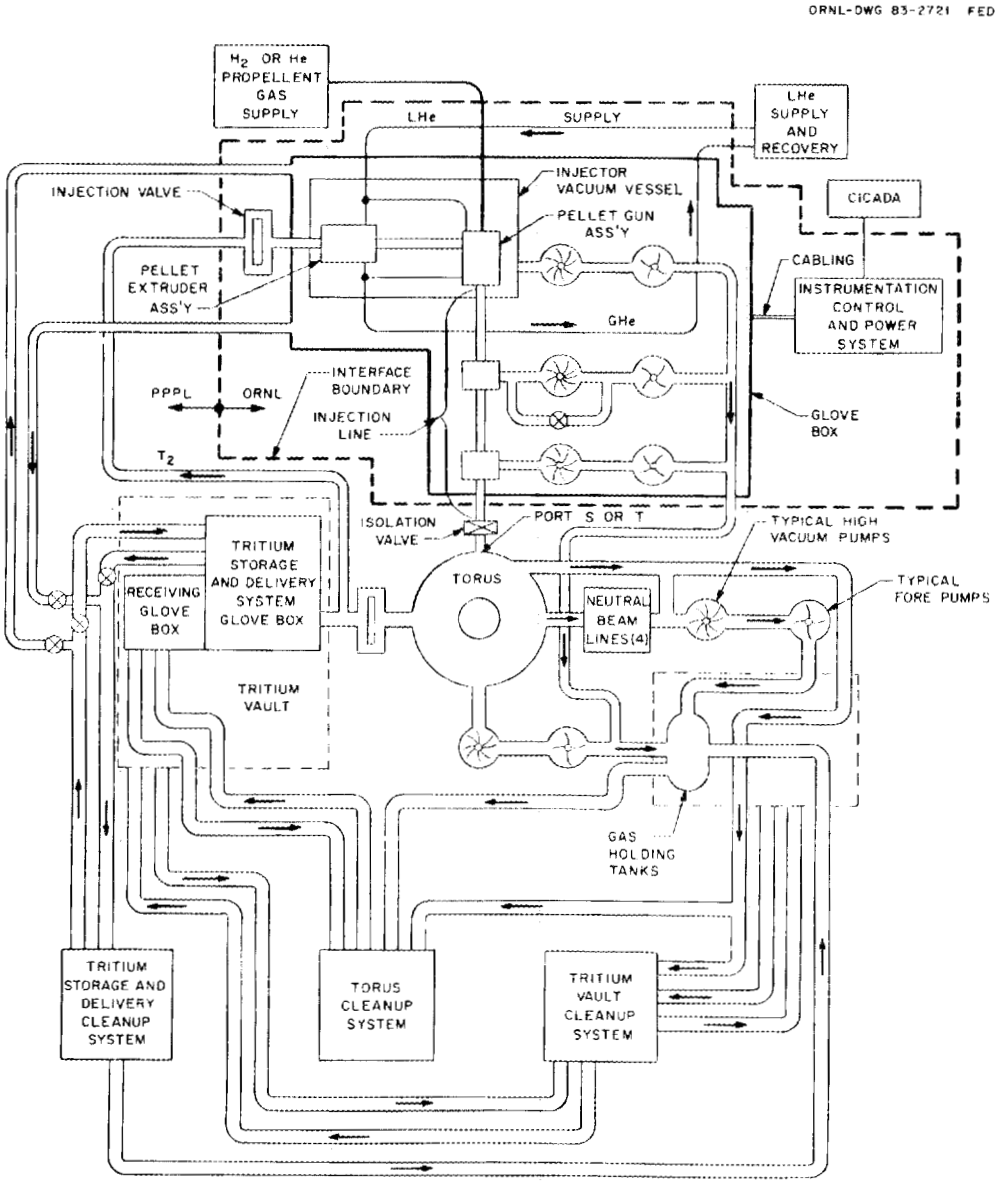

Fig. 6.8. Interfaces between tritium pellet injector and TFTR tritium handling systems.

6.2.2 Pellet Fueling Applications

6.2.2.1 Pellet injection in ISX-B

Improvements in plasma performance with pellet injection have been achieved in several tokamaks in recent experiments.[9–13] On the Impurity Study Experiment (ISX-B), an increase in plasma energy by as much as 50% has been observed following pellet injection. With 1.5-mm pellets, the value for τ_e^*, the gross energy confinement time determined from β_{equil}, has peaked at 1.7 times ISX-B scaling for $n_e = 6 \times 10^{13}$ cm^{-3} in both well-gettered and ungettered discharges.[13] Following the peak, in the well-gettered shots τ_e^* decays to 1.2 times ISX-B scaling within 50 ms after pellet injection. In the ungettered discharges τ_e^* follows the Z-mode scaling that is appropriate to the plasma conditions (P_b = 1.7 MW, I_p = 180 kA). Thus, pellet injection in ISX-B shows energy confinement better than that for gas puffing in clean discharges and matches the Z-mode improvement obtained in ungettered discharges.

Various explanations for the physics of this confinement improvement have been proposed, such as improvements in ion or electron confinement following pellet injection or a reduction in beam charge-exchange losses with pellets in neutral-beam-heated shots. Data from two plasma shots (a = 20 cm, I_p = 120 kA, P_b = 0.8 MW), each with injection of a single 1.0-mm hydrogen pellet, are shown in Figs. 6.9 and 6.10. The first shot (Fig. 6.9) shows no increase in beta following pellet injection; in contrast, the second shot (Fig. 6.10) shows a 30% increase in plasma energy following pellet injection. As observed for the improved-confinement plasma shots with the larger (1.5-mm) pellets, this shot shows a prompt decrease in the plasma internal inductance l_i, indicating a broadening of the plasma current profile, a change in plasma magnetohydrodynamic (MHD) behavior from sawtooth oscillations to quiescence immediately after the pellet, and a sharp 1-V spike in the loop voltage. Some 25 ms after the pellet, l_i has increased slightly above the preinjection level, and plasma MHD activity has grown to continuous large-scale oscillations (continuous m = 1 activity is observed with the 1.5-mm pellets). This shot also shows an improvement in particle confinement, as evidenced by a postpellet peaking of the line-averaged electron density on all chords.

Trajectory plots of plasma beta vs density for these two shots are shown in Fig. 6.11 overlaid with a comparison gas puff shot. It is clear from the data of Figs. 6.9, 6.10, and 6.11 that the observed plasma energy increase is not the result of a progressive decrease in transport or beam losses with increasing density but is a discrete plasma event triggered by the pellet. From other ISX-B experiments,[12–14] we know that the prerequisites to obtaining confinement improvement with pellets appear to be adequate pellet penetration and a good-quality shot (in terms of MHD) before injection. The H_α emission profiles from the two pellets are shown in Fig. 6.12. Both pellets penetrate far enough into the plasma ($\delta \sim$ 0.9) that the difference in penetration is not likely to be the sole reason for the different post-pellet evolution of these shots. The detailed shapes of the H_α signals and deposition profiles are slightly different, however, perhaps reflecting the pellet's transit through different temperature and density zones. This leads to the conjecture that the random timing of the pellet event relative to the sawtooth oscillation cycle produces post-pellet q profiles that lead to confinement improvement, no confinement change, or disruptions in otherwise

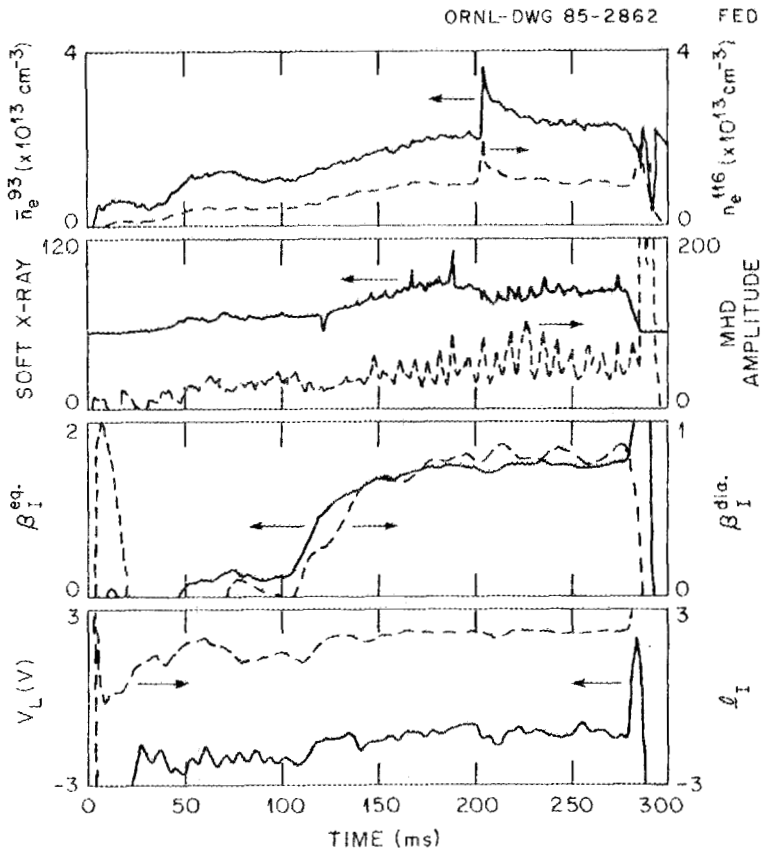

Fig. 6.9. Data from pellet injection into ISX-B plasma, showing no increase in beta following pellet injection.

identical shots. This explanation is consistent with the observation that high-q_{edge} shots (with no sawtooth oscillations) were required in the early ISX-B experiments[14] to produce density evolution similar to that of Figs. 6.9 and 6.10.

6.2.2.2 Pellet injection into ICRF-heated plasmas in PLT: preliminary results

The ISX-B/ATF four-shot pellet injector has been lent to PPPL for installation on the Princeton Large Torus (PLT). The objectives of this effort are to study confinement, heating, and density control in plasmas with high-power ion cyclotron resonant frequency (ICRF) heating and lower hybrid current drive (LHCD). Preliminary results obtained by injecting 1.5-mm-diam D_2 pellets into ohmically heated and low-power (600-kW), ICRF-heated discharges are shown in Figs. 6.13–6.15. In the ohmic shot, the pellet produces a line-averaged density increase from 2.8×10^{13} cm^{-3} to 4.8×10^{13} cm^{-3}, with a corresponding drop in $T_e(0)$ from 1.6 keV to 0.9 keV [Fig. 6.13(a)]. The central-chord visible bremsstrahlung increases 2.5 times, which is consistent with the T_e and $\bar{n}_e$ data and the pre-pellet value for Z_{eff}. In Fig. 6.14(a), one sees that the post-pellet T_e profile is slightly flatter than the pre-pellet profile and that the sawtooth inversion radius has

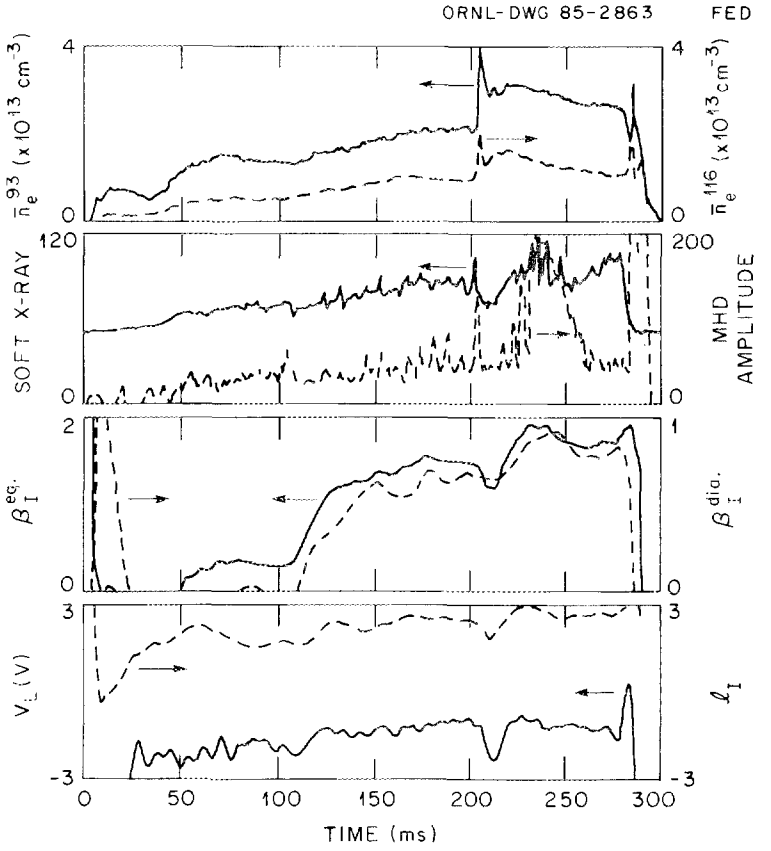

Fig. 6.10. Data from pellet injection into ISX-B plasma, showing a 30% increase in beta following pellet injection.

increased slightly. The sawtooth period has increased 1.5 times, which implies a 50% central density increase assuming constant radiation losses. Figure 6.15(a) shows neutron production, which increases threefold following pellet injection. Like $\bar{n}_e$, neutron production stays elevated for the duration of the shot, indicating good confinement of the particles deposited by the pellet.

Data for an ICRF-heated plasma shot with pellet injection are shown in Figs. 6.13(b), 6.14(b), and 6.15(b). A total of 600 kW of ICRF power at 30 MHz (He^3 minority heating) was brought up at 350 ms into the shot [Fig. 6.13(b)]. The pellet-induced changes in plasma density, central-channel bremsstrahlung, and $T_e(0)$ to the pellet are smaller than for the ohmic shot of Figs. 6.13(a), 6.14(a), and 6.15(a), which is not unexpected, given the additional heat flux to the pellet from fast ions generated by the ICRF heating. Both neutron production [Fig. 6.15(b)] and T_e [Fig. 6.14(b)] climb steadily following pellet injection as long as the heat stays on, a promising indication of improved ICRF heating or plasma confinement following pellet injection. Lengthening the ICRF pulse or applying additional ICRF power following pellet injection could boost neutron production even further.

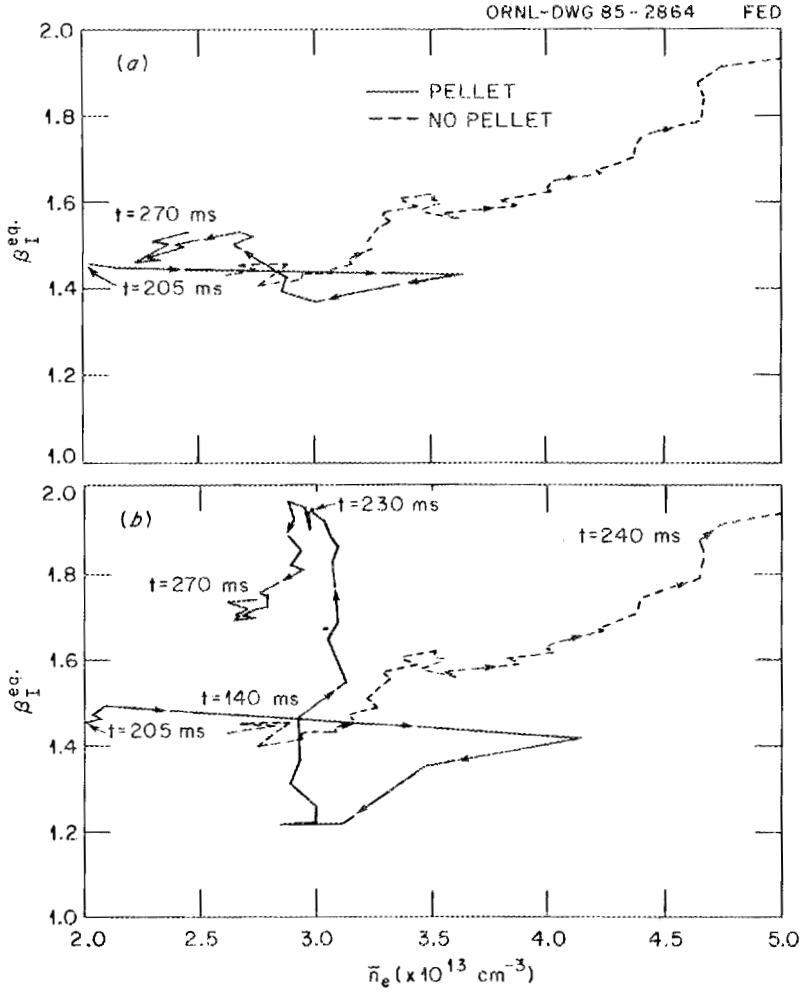

Fig. 6.11. Trajectory plots of plasma density vs beta for the two shots shown in Figs. 6.9 and 6.10. A gas puff shot is also shown for comparison.

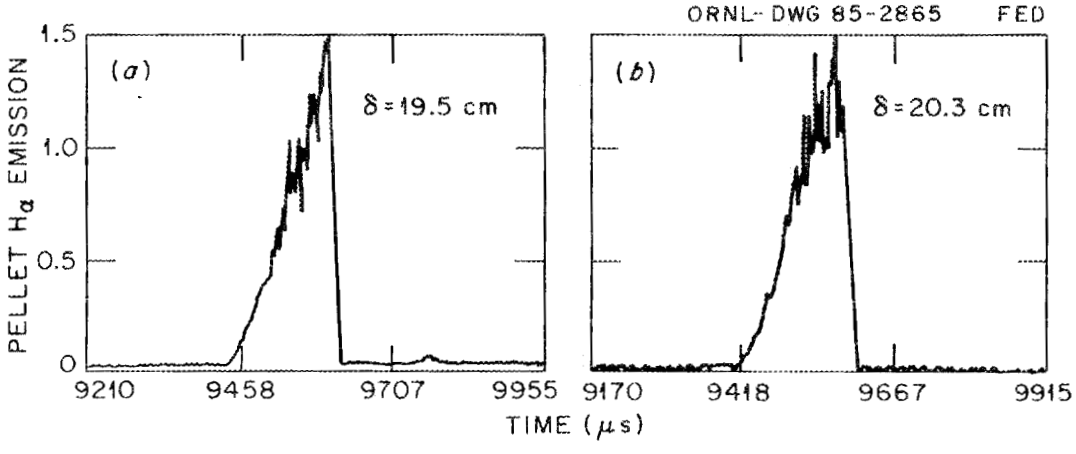

Fig. 6.12. H_α emission profiles for the two shots shown in Figs. 6.8 and 6.10.

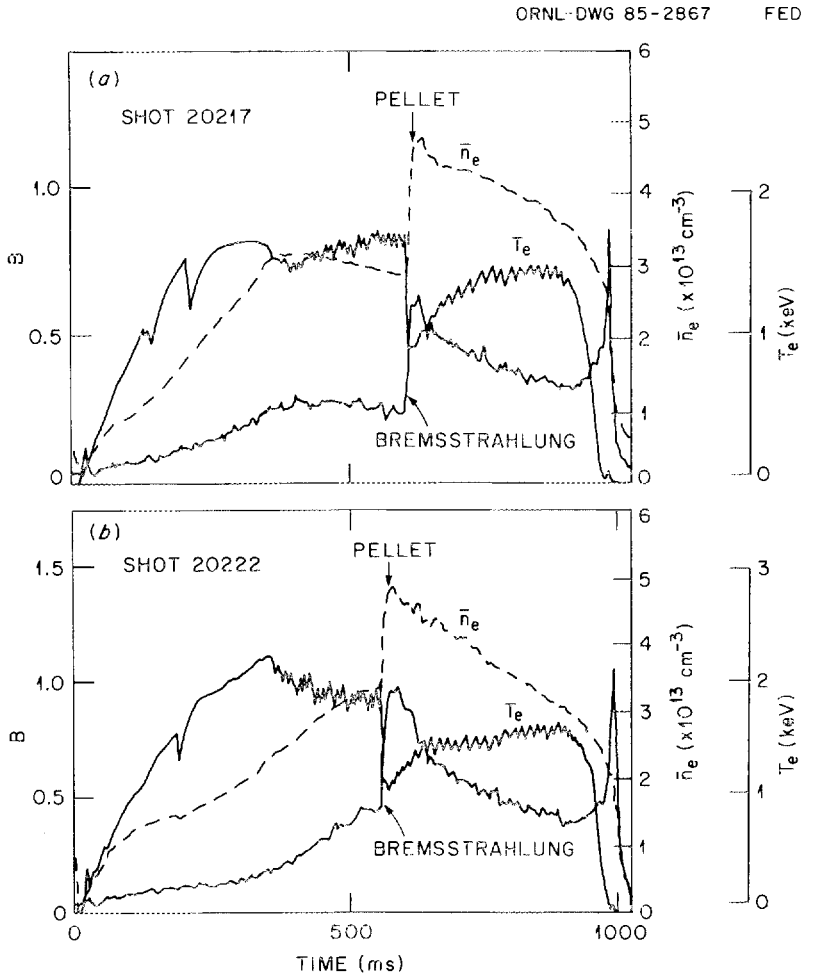

Fig. 6.13. Bremsstrahlung radiation, density, and temperature (measured with electron cyclotron emission) in (a) an ohmically heated and (b) an ICRF-heated discharge in PLT.

6.2.2.3 Pellet injection in Doublet III

A major experiment was performed on the DIII tokamak facility at GA Technologies, Inc., in cooperation with the Japan Atomic Energy Research Institute (JAERI) group. A centrifuge-type pellet injector, which was developed at ORNL, was used to continuously fuel plasmas in both divertor and limiter configurations. The injector could inject 1.3-mm-diam pellets of frozen deuterium at a speed of 800 m/s and a rate of up to 40 pellets/s. The pellet injector was shipped from ORNL in January 1984. Pellet experiments started in April and ran with high reliability through August, when DIII was shut down for a major upgrade. In the divertor-configuration experiments, the plasmas produced with pellets had much higher densities than those produced by edge fueling with gas. This was not surprising, since with gas injection the fuel must pass through the divertor, which is exhausting the plasma, whereas the pellets penetrate through the edge, depositing the fuel in the

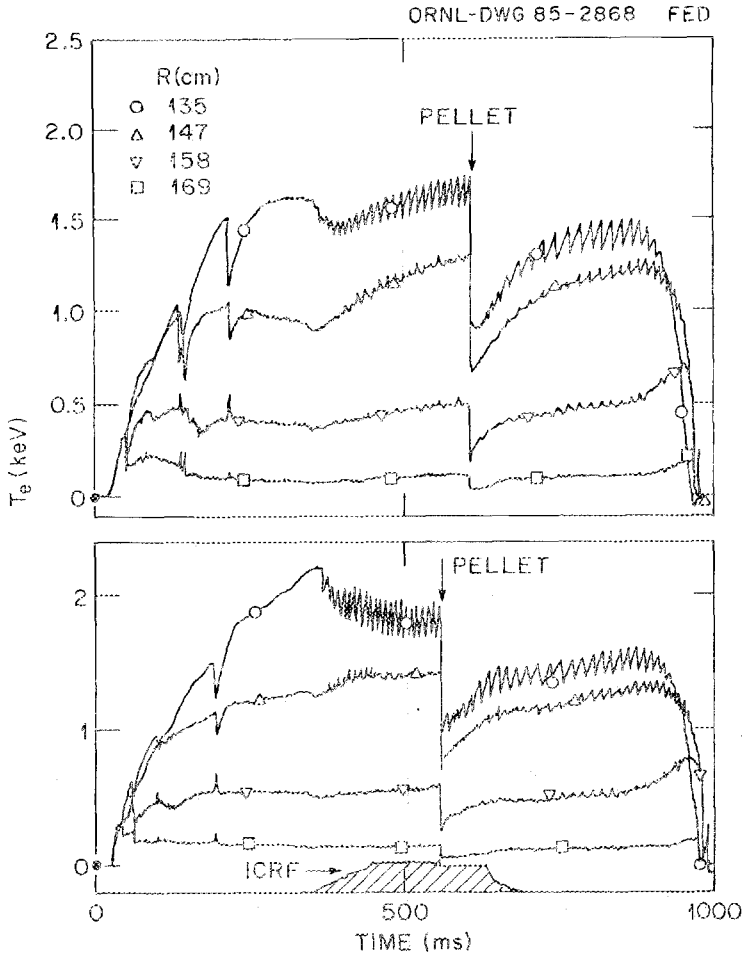

Fig. 6.14. T_e **profile in (a) an ohmically heated and (b) an ICRF-heated discharge in PLT.**

plasma interior. In the limiter configuration, pellet fueling produced superior discharges, especially for plasmas heated with high-power neutral beams. Due to a combination of the peaked density profiles and enhanced energy confinement, the fusion reaction rate in the pellet-fueled plasmas was ten times higher than that in a comparable gas-fueled plasma under otherwise similar conditions. This result is of considerable importance to the successful operation of TFTR, which is also a beam-heated, limiter-type tokamak.

6.2.2.4 Pellet injection in TFTR

Preparations were made for two pellet fueling applications on TFTR in support of the $Q = 1$ demonstration scheduled for 1988. The RPI was modified for use in 1985 in a series of preliminary experiments that will feature (1) injection of a single large pellet (4 mm) at high speed (>1500 m/s) and (2) injection of a burst of pellets (~5 pellets/s for 2 s) at lower speed (1300 m/s) into ohmic and neutral-beam-heated discharges. The

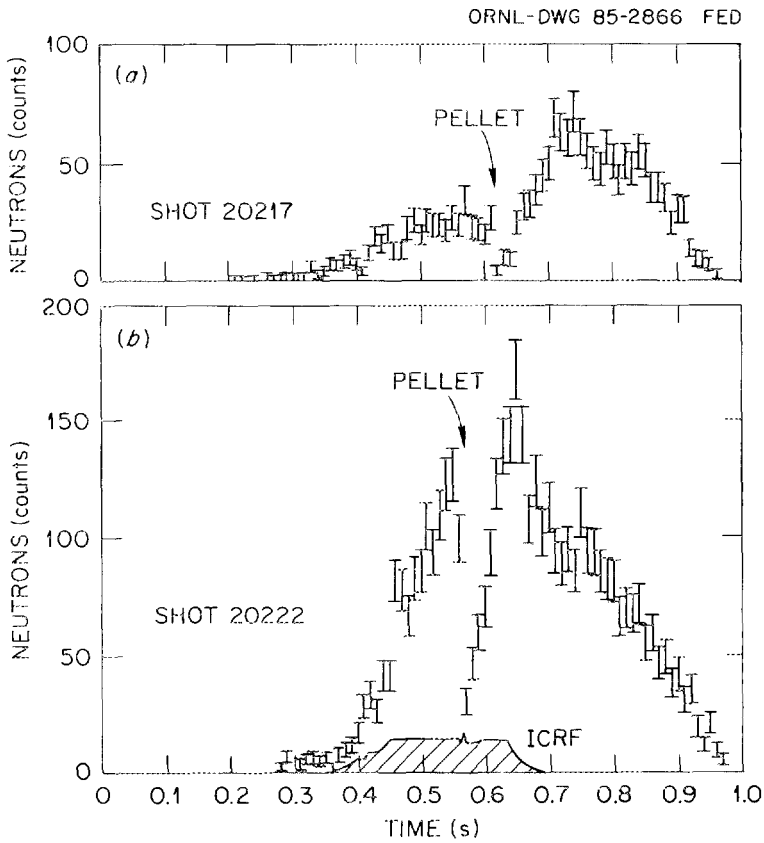

Fig. 6.15. Neutron production in (a) an ohmically heated and (b) an ICRF-heated discharge in PLT.

RPI should adequately meet the TFTR fueling needs through 1985 for neutral beam powers up to 10 MW.

The follow-on experiment to the RPI will feature a high-performance, eight-shot gun that can deliver pellets of varying size at speeds approaching 1600 m/s. This device is being built at ORNL in support of the high-power (27-MW) neutral beam experiments scheduled for 1986.

6.3 RF HEATING

6.3.1 National RF Research and Development Program

The National RF Research and Development (NRFRD) Program encompasses the development of rf technology at ORNL and the coordination of supporting research at some other institutions. The principal goal of the NRFRD Program is to develop and demonstrate the technology necessary to deliver long-pulse (to cw), high-power, ICRF energy to a reactor-grade plasma. The program has three major thrusts: (1) antenna systems development, (2) theoretical support, and (3) test facilities. An additional major

endeavor is the development of an rf power source that can serve as the basic element, or "building block," for the multimegawatt ICRF fusion systems of the future. A system that can provide over 2 MW of power at frequencies of 40–80 MHz with only one output tube is already under development. These capabilities are unmatched by those of any existing or planned system. This equipment, when delivered in May 1986, will be installed to provide for the antenna development tests to be conducted in the Radio-Frequency Test Facility (RFTF). As the designated lead laboratory for ICRF technology developments, ORNL has been carrying out the responsibilities of coordinating other complementary research at other institutions—for example, the waveguide launcher investigations at the University of Wisconsin and JAYCOR.

A critical emphasis of the NRFRD Program activity is the support of near-term fusion experiments with adaptations of ICRF developments. An example is the incorporation of many of the NRFRD antenna system achievements of 1984 into a high-power (>2-MW) launcher that will be tested on the DIII upgrade, DIII-D, in 1986.

Considerable progress in rf technology has been made in the last year. The improved rf system concepts that ORNL has analyzed and developed are expected to lead to an overall improvement of greater than an order of magnitude in the power that can be launched into a fusion device plasma. With future fusion machines expected to need 10–50 MW of rf power, the effectiveness of the rf elements is extremely important in cost and in performance.

6.3.2 RF Development Technology

Antennas for ion cyclotron resonance heating (ICRH) applications have been analyzed and optimized to extend the power limit per antenna by a factor of 2 to 3. Loop variations [simple loop, long loop, cavity, resonant double loop (RDL), asymmetric RDL (ARDL), and U-slot] have been built and studied. High voltage in the antenna structure generally limits the power. The matched RDL minimizes the voltage at the feedpoint. The ARDL not only minimizes the voltage at the feedpoint but also has the lowest voltages of any of the antennas. The electrical characteristics of each antenna and its magnetic field profiles have been measured and agree with simple models.

Faraday shields are used to protect the antennas and to polarize the wave while transmitting power. Experiments on 27 Faraday shields show that the shields in general use typically cut coupling in half and that simple designs can result in virtually no reductions. These optimum Faraday shields, in combination with the optimum antennas, can improve the rf launcher system's power handling by a factor of 6.

We have also tested Faraday shield materials by exposing them to 2000-A, 1-s, 26-kV neutral beam discharges. The heat flux was 4 kW/cm^2. All materials were bonded to a 3/8-in. copper swirl tube with a coolant flow rate of 3 gpm. Materials include copper; electroplated nickel, chromium, gold, and silver; plasma-sprayed TiC nickel, chromium, and aluminum; and brazed POCO graphite. The plasma spray techniques frequently did not offer sufficient conduction. Of particular interest is the graphite, which easily survived the tests with a minimum of erosion. These techniques can also be used for limiters.

The benefits of matched antennas are realized only with a matched feedthrough. High-power, 50-Ω feedthroughs have been built, tested, and modeled. Prototypes have an

insertion voltage standing-wave ratio (IVSWR) of <1.15 for frequencies of <400 MHz. This was well correlated with a 2-D Poisson solver that computes the feedthrough's impedance as a function of frequency. Other models that we have designed and are building are predicted to have an IVSWR < 1.03 for f < 400 MHz. The feedthroughs have been tested to 80 kV for 5 s and 610 A for 1 s with no problems. This is more than sufficient for 1- to 5-MW antennas.

6.3.3 RF Theoretical Support

6.3.3.1 Theory of feedthroughs: wave transmission and voltage characteristics of high-power current feeds for ICRH

J. H. Whealton, R. J. Raridon, D. J. Hoffman, T. L. Owens, M. A. Bell, F. W. Baity, J. L. Bledsoe,* and W. R. Becraft

Using circuit theory and solutions of a scalar 2-D Laplace equation for the electrostatic potential, we examined several feedthroughs for voltage holding, voltage standing-wave ratio (VSWR), and impedance characteristics. Suitable inhomogeneous Dirichlet, scalar boundary conditions were imposed for the potentials for the calculation of the electrostatic fields. The inhomogeneous vector Neumann boundary conditions on the surface of the dielectric were dispatched by use of a conformal mapping.

Several feedthroughs were examined: old PLT designs, designs for TEXTOR, and several ORNL designs that have been built and tested. Some of these feedthrough configurations have been optimized to provide constant 50-Ω impedance or minimum VSWR.

A high-power rf gas-vacuum interface, or feedthrough, is an important component of the rf transmission system. An optimal design must eliminate corona points, as described in ref. 15. It is also desirable to reduce the VSWR as much as possible. We solved Laplace's equation, including boundary conditions for dielectrics, for geometries of interest to determine field stress points. Also solved were differential circuit equations, from which impedances and VSWR are obtained. Some of the feedthroughs of ref. 15 were considered in this light, as were the old TEXTOR design[16] and more recent designs in which the VSWR has been minimized.

Nine feedthrough configurations were examined; geometries are shown in Fig. 6.16. The locations of the dielectrics are also shown. Equipotentials for all nine cases are shown in Fig. 6.17. Impedance as a function of length is shown in Fig. 6.18 for cases 2–6A. Figure 6.19 shows the VSWR for cases 2–6A.

Cases 1 and 2 were used on PLT and are described in ref. 15. Case 3 was used in TEXTOR at Jülich.[16] Cases 4–6 are new ORNL designs. The principal result is embodied in Fig. 6.19. The lower the VSWR, the fewer the voltage breakdowns that will occur in these feedthroughs. Thus, it is desirable to reduce the VSWR value to as close to unity as possible. The VSWRs of cases 4A, 5A, and 6A have been reduced by over an order of magnitude from the reference case 2 described in ref. 15. In addition, cases 4–6A all employ cylinder ceramic insulators that are available off the shelf. Cases 2–6A also avoid

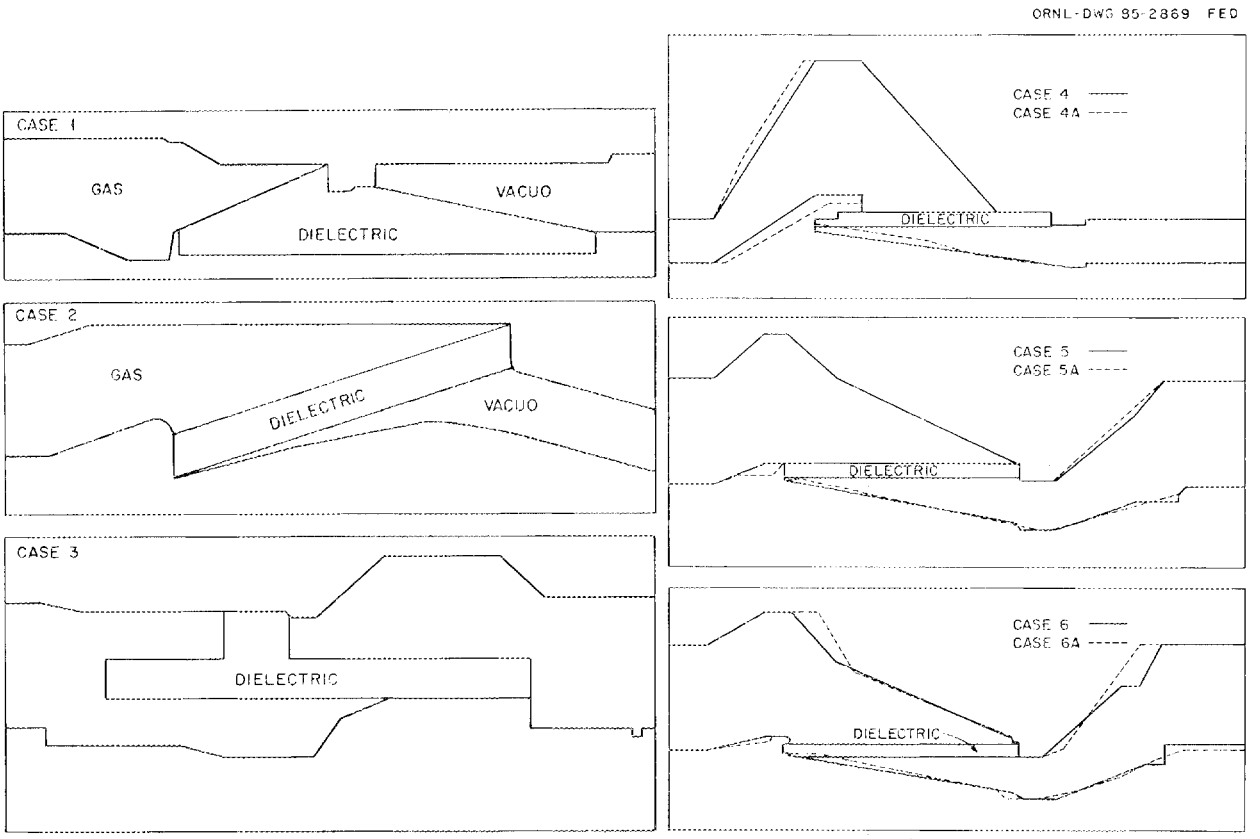

Fig. 6.16. Feedthrough configurations. All geometries are cylindrically symmetric.

corona points, which are shown in Fig. 6.17 for case 1. Therefore, geometries like those of cases 4A–6A are recommended for the most trouble-free feedthroughs for high-power ICRH launching structures.

*Computing and Telecommunications Division, Martin Marietta Energy Systems, Inc.

6.3.3.2 Multidimensional waveguide, cavity, and feedthrough calculations for the design of multimegawatt ICRH launchers

J. H. Whealton, R. J. Raridon, M. A. Bell, D. H. Wooten, R. W. McGaffey, D. J. Hoffman, S. Y. Ohr,* and W. R. Becraft

In a vacuum the three-dimensional (3-D) equations describing the electromagnetic fields of an ICRH launcher structure can be vector linear homogeneous Helmholtz equations for the electric or magnetic fields. These solutions are constrained by $\nabla \cdot \mathbf{E} = 0$. If

ORNL-DWG 85-2870 FED

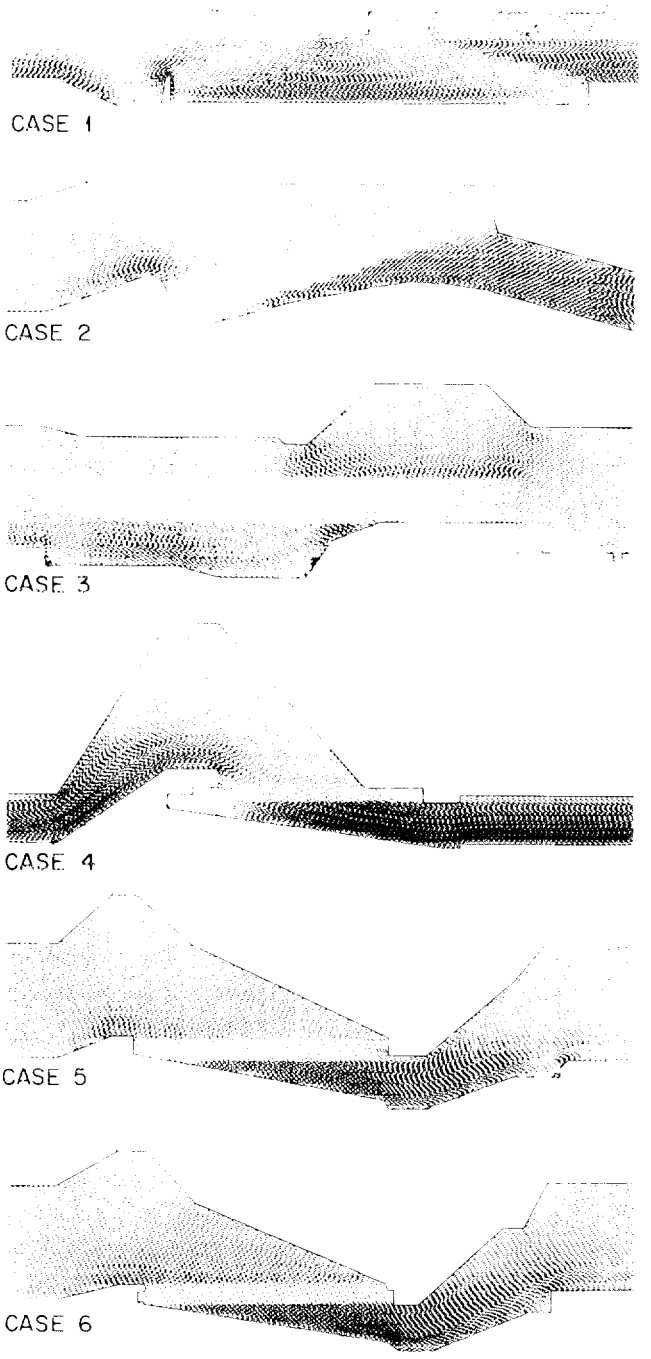

Fig. 6.17. Equipotentials for the feedthrough configurations of Fig. 6.16.

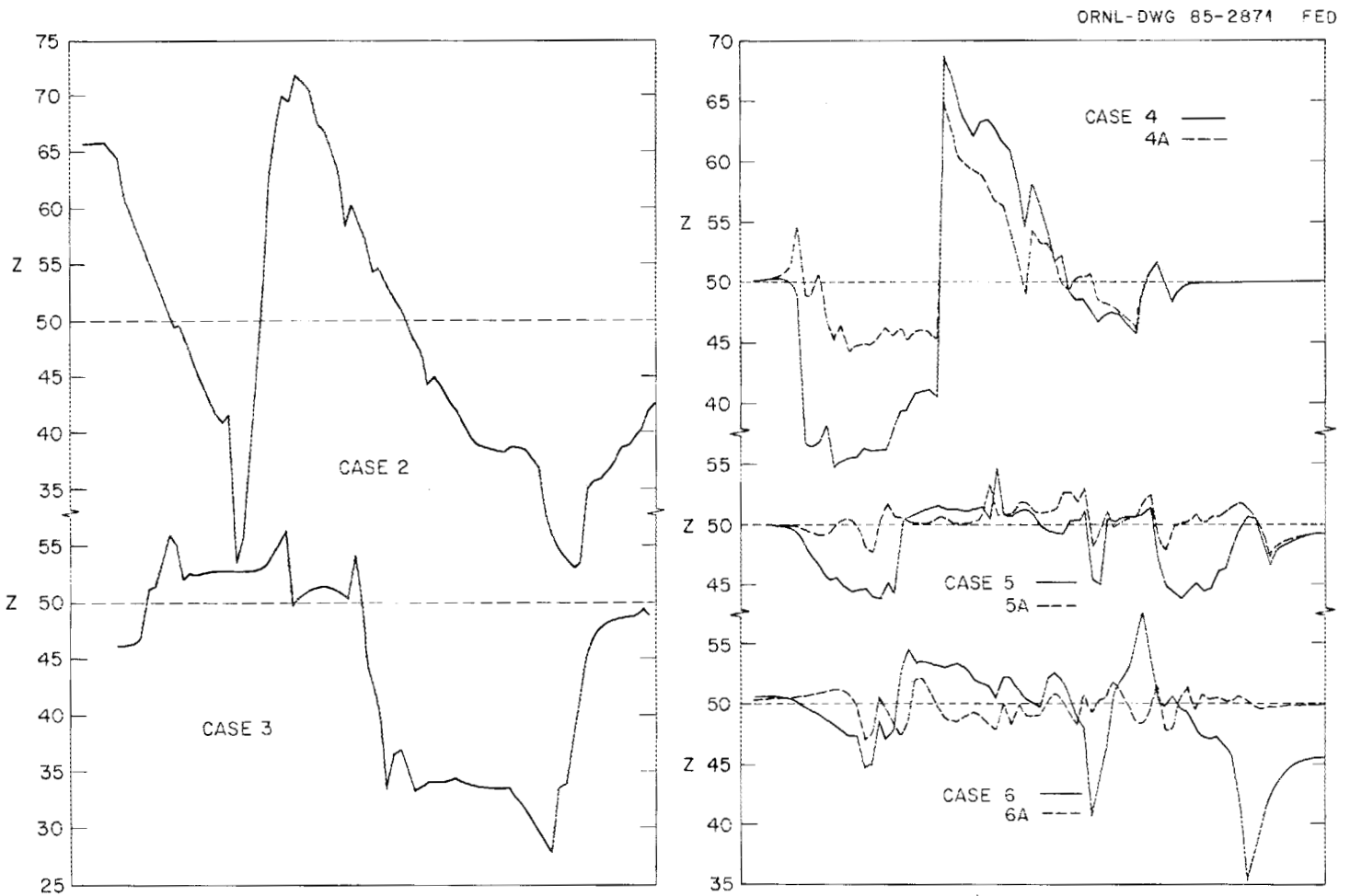

Fig. 6.18. Impedance as a function of length for cases 2–6A of Fig. 6.16.

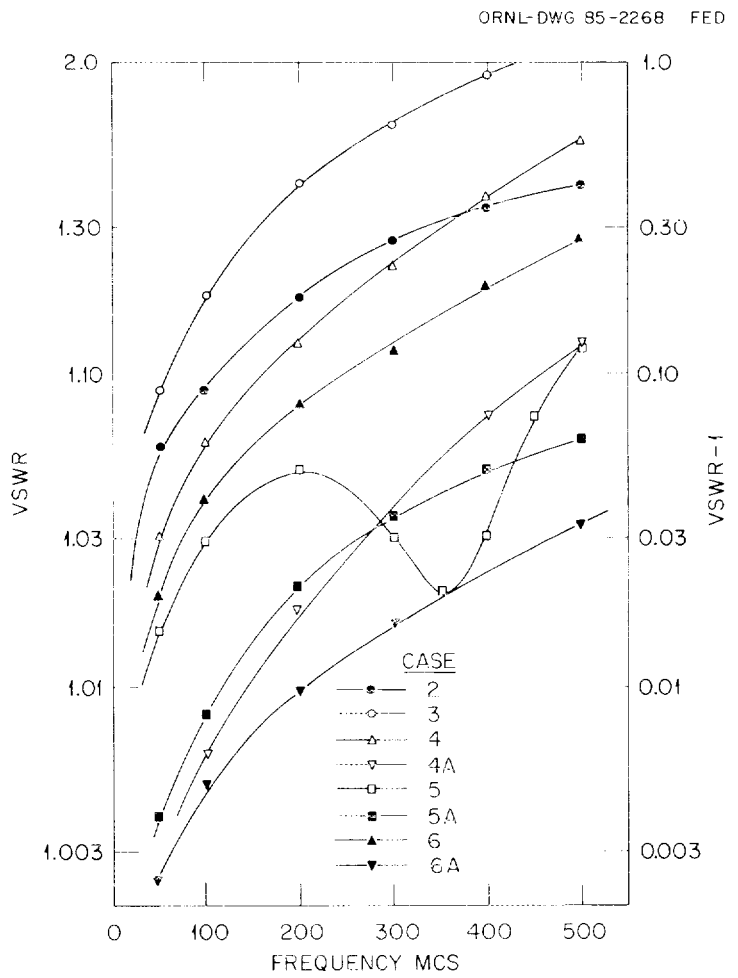

Fig. 6.19. VSWR for cases 2–6A of Fig. 6.16.

the boundary surfaces are normal or parallel to the coordinate surfaces, the boundary conditions are homogeneous Dirichlet or Neumann conditions for ideal metallic conductor boundaries. For boundaries not suitably arranged with respect to the coordinate system, the Neumann boundary conditions are linear inhomogeneous. For driven devices where wall currents are imposed, the Dirichlet boundary conditions are also linear inhomogeneous.

We solve these equations by a straightforward iteration technique that finds the correct eigenvalue and eigenfunction simultaneously. The coefficients of the difference equations are written out of core. The inhomogenous Neumann boundary conditions are iterated until convergence occurs.

An example of a solution with mod-E contours is shown in Fig. 6.20 for a TE mode in a ridge waveguide. A slow-wave launching structure is shown in Fig. 6.21. The device in Fig. 6.22 is similar to that in Fig. 6.21 except that a Faraday shield has been added to protect the antenna from the heated plasma.

We are implementing an algorithm to account for finite wall conductivity by a further iteration. The iteration will start with the solution for infinite conductivity. Wall currents will be computed from the solution to the magnetic field $\nabla \times \mathbf{H} = \mathbf{j}$, near the wall. A parallel electric field on the boundary will be computed from $\mathbf{j} = \sigma\mathbf{E}$, and the inhomogenous boundary condition will be imposed on the solution of the vector Helmholtz equation for $\mathbf{E}$. A new $\mathbf{E}$ and $\mathbf{H}$ will be computed, and the iterative process will continue.

---

*Computing and Telecommunications Division, Martin Marietta Energy Systems, Inc.

ORNL-DWG 85-2872 FED

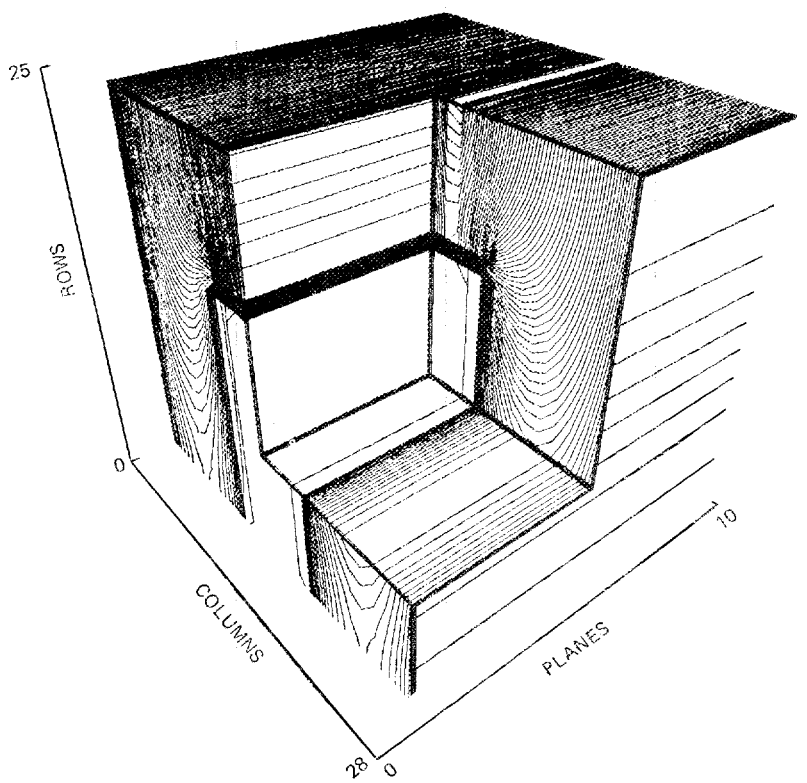

Fig. 6.20. TE mode in a ridge waveguide (2-D configuration).

ORNL-DWG 85-2873 FED

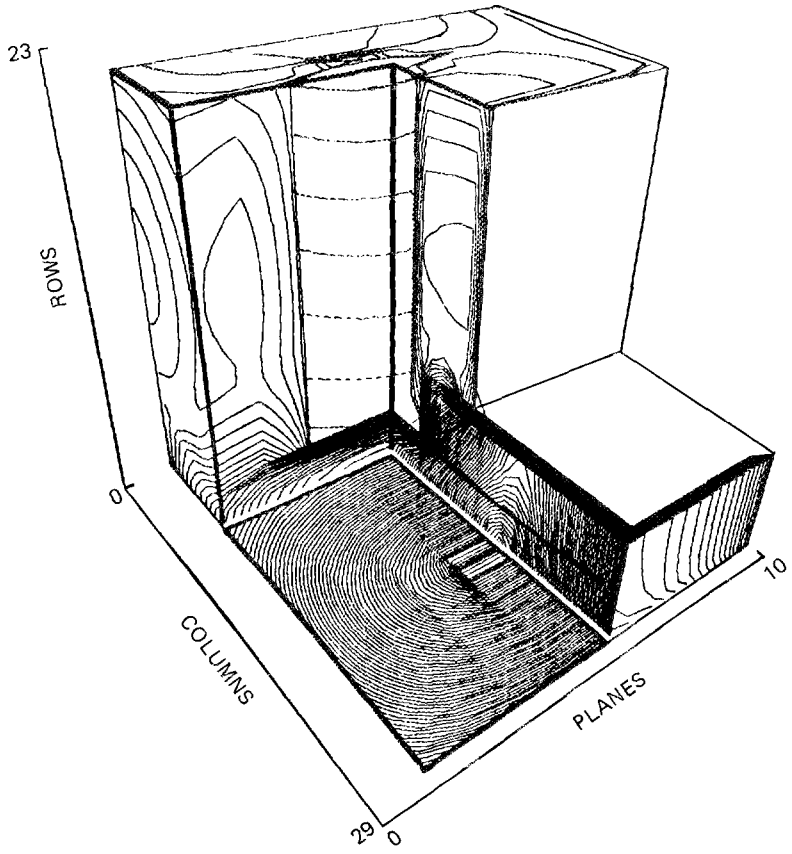

Fig. 6.21. Slow-wave launching structure. The vertical elliptical boundary is a current strap, and a cavity with capacitor plate is attached at the bottom. The structure is in lowest mode with no current in the current strap.

6.3.4 The ORNL RF Test Facility

H. C. McCurdy, W. L. Gardner, F. K. Booth,* G. F. Bowles,† R. A. Brown, J. L. Burke,† P. B. Burn,‡ E. J. Byrnes,† D. B. Campbell,* R. L. Livesey, J. B. Mankin,** T. J. McManamy, J. A. Moeller, J. A. Moore, K. W. Prince, L. A. Ray,* P. M. Ryan, J. P. Schubert,* C. K. Thomas,† R. A. Weaver,†† E. R. Wells,† J. A. White,* T. L. White, and R. E. Wright

6.3.4.1 Introduction

The RFTF is being constructed in Bldg. 9201-2 as a development support tool to provide the necessary environment for testing the high-power, pulsed or cw rf components and systems being developed for applications on plasma confinement devices. The facility is scheduled for completion by September 1985.

ORNL-DWG 85-2874 FED

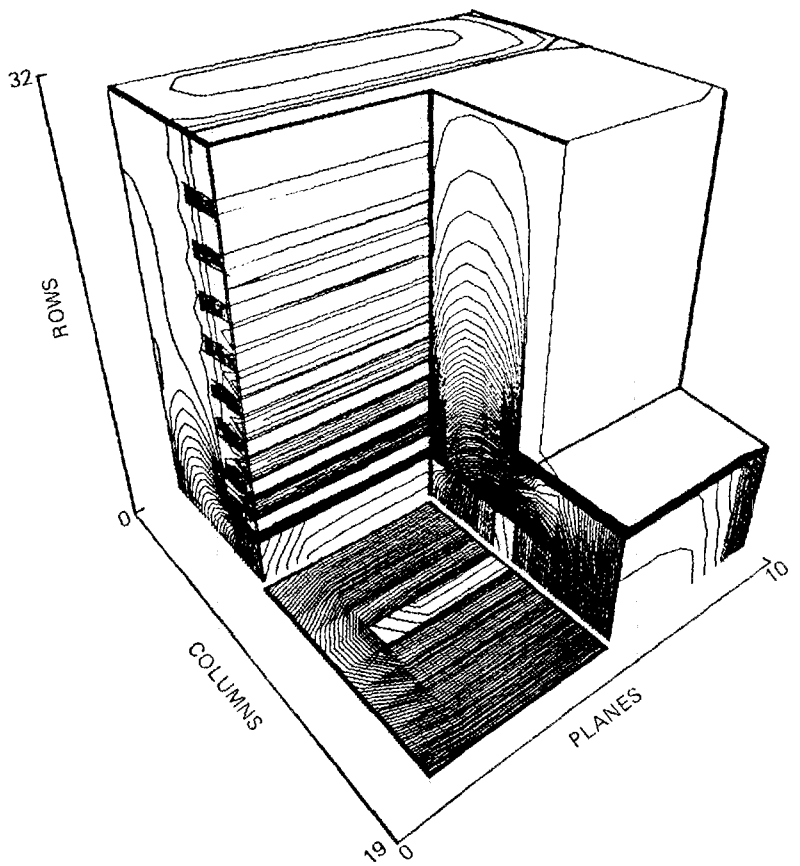

Fig. 6.22. Structure similar to that in Fig. 6.19, with a Faraday shield added to protect the antenna from the plasma.

The core of the RFTF is a simple magnetic-mirror configuration in a lead-shielded enclosure. The configuration consists of two superconducting magnets built for the ELMO Bumpy Torus (EBT) Proof-of-Principle project (see Sect. 2.2), placed on 112-cm centers and sandwiching a vacuum vessel, which serves as a test chamber for antennas and other rf components. A steady-state plasma can be formed in the test chamber by electron cyclotron resonance breakdown, using microwave power from an EBT 28-GHz gyrotron source.

The main access opening of the test chamber is 74 by 163 cm, which is large enough to allow testing of full-size launching structures proposed for DIII-D and TFTR. Additional access for test components and diagnostics is provided by a large (35 by 25 cm) port on top and several smaller, round ports. Subsystems include a turbopump-based vacuum system; a closed-loop, helium refrigerator/liquefier system; and an instrumentation and control center located in part of the former EBT-Scale control room. The facility arrangement is shown conceptually in Fig. 6.23.

Components and systems to be tested can be energized with rf power from a variety of rf sources available in the development program. When the facility is brought to full

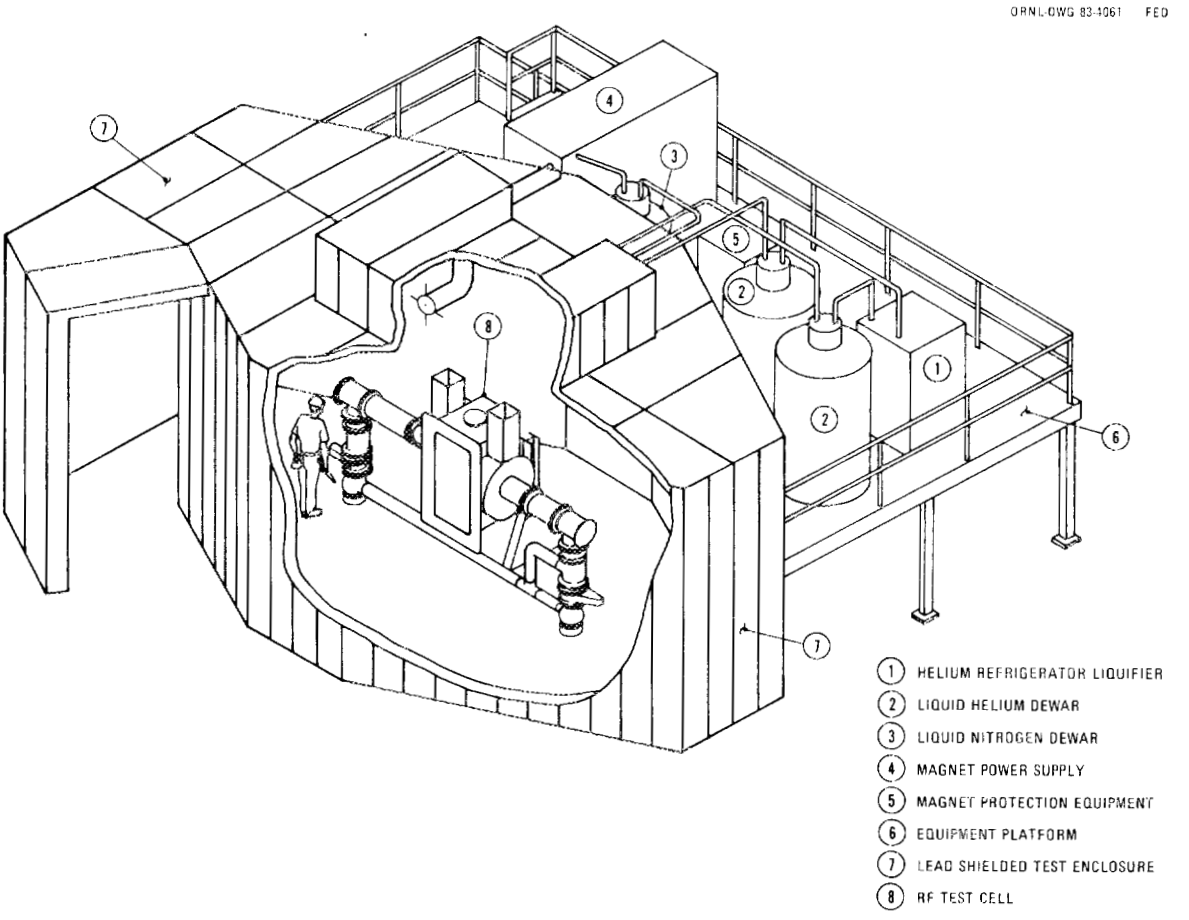

Fig. 6.23. Cutaway drawing of the RFTF.

operating status by installing water-cooled panels (being prepared under a related program), it will test rf components and systems to 1-MW cw power levels in the frequency range of 40–80 MHz.

6.3.4.2 Status

During the first part of 1984, approval to proceed with fabrication and construction was withheld pending review of the conceptual design by potential users. As a result of this review, the test chamber was enlarged to its present size to make the main access opening as wide as the largest port on TFTR. Full approval was received in May 1984 after the project management plan was accepted by the Department of Energy (DOE).

An engineering review of the overall design was held in November, when the detailed design was approximately 80% complete. The review gave confidence that the design was technically sound and consistent with the project criteria. At the end of the report period, the design was approximately 90% complete.

Major procurement and fabrication are about 75% complete. The vacuum vessel was fabricated by Y-12 shops and delivered on schedule; the helium refrigerator/liquefier is reported by the supplier to be complete and ready for testing in January 1985. Testing of the magnets has been completed (Sect. 2.2), and the magnets are on site and ready for installation.

Construction and installation of equipment is about 20% complete. Rust Engineering completed construction of the facility enclosure and equipment platform and began installing utilities. Figures 6.24 and 6.25 show the vacuum vessel and the facility enclosure at the end of the report period.

---

*Engineering Division, Martin Marietta Energy Systems, Inc.
†Management Services Section.
‡Quality Assurance and Inspection Division.
**Computing and Telecommunications Division, Martin Marietta Energy Systems, Inc.
††Purchasing Division, Martin Marietta Energy Systems, Inc.

6.4 GYROTRON DEVELOPMENT

G. R. Haste

The contracts with Hughes Electron Dynamics Division and Varian Associates for the development of 60-GHz gyrotrons were completed during 1984. Both programs have resulted in tubes that have been sent to plasma physics experiments.

The Varian cw program has resulted in an impressive performance. One tube produced 200 kW with 95% of the output in the TE_{02} mode. This power was produced in a cw test for a period of 2 h. In a repetitive test, the tube was pulsed on for 3 s, then off for 5 s, 10,000 times. In another type of pulse test, the tube was turned on for 30 s. During that time the beam current can be expected to decay due to cooling of the cathode as the electrons are emitted. However, a technique was demonstrated for applying additional cathode power to compensate for the cooling, with the result that the current stayed constant during the 30-s pulse, except for a 5% overshoot at the beginning of the pulse. The contract reached an end before the last tube in the development chain could be brought to the same operational performance.

Bids were received from four different tube manufacturers for a program to develop a 1-MW cw gyrotron at 120 GHz. Those bidding were Hughes, Litton, Raytheon, and Varian. These bids were evaluated, but no contract was let, at the direction of DOE.

A contract was let in March 1984 with Varian Associates for a gyrotron power source at 140 GHz. This contract is expected to take 32 months and to result in a source that will produce 200 kW cw with two 100-kW tubes. The design of the first tube in the development chain was completed in 1984.

Varian received the modulator/regulator equipment from UVC for use on the superpower test facility. An extensive effort by Varian engineers was then undertaken to adapt the equipment to the Varian test stand.

ORNL-PHOTO 6630-85

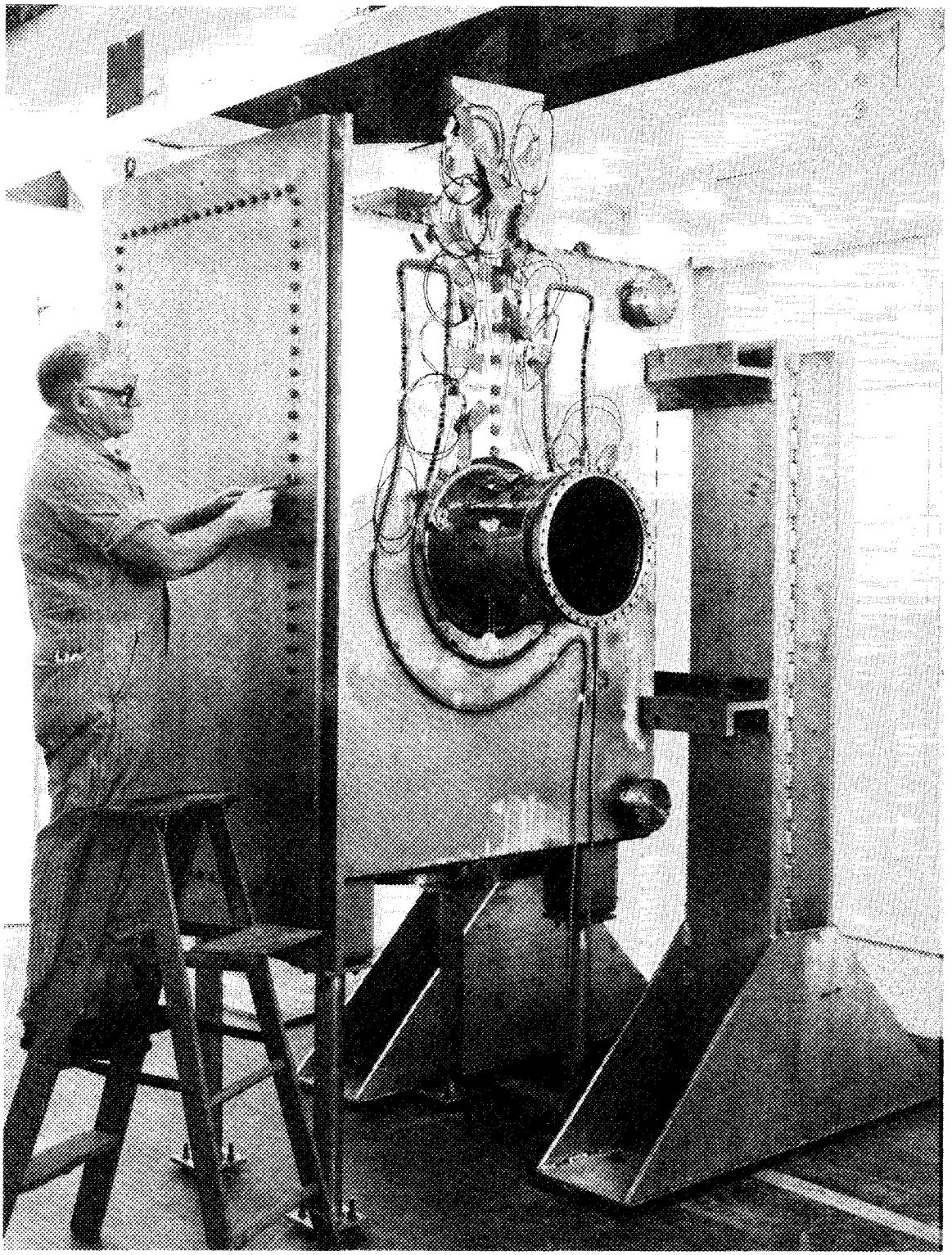

Fig. 6.24. RFTF vacuum vessel and magnet supports in place in enclosure. View shows auxiliary cooling lines and instrumentation on west side of vessel.

ORNL-PHOTO 6628-85

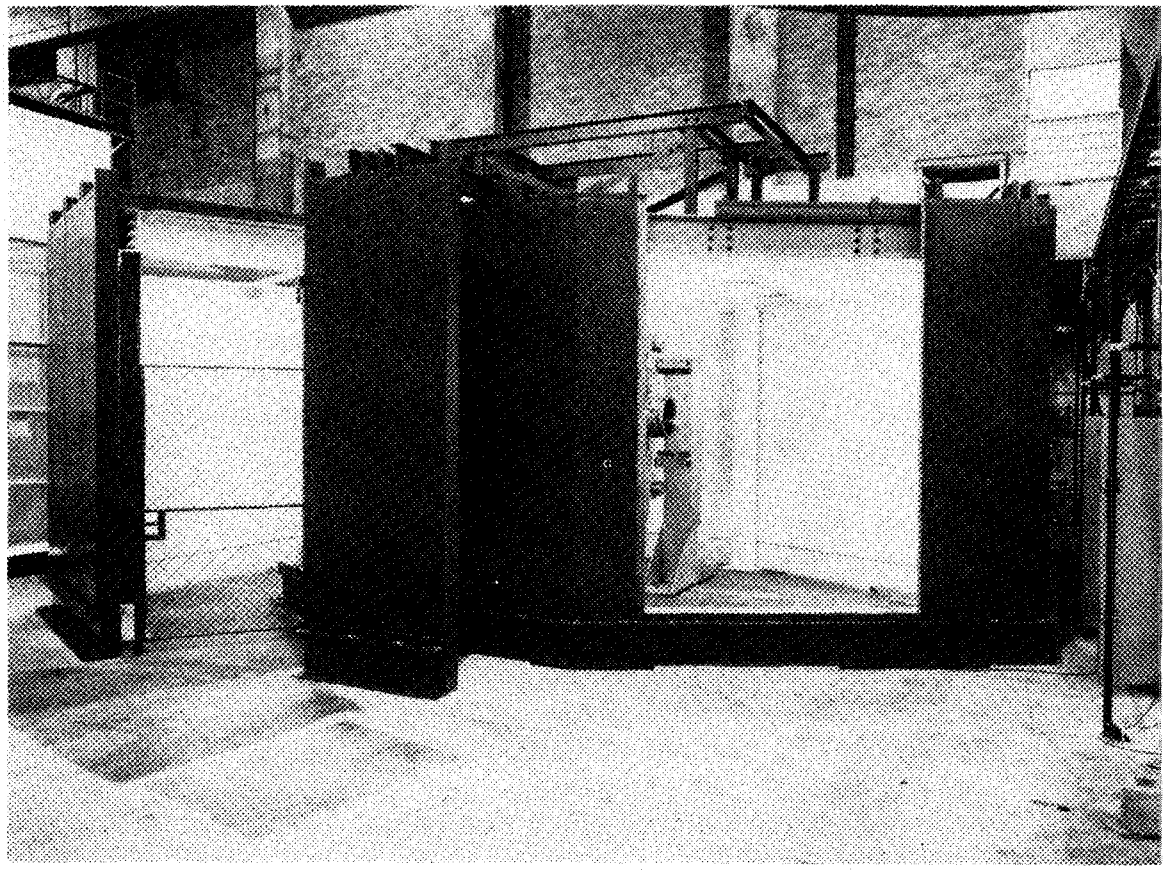

Fig. 6.25. RFTF enclosure during construction in Bldg. 9201-2. Some shield panels have been removed to allow installation of equipment. Vacuum vessel and one magnet support can be seen through the opening.

The window development activities resulted in data showing the importance of slow crack growth in alumina and beryllia. The relation between the applied stress and the growth rate for crack propagation was determined. The growth rate was shown to increase in the presence of moisture, as a result of the chemical activity.

Measurements of microwave absorption by candidate materials for gyrotron windows have led to the selection of sapphire as the best choice for the 140-GHz gyrotron. The most recent samples have shown absorption roughly one-fourth that of alumina, the next best candidate. Although the sapphire is not as tough as the alumina, the lower absorption results in less heating, less thermal stress, and a greater margin of safety.

REFERENCES

1. M. M. Menon et al., "A Quasi-Steady-State Multi-Megawatt Ion Source for Neutral Beam Injection," Rev. Sci. Instrum., accepted for publication (1985).

2. W. K. Dagenhart and W. L. Stirling, "Intense Li^0 Beam Production with an ORNL SITEX Li^- Source," presented at the Annual Meeting of the Division of Plasma Physics, American Physical Society, Boston, Oct. 29–Nov. 2, 1984.

3. W. K. Dagenhart et al., *Nucl. Technol./Fusion* **4**(2), 1430 (1983).

4. M. A. Bell et al., "New Accelerator Designs for Positive and Negative Ions," presented at the Annual Meeting of the Division of Plasma Physics, American Physical Society, Boston, Oct. 29–Nov. 2, 1984.

5. J. H. Whealton, "Ion Extraction and Optics Arithmetic," *Nucl. Instrum. Methods* **18**, 55 (1981).

6. J. H. Whealton, "Expeditious Vlasov Solver for Computation of Ion Extraction from a Plasma," *J. Comput. Phys.* **40**, 491 (1981).

7. J. H. Whealton, *Bull. Am. Phys. Soc.* **27**, 1136 (1983).

8. M. A. Bell et al., *Bull. Am. Phys. Soc.* **28**, 1200 (1983).

9. S. Sengoku et al., "Improvement of Beam Heated Limiter Discharges by Continuous Pellet Fueling in Doublet-III," *Nucl. Fusion*, accepted for publication (1985).

10. M. Greenwald et al., "Pellet Fueling Experiments in Alcator-C," in *Proceedings of the 10th International Conference on Plasma Physics and Controlled Nuclear Fusion Research (London 1984)*, Int. Atomic Energy Agency, Vienna, in press.

11. C. A. Foster et al., "Results of Continuous Pellet Fueling Experiments on Doublet-III," *Bull. Am. Phys. Soc.* **29**, 1321 (1984).

12. D. D. Schuresko, "Pellet Injection into NBI-Heated and Ohmic Discharges," unpublished data, Feb. 1, 1984.

13. D. D. Schuresko, "Pellet Injection Results from ISX-B," presented at the Workshop on the Physics of Pellet Fueling, Baltimore, July 22–23, 1984.

14. S. L. Milora et al., "Results of Hydrogen Pellet Injection into ISX-B," *Nucl. Fusion* **20**, 1491 (1980).

15. D. Q. Hwang, G. Grotz, and J. C. Hosea, *J. Vac. Sci. Technol.* **20**, 1273 (1982).

16. R. R. Weynants, personal communication with the authors.

Chapter 7

Superconducting Magnet Development

P. N. Haubenreich, Large Coil Program Manager
M. S. Lubell, Magnetics and Superconductivity Section Head

J. K. Ballou
L. R. Baylor[1]
R. D. Benson[1]
R. E. Bohanan
C. Bridgman[1]
R. L. Brown
J. A. Clinard[2]
L. Dresner
B. C. Duggins[1]
J. F. Ellis
D. T. Fehling
W. A. Fietz
C. M. Fitzpatrick
W. M. Fletcher[1]
G. M. Friesinger[3]
W. H. Gray
E. L. Halstead[1]
D. R. Hatfield[1]
R. L. Hendren
D. L. James
T. Kato[4]
W. J. Kenney
R. K. Kibbe
J. O. Kiggans
K. Koizumi[4]
L. R. Layman[1]
J. W. Lue
J. N. Luton, Jr.
J. R. May
T. J. McManamy[1]
H. E. Miller[1]
J. F. Monday[1]
J. N. Money
M. F. Nishi[4]
T. C. Patrick
L. Riester
J. P. Rudd
T. L. Ryan[1]
Y. Sanada[4]
S. W. Schwenterly
L. S. Scruggs[5]
S. S. Shen
B. C. Smith
R. E. Stamps
R. Takahashi[4]
D. J. Taylor[1]
S. F. Vaughan[5]
C. A. Wallace
P. L. Walstrom
C. T. Wilson[1]
L. V. Wilson[1]
R. E. Wintenberg[6]
R. J. Wood[1]
W. L. Wright[1]
K. Yoshida[4]
G. R. Zahn[3]
K. L. Zell[5]
J. A. Zichy[7]

1. Engineering Division, Martin Marietta Energy Systems, Inc.
2. Engineering Technology Division.
3. Assignee from Kernforschungszentrum Karlsruhe, Federal Republic of Germany.
4. Assignee from Japan Atomic Energy Research Institute, Ibaraki, Japan.
5. Program/section secretary.
6. Instrumentation and Controls Division.
7. Assignee from Swiss Institute for Nuclear Research, Villigen, Switzerland.

CONTENTS

SUMMARY OF ACTIVITIES 7-5
7.1 INTRODUCTION 7-5
7.2 LARGE COIL TASK 7-6
7.2.1 Test Coils 7-6
7.2.2 Program Management 7-7
7.2.3 Facility Operation 7-8
7.2.4 Coil Tests 7-9
7.2.5 Installation and Modifications 7-10
7.2.6 LCP Research and Development 7-11
7.2.6.1 Tests of Westinghouse conductor 7-11
7.2.6.2 High-voltage, low-energy test of GE coil 7-12
7.2.6.3 Improvement of GD/C sensor lead protection 7-12
7.2.6.4 Vapor-cooled lead test 7-13
7.2.6.5 Breakdown location by acoustic emission 7-13
7.3 ADVANCED CONDUCTOR DEVELOPMENT 7-13
7.3.1 Stability of Cable-in-Conduit Superconductors Cooled by He-II 7-13
7.3.2 Summary of "Superconductor Stability, 1983: A Review" 7-14
7.3.3 Abstract of "Quench Energies of Potted Magnets" 7-14
7.3.4 Protection of Helium-Level Probes 7-14
7.3.5 Laboratory Facility Magnet 7-15
7.4 MAGNET TECHNOLOGY 7-15
7.4.1 EBT-P Magnet Development Program 7-15
7.4.1.1 First two-coil test 7-15
7.4.1.2 Second two-coil test 7-16
7.4.2 ATF Helical Field Coil Joint Tests 7-16
7.4.3 Computer Graphics 7-17
REFERENCES 7-19

7. SUPERCONDUCTING MAGNET DEVELOPMENT

Summary of Activities

Major strides were made in the implementation of the international Large Coil Task (LCT) during 1984. Three of the six test coils were delivered, facility shakedown was accomplished, and preliminary operational tests were performed on three coils.

The Swiss coil was delivered in February, the European Atomic Energy Commission (EURATOM) coil in November, and the General Electric Company coil in November (after extensive modifications and completion by shops at Oak Ridge Gaseous Diffusion Plant). Meanwhile, Westinghouse Electric Corporation finished installing conductor in their coil and made substantial progress on the final assembly tasks.

The first period of shakedown operation, with the Japanese and General Dynamics/Convair (GD/C) coils in place, ended when leaks developed in the GD/C coil. While the leaks (in urethane injection tubes) were being repaired, the Swiss coil was set in the test stand and its helium and instrumentation were connected. Operation resumed in June and continued into September, including 59 days at temperatures below 80 K, without any new leaks in any coil or any major breakdown of equipment. Operation showed that in only one important area—the liquid helium system—were substantial improvements required. Despite the deficiencies in the helium system, which must be remedied before six-coil tests begin, a satisfactory availability factor was achieved, and performance met the needs of the partial-array test. Indicated needs for other repairs, adjustments, and modifications of the facility systems were relatively minor.

In the coil tests, the Japanese and GD/C coils were each operated up to full design current (10.2 kA) with the other coil serving as an adjacent background coil at 40% of full current. Cryostatic stability was demonstrated by spontaneous recovery after half-turns (5 m) of conductor were driven normal by embedded heaters. The forced-flow cooling of the Swiss conductor and coil case worked well, enabling good control of temperatures during cooldown and warmup. None of the coils developed helium leaks during the tests.

Numerous research and development tasks were accomplished in 1984 in support of the LCT, including verification tests of some elements of the Westinghouse coil and various tests to shed light on questions arising during installation and coil testing. Work on advanced conductors and magnet technology also produced some notable progress.

7.1 INTRODUCTION

For more than a decade the ORNL Fusion Energy Division has had a leading role in the development of superconducting magnet systems for toroidal fusion reactors. Since 1977, the greatest part of the effort has been devoted to the Large Coil Program (LCP) and its outgrowth, the international Large Coil Task (LCT). The International Fusion Superconducting Magnet Test Facility (IFSMTF) (previously called the Large Coil Test

Facility) at Oak Ridge is the focal point for the collaboration by the United States, the European Atomic Energy Commission (EURATOM), Japan, and Switzerland in the LCT under terms of an International Energy Agency agreement. In the IFSMTF, six different toroidal field (TF) coils will be operated as a toroidal magnet system, with each coil tested in turn to determine its capabilities. The United States is providing the facility and three of the test coils; the other participants, one coil each. On behalf of the United States, ORNL acts as the operating agent for the LCT. The facility is operated by qualified members of the division staff. On-site representatives of all LCT participants work together in planning and carrying out the coil tests.

In previous years, facility construction was completed and the coils from Japan and from General Dynamics/Convair (GD/C) were installed. Shakedown operation of the facility with the two coils in place had just begun at the end of 1983.

Research and development (R&D) activities in direct support of the LCP, carried out in the division's Magnetics and Superconductivity Section, include work on coil diagnostics, instrumentation for cryogenic service, conductor verification tests, and cryogenic tests of various components.

In addition to the LCT, work at ORNL continued to advance superconducting magnet technology in areas specific to fusion applications by developing better analysis techniques, generating basic design information, and evaluating small quantities of experimental conductor embodying advanced concepts.

Other magnet technology activities have included participation in the fabrication and testing of development coils for the ELMO Bumpy Torus Proof-of-Principle (EBT-P) Project and development of joints for the Advanced Toroidal Facility (ATF) coils.

7.2 LARGE COIL TASK

7.2.1 Test Coils

Three of the six LCT test coils were delivered to the IFSMTF during 1984. The Swiss coil, constructed by Brown Boveri, was delivered in February and placed in the test stand in March. The EURATOM coil, after being tested alone at currents up to 10 kA at Karlsruhe, Federal Republic of Germany, was shipped to Oak Ridge, arriving in November, and placed in the test stand in December. The second U.S. coil was delivered to the IFSMTF as soon as the EURATOM coil was in place.

This coil was designed and partially completed by the General Electric Company (GE), Schenectady, N.Y. Work on this coil at GE was stopped in 1982, when design deficiencies became evident and manufacturing efforts were hampered by organizational problems at Schenectady. The Department of Energy (DOE) and ORNL put the coil in storage while its fate was decided. It was found that the coil could be upgraded for full service by means of sophisticated design and high-quality fabrication. This work began in the shops at the Oak Ridge Gaseous Diffusion Plant (ORGDP) in 1983, and the foreseen bolting and welding were completed that year. Work on the coil was prolonged, however, by additional problems discovered in the course of the planned tasks. Correction of these problems at ORGDP was completed late in November 1984.

During the first nine months of 1984, Westinghouse Electric Corporation (Westinghouse), using two winding lines and an extended work schedule, finished installing conductor and sensors in the grooved aluminum plates of the third U.S. coil. As each of the 24 plates was wound, another was placed on top of it, the conductors connected, and the new plate wound with insulated conductor. Electrical tests at each step verified the voltage withstand capability. In this manner two coil halves were built up. The two halves were brought together in October. The remainder of 1984 was spent installing the bolts that hold the plates together. This task entailed drilling out the 526 holes to provide snug fits for the high-strength bolts.

7.2.2 Program Management

Program management in 1984 successfully dealt with a wide variety of tasks. Developments in the Westinghouse coil project called for management actions affecting both business and technical aspects of the project. Program costs were a major concern, especially because of the substantial, unanticipated effort required to repair leaks in the GD/C coil. Because of major perturbations in the planned test program, the importation of two coils with associated equipment, and the assignment of numerous on-site representatives, international collaboration in the LCT was again put to the test. As before, the international organization proved effective in working out mutually acceptable solutions to problems.

Coordination of coil installation, facility modifications, operations, and coil testing continued throughout the year. Costs and benefits of numerous proposals for modifications or additions to the facility were evaluated and decisions reached. The pulse coil system and the helium refrigeration system received especially intensive evaluations.

Interaction with Westinghouse management resulted in an agreement to share costs, substantially reducing the ultimate cost to the government. Technical monitoring of Westinghouse work continued as required throughout the year. Westinghouse proposals for revision of schedules and cost estimates were scrutinized in detail, and acceptable agreements were reached.

When leaks interrupted facility shakedown in January 1984, program management conferred with advisors, then met with LCT project officers in a special meeting in February to consider alternative proposals for testing with one, two, or three coils. Afterward, ORNL worked out detailed schedules with on-site representatives and submitted a proposal to the LCT Executive Committee. Plans for partial-array tests were developed, and approval was secured in the semiannual LCT meetings at Oak Ridge in May. A steering committee including both ORNL and foreign participants met weekly throughout the year.

Program management dealt with duty-free import of the Swiss coil and special equipment and with the assignments of additional Japanese, EURATOM, and Swiss representatives to work at the IFSMTF.

Government-owned equipment was moved from GE's Schenectady plant to storage at Princeton Plasma Physics Laboratory. In response to a request from the Massachusetts Institute of Technology (MIT) fusion laboratory for surplus unreacted Westinghouse/Airco conductor, LCP management released this material as soon as warranted by winding progress at Westinghouse. ORNL worked with Oxford Airco to obtain required documentation and archival samples and to store other government property.

In response to a request by the DOE Office of Fusion Energy (DOE-OFE), LCT experience was reviewed. A report on lessons learned that would be of benefit to the fusion program was completed, approved by ORNL management, and submitted to DOE. Useful information derived from the experience with U.S. coils and the test facility was disseminated to U.S. fusion program planners and magnet designers through quarterly reports and technical papers.

Program management maintained closest contact with the work at ORGDP on the GE coil, arranging for specialized support and providing guidance on technical and schedule matters.

At the October meetings of the LCT project officers and executive committee, the results of activities at the IFSMTF were assessed and agreements were reached on plans for installation of the remaining coils and equipment. Arrangements were made for the receipt of the EURATOM coil and special equipment, the assignment of Kernforschungszentrum Karlsruhe (KfK) staff members to participate in its installation, and an appropriate ceremony marking its arrival.

7.2.3 Facility Operation

A major step in the international program was accomplished in 1984, when the IFSMTF was operated for a substantial period of time, with acceptable availability, providing all services necessary for testing an array of three coils from Japan, Switzerland, and the United States. This took place from mid-June through September.

At the first of the year, integrated operation of all facility systems had just begun. The refrigerator was put into operation and cooldown of the test stand began in the first half of January. When the temperature reached 170 K, helium began to leak excessively from the GD/C coil. The test stand was warmed back up and the vacuum tank was opened to hunt the leaks, concluding this period of operation.

After repair and reinstallation of the GD/C coil and (partial) installation of the Swiss coil (described in Sect. 7.2.5), the vacuum tank was closed in mid-June. Startup operations were interrupted by a helium leak at a bellows joint in a superconducting bus jacket. The tank was opened, repairs made, and the tank evacuated again by the end of June.

Cooldown by circulation of helium gas cooled with liquid nitrogen began on July 3. With the conservative limits on allowable temperature differences set by the Testing and Analysis Group, the rate was limited to about 20 K per day, but control was quite good. When the temperature reached about 100 K, cooldown was interrupted to liquefy the amount of helium required for operation and then continued with the refrigerator operating to produce low-temperature helium gas. Superconductivity was observed in all three coils on July 23, and by July 26 all coils had been filled with liquid and were fully superconducting. Escalation of coil currents was delayed two weeks when air leaked into the vacuum jacket on the helium storage dewar, resulting in the loss of some helium and the need to dry the jacket, repair the vacuum system, and reliquefy helium. In an intensive period of operation between August 13 and September 3, all planned coil tests were satisfactorily completed.

After the electrical tests, the helium system was operated in a simulation of forced-flow coil tests. The bath in the auxiliary cold box was operated at 0.5-atm pressure to reduce

the temperature of the helium going to the Swiss coil to 3.8 K. These conditions were reached, but air leaking through a defective rupture disk froze in the cold box and prevented further operation. On September 14, warmup of the test stand began. Again, temperature differences were well controlled and held within conservative limits. By the end of the month, the test stand was up to about 250 K, and continuous attendance by an operating crew was discontinued. The final stages of warmup were quite slow, as there was no provision for heating the circulating helium gas.

During the partial-array operation, all objectives established by LCT project officers were accomplished except for operation of the helium system at subatmospheric pressure for a substantial period of time. (See Sect. 7.2.5.)

7.2.4 Coil Tests

The first attempt at coil tests, in January 1984, with the Japanese and GD/C coils in the test stand, progressed only through the point of partially verifying cooldown capabilities before the failure of defective seal welds on the GD/C coil. The second attempt, following repair of the GD/C coil and installation of the Swiss coil (except for high-current leads), was completely successful.

Cooldown of the test stand with three coils in July was an experiment in the distribution of helium flows among coil structures and windings and test stand components. Conservative limits on temperature differences within each coil or component were met without any problem other than slowing the cooldown. The ability to keep the coil case colder than the winding in the forced-flow Swiss coil was gratifying, as it ensured that the potted winding was kept in compression. Best of all, no cold leak developed during the cooldown and subsequent coil testing.

The sequence of the high-current tests of the GD/C and Japanese coils was ordered with relevance to shakedown of facility systems, checkout of coil instrumentation, extent of risks, and importance of information to later full-array tests. In single-coil tests, each coil was individually charged to full design current of 10.2 kA, producing a peak field at the conductor of 6.4 T. There was no evidence of training and no quench during any test. Three unintended "dumps" (rapid discharges) of the Japanese coil were caused by a thunderstorm interruption of refrigerator operation, a coil supply control fault, and slightly slow recovery of a normal zone deliberately induced by heaters during an experiment. Test dumps of both coils were initiated by various simulated quench signals and by manual dump switches. Helium boiloffs during dump transients were acceptably low.

In two-coil charging/discharging tests, currents ranged up to 100% of design current in one coil with the other coil at 40% of design current. Calculations had indicated that limiting stresses would be reached in part of the test stand structure at this level; observations of strain gages confirmed this prediction. Displacement of winding packs relative to the coil cases, observed during charging and discharging, did not always compare favorably with expectations.

Acoustic emission from the coils was recorded. Some intriguing features, including differences between GD/C and Japanese coils, were observed. Testing and analysis personnel at ORNL collaborated with MIT personnel in obtaining and analyzing these data.

Recovery tests designed to explore the inherent stability designed into the GD/C and Japanese coils were successfully conducted and analyzed. Both coils recovered from a condition of a half-turn driven normal while operating at 10.2 kA and fields up to 6.4 T.

The partial-array tests proved the unique pickup coil compensation scheme developed at ORNL for multicoil operation, which makes it possible to distinguish small resistive voltages indicative of normal zones from the larger inductive voltages encountered.

On-site representatives of all LCT participants actively engaged in testing and analysis activities. The work is documented in a paper presented at the Applied Superconductivity Conference only two weeks after the conclusion of the tests.[1]

7.2.5 Installation and Modifications

During a total of seven months in 1984, the principal activities at the IFSMTF were installation of coils and equipment, repairs, and modifications.

Immediately after the vacuum tank was opened on January 26, leaks were found at tubes that had been welded shut by GD/C after polyurethane was injected through them between the winding pack and coil case. Since some of the leaks were in the coil face against the bucking post, the coil had to be completely disconnected and removed from the test stand for repairs. Inspection showed that urethane vapors had contaminated closure welds, leading to subsequent cracking and leakage. All port welds were cut out, urethane was removed, and new plugs were welded in place. After sensitive helium leak tests, cover plates (or additional weld metal) were applied to further reduce the risk of leakage. Tests of all sensor lead feedthroughs and thin-section welds on the GD/C coil detected no leaks.

Because of previous experience with damage to sensor lead insulation during work inside the tank, steps were taken while the coil was out to improve the electrical insulation and protection of all 120 cables from sensors inside the coil that might see high voltage during a dump. Teflon tubing was shrunk onto each cable, and bundles of cables were sheathed in larger tubing. Tests showed no breakdown in the leads after this treatment.

Meanwhile, the Swiss coil arrived at the IFSMTF on February 2. With active participation of the Swiss representatives, it was quickly tested and prepared for installation. Following the decision of the LCT Executive Committee to install the Swiss coil except for high-current leads, the coil was set into the test stand on March 22 and its installation began.

Repairs on the GD/C coil were completed and it was returned to the test stand on May 10. The installation work on the GD/C and Swiss coils was completed, access equipment was removed, and the vacuum tank was closed on June 14.

Helium leakage detected inside the tank during startup was traced to a welded joint between bellows and pipe sections of the helium jacket on a superconducting bus. A backup seal with silver solder proved to be an acceptable repair. During operation, a small leak persisted but did not increase in size. (Leakage rates changed only with temperature-dependent helium properties.)

Measurement of voltage withstand capabilities at the end of cooldown, with coils and lead dewars filled, showed incipient breakdown in the GD/C system at 600 V, while the Japanese coil passed 1500 V. An acceptable operating margin for dumps up to 40%

current was obtained by soft-grounding the center tap on the GD/C dump resistor and reducing its value by 33%.

During the operating period, Y-12 Maintenance forces were preparing for installation of the pulse coil system and the other test coils. By October 15, all temperatures were above the dewpoint of the air, and the tank lid was removed. Access equipment was installed, and structural elements of the test stand were removed as necessary for installation of the other test coils.

Installation of the pulse coil system began in November with the six supports for the segmented, circular track. Half of the track was installed (through the bores of the three test coils already in place). Then the coil/torque beam assembly was set in place on December 11.

As expected, the shakedown operation of the facility showed a need for numerous minor repairs, adjustments, and modifications. In general, however, indications were that the facility, with the notable exception of the helium system, would perform satisfactorily during the ultimate six-coil tests. All participants agreed that the performance of the helium refrigerator/liquefier and distribution/storage system would have to be upgraded. Plans for upgrading the helium system were worked out with consultants and LCT foreign participants.

Vacuum-jacketed helium transfer lines that had excessive heat leakage during shakedown were removed, repaired, and replaced. The anomalously high boiloff from the vapor-cooled leads and dewars was investigated by a laboratory test of a lead (see Sect. 7.2.6.4).

The EURATOM coil was transported from Karlsruhe, arriving at the IFSMTF on November 28. Inspection showed it to be in excellent condition. Preparation for installation began immediately, with participation of several KfK staff members. On December 13 the coil was the center of a ceremony involving high-ranking DOE, German, and EURATOM officials. It was then set into the test stand on December 17.

The GE coil was delivered from the ORGDP shops on December 20. The coil was cleaned and inspected, and installation of external instrumentation began.

7.2.6 LCP Research and Development

7.2.6.1 Tests of Westinghouse conductor

A series of short-sample tests of full-size, prereacted Nb_3Sn conductor was performed to check the use of conductor with known manufacturing or handling flaws. The conductor was manufactured by Airco Superconductors for the Westinghouse coil. Its bending history in the coil was duplicated for the tightest bend (18-in. radius) in the high-field region. (Bending at the plate entry may be of smaller radius, but fields at these points are much lower.) The two samples were representative of the two worst cases anticipated in the coil—a length that was heavily sintered during the heat-treating process and one that had been bent in the wrong direction and then restraightened before bending correctly. The samples were tested to the full peak field (8.8 T) and current (24 kA) expected in the extended operation (140%) case. The results showed that in spite of the severe handling, the conductor will probably perform acceptably even under extended operating conditions.

Eight samples of full-scale LCP conductor and two resistance-welded joints were tested in a split solenoid capable of up to 8 T over a conductor length of 15 cm. The available current supply could provide 24 kA to two samples connected in series with a joint at the lower end in a low-field region. The samples included sections of the transition between swaged end and cable, good-quality conductor, and some heavily sintered conductors. All were bent around various diameters, then straightened for testing. Since 24 kA at 8 T was less than the critical current of the good conductors, a quantitative determination of degradation due to these various factors could not be made. However, only two samples of the eight tested showed degradation to about 21–24 kA at 7.6 T, which gives confidence that the conductor performance should not be limited by the various bending operations in the coil, if the conductor is handled carefully. The resistance-welded joints showed a resistance of $10^{-9}\ \Omega$ at 20 kA and 3 T, a satisfactory value for the LCP coils.

7.2.6.2 High-voltage, low-energy test of GE coil

Shorts or breakdowns between sensor leads and from leads to conductor or coil case were encountered during assembly of the GE coil. Concerns about possible damage during a dump from high-current operation called for a method of testing a coil with high voltage from terminal to terminal but with negligible risk of damage. Such a method was devised and applied to the GE coil at ORGDP. The coil was charged to very low currents (in the milliampere range), the circuit was opened suddenly with an electronic switch, and the coil was allowed to "ring down" at its natural frequency while the terminal-to-terminal voltage and wave shape were monitored with a real-time oscilloscope. This demonstrated linearity at low voltages. The low-current data were extrapolated to require a 1-A charging current to produce the desired 1-kV terminal voltage. The total stored energy corresponding to 1 A is 1 J, an amount previously shown to be too small to thermally enlarge preexisting defects even if the total energy were available for deposition at the supposed fault. For the full test, we increased the charging current in small increments, beginning at 1 mA and ending at 1075 mA when the peak terminal-to-terminal voltage reached the desired 1000 V.

7.2.6.3 Improvement of GD/C sensor lead protection

Because of experience with physical damage to lead insulation and undesirably low breakdown voltages in the GD/C coil electrical system, a procedure for improvements was developed in the laboratory and applied while the GD/C coil was out of the tank for repair of seal welds on the polyurethane ports. The upgrade consisted of sleeving individual cables with heat-shrinkable Teflon tubing, separating the cables into 38 bundles, inserting each bundle inside a 0.75-in. Teflon semirigid conduit with 0.040-in.-thick walls, casting new Blue Stycast 2850 FT potting on the coil connector potting to extend over the ends of the heat-shrunk Teflon-sleeved cables, and heat shrinking larger polyolefin tubing over the transition length between coil connector and 0.75-in. Teflon conduit.

High potential voltage (hi-pot) tests were performed on the cable bundles before the polyolefin tubing was put in place. The coil connectors were bagged, and helium was introduced into the bag and flowed out of the free end of the 0.75-in. conduits. Calibrated spark gaps were used to ensure the purity of the exiting helium. Electric potentials of up to 8.5 kV dc were applied to a bare copper wire that ran the whole length of the cable bundle

inside the conduit and wrapped around the connector Stycast potting. The shield wires of the cables and all other grounded parts were the negative electrode. There were 35 bundles of cables and 21 coil connectors; defects involving 8 connectors or their associated bundles were found and repaired. Most of the defects were pinholes or cuts in the Teflon shrink tubing, but there were some defects in the connector potting, some broken wires, and one cracked potting. After the repairs, all bundles passed the 8.5-kV test in helium at atmospheric pressure.

7.2.6.4 Vapor-cooled lead test

To contribute to the understanding of performance observed during the partial-array operation of the IFSMTF, a heat-load test of one vapor-cooled lead (VCL) was performed in a facility lead dewar. Helium boiloff rate as a function of VCL flow was measured. Other test variables included heating or not heating on the top of the lead and dewar shield tracing with and without liquid nitrogen cooling. The observed strong dependence on VCL flow was similar to the trend of data taken during the partial-array coil tests. Little difference was seen within the range of other variables used. The results are consistent with the 1982 lead tests by Miller and Lue[2] and showed a standby loss of about 24 L/h with all of the boiloff gas flowing through the VCL.

7.2.6.5 Breakdown location by acoustic emission

Equipment and procedures were developed for using acoustic emission to determine the location of electric breakdown. (The general technique was applied previously in Japan.) The requirement originated with the GD/C coil. Even after the protection of the sensor leads was upgraded, hi-pot tests of the coil electrical system showed anomalously low breakdown voltages. Certain feedthroughs in the coil case were thought to be the most likely locations, but there was no way to subdivide electrically to verify this hypothesis. It was determined that significant acoustic emission accompanied the breakdown, so techniques were developed for measurement (using existing equipment) and analysis. Tests by the end of 1984 showed that breakdown was occurring in or near two adjacent feedthroughs on the side of the GD/C coil.

7.3 ADVANCED CONDUCTOR DEVELOPMENT

7.3.1 Stability of Cable-in-Conduit Superconductors Cooled by He-II

During 1984, an explanation was sought for some observations made by J. C. Lottin and J. R. Miller,[3] who measured the stability margin of cable-in-conduit superconductors cooled by superfluid He-II. They found that below the limiting current the stability margin was nearly the same as when the conductor was cooled by He-I, but beyond the limiting current, until the transport current reached a certain cutoff current, the stability margin of He-II was much larger than that of He-I. Calculations were performed that attempted to explain these experimental results by showing that the cutoff current is determined by the Kapitza interfacial resistance; however, the required Kapitza resistance was much larger than directly measured values. A program note was written to describe this phase of the work.

Later in 1984, a rapid, semiempirical method was developed for calculating the stability margins of superconductors cooled with subcooled He-II. The method, based on a model of Seyfert et al.,[4] was compared with the heat transfer data of ref. 4, the stability data of Meuris,[5] and the stability data of Lottin and Miller.[3] The calculations are consistent with the data of Seyfert et al. and Meuris but disagree with the data of Lottin and Miller. According to Miller,[6] the disagreement can be explained by a failure of complete current sharing in the experiment of Lottin and Miller. This failure of current sharing also explains the cutoff current of ref. 3, eliminating the need for any other explanation. (This second phase of the work was performed by L. Dresner while he was on assignment at the Applied Superconductivity Center of the University of Wisconsin, Madison.)

7.3.2 Summary of "Superconductor Stability, 1983: A Review"[7]

L. Dresner

This review paper, developed from an invited paper at the 1983 International Cryogenic Engineering Conference, brings together in one article concepts and methods, many of them original to the author and his colleagues, of using the various low-temperature phases of helium to stabilize superconductors. Special emphasis has been placed on three topics: internally cooled superconductors, cooling by superfluid helium, and metastable magnets.

7.3.3 Abstract of "Quench Energies of Potted Magnets"[8]

L. Dresner

The quench energy of potted magnets has been studied for two extreme models of the winding: (1) treating it as an ansiotropic three-dimensional continuum and (2) ignoring heat conduction in the epoxy and treating it as a one-dimensional continuum. For each model, we have obtained a formula for the point-source quench energy, complete up to a single undetermined constant, by applying a combination of dimensional and group-theoretic arguments to the heat balance equation. The undetermined constant has been estimated by solving the heat balance equation approximately. Correction factors are given for taking into account the source's being distributed in space and time. The formulas are compared with available experimental data; agreement is fair.

7.3.4 Protection of Helium-Level Probes

Superconducting liquid-helium-level probes of the type developed by American Magnetics, Inc., and used in IFSMTF will burn up if the signal conditioning unit is turned on while the probe is in vacuum. The usual mechanism of failure is for the superconducting wire to burn in two, stopping current flow in the heater, which is in series with the NbTi element. If the increase in the resistance of the superconducting NbTi element above room temperature is large enough, it should be possible to add to the existing level readout electronics an additional comparator and a current shutoff relay that would sense overheating of a probe and automatically switch off the current. The current could then be turned on again with a push button when desired. With these considerations in mind, the resistance of a length of bare NbTi wire of the type used in American Magnetics level probes was

measured over the interval from 24°C to 200°C. The resistance increased linearly with temperature over the interval and at 200°C attained a value 8.45% greater than that at 24°C. This resistance change is large enough to trigger active circuitry for switching off a superconducting level probe and thereby protecting it from overheating and burning up in a vacuum.

7.3.5 Laboratory Facility Magnet

For more efficient operation of the Coil Winding Test Experiment (CWTX) facility (an 8-T, 40-cm-bore magnet with a 12-T, 22-cm-bore insert), a new cryogenic dewar system was purchased and delivered in October 1984. The system, which has an inside diameter of 1 m and is 1.8 m high, was manufactured by Cryofab Company. It also includes the stainless steel structural support for the CWTX magnets and a test fixture designed for insert sample coil testing. This system, combined with our laboratory 140-W or 40-L/h refrigerator, will provide a complete facility for testing large conductors or coils for high-field applications, such as those in reactor designs. The listed values (8 T and 12 T) are working field values in the bore of the magnet.

7.4 MAGNET TECHNOLOGY

In reporting the work accomplished in 1984, we also discuss those aspects of magnet technology work performed for others. It seems consistent to report all of our magnet technology development in one place, even though much of it is funded by other projects.

7.4.1 EBT-P Magnet Development Program

7.4.1.1 First two-coil test

The two-coil test of the EBT-P development coils D1 and D2 was successfully completed. The two coils were mounted side by side with their centers 60 cm apart and were charged in series to 1200 A three times. At 1200 A, the magnets produced the maximum design out-of-plane mechanical load of 73,000 lb on each magnet. The applied maximum current was the same as that planned for the Radio-Frequency Test Facility (RFTF), but the load was more than twice that to be experienced in RFTF (because of the close spacing in the present experiments). The test verified that the magnets can be operated stably with the out-of-plane load applied and that the structures are mechanically sound. This is a significant point and should not in the least be considered a routine test. When a magnet is tested by itself as these magnets were, the magnetic forces are radially outward and axially toward the center (i.e., the magnet tends to compress in length). However, in a two-coil test configuration, the forces on the respective windings are attractive (i.e., toward one side plate of the bobbin). If the magnets were not wound extremely tightly, then the single-coil tests would create some space for small motion in the two-coil test, and the magnets would then either quench or train (i.e., these are high-current-density, high-performance, noncryostabilized designs). Since quenching and training *did not occur*, this test serves as a confirmation of the soundness of the design and a tribute to the care and magnet fabrication technology employed.

Tests were made with helium bath pressure up to 18.5 psia. Thus, the overpressure of several pounds per square inch in the proposed RFTF operation with a closed-cycle refrigerator should not cause any problem.

A helium leak developed in the stack area of D1 from the helium space into the vacuum space, causing a heat leak in D1 about three times that in D2. The use of D1 in RFTF is now doubtful. Plans were made to test and use D2 and D3 in series and to retain D1 for emergency use.

7.4.1.2 Second two-coil test

The two-coil test of EBT-P development coils with D2 and D3 (prototype coil fabricated by GD/C) in series was successfully completed. Operation at 5 T with a 73,000-lb out-of-plane load was required to verify the basic EBT-P design. On June 14, the magnets were ramped once up to 1200 A and back down; however, on subsequent attempts the magnets were tripped out automatically one or two minutes after reaching 1200 A. Investigation revealed a power supply problem that was circumvented by inverting the polarity of the power supply. On June 26, the magnets were operated successfully at 1200 A and 5.1 T and held in steady state for nearly 1 h. The magnets were intentionally dumped from full field. No significant problems were discovered, and the strain data agreed well with the predictions. The measured liquid helium use was within the range of prediction. This completed the planned testing, and the magnets were considered qualified for use in RFTF.

At the outset of this program, we stated that development was needed for the conductor and winding technology. We further stated that with completion of the development coils, our R&D effort would cease and our only involvement would be during the testing phase. We are pleased to report that this commitment was kept. We finished the necessary development work and went on to other work. Over the last few years, we have been involved only with testing. This report concludes the testing phase.

7.4.2 ATF Helical Field Coil Joint Tests*

After thermally and electrically testing 20 joint concepts, Engineering Division staff selected (with approval from Fusion Energy Division) the joint they considered most likely to succeed. A backup joint was also selected. This milestone decision was exactly on schedule. The joint will electrically connect the helical coil segments and must satisfy very stringent electrical, thermal, and mechanical requirements. The joint selected is a lap-bar combination that provides better-than-average adjustments for alignment between coil segments. It has a separate copper piece between conductors with an added cooling channel. All tests indicated that any separate pieces need supplemental cooling. Several more joint concepts will be tested before the first phase of the joint development program ends. The next phase, already under way, is to construct a full-scale prototype to verify the feasibility of assembling the selected concept. Also, more electrical, tolerance, and fatigue testing and analysis are planned.

---

*Funded by the ATF project.

7.4.3 Computer Graphics

For several months the ATF project had difficulties with an error in the PAFEC Interactive Graphics Suite (PIGS) computer code. For no apparent reason, during a grid generation sequence, the PIGS program would type out "DATA OVERFLOW. PLEASE REENTER" when in fact the data were correct. To compound the difficulty of analyzing where the error occurred, there seemed to be no 100% reproducible path to simulate this error. Eventually, the error was tracked down to improper initialization of a common block variable in an overlaid subroutine. The program was fixed by moving the initialization of the offending variable to the root link of the overlaid code.

REFERENCES

1. J. N. Luton et al., "Preliminary Results of the Partial-Array LCT Coil Tests," *IEEE Trans. Magn.* **MAG-21**, 238–41 (1985).

2. J. R. Miller and J. W. Lue, "Vapor-Cooled Current Leads for LCTF," pp. 202–3 in *Fusion Energy Division Annual Progress Report for Period Ending December 31, 1982*, ORNL-5919, Union Carbide Corp. Nuclear Div., Oak Ridge Natl. Lab., November 1983.

3. J. C. Lottin and J. R. Miller, *IEEE Trans. Magn.* **MAG-19**, 439–42 (1983).

4. P. Seyfert, J. Lafferranderie, and G. Claudet, "Time-Dependent Heat Transport in Subcooled Superfluid Helium," *Cryogenics* **22**, 401–8 (1982).

5. C. Meuris, "Thermal Stability of Superconductors," *J. Phys. (Paris) Colloq.* **C1** [suppl.: *Proceedings of the 8th International Conference on Magnet Technology (MT-8), Grenoble (France), Sept. 5–9, 1983*], 503–14 (1984).

6. J. R. Miller, Lawrence Livermore National Laboratory, Livermore, Calif., personal communication to L. Dresner, 1984.

7. L. Dresner, "Superconductor Stability, 1983: A Review," *Cryogenics* **24**, 283–92 (1984).

8. L. Dresner, "Quench Energies of Potted Magnets," *IEEE Trans. Magn.* **MAG-21**, 392–5 (1985).

Chapter 8

Advanced System Studies

Fusion Engineering Design Center

T. E. Shannon[1]

R. J. Barrett[2]
D. T. Blackfield[3]
S. K. Borowski
T. G. Brown[4]
M. K. Bullock[5]
G. T. Bussell[6]
L. C. Caldwell[1,7]
A. Dabiri[8]
L. S. Dale[7]
G. R. Dalton[9]
M. V. Dunn
C. A. Flanagan[10]
P. J. Fogarty[1]
S. A. Freije[3]
J. D. Galambos[11]
G. E. Gorker[12]
J. R. Haines[13]
W. R. Hamilton[1]
N. R. Irby[7]
S. S. Kalsi[12]
D. C. Keeton[14]
M. H. Kunselman[1]
V. D. Lee[13]
D. C. Lousteau[15]
W. D. Nelson[12]
Y-K. M. Peng
P. A. Powell[7]
R. L. Reid[1]
B. W. Riemer[4]
K. E. Rothe[11]
P. T. Spampinato[4]
V. C. Srivastava[12]
P. Stevens[16]
D. J. Strickler[11]
M. E. Talley[7]
G. E. Taylor[13]
S. L. Thomson[17]
N. A. Uckan
F. W. Wiffen[18]
K. F. Wu[1]

Fusion Environmental Assessment Program

J. B. Cannon,[19] Program Manager

---

1. Engineering Division, Martin Marietta Energy Systems, Inc.
2. Burns & Roe, Oradell, N.J.
3. TRW Inc., Redondo Beach, Calif.
4. Grumman Aerospace Corp., Bethpage, N.Y.
5. American Technical Associates, Knoxville, Tenn.
6. Stone & Webster Engineering Corp., Boston.
7. Section secretary.
8. Science Applications International Corp., Boulder, Colo.
9. University of Florida, Gainesville.
10. Westinghouse Electric Corp., Madison, Pa.
11. Computing and Telecommunications Division, Martin Marietta Energy Systems, Inc.
12. General Electric Co., Schenectady, N.Y.
13. McDonnell Douglas Astronautics Co., St. Louis.
14. Tennessee Valley Authority, Chattanooga, and Electric Power Research Institute, Palo Alto, Calif.
15. Operating Contractors Project Office, Martin Marietta Energy Systems, Inc.
16. The University of Tennessee, Knoxville.
17. Bechtel National, Inc., San Francisco.
18. Metals and Ceramics Division.
19. Energy Division.

CONTENTS

SUMMARY OF ACTIVITIES 8-5
8.1 FUSION ENGINEERING DESIGN CENTER 8-5
8.1.1 Fusion Power Demonstration Reactor Studies 8-5
8.1.1.1 FPD-I 8-8
8.1.1.2 FPD-II 8-10
8.1.1.3 FPD-III 8-12
8.1.2 Tokamak Fusion Core Experiment 8-15
8.1.2.1 Superconducting devices 8-18
8.1.2.2 CCTF concept 8-40
8.1.3 Ignition Spherical Torus 8-46
8.1.3.1 Results of initial assessments 8-48
8.1.3.2 Reference configuration 8-49
8.1.4 Supporting Activities 8-52
8.1.4.1 Tandem Mirror Reactor Systems Code 8-52
8.1.4.2 INTOR 8-59
8.1.4.3 Cost engineering 8-61
8.1.4.4 Availability program 8-65
8.2 FUSION ENVIRONMENTAL ASSESSMENT PROGRAM 8-67
REFERENCES 8-68

8. ADVANCED SYSTEM STUDIES

Summary of Activities

Advanced system studies in the ORNL Fusion Program are carried out by the Fusion Engineering Design Center and the Fusion Environmental Assessment Program. The activities of the Design Center included work on the Tokamak Fusion Core Experiment (TFCX), the Fusion Power Demonstration (FPD) tandem-mirror reactors, and the Ignition Spherical Torus (IST). In the assessment program, work continued on the generic environmental impact statement (GEIS) that will be required as the national fusion program advances.

In 1984, the Design Center participated in a wide variety of design studies for the U.S. Department of Energy. In the first half of the year, the major emphasis was on the TFCX devices. The Design Center developed the superconducting coil options and an independent copper coil option for the TFCX project and contributed substantially to selected design areas, such as rf systems, superconducting magnet systems, plant design, plasma analysis, and cost engineering. Design studies for the FPD series of tandem-mirror reactors continued throughout the year and resulted in the development of configurations for three possible devices. In the second half of the year, the tokamak effort concentrated on the IST, which is a device with very small aspect ratio proposed by the Design Center as an ignition experiment that is potentially much less expensive than the TFCX concepts. In addition to the design studies, the Design Center led the development of a tandem-mirror systems code, completed two tasks for the International Tokamak Reactor, developed the fusion cost data base and associated methodology, and performed an assessment of the availability of fusion reactors.

The Fusion Environmental Assessment Program continued to focus on developing the GEIS for fusion. A revised preliminary draft GEIS prepared in 1984 addressed a number of issues related to the introduction of central-station fusion power plants into the U.S. energy economy.

8.1 FUSION ENGINEERING DESIGN CENTER

8.1.1 Fusion Power Demonstration Reactor Studies

The Fusion Engineering Design Center (FEDC) supported the Lawrence Livermore National Laboratory (LLNL) in 1984 by developing configurations and performing subsystem designs for the Fusion Power Demonstration (FPD) series of tandem-mirror reactor (TMR) studies. The FPD device is an engineering test reactor (ETR) that includes all systems required to demonstrate power production. Three designs were developed to meet the following common goals:

1. The central cell should be ignited; that is, the power deposited by the fusion alpha particles in the central-cell plasma volume should balance the total power loss (energetic particles and radiation) from this volume.
2. The central cell should be no longer than necessary to achieve ignition.
3. The device should generate net electrical power; that is, the engineering Q (gross electric power divided by recirculating electric power) should be greater than or equal to unity.
4. The device should operate in a long pulse (hours) and achieve 50% availability over a 20-year life.

The objective of the FPD studies was to select a single concept as a baseline for further detailed design and analysis. To this end, these three configurations were developed in enough detail to estimate their relative costs and to evaluate the fuel cycle, power conversion systems, rf and neutral beam injection (NBI) systems, magnet systems, and maintainability of each one. The principal parameters for the three versions of FPD are shown in Table 8.1.

The plasma engineering configurations of FPD-I and FPD-II follow the principles employed in the Mirror Advanced Reactor Study (MARS)[1] and comprise a low-field (2.5-T), solenoidal central-cell region; high-field (24-T), central-cell choke coils; and an end-cell magnet system that is composed of a double-quadrupole, anchor/plug, yin-yang pair (Fig. 8.1). Central-cell passing particles that become trapped in the long end-cell transition regions are radially "drift pumped" to the plasma halo and represent a major power loss from the system. The engineering design philosophy for FPD-I and FPD-II reflects the configuration developed in the 1983 Tandem-Mirror Fusion Test Facility (MFTF-B) upgrade studies that minimizes size and emphasizes ease of maintenance.[2]

The FPD-I configuration has a 74-m-long central cell and produces 360 MW of fusion power. With a recirculation power of approximately 170 MW, this option, with minor revisions, could reach engineering breakeven. The most visible difference between the MARS

Table 8.1. FPD engineering parameters

Parameter	FPD-I	FPD-II	FPD-III
Fusion power, MW	360	480	140
Q	28	36	12
Wall loading, MW/m^2	1.4	1	0.9
Fueling current, kA	0.66	0.25	0.08
Magnet configuration (end cell)	MARS	MARS	Octopole
Choke field, T	24	24	24
Central-cell length, m	74	96	32
First wall radius, m	0.81	0.67	0.67

ORNL-DWG 85-2662 FED

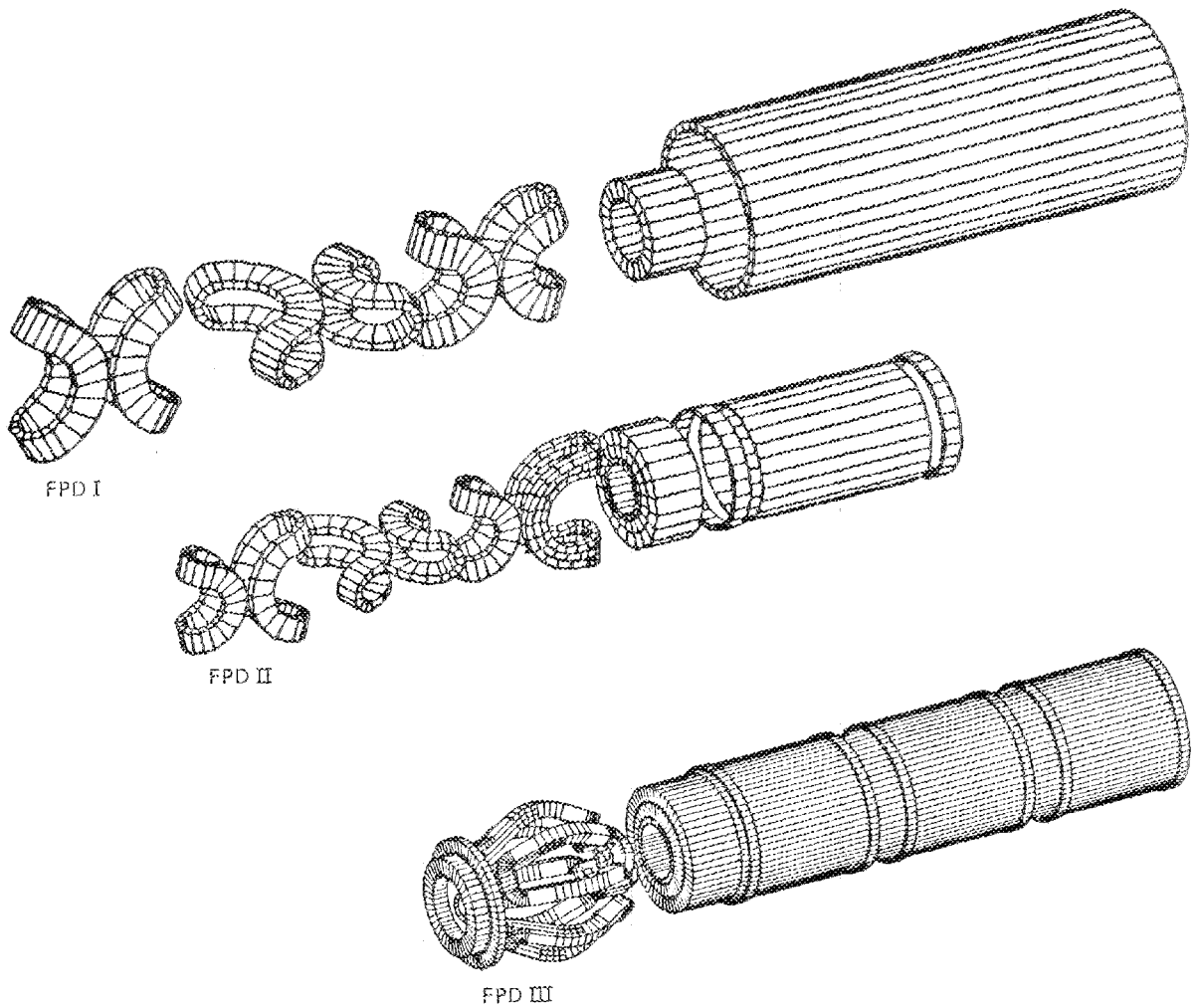

Fig. 8.1. Magnet configurations for FPD-I, FPD-II, and FPD-III.

and FPD-I concepts is the application of sheet coils to the central cell in FPD-I, which reduces field ripple and improves performance. A test cell is included in the FPD-I concept; it will develop a wall loading of 2 MW/m^2 of uncollided, 14-MeV neutrons.

The FPD-II configuration has a 96-m-long central cell and produces 480 MW of fusion power. At this power level, this device could produce about 200 MW of net electrical power using a reasonably efficient turbine plant. A test cell is included in the FPD-II concept; it will develop a wall loading of 4 MW/m^2 of uncollided, 14-MeV neutrons. A revision of the geometry and a better understanding of the physics account for the differences in performance between this device and FPD-I.

The FPD-III configuration differs from prior TMR configurations in that the end cell is based on an octopole coil concept. The configuration meets the design goals with a 32-m-long central cell and 140 MW of fusion power. Of the three machines studied, FPD-III stands out as the most cost-effective. Detailed descriptions follow.

8.1.1.1 FPD-I

The configuration study for FPD-I (Fig. 8.2) broke new ground with the first look at the semicontinuous central-cell solenoid design. The central cell uses six 10-m-long modules, each one made up of a pair of 5-m-long blanket modules (cooled with liquid lead-lithium) that can be inserted from opposite ends. This length was chosen to limit the module weight and the magnetohydrodynamic (MHD) effects on the blanket. The central cell is divided into six 10-m modules and two 5-m modules. The smaller modules are joined with the choke coils so the high axial force on these solenoids can be carried out by permanent structure. The complete 10-m module, when drained, will weigh less than 455 Mg (500 tons), which is judged to be a reasonable limit for handling and positioning by an overhead bridge crane.

Surrounding the blanket is a nuclear shield supported by a circumscribing truss so the shield can be extracted from the end of the module. Between the outer vessel wall and the nuclear shield lies a 9.25-m-long superconducting solenoid coil that provides the 2.5-T central field. This coil, which uses a long, thin solenoid, was developed to produce minimum magnetic field ripple. Low ripple is related to achieving high central-cell beta.

The choke coils create a peak field on axis of 24 T. As configured by General Dynamics, each coil is constructed using a normal-conducting insert coil and a superconducting background coil. The copper insert coil can be removed separately since it is not envisioned as a lifetime component. The winding pancakes are separated slightly at the horizontal center to allow radial injection of fueling pellets from a rail gun.

The two end cells are configured to permit easy assembly of the machine and replacement of all internal components, including the large C coils. The double-walled end-cell vessel has large hatches and contains water, forming a part of the biological nuclear shield.

The six C-shaped and one solenoid-coil superconducting magnets are placed on cold tables supported by truss struts. Axial loads are supported by struts to the end of the vessel. Coils can be replaced with minimum disruption of other coils and components. Adequate nuclear shielding permits the magnets to be lifetime components.

The end-cell heating systems use ion cyclotron resonance heating (ICRH), electron cyclotron resonance heating (ECRH), drift pumping, and NBI. The ICRH is applied to the transition region using four-loop antennas. There is not enough space for rigid waveguides. The ECRH is applied at two locations using quasi-optical transport and launching systems, also selected because of limited space. The launchers are arrayed axially so that the beams can pass through the major radius of the anchor coil. The sources (gyrotrons) are mounted on a winglike vacuum box with gate valves so that they can be replaced without bringing the system up to air.

Integrating the 475-keV, negative-ion NBI into the configuration proved difficult. The locations of the plasma target point and the C coils make axial fanning of the beams from each of the three required sources impossible. The three beams, two active and one on-line

ORNL–DWG 85-2663 FED

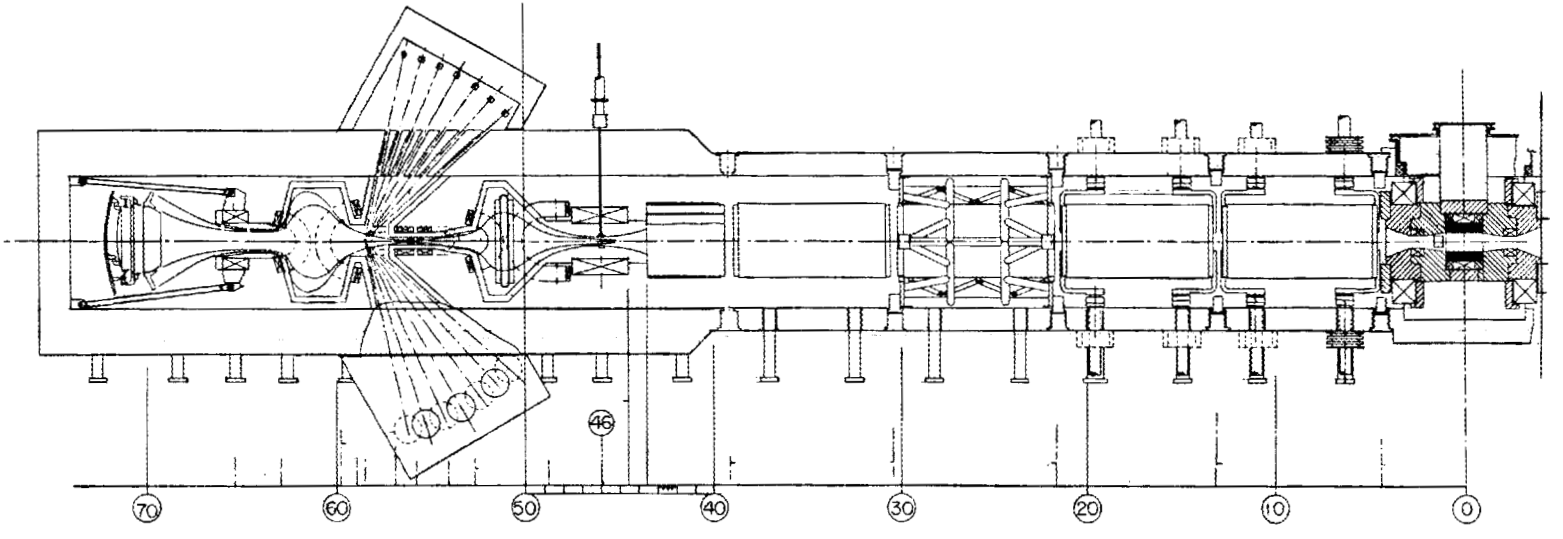

Fig. 8.2. Plan view of FPD-I.

spare, must be arranged in a circumferential fan, which allows only marginal nuclear shielding.

The halo scraper and direct convertor are considered lifetime components. However, these components can be removed by lifting them through their hatch. This arrangement minimizes the length of the reactor vault and is compatible with the vertical access philosophy of the other subsystems.

8.1.1.2 FPD-II

FPD-II has a 96-m-long central cell. This length and an improved end-plug design increase the fusion power to 480 MW. This design can supply 200 MW of net electric power when operated without the D-T axicell module. As in the FPD-I design, tritium-breeding blanket modules cooled with liquid lead-lithium make the FPD-II reactor self-sufficient in tritium. Thus, this device should be a true fusion power demonstration reactor. The overall configuration of FPD-II is shown in Fig. 8.3. The baseline design includes a nuclear testing station (or D-T axicell), central-cell modules with the semicontinuous solenoid concept, and small end-cell magnets.

The D-T axicell arrangement was developed to provide a large test area at very high wall loading. It was based on the MFTF-α+T configuration. The axicell has a 2-m-long nuclear test module to which 4–5 MW/m^2 of neutron power can be applied. The axicell module, shown in Fig. 8.4, consists of two superconducting background coils, two copper choke coils, one copper field-enhancing coil, the nuclear shielding, the test module, the vacuum vessel, and the support structure. The CS0 copper coils are an integral part of the test module, which has a separate hatch. The axicell nuclear shield consists of steel balls and water and satisfies the shutdown dose rate requirement of 0.5 mrem/h, 24 h after shutdown, for a 5-MW/m^2 wall loading.

The central cell is configured using eight full-length (8.7-m-long) modules and two half-length modules that are mated to the choke coils. The central-cell module for FPD-II is similar to that for FPD-I, except that there is enough nuclear shielding within the bore of the solenoid coil to lower the shutdown dose rate to an acceptable level. Therefore, instead of a double-walled vessel with a water shield, a single-walled shell with external ring stiffeners is provided.

The end cell is also similar to that of FPD-I, with several significant improvements. First, the biological shield is much smaller because of the reduced neutron source, which allows the use of a double-walled vessel only 0.6 m thick. Second, because ICRH subsystem power requirements are reduced, it is unnecessary to incorporate a four-loop antenna. A rigid waveguide simplifies the integration of this subsystem. Third, the point *b* ECRH subsystem uses two fewer gyrotrons. This permits more nuclear shielding and a less costly nuclear shield design. Fourth, reduced sloshing-ion beam power requirements, together with improved target point-to-coil geometry for FPD-II (the angle to the z-axis being relaxed to permit 90° injection), allow a much improved mechanical arrangement. Fifth, the injection point for pellet fueling has been moved so that it does not pass through the insert choke coil; it is located toward the central-cell side of the choke coil.

Maintenance for FPD-II calls for vertical lifting through dedicated hatches. This makes installation easier, shortens the reactor building, and improves our ability to replace subsystems or upgrade to a new concept, if necessary or desirable.

ORNL–DWG 85-2654 FED

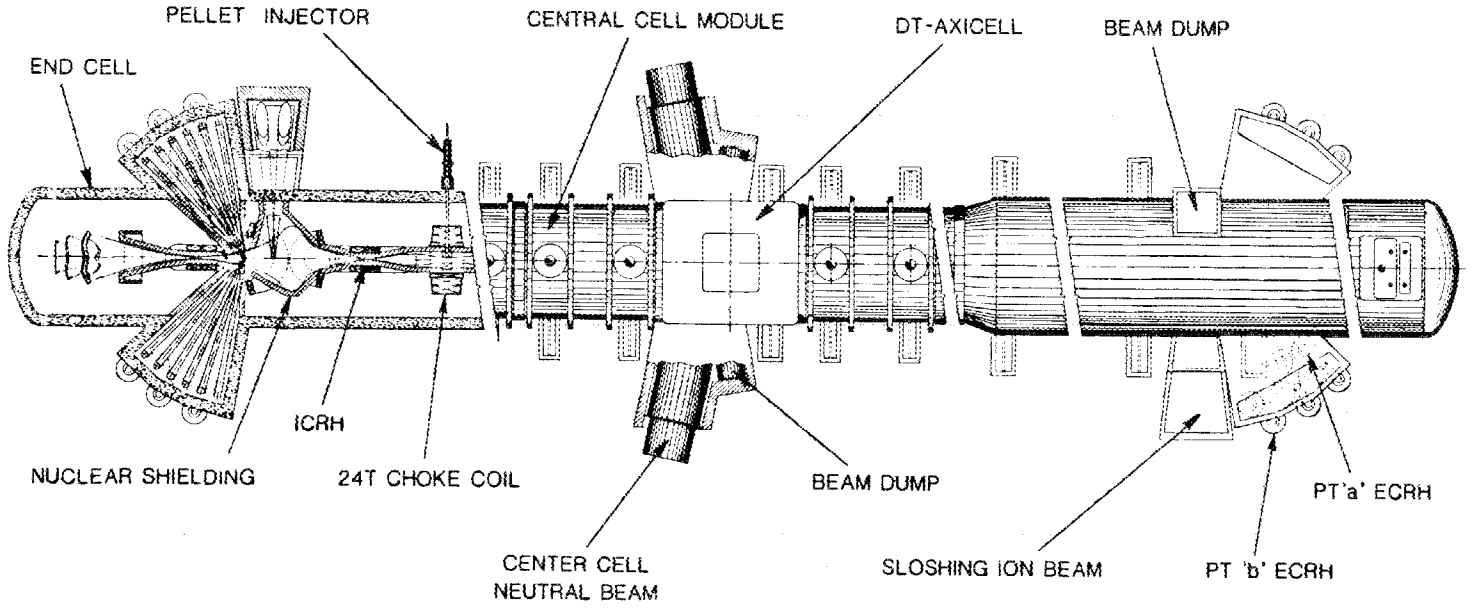

Fig. 8.3. Sectionalized plan view of FPD.

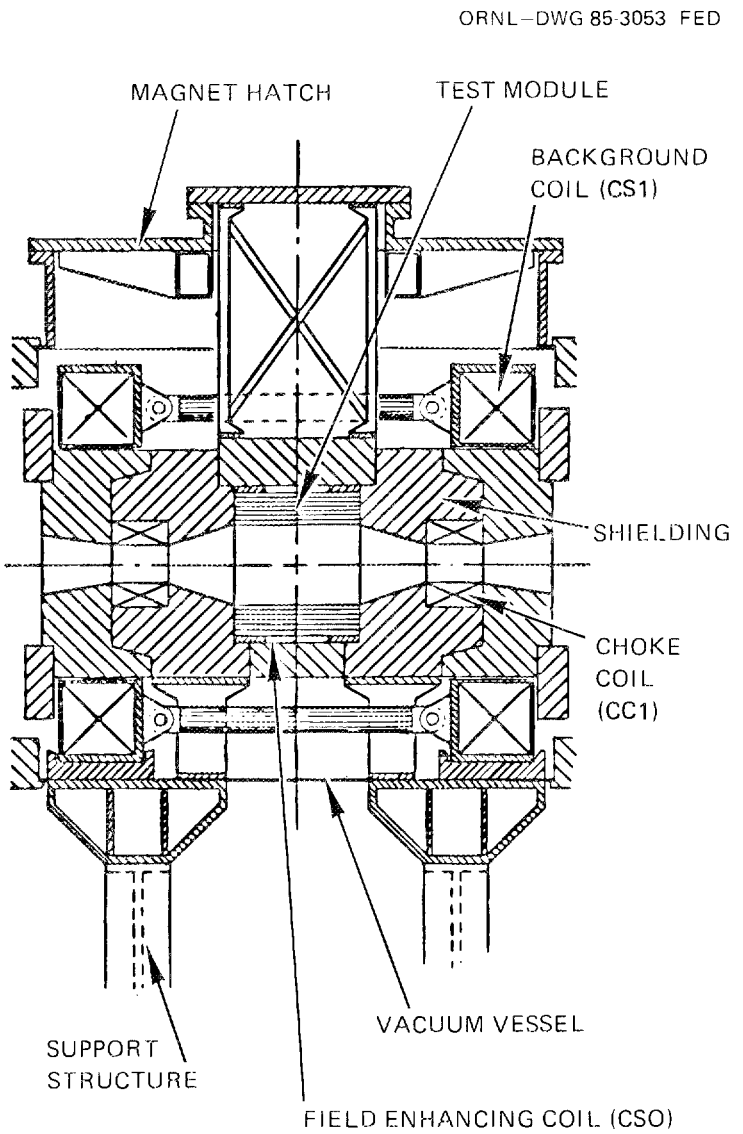

Fig. 8.4. Central-cell module of FPD-II.

The FPD-II configuration is an improved design primarily because of a significantly better end-cell plug design that reduces the end-cell nuclear source strength and heating system power requirements. The central-cell module design is also improved, requiring only a single-walled vacuum vessel. The D-T axicell was optimized with a wall loading of 5 MW/m^2.

8.1.1.3 FPD-III

The third version of the FPD device is designed to produce 140 MW of fusion power. As shown in Fig. 8.5, the device is 67.5 m long and 8.2 m in diameter, with a centerline

ORNL-DWG 85-2666 FED

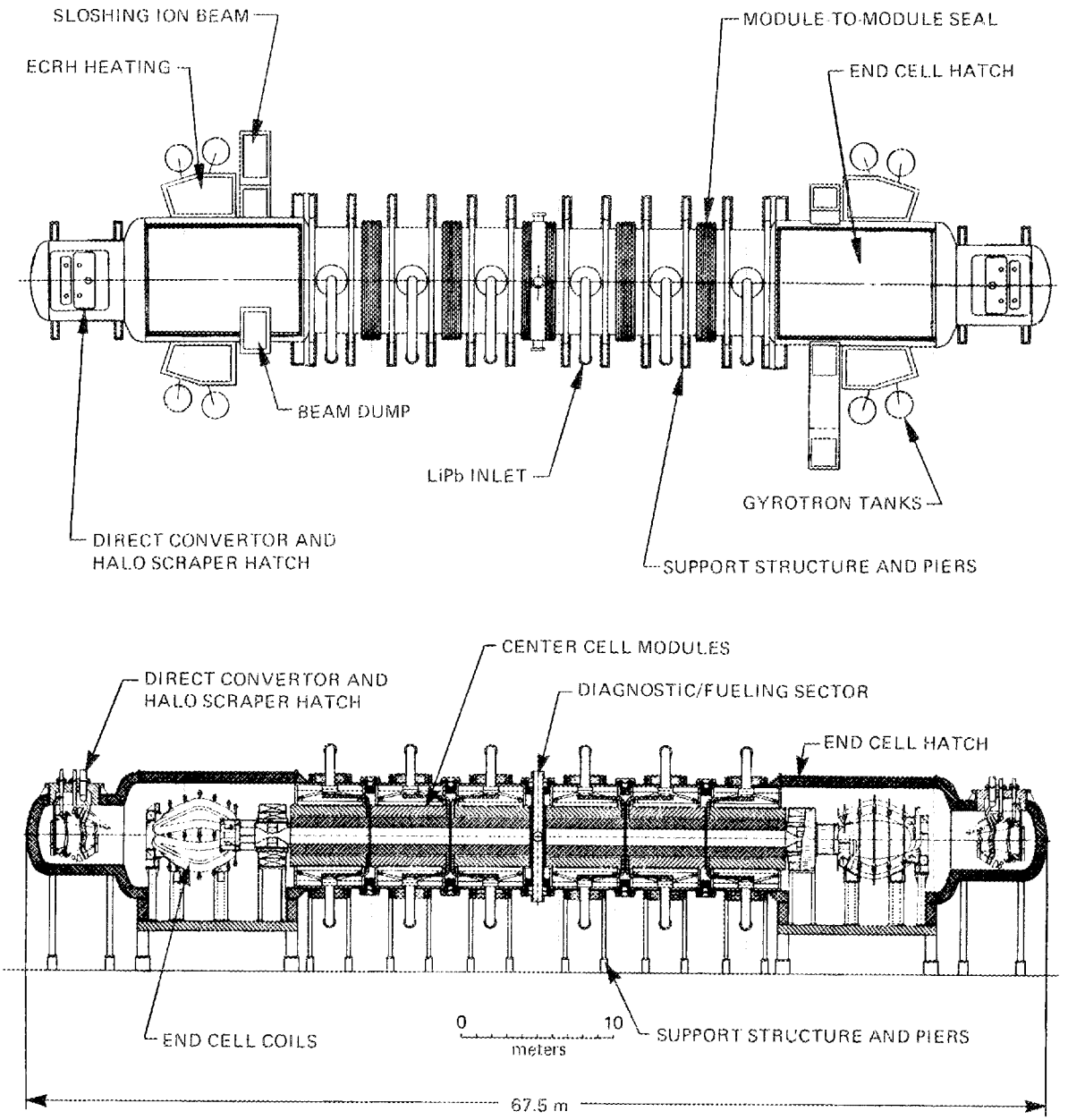

Fig. 8.5. Plan and elevation views of FPD-III.

height of 9 m. The device is assembled from six modular central-cell sections, a fueling/diagnostic sector, and two end cells with direct convertors.

Each central-cell module is 5.5 m long and 7 m in diameter and contains the blanket, shield, solenoid coil, and vacuum tank required to make it a "standalone" unit. All units, except the end units (those closest to the end cells), are interchangeable. The length of the

central-cell modules was again chosen to limit MHD effects in the blanket. Without fluids in the shield and blanket, the estimated weight of a module is 250 Mg (275 tons). Central-cell modules are structurally connected by tie bolts that resist the axial load and by bellows that form the circumferential vacuum seal. The four central modules can be independently removed from the device for maintenance or repair.

FPD-III differs from prior TMR configurations in that the end cell is based on an octopole coil concept. The end-cell coil set consists of choke coils, a transition octopole, the large octopole, and an outer mirror coil. The end cell also contains provisions for negative-ion neutral beam heating and ECRH, drift pumping, a halo scraper, and a direct convertor. The end-cell vacuum vessel is 8.2 m in diameter and 18 m long. The vacuum boundary is extended in winglike appendages for the ECRH and coils.

The principal feature of the end cell is the octopole magnet. Three concepts were considered before the preferred arrangement was selected. A continuously wound octopole magnet provides the required access for the neutral beams but would be very difficult to build and maintain. An octopole assembled from eight individually wound window frames, while easy to build, results in very limited access for beam injection. The selected scheme, using four window frames, combines the manufacturing/maintenance and beam access advantages of the other schemes. A demountable, circumferential support structure allows the upper window frame to be independently removed from the vacuum vessel, exposing other components to top access. Other magnets include a smaller "transition" octopole, a correction coil, and an outer mirror coil. All coils, except a resistive insert coil in the high-field region of the choke, are superconducting. The window-frame octopole concept requires a correction coil to compensate for the end currents. Because the correction coil must be close to the octopole, the end of the octopole must be stepped and the correction coil staggered in the axial direction.

ECRH is applied at three locations in each end cell. The thermal barrier at point *b* and the electron mantle are at the same axial location, 31 cm beyond the midplane of the large octopole magnet. The point *b* region is on axis, while the mantle is centered 90 cm off axis. A third ECRH system is required for the potential peak at point *a*. The point *a* system requires one 200-kW gyrotron, while the point *b* and mantle systems each use six 1-MW gyrotrons per end. The thermal barrier system for FPD-III uses a quasi-optical launching and transport system centered on the horizontal midplane. Launchers are arrayed axially so that the ECRH passes between the coil windings. The launchers for the point *a* and mantle systems are inside the vacuum vessel. A waveguide interface penetrates the vessel, carrying the power from the gyrotrons to the launcher. The total prime power requirement for the three systems is approximately 45 MW.

The 475-keV, negative-ion-based NBI system is positioned to produce the sloshing-ion distribution in each plug. Integrating this system again proved difficult because of the lack of space in the required location, the midplane of the small octopole. The beam must pass through an area already crowded by magnetic windings and structure, neutron shielding, and coil crossovers. One beam line is centered on the azimuthal midplane; the beam line at the other end of the device enters at an angle of 45° below midplane.

Drift pumping coils are placed at two axial locations in each end cell. A slotted antenna encircles the plasma to pump the ion species trapped in the plasma core near the small octopole. In the outer end of the large octopole, four split-coaxial sections follow the lobes of the plasma edge surfaces.

The double-walled end-cell vacuum vessel has 60 cm of biological shielding and water between the walls. A hatch that extends axially from the choke coil to the outer mirror coil is wide enough to allow installation/removal of the end-cell magnets. The vacuum tank diameter is reduced near the halo scraper/direct convertor, which is installed through a port on top of the vessel.

8.1.2 Tokamak Fusion Core Experiment

The Design Center participated in the Preconceptual Design Study for the Tokamak Fusion Core Experiment (TFCX), which developed four options for presentation to the Department of Energy (DOE) in July 1984. In the first part of the year, most work was devoted to characterizing the nominal and high-performance superconducting options and to the support of Princeton Plasma Physics Laboratory (PPPL), which led the TFCX studies, in selected areas. The Design Center also developed a TFCX design using continuous copper toroidal field (TF) coils, which was not selected as one of the TFCX options.

The four TFCX options were designed with a common physics base, specified gaps and thicknesses, and material properties. Key plasma parameters that were fixed include the following:

Elongation κ	1.6
Triangularity δ	0.3
Safety factor at edge q	2.4
Temperature, keV	10
Ignition parameter C_{ig}	1.5

The ignition parameter was specified by:

$$C_{ig} = 0.295\beta\tau_E B_t^2,$$

where

$$\beta = 0.2(1 + \kappa^2)/2Aq,$$

$$\tau_E = (0.39 \times 10^{-6})aI_p,$$

B_t is the field on axis, A is the aspect ratio, a is the plasma radius, and I_p is the plasma current. In addition, the pulse length was specified to be 70% of the internal plasma flux divided by the toroidal loop voltage during burn.

Important design features common to all options included:

- current drive with lower hybrid resonant frequency (LHRF) heating to provide most of the power to ramp up the plasma current, augmented by ion cyclotron resonant frequency (ICRF) heating to heat the plasma to ignition;
- 16 TF coils, with a window between the outer legs that allows direct radial extraction of the main shield modules;

- poloidal field (PF) coils located outside the TF coil bore, with locations restricted to allow access to shield modules; and
- a flat, single-leading-edge limiter at the bottom of the plasma, with vacuum ducts connected to the underside of the vacuum vessel.

The characteristics of the four TFCX options are shown in Table 8.2. The nominal superconducting option (Fig. 8.6) is based on the previous Fusion Engineering Device (FED)/TFCX designs. In the high-performance superconducting option, the nuclear heating in the TF coils is allowed to increase from 1 to 50 mW/cm^3, with a corresponding decrease in required inboard shielding. The two copper TF coil options were developed by PPPL and are not described here.

Because the TFCX system definition studies have been a national undertaking, a special approach to the management of this effort has been needed. The criteria for the management approach are:

- providing a means for developing a national consensus on technical and cost issues,
- providing a means for controlling this diverse activity, and
- having flexibility for adapting to new innovations.

Table 8.2. TFCX option characteristics

	Superconducting		Copper	
Parameter	Nominal	High performance	Nominal	High performance
Major radius, m	4.08	3.61	3.35	2.60
Minor radius, m	1.52	1.30	1.30	1.04
Aspect ratio	2.69	2.77	2.58	2.49
Field on axis, T	3.73	4.23	4.00	4.50
Inboard shielding, m	0.62	0.36	0.12	0.015
Fusion power, MW	267	270	229	197
Wall loading, MW/m^2	0.69	0.92	0.85	1.17
Plasma current, MA	11.2	10.5	10.9	10.4
Pulse length, s	618	452	458	298
LHRF power, MW	32	26	26	19
ICRF power, MW				
Initial	6	10	7	7
Final	31	36	28	26
TF power, MW			405	333
PF power, MW			51	108
Beta, %	5.51	5.35	5.76	5.95
Mirnov ignition parameter C_{ig}	1.5	1.5	1.5	1.5

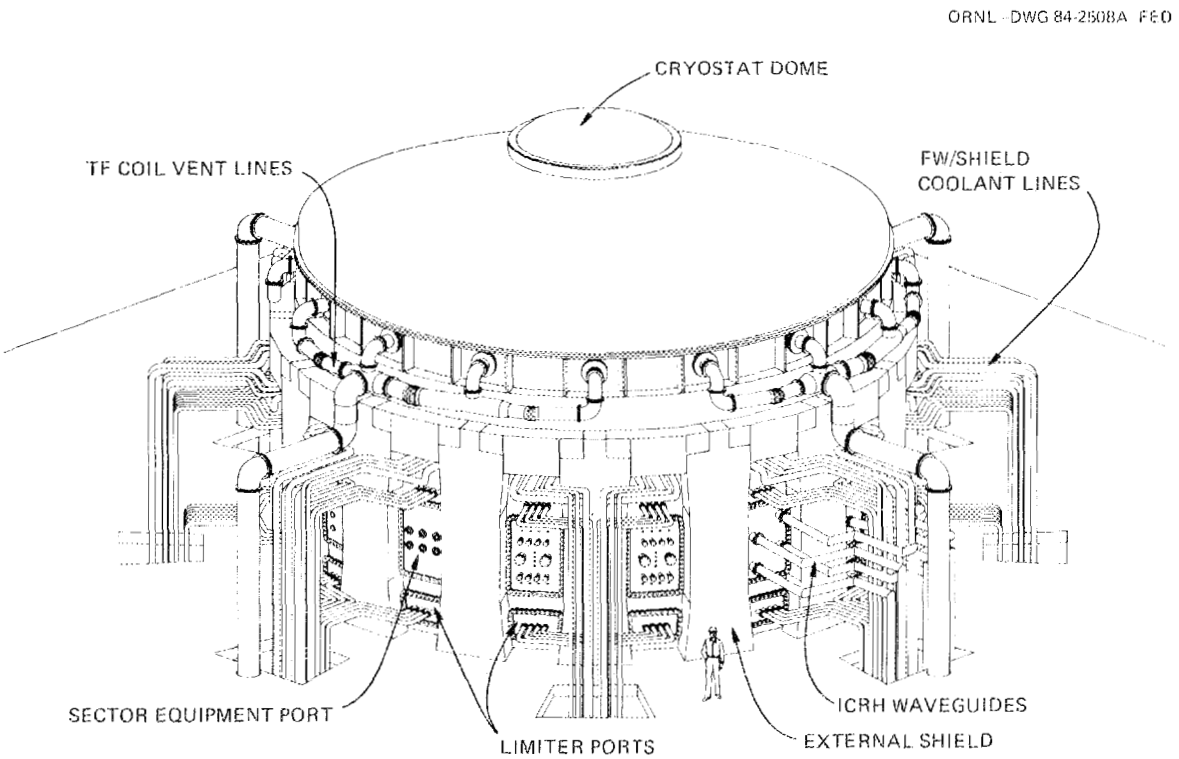

Fig. 8.6. TFCX superconducting option, TFCX-S.

The approach to organizing and managing the project has the following characteristics:

- Technical and costing approaches (discussed below) have been adopted.
- Within the framework of these approaches, the options have been separated into distinct classes. Responsibility for developing the designs for specific classes has been assigned to a design group at the Design Center and to another group centered at PPPL.
- Ideas for innovative design approaches have been fostered from fusion laboratories at the Massachusetts Institute of Technology (MIT) and LLNL.
- Many workshops have been organized to develop a consensus on the options to be pursued, along with the specific design and costing approaches to be used.
- Substantial documentation has been developed to facilitate a broad review of the design and costing basis.

The objective in establishing the technical approach to the TFCX engineering design was to provide a mechanism for the development, by a national design team, of several design options on a common engineering and physics basis. The technical approach used was to establish a detailed design specification to control the design effort.

Fusion projects prior to TFCX have often had as their only specifications a list of physics parameters that the device had to satisfy. With the TFCX approach, a set of prescriptions was developed for sizing the elements of the device. As the analysis proceeds, these

prescriptions are refined and the range of options more precisely defined. These prescriptions are detailed in the TFCX preconceptual design specifications.[3]

The costing of the options for TFCX is being carried out in a manner similar to the technical approach. A cost specification has been developed to specify and control the method for costing the options.

Two methods are used for TFCX subsystems. Where a solid, historical data base is available for costing a particular subsystem, this data base is distilled for the cost specification and applied to all options for that subsystem. An example is the TFCX TF coils. Large copper and superconducting coils have been built for other fusion devices, yet the TF coils for TFCX will be, in detail, unique. An excellent method to estimate the costs of such devices is to base costs on previously delivered cost per unit (weight, volume, area, etc.) of similar components.

8.1.2.1 Superconducting devices

Configuration

The configuration design approach incorporated in the TFCX superconducting studies is based on the design features that have evolved from the FED/International Tokamak Reactor (INTOR) studies. Distinguishing features of this approach are the modularity in design of as many components as possible and the arrangement of components for ease of maintenance. In particular, care has been taken to ease the maintenance of components that may require frequent replacement, such as the limiter blades and rf modules. Other components are also replaceable but with increasing difficulty, such as the shield modules, the PF coils, and the TF coils. Figures 8.7 and 8.8 show elevation and plan views of the nominal superconducting option. The design details of the major components and the device interface with the device hall facility have been carefully developed to integrate the main coolant, electrical, and vacuum lines with the device and to better understand the space needed for the ancillary equipment. To provide more space and improve access for installing the ancillary equipment, a steel floor and substructure were designed to circle the entire device.

The vacuum topology consists of a combined vacuum boundary between the plasma and superconducting magnetic system, formed by welding three major structural members together: the vacuum ring module, the window module, and the outboard wall structure (see Fig. 8.9). The ring and window modules are welded along poloidal seals formed at their interface. A single-turn vacuum seal is added to provide the primary vacuum interface with the plasma.

Eight cryosorption pumps, located below floor level, are equally spaced around the device. Shielded vacuum ducts are attached to the vacuum structure in the spaces between the 16 TF coils. They provide the gravity support for the torus. The conductance of the vacuum system is limited by the area available for the vacuum ducts located between the TF coils.

The TF coils have been sized to allow a two-piece limiter blade to be extracted from the torus. An intercoil support structure at the top and bottom of the TF coil has been developed. A local structure stiffens the case and is flared outward locally to pick up the outer-ring beam structure. Bolted TF coil interfaces are located between TF coils along the

ORNL-DWG 85-2667 FED

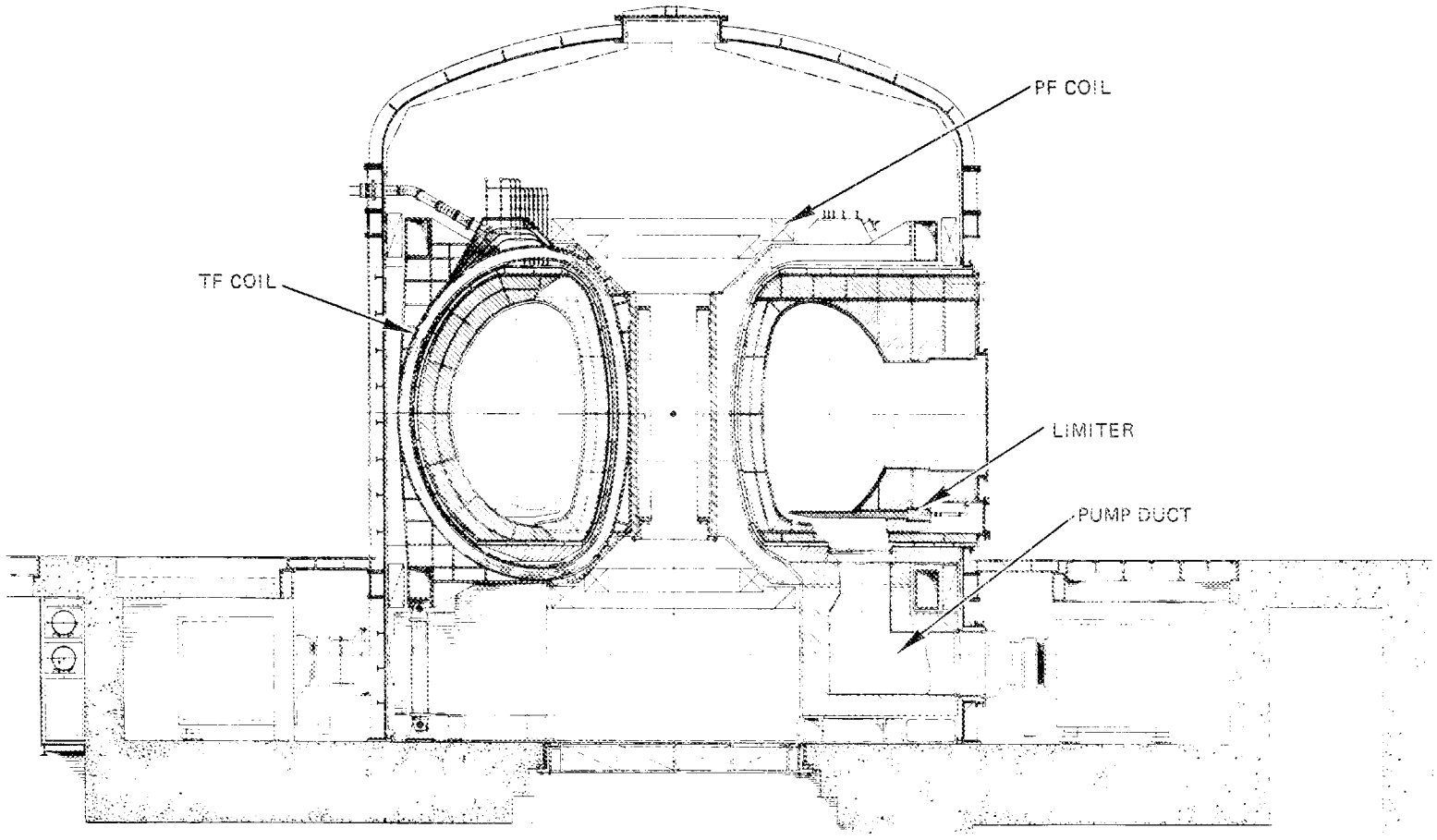

Fig. 8.7. Elevation view of TFCX-S.

ORNL DWG 85-2668 FED

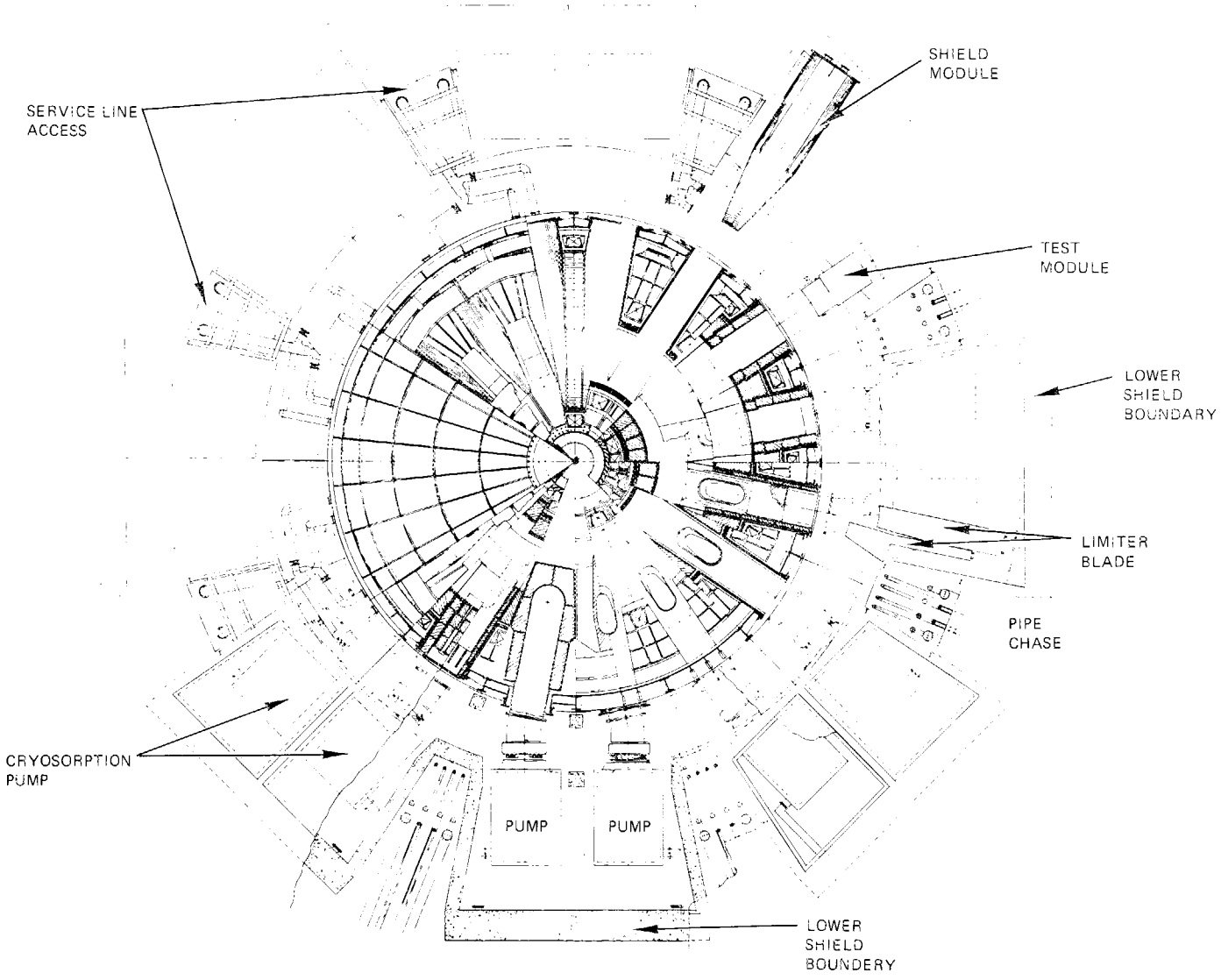

Fig. 8.8. Plan view of TFCX-S.

ORNL-DWG 85-2669 FED

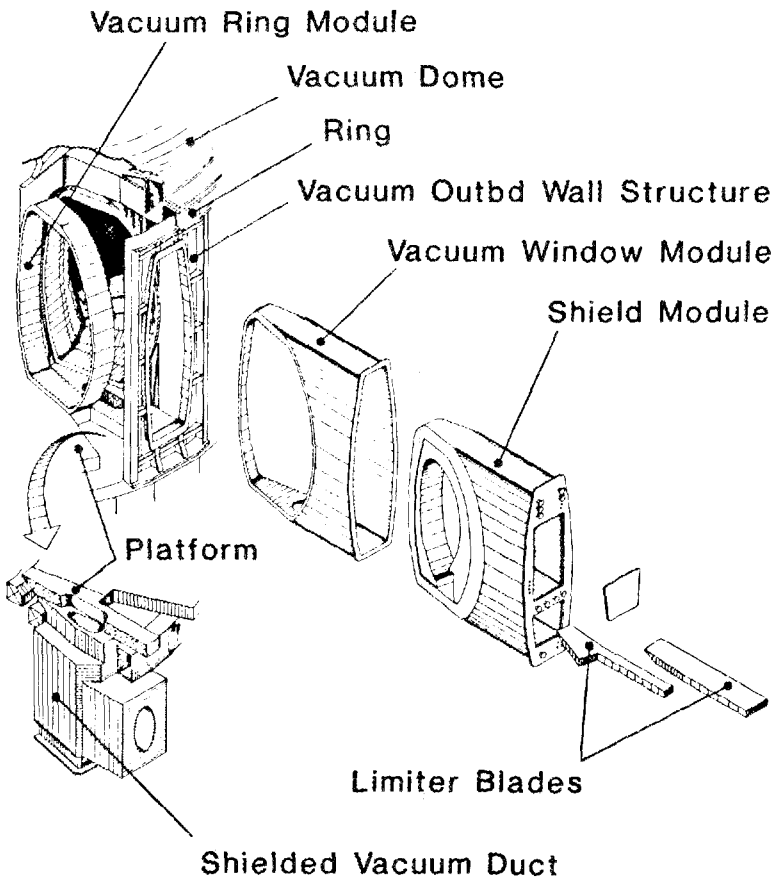

Fig. 8.9. Vacuum vessel and shield configuration.

inboard region of the TF coil corners and at the midsection of the upper-ring beam. The upper-ring beam provides bolt access around the joint to prevent interference with the outboard equilibrium field (EF) coils.

Coolant lines servicing the shield, first wall, and reactor components penetrate the reactor floor behind every other TF coil. Helium and superconducting electrical lines leaving the TF coils and upper PF coils penetrate the vacuum boundary through a ring structure, so the vacuum dome can be removed without disturbing any lines.

A mechanical pump limiter removes helium ash and hydrogen particles from the plasma. The limiter forms a continuous toroidal belt at the bottom of the device and has a single leading edge, with a flat surface facing the plasma. The limiter blade is divided into two segments per sector so that the limiter can be installed through the access opening in the bottom of each sector. The limiter blades are protected by a removable, expendable sleeve of armor tiles bonded to an actively cooled copper substrate. Candidate materials for the tiles are beryllium and graphite.

Erosion determines the lifetime of the protective surface. Therefore, tile size was studied to find the maximum allowable tile thickness, based on the thermal loads experienced by the limiter. Temperature and thermal-stress distributions were calculated as a function of tile thickness. Limits based on maximum temperature, material strength, and fatigue were determined for limiter configurations with either graphite or beryllium tiles brazed to a copper substrate.

Erosion of the limiter surface by both sputtering and disruption-induced melting and vaporization was evaluated. Disruption erosion is the dominant erosion mechanism for TFCX. Using the calculated tile thicknesses and erosion rates, calculated erosion lifetimes for the nominal superconducting option are: for graphite, 1.1 years of operation with a temperature limit of 400°C and 2.8 years of operation with a temperature limit of 1000°C; for beryllium, 0.1 year of operation assuming that the entire melt layer is lost and 0.5 year of operation assuming the melt layer remains intact. Lifetimes for the high-performance option are approximately 20% less, as shown in Fig. 8.10.

The inboard region of the first wall consists of Graphol graphite tiles, attached directly to the inboard shield surface with one graphite bolt per tile. The tiles are passively cooled,

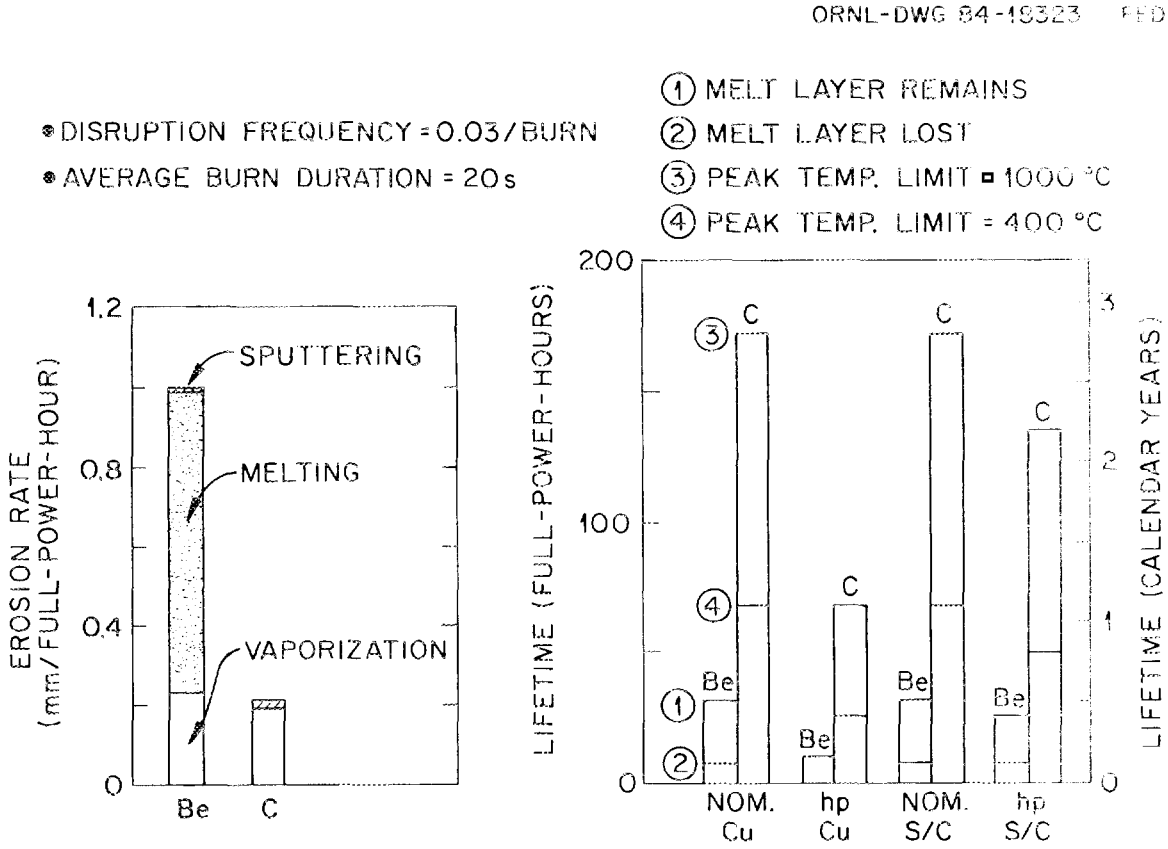

Fig. 8.10. Limiter erosion rate and lifetime.

radiating their heat load to the cooled shield surface and to the actively cooled outboard panels. The graphite bolts permit the in situ replacement of a single tile by remote means. The 3-cm-thick graphite tiles are square (10 cm on a side).

The outboard region of the first wall consists of seven actively cooled, stainless steel panels. These panels are mounted to the shield structure with pinned brackets to allow thermal expansion in both toroidal and poloidal directions. The lifetime of both the inboard and outboard first walls for both options is longer than that of the device.

The shielding was designed to meet the following requirements:

- The shield must limit the nuclear heating in the TF coil windings to 1 mW/cm^3 in the nominal case or 50 mW/cm^3 in the high-performance case.
- The maximum dose to the TF coil winding insulator must not exceed 2.5×10^8 rad, and the maximum dose to the thermal insulator for the TF coil must not exceed 5×10^9 rad in the nominal case, or ten times those limits in the high-performance case.
- The displacements per atom (dpa) for the copper stabilizer in the TF coil windings must not exceed 2×10^{-4} dpa.
- The shutdown dose rate at the outer surface of the reactor island and any other region within the device island requiring contact maintenance must not exceed 1 mrem/h at 24 h after shutdown.

The shield design is the same for both options, except for the inboard shield thickness, which at midplane is 0.63 m for the nominal case and 0.36 m for the high-performance case. The inboard bulk shield is 80% Nitronic-33 stainless steel plate with machined passages for the water coolant that is 20% of the volume. The intermediate region of the shield module is a composition of 60% stainless steel and 40% water. Here the steel consists of Nitronic-33 stainless steel balls, which are significantly cheaper than a machined plate. The thickness of this region at midplane is 0.70 m. In the outboard region of the shield module, water is the bulk-shield material. The thickness of this region at midplane is 1.58 m.

Plasma operations

MHD equilibrium: The goal of the TFCX MHD equilibrium studies is to determine the characteristics of the PF coil system for each TF coil option in order to minimize the machine size while satisfying

- plasma volt-second requirements,
- mechanical configuration constraints,
- maximum field and current density constraints, and
- plasma shape requirements.

In the TFCX preconceptual design analysis, the PF system consists of three coil groups: a central solenoid, shaping field coils, and outboard EF coils. The fields of the three coil sets are coupled, reducing the total ampere-turns and allowing the magnetic energy stored in the system to be used for both plasma current maintenance and MHD equilibrium.

The copper TF device design parameters were chosen using a plasma scaling based on a set of numerical equilibria. The PPPL Generalized Flux Coordinate Equilibrium Code is

used to generate data from which the coefficients of expressions relating the plasma current I_p, the toroidal field B_t, and the internal flux $\Delta\psi$ to the aspect ratio are derived.[3] This fixed-boundary code allows prescribed profiles of plasma shape, pressure, and safety factor q. Vacuum fields consistent with these equilibria are represented by toroidal multipoles,[4] also given as functions of plasma geometry, and are used in designing the PF coil system.

The superconducting TF device design parameters are the result of an iterative process involving the tokamak systems code (with the TFCX plasma scaling), the EFFI magnetics code, and the FEDC MHD equilibrium code.[5] This process is shown in Fig. 8.11. The FEDC equilibrium code computes the coil currents necessary to maintain a plasma approximating a prescribed shape for given pressure and toroidal field ($F = RB_t$) profiles. The two MHD equilibrium codes have been satisfactorily compared.[6,7]

When the design points have been established, PF coil currents representing the time-dependent plasma operation scenario are simulated by a set of equilibria with specific properties. For example, the volt-second requirement during burn is taken to be $\Delta\Phi_{PF} = 0.7\Phi_{int}$, where Φ_{int} is the internal flux of the plasma and $\Delta\Phi_{PF} = \sum_i \Delta(M_{ip}I_i)$ is the externally applied flux due to the PF system. During plasma bulk heating, the requirement is $\Delta\Phi_{PF} = \Delta\Phi_{res} + \Delta\Phi_{ind}$, where $\Delta\Phi_{res}$ and $\Delta\Phi_{ind}$ are the resistive and inductive flux, respectively. The current in the ohmic heating (OH) solenoid is adjusted in equilibrium calculations until the appropriate volt-second values are matched at

- low beta, before heating,
- high beta, at start of burn, and
- end of burn.

Neutral transport for the pump limiter and divertor: Pumping rates for TFCX are discussed for both the pump limiter and the divertor options. In particular, a coupled plasma-neutral transport model is used to account for the effects of neutral recycling near the neutralizing plate. The primary effect introduced by neutral recycling is an increase in the pumping probability per ion flowing into the divertor (or limiter shadow). Pumping rates sufficient to exhaust helium ash are found for both options.

Plasma transport along the magnetic field line is evaluated using the ZEPHYR code[8] coupled with a simplified neutral transport model.[9] Input to ZEPHYR for the radial scrapeoff width and "watershed" density and temperature is provided by a radial transport model based on the transport equations.[10] This model uses a two-point method[11] to calculate particle and energy losses (including conduction) along the field line and uses an assumed recycling profile. The two models are iterated until the recycling calculated with ZEPHYR is consistent with that used in the radial transport model. Also, the simplified neutral transport model used in ZEPHYR is benchmarked with the DEGAS neutral transport code.[12]

The pump limiter case consists of 16 ducts, each with a conductance of 1.9×10^4 L/s and a pump speed of 5×10^4 L/s (a total effective pumping speed of 2.2×10^5 L/s). The plasma parameters at the main plasma/scrapeoff interface are taken to be $n = 3 \times 10^{13}$ cm^{-3} and $T = 200$ eV, for a total heat flux of $\approx$50 MW on the limiter over the entire scrapeoff. Figure 8.12 shows the calculated density and temperature profiles in the

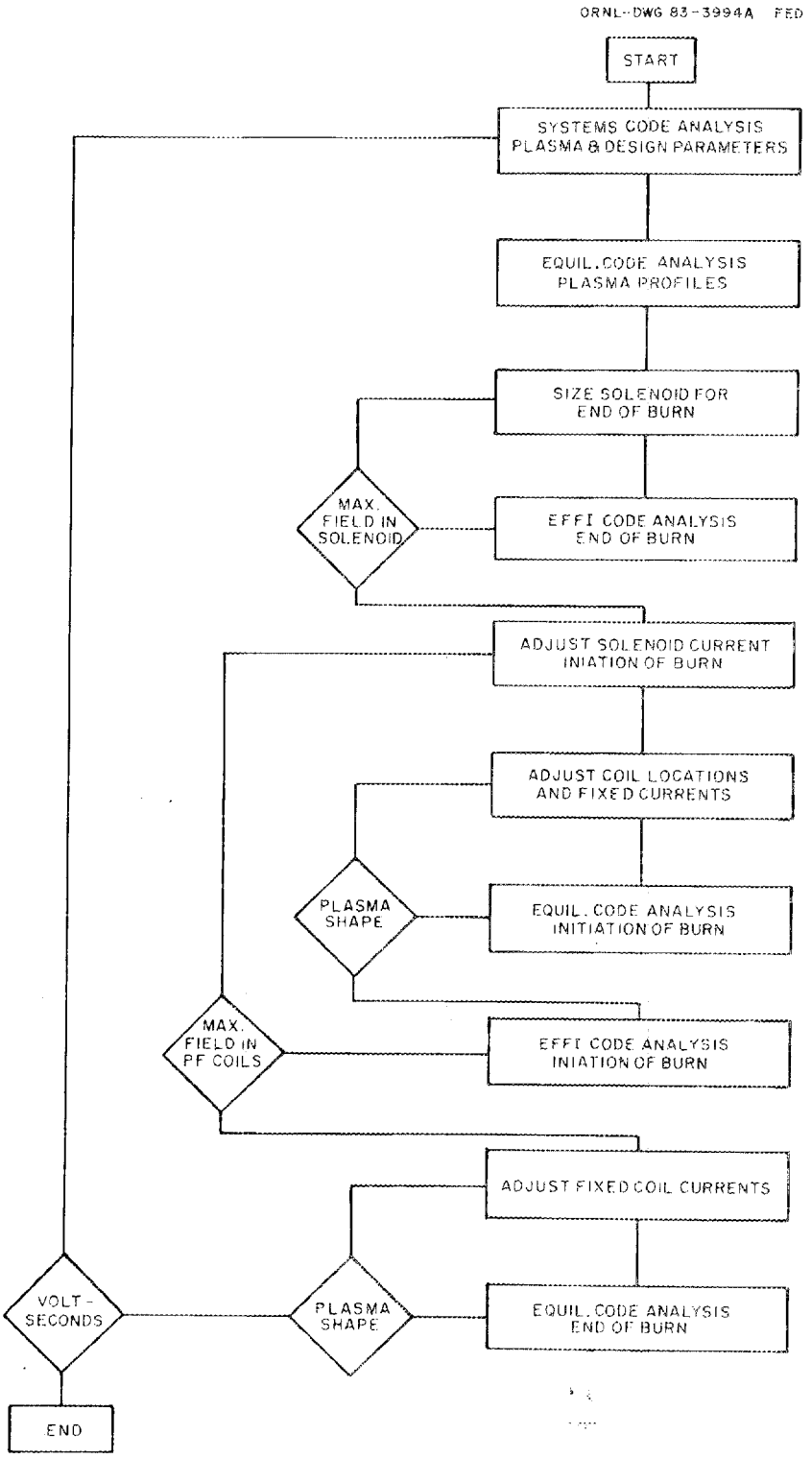

Fig. 8.11. Magnetics analysis flow chart.

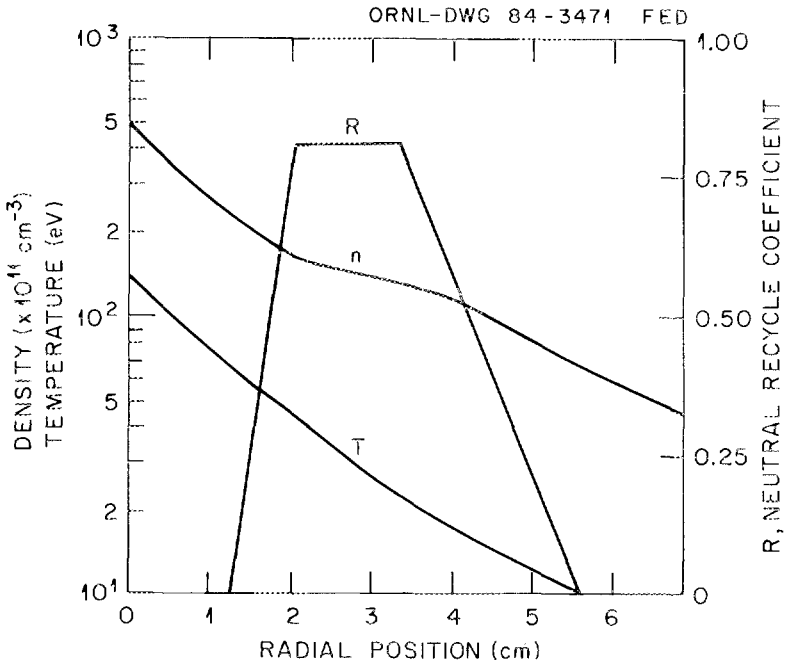

Fig. 8.12. Limiter scrapeoff profiles.

scrapeoff. The limiter leading edge is positioned where the heat flux (in the poloidal direction) has fallen to 200 W/cm^2. For this case, the leading edge is 2.3 cm into the scrapeoff. Beyond this point, plasma flows below (into the "throat" of) the limiter and is available for pumping; in this case, the total flow rate into the limiter throat is 4.2×10^{21} s^{-1}. The low flow rate is due to the high neutral recycling that occurs below the limiter ($R = 0.82$), which results in a low Mach number ($M = 0.13$) at the throat entrance. The high neutral recycling also results in the pumping of a large fraction (66%) of the plasma that flows below the limiter, corresponding to a total pumping rate of 2.8×10^{21} s^{-1}. Although the pumping efficiency for the plasma that flows below the limiter is high, the pumping rate is only about 1% of the total flow rate onto the entire limiter, because most of the flow is on the front surface of the limiter. The predicted pumping rate of 2.8×10^{21} s^{-1} should be sufficient to exhaust the 10^{20} alpha products produced each second (60-MW charged fusion power), assuming a 5% helium density ratio and equivalent helium-hydrogen transport.

The divertor case consists of 16 ducts, each with a conductance of 1.9×10^4 L/s and a pump speed of 2×10^4 L/s (a total effective pump speed of 1.6×10^5 L/s). The entire scrapeoff plasma flows into the divertor region and is subject to pumping, although only the outboard diverted plasma is considered to be pumped here. The density and temperature at the scrapeoff/main plasma interface are taken to be $n = 3 \times 10^{13}$ cm^{-3} and $T = 350$ eV, which results in a scrapeoff plasma depositing approximately 50 MW to the divertor. The resultant radial profiles for the density and temperature are shown in Fig. 8.13. The neutral recycling for the divertor case is higher ($R = 0.91$) than for the limiter case and causes low flow rates into the divertor. This is reflected in the flat density profile

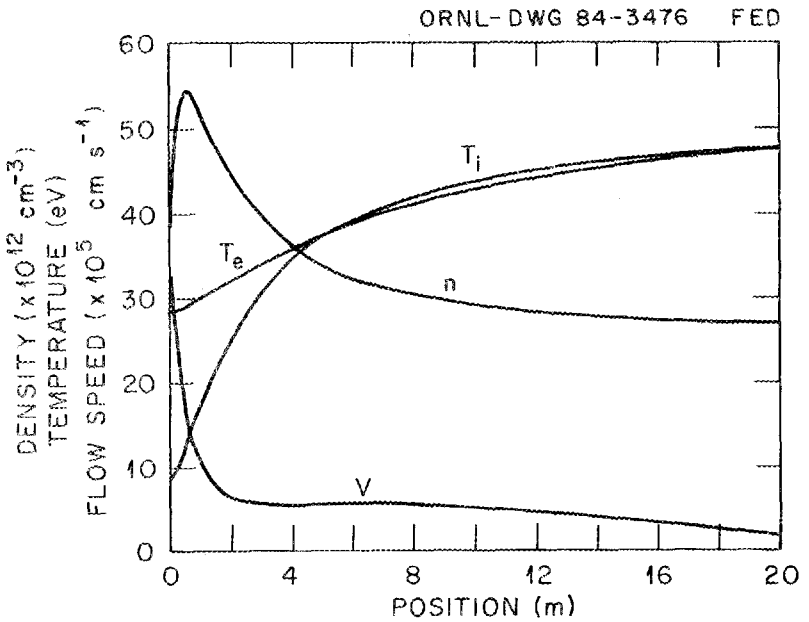

Fig. 8.13. Divertor scrapeoff profiles.

shown in Fig. 8.12. The total plasma flow rate into the divertor chamber is 1.9×10^{22} s^{-1}, of which approximately 50% is pumped (9.0×10^{21} s^{-1}). This pumping rate is greater than that required for helium exhaust and indicates that even lower pump rates may be adequate.

Plasma operation contours: The ORNL tokamak transport code, WHIST, was used for one-and-one-half-dimensional (1½-D) plasma simulations. The nominal copper design for TFCX [R_0 = 3.25 m, a = 1.30 m, κ = 1.6, δ = 0.3, B_0 = 4 T, $q(a)$ = 2.4] was chosen as a representative example. The model includes noncircular plasma equilibria (consistent with pressure and current profiles), particle balance (five ion species and electrons), energy balance (ions and electrons), poloidal flux diffusion, and fixed impurities. Ohmic heating and local, instantaneous alpha deposition are supplemented by a Gaussian heating profile, $-\exp[-(r/r_0)^2]$, to represent the rf heating profile. The auxiliary power is split between ions (75%) and electrons (25%) with r_0 = 0.8 m. Current profile evolution causes sawtoothing; the density, temperature, and current profiles are periodically flattened (τ_{st} = 400 ms) consistent with particle, energy, and helical flux conservation inside the sawtoothing region. The affected region typically extends to $r \sim 0.75a$. Plasma losses are then dominated by confinement in the edge plasma, where gradients are large. Fueling is by gas puffing and recycling (95%). Neoclassical transport is taken as twice that given by Hinton and Hazeltine. The Hastie-Hitchon model is used for thermal ion-conduction loss by toroidal field ripple, assuming an edge ripple of 1.5% and 16 TF coils. Ripple losses increase as the magnetic axis shifts outward during evolution of the MHD equilibrium. Anomalous electron energy confinement and particle diffusion are a combination of neo-Alcator scaling and a modified form of GMS scaling that includes a finite-beta enhancement term $f(B)$. Table 8.3 describes the confinement modules used in this study. Figure 8.14 shows plasma operation contours with an oxygen impurity density of 6×10^{11} cm^{-3}.

Table 8.3. Plasma transport models

Scrapeoff layer, m	0.1
Fueling	Gas puffing and recycling at wall
Ion energy confinement χ_i	$2\chi^{neo} + \chi_{RT}^{rip} + \chi_{BD}^{rip}$
Electron energy confinement χ_e	$2\chi^{neo} + \chi_E$
χ_E, cm^2/s	$\chi_{NA} + 0.72\chi_{GMS} \times f(B)$
χ_{NA}, cm^2/s	$[(1.5 \times 10^{17})/n_e(r)](a\sqrt{\sigma}/83\ \text{cm})(250\ \text{cm}/R_0)^2$
χ_{GMS}, cm^2/s	$65\ [1 + 4(r/a)^2](a\sqrt{6}/I)$
$f(B)$	$0.384 \exp(\beta/\beta_c)^2$
β_c	$a(1 + \sigma^2)/[10R_0q(a)]$
Particle confinement D	$2D^{neo} + 0.2\chi_{GMS}$
TF ripple	Ripple trapping + banana drift, $\chi_{RT}^{rip} + \chi_{BD}^{rip}$
Discrete sawtoothing	
Sawtoothing for $q(r = 0)$	<1.0
Alpha particle power deposition	Local, instantaneous
Heating	Ohmic; ICRH auxiliary (Gaussian spatial deposition)

The minimum ignition density lies at 10^{14} cm^{-3} and 8 keV, corresponding to $\beta_t = 4.5\%$, $\beta_p = 0.5$, and 150 MW of fusion power. The finite beta enhancement to χ_E limits the ignition region to $B_t \leq 7\%$. The auxiliary power at equilibrium (P_{aux}^{eq}) is the power required to maintain the operating point at a given density n and temperature T. High power at low n and high T is needed to overcome thermal ion losses due to TF ripple; high power at low T and high n is required to offset impurity radiation. The powers shown assume perfect coupling between the rf source and the plasma. An ICRH power of 25 MW is adequate to surmount the saddle point in Fig. 8.12; the excess power of 15 MW reduces the startup time to ≤5 s.

RF systems

The TFCX designs include two rf systems. An LHRF system will drive the plasma current from startup to an operational (ignition) level and will be used for bulk plasma heating. An ICRF system will augment the LHRF system during heating to ignition. The LHRF system will operate at a frequency of approximately 2.7 GHz and will use a phased waveguide-array launcher. Present power klystron technology facilitates a system configuration using between 56 and 112 klystrons, depending upon the system power required. Each klystron will drive four waveguides, consistent with a waveguide power density of 5 kW/cm^2. The waveguides will be grouped so that each waveguide in a group is driven

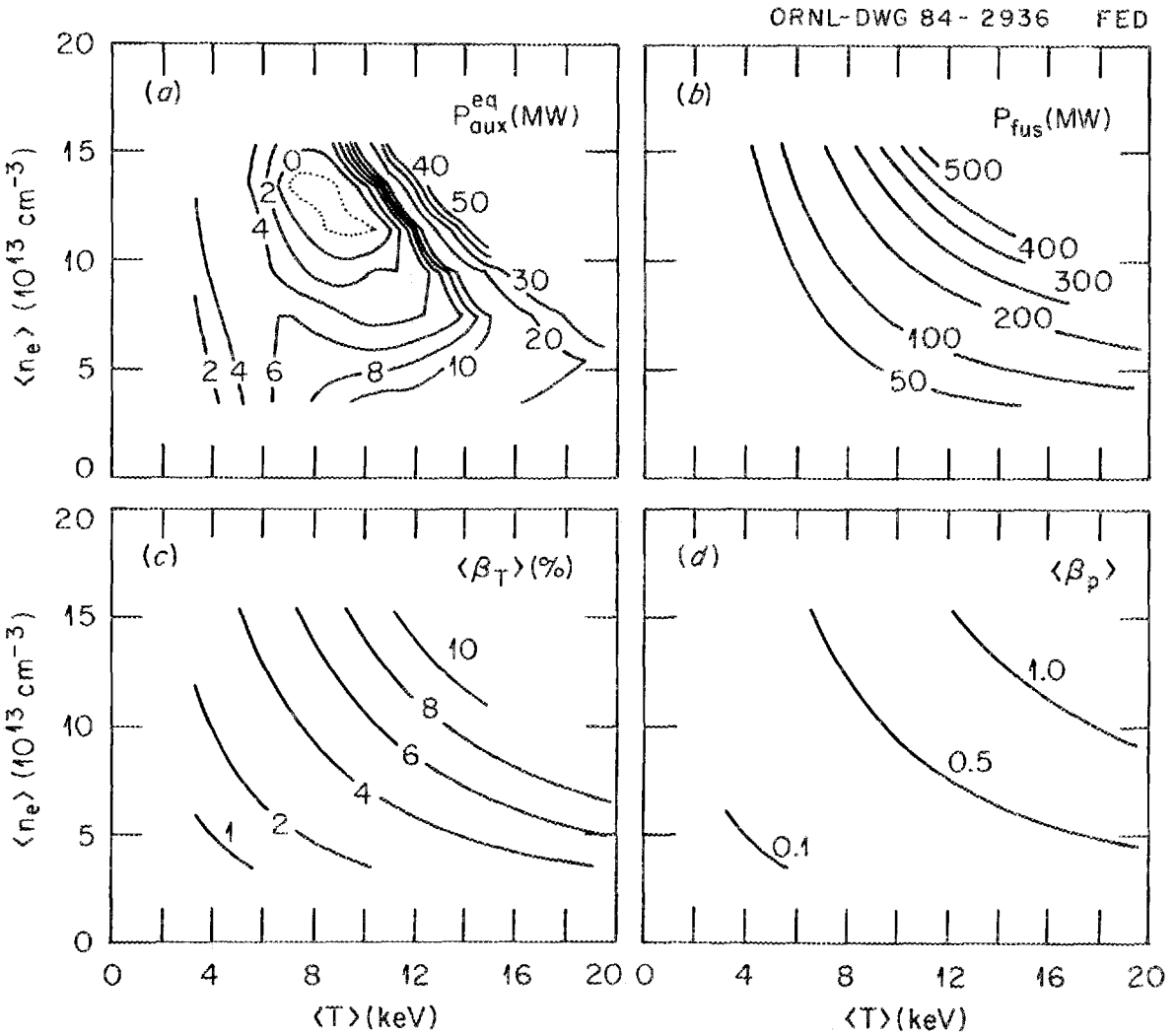

Fig. 8.14. Ignition contours.

by a klystron, the phase of which is adjusted relative to that of klystrons driving the other waveguides in the group. Waveguide grouping and phase adjustments will be designed to optimize the spatial power-density pattern characterizing the collective performance of the array. The number of klystrons required can be reduced by the development of higher power designs capable of operation at the required frequency.

The LHRF power needed is 32.5 MW for the nominal and 26.4 MW for the high-performance superconducting options and 27.5 MW for the nominal and 15.9 MW for the high-performance copper options.

Figure 8.15 shows views of a typical LHRF launcher. The basic module is an eight-waveguide subarray with a spacing of 1.3 cm center-to-center. At the 2.7-GHz frequency, the maximum *n*-parallel (*nz*) is 4.4. For the current-drive mode, the maximum *nz* used is 1.6. In the bulk heating mode, the phasing is done by pairs of elements that essentially

ORNL–DWG 85–2670 FED

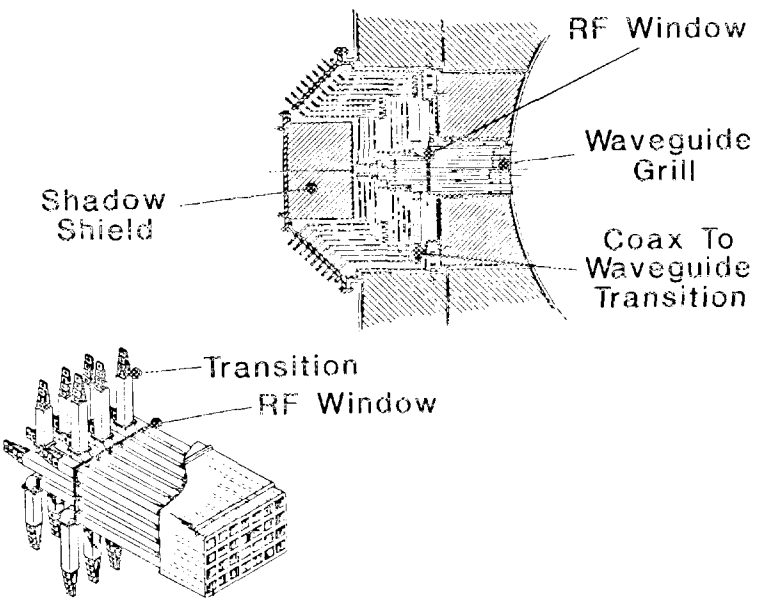

Fig. 8.15. Lower hybrid system.

double the spacing, making the maximum nz about 2.2. All the options use a subarray arrangement of four rows. Each has seven columns, except the small copper TF option, which uses four columns. The window is an eight-pane arrangement positioned at the back of the bulk shield. The fluence at this point is 0.03 that at the first wall. Behind this window, the guide and coaxial cable are pressured.

The transmission system efficiency is typically 57%. Hence, each of the 56 klystrons must generate 103 kW/waveguide, or a total of 413 kW. There are two sets of 56 klystrons. One set drives the top and bottom rows, and the other set drives the two center rows, so the two center rows can be used for startup. An alternative approach would use one large tube to drive all rows in one column. The overall system efficiency is 33%, so this option would use 80 MW of prime power.

The rf module uses a klystron power amplifier. For the large-tube option, this could be satisfied by strapping approximately 500 1-kW (8270) tubes together. A 1-MW tube is under development by two manufacturers in Japan. The drive circuit for each klystron consists of a phase shifter, an attenuator directional coupler, and a circulator. An efficiency of approximately 70% is expected for the klystron. In the output circuit, there is a lineup of circulator–directional coupler and window. This window, which serves as a tritium block in case of an accident, is positioned in the mezzanine. The transmission efficiency for this output is estimated to be approximately 0.88. For the approximate 1-MW power level, this results in a 120-kW cooling requirement for each output circuit. Each of the components must be water cooled.

The transmission and distribution network is composed of a 35-m run of waveguide, power splitters, circulators, directional couplers, and coaxial cables. With any of these arrangements, the transmission efficiency (without partitioning fraction) is 62%. A total power dissipation of about 350 kW is expected in these components, and therefore they will be water cooled. It is preferable to have this distribution equipment as close to the launcher as possible but out of the test cell. Therefore, these components are located below the test-cell floor.

Each rf port requires approximately 500 kW of cooling to handle the rf losses alone. Additional heat sources of ≈200 kW are due to volumetric heating by the neutrons and the plasma heat flux. The spaces between each subarray and between the waveguide array and shadow shield are flooded with water to carry away this heat. At present, the launcher life is not limited by particle erosion of the vacuum section or by neutron fluence of the BeO window. This is because the seconds of D-T operation are only 2×10^5. The neutron flux is a problem from a streaming standpoint. The 14-MeV content leaving the waveguide grill is large and therefore must be locked by the 40-cm-thick shadow shield.

The ICRF system will operate at a frequency between 60 and 100 MHz. The rf power required is between 6 and 36 MW. Launcher spectrum formation and power density considerations support the use of an array of launcher elements. Several types of elements (loops, cavity, etc.) are under consideration, with a ridge-loaded waveguide appearing to be the best choice. Six such waveguides, each with a calculated power-handling capability of 6 MW, could provide the required ICRF power. The associated power generation requirement can be met with a modest array of power tetrode tubes. Phasing the rf power delivered by each array element will be accomplished by phasing the low-level rf applied to each power amplifier module.

A unique feature of the ICRF system is the array launcher. The spectrum formed matches that of the plasma power absorption pattern. Figure 8.16 shows how ridge-loaded waveguides can be interleaved to create a grill with a main response in the nz range of 4–8 and an ambiguity spacing of 40 for all options except the small copper device (with ambiguity spacing of about 30). Assuming there is no coupling between neighboring launchers, the main response will have a width of about 5. Because these ports will be phased to form an interport array, the resolution is expected to be better than that of a single port, possibly by 2:1. Other array elements have been considered, such as the resonant cavity [on Doublet III (DIII)], the U-slot [on the Tokamak Fusion Test Reactor (TFTR)], and the radome covered loop (on INTOR). Any of these could be arranged in a continuous array to form a comparable spectrum. A power density of at least 1.2 kW/cm^2 is required from each element. Estimates of plasma-loaded loops (1 m long) indicate that the impedances are in the range of $97 + j78$. A corresponding impedance of $15 + j68\ \Omega$ was estimated for the waveguide element. The waveguide shown is excited by a pair of current loops, one on each side of the ridge. These are phased relative to one another since they are coupled. The calculated power-handling capability is 6 MW for the ridge-loaded guide, but for these applications no more than 2.5 MW (small copper device) is required.

Figure 8.16 shows the vacuum break positioned behind the bulk shield. Ceramic (BeO) isolators have a lifetime fluence of about 10^{20} neutrons/cm^2. For the present TFCX duty factor, this represents a 2.5:1 safety factor. By positioning the break behind the shield,

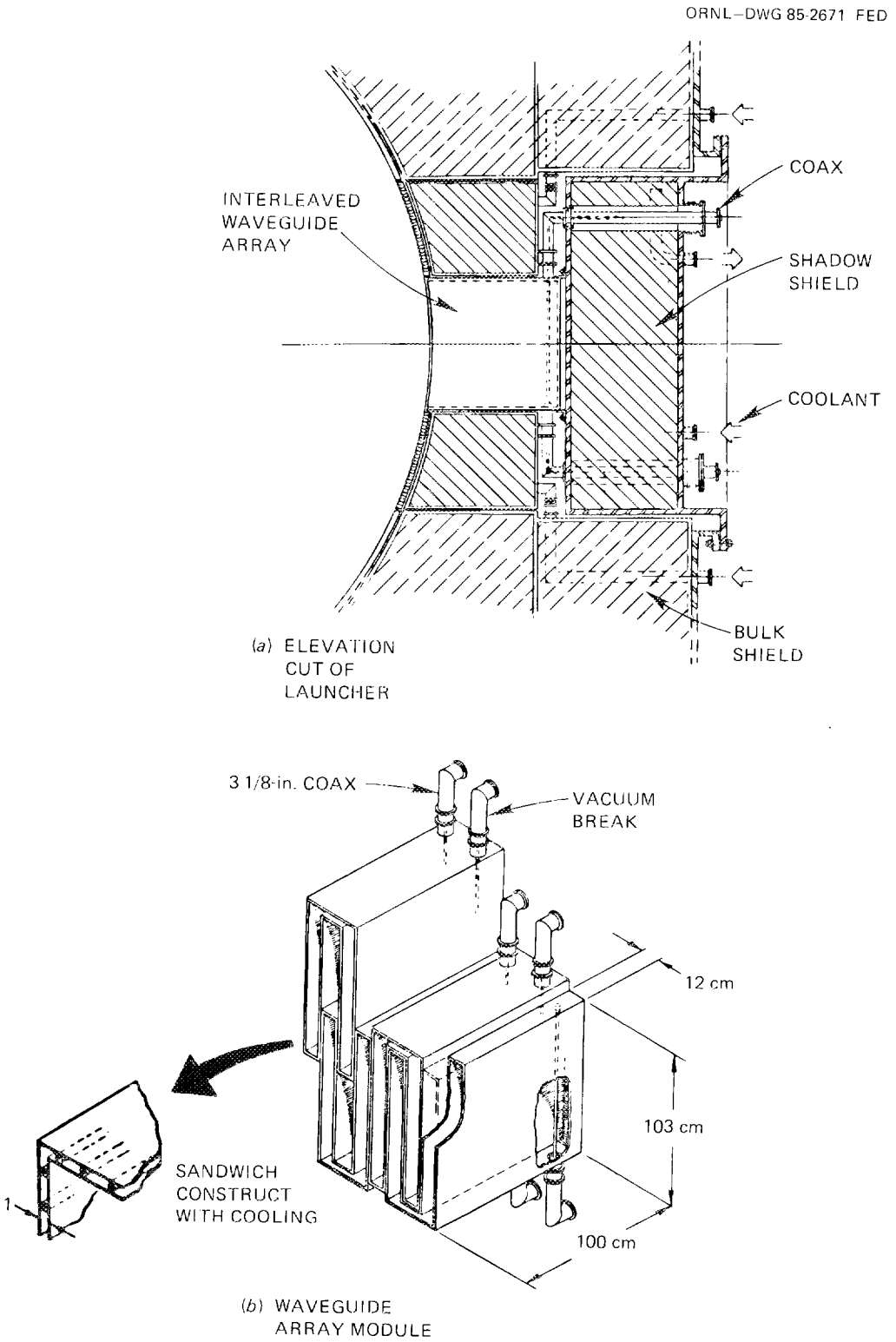

Fig. 8.16. Ion cyclotron system.

allowance is made for upgrades in fluence by an order of magnitude or more. Each transmission line is cooled and pressurized to accommodate the required power level. There is one power module per launcher to allow the use of low-power phase shifters ahead of the final amplifiers. A 75% transmission system efficiency is typical. Therefore, the two nominal options require power modules of about 1.2 MW, while the high-performance superconducting and copper TF devices need 1.9 MW and 3.3 MW, respectively. If the coupling between ports is poor, higher power modules, with power splitters to drive multiple elements in different ports, would be more economical. The overall system efficiency is expected to be about 50%. Therefore, the prime power needed ranges from 14 to 30 MW.

Magnet systems

TFCX reference design: A major task of the TFCX study was to develop superconducting magnet designs that maximize the winding current density and the ability to withstand nuclear heating. The TFCX design specification calls for a winding current density of 3500 A/cm^2 at a 10-T peak field and for peak nuclear heat load limits of 1 mW/cm^3 for the nominal design and 50 mW/cm^3 for the high-performance design. Past studies have shown that NbTi conductors at 10 T can achieve about 2000 A/cm^2 (superfluid, bath-cooled) to 2200 A/cm^2 (FED baseline, forced-flow conductor subcooled to 3.1 K), with a limited ability to remove nuclear heat. Several approaches to higher winding current densities were considered:

- Use of forced-flow Nb_3Sn conductors, similar to the Westinghouse Large Coil Program (LCP) conductor. Nb_3Sn has a higher current-sharing temperature than NbTi, which greatly increases the ability to withstand nuclear heat.
- Epoxy impregnation of the winding. Test results in arrays of cable-in-conduit conductors show that the potting compound in the interstices between conduits advantageously alters the load path by which transverse-compressive winding loads are transmitted to the case and justifies elimination of co-wound structural material.
- Designing to 80% of critical current, rather than 67% as done previously.
- Reacting the conductor after winding to anneal out the strains induced during coil-winding operations, thereby increasing the critical current.
- Use of Incoloy as the conduit material. The cooldown contraction of Incoloy-wrapped conductors closely matches that of Nb_3Sn, thereby reducing cooldown strains and increasing the critical current.

Table 8.4 summarizes the TF coil performance and design requirements for the superconducting options and gives the key TF coil parameters. The nominal TF coil design uses the Westinghouse LCP conductor; that is, Nb_3Sn conductor wrapped in a JBK-75 stainless steel conduit. The conduit thickness is 1.7 mm, and the void fraction inside the conduit is 32%. The winding can withstand all credible heat loads arising during normal pulsed operation and during plasma disruption without quenching.

The peak conductor temperature in the high-performance design is 5.5 K, compared with 4.5 K in the nominal design. To offset the degradation of critical current at the higher temperature, the conductor must be reacted after winding. Additional critical current capability is obtained by increasing the void fraction from 32% to 41% and by

Table 8.4. TF coil requirements and parameters

	Nominal	High performance
Requirements		
Plasma major radius, m	4.08	3.61
Field on plasma axis, T	3.73	4.23
Maximum ripple, %		
Edge	1.5	1.5
Plasma centerline	0.1	0.1
Maximum field at TF coil, T	10.0	10.0
Nuclear heating rate in winding, mW/cm^3	1.0	50.0
Parameters		
Number of TF coils	16	16
Winding bore size, m × m	5.2 × 7.7	4.4 × 6.4
Mean coil perimeter, m	23.0	19.2
Combined ampere-turns, MAT	76.0	76.0
Conductor current, A	20,300	20,300
Number of turns per coil	234	234
Winding current density, A/cm^2	3,310	3,310
Overall current density, A/cm^2	1,970	1,970
Stored energy, MJ	440	340
Weight of winding, kg (per coil)	15,200	12,900
Weight of case, kg (per coil)	17,600	14,900
Weight of intercoil structure, kg (per coil)	2,900	2,900

replacing the JBK-75 conduit in the Westinghouse/Airco design with an Incoloy conduit that greatly reduces the cooldown strain. These design changes alter the conductor cross-sectional dimensions, although the current density remains about the same.

Figure 8.17 shows the helium manifolding scheme for the high-performance coil. To limit the helium exit temperature to 5.5 K, the coolant path length is limited to one turn in the first third of the winding, to two turns in the next third, and to five turns in the remainder of the winding. Manifolding connections are brought from various points within the winding through the case sidewall to a common manifold. Each line is at a different electrical potential and is insulated from the common manifold. Although the winding is epoxy-impregnated for structural rigidity, the multiple penetrations by the coolant lines through the case sidewall make it necessary to reinforce this portion of the case.

Analysis of critical current: The selection of the actual conductor operating current depends upon the critical current, which is a function of many variables, including

- maximum field,
- residual compressive cooldown strain in the conductor,

ORNL--DWG 85--2672 FED

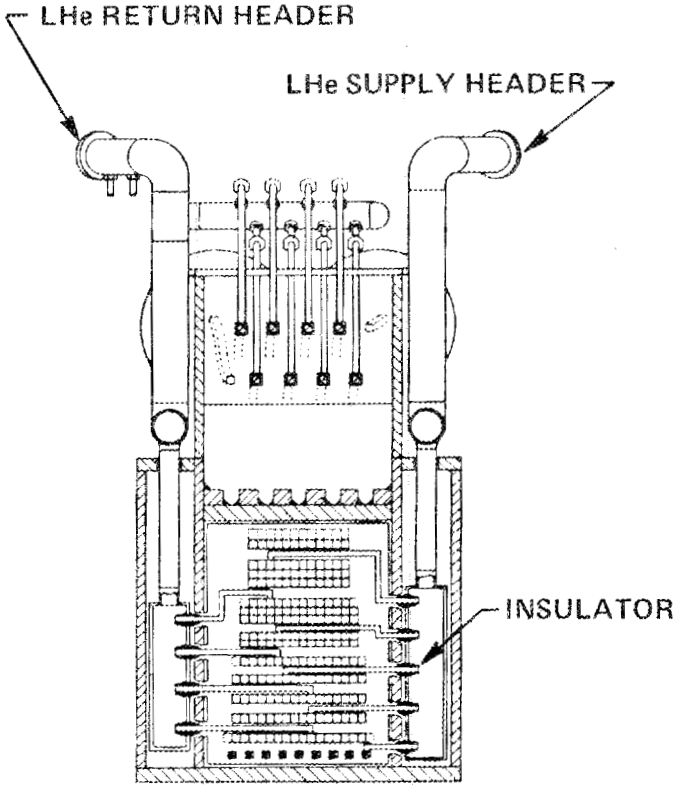

Fig. 8.17. Cooling and manifolding for the high-performance case.

- choice of jacket material and heat treatment, both of which affect the residual cooldown strain,
- strain level developed in conductor when it is bent into the minimum radius of curvature during coil winding (which can be relieved if the conductor is reacted after winding), and
- strain level in conductor resulting from operating loads.

At the 10-T field, the critical current of the Westinghouse LCP conductor is 24 kA with no imposed tensile strain and 41 kA for an imposed tensile strain of 0.75%.[13] The 0.75% imposed strain is therefore equal and opposite to the residual compressive strain due to cooldown plus winding; research at MIT has determined that the cooldown portion alone is −0.5%. A compressive strain of 0.75% therefore degrades the critical current to 59% of its value in the strainfree state (24 vs 41 kA). This fractional degradation is in reasonably good agreement with Ekin's strain scaling law.[14]

For a TFCX-size coil, the minimum radius of curvature imposed on the conductor during coil winding is about 1.5 m, corresponding to a bending strain in the conduit wall of about 0.7%. According to ref. 15, the strands experience about one-third the bending strain developed in the conduit, or about 0.23%. Furthermore, when the coil is energized, a dilational tensile strain of about 0.1% is developed. Thus, the net strain, including cooldown strain, is $-0.50 - 0.23 + 0.10 = -0.63$. Ekin's formula, with $\epsilon = -0.0063$ and $B = 10$ T, gives $I/I_0 = 0.64$. Under TFCX conditions, the critical current at 10 T becomes $0.64 \times 41 = 26.3$ kA at 4.2 K.

The maximum conductor temperature depends on the amount of nuclear heat that the coil must withstand. A separate analysis has shown that for 1 mW/cm^3, a temperature rise of about 0.5 K occurs. Hudson et al.[16] predict that the critical current at temperature T degrades from its 4.2 K value by the fraction of 0.935, so that the critical current at 4.5 K is 24.6 kA. If the conductor current is set at 80% of the critical current, it follows that the Westinghouse LCP conductor, without modification, would operate in a TFCX application at 19.7 kA at 10 T. This corresponds to an average current density (with a single grade) of 3500 A/cm^2, which meets the design specification.

A similar analysis of the critical current data has been made for the combinations of six possible conditions:

- JBK-75 or Incoloy jacket (affects cooldown strain),
- react-and-wind or wind-and-react (affects winding strain), and
- 10- or 12-T peak field.

Figure 8.18 summarizes the attainable current density as a function of peak conductor temperature for each combination of jacket material, manufacturing sequence, and peak field.

As the nuclear heat load rises, more and more helium must be circulated. Not only does this increasing mass flow increase the pressure drops, but also the associated frictional heating increases the heat load further. In conventional piping system designs, these frictional heat terms are negligible, but in cryogenic systems they are of the same order of magnitude as the imposed heat load. These heat loads limit the length of the coolant path and therefore affect the required number of coolant lines.

Helium outlet conditions were calculated using a computer program that accounts for spatial variation of the nuclear heat load around the perimeter of the TF coil and also accounts for attenuation of the nuclear heat load turn-to-turn. Pressure drops and frictional heat are calculated using the friction factor correlation in ref. 13.

A mean TF coil perimeter of 18 m was assumed, and coolant path lengths of one-half, one, and four turns were considered. The TF coil configuration has a radial build of 12 turns; if it is assumed that the coil is wound three-in-hand, a path length of four turns is considered about as simple a manifolding scheme as is reasonably achievable. The shorter path lengths represent more complex manifolding but offer the potential for higher incident nuclear heat.

Table 8.5 summarizes the maximum nuclear heat capability for three cooling system configurations (denoted A, B, and C) that differ in flow path length and in helium inlet and outlet conditions. A nuclear heat level of 10 to 12 mW/cm^3 appears feasible from a heat-removal standpoint for a practical manifolding arrangement, whereas up to about

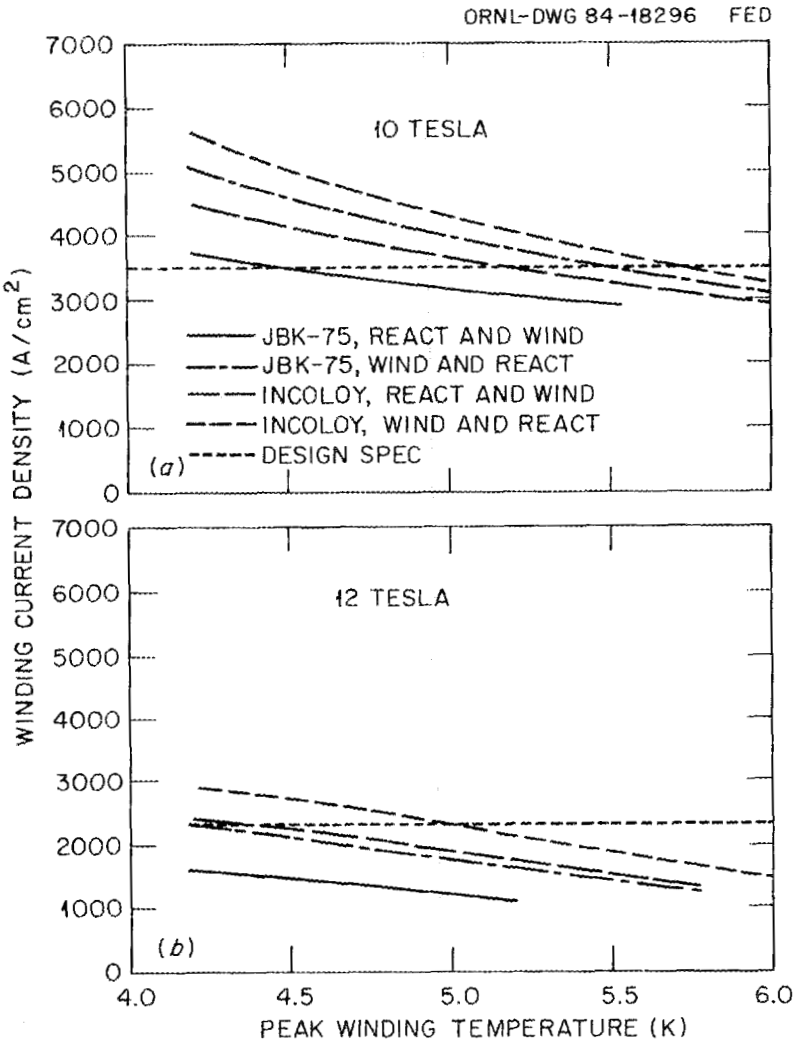

Fig. 8.18. Achievable current density vs peak conductor temperature at 10 T and 12 T.

100 mW/cm^3 can be accommodated with many short helium flow paths. The nuclear heat load may be limited to lower values, however, to avoid unacceptable degradation of the critical current.

Buildings, facilities, and site utilities

The TFCX site plan shown in Fig. 8.19 is representative of a generic site and lays out a typical arrangement for the tokamak support buildings, auxiliary facilities, support facilities, site utilities, roads, and paved areas.

The facility layout has been designed on the basis of functional, operational, and cost considerations. The tokamak support buildings provide space for direct support of the tokamak and include the following areas:

Table 8.5. Nuclear heat capability for three cooling system configurations

	Configuration		
	A	B	C
Number of turns in coolant path	4	1	0.5
Coolant path length, m	72	18	9
Helium inlet temperature, K	4.2	4.2	4.2
Helium outlet temperature, K	5.8	6.0	5.9
Helium inlet pressure, atm	9.0	8.0	10.0
Helium outlet pressure, atm	2.7	2.3	2.6
Helium flow rate per channel, g/s	15	30	50
Maximum nuclear heat, mW/cm^3	12	75	100

- tokamak test cell, for machine housing and operation functions;
- transfer area, for transport and handling functions;
- decontamination cell, for decontamination functions;
- hot cell, for remote repair and maintenance functions;
- warm cell, for hands-on repair and maintenance functions; and
- tritium area, for storage, delivery and cleanup functions and pump housing.

The auxiliary facilities provide space for auxiliary functions, including

- instrumentation and control (I&C) and data acquisition (DA) systems,
- diagnostics,
- field coil power conversion,
- rf heating power conversion,
- cryogenics,
- component cooling water,
- fabrication, assembly, and mock-up area,
- power factor correction, and
- I&C and DA tunnel.

The support facilities provide space for

- offices, drafting area, and laboratory,
- emergency services,
- library,
- cafeteria,
- maintenance, shop, and warehouse areas,
- fabrication and assembly areas,

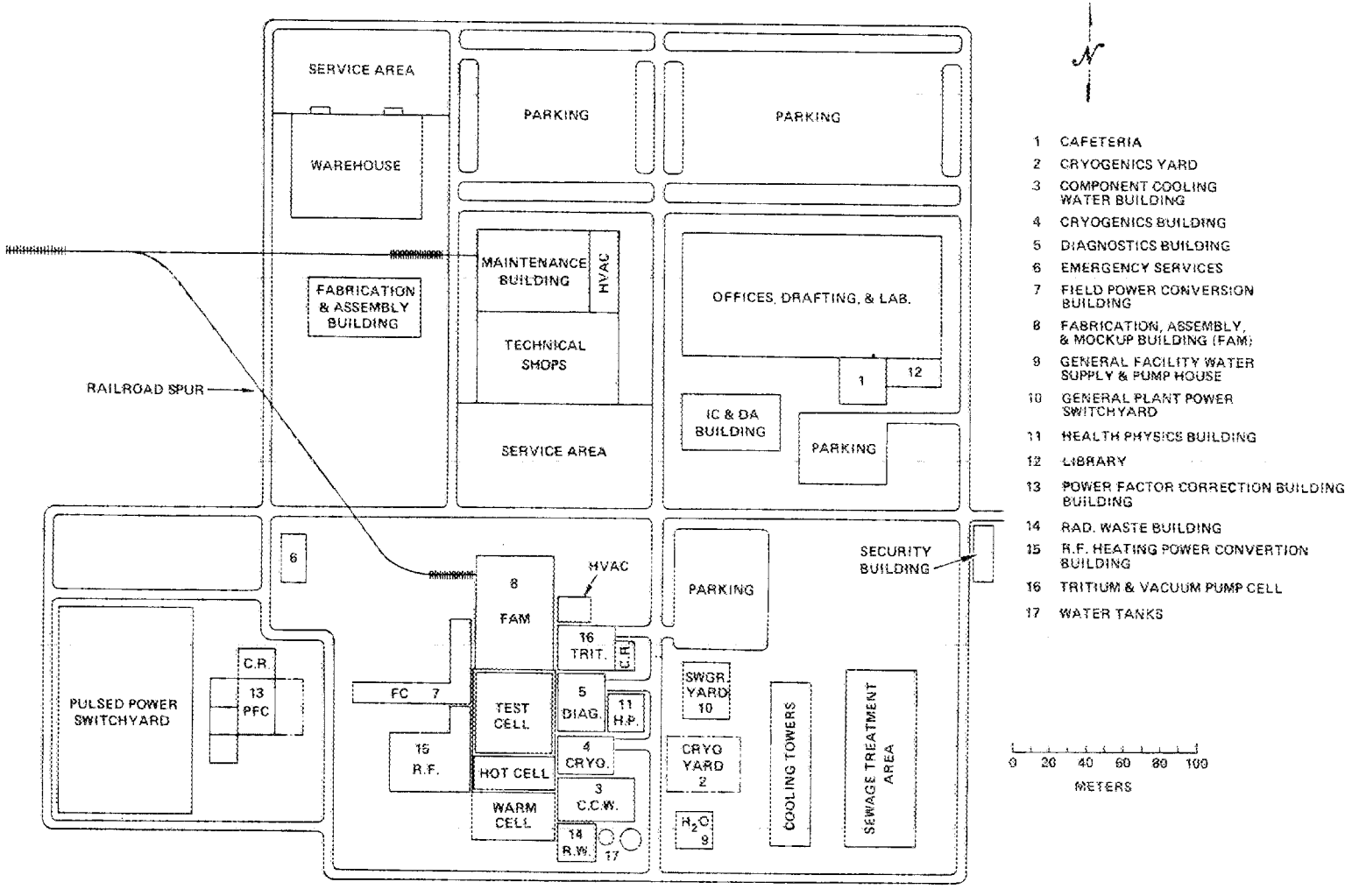

Fig. 8.19. TFCX plot plan.

- building heating, ventilating, and air conditioning (HVAC), and
- health physics.

The site also contains the required site utilities, including

- general-purpose facility water supply and distribution;
- fire protection water distribution;
- boiler house, steam, and condensate system;
- area lighting;
- general plant power;
- waste and effluent management;
- communications and security alarm systems; and
- roads, grounds, and parking.

The TFCX test cell (Fig. 8.20) (including grade level and basement) is designed to survive operationally the "most probable" earthquake and tornado, to withstand the "most intense" natural phenomena from the standpoint of pressure boundary integrity, and to withstand the impact of a light aircraft. The test cell must also provide shielding from ionizing radiation sources and provide for containment and handling of radioactively contaminated components.

The test-cell roof, wall, and floor thicknesses are based upon structural and radiation shielding requirements. Because of the structural strength and radiation shielding requirements, the test cell must be constructed of reinforced concrete with wall, roof, and floor systems approximately 2 m thick. The test cell inside-clear dimensions must be approximately 44 m long, 40 m wide, and 28.7 m high for the baseline machine (the nominal superconducting machine). The test cell is designed to support a bridge crane with a capacity of 400 tons.

The test-cell basement has the same clear dimensions as the test-cell grade level, except it is 10.5 m high. The test-cell basement houses a portion of the machine sector and component transfer area, the compound cryogenic vacuum pumps, piping, valves, bus bars, and the machine structural support system. Part of the basement provides a tritium boundary and structural containment. Access to the basement from the grade level is through a 7.6- by 7.6-m hatch.

8.1.2.2 CCTF concept

The Long-Pulse Ignited Test Experiment (LITE) series of tokamak designs featuring quasi-continuous, Bitter-plate TF magnets has been proposed as an attractive concept for TFCX[17] or the next FED. The magnet concept has a large amount of copper in each turn, which reduces the resistive power losses, and has a high copper filling factor in the throat region of the magnet, which reduces the radial build. These factors are perceived to result in a design with a reduced initial capital cost and a lower operating cost.

To assess the mechanical design features of the quasi-continuous magnet concept, a conceptual design study—the Continuous Copper Toroidal Field (CCTF) concept—was performed by the Design Center, with input and collaboration from MIT. The CCTF concept is a variation of the LITE-R[17] concept proposed by MIT. The parameters, radial

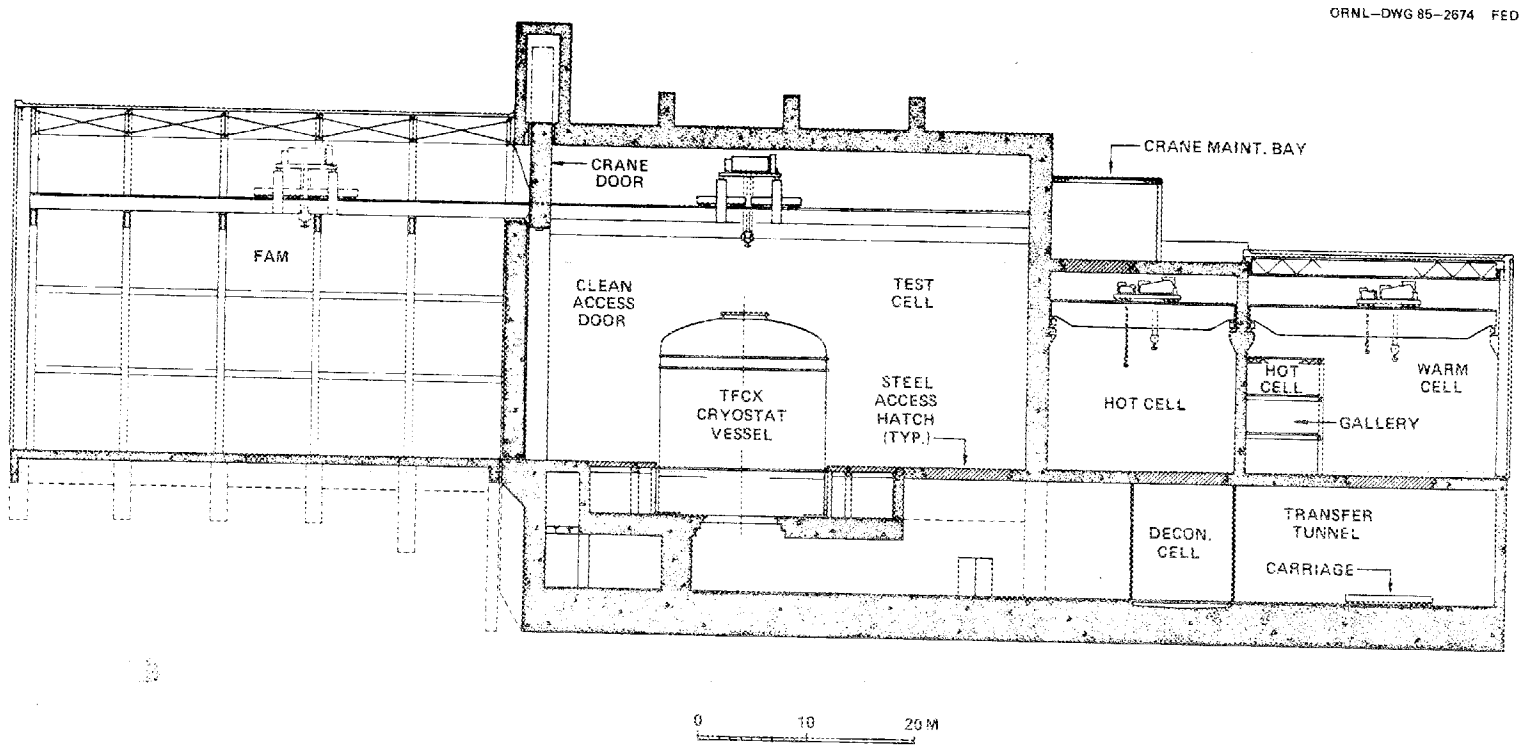

Fig. 8.20. Longitudinal section of tokamak support buildings.

build, and general shape of the TF coils are essentially the same in both concepts. The LITE-R concept is a free-standing, toroidal array of copper plates with interspersed radial plate flanges. Steel plate shims are installed between each turn on the outboard leg. The CCTF concept has essentially the same toroidal array of copper plates but uses the same radial plate flanges to form an encasement to react forces with a pinned shear bar to make the sector-to-sector attachment. Both concepts use wedging in the nose region of each sector to react the net centering forces.

If both concepts provide an equally acceptable structural design, then the trade-off between the concepts involves such factors as ease of manufacture, assembly, installation, operation, and maintenance. These factors eventually translate to the most economical concept. However, it is more meaningful to assess the fundamental features of the quasi-continuous TF coil concept that are inherent to both concepts.

Configuration

The CCTF torus has a major radius of 2.44 m and a minor radius of 0.84 m. The field on axis is 6.13 T. Table 8.6 lists the significant plasma parameters. The torus is made of 16 removable sectors that include a cased magnet with nuclear shielding, first wall, and pumped limiter components, nestled in the bore of the TF coil. An elevation view is shown in Fig. 8.21, and a plan view at midplane is shown in Fig. 8.22.

Access is provided at the centerline of each sector, as shown in Fig. 8.21. The access opening in each sector is 0.55 m wide and 1.2 m high, providing a total access area of more than 10 m^2. Coolant lines to the first wall and shielding components are routed at the top and bottom of the access openings. Diagnostics, instrumentation, materials, blanket test modules, and fueling and rf heating components are installed in the access openings. The limiter can be removed through the access opening after these components are removed.

The plasma vacuum boundary is at the inner periphery of the TF coil magnet encasement, as shown in Fig. 8.21. The bore of the magnet encasement becomes the vacuum vessel. The vacuum boundary is extended to the outboard face of the device by welding the access port walls to the magnet encasement. An access port door with welded metal vacuum seals closes the boundary. The vacuum boundary is extended to the vacuum pumping duct interface in a similar manner. The sector-to-sector vacuum boundary is established by bringing the vacuum boundary in toward the plasma, as shown in Fig. 8.22. A welded metal plate in the radial parting plane brings the vacuum boundary from the inner periphery of the TF coil encasement to the inner periphery of the shield. The sector-to-sector continuity of the vacuum boundary is provided by a welded metal bellows seal.

The sector-to-sector attachment is shown in Fig. 8.23. The sectors are installed radially so that the side plates in the inboard nose region are in contact, forming a wedging contact area across the total thickness of the inboard leg to react the inplane Lorentz forces. Out-of-plane Lorentz forces produce a net overturning that is reacted by a shear plate attached to the outboard face of the sector-to-sector joint. A total of 120 shear pins, each 4.45 cm (1.75 in.) in diameter, are required at each sector-to-sector joint.

Each sector contains 24 coil turns, for a total of 384 coil turns in the device. The coil turns are encased between four radial-plate flanges, which are made of stainless steel, and are arranged in a sequence of 6 turns, 12 turns, and 6 turns between the plate flanges.

Table 8.6. CCTF parameters

Major radius, m	2.44
Minor radius, m	0.84
Plasma elongation	1.60
Plasma triangularity	0.30
Inboard shield thickness, m	0.15
Magnetic field	6.13
Plasma current (q = 2.4), MA	8.11
Beta β	0.051
$(n\tau_E)$Mirnov/$(n\tau_E)$ign	1.50
Neutron wall loading, MW/m^2	2.33
Fusion power, MW	300
Total D-T burn time, s	2×10^5

Four radial-plate flanges form the central skeleton of the encasement. Flat plates form the top, bottom, inboard, and outboard surfaces and are welded to the outer periphery of the radial flanges. Roll-contoured plates are similarly welded to form the coil bore encasement. Flat plates are also welded to the flanges, establishing the encasement boundary for the vacuum pumping duct and access port openings.

Summary

The FEDC Tokamak Systems Code was used to assess the cost of the CCTF concept; the result was a cost about 85% that of the nominal superconducting option. Thus, the CCTF concept with its quasi-continuous TF coils appears to fall in the cost category of high-performance copper devices.

The large amount of copper in the TF coil turns results in a relatively small resistive power requirement (275 MW for LITE-R and 325 MW for CCTF). It is in the same range as the TFCX high-performance copper concept, which has a resistive power of 333 MW.

The very nature of the quasi-continuous TF coils presents some maintenance difficulties for the internal plasma chamber. Since the entire periphery of the torus is either TF coil conductor or encasing flange structure, access is achieved only by routing portions of the TF conductor out-of-plane and around the access openings. This leads to small opening areas but also long accessway lengths since the conductor routing around the openings adds length to the accessway. Even after access is gained to the inner chamber, its small bore makes in-vessel maintenance tasks very difficult due to lack of maneuvering space.

Two remote maintenance tasks are vital to this configuration: limiter installation or removal and vacuum bellows seal welding or cutting operations. These tasks must be performed remotely in order to remove a typical sector. The limiter must be removed to permit access to cut the bellows seal. Therefore, limiter installation or removal must be an in situ task. Maintenance of other first wall components could be performed after sector removal to the hot cell.

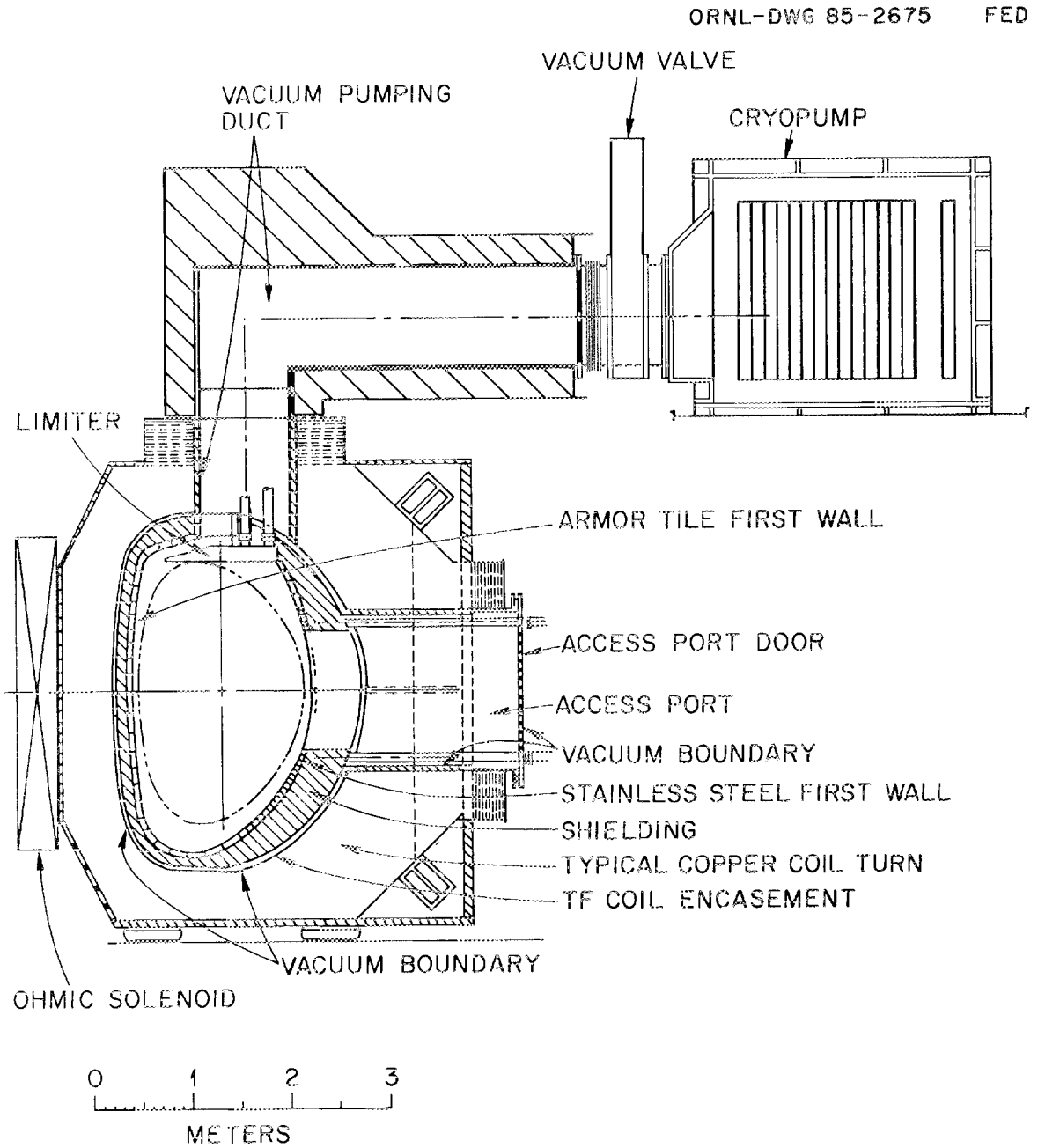

Fig. 8.21. Elevation view of CCTF.

Several manufacturing considerations should be discussed. A single turn cannot be manufactured from one plate since plates of this size are unavailable. The turn will have to be manufactured in segments and welded together. The CCTF plates are tapered the full radial dimension. The LITE-R plates are tapered to a specific radius and then become a constant thickness. Steel shims complete the toroidal angle. Either concept will require an

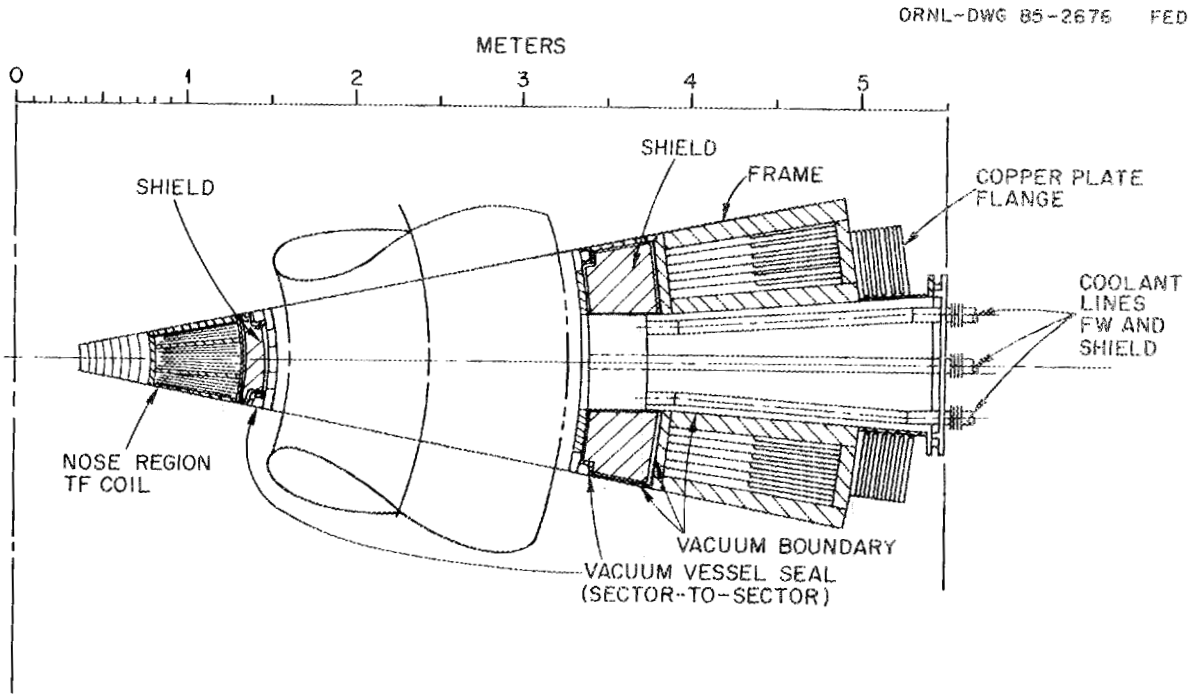

Fig. 8.22. Midplane section to CCTF.

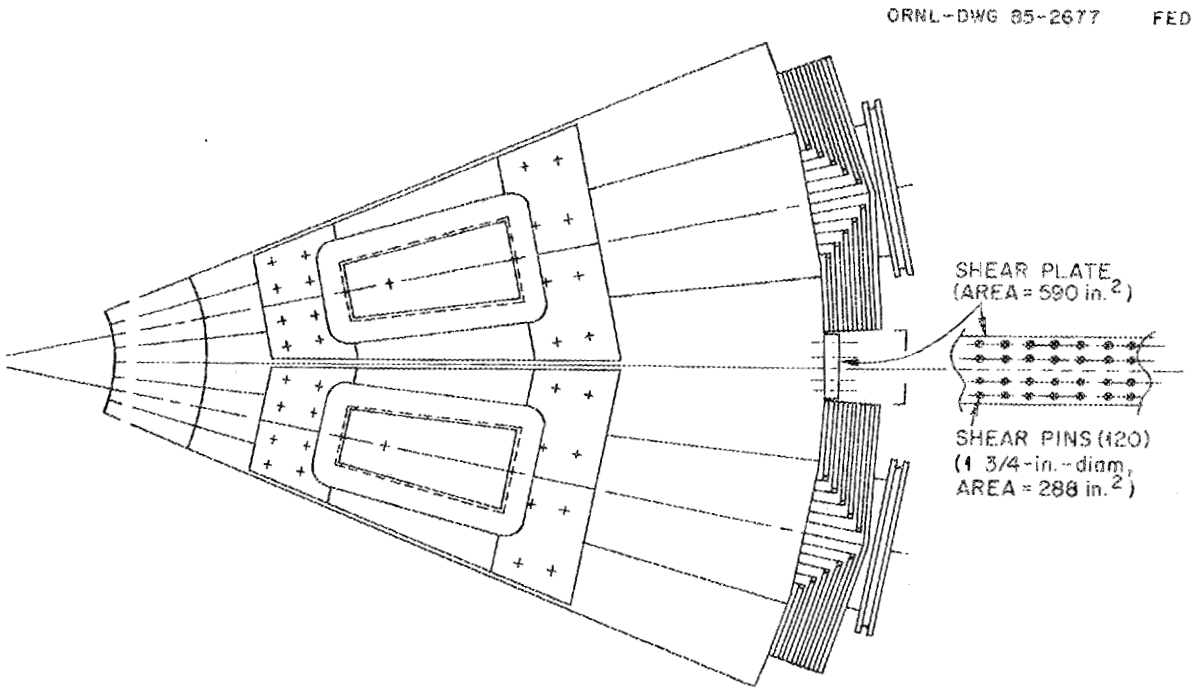

Fig. 8.23. CCTF sector-to-sector arrangement.

extraordinary amount of surface machining on both the coil turns and the steel flanges and shims. The CCTF concept has the added requirement of a welded steel encasement structure, while the LITE-R has the difficult requirement of machined keys and keyways. Final assembly sequences represent about the same level of difficulty. Although a qualitative manufacturing cost comparison was not done, the amount of welding and machining of thicker coil turn plates and encasement plates undoubtedly would make the CCTF concept more costly. The manufacturing techniques required to produce either concept are typical state-of-the-art methods and, as such, would require no technology development.

8.1.3 Ignition Spherical Torus

Ignition Spherical Torus (IST) design studies were initiated at the Design Center to explore a lower-cost alternative to the TFCX options. The basic approach was to reduce the aspect ratio of the device to the minimum possible. Under the stability and confinement constraints as now understood and used in the TFCX studies, the low aspect ratio allows an ignition device with compact geometry and low magnetic field. The spherical torus assessment resulted in the definition of an ignition device with a cost half that of the TFCX high-performance copper option.

A spherical torus is obtained by retaining only the indispensable components on the inboard side of a tokamak plasma, such as a cooled, normal conductor that carries current to produce a toroidal magnetic field. The resulting device features an exceptionally small aspect ratio (typically around 1.5), a naturally elongated, D-shaped plasma cross section (typically 2-to-1 elongation), and rampup and maintenance of the plasma current primarily by noninductive means. The tokamak plasma takes on the spherical shape with a modest hole through the center, suggesting the name of spherical torus[18] (Fig. 8.24).

A spherical torus plasma is characterized by comparable currents in the plasma, the TF coils, and the PF coils; comparable toroidal and poloidal beta; comparable toroidal and poloidal magnetic fields; and strong paramagnetism. As a result of the favorable dependence of the tokamak plasma behavior on decreasing aspect ratio and increasing plasma current, a spherical torus is projected to have high beta, small size, and modest field. With TF coils made of normal conductors and inorganic insulators, eliminating the inboard nuclear shield causes only a small percent of the fusion neutrons to be lost to the center conductor, permitting potentially dramatic simplifications in the configuration of a fusion spherical torus.

Assuming confinement scalings with favorable dependences on the plasma current, an IST at a field of 2 T features a major radius of 1.5 m, a minor radius of 1 m, a plasma current of 14 MA at a safety factor (inverse rotational transform of the magnetic field) of 2.4, an average toroidal beta of 24% (with respect to the externally applied toroidal field), and a fusion power of 50 MW. At 2 T, a scientific breakeven ($Q = 1$) spherical torus will have a major radius of 0.8 m, a minor radius of 0.5 m, and a fusion power of a few megawatts. Assuming a high-technology copper coil that permits tripling of the conductor current density up to 10 kA/cm^2, a spherical torus suitable for fusion engineering and technology development would have a field of 3 T, a major radius of 0.7 m, a minor radius of 0.45 m, a D-T fusion power of 40 MW, and a neutron wall load of 2 MW/m^2.

ORNL-DWG 84-3421 FED

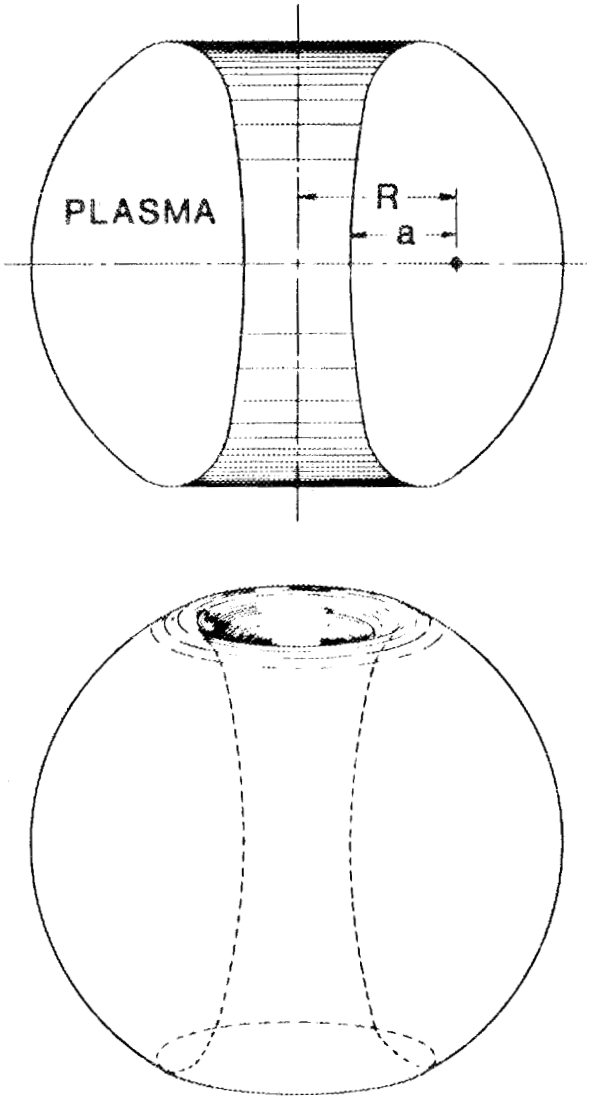

Fig. 8.24. The plasma configuration of a spherical torus, a tokamak plasma with very small aspect ratio and large elongation.

Although the plasma properties projected for the spherical torus are consistent with the present-day tokamak data base, having aspect ratios ranging from 2.5 to 5, its unique properties identify a new and unexplored tokamak physics regime. A small spherical torus experiment (STX) is being defined at ORNL (see Sect. 1.3 of this report) to resolve major physics scaling questions of the conventional tokamaks and to provide concrete data in the regime.

8.1.3.1 Results of initial assessments

An initial assessment of the IST has been completed. The purpose of this study is to quantify the potential and challenges of an IST, to characterize its critical issues, and to highlight its data base needs. An IST is to achieve ignition for pulse lengths on the order of tens of seconds with at least the minimum number of cycles sufficient to demonstrate repeatability of results and at the lowest overall cost, consistent with the initial guidelines of the Office of Fusion Energy (OFE) Mission I Ignition Studies during the first phase of FY 1985.

The major physics assumptions of an IST include:

1. the critical beta scaling proposed by Troyon, with $\beta_c = 0.035$ and $\beta_{DT} = 0.77\beta_c$;
2. energy confinement scalings with the options of Mirnov and neo-Alcator;
3. plasma current determined by free boundary MHD equilibrium calculations, taking advantage of the natural elongation at very low aspect ratios;
4. paramagnetism as exhibited by the plasma enhancement of the toroidal field over the externally applied field at the plasma axis, B/B_0;
5. LHRF current rampup with inductive assist only from vertical field coils and some plasma current decay during plasma heating, ignition, and burn, lasting for tens of seconds, a time scale much shorter than the resistive decay time of the burning plasma; and
6. plasma density below the Murakami limit.

Because the field for this concept should be modest, only conventional engineering assumptions are used in this study, with one exception. The option of using a high-strength copper alloy, C-17510 (Cu-Ni-Be), in the center conductor post is considered to allow for a highly compact IST and for more objective comparison with the IGNITOR class of short-pulse ignition tokamaks. Otherwise, the engineering and costing approaches are in accordance with the recent TFCX practices.

The major results of this study are summarized as follows.

1. A nominal IST with conventional coil current density (about 3 kA/cm^2) and Mirnov scaling is estimated to have $B_0 = 2$ T, $R = 1.6$ m, $a = 1.0$ m, $I_c = 16.2$ MA, $I_p = 14$ MA, $P_{DT} = 55$ MW, and $C_{ig} = 2.3$. The estimated constructed cost of the IST project, ready for operation at an initially undeveloped site, is \$576 million in 1984 dollars. The total direct cost of the nuclear island is estimated to be \$119 million. Based on neo-Alcator scaling, C_{ig} for this device would be 0.22.

2. The rationale for using high-strength copper alloy for the center conductor is to permit a highly compact IST with $B_0 = 3$ T, $R = 1.0$ m, $a = 0.61$ m, $I_c = 15.1$ MA, $I_p = 11.9$ MA, $C_{ig} = 2.8$, and $P_{DT} = 56$ MW. The direct cost of the nuclear island can then be reduced by about \$20 million, while the total direct cost can be reduced by about \$30 million.

3. The plasma paramagnetism is shown to increase strongly when the aspect ratio is decreased below 2.5 and when the plasma elongation is increased beyond 2. The ratio B/B_0 ranges between 1.5 and 2.3 at an aspect ratio of 1.6 when the plasma is elongated from 1.9 to 3.0. The impact of such strong paramagnetism is to allow an IST with $B_0 = 2$ T, $R = 1.1$ m, and $a = 0.62$ m to have $C_{ig} = 1.5$ based on the neo-Alcator scaling. The data base

for application of the plasma-enhanced field to the plasma scaling laws is currently inadequate. When this possible effect of paramagnetism is not included, C_{ig} would be smaller by roughly an order of magnitude.

4. By combining the center conductor engineering design trade-off with the IST parameter space trade-off, it is assessed that the use of the C-17510 alloy permits feasible IST designs with J_c as high as 11 kA/cm^2 without exceeding the stress limits of the alloy conductor, if it is cooled with high-velocity pressurized water in a highly compact IST at a relatively moderate field (between 3 T and 5 T).

5. An IST configuration is derived that features internal restraining and supporting structures to allow the TF configuration to be essentially free-standing. This approach, while preliminary in nature, has high potential for decoupling the torus from the shield structure, contributes to minimizing the "disposable" portion of the nuclear island, and eases maintenance without significantly compromising the need to achieve a very small aspect ratio.

The results of this study, although preliminary, indicate the high potential of the spherical torus concept in permitting compact fusion at modest field. The prevailing confinement and beta scaling laws, while relatively secure in their application to large tokamaks of conventional aspect ratios, indicate uncertainties of an order of magnitude in spherical tokamaks. An absence of physics data base at present stands out as the primary handicap to significant progress in our understanding of the highly paramagnetic spherical tokamaks.

8.1.3.2 Reference configuration

Reference parameters for the nominal IST design are shown in Table 8.7, and elevation and plan views are shown in Figs. 8.25 and 8.26, respectively. The primary features of the reference concept are: (1) a 36-turn TF coil system connected in series with the top leg of each coil removable for access, (2) a thick-walled vacuum vessel/first wall structure that also functions as an intercoil structure, and (3) an external shielding system of 2.5 m of water in steel tanks, which can be added by phased construction before D-T operation.

The TF coils are rectangular in shape, with the center leg wedged between adjacent TF turns. In the radial build, the center leg begins at a radius of 5 cm and ends on a radius of 40 cm. The toroidal wedge angle is 10°, and the current density is 3 kA/cm^2.

The outer leg of each TF coil turn has a toroidal width of 40 cm and a thickness of 10 cm. The current density in the outer leg is 1 kA/cm^2. The 40-cm width for each of the 36 TF coil outer legs arranged in a toroidal array allows access openings (60 cm in toroidal width) at 6 equally spaced locations. Access openings at midplane are for LHRF heating units. Access openings at the limiter elevation are provided for coolant and attachment connections.

The top and outer legs of the TF coil are removable. The center leg mates with the top leg by means of an eight-finger lap joint with two bolts. The top leg mates with the outer leg by means of a bolted lap joint. Turn-to-turn electrical connection occurs between the outer leg and the bottom leg of the adjacent turn at floor level. The turn-to-turn connector lies on top of the inlet electrical bus, which makes a full toroidal loop around the machine before mating with the bottom leg of the first turn. Current in the turn-to-turn

Table 8.7. Reference parameters for a nominal IST

Description	Value
Geometry	
Major radius R_0, m	1.62
Plasma radius a, m	1.01
Plasma elongation κ	2.0
Aspect ratio A	1.60
Scrapeoff layer, m	0.10
Distance from scrapeoff to conductor post, m	0.11
Plasma	
Average ion temperature $\langle T_i \rangle$, keV	20
Safety factor (edge) q (flux surface average)	2.4
Effective charge (during burn) Z_{eff}	1.5
Plasma current I_p, MA	14.0
Average electron density $\langle n_e \rangle$, cm^{-3}	0.62×10^{14}
Average D-T density $\langle n_{DT} \rangle$, cm^{-3}	0.44×10^{14}
Epsilon beta poloidal	0.20
Total beta $\langle \beta \rangle$, %	24.3
D-T beta $\langle \beta_{DT} \rangle$, %	18.7
Toroidal field at plasma B_t, T	2.0
Q	Ignited
Operating mode	
Maximum burn time t_{burn}, s	50
Average burn time t_{bave}, s	20
Fusion power P_{fus}, MW	55
Cumulative D-T burn time, s	2×10^4
Years of operation	10
First wall and vacuum vessel	
Coolant	H_2O
Average neutron wall load at plasma edge, MW/m^2	0.41
Average neutron wall load at first wall, MW/m^2	0.26
Average thermal wall load, MW/m^2	0.03
First wall/vacuum vessel thickness, m	0.10

Table 8.7 (continued)

Description	Value
Shield	
Inboard shield thickness	0
Dose rate to TF coil insulation, rad	1×10^{10}
Time after shutdown to permit personnel access (2.5 mrem/h), h	36
Outboard shield thickness (90% water, 10% stainless steel), m	2.50
Maximum structure temperature, °C	200
Vacuum	
Initial base pressure, torr	10^{-7}
Preshot base pressure, torr	10^{-5}
Postshot base pressure, torr	3×10^{-4}
Pressure at duct inlet during burn, torr	10^{-2}
TF coils	
Number	36
Peak design field at winding, T	8.1
Conductor current density, A/cm^2	3250
PF coils	
Total flux capability, Wb	9.44
EF flux, Wb	9.44
Total maximum ampere-turns, MAT	11.61
Total maximum EF ampere-turns, MAT	11.61
Conductor winding pack current density, A/cm^2	1500
Current rampup	
Lower hybrid current	
Rise time, s	50
Power, MW	8
Frequency, GHz	0.564
Bulk heating	
Lower hybrid current	
Time, s	10
Power, MW	8
Frequency, GHz	1.325

ORNL-DWG 85-2678 FED

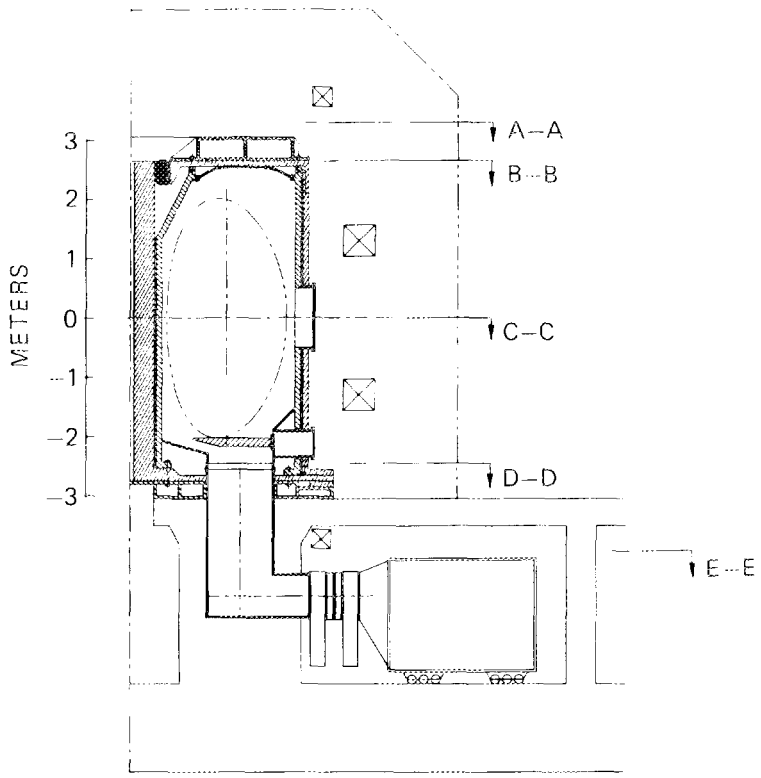

Fig. 8.25. Elevation view of IST.

connector flows in the direction opposite to the current flowing in the inlet bus, canceling the fields generated.

The inner and outer rings of the vacuum vessel function as TF intercoil structures for both in-plane and out-of-plane TF coil loads. The lid of the vacuum vessel is removable for access to the plasma chamber.

8.1.4 Supporting Activities

8.1.4.1 Tandem-mirror reactor systems code

A computer code was developed to self-consistently determine the configuration, performance, and cost of a TMR as a function of plasma, magnetic, and engineering parameters. The first version of the Tandem Mirror Reactor Systems Code (TMRSC) models a configuration similar to MARS[1] and FPD[2] that incorporates a solenoidal central cell and an end cell consisting of a choke coil, a C coil transition region, an anchor C coil set, a plug C coil set, and a recircularizing coil. The thermal barrier in this configuration is located in the plug.

ORNL-DWG 85-2679 FED

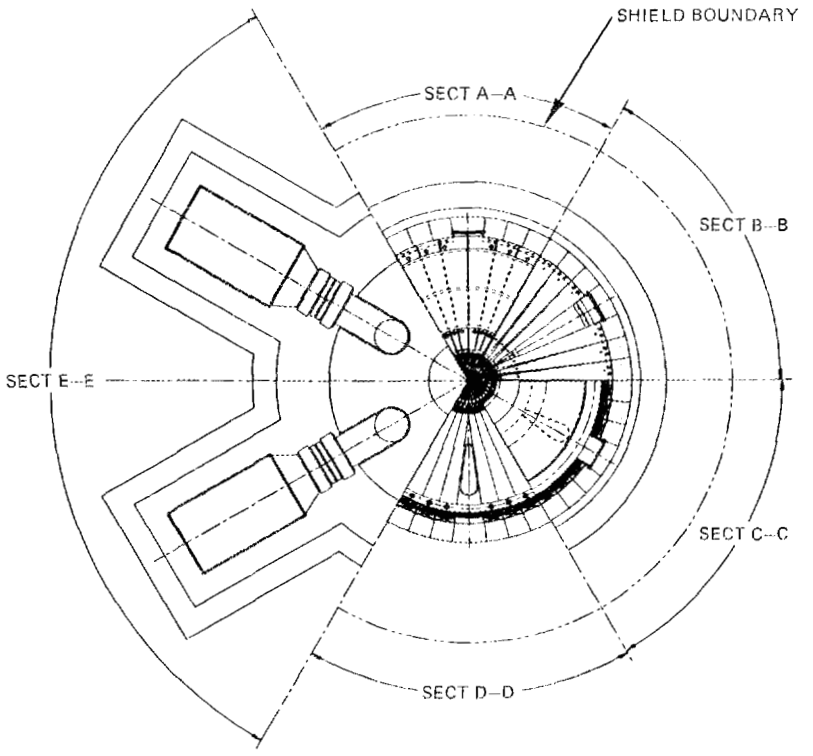

Fig. 8.26. Plan view of IST.

The modules that make up the TMRSC were provided by various sources within the fusion community. The physics, magnetics, magnet, and facility modules were the responsibility of LLNL. Neutronics, shielding, and tritium modules were modeled by Argonne National Laboratory (ANL). Blanket thermal hydraulics, heat transport/power conversion, cryogenics, direct convertor, and plasma heating systems were provided by TRW, Inc. Magnet electrical, ac power, vacuum vessel, fueling, maintenance equipment, and I&C modules were modeled by the Design Center, and the integration of the modules into the TMRSC was the responsibility of the Design Center. Figure 8.27 is a flow diagram.

The modules, each describing a reactor component or system, are connected by a driver. Three feedback loops are indicated by dashed lines. These loops are necessary due to the strong coupling between the plasma physics, the magnetics, neutronics, and magnet design parameters.

The calculational procedure is to start at the plasma centerline of the central cell and proceed radially. The central-cell length and plasma radius are determined primarily from the desired fusion power, field on axis, beta, and plasma temperature. The central-cell blanket thickness is determined based on the desired energy multiplication and tritium breeding ratio. The shield thickness is set by nuclear response limits in the superconducting

ORNL-DWG 85-2622 FED

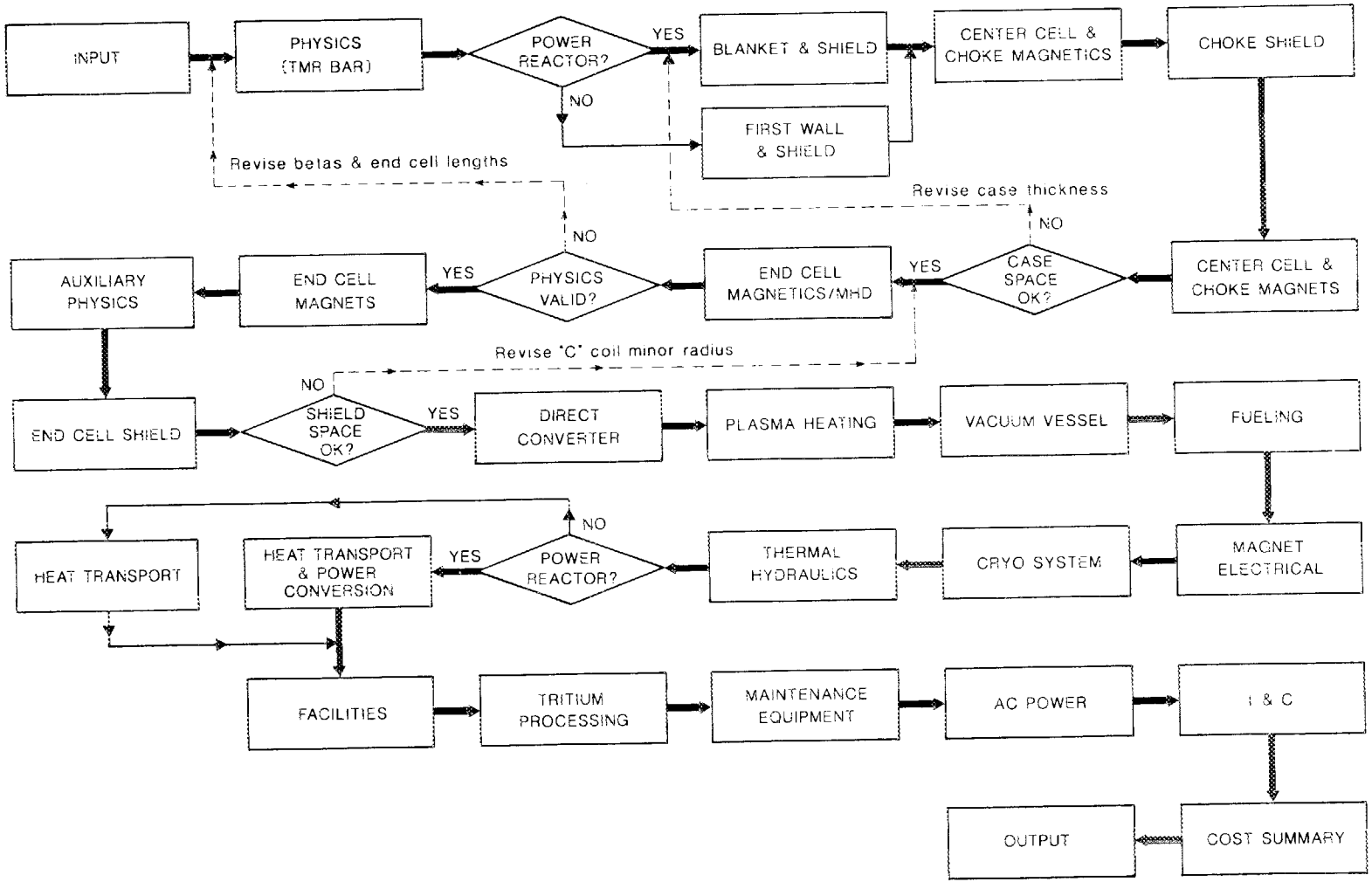

Fig. 8.27. Flow diagram of TMRSC.

solenoidal coils. The central-cell, solenoidal coil radius is then determined from the summation of the plasma radius, blanket and shield thickness, and assembly gaps. Coil currents and conductor areas for the solenoidal coils are determined as functions of the coil radius, desired field on axis, and allowable coil current density.

The code now proceeds axially to the choke coil and end-cell regions. The plasma radius at the choke coil is determined from the desired field on the choke coil axis and the requirement to pass the central-cell magnetic flux. With the plasma radius at the choke coil known, a choke coil (superconducting portion plus copper insert portion) is sized, based on required currents and allowable current densities, to deliver the desired field on axis. Space for shielding the choke coil is provided.

The C coil radii in the end cells are consistent with the plasma boundary, the desired field on axis, requirements for shielding, desired sweep angle, and allowable current densities. Axial positions of the coils are chosen to allow recircularizing the flux in the anchor and plug wells and reducing the average geodesic curvature to zero. As previously noted, a feedback loop ensures compatibility between coil geometry, neutronics, magnetics, and plasma stability. Modules downstream of the iteration loops are executed in a once-through manner according to the sequence shown in the flow diagram.

Brief summaries of the modules follow.

Physics

The physics module computes the steady-state plasma power and particle balance and the plasma supplemental heating requirements for TMRs by solving multiple, nonlinear, linked equations. Quasi-neutrality is maintained at several cardinal points in the end-cell region. Volumes, densities, potentials, and fusion power values are determined. Options to find minimum length, maximum power, or maximum Q are available. The central cell may be specified to be ignited or driven.

Neutronics

Options are available to select from various breeding, reflector, and structural materials in the central-cell blanket and shield module. Tritium breeding ratio, energy deposition, and nuclear response in the coils are determined consistent with the neutron wall loading and material composition and thickness. End-cell shielding is based on the neutron source strength. Costs of the blanket and shield are estimated.

Blanket thermal hydraulics

Coolant inlet and outlet temperature, pressure drops, pumping power, and structural temperatures are determined for liquid-metal and gas-cooled components.

Magnetics

Magnetics for the central-cell solenoid coils, the choke coil, and the end-cell C coils are determined. Required currents are computed based on the magnetic field profile, the coil radii, and the coil axial location. The central-cell coils may be discrete coils or a current sheet. Conductor current density and coil dimension or coil aspect ratio are input

items. The end-cell C coils are sized and positioned to provide (1) the desired magnetic field profile, (2) flux tube circularity in the magnetic wells, and (3) zero average geodesic curvature. This module runs the EFFI magnetic field code and the Tandem Equilibrium and Stability Code (TEBASCO). Allowable values of beta in the central cell, anchor, and plug are determined to be consistent with MHD equilibrium and stability. These values of beta are coupled to the plasma physics through an external feedback loop.

Magnets

Central-cell and end-cell magnets are modeled. Magnet designs are consistent with limitations of current density, maximum field, cryostability, and fluence for various conductor types. Coil case thickness is based on allowable stress. Cost for each magnet is estimated.

Neutron source (auxiliary physics)

The module determines the neutron source strength in the end cells (needed to determine shielding requirements), frequency requirements for the plasma rf heating and drift pumping systems (ECRH, LHRH, ICRH), and magnetic flux, heat flux, magnetic field profile, and net electrical power associated with the direct convertor.

Direct convertor

The direct convertor is based on a gridless design and consists of four concentric collectors at each end. Radial drift pumping forces most of the ions in the plasma onto the halo, which is kept at ground potential by the outer two collectors. Electrons flow axially through the middle of the magnet sets and are deposited on the inner two collectors, which are biased on the order of 100 kV. Direct electrical power is produced by the electrons; heat deposited by the ions and alphas can be recovered by a thermal cycle.

The model calculates the collector area required for each of the four regions, based on a maximum energy flux (input parameter). The electrical power produced, effective radii of the collectors, length of the direct convertor, and size of the enclosing vacuum tank are also calculated. The thermal power is sent to the heat transport module. Costs are computed based on collector area for each region, direct electrical power for inverting equipment, and vacuum pumping requirements.

Plasma heating

This module sizes rf or NBI heating systems to supply the required plasma supplemental heating in the central-cell and end-cell plasma regions. For the rf systems, the output includes required circulating power, efficiency, cost, and component sizes consistent with available space for access and required power at the launcher. For the negative-ion NBI system, the output includes circulating power, efficiency, cost, and the number of sources and associated currents to deliver the required power to the plasma. Heating system component characteristics, such as power supplies, amplifiers, waveguides, launchers, and neutralizers are determined. Positive-ion heating systems are not now included in the module but may be added later.

The module also includes rf systems for drift pumping. The drift pumping system removes ions that have become trapped in the end cells as they pass to the potential peaks. The model is based on the MARS system and produces a perturbation field normal to the ambient magnetic field. Physics requirements of ion pumping speed, frequency, and geometry are used to calculate required rf frequency, current in the coils, and number and width of individual driver frequencies. Total power consumption and system cost are estimated.

Vacuum vessel

A vacuum vessel outside the solenoid coils, end-cell C coils, and direct convertor is sized and costed.

Cryogenic system

The cryogenic system module accumulates cryogenic loads from each subsystem requiring cryogens and generates the required electrical power and capital cost of the cryoplant.

Heat transport/power conversion

The heat transport and power conversion module sizes and costs the power conversion system. The blanket/reflector inlet and outlet temperatures and flow rates determine the cycle parameters. Thermal input from the end cell is also incorporated. The module consists of a heat transport routine to generate steam conditions, a turbine efficiency routine, and a costing routine. An option is available to dump the thermal power for experimental TMR designs (nonelectrical power producers).

Tritium processing

The tritium module determines mass flow rates for the primary tritium/deuterium fuel cycle based on input from the physics module. In the fueling section, an option of using tritium neutral beams during the burn is included. Tritium inventories in all major systems are calculated. The cost of the tritium needed per year is calculated both with and without a breeder blanket. An atmospheric tritium recovery system is assumed in four areas (reactor hall, hot cell, tritium building, and radioactive waste building). Capital costs for the major tritium processing and tritium recovery systems are computed.

Fueling module

The fueling module computes pertinent design requirements and cost data for the gas injectors, first-stage pellet injectors, second-stage EM rail-run accelerators, and their support systems. The pellet velocity, pellet size, pellet rate, vacuum power, helium/nitrogen refrigeration, and cost of the major equipment are determined.

AC power

The ac power systems code module calculates characteristic design and cost data for the electrical power system needed to operate the reactor. This module identifies and computes the cost for major equipment such as circuit breakers, switches, transformers, lightning arrestors, diesel generators, load control centers, and power feeders. This module does not include the turbine generator or the dc direct convertor in the end cells, but it does include the switch gear and dc-to-ac invertors that interface with the main substation. An electrical power summary is generated.

Magnet electrical systems

The magnet electrical module computes design and cost data for the power supplies and coil protection equipment of the central-cell and end-cell magnets. Design and cost data for power supplies, busing, load centers, dump resistors, dc current breakers, and associated local controls and instrumentation are determined.

I&C systems

This module determines the costs of process I&C, plasma diagnostic instrumentation, data transmission, data processing, and consoles located in the control building. The cost of each I&C process and diagnostic includes both hardware and software.

In this module, I&C refers to the supervisory control and data system located in the main control building and the associated data links to local control and instrumentation. It does not include the local process control and instrumentation located near the reactor vault.

Maintenance equipment

This module consists of a list of reactor-cell and hot-cell equipment and unit costs. The user chooses the appropriate equipment for a particular device configuration from the comprehensive listing. The size and cost of the equipment either scale with reactor parameters or are fixed.

Facility

The facility module estimates the size and cost of buildings based on reactor size, thermal power from the blanket and other components, gross electrical power output, and number and capacity of turbine generators. Facilities considered include reactor building, hot-cell building, tritium building, steam generator building, power supply building, cryogenics building, and central building.

The costs of radwaste systems equipment, miscellaneous reactor and balance of plant equipment, and special materials are also estimated in this module.

8.1.4.2 INTOR

INTOR technical benefit assessment

In this phase of INTOR, one critical issue has been an evaluation of the technical benefit of dividing the design and component production tasks of all major advanced technologies among all of the participants. Two approaches were evaluated: (1) a "splitting" approach, in which each country provides one-fourth of the components of each major system (e.g., 3 of 12 TF coils), and (2) a "branching" approach, in which each country provides all of the components of selected major systems (e.g., one country provides all TF coils, another country provides all torus sectors, etc.).

In the context of this study, the term "technical benefit" means the development of industrial capability and experience to permit advancing with the development of future fusion technology. Therefore, the concept of partitioning the design and fabrication of all of the major advanced technology components and systems was put forward for evaluation. This study focused on establishing as concisely as possible the technical benefit to be derived by each participant from conducting the project on an international basis.

It was decided in the United States to adopt two criteria in determining the candidate major systems amenable for partitioning the design and fabrication. First, the system must involve advanced technology; second, the system must involve multiple units so production can be partitioned. Systems that use standard technology and systems that involve only one (or a few) units were judged *not* to be candidates for partitioning of design or fabrication. The major systems that satisfy both criteria are the following:

magnets—TF coils and PF coils;
nuclear—torus, first wall, test modules, divertor plates;
heating—ICRH systems; and
tritium—atmospheric tritium recovery.

An evaluation was performed for each of the advanced major systems and components selected by the INTOR Workshop. Input for the evaluation was obtained from a detailed questionnaire developed by the INTOR Workshop participants and completed by industrial representatives. In each case, an industrial member of the Design Center led the U.S. effort. The questions were designed to quantify the incremental time and cost associated with either the splitting or the branching scenario. Estimates were obtained on cost increments for component/system design, procurement, fabrication, transportation, design control, cooling requirements, component verification and testing, quality assurance, spare parts, and facility requirements. In addition, the associated complexity in management coordination, project engineering, staffing requirements, and the project-related research and development (R&D) were included in the incremental estimates to the overall project cost.

The total estimated cost increase is a factor of 1.66 for splitting and a factor of 1.20 for branching. This indicates that the total cost increase of an international project is 66% using the splitting approach and 20% using the branching approach. The cost to each participant for the splitting scenario is 41% of the total cost of building the project nationally. For the branching scenario, the cost to each participant is 30% of the total cost of building the project nationally.

Several possible qualitative benefits were identified for the splitting or branching approach:

- Having several vendors involved in the fabrication process could be advantageous, particularly where the fabrication of a given component or system is highly developmental and truly advancing the art.
- Experience in U.S. projects suggests that the use of selected vendors may actually reduce some time or costs for a national project. Having the entire international community of vendors to choose from could make it possible to select the "best" vendor.
- Depending on the difficulty and complexity associated with a given advanced component system, the risk of either splitting or branching could actually prove to be lower than that associated with a national project approach. Therefore, it would be beneficial to either branch or split the fabrication.

Based on these considerations, the benefit from splitting or branching could counteract the estimated increase in cost and make the splitting or branching scheme very worthwhile.

INTOR maintenance studies

The INTOR activities for 1984 included a study of the critical issue of maintainability, to compare the benefits and costs of personnel access maintenance procedures vs those of all-remote maintenance procedures. The study used the INTOR Phase 2A baseline configuration as the basis for comparison. A configuration based on all-remote operations for maintaining both the internal and external reactor components has not been developed. The reference configuration could be modified to model the all-remote case by reducing the outboard shielding by 50 cm, with a corresponding reduction in TF coil bore. However, this approach was not taken. Complexities of the modified design would include increased shielding requirements to protect the area outside the reactor building, increased activation in the reactor building, and increased TF coil heating. The study approach was to use the reference design for both approaches and to compare them by taking into account the induced activities and dose rates, waste disposal materials, estimated possible radioactive releases, shield requirements, assembly/disassembly procedures and maintenance-related device downtime, maintenance equipment requirements, tritium containment and control, reactor building and other facility requirements, capital and operational costs, and flexibility of operations.

The control of radioactive particulates is an important consideration for maintenance operations with both designs. For the personnel access case, activated particulates may render hands-on operations unacceptable; for the all-remote case, remote equipment may become unnecessarily contaminated. Collecting the particulates in situ before removing device components can minimize the potential for contaminating the reactor cell or maintenance equipment. If this is not sufficient, the area must be decontaminated before hands-on operations in the personnel access case, and equipment must be decontaminated after maintenance in the all-remote case. An alternative approach is to remove device components into casks that are attached (sealed) to the outboard shield so that loose particulate matter is contained until the component can be appropriately decontaminated. This

procedure implies the use of remotely operated or automated cask equipment; since components must be removed without personnel for both designs in any event, this type of equipment may not add much additional complexity or downtime. In fact, if it is possible to develop casks with vacuum sealing capability in addition to the mechanical requirements needed for remote extraction, significant downtime reductions are possible, because for this approach the plasma chamber may be kept under vacuum, and the 60 h for detritiation and 168 h for plasma chamber reconditioning may be waived.

It was determined that the tritium-handling requirements applied to both approaches, including the need for atmospheric tritium recovery systems determined on the basis of accident conditions and public safety. For operations in the reactor cell, it was shown that exposures for the personnel access approach are within acceptable limits, and maintenance operations outside the reactor cell are expected to be the same for both approaches. The reactor building for both is based on meeting accident criteria that limit the dose rate at the site boundary to 10 mrem/y. From this it was shown that tritium cleanup requirements are the same for both designs.

Maintenance scenarios that are representative of scheduled and unscheduled operations were selected to assess device downtime and to estimate personnel exposure levels. Each scenario was developed using limited personnel access and no personnel access. The following replacement scenarios were considered: divertor modules, rf heating module, test module, cryopump module, torus sector, and TF coil.

A comparison of total downtime for both designs indicates very little difference between the use of personnel access and all-remote operations. This is partially explained by the fact that personnel access to the device is limited and that much of the maintenance and disassembly must be accomplished remotely. The average annual downtime for the personnel access case is 4150 h; for the all-remote case, 4200 h. This means that on average, the device will have approximately 20 fewer days of downtime for the personnel access case. This difference is not significant because the average annual downtime is, at best, a first-order approximation. Therefore, the conclusion is that the impact on device downtime is the same for both approaches.

If personnel exposure is a critical issue for maintenance activities, then the all-remote case may be advantageous. The total personnel exposure is 233 rem for the device lifetime, or approximately 25 rem/y for reactor-cell operations. This indicates that 25 mechanics may spend as much as 400 h per year at the device shield boundary if the dose level is 2.5 mrem/h, or 2000 h per year if the dose level is 0.5 mrem/h. These numbers are based on limiting personnel exposure to ≤ 1 rem/y. An annual exposure level of 25 rem in the reactor cell is quite low, particularly compared to fission plant experience. Hence, personnel access is an acceptable approach that does not impose excessive dose levels. No significant cost differences were identified; maintenance equipment costs for the all-remote approach are 10% higher (~$7 million), and operating costs are the same.

8.1.4.3 Cost engineering

The accumulation of a cost data base derived from fusion project experience was initiated at the Design Center in October 1983. A major part of this effort has been the explicit definition of the elements of project and component costs, which is essential to the

evaluation of cost data for consistency. The intent of these definitions is to record cost data obtained from fusion projects so that the data are directly useful in estimating the costs of future projects.

Accurately estimating project costs requires considerable information in addition to the component purchase price. The costs incurred by component development, engineering, management, and construction are substantial. The Design Center has developed uniform definitions and procedures to estimate the total costs of future projects. The method is based largely on commercial power industry practice but is sufficiently general to be used for next-generation experimental devices.

The overall approach to assembling a project cost estimate consists of parallel project design and cost data base activities. At the onset of a project, a detailed code of accounts (work breakdown structure), compatible with the particular project, is developed below the mandatory level of the FEDC Code of Accounts. The FEDC Code of Accounts is applicable to all magnetically confined fusion concepts (tokamaks, mirrors, etc.) and project types (experimental device, power reactor) and is flexible with regard to contracting arrangement. Cognizant engineers are assigned the responsibility of providing the technical input to the cost estimate and submit standardized component subsystem design data sheets along with supporting material for their assigned elements in the code of accounts. These component/subsystem design data sheets, in conjunction with the Cost Data Base File, form the basis for the project cost estimate. The Cost Data Base File, which is a catalog of cost coefficients, algorithms, and component costs arranged in a standard format, is the product of the ongoing fusion component cost data base activity.

Cost estimating methodology

The flowchart shown in Fig. 8.28 outlines the methodology for calculating the total constructed cost of a reactor plant or experimental device. The equipment cost of a specific component or subsystem is first calculated using the design description and parameters list submitted by the cognizant engineer and the cost data on a similar component from the Cost Data Base File. Engineering cost and labor cost for the component/subsystem are calculated using a percentage of equipment cost extracted from the Cost Data Base File. A design allowance is added to the subtotal of component/subsystem engineering, equipment, and labor costs to account for uncertainty in the estimate for new equipment. The sum of equipment cost, engineering cost, and labor cost (with design allowance) is the direct cost of the component or subsystem. The direct costs of all the components and subsystems in the code of accounts are summed to form the total direct cost of the facility, which represents those costs associated with a specific, permanent component or subsystem in the plant. A separate systems contingency is then determined for each major section of the facility.

Four indirect cost elements are calculated, by subelement if necessary, using percentages of total direct cost extracted from the Cost Data Base File. These four elements are summed to form the total indirect cost of the facility, which is defined as cost not identified with specific, permanent plant facilities, equipment, or systems but incurred by the project as a whole. The total direct and indirect costs are summed, and a construction contingency is added to account for project uncertainties. The sum of direct and indirect costs and contingency is the total constructed cost of the facility.

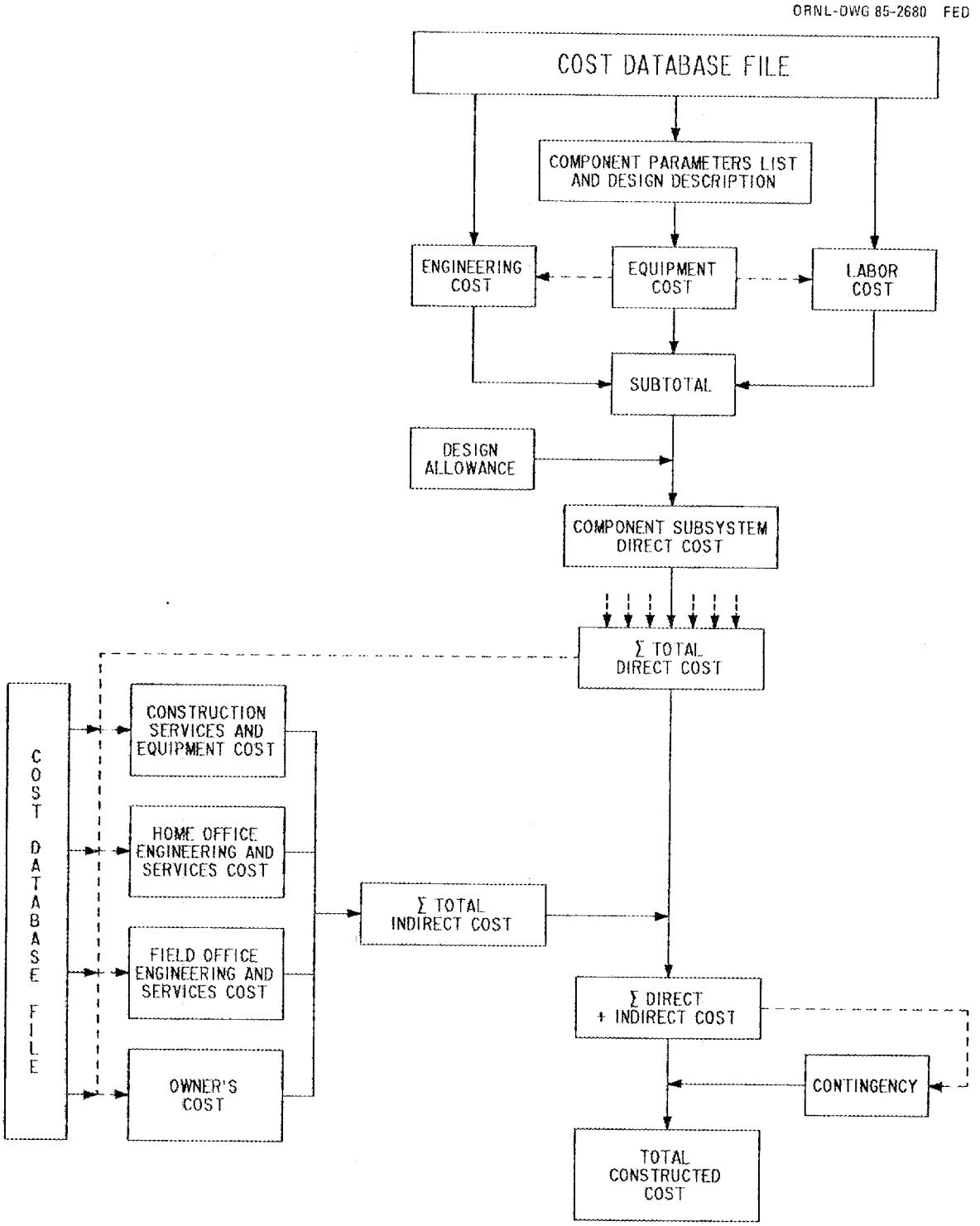

Fig. 8.28. FEDC cost estimating methodology.

Cost data base development

Past experience has demonstrated that "bottom-up" cost estimates made at preconceptual design levels for devices on the leading edge of technology are consistently inaccurate. This traditional estimating method involves summing the cost of subsystem components, beginning with the smallest details and combining these into larger and larger assemblies until the entire subsystem is complete. The bottom-up method is an excellent method when the design has matured to a fine level of detail and the components are standard, off-the-shelf items with precisely known costs. However, absence of a mature design at the preconceptual level makes total bottom-up cost estimating very difficult, at best, due to the inherent lack of design definition and detail.

The FEDC Cost Data Base is being derived from actual cost experience within and outside the fusion community and includes engineering, equipment, and labor cost data for specific components/subsystems, in addition to project-level indirect cost data. Major sources of cost data are

- fusion projects now operating or under construction,
- fusion component development projects,
- fusion project cost estimates,
- industrial manufacturers of fusion components/subsystems,
- manufacturer's quotes/price lists, and
- other nuclear projects.

The extent and format of the cost data available for a specific component depend on the component's origin. If the component is commercially available, then only the purchase price need be reported. If the component is specially fabricated, all applicable direct cost subelements (engineering cost, equipment cost, labor cost) should be reported. These subelements depend on the contracting method—built to print, built to specification, installed, etc. In some instances, fabrication cost and fabrication engineering cost can be reported separately, depending on whether the manufacturer directly charges fabrication engineering or includes it in overhead.

The most difficult cost data to refine for use in predicting the cost of future projects are those from one-of-a-kind component development programs. Figure 8.29 outlines the general methodology used to refine component development cost data. Program-unique costs are quantified and subtracted from the total contract cost to yield the cost of the next unit. Unique costs include costs incurred due to imposed budget and schedule constraints, costs attributable to unique requirements that would not apply to production units, and costs due to problems that would not be repeated on succeeding units. The cost of the next unit is then divided into recurring and nonrecurring cost elements. Subelements of nonrecurring costs are engineering and tooling. Recurring costs include the cost of fabrication and the cost of fabrication support engineering. The fabrication cost of the component or subsystem is broken down into its subelements, if necessary, and fabrication engineering is prorated among these subelements. In cases where fabrication engineering support is not directly charged by the manufacturer, it should be included in the overhead rate applied to fabrication labor. An assumed learning curve is then applied to the subelement cost, based on the desired quantity, and tooling cost is added to yield the cost of the production units.

ORNL-DWG 85-2681 FED

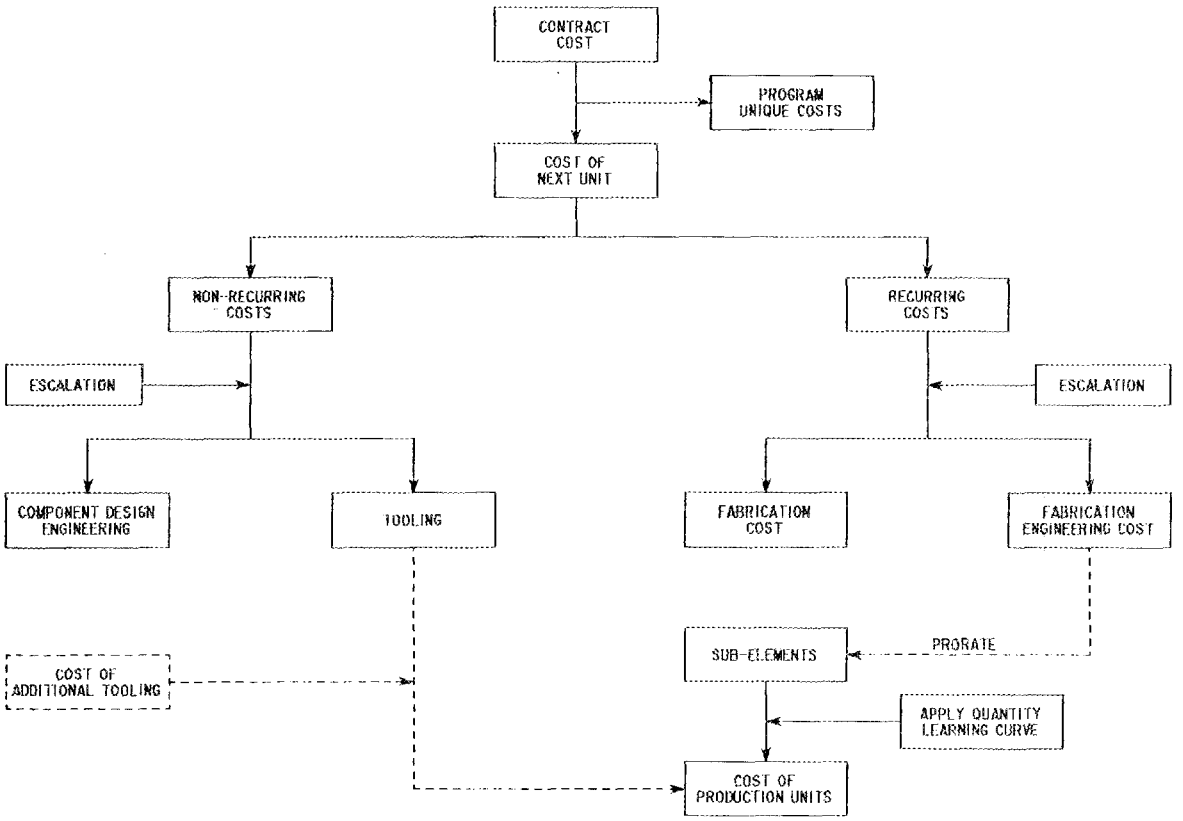

Fig. 8.29. Methodology for refinement of component development cost data.

This same methodology can be used, to a lesser extent, to refine cost data from production units.

After the cost data have been refined, they are recorded in the Cost Data Base File. This file is a catalog of cost coefficients, cost algorithms, and "component takeoff costs" formatted onto separate cost data sheets corresponding to specific components and subsystems. Each cost data sheet contains equipment, labor, and engineering cost data, in addition to pertinent design parameters, for different configurations and types of the specific component or subsystem. The Cost Data Base File is arranged to correspond to the FEDC Code of Accounts.

8.1.4.4 Availability program

An Availability Working Group was formed within the OFE in March 1984 to consider the establishment of an availability program for magnetic fusion. The scope of this program is defined to include the development of (1) a comprehensive data base, (2) empirical correlations, and (3) analytical methods for application to fusion facilities and

devices. The long-term goal of the availability program is to develop a validated, integrated methodology that will serve to provide (1) projections of plant availability and (2) input to design decisions on maintainability and system reliability requirements.

The Phase I study group was commissioned at the Design Center to assess the status of work in progress relevant to the Availability Program. The scope of Phase I included surveys of existing data and data collection programs at operating fusion facilities, the assessment of existing computer models to calculate system availability, and the review of methods to predict and correlate data on component failure and maintenance.

The review of existing availability calculation models shows that they are sufficient to meet the needs of the fusion program. The deterministic model developed by the Electric Power Research Institute (EPRI) for advanced power system applications, UNIRAM, is recommended for rapid assessment of the effect of design and input data changes on the overall system availability. Two stochastic codes developed specifically for fusion systems (the University of Wisconsin and the FEDC models) are recommended for more detailed systems analysis. These stochastic codes are capable of assessing more complex operating and maintenance scenarios, and they provide a more realistic model of the plant than the deterministic code.

It was found that the availability models are not routinely used in design studies and are not used to their full potential because the models are already well advanced compared to the availability and quality of the input data. Effective use of the models requires detailed design definition and realistic inputs for failure rates and repair times. Essential elements of the design definition are the complete system and component definition, the identification of failure modes and consequences, and the specification of the maintenance approach. The degree of definition in most preconceptual design studies does not warrant the use of a sophisticated availability model. The fusion component failure and repair inputs to the models at present are estimates based largely on the experience of persons familiar with the development of similar components. These data are useful for rough estimates of plant availability or, as is more commonly the case, for apportionments of the availability of each component to achieve the plant target availability. Simulation of mechanical motions by computer-aided design (CAD) kinematics software may become the best source for maintenance data in the future. This would allow an assessment of new designs without requiring physical mock-ups and would be conveniently connected to designs in progress on the CAD system. Correlations of reliability data can be discovered and estimates of future performance obtained by formal interrogation of fusion personnel, such as by Bayesian interrogation of experts.

The key issue in the data base assessment is whether it is worthwhile to collect data from existing experimental devices. Data should only be collected to the extent that, and in a manner such that, the data will be of use. Potential users of reliability, availability, and maintainability (RAM) data are those engaged in the conceptual design of next-generation devices and the operators of existing devices.

Operating logs and other records are used selectively and individually by experimental projects to identify downtime drivers. Although these devices do not have high availability as a goal, the projects are judged by the experiment time accomplished. The need for centralization of the device RAM data is questionable, because the device-specific problems are perceived to be more important than generic problems and because professional

exchanges serve to identify generic problems. Comprehensive collection of RAM data is justified if the cost of collecting the data is less than the value of the data to the experimental project or if one of the objectives of the project is to provide RAM data for future application. The first condition is met by projects that are so large, expensive, and controlled that a quality assurance and control program is implemented. This is true of TFTR and will be true of MFTF-B. The second condition is met by the technology development programs, such as the Tritium Systems Test Assembly (TSTA) and LCP.

The long-term objectives of the availability program, to project fusion plant availability and guide designs, will require a comprehensive data base. The value of data from current experimental projects is arguable, but these data are better than no data, if properly used. The goal of the fusion program is to provide the information required for the private sector to invest in fusion. A key element of this information will be the projection of plant availability. Availability analysis and projection should become as much a part of reactor design studies as cost analysis and projection. Historically, availability analysis has been used to improve the performance of existing or fully characterized systems. It is ambitious for the fusion program to intend to confidently predict the availability of a power plant before a full prototype has been operated. However, the capital investment required for a fusion plant mandates this projection. In the long run, the existence of a comprehensive and validated RAM data base will be of high value to the fusion program.

8.2 FUSION ENVIRONMENTAL ASSESSMENT PROGRAM

The Fusion Environmental Assessment Program provides technical assistance to the DOE–OFE in coordination and preparation of National Environmental Policy Act (NEPA) compliance documents. The program is administratively part of the Environmental Impact Section of the ORNL Energy Division, but it draws on the technical expertise of staff from the Chemical Technology, Engineering Physics and Mathematics, Environmental Sciences, Fusion Energy, Health and Safety Research, Information, and Metals and Ceramics divisions as well.

Since the program's inception in 1979, its focus has been the development of a generic environmental impact statement (GEIS), which is required by NEPA regulations as the national fusion program advances from basic and applied research to engineering development. In 1984, a revised preliminary draft GEIS was prepared. The following issues, which are related to introduction of central-station fusion power plants into the U.S. energy economy, were addressed: radioactive inventories, plant effluents, occupational safety and health, reactor safety, radioactive waste management, and availability of basic constituent materials. The technical basis for analysis of these issues in the GEIS is included in a previous report.[19] The draft GEIS is expected to be issued by DOE in FY 1986.

REFERENCES

1. *Mirror Advanced Reactor Study (MARS), Final Report, Commercial Fusion Electric Plant*, UCRL-53480, Lawrence Livermore Natl. Lab., Livermore, Calif., July 1984.

2. J. N. Doggett, *Fusion Power Demonstration -I and -II*, UCID-19975-1, Lawrence Livermore Natl. Lab., Livermore, Calif., January 1985.

3. G. V. Sheffield and W. T. Reiersen, *TFCX Preconceptual Design Specifications*, Rev. 1, Princeton Plasma Physics Lab., Princeton, N.J., March 1984.

4. G. V. Sheffield, *Nucl. Fusion* **23**, 1039–42 (1983).

5. D. J. Strickler et al., *Equilibrium Modeling of the TFCX Poloidal Coil System*, ORNL/FEDC-83/10, Oak Ridge Natl. Lab., April 1984.

6. W. T. Reiersen, *TFCX Plasma Current Scaling*, TFCX-E-102, Princeton Plasma Physics Lab., Princeton, N.J., May 1984.

7. D. J. Strickler and J. B. Miller, *Equilibrium Comparison*, FEDC-M-84-PE-047, Fusion Engineering Design Center, Oak Ridge Natl. Lab., May 1984.

8. P. J. Harbour and J. G. Morgan, *Models and Codes for the Plasma Edge Region*, CLM-R234, Culham Lab., Abingdon, England, 1982.

9. M. F. A. Harrison, P. J. Harbour, and E. S. Hotson, *Nucl. Technol./Fusion* **3**, 432 (1983).

10. H. C. Howe, *Physics Considerations for the FED Limiter*, ORNL/TM-7803, Union Carbide Corp. Nuclear Div., Oak Ridge Natl. Lab., 1981.

11. J. D. Galambos and Y-K. M. Peng, *Two-Point Model for Divertor Transport*, ORNL/FEDC-83/4, Oak Ridge Natl. Lab., 1984.

12. D. Heifetz, D. Post, M. Petranic, J. Weisheit, and G. Bateman, *A Monte-Carlo Model of Neutral Particle Transport in Diverted Plasmas*, PPPL-1843, Princeton Plasma Physics Lab., Princeton, N.J., 1981.

13. *Superconducting Magnet Coils for the Large Coil Program*, Westinghouse Electric Corp., ORNL Contract No. 22X-31747C (March 1980).

14. M. M. Steeves and M. O. Hoenig, "Experimental Parameter Study of Subsize Nb_3Sn Cable-in-Conduit Conductors," *IEEE Trans. Magn.* **19**(3) (1983).

15. Ref. 13, vol. VI, Pt. 1, pp. 7–55.

16. P. A. Hudson, F. C. Yin, and H. Jones, *The Critical Current Density of Filamentary Nb_3Sn as a Function of Temperature and Magnetic Field*, Clarendon Lab., Oxford University, Oxford, England, November 1983.

17. L. Bromberg, D. R. Cohn, J. E. C. Williams, T. Yang, and D. L. Jassby, "Engineering Aspects of LITE (Long-Pulsed Ignited Test Experiment) Devices," presented at the 10th Symposium on Fusion Engineering, Philadelphia, December 5–9, 1983.

18. Y-K. M. Peng, *Spherical Torus, Compact Fusion at Low Field*, ORNL/FEDC-84/7, Oak Ridge Natl. Lab., February 1985.

19. J. B. Cannon et al., *Background Information and Technical Basis for Assessment of Environmental Implications of Magnetic Fusion Energy*, DOE/ER-0170, U.S. DOE, August 1983.

Chapter 9

Materials Research and Development

E. E. Bloom, Fusion Materials Program Manager

D. N. Braski[1]	R. L. Klueh[1]	J. L. Scott[1]
R. R. Coltman, Jr.[2]	K. C. Liu[1]	P. F. Tortorelli[1]
M. L. Grossbeck[1]	P. J. Maziasz[1]	J. M. Vitek[1]
C. E. Klabunde[2]	A. F. Rowcliffe[1]	F. W. Wiffen[1]

1. Metals and Ceramics Division.
2. Solid State Division.

CONTENTS

SUMMARY OF ACTIVITIES 9-5

9.1 ALLOY DEVELOPMENT FOR IRRADIATION PERFORMANCE 9-6

9.1.1 Low-Activation Materials—Abstracts 9-6

9.1.1.1 "Low-Activation Materials for Fusion Applications" 9-6

9.1.1.2 "The Development of Austenitic Stainless Steels for Fast Induced-Radioactivity Decay for Fusion Reactor Applications" 9-7

9.1.1.3 "The Development of Ferritic Steels for Fast Induced-Radioactivity Decay for Fusion Reactor Applications" 9-8

9.1.2 Austenitic Stainless Steels—Abstract of "Molybdenum Solubility Differences in MC Phases Formed in Titanium and Niobium Modified Austenitic Stainless Steels Determined Using AEM" 9-8

9.1.3 Nickel-Base Alloys—Abstract of "Fatigue Performance of HFIR-Irradiated Nimonic PE-16 at 430°C" 9-8

9.1.4 Refractory Metals and Alloys—Abstract of "A Modified Tritium Trick Technique for Doping Vanadium Alloys with Helium" 9-9

9.1.5 Martensitic Steels—Abstracts 9-9

9.1.5.1 "Elevated-Temperature Tensile Properties of Irradiated 2¼ Cr–1 Mo Steel" 9-9

9.1.5.2 "Effect of Specimen Size and Nickel Content on the Impact Properties of 12 Cr–1 MoVW Ferritic Steel" 9-10

9.1.6 Copper and Copper Alloys—Abstract of "Low-Cycle Fatigue Behavior of Oxygen-Free High-Conductivity Copper at 300°C in High Vacuum" 9-10

9.2 MATERIALS COMPATIBILITY—ABSTRACTS 9-11

9.2.1 "Mass Transfer Kinetics in Lithium–Stainless Steel Systems" 9-11

9.2.2 "Liquid Metal Corrosion Considerations in Alloy Development" 9-11

9.3 DAMAGE ANALYSIS AND FUNDAMENTAL STUDIES—ABSTRACTS 9-11

9.3.1 "The Effect of Microstructure on the Minimum Critical Radius for Bias-Driven Growth During Irradiation" 9-11

9.3.2 "Critical Radius and Critical Number of Gas Atoms for Cavities Containing a Van der Waals Gas" 9-12

9.3.3 "Ion Bombardment Damage in a Modified Fe–9 Cr–1 Mo Steel" 9-12

9.3.4 "Analytical Solutions for Helium Bubble and Critical Radius Parameters Using a Hard Sphere Equation of State" 9-13

REFERENCES 9-14

9. MATERIALS RESEARCH AND DEVELOPMENT

Summary of Activities

The Office of Fusion Energy Reactor Materials Program consists of four major task areas: Alloy Development for Irradiation Performance (ADIP), Damage Analysis and Fundamental Studies (DAFS), Plasma-Materials Interaction (PMI), and Special-Purpose Materials (SPM). The PMI research is reviewed in Chapter 5. This chapter covers research on the ADIP, DAFS, and SPM tasks.

Our ADIP and DAFS programs are concerned with fusion reactor structural materials and have as their primary objectives

1. to develop an understanding of the mechanisms involved in radiation damage and corrosion phenomena;
2. to provide information on materials properties necessary for the design of near-term fusion devices and for fusion power reactor conceptual design and trade studies; and
3. to develop a sound technological basis for development of materials that will allow fusion to be developed to its full potential.

Our research on austenitic stainless steels has focused on development of microstructures that are stable at high temperatures to high irradiation damage levels and that will trap transmutation-produced helium on a very fine scale. Such microstructures should extend the incubation period for void swelling and increase the temperature at which helium embrittlement occurs, thus expanding the temperature-fluence design window. Exploratory research including basic physical metallurgical studies, irradiations in the Fast Flux Test Facility (FFTF), and dual-ion irradiations was initiated on manganese-stabilized austenitic stainless steels, which are possible low-activation structural alloys.

Research on vanadium alloys has continued to expand. Development of an apparatus for introducing helium at elevated temperature using the "tritium trick" was completed. Helium was introduced into three vanadium alloys with no significant interstitial element pickup. The three alloys (V–15 Cr–5 Ti, V–3 Ti–1 S, and VANSTAR-7) show varying responses of the tensile ductility and fracture behavior to the presence of helium. These results show that the resistance of vanadium alloys to helium embrittlement can be significantly improved through further alloy development. Samples are being irradiated in FFTF to investigate the combined effects of helium and displacement damage.

In the ferritic steels area we have continued to scope the response of our reference alloys, HT-9 and 9 Cr–1 Mo, to neutron damage, with particular emphasis on impact and tensile properties. To create radiation damage conditions similar to those produced by 14-MeV neutrons (displacement damage coupled with helium production), we have pioneered the technique of isotopic tailoring. To structural alloys, we deliberately add selected isotopes that will enhance helium production during irradiation in a mixed-spectrum fission reactor. An extensive study of the effects of doping ferritic steels with small concentrations of natural nickel has established that the basic metallurgical response

of the tempered martensitic structure is retained. Sets of doped and undoped alloys currently undergoing irradiation in the High-Flux Isotope Reactor (HFIR) will allow us to explore, for the first time, the response of these promising materials to high levels of damage (~100 dpa) and helium (~1500 appm). Subsequent experiments are planned using lower concentrations of ^{58}Ni to stimulate helium production and identical concentrations of ^{60}Ni for controls. Our approach to developing low-activation versions of the ferritic steels is to explore the metallurgical consequences of substituting tungsten or vanadium for molybdenum and niobium in an experimental set of alloys with chromium ranging from 2% to 12%. Although our initial studies are promising, a great deal remains to be done to investigate the ductile-to-brittle transition, high-temperature strength, corrosion properties, and radiation response of this new class of materials.

Corrosion studies have the objectives of (1) establishing compatible structural material, coolant, and breeder combinations and (2) understanding the mechanisms of corrosion and mass transfer to provide a basis for predicting kinetics in reactor systems and developing techniques for control. Estimates of the maximum allowable temperature in austenitic and ferritic stainless steel systems using lithium and Pb-Li as coolants/breeders have been established. In general, the compatibility of the ferritic steel is superior to that of the austenitic steel in the liquid-metal environments. The compatibility of vanadium alloys with Pb-Li and lithium is being addressed with prime emphasis on interstitial mass transport and reactions in dissimilar alloy systems.

The DAFS research has focused on developing an understanding of the effects of helium on microstructural evolution, swelling, and mechanical properties. The research includes theory, modeling, and experiment. Helium is found to reduce the critical radius for bias-driven growth. In the design of swelling-resistant materials, the helium must be trapped in a distribution of very fine bubbles, which because of their high concentration are delayed in reaching the critical size for growth as voids.

The program on insulators and stabilizers for superconducting magnets (SPM Program) has focused on providing facilities at the National Low-Temperature Neutron Irradiation Facility (NLTNIF) for research in the area of radiation effects on magnet materials. This facility will provide temperatures and irradiation conditions similar to those at the magnets of a fusion reactor.

9.1 ALLOY DEVELOPMENT FOR IRRADIATION PERFORMANCE

9.1.1 Low-Activation Materials—Abstracts

9.1.1.1 "Low-Activation Materials for Fusion Applications"[1]

R. W. Conn,[*] E. E. Bloom, J. W. Davis,[†] R. E. Gold,[‡] R. Little,[**] K. R. Schultz,[††] D. L. Smith,[‡‡] and F. W. Wiffen

Radioactivity in fusion reactors can be effectively controlled by materials selection. The detailed relationship between the use of a material for construction of a magnetic fusion reactor and the material's characteristics important to waste disposal, safety, and system

maintainability has been studied. The quantitative levels of radioactivation are presented for many materials and alloys, including the role of impurities, and for various design alternatives. A major outcome has been the development of quantitative definitions to characterize materials based on their radioactivation properties. Another key result is a four-level classification scheme to categorize fusion reactors based on quantitative criteria for waste management, system maintenance, and safety. A recommended minimum goal for fusion reactor development is a reference reactor that (a) meets the requirements for Class C shallow land burial of waste materials, (b) permits limited hands-on maintenance outside the magnet's shield within two days of a shutdown, and (c) meets all requirements for engineered safety. The achievement of a fusion reactor with at least the characteristics of the reference reactor is a realistic goal. Therefore, in making design choices or in developing particular materials or alloys for fusion reactor applications, consideration must be given to both the activation characteristics of a material and its engineering practicality for a given application.

---

*School of Engineering and Applied Science, University of California, Los Angeles.
†McDonnell Douglas Astronautics Co., St. Louis.
‡Westinghouse Electric Corp., Pittsburgh.
**Princeton Plasma Physics Laboratory, Princeton, N.J.
††GA Technologies, Inc., San Diego.
‡‡Argonne National Laboratory, Argonne, Ill.

9.1.1.2 "The Development of Austenitic Steels for Fast Induced-Radioactivity Decay for Fusion Reactor Applications"[2]

R. L. Klueh and E. E. Bloom

Austenitic stainless steels (primarily type 316 and variations on that composition) are leading candidates for the structural components for future fusion reactors. However, irradiation of such steels in a fusion environment produces long-lived radioactive isotopes. These isotopes lead to difficult radioactive waste disposal problems once the structure is removed from service. Such problems could be reduced by developing steels that contain only elements that produce radioactive isotopes that decay to low levels in a reasonable time (tens of years instead of hundreds or thousands of years). This paper discusses the development of such austenitic steels by making elemental substitutions in the steels now under consideration. Nickel and molybdenum must be replaced in these steels; the nitrogen concentration must be limited and the niobium maintained at extremely low levels. Manganese appears to be an appropriate substitution for nickel. Because manganese is not as effective an austenite-stabilizing element as nickel, a simple one-to-one substitution is not possible. Therefore, the first step in an alloy development program will be the determination of a stable Fe-Cr-Mn-C composition, after which alloying additions can be made to improve strength and irradiation resistance.

9.1.1.3 "The Development of Ferritic Steels for Fast Induced-Radioactivity Decay for Fusion Reactor Applications"[3]

R. L. Klueh and E. E. Bloom

The Cr-Mo ferritic (martensitic) steels are leading candidates for the structural components for future fusion reactors. However, irradiation of such steels in a fusion environment produces long-lived radioactive isotopes that lead to difficult waste disposal problems once the structure is removed from service. One method proposed to alleviate such problems is the development of steels that contain only elements that produce radioactive isotopes that decay to low levels in a reasonable time (tens of years instead of hundreds or thousands of years). For such a solution for the Cr-Mo steels, molybdenum must be eliminated. In addition, niobium must be maintained at extremely low levels. Tungsten is proposed as an appropriate substitution for molybdenum, and the procedures for developing Cr-W steels analogous to the Cr-Mo steels are discussed.

9.1.2 Austenitic Stainless Steels—Abstract of "Molybdenum Solubility Differences in MC Phases Formed in Titanium and Niobium Modified Austenitic Stainless Steels Determined Using AEM"[4]

P. J. Maziasz

Molybdenum is added to improve elevated-temperature strength and corrosion resistance for type 316 compared to type 304 stainless steel. Strong carbide-forming elements, like titanium and niobium, are also added to these steels to improve creep strength and reduce stress corrosion cracking, as well as to improve resistance to irradiation-induced swelling and helium embrittlement. This work shows that fairly pure TiC and NbC form in Ti- and Nb-stabilized versions of type 304 stainless steel (types 321 and 347, respectively); however, the Ti-rich MC dissolves molybdenum considerably, whereas the NbC remains compositionally quite pure when these phases form in Ti- and Nb-modified type 316 stainless steels, respectively. The modified type 316 stainless steels depend upon stability of fine MC particles for their creep or irradiation resistance advantage over unmodified alloys. Differences in phase stability may correlate with differences in phase composition. For example, the Ti-rich MC would seem sensitive to molybdenum alloy content or formation of molybdenum-rich phases, whereas the NbC would not. Such ideas can lead to alloy development strategies for properties improvement that would be unsuspected without analytical electron microscopy (AEM) phase analysis.

9.1.3 Nickel Base Alloys—Abstract of "Fatigue Performance of HFIR-Irradiated Nimonic PE-16 at 430°C"[5]

M. L. Grossbeck and K. C. Liu*

Nimonic PE-16 was irradiated in the HFIR to 6 to 9 dpa and 560 and 1000 appm He at 430°C. Postirradiation fatigue tests revealed a reduction in fatigue life by about a factor of ten at 430°C. In contrast to AISI type 316 stainless steel, no endurance limit was

observed. All irradiated specimens exhibited some intergranular fracture with an increasing tendency toward "cleavagelike" intragranular fracture for low strain ranges.

*Metals and Ceramics Division.

9.1.4 Refractory Metals and Alloys—Abstract of "A Modified Tritium Trick Technique for Doping Vanadium Alloys with Helium"[6]

D. N. Braski and D. W. Ramey*

A modified tritium trick technique was used to implant three different levels of ^{3}He in V–15 Cr–5 Ti (wt %) and VANSTAR-7 specimens before irradiation in FFTF. The modifications include (1) wrapping of the specimens with tantalum foil to minimize oxygen contamination and (2) a 400°C decay-time treatment to prevent vanadium tritide formation and to produce a ^{3}He bubble distribution similar to that produced during elevated temperature irradiation. Preliminary results show that both modifications were successful. However, the tritium removal step at 700°C was probably too excessive, especially at higher helium levels, because large ^{3}He bubbles formed in the grain boundaries and severely embrittled the V–15 Cr–5 Ti alloy. Reduction of the tritium removal step to 400°C should alleviate this problem. VANSTAR-7 specimens consistently absorbed about half as much tritium and subsequently contained half as much ^{3}He as V–15 Cr–5 Ti. Implanting ^{3}He in vanadium alloys via the tritium trick offers a convenient technique to study the mechanism of helium embrittlement *without* irradiation and should provide a rapid screening method to help develop embrittlement-resistant vanadium alloys.

*Operations Division.

9.1.5 Martensitic Steels—Abstracts

9.1.5.1 "Elevated-Temperature Tensile Properties of Irradiated 2¼ Cr–1 Mo Steel"[7]

R. L. Klueh and J. M. Vitek

The effect of neutron irradiation on the tensile properties of normalized-and-tempered 2¼ Cr–1 Mo steel was determined for specimens irradiated in the Experimental Breeder Reactor (EBR-II) at 390°C to 550°C. Two types of unirradiated control specimens were tested: as-heat-treated specimens and as-heat-treated specimens aged for 5000 h at the irradiation temperatures. Irradiation to approximately 9 dpa at 390°C increased the strength and decreased the ductility compared to the control specimens. Softening occurred in samples irradiated and tested at temperatures of 450°C, 500°C, and 550°C; the amount of softening increased with increasing temperature. The tensile results were explained in terms of the displacement damage caused by the irradiation and changes in carbide precipitates that occur during elevated-temperature exposure.

9.1.5.2 "Effect of Specimen Size and Nickel Content on the Impact Properties of 12 Cr–1 MoVW Ferritic Steel"[8]

W. R. Corwin,* R. L. Klueh, and J. M. Vitek

The ferritic steel 12 Cr–1 MoVW is a candidate material for use in the first wall of magnetic fusion reactors. One of the primary concerns of materials in this application is service-induced embrittlement from aging and irradiation. Unirradiated Charpy impact data have been developed on three typical heats of 12 Cr–1 MoVW steel and on heats that have been modified with nickel and chromium additions for subsequent simulation of helium effects of irradiation. The ductile-to-brittle transition temperature and the upper-shelf energy were reduced by nickel additions. The addition of nickel while simultaneously maintaining a constant net chromium equivalent caused the transition temperature to increase. The use of a subsize specimen is mandated by the small volume and high gamma heating in high-flux research reactors used for very high fluence irradiation experiments. Therefore, an understanding of the behavior of the subsize specimen is important in predicting corresponding irradiation-induced transition temperature shifts and upper-shelf drops of full-size Charpy specimens. Data are reported from subsize Charpy impact specimens, and the full-size and subsize specimens are compared. The effect of specimen size on the upper-shelf energy of this material can be reduced better by volume normalization than by area normalization.

---

*Metals and Ceramics Division.

9.1.6 Copper and Copper Alloys—Abstract of "Low-Cycle Fatigue Behavior of Oxygen-Free High-Conductivity Copper at 300°C in High Vacuum"[9]

K. C. Liu* and C. M. Loring, Jr.†

In-vacuum fatigue tests were performed on commercially pure OFHC copper and 35% Au–65% Cu brazing filler metal at 300°C. Excessive recrystallization due to exposure in the 1025°C brazing temperature cycle was detrimental to the fatigue life of the base metal; cold work was beneficial to the fatigue resistance. Triple-point cracking and grain boundary sliding were the prevailing modes of fatigue failure observed in the full-size specimens. However, a mixed morphology of ductile and cleavagelike fracture was observed on the fracture surface of the subsize specimen in which the grain structure appeared to have undergone a change because of the presence of surface cold work. The braze has superior fatigue resistance, but to exploit the maximum strength, the brazed joint must be devoid of defects such as cavities and cracks.

---

*Metals and Ceramics Division.

†Fusion Energy Division.

9.2 MATERIALS COMPATIBILITY—ABSTRACTS

9.2.1 "Mass Transfer Kinetics in Lithium–Stainless Steel Systems"[10]

P. F. Tortorelli and J. H. DeVan

Austenitic stainless steels have been studied using lithium thermal-convection loops that allow periodic specimen examination without significantly disrupting the lithium flow. Weight change measurements were made as a function of exposure time to characterize the reaction kinetics of both the dissolution and deposition processes. A power curve law was found to accurately describe the weight loss and gain behavior over the entire exposure interval, whereas both power curve and straight-line fits adequately reflected the weight changes as a function of time at longer exposures. However, weight changes ultimately approached a steady state, in which the dissolution and deposition rates are constant (that is, the weight changes were linearly proportional to exposure time). An Arrhenius analysis of the dissolution rates from a loop experiment in which the maximum loop temperature was varied while the ΔT remained fixed yielded an apparent activation energy consistent with a phase boundary reaction as the rate-determining step. Determination of steady-state deposition rates for the long-term loop experiments showed that the maximum rate of weight gain was generally not at the minimum-temperature specimen position.

9.2.2 "Liquid-Metal Corrosion Considerations in Alloy Development"[11]

P. F. Tortorelli and J. H. DeVan

Liquid-metal corrosion can be an important consideration in developing alloys for fusion and fast breeder reactors and other applications. Because of the many different forms of liquid-metal corrosion (dissolution, alloying, carbon transfer, etc.), alloy optimization based on corrosion resistance depends on a number of factors such as the application temperatures, the particular liquid metal, and the level and nature of impurities in the liquid and solid metals. The present paper reviews the various forms of corrosion by lithium, lead, and sodium and indicates how such corrosion reactions can influence alloy optimization.

9.3 DAMAGE ANALYSIS AND FUNDAMENTAL STUDIES—ABSTRACTS

9.3.1 "The Effect of Microstructure on the Minimum Critical Radius for Bias-Driven Growth During Irradiation"[12]

W. A. Coghlan* and L. K. Mansur†

It has been shown theoretically that bias-driven cavity swelling can only occur after either a critical cavity radius has been achieved or a critical number of gas atoms has accumulated in a cavity. These possibilities merge into each other, as increasing the contained gas lowers the critical radius until at the critical number of gas atoms the minimum critical radius is achieved. With the addition of any more gas, the critical radius disappears and cavity swelling is ensured. It is found that these critical quantities are highly sensitive to irradiation conditions and material parameters. Under fixed irradiation conditions, the

critical quantities are remarkably strong functions of dislocation density and bias. These results are described and their implications for the design of swelling-resistant materials are discussed.

*Arizona State University, Tempe.

†Metals and Ceramics Division.

9.3.2 "Critical Radius and Critical Number of Gas Atoms for Cavities Containing a Van der Waals Gas"[13]

W. A. Coghlan* and L. K. Mansur†

The effect of gas on void nucleation and growth is particularly important for structural materials in fusion reactors because of the high production of helium by neutron-induced transmutation reactions. Gas reduces the critical radius for bias-driven growth, and there is a critical number of gas atoms n_g^* at which the critical radius is reduced essentially to zero. The significance of this is that the time interval to the accumulation of n_g^* gas atoms may determine the time to the onset of bias-driven swelling where n_g^* is large. In previous papers these critical quantities were given for an ideal gas. Recently, we presented the results for a Van der Waals gas. Here the derivation of these relations is presented and further results of calculations are given. At low temperatures (high pressures) the results depart from those of the ideal gas, with the critical number affected more strongly than the critical radius. Comparisons are made with earlier calculations.

*Arizona State University, Tempe.

†Metals and Ceramics Division.

9.3.3 "Ion Bombardment Damage in a Modified Fe–9 Cr–1 Mo Steel"[14]

K. Farrell* and E. H. Lee

A normalized-and-tempered Fe–9 Cr–1 Mo steel, modified with small quantities of niobium and vanadium, was bombarded with 4-MeV iron ions to a nominal displacement level of 100 dpa at temperatures of 400°C, 450°C, 500°C, 550°C, and 600°C. The major microstructural damage feature created in the lathlike α-ferrite grains was dislocation tangles, which coarsened with increasing bombardment temperature. Sparse cavities were heterogeneously distributed at 500°C and 550°C. Incorporation of helium and deuterium simultaneously in the bombardments at rates of 10 and 45 appm/dpa, respectively, introduced very high concentrations of small cavities at all temperatures, many of them on grain boundaries. These cavities were shown to be promoted by helium. A small fraction of the matrix cavities exhibited bias-driven growth at 500°C and 550°C, with swelling less than 0.4%. This is a very narrow temperature range for bias-driven swelling. It is about 125°C higher than the peak swelling temperature found in neutron irradiations, which is

compatible with the higher damage rate used in the ion bombardments. High concentrations of subgrain boundaries and dislocations, resulting from the heat treatment, and unbalanced cavity and dislocation sink strengths in the damage structures contribute to the swelling resistance. Such resistance may not be permanent. High densities of bubbles on grain boundaries indicate a need for helium embrittlement tests.

*Metals and Ceramics Division.

9.3.4 "Analytical Solutions for Helium Bubble and Critical Radius Parameters Using a Hard Sphere Equation of State"[15]

R. E. Stoller* and G. R. Odette†

Considerable theoretical and experimental work has verified the role of helium-stabilized bubbles as the precursor to void formation in fast-neutron-irradiated stainless steels. The concept of the critical bubble radius or critical helium number for bubble-to-void conversion has received particular attention. A hard sphere equation of state is used to compute these parameters for a variety of irradiation conditions, and the results are compared with those computed using the ideal gas law. Simplified analytical solutions are developed which permit the calculation of the bubble radius and the critical bubble parameters without resorting to iterative techniques and yet retain the accuracy of the hard sphere equation of state. The use of these solutions is illustrated using a rate theory model of void swelling which has been calibrated using fast reactor swelling data.

*Metals and Ceramics Division.

†University of California, Santa Barbara.

REFERENCES

1. R. W. Conn, E. E. Bloom, J. W. Davis, R. E. Gold, R. Little, K. R. Schultz, D. L. Smith, and F. W. Wiffen, "Lower Activation Materials and Magnetic Fusion Reactors," *Nucl. Technol./Fusion* **5**, 291–310 (1984).

2. R. L. Klueh and E. E. Bloom, "The Development of Austenitic Steels for Fast Induced-Radioactivity Decay for Fusion Reactor Applications," in *Tailoring and Optimizing Materials for Nuclear Applications*, American Institute Metallurgical Mining Engineers, in press, 1985.

3. R. L. Klueh and E. E. Bloom, "The Development of Ferritic Steels for Fast Induced-Radioactivity Decay for Fusion Reactor Applications," *Nucl. Eng. Des.*, accepted for publication (1985).

4. P. J. Maziasz, "Molybdenum Solubility Differences in MC Phases Formed in Titanium and Niobium Modified Austenitic Stainless Steels Determined Using AEM," pp. 496–7 in *Proceedings, 42d Annual Meeting of the Electron Microscopy Society of America, Detroit, Michigan, August 13–17, 1984*, ed. G. W. Bailey, San Francisco Press, San Francisco, 1984.

5. M. L. Grossbeck and K. C. Liu, "Fatigue Performance of HFIR-Irradiated Nimonic PE-16 at 430°C," *J. Nucl. Mater.* **122 & 123**, 682–6 (1984).

6. D. N. Braski and D. W. Ramey, "A Modified Tritium Trick for Doping Vanadium Alloys with Helium," paper presented at the 12th International Symposium on Effects of Radiation on Materials, Williamsburg, Va., June 18–20, 1984; proceedings to be published as ASTM-STP-870, American Society for Testing and Materials.

7. R. L. Klueh and J. M. Vitek, "Elevated-Temperature Tensile Properties of Irradiated 2¼ Cr–1 Mo Steel," *J. Nucl. Mater.* **126**, 9–17 (1984).

8. W. R. Corwin, R. L. Klueh, and J. M. Vitek, "Effect of Specimen Size and Nickel Content on the Impact Properties of 12 Cr–1 MoVW Ferritic Steel," *J. Nucl. Mater.* **122 & 123**, 343–8 (1984).

9. K. C. Liu and C. M. Loring, Jr., "Low-Cycle Fatigue Behavior of Oxygen-Free High-Conductivity Copper at 300°C in High Vacuum," *J. Nucl. Mater.* **122 & 123**, 783–8 (1984).

10. P. F. Tortorelli and J. H. DeVan, "Mass Transfer Kinetics in Lithium-Stainless Steel Systems," in *Proceedings of the Third International Conference on Liquid Metal Engineering and Technology*, vol. 3, British Nuclear Energy Society, London, in press.

11. P. F. Tortorelli and J. H. DeVan, "Liquid Metal Corrosion Considerations in Alloy Development," in *Proceedings of the Symposium on Tailoring and Optimizing Metals for Nuclear Applications*, American Institute Mining, Metallurgical, and Petroleum Engineers, in press.

12. W. A. Coghlan and L. K. Mansur, "The Effect of Microstructure on the Minimum Critical Radius for Bias-Driven Growth During Irradiation," paper presented at the 12th Symposium on Effects of Radiation on Materials, Williamsburg, Va., June 18–20, 1984; proceedings to be published as ASTM-STP-870, American Society for Testing and Materials.

13. W. A. Coghlan and L. K. Mansur, "Critical Radius and Critical Number of Gas Atoms for Cavities Containing a Van der Waals Gas," *J. Nucl. Mater.* **122 & 123**, 495–501 (1984).

14. K. Farrell and E. H. Lee, "Ion Bombardment Damage in a Modified Fe–9 Cr–1 Mo Steel," paper presented at the 12th Symposium on Effects of Radiation on Materials, Williamsburg, Va., June 18–20, 1984; proceedings to be published as ASTM-STP-870, American Society for Testing and Materials.

15. R. E. Stoller and G. R. Odette, "Analytical Solutions for Helium Bubble and Critical Radius Parameters Using a Hard Sphere Equation of State," *J. Nucl. Mater.*, accepted for publication (1985).

Chapter 10

Neutron Transport

R. G. Alsmiller, Jr.[1]

J. M. Barnes[2]
J. L. Bartley[1]
G. T. Chapman[3]
C. Y. Fu[1]
D. M. Hetrick[2]
D. C. Larson[1]
J. F. Manneschmidt[2]
G. L. Morgan[5]
R. W. Roussin[1]
R. T. Santoro[1]
P. D. Soran[6]
D. K. Trubey[1]
J. E. White[1]

1. Engineering Physics and Mathematics Division.
2. Computing and Telecommunications Division, Martin Marietta Energy Systems, Inc.
3. Roane State Community College, Harriman, Tenn.
4. Physics Division.
5. Los Alamos National Laboratory, Los Alamos, N.Mex.
6. Schlumberger Well Services, Houston.

CONTENTS

SUMMARY OF ACTIVITIES 10-5
10.1 ABSTRACTS 10-5
10.1.1 *Fusion Reactor Shielding Benchmark* 10-5
10.1.2 *Fusion Reactor Shielding Benchmark: II. Duct Streaming and Analyses* 10-5
10.1.3 *Calculations to Evaluate the Use of the Attenuation of D-D Neutrons in Liquid Oxygen as a Means of Measuring Plasma Ion Temperature* 10-6
10.1.4 *ORACT: A 174-Neutron-Group Cross-Section Library for Fusion and Fission Reactor Design Studies* 10-6
10.1.5 *Multigroup Energy-Angle Distributions for Neutrons from the* $T(d,n)^4He$ *Reaction* (E_d = *100–400 keV*) 10-7
10.2 DATA EVALUATION AND PROCESSING FOR FUSION NEUTRONIC DATA NEEDS 10-7
10.3 RADIATION SHIELDING INFORMATION CENTER 10-8
REFERENCES 10-9

10. NEUTRON TRANSPORT

Summary of Activities

The neutron transport program includes both experimental and analytic phases. The experimental program is designed to provide the data necessary for verifying the analytic method and cross-section data used for fusion reactor neutronics design calculations. Experiments are carried out to determine neutron and photon transport in typical fusion reactor shield materials and configurations and to determine the effects of penetrations in these shields. The analytic program supports the design of the integral experiments and compares calculated data with data obtained experimentally. Work is also performed in the area of nuclear data evaluation and cross-section processing, and the Radiation Shielding Information Center has continued to supply a broad range of services to the fusion energy research community.

10.1 ABSTRACTS

10.1.1 *Fusion Reactor Shielding Benchmark*[1]

G. T. Chapman, G. L. Morgan, J. W. McConnell,* R. T. Santoro, R. G. Alsmiller, Jr., and J. M. Barnes

Integral experiments to measure the energy spectra of neutrons and gamma rays due to the transport of ~14-MeV $T(d,n)^4He$ through laminated stainless steel and borated polyethylene shield configurations have been performed at ORNL. The data from these experiments have been accepted as a fusion shielding benchmark by the Cross Section Evaluation Working Group Benchmark Committee. The document includes, in addition to all of the experimental data, a complete description of the experiments and comparisons obtained at ORNL between the experimental data and calculated results.

*Physics Division.

10.1.2 *Fusion Reactor Shielding Benchmark: II. Duct Streaming Experiments and Analyses*[2]

G. T. Chapman, R. T. Santoro, R. G. Alsmiller, Jr., J. S. Tang,* and P. D. Soran

Integral experiments to measure the energy spectra of neutrons and gamma rays due to the streaming of ~14-MeV $T(d,n)^4He$ neutrons through a cylindrical iron duct have

been performed. The data from these experiments have been submitted as a fusion benchmark to the Cross Section Evaluation Working Group Benchmark Committee. The document includes, in addition to all of the experimental data, a complete description of the experiments and comparisons obtained at ORNL between the experimental data and calculated results.

*Computing and Telecommunications Division, Martin Marietta Energy Systems, Inc.

10.1.3 *Calculations to Evaluate the Use of the Attenuation of D-D Neutrons in Liquid Oxygen as a Means of Measuring Plasma Ion Temperature*[3]

R. G. Alsmiller, Jr., R. T. Santoro, J. F. Manneschmidt, and J. M. Barnes

The ion temperature of a deuterium plasma with a Maxwellian distribution may be determined by measuring the transmission of the D-D neutrons, i.e., neutrons produced by the reaction $D + D \rightarrow n + {}^3He$, through liquid oxygen. In practice the measurement requires both collimation and shielding to ensure that the attenuation of only those neutrons emitted directly from the plasma is measured. Calculated results are presented of the collimation and shielding required to reduce the background so that the ion temperature may be measured. The geometric configuration used in the calculations is that of the Impurity Study Experiment (ISX) at ORNL, but the results will provide insight into the application of the measurement method at other plasma facilities. Results are presented for D-D plasma temperatures of 2, 6, and 10 keV and for two sizes of NE-213 detectors. It is concluded that the counting rates are too low to make the measurement feasible at ISX.

10.1.4 *ORACT: A 174-Neutron-Group Cross-Section Library for Fusion and Fission Reactor Design Studies*[4]

R. T. Santoro, J. E. White, and J. D. Drischler*

A 174-neutron-group activation cross-section library for 233 ground-state target isotopes and 22 isomeric target isotopes is described. The library, ORACT, was derived from the ACTL Evaluated Neutron Activation Cross-Section Library and was developed for use with existing computer codes that calculate induced activation by convoluting the cross-section data with neutron scalar flux distributions. The activation cross sections extend over the energy range from thermal to 20 MeV and are useful for fusion and fission reactor nuclear design studies as well as other applications.

*Engineering Physics and Mathematics Division.

10.1.5 *Multigroup Energy-Angle Distributions for Neutrons from the $T(d,n)^4He$ Reaction (E_d = 100–400 keV)*[5]

R. T. Santoro, J. M. Barnes, J. D. Drischler,* and R. G. Alsmiller, Jr.

The angle-energy dependence of neutrons produced in the $T(d,n)^4He$ reaction from 100–400 keV deuterons incident on a 4-mg/cm^2-thick titanium tritide target has been calculated.

---

*Engineering Physics and Mathematics Division.

10.2 DATA EVALUATION AND PROCESSING FOR FUSION NEUTRONIC DATA NEEDS

D. C. Larson, C. Y. Fu, D. M. Hetrick, and R. W. Roussin

Evaluated and processed neutron cross-section data are produced to meet the needs of fusion reactor designers. Nuclear data needs for the Magnetic Fusion Energy Program are given in ref. 6 and include evaluated cross sections for copper, nickel, and chromium. Nuclear model codes were used to compute cross sections for ^{63}Cu and ^{65}Cu for incident energies from 1 to 20 MeV. The input parameters for the model codes were determined through analysis of extensive experimental data in this energy region. The models and their input data and resulting calculations are compared extensively to measured data and to the Evaluated Nuclear Data File (ENDF/B-V) for copper in a recent report by Hetrick, Fu, and Larson.[7] Evaluated nuclear data files were compiled from the calculations for both ^{63}Cu and ^{65}Cu in the new ENDF/B-VI format. The resulting evaluated data sets were transmitted to the National Nuclear Data Center at Brookhaven National Laboratory and are available for processing.

Work has been initiated on evaluating cross sections for ^{58}Ni, ^{60}Ni, and ^{52}Cr in a manner similar to that for preparing the evaluations for ^{63}Cu and ^{65}Cu.

Evaluated cross sections must be processed into forms which can be used in radiation transport computer codes. The focus of this effort has been the development of VITAMIN-E,[8] a 174-neutron, 38-gamma-ray group cross-section library. It can be used in conjunction with the AMPX-II system[9] to derive cross-section data suited to a particular application. The initial version of VITAMIN-E is based on ENDF/B-V.[10]

There is a continuing effort to maintain VITAMIN-E and the relevant AMPX-II computing technology on the National Magnetic Fusion Energy Computer Center at Lawrence Livermore National Laboratory. The VITAMIN-E data and AMPX-II computing technology are also available from the Radiation Shielding Information Center at ORNL.

10.3 RADIATION SHIELDING INFORMATION CENTER

R. W. Roussin, D. K. Trubey, J. E. White, and J. L. Bartley

The Radiation Shielding Information Center (RSIC) serves an international community by responding to inquiries about radiation transport problems. Staff members provide guidance by drawing on a technical data base that includes a computerized literature file, a collection of complex computer programs, and a substantial body of nuclear data libraries pertinent to the solution of such problems.

Acquiring the needed computer-based technology base requires the collaboration of the neutronics community with RSIC staff members to collect, organize, process, evaluate, and package relevant technology developed in the community. This technology is disseminated throughout the community with a mechanism for feedback of experience through usage, which results in an improved product. The resulting technology base provides an overall advancement of the state of the art.

A selected few of the products of this information cycle that are relevant to fusion neutronics are listed below. An updated version of the multigroup Monte Carlo code (CCC-203/MORSE-CG)[11] was provided by ORNL, and Los Alamos National Laboratory (LANL) provided the latest version of their point Monte Carlo code (CCC-200/MCNP).[12] A new version of an atomic displacement code (PSR-137/MARLOWE)[13] was contributed by ORNL. A cross-section handling routine (PSR-206/TRANSX-CTR)[14] for multigroup data in MATXS format was placed in RSIC by LANL. The Japan Atomic Energy Research Institute updated CCC-410/THIDA,[15] a dose calculation system for fusion facilities, and the United Kingdom Atomic Energy Authority contributed an updated version of their evaluated neutron cross-section library (DLC-107/UKNDL-81).[16]

This selection represents only a small portion of the total activity of the center. Information processing (including evaluation and packaging) is a daily concern. In addition to a comprehensive literature data base, RSIC-packaged products include 115 data packages (DLC), 464 neutronics and shielding code packages (CCC), and 208 data processing and other miscellaneous code packages (PSR).

REFERENCES

1. G. T. Chapman, G. L. Morgan, J. W. McConnell, R. T. Santoro, R. G. Alsmiller, Jr., and J. M. Barnes, *Fusion Reactor Shielding Benchmark*, vol. II in *Cross Section Evaluation Working Group Benchmark Specifications*, ed. P. F. Rose and R. W. Roussin, BNL-19302 (ENDF-202), Brookhaven Natl. Lab., 1984.

2. G. T. Chapman, R. T. Santoro, R. G. Alsmiller, Jr., J. S. Tang, and P. D. Soran, *Fusion Reactor Shielding Benchmark II. Duct Streaming Experiments and Analyses*, submitted to the Cross Section Evaluation Working Group Benchmark Committee, Evaluated Nuclear Data File, 1984.

3. R. G. Alsmiller, Jr., R. T. Santoro, J. F. Manneschmidt, and J. M. Barnes, *Calculations to Evaluate the Use of the Attenuation of D-D Neutrons in Liquid Oxygen as a Means of Measuring Plasma Ion Temperature*, ORNL/TM-9230, Oak Ridge Natl. Lab., 1984; also accepted for publication in *Fusion Technology*.

4. R. T. Santoro, J. E. White, and J. D. Drischler, *ORACT: A 174-Neutron-Group Activation Cross-Section Library for Fusion and Fission Reactor Design Studies*, ORNL/TM-9203, Oak Ridge Natl. Lab., 1984.

5. R. T. Santoro, J. M. Barnes, J. D. Drischler, and R. G. Alsmiller, Jr., *Multigroup Energy-Angle Distributions for Neutrons from the $T(d,n)^4He$ Reaction (E_d = 100–400 keV)*, ORNL/TM-9251, Oak Ridge Natl. Lab., 1984.

6. E. T. Cheng, D. R. Mathews and K. R. Schultz, *Magnetic Fusion Energy Program Nuclear Data Needs*, GA-A17324, GA Technologies, Inc., San Diego, 1984.

7. D. M. Hetrick, C. Y. Fu, and D. C. Larson, *Calculated Neutron-Induced Cross Sections for $^{63,65}Cu$ from 1 to 20 MeV and Comparisons with Experiments*, ORNL/TM-9083, Oak Ridge Natl. Lab., 1984.

8. R. W. Roussin et al., *VITAMIN-E: A Coupled 174-Neutron, 38-Gamma-Ray Multigroup Cross-Section Library for Deriving Applications-Dependent Working Libraries for Radiation Transport Calculations* [computer program], available from the Radiation Shielding Information Center, Engineering Physics and Mathematics Division, Oak Ridge National Laboratory, as DLC-113/VITAMIN-E.

9. N. M. Greene et al., *AMPX: A Modular Code System for Generating Coupled Multigroup Neutron Gamma Libraries from ENDF/B*, ORNL-3706, Union Carbide Corp. Nuclear Div., Oak Ridge Natl. Lab., 1976.

10. R. Kinsey, comp., *ENDF/B Summary Documentation*, 3d ed. (ENDF/B-V), BNL-NCS-17541 (ENDF-201), Brookhaven Natl. Lab., Upton, N.Y., 1979.

11. M. B. Emmett, *The MORSE Monte Carlo Radiation Transport Code*, ORNL-4972, Union Carbide Corp. Nuclear Div., Oak Ridge Natl. Lab., 1975.

12. W. L. Thompson, *MCNP—A General-Purpose Monte Carlo Code for Neutron and Photon Transport, Version 2B*, LA-7396-M, Los Alamos Natl. Lab., Los Alamos, N.Mex., 1981.

13. M. T. Robinson, *MARLOWE User's Guide (Version 12)*, Oak Ridge Natl. Lab., unpublished, July 1984.

14. R. E. MacFarlane, *TRANSX-CTR: A Code for Interfacing MATXS Cross-Section Libraries for Nuclear Transport Codes for Fusion Systems Analysis*, LA-9863-MS, Los Alamos Natl. Lab., N.Mex., 1984.

15. H. Iida, *THIDA: Dose Calculation Systems for a Nuclear Fusion Facility*, ORNL-tr-471 (JAERI-M 8019), Union Carbide Corp. Nuclear Div., Oak Ridge Natl. Lab., 1978.

16. J. S. Story and R. W. Smith, *The 1981 Edition of the United Kingdom Nuclear Data Library—A Status Summary*, unpublished, 1981.

Chapter 11

Generic Magnetic Fusion Reactor Analysis

J. Sheffield[1]

R. A. Dory[2] J. G. Delene[4] D. E. T. F. Ashby[5]
S. M. Cohn[3] L. F. Parsly[4] W. T. Reiersen[6]

1. Associate division director.
2. Plasma Theory Section.
3. Energy Division.
4. Engineering Technology Division.
5. Culham Laboratory, Abingdon, Oxfordshire, England.
6. Present address: Plasma Physics Laboratory, Princeton Univ., Princeton, N.J.

11. GENERIC MAGNETIC FUSION REACTOR ANALYSIS

Summary of Activities

The economics of magnetic fusion will be an important factor in the acceptance and commercialization of this energy source. A study of a "generic" magnetic fusion reactor, which incorporates the elements common to a number of configurations, has led to the conclusion that the cost of fusion energy will be close to that for fission and fossil energy if certain physics and technology requirements are met. These requirements represent only moderate advances beyond current achievements and are the focus of existing development programs. The generic reactor model provides confidence that fusion can be a competitive energy source if the challenge of combining its elements into a single attractive reactor can be met. The challenge is a tremendous one, but we are confident that it can be met through a continuing commitment to the development of fusion as a source of energy for the future.

Over the past decade, numerous articles have been written discussing the potential economics of magnetic fusion reactors. In some of these articles it is argued that, because fusion reactors may be larger than fission reactors, the cost of electricity (COE) from them will be prohibitively high. In countering this argument, the point is made that the higher capital cost of a fusion reactor is offset by lower fuel costs. Thus, the debate centers in part on costing procedures and in part on the somewhat uncertain scale of the ultimate fusion reactor. Compounding the difficulty of unraveling this issue has been the use in some fusion studies of overly optimistic costing procedures and the continuing debate about which magnetic configuration will turn out to be the best.

As a contribution toward resolving these questions, a study has been undertaken at ORNL of what we call a "Generic Magnetic Fusion Reactor." This reactor includes all of the components of the various types of magnetic fusion reactors—among them, superconducting coils, lithium breeding blankets for tritium production, plasma heating systems, power supplies, fuel cycle components, shielding, remote handling equipment, buildings, generators, and cooling towers. However, the reactor is not any particular configuration, and it serves to emphasize what is common to all configurations. It is based on conservative assumptions about the reactor form and about the costing. Thus, the superconducting coils invoked are close to those available today. Their cost is based on today's costs, even though it is reasonable to expect substantial advances in this relatively young technology. The limit on scale is set, in the first instance, by the generic limits such as fusion reaction rates, shielding distances, acceptable material stresses, and the like. The cost procedure is that used in assessments of fission and fossil COEs.[1]

The model is used to identify the self-consistent requirements for a fusion reactor: how small must it be in order to compete with fission systems in the 21st century? The financial requirement is that the COE, in 1984 dollars, should be about 0.045–0.055 $/kWh(e). This is comparable to present fission and fossil costs, which typically range from 0.035 to 0.045 $/kWh(e) at the power plant output. We argue that at this stage it is necessary only to show that fusion is in the same ball park. The potential environmental advantages of fusion, coupled with the eventual increasing cost of fission and fossil fuels, will be the deciding factor in a choice. The question is then "Are the requirements in physics and technology for such a reactor attainable?"

The results of the study are simply stated and encouraging. They support the argument that many of the earlier fusion reactor reference designs were too big—typically, the weight of the fusion island was 25,000 tonnes for a 1200-MW(e) plant. Such plants have a COE of 0.07–0.08 $/kWh(e) in this model. By the same token, the study shows that fusion can be an attractive alternative if the fusion island weight is reduced to about 10,000 tonnes for a 1200-MW(e) plant, as shown in Fig. 11.1 and Table 11.1. An interesting result from the model is that smaller fusion power plants down to 300 MW(e) could be competitive in multiple units.

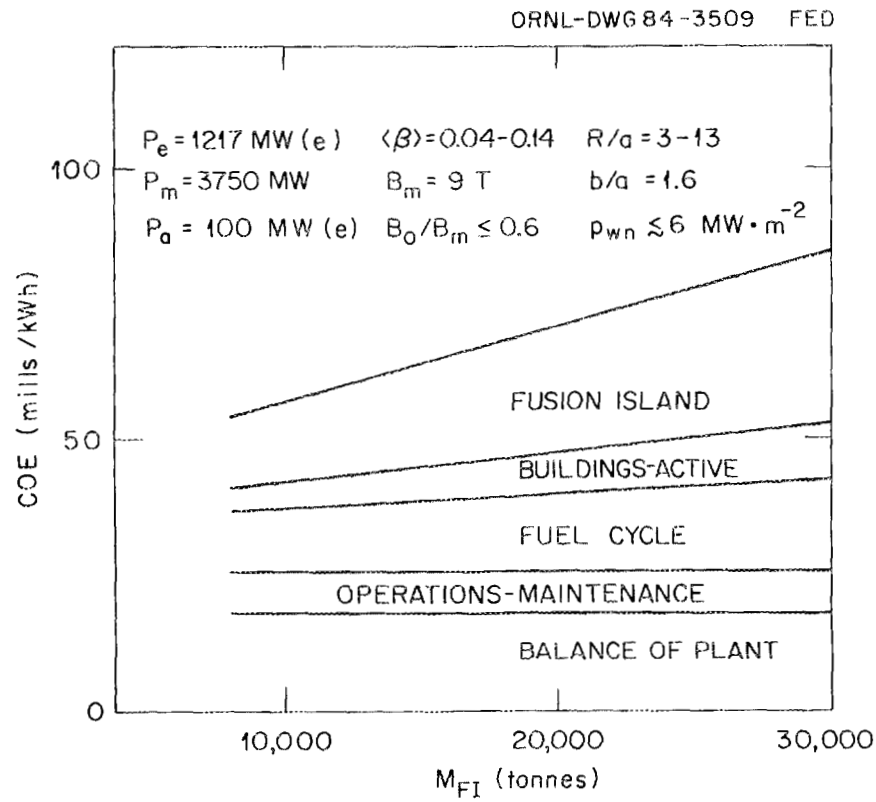

Fig. 11.1. COE vs mass of fusion island M_{FI}, showing decrease in cost as the mass decreases.

Table 11.1. Parameters of improved fusion reactors with thermal power P_t of 3750 MW(t)

Electric power, MW(e)	1,236	1,236	1,217	1,217	1,217	1,217	1,236	1,217
Auxiliary power to plasma, MW(e)	50	50	100	100	100	100	50	100
Maximum coil magnetic field, T	9	9	9	9	9	9	8	10
Beta $\langle\beta\rangle$	0.10	0.10	0.10	0.08	0.10	0.08	0.12	0.08
Major radius R	6.44	6.50	6.83	7.18	7.49	7.84	7.87	7.05
Minor radius a	1.61	1.08	1.14	1.44	1.07	1.31	0.98	1.18
R/a	4	6	6	5	7	6	8	6
Ellipticity b/a	1.6	2.0	1.6	1.6	1.6	1.6	2.0	1.6
Mass, tonnes	9,160	8,600	8,640	9,880	8,710	10,260	8,640	10,610
Volume, m^3	2,340	2,080	1,970	2,500	1,970	2,500	1,970	2,500
Ratio of mass to thermal power, tonne/MW(t)	2.44	2.30	2.30	2.63	2.32	2.74	2.30	2.83
Ratio of thermal power to volume, MW(t)/m^3	1.6	1.8	1.9	1.5	1.9	1.5	1.9	1.5
Neutron flux to first wall, MW/m^2	4.5	5.1	5.5	4.5	5.9	4.6	5.1	4.8
COE, \$/kWh(e)	0.0522	0.0474	0.0558	0.0573	0.0589	0.0558	0.0472	0.0591

As to whether such plant sizes are realizable, the answer is yes. Both the physics and the technology represent only a moderate advance over present-day achievements and are not beyond the projections of our development programs. For example, a key parameter is beta, the ratio of plasma pressure to magnetic pressure. Values for beta of 8% or greater are required, depending on configuration and superconducting coil performance. Such values have been attained in some configurations and are accessible theoretically to a wide range of configurations, including the tokamak, stellarator, reversed-field pinch, and tandem mirror, for example. Equally, we may achieve the level of thermal insulation required to maintain the hot reacting plasma by a number of routes. We have built and operated superconducting coils with parameters close to those required and, in fact, may expect further advances. We have made substantial progress in the development of the required materials and heating and fueling systems.

The generic reactor model has been reviewed widely by other fusion laboratories, by universities, and—of particular importance—by industries and utilities. Although many valuable suggestions have been made to improve the model, there has been no disagreement with the basic model or its output.

Having said all of this, we should not overlook the tremendous challenge of combining all of those elements into a single attractive reactor. However, the history of technology development is one in which what was "inconceivable" in one decade has become commonplace in another—television, space travel, air travel with its myriad of complicated components (radar, jet engines, movies in flight, supersonic transport, global coverage, operation on schedule, etc.), computers, pocket calculators, and cancer cures, to name only a few.

We are convinced that magnetic fusion can be a viable source of energy for the future. The time scale for the deployment of any energy system is so great (tens of years) that it is important to push development now, even though deployment will not occur until the 21st century, so that it will be possible to have a choice.

REFERENCE

1. *Nuclear Energy Cost Data Base*, DOE/NE-0044/2, U.S. Department of Energy, 1983.

Chapter 12

Management Services

V. C. Kruzic, Section Head

S. K. Adkins[1]	R. P. Jernigan	W. K. Russell
D. R. Alford	C. H. Johnson[2]	S. R. Schwartz[2]
D. R. Baumgardner[2]	D. Y. Johnson[2]	S. S. Scott[2,4]
B. J. Beem[1]	J. K. Johnson[2]	D. G. Sharp
G. F. Bowles	M. N. Johnson	G. G. Shearin
T. H. Brady[3]	C. H. Jordan	B. J. Smith[2]
D. P. Brooks	L. M. Jordan	B. L. Straine[1]
J. L. Burke	T-C. Liu[2]	P. A. Sumner[2]
E. J. Byrnes	J. C. Neeley[2]	M. G. Talley[1]
E. L. Cagle[2]	M. J. Owens	C. K. Thomas
M. W. Darnell[2]	J. C. Parrott[2]	A. S. Travis[2]
K. M. Dobbs[2]	E. N. Patterson	M. A. Vornehm[1,4]
M. V. Dunn	L. A. Pollard[1,4]	E. E. Webster[2,4]
H. W. Jernigan	P. L. Ray	E. R. Wells
J. R. Jernigan[1,4]	E. M. Ruckart	B. J. Williams[2]

1. Section secretary.
2. Information Division.
3. Finance and Materials Division, Martin Marietta Energy Systems, Inc.
4. Part-time.

CONTENTS

SUMMARY OF ACTIVITIES 12-5
12.1 OFFICE OF THE MANAGER FOR GENERAL ADMINSTRATION AND PROCUREMENT 12-5
12.1.1 Personnel Functions 12-5
12.1.2 Subcontracts 12-6
12.1.3 National and International Agreements 12-6
12.1.4 Procurement 12-6
12.2 ENGINEERING SERVICES 12-6
12.3 FINANCE 12-7
12.4 LIBRARY 12-7
12.5 PUBLICATIONS OFFICE 12-9
12.6 SAFETY, EMERGENCY PLANNING, AND QUALITY ASSURANCE 12-11
12.6.1 Safety and Emergency Planning 12-11
12.6.2 Quality Assurance 12-11

12. MANAGEMENT SERVICES

Summary of Activities

The Management Services Section supports the programmatic research and development activities of the Fusion Energy Division. Areas of support include the following:

- general personnel administration, material and service procurement, subcontracting, and coordination of national and international agreements;
- nonprogrammatic engineering services for support systems and equipment, planning and coordination of general plant project and facility improvements, coordination of maintenance and machine shop work, labor relations, and telecommunications;
- financial management;
- library services and resources;
- publications services, including editing, word processing, graphic arts, and reproduction; and
- safety, emergency planning, and quality assurance.

Support is provided through interpersonal relations with division programmatic staff and through coordination of support resources from a variety of disciplines outside the division.

12.1 OFFICE OF THE MANAGER FOR GENERAL ADMINISTRATION AND PROCUREMENT

12.1.1 Personnel Functions

Travel and off-site assignments increased significantly during 1984. There were 18 long-term assignments (foreign and domestic). Apartments near Princeton Plasma Physics Laboratory (PPPL) were rented to accommodate personnel involved in accelerated cooperative research between ORNL and PPPL.

Attrition from the division was heavy. There were 5 retirements, 5 transfers to other ORNL divisions, 16 resignations, and 1 death. This resulted in a net loss of 20 employees, which included 7 physicists and 7 engineers. To improve the quality assurance (QA) for fusion projects, two highly qualified engineers were hired.

The summer program was reduced to five technical students, one faculty member, and one clerical employee. Two additional university students came under the sponsorship of the Oak Ridge Associated Universities (ORAU) program. Assignments were processed for 108 scientific guests and subcontractor personnel. Of these, 53 were foreign participants,

28 were with the Large Coil Program (LCP), 13 were with the beryllium limiter experiment carried out for the Joint European Torus (JET), and 4 were involved in the collaboration between the United States and Spain.

The usual activities of personnel matters and security items continued.

12.1.2 Subcontracts

Industrial participation through subcontracts cost approximately $15 million. Phasing out the contracts for coils for the LCP is represented in this cost. Contracts for microwave sources with Varian and industrial contracts for the Fusion Engineering Design Center (FEDC) continued. Many subcontracts were terminated, and others were greatly reduced for FY 1985. Personnel associated with the closed-out subcontracts have left ORNL.

12.1.3 National and International Agreements

With the arrival of the coils from Japan, Switzerland, and Germany and the two U.S. coils, there has been a flurry of activity in the Implementing Agreement for the Large Coil Task. Local agreements approved by the DOE Oak Ridge Operations Office to assist the assignees to this program in obtaining materials and services have been implemented. A contract for a beryllium limiter experiment on the Impurity Study Experiment (ISX-B) was executed. This international collaboration for JET was very successful. Administrative matters went smoothly.

A new agreement between the United States and Spain was also implemented during this reporting period.

12.1.4 Procurement

During 1984, the procurement group processed 1397 requisitions, representing a dollar value of approximately $4.1 million. Processing of 421 shipping orders was completed. This included major loan agreements of equipment to PPPL, the Massachusetts Institute of Technology (MIT), and TRW, Inc. The group assisted in implementing special procurement for the Japanese and Swiss site representatives to the LCP.

12.2 ENGINEERING SERVICES

The Engineering Services Group coordinates all engineering work performed in the division. This includes providing or directing the engineering for all nonprogrammatic work, coordinating maintenance and machine shop work, supervising the inventory and storage of materials, and coordinating telecommunications. The group also oversees all General Plant Projects (GPP), Multi-General Purpose Facilities (MGPF), and Line Item and General Plant Equipment (GPE) improvements. In addition, the group is responsible for maintaining building facilities and planning future facilities. Some highlights of the 1984 activities follow.

1. Completed engineering and bidding and awarded a fixed-price contract on the construction and installation of a new cooling tower and heat exchanger (MGPF). This will improve the reliability of the demineralized cooling-water system in Bldg. 9201-2.

2. Completed design, awarded a contract, and completed installation of instrumentation and controls on a demineralized cooling-water system for Bldg. 9204-1.
3. Completed design and awarded construction (to Rust Engineering) of the electrical upgrade (MGPF) of the Bldg. 9201-2 facility. This consists of adding an additional 50-MW transformer, connecting line 2 (161 kV) from Elza switchyard to a new transformer, installing new switchgear, and connecting heavy pulsed loads to new switchgear. This will increase available power to Bldg. 9201-2 and improve the reliability of the overall electrical system.
4. Completed hookup of the broadband video-data link to Bldg. 9201-2, Bldg. 9204-1, and the FEDC building. Internal wiring has been completed in the FEDC building and is in process in Bldg. 9201-2. This improves both computer and audio-video communications between X-10 and Y-12 and within division facilities.
5. Continued to improve general appearance of division building by adding new entrance to Bldg. 9201-2, installing new tile in hallways, painting selected areas, and continuing to remove obsolete equipment from buildings.
6. Assisted in the installation of three coils for operation of the International Fusion Superconducting Magnet Test Facility. This involved the coordination of engineering, maintenance, and shop fabrication and required following these areas on a daily basis until the facility was ready for the three-coil test.
7. Shop fabrication consisted of 147 jobs requiring 25 work-years of effort at a cost of approximately $2 million. This work was placed in shops at ORNL, Y-12, and the Oak Ridge Gaseous Diffusion Plant (ORGDP). Several small jobs were placed outside in local shops. This does not address the large fabrication efforts on LCP or the Advanced Toroidal Facility (ATF), which were awarded through purchase orders to outside vendors. One of the largest efforts was the rework of the General Electric Company coil, which was completed at ORGDP shops as described in Chap. 7.

12.3 FINANCE

The Finance Office, a functional part of the Management Services Section, provides financial management support for division administrative, engineering, and research personnel in areas including budget preparation, cost scheduling, and variance analysis. This office also provides meaningful and appropriate accounting and cost control. Interaction with division management is an essential part of administering the budget, accounting policies, and procedures.

Table 12.1 and Fig. 12.1 show the funding trends for the Fusion Program. Funding of this magnitude creates a need for great efficiency and continued improvement in the specific areas of financial control. In this spirit, the Finance Office must continue to develop innovative techniques to meet the growing and changing financial needs of the division.

12.4 LIBRARY

The Fusion Energy Library, along with other branch libraries in the ORNL Library System, introduced its computerized on-line catalog and circulation system, the Library Information Online Network (LION), in December 1984. LION replaces the traditional card catalog and provides a new approach to using the library's resources.

Table 12.1. Fusion Program expense funding (in thousands of dollars)—budget outlay (B/O)

Activity	FY 1982 actual cost	FY 1983 actual cost	FY 1984 actual cost	Funding as of February 1985	FY 1986 budget submission	FY 1987 budget submission
Applied plasma physics						
Fusion plasma theory	$ 3,031	$ 3,237	$ 3,424	$ 3,045	$ 3,010	$ 3,210
Experimental plasma research	1,129	1,344	1,405	1,400	2,105	2,705
National MFE computer network	332	352	336	432	350	400
Technical program support	0	38	185	276	200	200
	$ 4,492	$ 4,971	$ 5,350	$ 5,153	$ 5,665	$ 6,515
Confinement systems						
Toroidal systems						
Research operations	$ 9,448	$ 9,639	$ 9,233	$11,765	$16,315	$25,535
Major device fabrication	0	54	1,826	8,580	9,900	96
Magnet mirror systems						
Research operations	11,050	10,866	12,515	978	0	440
	$20,498	$20,559	$23,574	$21,323	$26,215	$26,071
Development and technology						
Magnetic systems	$11,456	$12,839	$12,794	$12,500	$11,350	$ 8,735
Plasma engineering	9,000	9,348	4,522	3,996	7,483	8,275
Reactor systems	765	765	569	477	1,001	1,004
Environment and safety	494	270	201	100	100	100
Reactor materials	4,883	5,615	6,292	6,609	7,756	8,133
Fusion Engineering Design Center	3,756	4,110	5,083	4,500	4,410	4,420
	$30,354	$32,947	$29,461	$28,182	$32,100	$30,667
TOTAL ORNL FUNDING	$55,344	$58,477	$58,385	$54,658	$63,980	$63,253

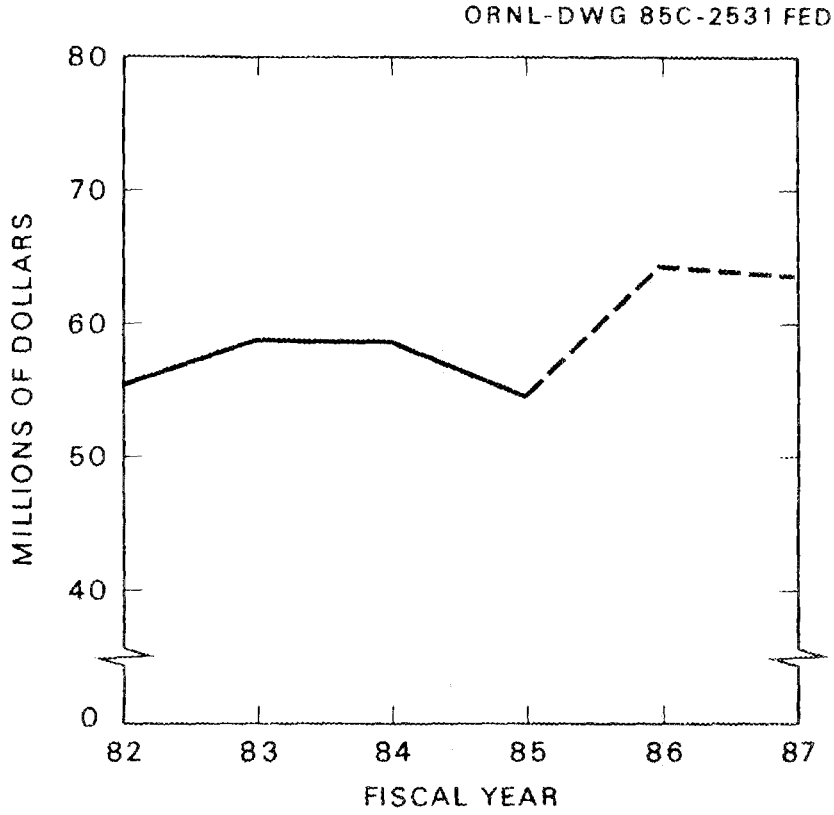

Fig. 12.1. Fusion Program expense funding (B/O).

Patrons can use LION terminals in the library to retrieve information about books, journals, and recent reports in the entire library system. The system gives the location of the work and whether or not it is on the shelf. The data base can be searched by author, title, subject, report number, keyword, and other identifiers. A tutorial brochure, "A Guide to Using LION," is available at each terminal, and library staff are helping users to learn the new system. Remote access to LION should become available in 1985 and will allow users to access the data base from any terminal using "System Select" or a dial-up line.

The library continues to offer traditional services, including on-line literature retrieval and assistance with references. The amount of on-line searching increased dramatically in 1984. The library has also been working closely with the fusion specialist at DOE's Office of Scientific and Technical Information to improve the coverage and accuracy of fusion literature in the DOE RECON Energy Data Base.

12.5 PUBLICATIONS OFFICE

More than 43,400 pages of reports, articles, conference papers, and graphics were edited, composed, drawn, and processed in the division publications office during 1984. The editors, compositors, and graphic artists processed nearly 193 pages each working day

(based on an average 225-day work-year). As shown by Table 12.2, this collective effort amounted to more than 25,000 work-hours, including 1,143 overtime hours (mostly contributed by the graphic arts and composition groups).

The publications office handled 362 separate jobs (Table 12.3) from division authors during the past year, including journal articles, conference papers, reports, presentation posters, full-color renderings, and viewgraphs, and cleared 215 abstracts.

The composition (word processing) group in the publications office has continued to make efficient use of the IS/1 UNIX* Text Management System instituted in the office in 1982. The system includes a TEDI-to-UNIX conversion program that allows transfer of files from division computers to the Publications Office for on-line editing, word processing, and outputting.

The graphic arts (GA) group produced more than 2100 new original drawings in the past year (Table 12.3); the total volume of work processed by the group was over 18,600 units [including more than 12,400 camera (Pos) copies].

The computer graphics program brought into full use in the last half of 1983 has continued to increase the efficiency of the GA group. During 1984, the illustrators produced 500 publication-quality drawings and visuals using the MAPPER program. Using the Tektronix equipment—a 4054 terminal and digitizing tablet, a 4114 terminal and digitizing tablet, and a 4631 hard-copy unit for proof copies—the illustrators send raw, digitized, or enhanced data to the FR80 camera for final black-and-white or color output. Color slides

Table 12.2. Production and work-hours for CY 1984 (≈225 work-days)

	Service pages[a]	Work-hours
Graphic arts	5,399	11,054
Editing	5,758	4,331
Proofreading	14,418[b]	934
Composition	6,299[c]	8,208
Makeup	2,272	346
Quality assurance	9,279	230
	43,425	25,103

[a]"Service pages" indicates the total number of pages handled by each functional group (e.g., editing). Pages corrected or reprocessed as a result of publications office error are *not* counted more than once.

[b]Abnormally large figure results from addition of proofreading pages from a two-year project completed in the summer of 1984.

[c]About 90% of the service pages in the composition category were first converted from TEDI to UNIX by the publications office compositors.

Table 12.3. Volume of publication services

Publications[a]	577
Graphic arts	
Drawings[b]	3,042
Visuals[c]	551
Camera (Pos) copies[d]	12,461
Other[e]	2,552
Xerox 9400 copies	>2,200,000

[a]Number of jobs processed, without regard to size of job; includes 215 abstracts cleared through the work reception office.

[b]Includes original and revised drawings.

[c]Includes original artwork for view graphs and slides.

[d]Includes glossy prints and view graphs.

[e]Includes posters, poster titles, signs, report covers, nameplates, diazo, etc.

can be made very inexpensively on the FR80 (for less than the cost of black-and-white viewgraphs).

*UNIX is a trademark of Bell Laboratories.

12.6 SAFETY, EMERGENCY PLANNING, AND QUALITY ASSURANCE

12.6.1 Safety and Emergency Planning

The division safety program included monthly safety inspections by individual sections and quarterly safety inspections by an independent inspection committee comprising the division safety officer, Y-12 safety representatives, and Y-12 Maintenance supervision. Monthly fire inspections were performed by professional fire inspectors. Six safety training sessions were held, at which attendance was mandatory for all division personnel. Two special safety meetings were presented, with emphasis on off-the-job accidents and slips and falls. Emergency evacuation drills were conducted, and a new alarm system was designed and installed in Bldg. 9204-1. Emergency training was continued, using American Red Cross instructors, to ensure maximum response to building emergencies.

12.6.2 Quality Assurance

The division's QA program continued to improve during 1984. Following the death of the division QA manager in an automobile accident, a search for a qualified replacement was carried out. During the last quarter of 1984, a new QA manager and an additional QA engineer were hired.

During the year, QA audits were conducted at vendors' sites and within the division on specific projects. The Department of Energy conducted an audit of the division QA

program and made several recommendations for improvement to both the division and the laboratory.

Appendix 1

ABBREVIATIONS AND ACRONYMS

ADIP	Alloy Development for Irradiation Performance
AEM	analytical electron microscopy
APIS	advanced positive-ion system
appm	atomic parts per million
ARDL	asymmetric resonant double loop
ATF	Advanced Toroidal Facility
ATFSR	ATF Stellarator Reactor
COM	constant of motion
CPU	central processing unit
CW	cold-worked
cw	continuous wave
CWTX	Coil Winding Test Experiment
DAFS	Damage Analysis and Fundamental Studies
dpa	displacements per atom
DOE	U.S. Department of Energy
DIII	Doublet III
DIII-D	upgrade of DIII
EURATOM	European Atomic Energy Commission
EBR-II	Experimental Breeder Reactor upgrade
EBS	ELMO Bumpy Square
EBT	ELMO Bumpy Torus
EBT-I	Initial EBT device and configuration (microwave power is ≤60 kW at 18 GHz, magnetic field is 5 kG)
EBT-P	EBT Proof-of-Principle
EBT-S	EBT-Scale device and configuration (microwave power is ≤200 kW at 28 GHz, magnetic field is 7.2 kG)
ECH	electron cyclotron heating
ECRF	electron cyclotron range of frequencies
ECRH	electron cyclotron resonance heating
FCT	flux-conserving tokamak
FEDC	Fusion Engineering Design Center
FFTF	Fast-Flux Test Facility
FIR	far-infrared
FLR	finite Larmor radius
FWHM	full width at half maximum
FY	fiscal year
GA	GA Technologies, Inc.
GD/C	General Dynamics Convair Division
GE	General Electric Company
GEIS	generic environmental impact statement
GPF	General Plant Equipment
GPP	General Plant Project
GUSS	graphics user service station
HBQM	High-Beta Q Machine
HF	helical field
HFIR	High-Flux Isotope Reactor
HIBP	heavy-ion beam probe

ICH	ion cyclotron heating
ICRF	ion cyclotron range of frequencies
ICRH	ion cyclotron resonance heating
IEA	International Energy Agency
IFSMTF	International Fusion Superconducting Magnet Test Facility
INTOR	International Tokamak Reactor
ISX	Impurity Study Experiment
ISX-B	Upgrade of ISX
IVSWR	insertion voltage standing-wave ratio
JAERI	Japan Atomic Energy Research Institute
JEN	Junta de Energia Nuclear
JET	Joint European Torus
KFA	Kernforschungsanlage
LH	lower hybrid
LHCD	lower hybrid current drive
LCP	Large Coil Program
LCTF	Large Coil Test Facility (now IFSMTF)
LIF	laser-induced fluorescence
LION	Library Information Online Network
LLNL	Lawrence Livermore National Laboratory
MDAC	McDonnell-Douglas Astronautics Company
MFE	magnetic fusion energy
MFECH	multiple-frequency electron cyclotron heating
MFEnet	NMFECC network
MFTF-α+T	upgrade of MFTF-B
MFTF-B	Tandem-Mirror Fusion Test Facility
MGPF	Multi-General Purpose Facility
MHD	magnetohydrodynamic
MHF	magnetohydrofriction
MIT	Massachusetts Institute of Technology
M&S	Magnetics and Superconductivity
NAP	network access port
NBI	neutral beam injection
NBT-1M	Nagoya Bumpy Torus
NLTNIF	National Low-Temperature Ion Irradiation Facility
NMFECC	National Magnetic Fusion Energy Computing Center
NRFRD	National RF Research and Development
NYU	New York University
O-mode	ordinary mode
ODE	ordinary differential equation
OFE	Office of Fusion Energy
OFHC	oxygen-free high-conductivity
OH	ohmic heating
OMA	optical mass analyzer

ORAU	Oak Ridge Associated Universities
ORGDP	Oak Ridge Gaseous Diffusion Plant
ORNL	Oak Ridge National Laboratory
ORR	Oak Ridge Research Reactor
PBX	Poloidal Bean Experiment
PDE	partial differential equation
PDX	Poloidal Divertor Experiment
PF	poloidal field
PLC	programmable logic controller
PLT	Princeton Large Torus
PMI	Plasma-Materials Interactions
PMT	photomultiplier tube
PPPL	Princeton Plasma Physics Laboratory
QA	quality assurance
RBS	Rutherford ion backscattering
RDL	resonant double loop
rf	radio frequency
RFP	reversed-field pinch
RFTF	Radio-Frequency Test Facility
RPI	repeating pellet injector
R&D	research and development
SARA	single-aperture reflex arc
SITEX	surface ionization by transverse extraction
SPM	Special-Purpose Materials
SRO	short-range-ordered
STX	Spherical Tokamak Experiment
Symmmotron	symmetric modular torsatron
TF	toroidal field
TFCX	Tokamak Fusion Core Experiment
TFTR	Tokamak Fusion Test Reactor
TPI	tritium pellet injector
USC	User Service Center
VCL	vapor-cooled lead
VF	vertical field
VSWR	voltage standing-wave ratio
X-mode	extraordinary mode
YAG	yttrium-aluminum-garnet
0-D	zero-dimensional
1-D	one-dimensional
1½-D	one-and-one-half-dimensional
2-D	two-dimensional
3-D	three-dimensional

Appendix 2

PUBLICATIONS AND PRESENTATIONS

BOOKS AND JOURNAL ARTICLES A-6
PRESENTATIONS A-12
REPORTS A-37
- ORNL Reports A-37
- ORNL Technical Memoranda A-37
- ORNL Computer Services Division Reports A-40
- ORNL Fusion Engineering Design Center Reports A-40
- Conference Proceedings Published by ORNL A-41
- Reports Prepared by ORNL Subcontractors A-41
- Reports Published by Other Institutions A-42

THESES AND DISSERTATIONS A-43

BOOKS AND JOURNAL ARTICLES

C. F. Barnett, contributions to *Applied Atomic Collision Physics, Vol. 2: Plasmas*, H. S. W. Massey, E. W. McDaniel, and B. Bederson, eds., Academic Press, New York, 1984:
Preface, pp. xiii–xiv
Introduction, pp. 1–25
Sect. 5D, "Particle Plasma Diagnostics," pp. 24–95

C. F. Barnett, "Status of the U.S. Effort in Atomic Physics Research Relevant to the Magnetically Confined Fusion Program," *At. Tek. Rubezom* **3**, 28 (1984)

C. F. Barnett and M. F. A. Harrison, vol. eds., *Applied Atomic Collision Physics, Vol. 2: Plasmas*, H. S. W. Massey, E. W. McDaniel, and B. Bederson, eds., Academic Press, New York, 1984

D. B. Batchelor, R. C. Goldfinger, and D. A. Rasmussen, "Detailed Modeling of Microwave Energy in EBT Devices," *Phys. Fluids* **27**, 948–61 (1984)

D. B. Batchelor, R. C. Goldfinger, and H. Weitzner, "Propagation and Absorption of Electromagnetic Waves in Fully Relativistic Plasmas," *Phys. Fluids* **27**, 2835–46 (1984)

J. D. Bell, J. L. Dunlap, V. K. Paré, J. D. Callen, H. C. Howe, E. A. Lazarus, M. Murakami, and C. E. Thomas, "Measurement of χ_e in ISX-B Beam-Heated Discharges by Heat Pulse Propagation," *Nucl. Fusion* **24**, 997 (1984)

E. E. Bloom, R. W. Conn, J. W. Davis, R. E. Gold, R. Little, K. R. Schultz, D. L. Smith, and F. W. Wiffen, "Low Activation Materials for Fusion Applications," *J. Nucl. Mater.* **122 & 123**, 17–26 (1984)

S. K. Borowski, Y-K. M. Peng, and T. Kammash, "Radio-Frequency-Assisted Current Startup in the Fusion Engineering Device," *Fusion Technol.* **6**, 7–29 (1984)

C. Bottcher, "Numerical Calculations on Electron-Impact Ionization," *Adv. At. Mol. Phys.* **20**, 241–66 (1984)

D. N. Braski, "Microstructure and Bend Ductility of a $(Fe, Ni)_3V$ Ordered Alloy Irradiated in HFIR," *J. Nucl. Mater.* **122 & 123**, 676–81 (1984)

D. N. Braski and P. J. Maziasz, "Tensile Properties of Unirradiated PCA from Room Temperature to 700°C" *J. Nucl. Mater.* **122 & 123**, 338–42 (1984)

B. A. Carreras, H. R. Hicks, J. A. Holmes, V. E. Lynch, and G. H. Neilson, "Zero-Current, High Beta Stellarator Equilibria with Rotational Transform Profile Control," *Nucl. Fusion* **24**, 1347 (1984)

L. A. Charlton, D. K. Lee, R. M. Wieland, B. A. Carreras, W. A. Cooper, and G. H. Neilson, "Ideal MHD Stability of the ISX-B Tokamak," *Nucl. Fusion* **24**, 33 (1984).

L. A. Charlton, R. M. Wieland, and G. H. Neilson, "Equilibrium Modeling of ISX-B Tokamak Discharges," *Phys. Fluids* **27**, 1738–42 (1984)

G. L. Chen, L. W. Owen, D. B. Batchelor, and C. L. Hedrick, "Stochastic Particle Diffusion in Velocity Space for EBT-S," *Phys. Fluids* **28**, 883–7 (1985)

O. K. Chopra and P. F. Tortorelli, "Compatibility of Materials for Use in Liquid-Metal Blankets of Fusion Reactors," *J. Nucl. Mater.* **122 & 123**, 1201–12 (1984)

R. E. Clausing, F. Waelbroeck, J. Winter, P. Wienhold, and L. Könen, "Effects of Wall Conditioning on Plasma Parameters, Impurities and Hydrogen Recycling in TEXTOR," *J. Nucl. Mater.* **121**, 249–53 (1984)

R. W. Conn, E. E. Bloom, J. W. Davis, R. E. Gold, R. Little, K. R. Schultz, D. L. Smith, and F. W. Wiffen, "Lower Activation Materials and Magnetic Fusion Reactors," *Nucl. Technol./Fusion* **5**, 291–310 (1984)

T. B. Cook, P. W. King, and J. B. Roberto, "Summary Abstract: Measurement of the Ionization Length for Neutral Iron Near the Wall in the ISX-B Tokamak Using Laser-Induced Fluorescence," *J. Vac. Sci. Technol. A* **2**, 707 (1984)

W. A. Cooper, "Centrifugal Force Effects from Toroidal Rotation on Incompressible Resistive Ballooning," *Plasma Phys. Controlled Fusion* **26**, 1351–4 (1984)

W. A. Cooper and T. C. Hender, "Ballooning Modes in 3-D Stellarators with Shear," *Plasma Phys. Controlled Fusion* **26**, 921–33 (1984)

W. R. Corwin, R. L. Klueh, and J. M. Vitek, "Effect of Specimen Size and Nickel Content on the Impact Properties of 12Cr-1MoVW Ferritic Steel," *J. Nucl. Mater.* **122 & 123**, 343–48 (1984)

P. H. Diamond, R. D. Hazeltine, Z. G. An, B. A. Carreras, and H. R. Hicks, "Theory of Anomalous Tearing Mode Growth and the Major Tokamak Disruption," *Phys. Fluids* **27**, 1449–62 (1984)

P. H. Diamond, P. L. Similon, T. C. Hender, and B. A. Carreras, "Kinetic Theory of Resistive Ballooning Modes," *Phys. Fluids* **28**, 1116–25 (1985)

L. Dresner, "Superconductor Stability, 1983: A Review," *Cryogenics* **24**, 283–93 (1984)

L. Dresner, "Transient Heat Transfer in Superfluid Helium—Part II," *Adv. Cryog. Eng.* **29**, 323–33 (1984)

O. C. Eldridge, D. J. Hoffman, and P. J. Kortman, "Status and Plans for U.S. and International Radio-Frequency Experiments on Fusion Devices," *Fusion Technol.* **6**, 145–73 (1984)

L. C. Emerson, P. K. Mioduszewski, and J. E. Simpkins, "Experience with Zr-Al Getter Pumps in the ISX-B Tokamak," *J. Nucl. Mater.* **123**, 1156 (1984)

L. C. Emerson, P. K. Mioduszewski, and J. E. Simpkins, "Performance of Zr-Al Getter Pumps Under Transient Load Conditions," *J. Vac. Sci. Technol. A* **2**, 1583–8 (1984)

A. C. England, "Electron Cyclotron Heating Experiments in Tokamaks and Stellarators," *IEEE Trans. Plasma Sci.* **PS-12**, 124–33 (1984)

K. Felch, R. Bier, L. Fox, H. Huey, L. Ives, H. Jory, N. Lopez, J. Manca, J. Shively, and S. Spang, "A 60 GHz, 200 kW cw Gyrotron with a Pure Output Mode," *Int. J. Electron.*, special issue, 1984

M. K. Ferber, H. D. Kimrey, and P. F. Becher, "Mechanical Reliability of Ceramic Windows in High Frequency Microwave Heating Devices," *J. Mater. Sci.* **19**, 3767–77 (1984)

J. D. Galambos and E. Greenspan, "Discrete Nuclear Elastic Scattering Effects in Cat-D and D-^{3}He Fusion Plasmas," *Nucl. Fusion* **24**, 739 (1984)

J. D. Galambos and Y-K. M. Peng, "Two-Point Transport Model for Cold Divertor Plasma," *J. Nucl. Mater.* **121**, 205–9 (1984)

L. Garcia, B. A. Carreras, J. H. Harris, H. R. Hicks, and V. E. Lynch, "Equilibrium Studies for Low-Aspect-Ratio Torsatrons," *Nucl. Fusion* **24**, 115 (1984)

M. J. Gouge, L. M. Hively, and D. K. Bhadra, "Alpha-Driven Currents in Tokamak Reactors," *Fusion Technol.* **6**, 537–42 (1984)

M. Greenwald, D. Gwinn, S. L. Milora, J. Parker, S. Wolfe, M. Besen, F. Camacho, S. Fairfax, C. Fiore, M. Foord, R. Gandy, C. Gomez, R. Granetz, B. LaBombard, B. Lipschultz, B. Lloyd, E. Marmar, S. McCool, D. Pappas, R. Petrasso, P. Pribyl, J. Rice, D. Schuresko, Y. Takase, J. Terry, and R. Watterson, "Energy Confinement of High-Density Pellet-Fueled Plasmas in the Alcator-C Tokamak," *Phys. Rev. Lett.* **53**, 352 (1984)

D. C. Griffin, C. Bottcher, M. S. Pindzola, S. M. Younger, D. C. Gregory, and D. H. Crandall, "Electron-Impact Ionization in the Xenon Isonuclear Sequence," *Phys. Rev. A* **29**, 1729–41 (1984)

D. C. Griffin, M. S. Pindzola, and C. Bottcher, "Calculations of the Contributions of Excitation-Autoionization to the Electron-Impact Ionization of Ca^+ and Ba^+ in the Distorted-Wave Approximation," *J. Phys. B* **17**, 3183–92 (1984)

M. L. Grossbeck and K. C. Liu, "Fatigue Performance of HFIR-Irradiated Nimonic PE-16 at 430°C," *J. Nucl. Mater.* **122 & 123**, 682–86 (1984)

J. H. Harris, J. N. Talmadge, T. D. Mantei, and J. L. Shohet, "Low-Frequency Coherent Fluctuations in the Proto-Cleo Torsatron," *Nucl. Fusion* **24**, 159 (1984)

J. H. Harris, O. Motojima, H. Kaneko, S. Besshou, H. Zushi, M. Wakatani, F. Sano, S. Sudo, A. Sasaki, K. Kondo, M. Sato, T. Mutoh, T. Mizuuchi, M. Iima, T. Obiki, A. Iiyoshi, and K. Uo, "Magnetohydrodynamic Activity in High-β, Currentless Plasmas in Heliotron-E," *Phys. Rev. Lett.* **53**, 2242–5 (1984)

D. E. Hastings, "Development of a Differential Equation for the Ambipolar Electric Field in a Bumpy Torus in the Low Collision Frequency Limit," *Phys. Fluids* **27**, 2372–4 (1984)

D. E. Hastings, "Electron Transport in the ELMO Bumpy Torus in the Low Collision Frequency Limit," *Phys. Fluids* **27**, 2272–86 (1984).

D. E. Hastings, "Neoclassical Transport Associated With Collisionless Detrapping in a Bumpy Torus," *Phys. Fluids* **27**, 935–8 (1984).

D. E. Hastings, "Neoclassical Transport Due to Large Orbit Effects in Bumpy Tori," *Phys. Fluids* **27**, 458–66 (1984).

D. E. Hastings, "Neoclassical Transport in a Bumpy Closed Field Line Device in the Collisional, Small Electric Field Regime," *Phys. Fluids* **27**, 2115–19 (1984)

D. E. Hastings, "Transport of a Multiple-Ion-Species Plasma in a Collisionless Regime in a Bumpy Torus," *Phys. Fluids* **27**, 939–47 (1984)

D. E. Hastings and T. Kamimura, "Transport Studies of ECH Heated Bumpy Torus Plasmas," *Nucl. Fusion* **24**, 473 (1984)

D. E. Hastings, J. S. Tolliver, and C. L. Hedrick, "Nonresonant ELMO Bumpy Torus Transport Coefficients in the Small Electric Field Regime," *Phys. Fluids* **27**, 467–71 (1984)

P. N. Haubenreich and M. S. Lubell, "ORNL Superconducting Magnet Development Program," *Superconductive Technology in Review* **84-2**, 7–8 (1984).

T. C. Hender and B. A. Carreras, "Equilibrium Calculations for Helical Axis Stellarators," *Phys. Fluids* **27**, 2101–9 (1984)

T. C. Hender, B. A. Carreras, W. A. Cooper, J. A. Holmes, P. H. Diamond, and P. L. Similon, "The Effects of Compressibility of the Resistive Ballooning Mode," *Phys. Fluids* **27**, 1439–48.

H. R. Hicks, B. A. Carreras, and J. A. Holmes, "The Effect of Diamagnetic Rotation on the Nonlinear Coupling of Tearing Modes," *Phys. Fluids* **27**, 909–15 (1984)

S. Hiroe, J. B. Wilgen, F. W. Baity, L. A. Berry, R. J. Colchin, W. A. Davis, A. M. El Nadi, G. R. Haste, D. L. Hillis, D. A. Spong, T. Uckan, and T. L. Owens, "Observation of Hot Electron Ring Instabilities in ELMO Bumpy Torus," *Phys. Fluids* **27**, 1019–29 (1984)

A. Hishinuma, N. H. Packan, E. H. Lee, and L. K. Mansur, "Effects of Pulsed and/or Dual Ion Irradiation on Microstructural Evolution in Ti and Si Modified Austenitic Alloys," *J. Nucl. Mater.* **122 & 123**, 260–65 (1984)

J. T. Hogan, "Collisional Transport of Momentum in Axisymmetric Configurations," *Phys. Fluids* **27**, 2308–12 (1984)

J. T. Hogan, "Properties of Magnetically Confined Plasmas in Tokamaks," Chap. 4 in *Applied Atomic Collision Physics, Vol. 2: Plasmas*, ed. C. F. Barnett and M. F. A. Harrison, Academic Press, New York, 1984

R. C. Isler, "Impurities in Tokamaks," *Nucl. Fusion* **24**, 1599 (1984)

R. L. Klueh, "Dissimilar-Metal Weld Failures in Boiler Tubing," *Power Eng.* **82**, 52–56 (1984)

R. L. Klueh, "Metals in the Nuclear-Fusion Environment," *Mater. Eng.* **99**(2), 39–42 (1984)

R. L. Klueh and M. L. Grossbeck, "A Comparison of the Irradiated Tensile Properties of a High-Manganese Austenitic Steel and Type 316 Stainless Steel," *J. Nucl. Mater.* **122 & 123**, 294–98 (1984)

R. L. Klueh and J. M. Vitek, "Elevated-Temperature Tensile Properties of Irradiated 2¼ Cr–1 Mo Steel," *J. Nucl. Mater.* **126**, 9–17 (1984)

S. H. Kim, J. W. Dawson, D. G. McGhee, and S. S. Shen, "AC Losses of 19-Strand Subcables for the ANL 3.3-MJ Coil," *Adv. Cryog. Eng.* **30**, 939–46 (1984)

A. Komori, "Observation of Low Frequency Plasma Fluctuations in ELMO Bumpy Torus," *Nucl. Fusion* **24**, 1173–82 (1984)

A. G. Kulchar, O. C. Eldridge, A. C. England, C. E. Bush, P. H. Edmonds, G. G. Kelley, C. M. Loring, Y-K. M. Peng, J. B. Wilgen, and S. K. Borowski, "Preionization and Startup in the ISX-B Tokamak Using Electron Cyclotron Heating at 28 GHz," *Phys. Fluids* **27**, 1869–79 (1984)

R. A. Langley, "IAEA Activities in the Plasma-Surface Interaction Field Relevant to Fusion," *J. Nucl. Mater.* **123**, 1607 (1984)

R. A. Langley, J. Bohdansky, W. Eckstein, P. Mioduszewski, J. Roth, E. Taglauer, E. W. Thomas, H. Verbeek, and K. L. Wilson, *Data Compendium for Plasma-Surface Interactions*, special issue of *Nuclear Fusion*, September 1984

R. A. Langley and H. C. Howe, "Determination of the Global Recombination Rate Coefficient for the ISX-B Tokamak," *J. Nucl. Mater.* **121**, 237 (1984)

E. A. Lazarus, J. D. Bell, C. E. Bush, A. Carnevali, J. L. Dunlap, P. H. Edmonds, L. C. Emerson, O. C. Eldridge, W. L. Gardner, H. C. Howe, D. P. Hutchinson, R. R. Kindsfather, R. C. Isler, R. A. Langley, C. H. Ma, P. K. Mioduszewski, M. Murakami, L. E. Murray, G. H. Neilson, V. K. Paré, S. D. Scott, D. J. Sigmar, J. E. Simpkins, K. A. Stewart, C. E. Thomas, R. M. Wieland, J. B. Wilgen, A. L. Wintenberg, W. R. Wing, and A. J. Wootton, "Confinement Improvement in Beam-Heated ISX-B Discharges with Low-*Z* Impurity Injection," *J. Nucl. Mater.* **121**, 61 (1984)

J. W. Lue, S. S. Shen, J. K. Ballou, T. J. McManamy, C. T. Wilson, and T. L. Mann, "Single Magnet Test Results of the First EBT-P Development Coil," *Adv. Cryog. Eng.* **29**, 41–48 (1984)

J. F. Lyon, V. E. Lynch, and J. A. Rome, "Particles and Field Lines Outside the ATF Plasma," *J. Nucl. Mater.* **121**, 415 (1984)

P. J. Maziasz, "Comparison of Swelling and Cavity Microstructural Development for Type 316 Stainless Steel Irradiated in EBR-II and HFIR," *J. Nucl. Mater.* **122 & 123**, 236–41 (1984)

P. J. Maziasz, "Swelling and Swelling Resistance Possibilities of Austenitic Stainless Steels in Fusion Reactors," *J. Nucl. Mater.* **122 & 123**, 472–86 (1984)

P. J. Maziasz and D. N. Braski, "Improved Swelling Resistance for PCA Austenitic Stainless Steel Under HFIR Irradiation Through Microstructural Control," *J. Nucl. Mater.* **122 & 123**, 311–16 (1984)

P. J. Maziasz and D. N. Braski, "Microstructural Design of PCA Austenitic Stainless Steel for Improved Resistance to Helium Embrittlement Under HFIR Irradiation," *J. Nucl. Mater.* **122 & 123**, 305–10 (1984)

P. K. Mioduszewski, L. C. Emerson, J. E. Simpkins, A. J. Wootton, C. E. Bush, A. Carnevali, J. L. Dunlap, P. H. Edmonds, W. L. Gardner, H. C. Howe, D. P. Hutchinson, R. R. Kindsfather, R. C. Isler, R. A. Langley, E. A. Lazarus, C. H. Ma, M. Murakami, G. H. Neilson, V. K. Paré, S. D. Scott, C. E. Thomas, J. B. Whitley, W. R. Wing, and K. E. Yokoyama, "Particle Removal with Pump Limiters in ISX-B," *J. Nucl. Mater.* **121**, 285 (1984)

G. H. Neilson, G. R. Dyer, and P. H. Edmonds, "A Model for Coupled Plasma Current and Position Feedback Control in the ISX-B Tokamak," *Nucl. Fusion* **24**, 1291 (1984)

T. L. Owens, F. W. Baity, and W. A. Davis, "Ion Heating in the Range of High Ion Cyclotron Harmonics on EBT," *Nucl. Fusion* **24**, 1561 (1984)

V. K. Paré, "Reconnection in Tokamaks," pp. 341–6 in *Magnetic Reconnection in Space and Laboratory Plasmas*, ed. E. W. Hones, Geophysical Monograph Ser. 30, American Geophysical Union, 1984

M. S. Pindzola, D. C. Griffin, C. Bottcher, D. H. Crandall, R. A. Phaneuf, and D. C. Gregory, "Electron-Impact Double Ionization of Rare-Gas Ions," *Phys. Rev. A* **29**, 1749–56 (1984)

R. L. Reid and Y-K. M. Peng, "System Studies for a Quasi-Steady-State Advanced Physics Tokamak," *Nucl. Technol./Fusion* **5**, 356–373 (1984)

A. F. Rowcliffe and M. L. Grossbeck, "The Response of Austenitic Steels to Radiation Damage," *J. Nucl. Mater.* **122 & 123**, 181–90 (1984)

K. C. Shaing, "Noise-Induced Transition of the Radial Electric Field in a Nonaxisymmetric Torus," *Phys. Fluids* **27**, 1924–6 (1984)

K. C. Shaing, "Stability of the Radial Electric Field in a Nonaxisymmetric Torus," *Phys. Fluids* **27**, 1567–9 (1984)

K. C. Shaing, J. A. Rome, and R. H. Fowler, "Transport Associated with the Collisionless Detrapping/Retrapping Orbits in a Nonaxisymmetric Torus," *Phys. Fluids* **27**, 1–4 (1984)

J. E. Simpkins, W. A. Gabbard, L. C. Emerson, and P. K. Mioduszewski, "A Practical Sublimation Source for Large-Scale Chromium Gettering in Fusion Devices," *J. Nucl. Mater.* **123**, 1481 (1984)

D. A. Spong, H. L. Berk, and J. W. Van Dam, "Radial Structure of Curvature-Driven Instabilities in a Hot-Electron Plasma," *Phys. Fluids* **27**, 2292–2307 (1984).

W. M. Stacey, Jr., R. B. Bennett, and D. J. Sigmar "Neutral Beam Driven Impurity Flow Reversal in Tokamaks," *J. Nucl. Mater.* **121**, 91–92 (1984)

W. M. Stacey and D. J. Sigmar, "The Effects of Neutral Beam Injection on Impurity Transport in Tokamaks," *Phys. Fluids* **27**, 2076–85 (1984)

D. J. Strickler, Y-K. M. Peng, J. B. Miller, K. E. Rothe, and J. A. Holmes, "Numerical Simulation of the Plasma Current Quench Following a Disruptive Energy Loss," *Fusion Technol.* **6**, 44 (1984)

P. F. Tortorelli and J. H. DeVan, "Mass Transfer Behavior of a Modified Austenitic Stainless Steel in Lithium," *J. Nucl. Mater.* **122 & 123**, 1258–63 (1984)

T. Uckan, "Direct Reading Fast Microwave Interferometer for ELMO Bumpy Torus," *Rev. Sci. Instrum.* **55**, 1874 (1984)

K. Uo, A. Iiyoshi, T. Obiki, O. Motojima, S. Morimoto, M. Wakatani, A. Sasaki, K. Kondo, M. Sato, K. Hanatani, T. Mutoh, H. Zushi, H. Kaneko, S. Besshou, M. Nakasuga, F. Sano, T. Mizuuchi, S. Sudo, J. H. Harris, J. E. Rice, J. L. Terry, I. Ohtake, M. Iima, H. Okada, K. Magome, "Neutral-Beam Injection Heating Experiment on Currentless Plasma in the Heliotron E Device," *Nucl. Fusion* **24**, 1551 (1984)

J. M. Vitek and R. L. Klueh, "Microstructure of 9Cr-1MoVNb Steel Irradiated to 36 dpa at Elevated Temperatures in HFIR," *J. Nucl. Mater.* **122 & 123**, 254–59 (1984)

T. L. White, H. D. Kimrey, T. S. Bigelow, D. D. Bates, and H. O. Eason, "The EBT-S 28-GHz, 200-kW, cs, Mixed-Mode Quasi-Optical Plasma Heating System," *Int. J. Infrared Millimeter Waves* **5**, 1129–52 (1984)

J. B. Whitley et al., "Improved Performance of TiC-Coated Graphite Limiters by Surface Texturing," *J. Nucl. Mater.* **123**, 1177 (1984)

R. A. Zuhr, "Impurity Measurements in the TEXTOR Plasma Edge Using Deposition Probe Techniques," *J. Nucl. Mater.* **122 & 123**, 1193 (1984)

PRESENTATIONS

Review of Tritium Pellet Injection for TFTR, Department of Energy, Gaithersburg, Maryland, January 10–11, 1984

W. A. Houlberg, "Tritium Pellet Injection in TFTR"

U.S. Department of Energy Data Base Committee Meeting, GA Technologies, Inc., San Diego, California, January 15–17, 1984

J. T. Hogan, presentation

Seminar, Courant Institute, New York University, New York, February 6–10, 1984

D. B. Batchelor, "Recent Developments on EBT and ELMO Bumpy Square"

EBT Senior Review Panel, February 7–8, 1984

N. A. Uckan, "EBT Advanced Concepts Program and EBS"

U.S.-Japan Workshop on Heliotron-E Results, Kyoto, Japan, February 13–17, 1984

R. C. Isler, "ISX-B Experimental Results"

G. H. Neilson, "Recent Progress on ATF"

Meeting on Joint JET ISX-B Beryllium Limiter Experiment and Program, Culham Laboratory, Abingdon, England, February 14–16, 1984

P. H. Edmonds, "Joint JET ISX-B Beryllium Limiter Experiment"

P. K. Mioduszewski, "Be-Limiter Experiment on ISX"

ORAU Traveling Lecture Program, Atlanta University, Atlanta, Georgia, February 15, 1984

E. C. Crume, "Transport of Impurities in Tokamaks"

U.S. Department of Energy, Washington, D.C., February 16, 1984

D. B. Batchelor, "Effects of Doppler Shift and Wave Field Profile on Energy Distribution in Plasma Heating"

C. L. Hedrick, "Equilibria and Transport in the ELMO Bumpy Square"

Workshop on Alpha Particle Diagnostics, Knoxville, Tennessee, February 22–23, 1984

D. P. Hutchinson et al., "Feasibility of Alpha Particle Measurement by CO_2 Laser Thomson Scattering"

Seminar, McDonnell Douglas Astronautics Company, St. Louis, Missouri, February 24, 1984

S. P. Hirshman, "3D MHD Calculations Using Inverse Method"

American Institute of Mining, Metallurgical, and Petroleum Engineers Annual Meeting, Los Angeles, California, February 26–March 2, 1984

D. N. Braski and C. T. Liu, "The Development of $(Fe,Ni)_3V$ Long-Range-Ordered Alloys for a Fusion Reactor First Wall"

R. L. Kluch and E. E. Bloom, "Alloy Development for Fast Induced Radioactivity Decay for Fusion Reactor Applications"

P. J. Maziasz, "Strategies and Results Underlying the Development of Advanced Austenitic Stainless Steels for Fusion"

P. F. Tortorelli and J. H. DeVan, "Liquid Metal Compatibility Considerations in Alloy Development"

Tenth Austin Symposium on Molecular Structure, University of Texas, Austin, Texas, February 27–29, 1984

D. C. Gregory, "Multiple Ionization of Ions by Electron Impact"

Office of Fusion Energy FTP/A Review for the ORNL EBT Experimental Program, Germantown, Maryland, March 8, 1984

N. A. Uckan, "The ORNL EBT Advanced Concepts Program and ELMO Bumpy Square"

U.S.-Japan Workshop on Computer Control and Data Acquisition, Naka, Japan, March 12–14, 1984

W. R. Wing, "CAMAC and Computer Hardware at ORNL"

W. R. Wing, "The ISX Data Acquisition System"

U.S.-Japan Workshop on Impurity and Particle Control, Theory, and Modeling, Nagoya University, Nagoya, Japan, March 12–16, 1984

D. J. Sigmar, "Impurity Control with Momentum Sources, Part I: Theory; Part II: Transport Modeling Results"

11th Annual Energy Technology Conference and Exposition, Washington, D.C., March 19–21, 1984

W. D. Nelson, "Fusion Energy: The Next Mirror and Tokamak Devices"

U.S.-Japan Workshop on 3-D MHD Studies, Oak Ridge, Tennessee, March 19–23, 1984. Proceedings published by Oak Ridge National Laboratory as CONF-840370, 1984. Editor: B. A. Carreras

L. A. Charlton, B. A. Carreras, J. A. Holmes, H. R. Hicks, and V. E. Lynch, "Calculations in Toroidal Geometry with Full MHD Equations," p. 174

C. L. Hedrick and L. W. Owen, "Magnetic Equilibria for Square and Circular EBTs," pp. 126–37

T. C. Hender, J. L. Cantrell, B. A. Carreras, L. Garcia, J. H. Harris, J. A. Rome, and V. E. Lynch, "Equilibrium Studies of Helical Axis Stellarators, " p. 21

J. A. Holmes, B. A. Carreras, L. A. Charlton, H. R. Hicks, and V. E. Lynch, "Stellarator Expansion Studies of a High Beta Torsatron," p. 42

INTOR Workshop on Plasma Position Control, Princeton, N.J., March 20, 1984

G. H. Neilson, "Vertical Position Control in ISX-B"

4th International Symposium on Heating in Toroidal Plasmas, Rome, March 21–28, 1984. Proceedings published as *Heating in Toroidal Plasmas: Proceedings of the Fourth International Symposium, Rome, March 1984* by International School of Plasma Physics and ENEA, Varenna, Italy, 1984. Editors: H. Knoepfel and E. Sindoni

D. B. Batchelor, EBT Experimental Group, and EBT Theory Group, "Comparison of Electron Cyclotron Heating Theory and Experiment in EBT" (invited paper), vol. II, p. 779

M. Greenwald, D. Gwinn, S. L. Milora, J. Parker, S. Wolfe, M. Besen, F. Camacho, S. Fairfax, C. Fiore, M. Foord, R. Gandy, C. Gomez, R. Granetz, B. LaBombard, B. Lipschultz, B. Lloyd, E. Marmar, S. McCool, D. Pappas, R. Petrasso, P. Pribyl, J. Rice, D. Schuresko, Y. Takase, J. Terry, and R. Watterson, "Confinement Results from Pellet Fueled Discharges in Alcator C" (invited paper)

H. Jory, "Status of Gyrotron Developments at Varian Associates"

O. Motojima, H. Kaneko, S. Besshou, H. Zushi, F. Sano, S. Sudo, A. Sasaki, K. Kondo, M. Sato, T. Mutoh, T. Mizuuchi, M. Iima, T. Baba, H. Okada, J. H. Harris, M. Wakatani, T. Obiki, A. Iiyoshi, and K. Uo, "Experimental Studies of Currentless, High Beta Plasma in the Heliotron-E Device," vol. II, p. 865

K. Uo, A. Iiyoshi, T. Obiki, O. Motojima, S. Morimoto, M. Wakatani, A. Sasaki, K. Knodo, M. Sato, K. Hanatani, T. Mutoh, H. Zushi, H. Kaneko, S. Besshou, F. Sano, T. Mizuuchi, S. Sudo, A. Sasaki, J. H. Harris, J. E. Rice, J. L. Terry, I. Ohtake, M. Iima, and H. Okada, "Neutral Beam Injection and RF Heating Experiments on the Currentless Plasma in Heliotron-E," vol. II, p. 947

T. L. White, H. D. Kimrey, and T. S. Bigelow, "Mixed-Mode Distribution Systems for High Average Power Electron Cyclotron Heating" (invited paper), vol. II, p. 1444

A. J. Wootton, J. D. Bell, C. E. Bush, B. A. Carreras, A. Carnevali, J. L. Dunlap, P. H. Edmonds, O. C. Eldridge, A. C. England, W. L. Gardner, G. Hallock, R. L. Hickok, H. C. Howe, D. P. Hutchinson, R. C. Isler, W. Jennings, K. A. Kannan, R. R. Kindsfather, R. A. Langley, E. A. Lazarus, C. H. Ma, J. Mathew, M. Murakami, J. Munro, G. H. Neilson, V. K. Pare, S. D. Scott, D. J. Sigmar, C. E. Thomas, R. M. Wieland, W. R. Wing, and K. Yokoyama, "Balanced Beam Injection on ISX-B" (invited paper), vol. I, p. 69

Seminar, Massachusetts Institute of Technology, Cambridge, Massachusetts, March 22–23, 1984

D. E. Hastings, "EBT Neoclassical Transport"

Second Workshop on Examination of Radioactive Materials by Electron Beam Methods, Savannah River Laboratory, Aiken, South Carolina, March 29–30, 1984

D. N. Braski and J. R. Gibson, "Modification of an SEM for Examination of Radioactive Materials"

Seminar, Université Catholique de Louvain, Louvain-la-Neuve, Belgium, March 30, 1984

D. C. Gregory, "Indirect Processes in Electron Impact Ionization of Ions"

Fusion Power Associates Symposium on Fusion Power Development—The Next Decade, Livermore, California, April 2–3, 1984

J. Sheffield, "Generic Magnetic Fusion Reactor Cost Assessment"

J. Sheffield, "The Potential Economics of Magnetic Fusion"

Seminar, Department of Metallurgical, Chemical, and Polymer Engineering, University of Tennessee, Knoxville, April 3, 1984

P. F. Tortorelli, "Liquid Metal Corrosion Studies"

Fusion Energy Division Annual Information Meeting, April 9–10, 1984

S. L. Milora, "Pellet Fueling: State-of-the-Art Development and Applications"

J. L. Scott, E. E. Bloom, D. N. Braski, M. L. Grossbeck, R. L. Klueh, P. J. Maziasz, A. F. Rowcliffe, P. F. Tortorelli, J. M. Vitek, J. A. Conlin, Jr., I. T. Dudley, E. M. Lees, C. D. West, and R. D. Lillie, "Fusion Materials Program"

D. W. Swain, "Measurement of the Core Electron Distribution Function in EBT"

N. A. Uckan, "The ELMO Bumpy Square"

Third International Conference on Liquid Metal Engineering and Technology in Energy Production, Oxford, England, April 9–13, 1984

P. F. Tortorelli and J. H. DeVan, "Mass Transfer Kinetics in Lithium–Stainless Steel Systems"

Annual Conference on Theoretical Aspects of Controlled Nuclear Fusion Research (Sherwood Meeting), Incline Village, Nev., April 11–13, 1984

J. D. Callen and K. C. Shaing, "Resistive MHD-Like Equations in the Banana-Plateau Collisionality Regime"

B. A. Carreras, H. R. Hicks, J. A. Holmes, and V. E. Lynch, "Approximate Flux Conserving Stellarator"

M. D. Carter, D. B. Batchelor, and J. D. Callen, "Second Harmonic Electron Cyclotron Heating"

L. A. Charlton, B. A. Carreras, H. R. Hicks, J. A. Holmes, and V. E. Lynch, "Incompressible MHD Modes in Toroidal Geometry"

G. L. Chen, D. B. Batchelor, and Y. Matsuda, "Fokker-Planck Modeling of Electron Cyclotron Heating and Direct Particle Loss in EBT and ELMO Bumpy Square"

W. A. Cooper and S. P. Hirshman, "Suppression of Spectral Pollution by Angle Renormalization"

E. C. Crume and D. E. Arnurius, "Simulation of Impurity Transport in the ISX-B Tokamak with Directed Neutral Beam Heating"

P. H. Diamond, Z. G. An, M. N. Rosenbluth, B. A. Carreras, T. C. Hender, H. R. Hicks, and J. A. Holmes, "Theory of Magnetic Fluctuations, Field Reverse Maintenance, and Anomalous Thermal Transport in the Reversed Field Pinch"

A. M. El Nadi, "Electrostatic Confinement in a Bumpy Torus with Hot Electron Rings"

R. H. Fowler, J. A. Rome, and K. C. Shaing, "Transport Associated with the Collisionless Detrapping/Retrapping of Orbits in a Nonaxisymmetric Torus II"

L. Garcia, B. A. Carreras, and H. R. Hicks, "Nonlinear Evolution of Microtearing Modes"

R. C. Goldfinger, D. B. Batchelor, and H. Weitzner, "Propagation and Absorption of Electromagnetic Waves in Fully Relativistic Plasmas"

D. E. Hastings, "Collisionless Neoclassical Nonresonant Transport in Bumpy Tori"

C. L. Hedrick and L. W. Owen, "Magnetic Equilibrium and Single Particle Orbits in EBS"

T. C. Hender, J. Cantrell, B. A. Carreras, J. H. Harris, and J. A. Rome, "Equilibrium Studies for Helical Axis Stellarators"

H. R. Hicks, B. A. Carreras, L. Garcia, and J. A. Holmes, "The Reliability of Initial Value MHD Calculations of Tokamak Disruptions"

S. P. Hirshman and J. T. Hogan, "Comparison of 3-D Moments and Finite Difference Inverse MHD Equilibrium Codes"

J. T. Hogan, L. Ibanez, and H. Grad, "Current Generation in Stellarators"

J. A. Holmes, B. A. Carreras, L. A. Charlton, H. R. Hicks, and V. E. Lynch, "Free Boundary Stellarator Expansion MHD Equilibrium and Stability Calculations"

W. A. Houlberg, S. P. Hirshman, and S. E. Attenberger, "Inverse Mapping Algorithm for Moments Formulation of MHD Equilibria"

L. Ibanez, H. Grad, A. Bayliss, and J. Hogan, "Long Pulse Evolution of Elongated, Rippled High-Beta Tokamaks"

K. Imre, H. Weitzner, and D. B. Batchelor, "Absorption, Reflection, and Mode Coupling at the Second Cyclotron Resonance in a Weakly Relativistic, Inhomogeneous Plasma"

E. F. Jaeger, C. L. Hedrick, and D. B. Batchelor, "Microwave Induced Neoclassical Transport in EBT Geometry"

R. L. Miller, C. S. Chang, and D. K. Lee, "Enhanced Neoclassical Diffusion of Nonresonant Particles in a Bumpy Torus"

J. A. Rome and R. H. Fowler, "Non-Local Transport in Tokamaks"

K. C. Shaing, "Stability of the Radial Electric Field in a Nonaxisymmetric Torus"

D. A. Spong, C. L. Hedrick, and J. W. Van Dam, "Ballooning Modes in the ELMO Bumpy Square Configuration Using the Generalized Kinetic Energy Principle"

W. M. Stacey, A. W. Bailey, and D. J. Sigmar, "Rotation and Impurity Flow Reversal in Tokamak Plasmas with Neutral Beam Injection"

J. S. Tolliver and C. L. Hedrick, "Monte Carlo Estimates of Transport Rates in EBT with Asymmetric Potential Profiles"

E. Uchimoto, J. D. Callen, L. Garcia, and B. A. Carreras, "MHD Equilibrium Studies of a Poloidal Divertor Tokamak Using the Chodura-Schlüter Method"

N. A. Uckan, L. W. Owen, L. A. Berry, C. L. Hedrick, and D. A. Spong, "Physics Overview of the ELMO Bumpy Square"

W. I. van Rij, G. Vahala, and D. J. Sigmar, "The Spectrum of the MHD and Kinetic Alfvén Waves in a Cylindrical Tokamak"

Seminar, Massachusetts Institute of Technology, Cambridge, Massachusetts, April 12, 1984

P. J. Maziasz, "Influence of Precipitate Evolution on Property Changes in Austenitic Stainless Steels for Fusion"

Seminar, Culham Laboratory, Abingdon, England, April 13, 1984

P. F. Tortorelli, "Liquid Metal Corrosion Considerations in Fusion Blanket Design"

Review of TFCX RF Assumptions and Assessments, Princeton, New Jersey, April 23–25, 1984

W. A. Houlberg, "ICRF Plasma Heating and Ignition Simulations with WHIST"

Seminar, Institut für Kernphysik, Justus-Liebig Universität, Giessen, Federal Republic of Germany, April 24, 1984

D. C. Gregory, "Indirect Processes in Electron Impact Ionization of Ions"

Seminar, Cornell University, Ithaca, New York, April 25, 1984

D. J. Sigmar

Seminar, Rensselaer Polytechnic Institute, Troy, New York, April 27, 1984

D. J. Sigmar, "The Role of the Ambipolar Potential in Tokamak Transport"

American Society for Metals Conference on Materials for Energy Systems, Washington, D.C., April 29–May 2, 1984

E. E. Bloom and D. L. Smith, "Fusion Reactor Blanket Structural Materials"

ETR-INTOR Workshop, Atlanta, Georgia, May 1–2, 1984

A. C. England and O. C. Eldridge, "Effects of Preionization by Electron Cyclotron Heating in INTOR"

R. C. Isler, "Impurity Studies in the Oak Ridge Tokamaks"

G. H. Neilson, M. G. Bell, P. A. Pribyl, and R. D. Stambaugh, "Equilibrium Control"

4th Annual Meeting of the Tennessee Valley Chapter, American Vacuum Society, Knoxville, Tennessee, May 1–3, 1984

D. N. Braski, P. D. Goodell, J. V. Cathcart, and R. H. Kane, "The Oxidation of Inconel Alloy MA754 at Low Oxidation Potential"

G. M. Fuller, "The Vacuum Design Features of the Toroidal Fusion Core Experiment (TFCX)"

J. Sheffield, "The Status of Magnetic Fusion"

N. A. Uckan, "Magnetic Fusion Reactors" (invited paper)

Mathematics of Finite Element and Applications Conference, Brunel University, London, May 2–7, 1984

J. E. Akin, J. Montgomery, and W. H. Gray, "A Raster Scan Algorithm for Generating Hidden Isoparametric Surfaces"

TFTR Tritium Pellet Injector Conceptual Design Review, Princeton Plasma Physics Laboratory, Princeton, New Jersey, May 7–8, 1984

W. A. Houlberg, presentation

Microwave Power Tube Conference, Monterey, California, May 7–9, 1984

H. Jory, R. Bier, K. Felch, L. Fox, H. Huey, N. Lopez, and S. Spang, "Progress in CW Gyrotron Oscillators"

A. Salop, "Computational Studies of Mode Conversion in Gyrotron Collectors"

S. Spang, R. Feezell, and N. Lopez, "Cyclic Fatigue Reduction in Gyrotron Collectors"

Seminar, Department of Metallurgical, Chemical, and Polymer Engineering, University of Tennessee, Knoxville, Tennessee, May 8, 1984

R. L. Klueh, "Alloy Development for Fusion Reactors"

Seminar, New York University, New York, New York, May 8–9, 1984

B. A. Carreras, "Overview of Stellarator MHD Studies in ORNL"

U.S. Department of Energy, Washington, D.C., May 10, 1984

W. A. Houlberg, presentation

Meeting on Heliac Studies, Princeton Plasma Physics Laboratory, Princeton, New Jersey, May 14–16, 1985

T. C. Hender, presentation

1984 IEEE International Conference on Plasma Science, St. Louis, May 14–16, 1984. Abstracts published in *Conference Record—Abstracts*, IEEE Publication No. 84CH1958-8, Institute Electrical and Electronics Engineers, New York, 1984.

S. Attenberger, W. Houlberg, and S. Hirshman, "Efficient Mapping Algorithms Between Flux Coordinates and Real-Space Coordinates for Toroidal Plasmas," p. 121

M. Gouge and L. Hively, "Alpha-Driven Currents in Tokamak Reactors," p. 59

J. Goyer, L. Solensten, K. Connor, and R. Hickok, "Heavy Ion Beam Probe Data Acquisition on EBT," p. 69

G. A. Hallock, J. Mathew, R. Hickok, W. Jennings, and A. J. Wootton, "Plasma Space Potential Measurements on ISX-B," p. 5

D. J. Hoffman, F. W. Baity, W. R. Becraft, S. K. Combs, T. L. Owens, F. Sluss, and J. W. Whealton, "U.S. National ICH Project: Results of Development, Simulation, and Testing of Antennas for the the Next Large U.S. Fusion Devices," p. 75

R. Juhala and S. P. Hirshman, "The Magnetohydrodynamic Equilibria in a Bumpy Torus with Toroidal Current," p. 93

J. Mathew, G. Hallock, R. Hickok, W. Jennings, and A. Wootton, "Measurement Accuracy and Resolution of the ISX-B Heavy Ion Beam Probe," p. 68

F. McDermott, G. Bekefi, S. Attenberger, D. Batchelor, P. Edmonds, R. Goldfinger, R. Kindsfather, E. Lazarus, M. Murakami, G. Neilson, and A. Wootton, "Measurement of the Extraordinary Mode Absorption at $\omega = \omega_{ce}$ in the ISX-B Tokamak," p. 96

T. L. Owens, F. W. Baity, and W. A. Davis, "Heating in the High Ion Cyclotron Harmonic Frequency Range on EBT," p. 95

P. Ryan, R. A. Langley, C. W. Magee, C. C. Tsai, M. M. Menon, S. K. Combs, S. L. Milora, and H. H. Haselton, "Evaluation of Crystal Implementation Technique for the Measurement of Neutral Beam Composition and Energy Spectra," p. 15

L. Solensten, J. Goyer, K. Connor, and R. Hickok, "EBT Plasma Potential Measurements," p. 69

C. Tsai, H. Haselton, R. McGaffey, M. Menon, D. Schechter, and J. Whealton, "Grid Loading Mechanisms in Ion Sources for Neutral Beam Applications," p. 15

Sixth International Conference on Plasma Surface Interactions in Controlled Fusion Devices, Nagoya, Japan, May 14–18, 1984. Proceedings published as *J. Nucl. Mater.* **128 & 129** (1984). Editors: A. Miyahara et al.

J. L. Cecchi, M. G. Bell, M. Bitter, W. R. Blanchard, N. Bretz, C. Bush, S. Cohen, J. Coonrod, S. L. Davis, D. Mimock, B. Doyle, H. F. Dylla, P. C. Efthimion, R. Fonck, R. J. Goldston, S.von Goeler, B. Grek, D. J. Grove, R. J. Hawryluk, D. Heifetz, H. Hendel, K. W. Hill, R. Hulse, J. Isaacson, D. Johnson, L. C. Johnson, R. Kaita, S. M. Kaye, S. Kilpatrick, J. Kiraly, R. J. Knize, R. Little, D. McCarthy, D. Manos, D. C. McCune, K. McGuire, D. M. Meade, S. S. Medley,
D. Mikkelsen, D. Mueller, M. Murakami, E. Nieschmidt, D. K. Owens, A. T. Ramsey, A. L. Roquemore, N. Sauthoff, P. Stangeby, J. Schivell, S. Scott, Sesnic, J. Sinnis, J. Sredniawski, J. Strachan, G. D. Tait, G. Taylor, F. Tenney, C. E. Thomas, J. Timberlake, H. H. Towner, M. Ulrickson, and K. M. Young, "Initial Limiter and Getter Operations in TFTR," p. 1

C. K. Chen, J. Bohdansky, W. Eckstein, and M. T. Robinson, "Energy Reflection for H^+ Ions at Energies Between 10 and 80 keV," p. 687

R. E. Clausing and L. Heatherly, "Control of Surface Composition and Hydrogen Recycling by Plasma Conditioning," p. 855

T. B. Cook, P. W. King, J. B. Roberto, K. A. Stewart, and K. E. Yokoyama, "Time-Resolved Erosion Measurements at a Reference Limiter in ISX-B Using Laser-Induced Fluorescence," p. 253

P. H. Edmonds, P. Mioduszewski, J. B. Roberto, R. D. Watson, and M. F. Smith, "The ISX-JET Beryllium Limiter Experiment," p. 422

K. Evans, Jr., D. Heifetz, D. Post, and P. K. Mioduszewski, "Monte Carlo Simulation of the ISX Pumped Limiter," p. 452

R. J. Fonck, M. Bell, K. Bol, R. Budny, P. Couture, D. Darrow, H. Dylla, R. Goldston, B. Grek, R. Hawryluk, K. Ida, K. Jaehnig, D. Johnson, R. Kaita, S. Kaye, H. Kugel, B. LeBlanc, D. Mansfield, T. McBride, K. McGuire, S. Milora, D. Mueller, M. Okabayaski, D. Owens, D. Post, M. Reusch, G. Schmidt, S. Sesnic, H. Takahashi, F. Tenney, and M. Ulrickson, "Particle Fueling and Impurity Control in PDX," p. 330

R. A. Langley, "Hydrogen Trapping, Diffusion, and Recombination in Austenitic Stainless Steels," p. 622

P. Mioduszewski, J. E. Simpkins, P. H. Edmonds, R. C. Isler, E. A. Lazarus, C. H. Ma, M. Murakami, and A. J. Wootton, "Studies on Impurity Control and Hydrogen Pumping with Chromium Gettering in ISX-B," p. 884

J. B. Roberto and R. Behrisch, "Synergistic Effects in Plasma-Surface Interactions," p. 764

J. B. Roberto, J. Roth, E. Taglauer, and O. W. Holland, "The Use of Isotopically-Enriched Carbon Probes for Erosion/Deposition Measurements in the ASDEX Divertor," p. 244

J. Roth, J. Bohdansky, and J. B. Roberto, "On the Influence of Impurities on the High Temperature Sputtering Yield of Graphite," p. 534

A. J. Wootton and P. K. Mioduszewski, "Discharge Cleaning and Plasma Purity in ISX-B," p. 886

Seminar, Department of Metallurgical, Chemical, and Polymer Engineering, University of Tennessee, Knoxville, Tennessee, May 15, 1984

J. M. Vitek, "Tempering Behavior of Ferritic Steel"

Institute of Electrical and Electronics Engineers, Minicourse on Fusion, St. Louis, Missouri, May 17, 1984

F. W. Wiffen, "Materials Requirements and Potential Solutions for Fusion Reactors"

Seminar, Massachusetts Institute of Technology, Cambridge, Massachusetts, May 17, 1984

S. P. Hirshman, "3-D Moments Equilibria"

Seminar, Institute for Fusion Studies, Austin, Texas, May 24–25, 1984

T. C. Hender, stellarator equilibrium calculations for helical axis devices

Workshop on Impurity Control Processes, Atlanta, Georgia, May 30–31, 1984. Proceedings published as ETR-INTOR/ICP/3, 1984

R. A. Phaneuf, "Atomic Processes Involving Impurities in the Plasma Edge," pp. 101–25

15th Annual Meeting of the Division of Electron and Atomic Physics, American Physical Society, Storrs, Connecticut, May 30–June 1, 1984. Abstracts published in *Bull. Am. Phys. Soc.* **29**(4) (1984)

A. M. Howald, R.A. Phaneuf, D. H. Crandall, and D. C. Gregory, "Single, Double, and Triple Ionization of Xe^{6+} by Electron Impact," p. 804

F. W. Meyer, "The ORNL ECR Multicharged Ion Source," p. 810

R. A. Phaneuf, C. C. Havener, and H. F. Krause, "Ion-Atom Merged Beams," p. 812

Annual Meeting of the American Nuclear Society, New Orleans, Louisiana, June 3–8, 1984

T. G. Brown, "Configuration Review of TFCX Design Options"

G. M. Fuller, "The Status of Fusion Maintenance"

J. Kirchner, "MFTF-α+T End Cell Vacuum Vessel and Nuclear Shield Trade Studies"

P. T. Spampinato, "An All-Remote Configuration for the ETR-INTOR Tokamak Design"

MFAC Panel IX, Oak Ridge, Tennessee, June 5, 1984

N. A. Uckan, "The ELMO Bumpy Square (EBS)"

TFCX Preconceptual Design Review, Princeton, New Jersey, June 6–8, 1984

T. G. Brown, "Superconducting Device Configuration"

G. T. Bussell, J. Commander, K. Watts, R. Fleming, and H. Murray, "TFCX Facilities Presentation"

S. A. Freije, "Lower Hybrid Current Rampup for TFCX"

G. M. Fuller, "TFCX—Bulk Shield Design—Superconducting TF Coil Concepts"

J. D. Galambos, "Particle Removal Rates for Pump Limiter and Divertor"

J. R. Haines, "Impurity Control and Vacuum System Analysis"

W. R. Hamilton, "TFCX Cost Database"

L. Hively, "Plasma Modeling"

S. S. Kalsi, R. Hooper, T. Mann, and V. Srivastava, "TFCX Superconducting Magnet Design"

D. H. Metzler, "RF Systems"

J. A. O'Toole, "TFCX Superconducting Options Structural Analysis"

T. E. Shannon, "Superconducting Options Design Overview"

D. J. Strickler, "TFCX Plasma Magnetics"

Conference de la Societé Belge de Physique, Louvain-la-Neuve, Belgium, June 7–8, 1984

P. Defrance, D. Belic, F. Brouillard, S. Chantrenne, D. Gregory, J. Jureta, and S. Rachafi, "Etude Experimentale de l'Ionization d'Ions Multichargés"

Gordon Conference on Multiphoton Ionization, New London, New Hampshire, June 11–15, 1984

C. Bottcher, "Quantal and Classical Theories of Multiphoton Dissociation"

Seminar on Tokamak and Stellarator Edge Turbulence, Institute for Fusion Studies, Austin, Texas, June 11–15, 1984

K. C. Shaing, "Rippling Mode in Tokamaks"

12th International Symposium on Effects of Radiation on Materials, Williamsburg, Virginia, June 18–20, 1984

D. N. Braski and D. W. Ramey, "A Modified Tritium Trick Technique for Doping Vanadium Alloys with Helium"

M. L. Grossbeck and K. C. Liu, "Fatigue Behavior at 650°C of 20%-Cold-Worked Type 316 Stainless Steel Irradiated at 550°C in the HFIR"

R. L. Klueh and M. L. Grossbeck, " Tensile Properties and Swelling of 20%-Cold-Worked Type 316 Stainless Steel Irradiated in HFIR"

G. R. Odette, P. J. Maziasz, and R. E. Stoller, "An Assessment of the Mechanisms Controlling Swelling Resistance of Titanium Modified Stainless Steels"

1984 International Conference on Plasma Physics, Lausanne, Switzerland, June 27–July 3, 1984

J. B. Wilgen, R. K. Richards, D. L. Hillis, D. W. Swain, T. L. White, B. G. Peterson, F. W. Baity, L. A. Berry, W. H. Casson, J. A. Cobble, R. J. Colchin, W. A. Davis, O. C. Eldridge, J. C. Glowienka, J. R. Goyer, O. E. Hankins, G. R. Haste, S. Hiroe, H. D. Kimrey, T. L. Owens, D. A. Rasmussen, L. Solensten, and T. Uckan, "EBT Electron Energy Confinement Experiments"

International Conference on the Physics of Highly Ionized Atoms, Oxford University, England, July 2–5, 1984

R. C. Isler, "Charge Exchange Spectroscopy for Plasma Diagnostics"

F. W. Meyer, "The ORNL ECR Ion Source"

IAEA Workshop on MHD Beta Limits in Tokamaks, Lausanne, Switzerland, July 4–6, 1984

G. H. Neilson, "Experimental Results on Tokamak Beta Limits from ISX-B"

Y-K. M. Peng, J. A. Schmidt, S. E. Attenberger, R. J. Barrett, S. Bernabei, A. Boozer, S. K. Borowski, P. Colestock, D. Elder, S. A. Freije, J. D. Galambos, L. M. Hively, W. A. Houlberg, D. Hwang, S. Jardin, J. Miller, C. Phillips, R. L. Reid, K. E. Rothe, and D. J. Strickler, "Plasma Design Assessments of Quasi-Steady-State, D-T Burn Tokamak Reactors"

INTOR TFTR/JET Workshop on Plasma Transport in Tokamaks, Princeton, N.J., July 9–10, 1984. Proceedings published as PPPL-2182, January 1985

G. H. Neilson and the ISX Group, "Experimental Results on Tokamak Beta Limits from ISX-B"

Fourth Analytical Electron Microscopy Conference, Lehigh University, Bethlehem, Pennsylvania, July 16–20, 1984

E. A. Konik and P. J. Maziasz, "Application of Extraction Replicas and Analytical Electron Microscopy to Precipitate Phase Studies"

J. M. Vitek (presented by D. Williams), "An EDS Round-Robin Evaluation of Type 308 Austenitic Stainless Steel"

17th Annual Meeting of International Metallographic Society, Philadelphia, Pennsylvania, July 17–18, 1984

P. F. Tortorelli, T. J. Henson, J. R. Mayotte, and J. H. DeVan, "Metallographic Evaluation of the Reactions Between Borated Graphite and Fe-Ni-Cr Alloys"

Third International Conference on Infrared Physics (CIRP-3), Zurich, Switzerland, July 23–27, 1984

D. P. Hutchinson, C. H. Ma, P. A. Staats, and K. L. Vander Sluis, "Far-Infrared Interferometry/Polarimetry on the ISX-B Tokamak"

Ninth International Conference on Atomic Physics, Seattle, Washington, July 23–27, 1984

P. M. Griffin and C. C. Havener, "EUV Radiation from keV Electron Impact on Ta"

Seminar, Oulu University, Oulu, Finland, July 26, 1984

J. M. Vitek, "Welding of Austenitic Stainless Steels"

NATO Advanced Study Institute Programme: International Course on Physics of Plasma-Wall Interactions in Controlled Fusion, Val Morin, Quebec, Canada, July 30–August 11, 1984. Proceedings to be published by Plenum Press.

E. C. Crume, Jr., "Effects of Momentum Input and Sonic Flow on Impurity Transport in Tokamaks"

P. K. Mioduszewski, "Advanced Limiters"

C. C. Tsai et al., "Testing Capability at ORNL for Simulation of Plasma-Wall Interactions in Controlled Fusion"

Atomic Physics Colloquium, Lawrence Livermore National Laboratory, Livermore, California, July 30, 1984

P. M. Griffin, "New Radiometric Sources for the EUV"

Seminar, Sandvik, Inc., Sandviken, Sweden, August 2, 1984

J. M. Vitek, "Ferritic Steel Research for Fusion Reactor Applications"

42d Annual Meeting of the Electron Microscopy Society of America, Detroit, Michigan, August 13–17, 1984. Proceedings published by San Francisco Press, San Francisco, 1984. G. W. Bailey, editor.

P. J. Maziasz, "Molybdenum Solubility Differences in MC Phases Formed in Titanium and Niobium Modified Austenitic Stainless Steels Determined Using AEM," pp. 496–97

Eighth European Congress on Electron Microscopy, Budapest, August 13–18, 1984

J. M. Vitek, "Round Robin EDS Evaluation of Fully Austenitic Stainless Steel"

19th Annual Intersociety Energy Conversion Engineering Conference, San Francisco, California, August 19–24, 1984

J. Sheffield and R. A. Dory, "Cost Assessment of a Generic Magnetic Fusion Reactor"

1984 Applied Superconductivity Conference, San Diego, California, September 9–13, 1984

L. Dresner, "Quench Energies of Potted Magnets"

J. F. Ellis, M. S. Lubell, S. S. Shen, P. L. Walstrom, R. J. Thome, and R. D. Pillsbury, "Shorts Due to Diagnostic Leads"

W. A. Fietz, "Test Short Samples of Nb_3Sn Conductor for the Westinghouse LCP Coil"

R. K. Kibbe, C. M. Amonett, R. D. Benson, R. O. Hussung, and W. D. Shipley, "Experience Highlights from the Design and Manufacture of U.S. LCT Coils"

J. N. Luton, F. D. Cogswell, L. Dresner, G. M. Friesinger, W. H. Gray, Y. Iwasa, K. Koizumi, M. S. Lubell, J. W. Lue, M. F. Nishi, S. D. Peck, S. S. Shen, R. Takahashi, R. E. Wintenberg, K. Yoshida, and J. A. Zichy, "Preliminary Results of the Partial-Array LCT Coil Tests"

T. J. McManamy, J. W. Lue, J. K. Ballou, T. L. Mann, S. S. Shen and C. T. Wilson, "EBT-P Magnet Development Program Summary"

S. W. Schwenterly, "A Review of Low-Temperature Electrical Insulation Techniques for the Superconducting Magnet Designer"

V. C. Srivastava, "High-Performance TF Coil Design for the Toroidal Fusion Core Experiment (TFCX)"

Seminar, Los Alamos National Laboratory, Los Alamos, New Mexico, September 11–14, 1984

S. P. Hirshman, seminar on the Oak Ridge Moments Code

10th International Conference on Plasma Physics and Controlled Nuclear Fusion Research, London, September 12–19, 1984. Proceedings to be published by the International Atomic Energy Association, Vienna, 1985.

Z. G. An, P. H. Diamond, R. D. Hazeltine, J. N. Leboeuf, M. N. Rosenbluth, R. D. Sydora, T. Tajima, B. A. Carreras, L. Garcia, T. C. Hender, H. R. Hicks, and J. A. Holmes, "Role of Multiple Helicity Nonlinear Interaction of Tearing Modes in Anomalous Thermal Helicity Transport and Dynamo in Reversed Field Pinch and the Major Disruption in Tokamaks"

L. A. Berry, F. W. Baity, F. M. Bieniosek, T. S. Bigelow, J. A. Cobble, R. J. Colchin, W. A. Davis, J. C. Glowienka, J. R. Goyer, G. R. Haste, D. L. Hillis, S. Hiroe, H. D. Kimrey, L. W. Owen, T. L. Owens, R. K. Richards, L. Solensten, D. W. Swain, N. A. Uckan, T. Uckan, T. L. White, and J. B. Wilgen, "Recent Advances in Confinement and Heating Physics on EBT-S"

B. A. Carreras, J. L. Cantrell, L. A. Charlton, W. A. Cooper, L. Garcia, J. H. Harris, T. C. Hender, H. R. Hicks, J. A. Holmes, J. A. Rome, and V. E. Lynch, "MHD Equilbrium and Stability for Stellarator/Torsatron Configurations"

P. C. Efthimion, N. Bretz, M. Bell, M. Bitter, W. R. Blanchard, F. Boody, D. Boyd, C. Bush, J. L. Cecchi, J. Coonrod, S. Davis, D. Dimock, H. F. Dylla, S. von Goeler, R. J. Goldston, B. Grek, D. J. Grove, R. J. Hawryluk, H. Hendel, K. W. Hill, R. Hulse, D. Johnson, L. C. Johnson, R. Kaita, S. Kaye, M. Kikuchi, S. Kilpatrick, J. Kiraly, R. Knize, P. LaMarche, R. Little, D. Manos, M. McCarthy, D. McCune, K. McGuire, D. M. Meade, S. S. Medley, D. R. Mikkelsen, D. Mueller, M. Murakami, E. B. Nieschmidt, D. K. Owens, A. T. Ramsey, A. L. Roquemore, N. R. Sauthoff, J. Schivell, J-L. Schwob, S. Scott, S. Sesnic, J. Sinnis, F. Stauffer, J. D. Strachan, S. Suckewer, G. D. Tait, M. Tavernier, G. Taylor, F. Tenney, H. Towner, M. Ulrickson, K-L. Wong, A. Wouters, H. Yamada, K. M. Young, and M. Zarnstorff, "Confinement Studies of Ohmically Heated Plasmas in TFTR"

H. P. Eubank, J. Bell, M. G. Bell, M. Bitter, W. R. Blanchard, F. Boody, D. Boyd, N. Bretz, C. Bush, J. L. Cecchi, J. Coonrod, S. L. Davis, D. Dimock, H. F. Dylla, P. C. Efthimion, A. C. England, R. Fonck, E. Fredrickson, H. P. Furth, L. R. Grisham, S. von Goeler, R. J. Goldston, B. Grek, D. J. Grove, R. J. Hawryluk, H. Hendel, K. W. Hill, D. L. Hillis, R. Hulse, D. Johnson, L. C. Johnson, P. LaMarche, R. Kaita, J. Kamperschroer, S. M. Kaye, M. Kikuchi, S. Kilpatrick, J. Kiraly, R. Knize, H. Kugel, R. Little, D. Manos, M. McCarthy, R. T. McCann, D. C. McCune, K. McGuire, D. M. Meade, S. S. Medley, D. R. Mikkelsen, D. Mueller, M. Murakami, E. Nieschmidt, D. K. Owens, V. Paré, B. Prichard, A. Ramsey, D. Rasmussen, M. H. Redi, A. L. Roquemore, R. H. Rutherford, N. R. Sauthoff, J. Schivell, J. L. Schwob, S. Scott, S. Sesnic, J. Sinnis, F. Stauffer, J. D. Strachan, S. Suckewer, G. Tait, M. Tavernier, G. Taylor, F. Tenney, H. H. Towner, M. Ulrickson, R. Wieland, M. Williams, K. L. Wong, A. Wouters, H. Yamada, K. M. Young, and M. C. Zarnstorff, "Neutral-Beam Heating in TFTR—Projections and Initial Results"

M. Greenwald, D. Gwinn, S. Milora, J. Parker, R. Parker, S. Wolfe, M. Besen, B. Blackwell, F. Camacho, S. Fairfax, C. Fiore, M. Foord, R. Gandy, C. Gomez, R. Granetz, B. LaBombard, B. Lipschultz, B. Lloyd, E. Marmar, S. McCool, D. Pappas, R. Petrasso, M. Porkolab, P. Pribyl, J. Rice, D. Schuresko, Y. Takase, J. Terry, and R. Watterson, "Pellet Fueling Experiments in Alcator C"

C. L. Hedrick, D. B. Batchelor, G. L. Chen, R. C. Goldfinger, D. E. Hastings, E. F. Jaeger, D. K. Lee, L. W. Owen, D. A. Spong, and J. S. Tolliver, "Coupled Transport and Heating in EBT and EBS"

INTOR Group, "Engineering and Nuclear Aspects of INTOR"

INTOR Group, "The Evolution of the INTOR Concept"

P. K. Mioduszewski, D. D. Schuresko, L. C. Emerson, J. E. Simpkins, C. E. Bush, P. H. Edmonds, A. C. England, H. C. Howe, D. P. Hutchinson, R. C. Isler, R. R. Kindsfather, R. A. Langley, E. A. Lazarus, C. H. Ma, S. L. Milora, M. Murakami, G. H. Neilson, J. Sheffield, C. E. Thomas, A. J. Wootton, and K. E. Yokoyama, "Particle Control with Pump Limiters and Pellet Fueling in ISX-B"

M. Murakami, P. H. Edmonds, G. A. Hallock, R. C. Isler, E. A. Lazarus, G. H. Neilson, A. J. Wootton, J. D. Bell, C. E. Bush, A. Carnevali, B. A. Carreras, J. L. Dunlap, A. C. England, W. L. Gardner, R. L. Hickok, H. C. Howe, D. P. Hutchinson, W. C. Jennings, R. R. Kindsfather, R. A. Langley, C. H. Ma, J. Mathew, P. K. Mioduszewski, J. K. Munro, V. K. Paré, M. J. Saltmarsh, S. D. Scott, D. J. Sigmar, M. L. Simpson, C. E. Thomas, R. M. Wieland, W. R. Wing, and K. E. Yokoyama, "Confinement of Beam-Heated Plasmas in ISX-B"

D. C. Robinson, N. R. Ainsworth, M. W. Alcock, D. Atkinson, P. R. Collins, A. N. Dellis, T. Edlington, A. Ferreira, Q. Gao, T. C. Hender, Z. Ma, A. W. Morris, M. O'Brien, B. Parham, A. C. Rivière, D. F. H. Start, S. Takamura, and T. N. Todd, "Limiting β Investigations at Low Collisionality"

S. Sengoku, M. Abe, K. Hoshino, K. Itoh, A. Kameari, A. Kitsunezaki, T. Koike, S. Konoshima, T. Matoba, M. Nagami, A. Oikawa, T. Ohga, M. Shimada, N. Suzuki, H. Takahashi, K. Tani, M. Washizu, C. A. Foster, S. L. Milora, S. E. Attenberger, R. Stockdale, S. I. Itoh, S. Wojtowicz, T. Angel, K. Burrell, F. Blau, R. W. Callis, A. F. Colleraine, E. Fairbanks, J. Fasolo, R. Groebner, R. M. Hong, J. Kim, D. B. McColl, P. I. Peterson, J. C. Phillips, R. Schissel, T. J. Scoville, R. Silagi, B. Sleaford, J. Smith, R. Stan, J. F. Tooker, and GA Doublet III Group, "Improvement of Beam Heated Limiter Discharges by Continuous Pellet Fueling in Doublet III"

K. C. Shaing, R. H. Fowler, D. E. Hastings, W. A. Houlberg, E. F. Jaeger, J. F. Lyon, J. A. Rome, J. S. Tolliver, and J. D. Callen, "The Radial Electric Field in a Nonaxisymmetric Torus"

G. Tait, J. Bell, M. G. Bell, M. Bitter, W. R. Blanchard, F. Boody, D. Boyd, N. Bretz, C. Bush, J. L. Cecchi, S. Cohen, J. Coonrod, S. L. Davis, D. Dimock, H. F. Dylla, P. C. Efthimion, A. C. England, R. Fonck, E. Fredrickson, H. P. Furth, S. von Goeler, R. J. Goldston, B. Grek, D. J. Grove, R. J. Hawryluk, H. Hendel, K. W. Hill, D. Hillis, R. Hulse, D. Johnson, L. C. Johnson, R. Kaita, S. M. Kaye, M. Kikuchi, S. Kilpatrick, J. Kiraly, R. Knize, P. LaMarche, R. Little, D. Manos, M. McCarthy, D. C. McCune, K. McGuire, D. M. Meade, S. S. Medley, D. R. Mikkelsen, D. Mueller, M. Murakami, E. Nieschmidt, D. K. Owens, V. K. Paré, A. Ramsey, D. Rasmussen, M. Redi, A. L. Roquemore, N. R. Sauthoff, J. Schivell, J. L. Schwob, S. Scott, S. Sesnic, J. Sinnis, F. Stauffer, P. Stangeby, J. D. Strachan, S. Suckewer, M. Tavernier, G. Taylor, F. Tenney, J. Timberlake, H. H. Towner, M. Ulrickson, K. L. Wong, A. Wouters, H. Yamada, K. M. Young, and M. C. Zarnstorff, "Adiabatic Toroidal Compression and Free-Expansion Experiments in TFTR"

K. Uo, A. Iiyoshi, T. Obiki, O. Motojima, S. Morimoto, M. Wakatani, A. Sasaki, K. Kondo, M. Sato, K. Hanatani, T. Mutoh, H. Zushi, H. Kaneko, S. Besshou, M. Nakawuga, F. Sano, T. Mizuuchi, S. Sudo, J. H. Harris, I. Ohtake, M. Iima, H. Okada, and Y. Nakashima, "NBI Heating of Currentless Plasmas in Heliotron-E"

Fifth Topical Conference on High Temperature Plasma Diagnostics, Tahoe City, California, September 16–20, 1984. Abstracts to be published in *Review of Scientific Instruments.*

C. A. Bennett, D. P. Hutchinson, K. L. Vander Sluis, and P. A. Staats, "Development of Sequence and Regular Band Lasers for Use as Local Oscillators in Thomson Scattering Alpha Particle Diagnostics"

W. H. Casson, D. P Hutchinson, C. H. Ma, P. A. Staats, and J. B. Wilgen, "Far-Infrared Laser Diagnostic on EBT and Extreme Far-Forward Laser Scattering on ISX"

J. A. Cobble, "The Evolution of Low-Density Thomson Scattering on EBT"

J. A. Cobble, "Thomson Scattering at Densities Below 10^{12} cm^{-3}"

D. P. Hutchinson, C. H. Ma, K. L. Vander Sluis, and P. A. Staats, "Feasibility of Alpha Particle Measurement by CO_2 Laser Scattering"

R. C. Isler and R. A. Langley, "Calibration of Grazing Incidence Spectrometers Using Charge-Transfer Excitation"

C. H. Ma, D. P. Hutchinson, P. A. Staats, and K. L. Vander Sluis, "FIR Interferometer/Polarimeter System on the ISX-B Tokamak"

E. B. Nieschmidt, H. W. Hendel, J. A. Isaacson, F. Y. Tsang, A. C. England, and D. L. Hillis, "Effects of the Neutron Energy Spectrum on the Efficiency Calibration of Epithermal Neutron Detectors"

H. Park, D. K. Mansfield, L. C. Johnson, and C. H. Ma, "A Multichannel Far-Infrared Interferometer/Polarimeter for TFTR"

JET Joint Undertaking, Abingdon, United Kingdom, September 21, 1984

P. K. Mioduszewski, "Joint JET-ISX Be-Limiter Experiment"

Stellarator Workshop, Madrid, Spain, September 21–22, 1984

B. A. Carreras, presentation

Conference on Robotics and Remote Handling in the Nuclear Industry, Toronto, Canada, September 23–27, 1984

P. T. Spampinato, "Remote Handling Requirements and Considerations for D-T Fusion Reactors"

U.S./U.S.S.R. Topical Meeting on Plasma Rotation and Ambipolar Electric Fields in Tokamaks and RF-Heating and Transport, Kurchatov Institute, Moscow, U.S.S.R., September 23–29, 1984

E. C. Crume, "Theory and Simulations of the Electrostatic Potential in Neutral-Beam-Driven Tokamaks and Effects on Impurity Transport"

G. A. Hallock, "Ambipolar Potential Measurements on ISX-B"

13th Symposium on Fusion Technology, Varese, Italy, September 24–28, 1984. Proceedings published as a supplement to *Fusion Technology*.

P. H. Edmonds, R. D. Watson, and M. F. Smith, "Design and Fabrication of a Beryllium Limiter for ISX-B," pp. 1275–82

C. A. Flanagan, T. G. Brown, G. M. Fuller, S. S. Kalsi, D. H. Metzler, Y-K. M. Peng, and T. E. Shannon, "Superconducting Toroidal Field Coil Options for the Tokamak Fusion Core Experiment (TFCX)"

P. N. Haubenreich, R. E. Bohanan, W. A. Fietz, J. N. Luton, and J. R. May, "Startup of Large Coil Test Facility"

5th International Workshop on Stellarators: IAEA Technical Committee Meeting on Plasma Confinement and Heating in Stellarators, Schloss Ringberg (near Lake Tegernsee, Bavaria), Federal Republic of Germany, September 24–28, 1984. Proceedings published as EUR 9618 EN by the Commission of the European Communities, Directorate-General XII — Fusion Programme, Brussels. Editors: F. Rau and G. G. Leotta

B. A. Carreras, J. L. Cantrell, L. A. Charlton, L. Garcia, J. H. Harris, T. C. Hender, H. R. Hicks, J. A. Holmes, and V. E. Lynch, "MHD Equilibrium and Stability for Stellarator Configurations," vol. I, p. 317

B. A. Carreras, J. L. Cantrell, L. Garcia, J. H. Harris, T. C. Hender, and V. E. Lynch, "The Flexible Heliac," vol. II, p. 729

T. C. Jernigan, "Design and Status of ATF," vol. II, p. 597

J. F. Lyon, "Status of the ATF Program," vol. II, p. 597

K. C. Shaing, R. H. Fowler, D. E. Hastings, W. A. Houlberg, E. F. Jaeger, J. F. Lyon, J. A. Rome, J. S. Tolliver, and J. D. Callen, "The Radial Electric Field in a Stellarator," vol. II, p. 483

T. N. Todd, S. Takamura, T. Hender, and CLEO Team, "ECRH in CLEO Stellarator," vol. I, p. 173

U.S.S.R. Exchange I.5, Topical Meeting on Limiter and Divertor Designs and Plasma Physics, Moscow, U.S.S.R., September 24–29, 1984

P. K. Mioduszewski, "Pumped Limiter Studies on ISX-B"

P. K. Mioduszewski, "Results of the JET ISX Beryllium Limiter Experiment"

II Jornadas de Fusion, Madrid, October 1–2, 1984

B. A. Carreras, "Configuration Studies: Methods"

B. A. Carreras, "Stellarator Theory"

T. C. Jernigan, "Engineering Aspects of Stellarator Program"

J. F. Lyon, "ORNL Collaboration in the TJ-II Project"

J. F. Lyon, "World Stellarator Program"

1984 Gyrotron User/Developer Meeting, Gaithersburg, Maryland, October 2, 1984

T. L. White et al., "ORNL ECH Transmission Systems for RFTF and ATF"

H. R. Jory, "The Varian Gyrotron Development Program"

Fusion Power Associates Symposium on New Directions in Magnetic Fusion, Rockville, Maryland, October 3, 1984

J. Sheffield, "The Role of Improved Fusion Concepts in the Program Plan"

Seminar, Princeton Plasma Physics Laboratory, Princeton, New Jersey, October 8–12, 1984

S. P. Hirshman, "Renormalized MHD Equilibrium Theory"

Thirty-Seventh Annual Gaseous Electronics Conference, Boulder, Colorado, October 9–12, 1984

J. H. Whealton, R. J. Raridon, W. L. Stirling, M. A. Bell, S. L. Milora, and C. C. Tsai, "Theory of the Plasma Edge: Recycling—Sheaths"

Visit of T. Fuketa, Office of Planning, Japan Atomic Energy Research Institute, to ORNL, October 23, 1984

J. L. Scott, "Status of US/Japan Collaborative Testing in HFIR and ORR"

Seminar, Department of Metallurgical, Chemical, and Polymer Engineering, University of Tennessee, Knoxville, Tennessee, October 23, 1984

P. J. Maziasz, "Phase Identification Using Analytical Electron Microscopy"

INTOR Workshop, Vienna, Austria, October 25–29, 1984. Proceedings to be published by the International Atomic Energy Agency, Vienna.

C. A. Flanagan, T. G. Brown, S. K. Borowski, M. Y. Gohar, J. R. Haines, R. J. Hooper, S. S. Kalsi, D. H. Metzler, C. E. Nelson, Y-K. M. Peng, B. W. Riemer, P. T. Spampinato, and R. J. Thome, "Engineering Tasks for October 1984 INTOR Workshop"

C. A. Flanagan, T. G. Brown, D. B. Montgomery, J. Schultz, R. J. Thome, J. R. Haines, D. H. Metzler, G. E. Gorker, K. Young, T. E. Shannon, "Chapter IX. Engineering Data Base"

C. A. Flanagan, G. T. Bussell, P. A. Finn, G. M. Fuller, G. E. Gorker, W. R. Hamilton, S. S. Kalsi, D. H. Metzler, "Chapter VII. Technical Benefit—Partitioning of Component Design and Fabrication"

P. T. Spampinato, P. A. Finn, Y. Gohar, S-T. Yang, C. Morrison, S. Russell, G. Shaw, R. Watts, F. W. Wiffen, C. Bradley, G. M. Fuller, H. M. Harvey, B. W. Riemer, "Chapter VI. Maintainability, Tritium Containment and Personnel Access vs Remote Maintenance"

Seminar, Max-Planck-Institut, Stuttgart, Federal Republic of Germany, October 29, 1984

J. M. Vitek, "Investigation of Ferritic Stability in Dupplex Austenitic Steels Using Analytical Electron Microscopy (AEM)"

26th Annual Meeting of the Division of Plasma Physics, American Physical Society, Boston, October 29–November 2, 1984. Abstracts published in *Bull. Am. Phys. Soc.* **29**(8) (1984).

J. L. Alvarez-Rivas, J. A. Fabregas, J. Guasp, A. P. Navarro, A. Perea, and the ATF Team, "Configuration Studies for the TJ-II Device," p. 1273

S. E. Attenberger and W. A. Houlberg, "Intersections of a Trajectory with Tokamak or Stellarator Flux Surfaces" (postdeadline paper)

A. W. Bailey, W. M. Stacey, Jr., and D. J. Sigmar, "Neutral Beam Driven Impurity Flow Reversal in PLT and ISX-B," p. 1426

F. W. Baity, D. J. Hoffman, and T. L. Owens, "ICRF Heating on ATF," p. 1222

G. C. Barber, W. R. Becraft, N. S. Ponte, and R. E. Wright, "A Multi-Megawatt RF Amplifier System for ICRH Experiments," p. 1221

D. B. Batchelor, "Core Plasma Heating in EBT-S and the Effect of Strongly Damped Cyclotron Waves," invited paper, p. 1287

D. B. Batchelor, K. S. Riedel, and H. Weitzner, "Strong Damping of Electron Cyclotron Waves in Nearly Parallel Stratified Plasmas," p. 1311

L. R. Baylor, J. R. Roth, D. Dehkordi, and M. Laroussi, "Anomalous Drift Waves Detected with Microwave Scattering in an Electric Field Dominated Plasma," p. 1197

C. O. Beasley, K. Molvig, and W. I. van Rij, "Drift Waves Destabilized by Pellet Injection" (postdeadline paper)

W. R. Becraft, F. W. Baity, J.B.O. Caughman II, D. J. Hoffman, and J. H. Whealton, "The Transmission of Power Through Faraday Shields for Fusion Applications," p. 1222

K. Behringer, E. Kallne, P. Morgan, N. Peacock, R. C. Isler, and R. V. Neidigh, "Impurity Concentrations and Fluxes in the Joint JET–ISX-B Beryllium Limiter Experiment," p. 1426

J. D. Bell, J. L. Dunlap, V. K. Pare, J. Wootton, "MHD Fluctuations in ISX-B," p. 1424

M. A. Bell, J. H. Whealton, R. J. Raridon, D. E. Wooten, and R. W. McGaffey, "New Accelerator Designs for Positive and Negative Ions," p. 1369

F. M. Bieniosek, J. B. Wilgen, R. K. Richards, J. A. Cobble, D. L. Hillis, S. Hiroe, T. Uckan, and T. L. White, "Pulsed Experiments on EBT-S," pp. 1417–8

T. S. Bigelow, D. A. Rasmussen, and D. B. Batchelor, "Fundamental and 2nd Harmonic Resonance Polarized Microwave Absorption Measurements on EBT," p. 1428

D. T. Blackfield, R. Campbell, R. Bulmer, M. Fenstermacher, Y-K. M. Peng, L. Perkins, R. L. Reid, and F. Wu, "Physics Optimization Studies of Tandem Mirror Reactors," p. 1253

S. K. Borowski, Y-K. M. Peng, and W. A. Houlberg, "A Numerical Model for Examining Noninductive Current Drive Scenarios in Ignition Tokamaks," p. 1215

C. E. Bush, M. Murakami, R. C. Isler, P. K. Mioduszewski, R. A. Zuhr, and D. H. J. Goodall, "Energy Flux to Walls and Limiters for Various Impurity Control Elements in ISX-B," p. 1424

J. D. Callen and K. C. Shaing, "A Pressure-Gradient-Driven Tokamak 'Neoclassical MHD' Instability in the Banana-Plateau Collisionality Regime," p. 1294

A. Carnevali, S. D. Scott, C. E. Thomas, G. H. Neilson, M. Simpson, J. K. Munro, and J. A. Moore, "Fast Ion Measurements in ISX-B," p. 1425

B. A. Carreras, T. C. Hender, L. A. Charlton, and J. A. Holmes, "The Effects of Toroidicity on Resistive MHD Instabilities in the RFP," p. 1356

M. D. Carter, J. D. Callen, and D. B. Batchelor, "Nonlinear Effects in Second Harmonic Electron Cyclotron Heating," p. 1428

W. H. Casson, J. B. Wilgen, and D. P. Hutchinson, "FIR Scattering on ISX and EBT," p. 1418

J.B.O. Caughman II, B. Blackwell, and D. J. Hoffman, "Measurements of the Transmission Characteristics of the Alcator-C ICRH Antenna," p. 1221–2

L. A. Charlton, B. A. Carreras, L. Garcia, J. A. Holmes, H. R. Hicks and V. E. Lynch, "Fully Toroidal Nonlinear MHD Calculations Without Ordering Assumptions" (postdeadline paper)

G. L. Chen, D. B. Batchelor, and Y. Matsuda, "Fokker-Planck Calculations of Core Plasma Heating by ECRH in EBT," p. 1417

R. E. Clausing, L. Heatherly, R. A. Langley, J. Roberto, R. A. Zuhr, T. B. Cook, J. von Seggern, and K. Tschersich, "Materials Transport and Cleanup During the Joint JET–ISX-B Beryllium Limiter Experiment," p. 1426

S. K. Combs, S. L. Milora, and C. R. Foust, "Repeating Pneumatic Pellet Injector," p. 1370

R. W. Conn, G. A. Campbell, D. M. Goebel, R. A. Zuhr, and W. R. Wampler, "Langmuir/Calorimeter Probe Measurements in TEXTOR," p. 1353

T. B. Cook, P. W. King, and K. A. Stewart, "Time-Resolved Measurements at a Reference Limiter in the ISX-B Tokamak Using Laser-Induced Fluorescence," p. 1425

W. A. Cooper, "Resistive Ballooning Modes in Toroidally Rotating Tokamak Plasmas," p. 1387

W. K. Dagenhart and W. L. Stirling, "Intense Li^0 Beam Production with an ORNL SITEX Li^- Source," p. 1314

W. A. Davis and R. J. Colchin, "Monte-Carlo Neutral Density Profiles for EBT," p. 1416

N. G. Demas and C. A. Ventrice, "Inferring Point-Wise Current Densities from FIR Interferometer/Polarimeter Integral Measurements," p. 1277

P. H. Diamond, "Resistivity Gradient Driven Turbulence and Edge Fluctuations in Tokamaks," invited paper, p. 1411

P. H. Edmonds, P. K. Mioduszewski, J. Dietz, R. Watson, and M. Smith, "The Joint JET–ISX-B Beryllium Limiter Experiment," p. 1352

P. C. Efthimion, M. Bell, M. Bitter, J. Coonrod, R. Goldston, B. Grek R. Hawryluk, H. Hendel, K. Hill, D. Johnson, R. Kaita, D. McCune, K. McGuire, S. Medley, E. Nieschmidt, A. Ramsey, J. Schivell, J. Sesnic, G. Taylor, F. Tenney, and S. D. Scott, "Confinement Studies of Large Ohmically-Heated Plasmas in TFTR," pp. 1382–83

C. Egert, W. L. Stirling, C. C. Tsai, and D. Tunison, "Characteristics of a Quasi Steady State Plasma Source," p. 1314

A. M. El Nadi, J. C. Whitson, and S. Hiroe, "Finite $K_{\parallel}$ High Frequency Fluctuations in EBT," p. 1416

L. C. Emerson, P. K. Mioduszewski, J. E. Simpkins, G. R. Dyer, and D.H.J. Goodall, "Thermal Studies of the Beryllium Limiter in ISX-B During Ohmic- and Beam-Heated Discharges," p. 1426

A. C. England, O. C. Eldridge, and G. G. Kelley, "Effects of Preionization by Electron Cyclotron Heating in INTOR and TFCX," p. 1428

E. S. Fairbanks, F. P. Blau, D. Schissel, J. R. Smith, R. E. Stockdale, and C. A. Foster, "Density and Temperature Profiles in Doublet-III During Pellet Injection," p. 1365

K. Felch, R. Bier, L. Fox, H. Huey, L. Ives, H. Jory, and S. Spang, "Development of a 140 GHz, 100 kW cw Gyrotron," pp. 1255–56

C. A. Foster, S. L. Milora, S. Sengoku, M. Nagami, the JAERI Team, and the Doublet III Group, "Results of Continuous Pellet Fueling Experiments on Doublet III," p. 1321

J. P. Freidberg and D. J. Sigmar, "Influence of Ideal Ballooning Modes on Confinement Scaling at High β," p. 1370

S. A. Freije and Y-K. M. Peng, "Parametric Assessments of Current Rampup by Lower Hybrid Current Drive in TFCX," p. 1307

J. Galambos, Y-K. M. Peng, and D. Heifetz, "Coupled Plasma-Neutral Transport Model for Scrape-off Plasmas," p. 1247

L. Garcia, B. A. Carreras, L. A. Charlton, H. R. Hicks, and J. A. Holmes, "Stability Calculations for High-Beta Torsatrons," p. 1272

W. L. Gardner, D. J. Hoffman, H. H. Haselton, T. J. McManamy, J. A. Moeller, and P. M. Ryan, "The Oak Ridge RF Test Facility," p. 1222

J. C. Glowienka, R. K. Richards, and W. A. Davis, "Fast Ion Decay Estimates of Neutral Densities and Particle Lifetimes in EBT-S," p. 1418

R. C. Goldfinger, D. B. Batchelor, and S. P. Hirshman, "Propagation and Absorption of Electron Cyclotron Waves in ATF" (postdeadline paper)

J. R. Goyer, L. Solensten, K. A. Connor, and R. L. Hickok, "Heavy Ion Beam Probe Measurements of Electron Density and Temperature on EBT," p. 1418

G. A. Hallock, J. Mathew, R. L. Hickok, W. C. Jennings, A. J. Wootton, and T. F. Rayburn, "Results and Calibration of the ISX-B Heavy Ion Beam Probe," p. 1424

C. R. Handy and S. P. Hirshman, "Accelerated Convergence of the Steepest Descent Method for Magnetohydrodynamic Equilibria" (postdeadline paper)

O. E. Hankins, D. L. Hillis, and J. B. Wilgen, "A Study of Hot-Electron Ring Formation and Decay Processes During EBT-I/S Operation," p. 1418

J. H. Harris, J. C. Cantrell, J. A. Rome, and A. J. Wootton, "Divertor Schemes for the ATF Torsatron," 1244

D. E. Hastings, "A Differential Equation for the Ambipolar Electric Field in a Multiple-Helicity Torsatron," p. 1272

C. L. Hedrick and E. F. Jaeger, "R-F and Microwave Induced Losses," p. 1323

T. C. Hender, "Equilibrium Studies for Helical Axis Stellarators," invited talk, p. 1287

T. C. Hender, J. L. Cantrell, B. A. Carreras, L. Garcia, J. H. Harris, H. R. Hicks, V. E. Lynch, and J. A. Rome, "Helical Axis Stellarator Equilibria," p. 1373

H. R. Hicks, B. A. Carreras, and J. A. Holmes, "Study of ATF-1 Torsatron Configurations Using the NYU Code BETA" (postdeadline paper)

D. L. Hillis, J. B. Wilgen, J. A. Cobble, W. A. Davis, S. Hiroe, D. A. Rasmussen, R. K. Richards, T. Uckan, O. E. Hankins, J. R. Goyer, and L. Solensten, "Electron Confinement in EBT-S Without the Influence of Hot Electron Rings—'The Ring Killer Experiment,'" p. 1419

S. Hiroe, J. A. Cobble, D. L. Hillis, J. R. Goyer, L. Solensten, and B. H. Quon, "Effect of Fluctuation and Potential on EBT Confinement," p. 1234

L. M. Hively and D. R. Mikkelsen, "Plasma Performance of TFCX and JET with Sawtoothing," p. 1214

D. J. Hoffman, F. W. Baity, P. M. Ryan, J. H. Whealton, and T. L. Owens, "The Technology Development of Antennas and Feedthroughs for TFCX, TFTR, and DIII-D," p. 1222

J. T. Hogan, "Beam-Induced Current Effects on Stellarator Transform," p. 1271

J. T. Hogan and S. P. Hirshman, "Comparison of 3D MHD Inverse Coordinates Codes," p. 1410

J. A. Holmes, B. A. Carreras, L. A. Charlton, and V. E. Lynch, "Free Boundary Equilibrium and Stability of a Moderate Aspect Ratio Torsatron Using the Stellarator Expansion" (postdeadline paper)

H. C. Howe, D. Schuresko, and W. A. Houlberg, "Anomalous Pellet Ablation in ISX-B Discharges," p. 1425

D. Q. Hwang, P. Colestock, G. Greene, J. Hosea, D. Manos, E. Mazzucato, E. Meservey, C. K. Phillips, P. Stangeby, S. Suckewer, R. Wilson, and D. Schuresko, "Propagation of the Fast Magnetosonic Wave in a Pellet Fueled PLT Plasma," p. 1332

K. Imre, H. Weitzner, and D. Batchelor, "Absorption of the Quasi-Perpendicular X-Mode in 2nd Harmonic Boundary Layer in a Weakly Relativistic Inhomogeneous Plasma," pp. 1420–1

R. C. Isler, A. J. Wootton, J. T. Hogan, and C. E. Thomas, "Correlation between Plasma Rotation and Ion Temperatures," p. 1351

E. F. Jaeger, J. H. Whealton, H. Weitzner, and D. B. Batchelor, "Full Wave Treatment of Wave Propagation in a Three-Dimensional Cavity Containing Cold Plasma," p. 1401

H. D. Kimrey, T. L. White, and T. S. Bigelow, "Performance of 28-GHz, 200-kW, cw, Gyrotron Oscillators on the ELMO Bumpy Torus–Scale (EBT-S) Experiment," p. 1256

R. A. Langley, "Measurement of α-Particles in Fusion Devices," p. 1309

E. A. Lazarus, "Improved Confinement in Beam Heated ISX-B Plasmas with Low-Z Impurities," invited paper, p. 1258

E. A. Lazarus, J. D. Bell, R. R. Kindsfather, J. T. Hogan, M. Murakami, G. H. Neilson, and R. M. Wieland, "Effects of low-Z Impurities on Electron Heat Conduction in Beam-Heated ISX-B Plasmas," p. 1352

C. H. Ma, D. P. Hutchinson, E. A. Lazarus, P. K. Mioduszewski, M. Murakami, G. H. Neilson, D. D. Schuresko, P. A. Staats, K. L. Vander Sluis, and A. J. Wootton, "FIR Diagnostics for Experiments on ISX-B Tokamak," p. 1424

D. K. Mansfield, H. Park, L. C. Johnson, and C. H. Ma, "A Multichannel Far-Infrared Interferometer/Polarimeter for TFTR," p. 1304

J. Mathew, G. A. Hallock, W. C. Jennings, R. L. Hickok, A. J. Wootton, R. C. Isler, and T. F. Rayburn, "Space Potential Measurements in Neutral-Beam-Heated ISX-B Plasmas," p. 1351

R. W. McGaffey, J. H. Whealton, R. J. Raridon, J. W. Wooten, and M. A. Bell, "Implementation of Vector Oblique Neumann Boundary Conditions for Perfect Metals in Modeling of 3D Launchers and Cavities," p. 1400

S. S. Medley, M. Bitter, R. J. Goldston, H. Hendel, R. Kaita, S. Kaye, D. McCune, E. Nieschmidt, A. L. Roquemore, H. Towner, K. M. Young, and S. D. Scott, "Ion Heating in TFTR Ohmic Discharges," p. 1384

M. M. Menon, C. C. Tsai, G. C. Barber, S. K. Combs, W. K. Dagenhart, W. L. Gardner, H. H. Haselton, N. S. Ponte, P. M. Ryan, D. E. Schechter, W. L. Stirling, J. H. Whealton, and R. E. Wright, "Operational Characteristics of a High Power (3.2 MW) Quasi-Steady-State duoPIGatron Ion Source," p. 1369

P. K. Mioduszewski, "Particle and Impurity Control Experiments with Limiters in ISX-B," invited paper, pp. 1258–9

P. K. Mioduszewski, L. C. Emerson, J. E. Simpkins, P. H. Edmonds, R. C. Isler, R. A. Langley, E. A. Lazarus, C. H. Ma, M. Murakami, G. H. Neilson, K. E. Yokoyama, and A. J. Wootton, "Particle Control with Pump Limiters in ISX-B," p. 1352

J. K. Munro, Jr., S. D. Scott, and M. Murakami, "Monte Carlo Analyses of Power and Toroidal Momentum Deposition from Co- and Counter-Injected Neutral Beams on ISX-B," p. 1425

M. Murakami, A. Carnevali, P. H. Edmonds, A. C. England, W. L. Gardner, H. C. Howe, R. R. Kindsfather, E. A. Lazarus, C. H. Ma, J. K. Munro, G. H. Neilson, S. D. Scott, M. L. Simpson, C. E. Thomas, R. M. Wieland, W. R. Wing, and A. J. Wootton, "Effects of Beam Directivity on Energy Confinement in ISX-B," p. 1351

G. H. Neilson and A. J. Wootton,"Beta Limits Deduced from ISX-B and Other Tokamaks," p. 1352

T. L. Owens, D. J. Hoffman, F. W. Baity, and J. H. Whealton, "Inductive Array Couplers for High-Power ICRF," p. 1222

R. J. Raridon, J. H. Whealton, M. A. Bell, D. J. Hoffman, E. F. Jaeger, D. E. Wooten, R. W. McGaffey, J. W. Wooten, and W. R. Becraft, "Cavity and Waveguide Field Modeling in 3D," p. 1400

D. A. Rasmussen, T. S. Bigelow, D. B. Batchelor, D. L. Hillis, G. R. Haste, B. H. Quon, and O. E. Hankins, "EBT-I Multifrequency ECH Experiments," p. 1419

J. A. Rome, "$\ell=1/\ell=2$ Torsatron Hybrids," p. 1271

P. M. Ryan, J. H. Whealton, R. J. Raridon, and R. W. McGaffey, "Theoretical Study of Electron Losses in an Ion Beam Energy Recovery Device," p. 1369

D. E. Schechter, W. R. Becraft, S. K. Combs, M. M. Menon, S. L. Milora, F. Sluss, and C. C. Tsai, "Tests of Materials on Actively Cooled Tubes for Faraday Shields," p. 1221

D. P. Schissel, B. Stockdale, and C. Foster, "Results of Frozen Deuterium Injection on Doublet III," p. 1364

J. Schivell, M. Bitter, K. W. Hill, R. Hulse, S. Sesnic, F. Tenney, S. von Goeler, and C. E. Bush, "Spatially-Resolved Bolometer Measurements in TFTR," p. 1383

D. D. Schuresko, D. Q. Hwang, S. L. Milora, R. Bell, A. Cavallo, P. Colestock, G. Greene, J. Hosea, S. Lippmann, E. Mazzucatto, M. Ono, G. L. Schmidt, G. Stratton, S. Suckewer, and J. R. Wilson, "Preliminary Results of Pellet Injection into PLT Plasmas," p. 1335

S. D. Scott, R. Kaita, S. S. Medley, and A. L. Roquemore, "Analysis of Charge-Exchange Ion Temperature Measurements on TFTR," p. 1303

S. Sengoku, M. Nagami, JAERI Team, C. A. Foster, S. L. Milora, and the Doublet III Group, "Improvement of Energy Confinement Time by Continuous Pellet Fueling in Doublet III Limiter and Divertor Discharges," p. 1362

K. C. Shaing and J. D. Callen, "A Kinetic Approach to a New Pressure Gradient Driven Tokamak Instability," p. 1294

J. Sheffield, "Physics Requirements for an Attractive Magnetic Fusion Reactor," invited paper, pp. 1285–6

J. E. Simpkins, P. K. Mioduszewski, P. H. Edmonds, R. C. Isler, E. A. Lazarus, C. H. Ma, and M. Murakami, "Impurity Control with Cr-Gettering in ISX," p. 1425

L. Solensten, J. R. Goyer, K. A. Connor, and R. L. Hickok, "EBT Plasma Potential Measurements," p. 1418

D. A. Spong, D. J. Sigmar, K. T. Tsang, W. A. Cooper, and D. E. Hastings, "Effects of Trapped Alpha Particles on Ballooning Modes," p. 1387

R. F. Steimle and K. H. Carpenter, "A Geometrical Model from MHD Equilibrium Concepts for Diamagnetic Currents in Hot Electron Rings Produced by ECH in Mirrors (Elmo) or Bumpy Tori (EBT)," p. 1416

W. L. Stirling and W. K. Dagenhart, "Volume Produced Negative Ions from a Reflex Discharge," p. 1314

R. Stockdale, D. P. Schissel, N. Brooks, S. S. Wojtowicz, and C. A. Foster, "Measurements of Particle Transport in Pellet-Injected Doublet-III Discharges," p. 1365

P. W. Terry, K. C. Shaing, P. H. Diamond, B. A. Carreras, and L. Garcia, "Spectrum of Rippling Mode Turbulence," p. 1239

C. E. Thomas, A. Carnevali, M. D. Galloway, S. D. Scott, and M. L. Simpson, "Asymmetric Distortion of the Ion Distribution Function with Neutral Beam Injection in ISX-B," p. 1351

J. S. Tolliver and J. A. Rome, "Bounce-Averaged Monte Carlo Calculations for Stellarators," p. 1322

C. C. Tsai, W. R. Becraft, H. H. Haselton, D. J. Hoffman, M. M. Menon, and D. E. Schechter, "Characteristics of a High Particle Flux Plasma Source for RF Technology Development," p. 1221

E. Uchimoto, J. D. Callen, L. Garcia, and B. A. Carreras, "Investigation into the Structure of Saturated Magnetic Islands in a Poloidal Divertor Tokamak," p. 1376

N. A. Uckan, "Current Drive Options for TFCX," p. 1307

T. Uckan,"Electron Temeprature Measurements from Induced Toroidal Current in EBT-S," p. 1418

L. Vahala, G. Vahala, and D. J. Sigmar, "Effects of α-Particles on CO_2 Laser Scattering From a Fusion Plasma," p. 1310

J. G. Watkins, K. Yokoyama, and A. J. Wootton, "Langmuir Probe Measurements in the Joint JET–ISX-B Beryllium Limiter Experiment," p. 1426

R. D. Watson and J. B. Whitley, "Materials Issues for Beryllium Limiters in Tokamaks," p. 1426

J. H. Whealton, "Transverse Emittance Compressor," p. 1262

T. L. White, H. D. Kimrey, and T. S. Bigelow, "A Quasi-Optical Electron Cyclotron Heating System for the Advanced Toroidal Facility (ATF)," p. 1284

R. M. Wieland, E. A. Lazarus, J. D. Bell, W. A. Cooper, S. P. Hirshman, and G. H. Neilson, "Toroidal Flow Analysis of ISX-B Density and Temperature Profiles," p. 1425

K. E. Yokoyama, H. C. Howe, D. P. Hutchinson, R. C. Isler, E. A. Lazarus, C. H. Ma, M. Murakami, G. H. Neilson, and A. J. Wootton, "Particle Confinement in ISX-B," p. 1351

U.S.-Japan Stellarator/Heliotron Workshop on Experimental Planning, Oak Ridge, Tennessee, November 5–9, 1984

F. W. Baity, "ICRF Preparations for ATF"

K. K. Chipley, "ATF Vacuum Vessel"

R. C. Goldfinger, "ECH Launch Optimization for ATF"

T. C. Jernigan, "ATF Helical Field Coils and Joints"

J. F. Lyon, "ATF Program Plan"

J. F. Lyon, "Particle and Impurity Control"

M. M. Menon, "ATF Neutral Beam Heating"

G. H. Neilson, "ATF Startup Options"

G. H. Neilson, "Diagnostics Strategy for ATF"

G. H. Neilson, "Equilbrium Control Using Poloidal Field Windings"

T. L. White et al., "ECH Planning for ATF"

Second Topical Conference on Cross Sections for Fusion and Other Applications, College Station, Texas, November 8–10, 1984

R. A. Phaneuf, "Many-Electron Effects in Electron-Impact Ionization of Multiply Charged Ions," invited paper

Eighth Conference on the Application of Accelerators in Research and Industry, North Texas State University, Denton, Texas, November 12–14, 1984

C. Bottcher, "Time-Dependent Hartree-Fock Studies of F^{9+} + Ne Collisions," invited paper

D. C. Gregory, "Indirect Processes in Electron Impact Ionization of Multiply Charged Ions"

Seminars, University of Wisconsin, Madison, Wisconsin, November 12–16, 1984

B. A. Carreras, "Equilibrium and Stabiliy Studies for High Beta Torsatron"

B. A. Carreras, "Nonlinear Resistive MHD: The Rippling Instability, Parts I, II, and III"

B. A. Carreras, "Tokamak Disruptions Versus RFP Dynamo Effect"

U.S.-Japan Workshop on Tokamak Diagnostics by X-Ray, VUV, and Optical Radiation, Nagoya, Japan, November 12–16, 1984

R. C. Isler, "Sources, Densities, and Transport of Impurities in Neutral Beam Injected Tokamaks"

U.S.-U.S.S.R. Atomic Energy Agreement for Scientific and Technical Cooperation for Peaceful Usage, Moscow, U.S.S.R., November 12–20, 1984

J. H. Harris, "ORNL Helical-Axis Stellarator Studies"

J. H. Harris, O. Motojima, H. Kaneko, S. Besshou, H. Zushi, M. Wakatani, F. Sano, S. Sudo, A. Sasaki, K. Kondo, M. Sato, T. Mutoh, T. Mizuuchi, M. Iima, T. Obiki, A. Iiyoshi, and K. Uo, "MHD Activity in High-Beta Currentless Plasmas in Heliotron-E"

U.S.-U.S.S.R. Stellarator Workshop, Kharkov, U.S.S.R., November 13–17, 1984

J. H. Harris, "ATF Physics Design"

J. H. Harris, "MHD Activity in High-Beta Currentless Plasmas in Heliotron-E"

Seminar, University of Colorado, Boulder, Colorado, November 25–27, 1984

D. E. Hastings, "A Stochastic Model of a Nonequilibrium Phase Transition in a Magnetic Fusion Device"

Seminar, Plasma Research Institute, Boulder, Colorado, November 28–29, 1984

D. E. Hastings, "Stellarator Transport—An Overview"

Seminar, University of Tokyo, Tokyo, Japan, November 30, 1984

P. J. Maziasz, "Radiation-Induced Precipitation Under Neutron Irradiaton and Its Sensitivity to Helium Content in Austenitic Stainless Steels"

First International Conference on Fusion Reactor Materials, Tokyo, Japan, December 3–6, 1984

P. J. Maziasz, "A Perspective on Present and Future Alloy Development Efforts on Austenitic Stainless Steels for Fusion Application"

J. L. Scott, F. W. Clinard, Jr., and F. W. Wiffen, "Special Purpose Materials for Fusion Application"

F. W. Wiffen, "Materials Engineering for TFCX and Other Near-Term Fusion Reactors"

31st National Symposium of the American Vacuum Society, Reno, Nevada, December 4–7, 1984. Proceedings published in *J. Vac. Sci. Technol. A* 3 (3), Pts. I and II (1985)

P. H. Edmonds, K. J. Dietz, P. K. Mioduszewski, R. D. Watson, L. C. Emerson, W. A. Gabbard, D. Goodall, J. E. Simpkins, and J. L. Yarber, "Technical Aspects of the Joint JET–ISX-B Limiter Experiment," p. 1100

R. A. Langley, P. M. Ryan, C. C. Tsai, M. M. Menon, E. M. Botnick, and C. W. Magee, "Measurement of Beam Species Mix and Beam Impurities in High-Power Neutral Beam Injectors," p. 1085

J. Sheffield for the ATF Team, "The Advanced Toroidal Facility," p. 1134

IEEE International Electron Devices Annual Meeting, San Francisco, California, December 9–12, 1984

K. Felch, R. Bier, L. Fox, H. Huey, L. Ives, H. Jory, and S. Spang, "Design Considerations for a 100 kW CW, 140 GHz Gyrotron Oscillator"

K. Felch, R. Bier, L. Fox, H. Huey, L. Ives, H. Jory, and S. Spang, "Development of a 140 GHz, 100 kW CW Gyrotron"

H. Jory, K. Felch, R. Bier, L. Fox, H. Huey, L. Ives, N. Lopez, J. Manca, J. Shively, and S. Spang, "A 60 GHz, 200 kW CW Gyrotron with High Output Mode Purity"

A. Salop and M. Caplan, "Computations of VSWR and Mode Conversion for Complex Gyrotron Window Geometries"

S. Spang, R. Feezell, L. Fox, and N. Lopez, "Cyclic Fatigue Reduction in Gyrotron Collectors"

American Society of Mechanical Engineers, Winter Meeting, New Orleans, December 10, 1984

P. N. Haubenreich, W. A. Fietz, W. H. Gray, R. K. Kibbe, and J. R. Miller, "Engineering Superconducting Magnet Systems for Fusion Reactors"

Seminar, Japan Atomic Energy Research Institute, Tokai-mura, Japan, December 10, 1984

P. J. Maziasz, "Radiation-Induced Precipitation Under Neutron Irradiation and Its Sensitivity"

Third U.S./Japan Workshop on High-Field Superconducting Materials for Fusion, Tsukuba, Japan, December 10–14, 1984

S. S. Shen, W. A. Fietz, and M. S. Lubell, "Progress Report of Advanced Conductor Development Program at ORNL"

Seminar, U.S. Department of Energy, Washington, D.C., December 13, 1984

D. E. Hastings, "Multiplicative Noise and the Radial Electric Field in a Nonaxisymmetric Torus"

ASME Annual Winter Meeting, New Orleans, Louisiana, December 10–14, 1985

P. N. Haubenreich, W. A. Fietz, W. H. Gray, R. K. Kibbe, and J. R. Miller, "Engineering Superconducting Magnet System for Fusion Reactors"

ICRH Workshop, Los Angeles, California, December 16–17, 1984

D. B. Batchelor, "ICRH on ATF, Experimental Plans and Theoretical Issues"

Cuarto Simposio Chileno de Fisica (Fourth Chilean Symposium of Physics), Santiago, Chile, December 26–28, 1984. Proceedings published by Universidad de Chile, Santiago, 1984.

W. A. Cooper and M. C. Depassier, "Helically Symmetric Magnetohydrodynamic Plasma Equilibrium," pp. 82–85

M. C. Depassier and W. A. Cooper, "Resistive Ballooning in Plasma Confinement Schemes with a Coordinate of Symmetry," pp. 86–88

REPORTS

ORNL Reports

ORNL-6015 *Fusion Energy Division Annual Progress Report for Period Ending December 31, 1983*
September 1984

ORNL-6052 *1982 Bibliography of Atomic and Molecular Processes*
C. F. Barnett, D. H. Crandall, H. B. Gilbody, D. C. Gregory, M. I. Kirkpatrick, E. W. McDaniel, R. H. McKnight, F. W. Meyer, T. J. Morgan, R. A. Phaneuf, M. S. Pindzola, and E. W. Thomas
April 1984

ORNL-6095 *1983 Bibliography of Atomic and Molecular Processes*
C. F. Barnett, D. H. Crandall, H. B. Gilbody, D. C. Gregory, M. I. Kirkpatrick, E. W. McDaniel, R. H. McKnight, F. W. Meyer, T. J. Morgan, R. A. Phaneuf, M. S. Pindzola, and E. W. Thomas
October 1984

ORNL Technical Memoranda

ORNL/TM-7906 *Observations of Low Frequency Plasma Fluctuations in ELMO Bumpy Torus*
A. Komori
October 1984

ORNL/TM-8851 *Electron Thermal Diffusivity in ISX-B from Observations of Sawtooth Oscillations*
J. D. Bell
March 1984

ORNL/TM-8924 *Options for an Ignited Tokamak*
J. Sheffield
March 1984

ORNL/TM-8985 *Reactor Assessments of Advanced Bumpy Torus Configurations*
N. A. Uckan, L. W. Owen, D. A. Spong, R. L. Miller, W. B. Ard, J. F. Pipkins, and R. J. Schmitt
February 1984

ORNL/TM-8994 *Alloy Development for Fast Induced Radioactivity Decay for Fusion Reactor Applications*
R. L. Klueh and E. E. Bloom
March 1984

ORNL/TM-9002 *Plasma Engineering Studies for Tennessee Tokamak (TENTOK) Fusion Power Reactor*
K. E. Yokoyama, J. T. Lacatski, J. B. Miller, W. E. Bryan, P. W. King, R. T. Santoro, T. E. Shannon, and N. A. Uckan
February 1984

ORNL/TM-9015 *Electron Transport in EBT in the Low Collision Frequency Limit*
D. E. Hastings
June 1984

ORNL/TM-9026 *An EBT Reactor Systems Analysis and Cost Code: Description and User's Guide (Version 1)*
R. T. Santoro, N. A. Uckan, J. M. Barnes, and D. E. Driemeyer
June 1984

ORNL/TM-9034 *A Technique for Measuring the Losses of Alpha Particles to the Wall in TFTR*
A. C. England
March 1984

ORNL/TM-9075 *Propagation and Absorption of Electromagnetic Waves in Fully Relativistic Plasmas*
D. B. Batchelor, R. C. Goldfinger, and H. Weitzner
May 1984

ORNL/TM-9083 *Calculated Neutron-Induced Cross Sections for $^{63,65}Cu$ from 1 to 20 MeV and Comparisons with Experiments*
D. M. Hetrick, C. Y. Fu, and D. C. Larson
August 1984

ORNL/TM-9090 *Feasibility of Alpha Particle Measurement by CO_2 Laser Thomson Scattering*
K. L. Vander Sluis, D. P. Hutchinson, C. H. Ma, and P. A. Staats
December 1984

ORNL/TM-9110 *ELMO Bumpy Square Status Report*
N. A. Uckan, C. L. Hedrick, D. A. Spong, T. Uckan, L. A. Berry, L. W. Owen, D. K. Lee, W. E. Bryan, T. J. McManamy, P. B. Thompson, and W. L. Wright
October 1984

ORNL/TM-9127 *The Reliability of Initial Value MHD Calculations of Tokamak Disruptions*
H. R. Hicks, B. A. Carreras, L. Garcia, and J. A. Holmes
June 1984

ORNL/TM-9128 *Comparison of Plasma Results in EBT-I and NBT-1M*
R. J. Colchin and J. C. Glowienka
July 1984

ORNL/TM-9133 *Accelerated Convergence of the Steepest Descent Method for Magnetohydrodynamic Equilibria*
C. R. Handy and S. P. Hirshman
June 1984

ORNL/TM-9147 *Equilibrium Calculations for Helical Axis Stellarators*
T. C. Hender and B. A. Carreras
April 1984

ORNL/TM-9148 *Nonlinear Interaction of Tearing Modes: A Comparison Between the Tokamak and the Reversed Field Pinch Configurations*
J. A. Holmes, B. A. Carreras, T. C. Hender, H. R. Hicks, V. E. Lynch, Z. G. An, and P. H. Diamond
April 1984

ORNL/TM-9175 *The EBT-S 28-GHz, 200-kW, cw, Mixed-Mode, Quasi-Optical Plasma Heating System*
T. L. White, H. D. Kimrey, T. S. Bigelow, D. D. Bates, and H. O. Eason
July 1984

ORNL/TM-9182 *Zero Current, High Beta Stellarator Equilibria with Rotational Transform Profile Control*
B. A. Carreras, H. R. Hicks, J. A. Holmes, V. E. Lynch, and G. H. Neilson
July 1984

ORNL/TM-9183 *A Numerical Model for Swirl Flow Cooling in High-Heat-Flux Particle Beam Targets and the Design of a Swirl-Flow-Based Plasma Limiter*
S. L. Milora, S. K. Combs, and C. A. Foster
November 1984

ORNL/TM-9185 *Magnetic Well Depth in EBT and Sensitivity to Hot Electron Ring Geometry*
E. F. Jaeger, L. A. Berry, C. L. Hedrick, and R. Richards
October 1984

ORNL/TM-9193 *Monte Carlo Studies of Transport in Tokamaks*
R. H. Fowler, J. F. Lyon, and J. A. Rome
August 1984

ORNL/TM-9026 *Stochastic Particle Losses in Velocity Space for EBT-S*
G. L. Chen, L. W. Owen, D. B. Batchelor, and C. L. Hedrick
August 1984

ORNL/TM-9201 *A Transient Waveform Acquisition System for the ELMO Bumpy Torus*
K. G. Young, R. D. Burris, D. L. Hillis, and D. R. Overbey
October 1984

ORNL/TM-9203 *ORACT: A 174-Neutron-Group Activation Cross-Section Library for Fusion and Fission Reactor Design Studies*
R. T. Santoro, J. E. White, and J. D. Drischler
June 1984

ORNL/TM-9206 *Stochastic Particle Losses in Velocity Space for EBT-S*
G. L. Chen, L. W. Owen, D. B. Batchelor, and C. L. Hedrick
August 1984

ORNL/TM-9210 *Electron Bounce Resonance Heating in a Bumpy Cylinder*
G. L. Chen
October 1984

ORNL/TM-9219 *Electrostatic Confinement in a Bumpy Torus*
A. M. El Nadi
November 1984

ORNL/TM-9230 *Calculations to Evaluate the Use of the Attenuation of D-D Neutrons in Liquid Oxygen as a Means of Measuring Plasma Ion Temperature*
R. G. Alsmiller, Jr., R. T. Santoro, J. F. Manneschmidt, and J. M. Barnes
July 1984

ORNL/TM-9239 *The Calculation of Stellarator Equilibria in Vacuum Flux Surface Coordinates*
T. C. Hender, B. A. Carreras, L. Garcia, J. A. Rome, and V. C. Lynch

ORNL/TM-9240 *Direct Reading Fast Microwave Interferometer for EBT*
T. Uckan
October 1984

ORNL/TM-9251 *Multigroup Energy-Angle Distributions for Neutrons from the $T(d,n)^4He$ Reaction (E_d = 100–400 eV)*
R. T. Santoro, J. M. Barnes, J. D. Drischler, and R. G. Alsmiller, Jr.
July 1984

ORNL/TM-9300 *Optimized Fourier Representations for Three-Dimensional Magnetic Surfaces*
S. P. Hirshman and H. K. Meier
November 1984

ORNL/TM-9302 *A Convergent Spectral Representation for Three-Dimensional Inverse MHD Equilibria*
S. P. Hirshman and H. Weitzner
October 1984

ORNL/TM-9306 *Magnetic Fluctuations, Field Reversal Maintenance, and Anomalous Thermal Transport in the Reversed Field Pinch*
P. H. Diamond, Z. G. An, M. N. Rosenbluth, B. A. Carreras, T. C. Hender, and J. A. Holmes
November 1984

ORNL/TM-9315 *Electron Temperature Measurements from Induced Toroidal Current in ELMO Bumpy Torus–Scale*
T. Uckan
December 1984

ORNL/TM-9319 *Inherent Magnetic Field Error Measurements in ELMO Bumpy Torus*
T. Uckan
December 1984

ORNL/TM-9351 *Theory and Calculation of Finite Beta Drift Wave Turbulence*
C. O. Beasley, Jr., K. Molvig, J. P. Freidberg, and W. I. van Rij
October 1984

ORNL/TM-9471 *Thomson Scattering on ELMO Bumpy Torus*
J. A. Cobble
December 1984

ORNL Computer Services Division Reports

ORNL/CSD/INF-84/2 *NITHLP: Structure for the DEC-10 HELP Files*
M. E. Jordan and A. C. Johnson

ORNL Fusion Engineering Design Center Reports

ORNL/FEDC-83/8 *Inductive Current Startup in Large Tokamaks with Expanding Minor Radius and RF Assist*
S. K. Borowski
February 1984

ORNL/FEDC-83/10 *Equilibrium Modeling of the TFCX Poloidal Field Coil System*
D. J. Strickler, J. B. Miller, K. E. Rothe, and Y-K. M. Peng
May 1984

ORNL/FEDC-83/11 *Analysis of Tandem Mirror Reactor Performance*
K. F. Wu, R. B. Campbell, and Y-K. M. Peng
November 1984

ORNL/FEDC-83/14 *Two-Point Model for Divertor Transport*
J. D. Galambos and Y-K. M. Peng
April 1984

ORNL/FEDC-84/1 *Plasma Performance of TFCX and JET with Sawtoothing*
L. M. Hively and D. R. Mikkelsen
November 1984

ORNL/FEDC-84/2 *Engineering Analysis of TFTR Disruption*
J. G. Murray, K. E. Rothe, and G. Bronner
September 1984

ORNL/FEDC-84/3 *Tokamak Fusion Core Experiment: Design Studies Based on Superconducting and Hybrid Toroidal Field Coils—Design Overview*
C. A. Flanagan
October 1984

Reports Prepared by ORNL Subcontractors

ORNL/Sub-7676/4,5, University of Missouri, Rolla
Research Support for Plasma Diagnostics on ELMO Bumpy Torus
No. 4: *Development of a Multichannel Hall-Probe Based Diamagnetic Diagnostic Instrument and Observation and Modeling of EBT Electron Rings*
K. H. Carpenter and R. H. Booker
No. 5: *Diamagnetic Measurements and Data Analysis, and Development of Ring Models for Realistic Representation of Fields Near the Plasma*
K. H. Carpenter and R. F. Steimle

ORNL/Sub-79/21453/16–19, Varian Associates, Inc., Palo Alto, Calif.
60 GHz Gyrotron Development Program Quarterly Reports
No. 16: April through June, 1983
No. 17: July through September, 1983
No. 18: October through December, 1983
No. 19: January through March, 1984
H. R. Jory et al.

ORNL/Sub-79/33200/15–17, Hughes Aircraft Co., Torrance, Calif.
Development Program for a 200-kW cw Gyrotron: Quarterly Reports
No. 15: January through March, 1983
No. 16: April through June, 1983
No. 17: July through August, 1983
W. J. DeHope et al.

ORNL/Sub-83/51926/1, Rockwell International Science Center, Thousand Oaks, Calif.
Millimeter Wave Dielectric Property Measurement of Gyrotron Window Materials
W. W. Ho

ORNL/Sub-83/59396/1, Raytheon Co., Waltham, Mass.
1 Megawatt, 100 GHz Gyrotron Study
N. Dionne, R. Mallavarpu, and A. Palevsky

Conference Proceedings Published by ORNL

CONF-840370 *Proceedings of the Workshop: U.S.-Japan Theory Workshop on 3-D MHD Studies*
B. A. Carreras, ed.
May 1984

Reports Published by Other Institutions

DOE/ER-0113/3	*Sixth Annual Progress Report on Special Purpose Materials for Magnetically Confined Fusion Reactors* J. L. Scott, comp. and ed. U.S. Department of Energy, Washington, D.C., May 1984
GTFR-47	*Rotation and Impurity Transport in a Tokamak Plasma with Directed Neutral Beam Injection* W. M. Stacey and D. J. Sigmar Georgia Institute of Technology, Atlanta, 1984
IFSR-116	*Theory of Anomalous Tearing Mode Growth and Major Tokamak Disruptions* P. H. Diamond, R. D. Hazeltine, Z. G. An, B. A. Carreras, and H. R. Hicks Institute for Fusion Studies, University of Texas, Austin, January 1984
IFSR-146	*Theory of Resistivity Gradient Driven Turbulence* L. Garcia, B. A. Carreras, P. H. Diamond, and J. D. Callen Institute for Fusion Studies, University of Texas, Austin, October 1984
MDC E2805	*ELMO Bumpy Torus Physics—Final Report* McDonnell Douglas Astronautics Company, August 1984
PFC/CP-84/12	*Confinement Results from Pellet Fueled Discharges in Alcator-C* M. Greenwald, D. Gwinn, S. Milora, J. Parker, R. Parker, S. Wolfe, M. Besen, F. Camacho, S. Fairfax, and C. Fiore Plasma Fusion Center, Massachusetts Institute of Technology, May 1984
PPG-765	*Technical Assessment of the Critical Issues and Problem Areas in the Plasma Materials Interactions Field* R. W. Conn et al., eds. ORNL contributors: H. Howe, J. Roberto, P. Mioduszewski, and C. C. Tsai Center for Plasma Physics and Fusion Engineering, University of California at Los Angeles, January 1984
PPPL-2175	*Particle Fueling and Impurity Control in PDX* R. J. Fonck, M. Bell, K. Bol, R. Budny, P. Couture, D. Darrow, H. Dylla, R. Goldston, B. Grek, R. Hawryluk, K. Ida, K. Jaehnig, D. Johnson, R. Kaita, S. Kaye, H. Kugel, B. LeBlanc, D. Mansfield, T. McBride, K. McGuire, S. Milora, D. Mueller, M. Okabayashi, D. Owens, D. Post, M. Reusch, G. Schmidt, S. Sesnic, H. Takahashi, F. Tenney, and M. Ulrickson Princeton Plasma Physics Laboratory, December 1984

THESES AND DISSERTATIONS

L. R. Baylor, "Microwave Scattering as a Plasma Diagnostic in a Penning Discharge," M.S., Electrical Engineering, the University of Tennessee, Knoxville

S. K. Borowski, "Inductive Current Startup in Large Tokamaks with Expanding Minor Radius and RF Assist," Ph.D., Nuclear Engineering, University of Michigan, Ann Arbor

M. J. Gouge, "Alpha-Driven Currents in Tokamak Reactors," the University of Tennessee, Knoxville

J. Mathew, "Investigation of the Electric Field Structure in Neutral Beam Heated ISX-B Plasmas," Ph.D., Electrical Engineering, Rensselaer Polytechnic Institute, Troy, New York

J. S. Tolliver, "Bounce-Averaged Monte Carlo Energy and Pitch Angle Scattering Operators," Ph.D., the University of Tennessee, Knoxville

A. L. Wintenberg, "An Instrument to Synchronize Thomson Scattering Diagnostic Measurements with MHD Activity in a Tokamak," M.S., the University of Tennessee, Knoxville

K. E. Yokoyama, "An Experimental Investigation of the Plasma Properties of the ISX-B Tokamak Using Multiple Langmuir Probes," M.S., Nuclear Engineering, the University of Tennessee, Knoxville

Appendix 3

FUSION ENERGY DIVISION ORGANIZATION CHART

ORNL-DWG 85-2482R FED

FUSION ENERGY DIVISION

MARCH 1, 1985

O. B. MORGAN, DIRECTOR
Z. S. BUCHANAN*
A. J. KING

QUALITY ASSURANCE
E. J. BYRNES
G. F. BOWLES*
C. M. JORDAN

SAFETY AND EMERGENCY PLANNING
E. R. WELLS*
G. F. BOWLES*

AFFIRMATIVE ACTION
R. P. JERNIGAN, JR.*
C. H. JORDAN* (ALTERNATE)

MANAGEMENT SERVICES SECTION
V. C. KRUZIC[1]
B. J. BEEM

GENERAL ADMINISTRATION AND PROCUREMENT
R. P. JERNIGAN, JR.*
J. R. JERNIGAN[2]
L. A. POLLARD[2]
M. A. VORNEHM[2]

PROCUREMENT
J. L. BURKE
S. K. ADKINS
P. L. RAY
G. G. SHEARIN

ENGINEERING SERVICES
E. R. WELLS*
B. L. STRAINE
D. R. ALFORD
H. W. JERNIGAN
W. K. RUSSELL
D. P. BROOKS
C. K. THOMAS

FINANCE OFFICE
T. H. SRADY[3]
R. P. JERNIGAN, JR.*
M. V. DUNN*
C. H. JORDAN*
M. J. OWENS
E. N. PATTERSON
E. M. RUCKART

LIBRARY
T.-C. LIU[4]
E. E. WEBSTER[2,4]

FED REPORTS OFFICE
A. S. TRAVIS*[,4]

EDITING
A. S. TRAVIS*[,4]
M. R. HALL[4]
M. N. JOHNSON

GRAPHICS
J. C. PARROTT[4]
M. W. DARNELL[4]
C. H. JOHNSON[4]
J. C. NEELEY[4]
S. R. SCHWARTZ[4]
S. S. SCOTT[2,4]
P. A. SUMNER[4]

WORD PROCESSING
E. L. CAGLE[4]
K. M. DOBBS[4]
D. Y. JOHNSON[4]
B. J. SMITH[4]

ADMINISTRATION
B. J. WILLIAMS[4]
D. G. SHARP–XEROX

ASSOCIATE DIVISION DIRECTOR FOR CONFINEMENT
J. SHEFFIELD
G. ROBINSON

TOROIDAL CONFINEMENT PHYSICS SECTION
J. L. DUNLAP*
D. L. AKERS
J. F. LYON*
O. V. JETT

TFTR COLLABORATION
J. L. DUNLAP*
M. MURAKAMI
C. E. BUSH
R. J. COLCHIN
L. C. EMERSON[5]
A. C. ENGLAND
R. R. KINDSFATHER
R. A. LANGLEY
C. H. MA[6]
V. K. PARÉ[7]
D. A. RASMUSSEN
R. K. RICHARDS
J. E. SIMPKINS
C. E. THOMAS
J. B. WILGEN

ATF PHYSICS
J. L. DUNLAP*
A. CARNEVALI[8]
W. R. WING
A. J. WOOTTON
R. C. ISLER
J. C. GLOWIENKA
S. HIROE
E. A. LAZARUS
J. F. LYON*
J. H. HARRIS

U. S.–SPAIN COLLABORATION
J. F. LYON*
J. P. BOTIJA[9]
A. F. LOPEZ*[,9]
R. G. MARTIN[9]
A. A. PUEBLAS[9]

CONFINEMENT PROJECTS SECTION
M. J. SALTMARSH
A. D. GUTTERY

ATF PROJECT
T. C. JERNIGAN
K. L. WARREN

ATF OPERATIONS
P. H. EDMONDS
G. H. NEILSON
D. D. BATES[7]
G. R. DYER
W. A. GABBARD
G. H. HENKEL
L. A. MASSENGILL
T. F. RAYBURN
J. L. YARBER

PLASMA–MATERIALS INTERACTIONS
P. K. MIODUSZEWSKI
R. A. FORTNER
R. E. CLAUSING[5]
D. L. HILLIS
P. W. KING
T. UCKAN
R. A. ZUHR[10]

ADVANCED STUDIES
N. A. UCKAN

PLASMA THEORY SECTION
R. A. DORY
C. L. HEDRICK*
D. J. SIGMAR*[,11]
G. M. WARREN
J. F. COX
D. J. TATE
N. Y. WRIGHT[2]

TOROIDAL AND ALTERNATE CONFINEMENT THEORY
B. A. CARRERAS
J. D. CALLEN[12]
W. A. COOPER
P. H. DIAMOND[13]
L. GARCIA
T. C. HENDER
A. F. LOPEZ*[,9]
E. RODRIGUEZ-SOLANO[9]
J. A. ROME
K. C. SHAING

C. L. HEDRICK*
D. B. BATCHELOR
D. E. HASTINGS
E. F. JAEGER
D. A. SPONG
H. WEITZNER[14]

D. J. SIGMAR*[,11]
C. O. BEASLEY
E. C. CRUME
J. P. FRIEDBERG[15]
S. P. HIRSHMAN
J. F. HOGAN
W. A. HOULBERG
H. C. HOWE
K. MOLVIG[15]
W. A. STACEY[16]

COMPUTING
J. W. WOOTEN[17]
H. E. KETTERER
D. R. OVERBEY
K. A. STEWART
G. B. WOOTTON
K. G. YOUNG
J. V. HUGHES
E. J. HAWN[18]

ASSOCIATE DIVISION DIRECTOR FOR DEVELOPMENT AND TECHNOLOGY
L. A. BERRY
J. C. McGILL

PLASMA TECHNOLOGY SECTION
H. H. HASELTON
P. F. RICE
D. W. SWAIN*
N. S. BRYSON

PROGRAM DEVELOPMENT
W. R. BECRAFT*[,19]

PARTICLE BEAM DEVELOPMENT
W. L. STIRLING
K. L. MAYS

ION SOURCE DEVELOPMENT
C. C. TSAI*
W. K. DAGENHART
G. G. KELLEY[20]
R. K. KIBBE*
M. M. MENON
D. E. SCHECHTER*
S. C. FORRESTER*

TECHNOLOGY MODELING
J. H. WHEALTON
G. L. CHEN

ELECTRICAL ENGINEERING
G. C. BARBER
N. S. PONTE[20]
R. E. WRIGHT
D. O. SPARKS

RF PLASMA HEATING
D. W. SWAIN*

ICH DEVELOPMENT
W. R. BECRAFT*[,19]
D. J. HOFFMAN
T. L. OWENS[21]
P. M. RYAN*
D. E. SCHECHTER*
C. C. TSAI*
S. C. FORRESTER*
F. SLUSS

ICH APPLICATIONS
F. W. BAITY
K. W. PRINCE[21]

GYROTRON DEVELOPMENT
G. R. HASTE
P. A. HOLLIDAY
H. D. KIMREY*

ECH DEVELOPMENT AND APPLICATIONS
T. L. WHITE
D. D. BATES[7]
T. S. RIGELOW
H. D. KIMREY*

RFTF PROJECT
H. C. McCURDY
W. L. GARDNER
J. A. MOELLER[19]
P. M. RYAN*
R. L. LIVESEY

PLASMA FUELING
S. L. MILORA
P. P. HELTON

TPI PROJECT

PELLET FUELING DEVELOPMENT
S. K. COMBS
C. A. FOSTER*
D. D. SCHURESKO*
C. R. FOUST

PELLET FUELING APPLICATIONS
C. A. FOSTER*
D. D. SCHURESKO*

MAGNETICS AND SUPERCONDUCTIVITY SECTION
M. S. LUBELL*
S. F. VAUGHAN*

ANALYTICAL
L. DRESNER*
J. N. LUTON*

EXPERIMENTAL
R. L. BROWN
J. F. ELLIS*
J. W. LUE*
S. W. SCHWENTERLY*
S. S. SHEN*
W. J. KENNEY*

LARGE COIL PROGRAM
P. N. HAUBENREICH
K. L. ZELL
M. S. LUBELL*
S. F. VAUGHAN*

TEST COILS
R. K. KIBBE*

LCTF INSTALLATION AND MAINTENANCE
R. E. BOHANAN
R. E. WINTENBERG[7]
J. P. RUDD

LCTF OPERATIONS
W. A. FIETZ
L. S. SCRUGGS
J. F. ELLIS*
S. W. SCHWENTERLY*
R. E. STAMPS
R. D. DONALDSON
D. T. FEHLING
R. L. HENDREN
D. L. JAMES
W. J. KENNEY*
J. C. KIGGANS
M. W. McGOFFIN
J. N. MONEY
T. C. PATRICK
W. J. REDMOND
L. RIESTER
C. R. SCHAICH
B. C. SMITH
C. A. WALLACE

COIL TESTING AND ANALYSIS
M. S. LUBELL*
S. F. VAUGHAN*
J. N. LUTON*
J. A. CLINARD[22]
L. DRESNER*
K. KOIZUMI[23]
J. W. LUE*
S. S. SHEN*
G. R. ZAHN[24]
J. A. ZICHY[25]

FUSION ENGINEERING DESIGN CENTER
T. E. SHANNON[26]
L. C. CALDWELL[26]

ADMINISTRATION
M. V. DUNN

PLASMA ENGINEERING
Y-K. M. PENG
M. E. TALLEY
R. J. BARRETT[27]
D. T. BLACKFIELD[28]
S. K. BOROWSKI
R. L. DALTON[29]
J. D. GALAMBOS[17]
M. T. GAMBLE[20]
J. B. MILLER[5]
R. L. REID[20]
P. J. STEVENS[8]
D. J. STRICKLER[17]

SYSTEMS ENGINEERING
T. G. BROWN[19]
L. S. DALE
M. K. BULLOCK[30]
G. T. BUSSELL[31]
A. DABIRI[32]
P. J. FOGARTY[26]
M. H. KONSELMAN[26]
D. C. LOUSTEAU[26]
B. W. RIEMER[19]
E. C. SELCOW[19]
P. T. SPAMPINATO[19]

NUCLEAR COMPONENT DESIGN
J. R. HAINES[21]
N. R. IRBY
V. G. LEE[21]
G. E. TAYLOR[21]
F. W. WIFFEN[5]

ELECTRICAL AND MAGNET SYSTEMS
W. D. NELSON*[,20]
P. A. POWELL
G. E. GORKER[19]
S. S. KALSI[19]
J. J. YUGO[22]

MIRROR PROJECTS
W. D. NELSON*[,28]

TOKAMAK PROJECTS
C. A. FLANAGAN[33]

COMMERCIAL APPLICATIONS
S. L. THOMSON[34]
W. R. HAMILTON[26]
D. C. KEETON[35]

* DUAL CAPACITY
[1] DIVISION TECHNOLOGY UTILIZATION OFFICER
[2] PART–TIME
[3] FINANCE AND MATERIALS DIVISION
[4] INFORMATION RESOURCES ORGANIZATION
[5] METALS AND CERAMICS DIVISION
[6] PHYSICS DIVISION
[7] INSTRUMENTATION AND CONTROLS DIVISION
[8] THE UNIVERSITY OF TENNESSEE
[9] JUNTA DE ENERGIA NUCLEAR, MADRID, SPAIN
[10] SOLID STATE DIVISION
[11] LEAVE OF ABSENCE
[12] UNIVERSITY OF WISCONSIN
[13] UNIVERSITY OF TEXAS
[14] NEW YORK UNIVERSITY
[15] MASSACHUSETTS INSTITUTE OF TECHNOLOGY
[16] GEORGIA INSTITUTE OF TECHNOLOGY
[17] COMPUTING AND TELECOMMUNICATIONS DIVISION
[18] CO–OP, UNIVERSITY OF TENNESSEE
[19] GRUMMAN AEROSPACE CORPORATION
[20] CONSULTANT
[21] McDONNELL DOUGLAS ASTRONAUTICS CORPORATION
[22] ENGINEERING TECHNOLOGY DIVISION
[23] JAPAN ATOMIC ENERGY RESEARCH INSTITUTE, TOKAI, JAPAN
[24] KERNFORSCHUNGSZENTRUM KARLSRUHE, KARLSRUHE, FRG
[25] SWISS INSTITUTE FOR NUCLEAR RESEARCH, VILLIGEN, SWITZERLAND
[26] MECHANICAL ENGINEERING DIVISION
[27] BURNS AND ROE
[28] TRW, INC.
[29] UNIVERSITY OF FLORIDA
[30] AMERICAN TECHNICAL ASSOCIATES
[31] STONE AND WEBSTER
[32] SCIENCE APPLICATIONS INTERNATIONAL CORPORATION
[33] WESTINGHOUSE ELECTRIC CORPORATION
[34] BECHTEL NATIONAL GROUP, INC.
[35] ELECTRIC POWER RESEARCH INSTITUTE

ORNL-6111
Dist. Category UC-20

INTERNAL DISTRIBUTION

1. D. R. Alford
2–6. R. G. Alsmiller, Jr.
7. S. E. Attenberger
8. F. W. Baity
9. G. C. Barber
10. C. F. Barnett
11. R. J. Barrett
12. D. B. Batchelor
13. D. D. Bates
14. C. O. Beasley, Jr.
15. W. R. Becraft
16. M. A. Bell
17–21. L. A. Berry
22. T. S. Bigelow
23. D. T. Blackfield
24. E. T. Blair
25–29. E. E. Bloom
30. G. F. Bowles
31. S. K. Borowski
32. T. H. Brady
33. R. A. Brown
34. R. L. Brown
35. T. G. Brown
36. R. D. Burris
37. C. E. Bush
38. G. T. Bussell
39. E. J. Byrnes
40. J. B. Cannon
41. B. A. Carreras
42. W. A. Casson
43. L. A. Charlton
44. G. L. Chen
45. D. N. Clark
46. R. E. Clausing
47. R. J. Colchin
48. R. R. Coltman, Jr.
49. S. K. Combs
50. T. B. Cook
51. W. A. Cooper
52. E. C. Crume, Jr.
53. A. Dabiri
54. W. K. Dagenhart
55. L. Deleanu
56. K. M. Dobbs
57–61. R. A. Dory
62. L. Dresner
63–67. J. L. Dunlap
68. M. V. Dunn
69. G. R. Dyer
70. P. H. Edmonds
71. J. F. Ellis
72. L. C. Emerson
73. A. C. England
74. J. R. Engel
75. C. A. Flanagan
76. S. C. Forrester
77. C. A. Foster
78. C. R. Foust
79. R. H. Fowler
80. W. A. Gabbard
81. J. D. Galambos
82. L. Garcia
83. W. L. Gardner
84. J. C. Glowienka
85. R. C. Goldfinger
86. G. E. Gorker
87. J. R. Goyer
88. D. E. Greenwood
89. D. C. Gregory
90. M. L. Grossbeck
91. J. R. Haines
92. W. R. Hamilton
93. C. E. Hammons
94. J. H. Harris
95–99. H. H. Haselton
100. G. R. Haste
101–105. P. N. Haubenreich
106. C. L. Hedrick
107. H. R. Hicks
108. D. L. Hillis
109. S. Hiroe
110. S. P. Hirshman
111. D. J. Hoffman
112. J. T. Hogan
113. J. A. Holmes
114. W. A. Houlberg

115. H. C. Howe, Jr.
116. R. C. Isler
117. E. F. Jaeger
118. D. W. Jared
119. G. R. Jasny
120. H. W. Jernigan
121. T. C. Jernigan
122–126. M. N. Johnson
127. R. L. Johnson
128. L. M. Jordan
129. K. L. Kannan
130. W. J. Kenney
131. S. S. Kalsi
132. H. E. Ketterer
133. R. K. Kibbe
134–143. S. G. Kimmett
144. H. D. Kimrey
145. R. R. Kindsfather
146. P. W. King
147–151. V. C. Kruzic
152. R. A. Langley
153. E. A. Lazarus
154. D. K. Lee
155. R. L. Livesey
156–160. M. S. Lubell
161. J. W. Lue
162. J. N. Luton, Jr.
163. V. E. Lynch
164. J. F. Lyon
165. F. C. Maienschein
166. T. L. Mann
167. W. L. Marsh
168. H. C. McCurdy
169. R. W. McGaffey
170. J. R. McGuffey
171. F. W. Meyer
172. S. L. Milora
173–177. P. K. Mioduszewski
178. J. A. Moeller
179–183. O. B. Morgan
184. R. N. Morris
185. J. K. Munro, Jr.
186. M. Murakami
187. G. H. Neilson
188. B. E. Nelson
189. W. D. Nelson
190. S. Y. Ohr
191. D. R. Overbey
192. L. W. Owen
193. V. K. Paré
194–195. J. C. Parrott
196. F. S. Patton
197. Y-K. M. Peng
198. R. A. Phaneuf
199–208. J. J. Pinajian
209. H. Postma
210. K. W. Prince
211. D. A. Rasmussen
212. J. A. Ray
213. W. J. Redmond
214. R. L. Reid
215. R. K. Richards
216. B. W. Riemer
217. J. A. Rome
218. M. W. Rosenthal
219. R. W. Roussin
220. P. M. Ryan
221–225. M. J. Saltmarsh
226. R. T. Santoro
227. D. E. Schechter
228. D. D. Schuresko
229. K. C. Shaing
230–234. T. E. Shannon
235–239. J. Sheffield
240. S. S. Shen
241. D. J. Sigmar
242. J. E. Simpkins
243. D. A. Spong
244. K. A. Stewart
245. W. L. Stirling
246. D. J. Strickler
247. D. W. Swain
248. C. E. Thomas, Jr.
249. S. L. Thomson
250. P. B. Thompson
251. J. S. Tolliver
252. A. S. Travis
253. C. C. Tsai
254. T. C. Tucker
255. N. A. Uckan
256. T. Uckan
257. W. I. van Rij
258. J. S. Watson
259. E. R. Wells
260. J. H. Whealton
261. J. A. White

262. J. C. Whitson
263. F. W. Wiffen
264. J. B. Wilgen
265. M. K. Wilkinson
266. W. R. Wing
267. R. E. Wintenberg
268. J. W. Wooten
269. R. E. Wright
270. W. L. Wright
271. R. B. Wysor
272. J. L. Yarber
273. S. Zinkle
274. R. A. Zuhr
275–276. Laboratory Records Department
277. Laboratory Records, ORNL-RC
278. Document Reference Section
279. Central Research Library
280–281. Fusion Energy Division Library
282–286. Fusion Energy Division Publications Office
287. ORNL Patent Office

EXTERNAL DISTRIBUTION

U.S. Department of Energy, Oak Ridge Operations Office, P.O. Box E, Oak Ridge, TN 37831

288. Office of Assistant Manager for Energy Research and Development

Office of Fusion Energy, Mail Station G-256, U.S. Department of Energy, Washington, DC 20545

289. D. S. Beard
290. S. E. Berk
291. R. A. Blanken
292. M. Cohen
293. D. H. Crandall
294. V. Der
295. W. F. Dove
296. S. A. Eckstrand
297. T. V. George
298. G. M. Haas
299. T. R. James
300. A. Katz
301. S. W. Luke
302. G. R. Nardella
303. E. Oktay
304. A. Opdenaker
305. R. E. Price
306. T. C. Reuther
307. W. Sadowski
308. H. S. Staten
309. P. M. Stone
310. J. M. Turner
311. J. W. Willis

Princeton Plasma Physics Laboratory, P.O. Box 451, Princeton, NJ 08544

312. K. Bol
313. T. K. Chu
314. H. P. Eubank
315. J. File
316. R. B. Fleming
317. J. W. French
318. R. J. Goldston
319. K. W. Hill
320. J. C. Hosea
321. S. Kaye
322. D. M. Meade
323. R. G. Mills
324. P. H. Rutherford
325. J. Schmidt
326. T. H. Stix
327. S. Yoshikawa

GA Technologies, Inc., P.O. Box 81608, San Diego, CA 92138

328. J. Alcorn
329. R. L. Freeman
330. J. Gilliland
331. M. P. Hacker
332. R. Harder
333. G. L. Jahns
334. A. Kitsunezaki, JAERI Group
335. C. H. Muller
336. D. Overskei
337. J. R. Purcell
338. T. Tamano
339. S. K. Wong

Massachusetts Institute of Technology, 77 Massachusetts Ave., Cambridge, MA 02139

340. G. Bekefi
341. D. R. Cohn
342. J. P. Freidberg
343. M. O. Hoenig
344. L. M. Lidsky
345. J. E. McCune
346. F. S. McDermott
347. K. Molvig
348. D. B. Montgomery
349. R. R. Parker
350. P. A. Politzer
351. D. J. Rose
352. J. Schultz
353. R. J. Thome
354. J. E. Tracey

Los Alamos National Laboratory, P.O. Box 1663, Los Alamos, NM 87545

355. J. L. Anderson
356. R. A. Krakowski
357. R. K. Linford
358. J. D. Rogers

McDonnell Douglas Astronautics Company, P.O. Box 516, St. Louis, MO 63166

359. W. D. Ard
360. R. J. DeBellis
361. D. A. DeFreece

National Bureau of Standards, Boulder, CO 80302

362. V. D. Arp
363. A. Clark
364. G. H. Dunn, JILA
365. A. V. Phelps, JILA
366. F. R. Fickett

Lawrence Livermore National Laboratory, P.O. Box 5511, Livermore, CA 94550

367. D. Baldwin
368. C. D. Henning
369. L. D. Pearlstein
370. R. F. Post
371. K. Thomassen

Bechtel Group, Inc., P.O. Box 3965, San Francisco, CA 94119

372. W. O. Allen
373. E. von Fischer
374. H. K. Forsen

Sandia National Laboratories, P.O. Box 5800, Albuquerque, NM 87185

375. W. J. Davis
376. W. B. Gauster, Div. 1837
377. D. M. Mattox, Div. 5834
378. A. W. Mullendore
379. F. L. Vook
380. J. B. Whitley

University of Texas, Austin, TX 78712

381. H. L. Berk, IFS
382. K. W. Gentle, Department of Physics
383. M. N. Rosenbluth, IFS
384. H. H. Woodson, Dept. of Electrical Engineering
385. A. J. Wootton

General Dynamics–Convair Division, P.O. Box 85377, San Diego, CA 92138

386. R. F. Beuligmann
387. D. S. Hackley
388. R. A. Johnson, MZ 16-1070
389. R. E. Tatro

Grumman Aerospace Corporation, Bethpage, NY 11714

390. R. Botwin
391. J. W. Coursen
392. R. J. Gran
393. C. von Keszycki
394. M. L. Rossi
395. F. Thomas

Naval Research Laboratory, Washington, DC 20375

396. K. R. Chu
397. V. L. Granatstein
398. B. Hui
399. J. Mathew
400. M. E. Read

Westinghouse Electric Corporation, Advanced Reactors Division, P.O. Box 158, Madison, PA 15663

401. A. Anderson
402. G. G. Gibson

Westinghouse Electric Corporation, 700 Braddock Avenue, East Pittsburgh, PA 15112

403. S. K. Singh

Rensselaer Polytechnic Institute, Troy, NY 12181

404. G. A. Hallock
405. R. L. Hickok
406. J. C. Jennings
407. D. Steiner

Electric Power Research Institute, P.O. Box 10412, Palo Alto, CA 94303

408. F. L. Culler
409. F. R. Scott

Pacific Northwest Laboratories, Battelle Boulevard, P.O. Box 999, Richland, WA 99352

410. D. A. Dingee
411. B. Gore
412. L. L. Schmid

University of Wisconsin, Madison, WI 53706

413. J. D. Callen
414. J. R. Conrad
415. D. W. Kerst
416. D. C. Larbalestier
417. J. L. Shohet
418. J. C. Sprott
419. J. Tataronis

Georgia Institute of Technology, Atlanta, GA 30332

420. J. N. Davidson
421. R. Feeney
422. T. G. Heil
423. W. M. Stacey
424. E. W. Thomas

TRW, Inc., 1 Space Park, Redondo Beach, CA 92078

425. J. Lassoon
426. N. H. Lazar
427. J. A. Maniscalco
428. K. E. Yokoyama

EG&G ORTEC, 100 Midland Road, Oak Ridge, TN 37830

429. J. Ayers
430. D. A. Gedcke

Courant Institute for Mathematical Sciences, New York University, 251 Mercer Street, New York, NY 10012

431. H. Grad
432. H. Weitzner

Oak Ridge Associated Universities, P.O. Box 117, Oak Ridge, TN 37831

433–512. J. M. Haffey, Information Services
513. A. M. Weinberg, IEA
514. University Programs Department
515. Institute for Energy Analysis

The University of Tennessee, Knoxville, TN 37916

516. I. Alexeff, Dept. of Electrical Engineering
517. E. G. Harris, Dept. of Physics
518. J. R. Roth, Dept. of Electrical Engineering
519. J. Smith, Dept. of Mathematics
520. P. N. Stevens, Dept. of Nuclear Engineering

Denison University, Granville, OH 43032

521. W. A. Hoffman
522. R. R. Winters

Auburn University, Auburn, AL 36830

523. R. Kreibel, Dept. of Physics
524. M. S. Pindzola, Dept. of Physics
525. G. Swanson

Brookhaven National Laboratory, Upton, NY 11973

526. K. Prélec
527. P. J. Reardon

Magnetics Corporation of America, 179 Bear Hill Road, Waltham, MA 02154

528. E. J. Lucas
529. Z. J. J. Stekly
530. B. P. Strauss

Atlanta University, Atlanta, GA 30314

531. C. R. Handy
532. R. E. Mickens

Australian National University, P.O. Box 4, Canberra, A.C.T. 2000, Australia

533. S. M. Hamberger, Institute for Advanced Studies
534. Plasma Research Laboratory

International Centre for Theoretical Physics, Trieste, Italy

535. A. M. Hamende
536. Library

Centre des Récherches en Physique des Plasmas, Ecole Polytechnique de Lausanne, 21 Avenue des Bains, 1007 Lausanne, Switzerland

537. Bibliothèque
538. F. Troyon

Centre d'Etudes Nucléaires, B.P. No. 85, Grenoble, France

539. G. Briffod
540. Documentation SIGN, Departement de la Physique du Plasma et de la Fusion Controllée

Laboratorio Nazionali, C.P. 70, 00044 Frascati (Roma), Italy

541. N. Sacchetti
542. G. Sacerdoti
543. M. Spadoni

Commissariat a l'Energie Atomique, B.P. No. 6, 92 Fontenay-aux-Roses, France

Service du Confinement des Plasmas

544. Bibliothèque
545. F. Prevot

Service des Récherches sur la Fusion Controllée

546. P. Hubert
547. C. Mercier
548. J. Tachon
549. M. Trocheris

CEN/Saclay, B.P. No. 2, F-91190 Gif-sur-Yvette, France

550. H. Desportes, STIPE
551. J. C. Lottin

Plasma Research Center, University of Tsukuba, Sakura, Niihari, Ibaraki 305, Japan

552. Y. Kiwamoto
553. S. Miyoshi

Laboratorio Gas Ionizzati, C.P. 65, 00044 Frascati (Roma), Italy

554. H. E. Knoepfel
555. Library

Institute of Plasma Physics, Nagoya University, Nagoya 464, Japan

556. T. Amano
557. M. Fujiwara
558. K. Husimi
559. H. Ikegami
560. Research Information Center
561. K. Takayama
562. D. T. Uchida
563. Library

Japan Atomic Energy Research Institute, Tokai Research Establishment, Tokai, Ibaraki 319-11, Japan

564. M. Azumi
565. S. Kasai
566. M. Nozawa
567. S. Shimamoto
568. K. Shiraishi
569. M. P. Tanaka
570. Thermonuclear Library

KFA Jülich, Postfach 1913, D-5170 Jülich 1, Federal Republic of Germany

571. Bibliothek
572. H. Conrads
573. E. Hintz
574. A. Rogister
575. B. Schweer
576. F. Wälbröck

FOM-Instituut voor Plasmafysica, Edisonbaan 14, NL-3430 Nieuwegein, the Netherlands

577. C. M. Braams
578. Library

Max-Planck-Institut für Plasmaphysik, D-8046 Garching, Federal Republic of Germany

579. Bibliothek
580. G. von Gierke
581. G. Grieger
582. J. Junker
583. M. Kaufman
584. M. Keilhacker
585. A. Knobloch
586. R. Lengye
587. L. L. Lengyel
588. A. Martinelli
589. D. Pfirsch
590. K. Pinkau
591. M. Salvat
592. A. Schlüter
593. K. Schmitter
594. R. Toschi

Kernforschungszentrum Karlsruhe GmbH, Postfach 3640, D-7500 Karlsruhe 1, Federal Republic of Germany

595. O. Hagena
596. W. Klose
597. P. Komarek
598. A. Ulbricht
599. J. E. Vetter

Plasma Physics Laboratory, Kyoto University, Gokasho, Uji, Kyoto 611, Japan

600. Library
601. K. Uo
602. M. Wakatani

JET Group, Culham Laboratory, Abingdon, Oxon OX14 3DB, England

603. R. J. Bickerton
604. K. J. Dietz
605. A. Gibson
606. P. H. Rebut

UKAEA, Culham Laboratory, Abingdon, Oxon OX14 3DB, England

607. J. G. Cordey
608. R. Hancox
609. T. C. Hender
610. Library
611. M. Lomer
612. R. S. Pease
613. T. E. Stringer
614. J. B. Taylor
615. E. Thompson

Division de Fusion, Junta de Energia Nuclear, Avenida Complutense 22, Madrid (3), Spain

616. A. Perez Navarro
617. M. Soler
618. B. Zurro

Department of Physics, Risø, Roskilde, Denmark

619. C. T. Chang
620. V. O. Jensen
621. C. Kofoed-Hansen

Swiss Institute for Nuclear Research, CH-5234 Villigen, Switzerland

622. Library
623. G. Vécsey

624. M. P. G. Avanzini, NIRA S.p.A., Casella Postale 1166, 16100 Genova, Italy
625. D. M. Axelrod, Consulting Engineer, Department of Advanced Engineering, United Engineers and Constructors, Inc., 30 S. 17th Street, Philadelphia, PA 19101
626. K. Azuma, The Bank of Tokyo, Nihombashi, P.O. Box 8, Tokyo 103-91, Japan
627. W. Bauer, Sandia National Laboratories, Livermore, CA 94550
628. P. R. Bell, 132 Westlook Circle, Oak Ridge, TN 37830
629. R. A. Berry, Varian Associates, Inc., 611 Hansen Way, Palo Alto, CA 94303
630. G. Bohner, Forschungslaboratorien, Siemens Aktiengesellschaft, Postfach 325, D-8520 Erlanger 2, Federal Republic of Germany
631. R. A. E. Bolton, IREQ Hydro-Quebec Research Institute, 1800 Montée Ste.-Julie, Varennes, P.Q. JOL 2PO Canada
632. M. H. Brennan, Australian Atomic Energy Commission, Lucas Heights Research Laboratories, New Illawarra Road, Lucas Heights, Private Mail Bag, Sutherland, N.S.W., Australia 2232
633. P. J. Catto, Science Applications, Inc., 934 Pearl Street, Suite A, Boulder, CO 80302
634. R. N. Cherdack, Burns & Roe, Inc., 700 Kinder Kamack Road, Oradell, NJ 07649
635. G. Clemens, University Library of Essen, Gustav-Hicking-Strasse 15, D-4300 Essen, Federal Republic of Germany
636. E. W. Collings, Battelle Memorial Institute, 505 King Ave., Columbus, OH 43201
637. E. C. Creutz, National Science Foundation, Washington, DC 20550
638. J. G. Crocker, EG&G Idaho, Inc., Idaho National Engineering Laboratory, Idaho Falls, ID 83401
639. R. A. Dandl, Applied Microwave Plasma Concepts, Inc., 2210 Encinitas Boulevard, Suite F, Encinitas, CA 92024
640. S. O. Dean, Science Applications, Inc., 2 Professional Drive, Suite 249, Gaithersburg, MD 20760
641. H. W. Deckman, Advanced Energy Systems Laboratory, Exxon Research and Engineering Company, P.O. Box 8, Linden, NJ 07306
642. J. Denavit, Department of Mechanical Engineering, Northwestern University, Evanston, IL 60201
643. Department of Nuclear Engineering Sciences, 202 Nuclear Science Center, University of Florida, Gainesville, FL 32611
644. Director, Technical Library, Defense Atomic Support Agency, Sandia Base, Albuquerque, NM 87185

645. D. R. Dobrott, Science Applications International Corporation, P.O. Box 2351, La Jolla, CA 92038
646. T. J. Dolan, Department of Nuclear Engineering, University of Missouri, Rolla, MO 65401
647. G. W. Donaldson, School of Electrical Engineering, University of New South Wales, P.O. Box 1, Kensington, N.S.W., Australia
648. L. J. Drooks, Department 621, Bell Telephone Laboratories, Whippany, NJ 07981
649. E. Dullni, NB-05/639, Experimentalphysik, Ruhr-Universitaet Bochum, D-4630 Bochum, Federal Republic of Germany
650. R. W. Fast, Experimental Facilities, National Accelerator Laboratory, P.O. Box 500, Batavia, IL 60510
651. Y. Furuto, Superconducting Group, Central Research Laboratory, Furukawa Electric Company, Ltd., 915, 2-Chome, Futaba, Shinagawaku, Tokyo 141, Japan
652. A. Gaines, Combustion Engineering, 1000 Prospect Hill Road, Windsor, CT 06096
653. F. C. Gilbert, Division of Military Applications, Department of Energy, Washington, DC 20545
654. H. B. Gilbody, Department of Pure and Applied Physics, Queens University, Belfast, Northern Ireland, United Kingdom
655. R. W. Gould, California Institute of Technology, Building 116-81, Pasadena, CA 91125
656. H. R. Griem, Department of Physics, University of Maryland, College Park, MD 20742
657. D. C. Griffin, Rollins College, Winter Park, FL 32789
658. R. A. Gross, Department of Mechanical Engineering, Columbia University, New York, NY 10027
659. R. L. Hirsch, ARCO Oil & Gas Co., P.O. Box 2819, Dallas, TX 75221
660. R. Huse, PSE&G Research Corp., 80 Park Place, Newark, NJ 07101
661. W. R. Husinsky, Technical University of Vienna, Vienna, Austria
662. S. Ihara, Energy Division, Electrotechnical Laboratory, Sakura, Niihari, Ibaraki 305, Japan
663. M. Iwamoto, Central Research Laboratory, Mitsubishi Electric Corporation, 80 Nakano, Minamishimizu, Amagasaki, Kyogo 660, Japan
664. C. K. Jones, Cryogenic Research Laboratory, Westinghouse Electric Corporation, Research and Development Center, 1310 Beulah Road, Pittsburgh, PA 15235
665. R. Jones, Department of Physics, National University of Singapore, Bukit Timah Road, Singapore 10.25
666. K. K. Kim, Department of Electrical Engineering, University of Illinois, Urbana, IL 61801
667. D. Klein, Westinghouse Electric Corporation, Strategic Operations Division, P.O. Box 598, Pittsburgh, PA 15230
668. A. C. Kolb, Maxwell Laboratories, Inc., 9244 Balboa Avenue, San Diego, CA 92123
669. K. Koyama, Electrotechnical Laboratory, 5-4-1 Mukodaicho, Tanashi, Tokyo, Japan
670. N. A. Krall, JAYCOR, P.O. Box 85154, San Diego, CA 92139
671. A. H. Kritz, 69 Lillie Street, Princeton, NJ 08540

672. C. A. Kukielka, Science Applications, Inc., P.O. Box 843, Oak Ridge, TN 37831
673. K. Kuroda, Ltd., Central Research Laboratory, 1-280, Higa Shiko Igakubo, Kokubumji, Tokyo 185, Japan
674. Laboratory for Plasma and Fusion Studies, Department of Nuclear Engineering, Seoul National University, Shinrim-dong, Gwanak-ku, Seoul 151, Korea
675. Laser Fusion Group, Department of Mechanical and Aerospace Science, River Campus Station, University of Rochester, NY 14627
676. E. Lehnert, Royal Institute of Technology, Stockholm 70, Sweden
677. C. M. Loring, Eimac Division of Varian, 301 Industrial Way, San Carlos, CA 94070
678. M. Lotker, Advanced Energy Conversion Research, Northeastern Utilities Service Company, P.O. Box 270, Hartford, CT 06101
679. R. Lucey, JAYCOR, 205 South Whiting Street, Alexandria, VA 22304
680. V. A. Maroni, Chemical Engineering Division, CEN 205, Argonne National Laboratory, Argonne, IL 60439
681. E. A. Mason, Brown University, Providence, RI 02912
682. D. G. McAlees, Exxon Nuclear Company, Inc., 2101 Horn Rapids Rd., Richland, WA 99352
683. F. Moon, Department of Theoretical and Applied Mechanics, Cornell University, Ithaca, NY 14850
684. T. J. Morgan, Physics Department, Wesleyan University, Middletown, CT 06457
685. K. G. Moses, JAYCOR, 2811 Wilshire Boulevard, Suite 690, Santa Monica, CA 90403
686. C. Oberly, Aero Propulsion Laboratory, Power Distribution Branch, Wright-Patterson Air Force Base, OH 45433
687. T. Ogasawara, Department of Physics, College of Science and Engineering, Nihon University, Kanda-Surugadi, Chiyoda, Tokyo, Japan
688. H. Ogiwara, Toshiba Research and Development Center, 1 Komukai Tsohibacho, Saiwai, Kawasaki, Kanagawa 210, Japan
689. R. J. Onega, Nuclear Engineering Group, College of Engineering, Virginia Polytechnic Institute and State University, Blacksburg, VA 24061
690. B. Outten, Jr., Western Metal Products Company, 1300 Weber Street, Orlando, FL 32803
691. D. Palumbo, EURATOM, 51 Rue Belliard, Brussels 5, Belgium
692. B. H. Quon, Building R-1, TRW Defense and Space Systems, 1 Space Park, Redondo Beach, CA 90278
693. F. L. Ribe, 3910 Benson Hall BF 10, University of Washington, Seattle, WA 98195
694. F. Ring, Lockheed Missile and Space Company, Jackson Plaza, Suite 103, 800 Oak Ridge Turnpike, Oak Ridge, TN 37830
695. F. C. Rock, Plasma Physics Laboratory, Department of Physics and Astronomy, Brigham Young University, Provo, UT 84602
696. R. H. Rohrer, Department of Physics, Emory University, Atlanta, GA 30322
697. P. A. Sanger, Airco, 600 Milik St., Carteret, NJ 07008

698. S. St. Lorant, Stanford Linear Accelerator Center, Stanford Univ., Palo Alto, CA 94304
699. M. M. Satterfield, The Nucleus, 461 Laboratory Road, Oak Ridge, TN 37830
700. Y. Sawada, Heavy Apparatus Engineering Laboratory, Tokyo Shibaru Electric Company, Ltd., 4-2 Chome, Suehiro, Tsurumi, Yokohama, Japan
701. J. H. Schneider, Joint Research Centre, Ispra Establishment, 21020 Ispra (Varese), Italy
702. G. Siegel, Tennessee Valley Authority, 1360 Commerce Union Bank Building, Chattanooga, TN 37401
703. U. Stiefel, Eidg. Institut fuer Reaktorforschung, 5303 Wurenlingen, Switzerland
704. W. Sutton, Department of Nuclear Engineering, University of Illinois, Urbana, IL 61807
705. K. Tachikawa, Chief, Electric Materials Laboratory, National Research Institute for Metals, 3-12, 2-Chome, Nakameguro, Meguru, Tokyo, Japan
706. R. J. Taylor, Center for Plasma Physics and Fusion Engineering, University of California, Los Angeles, CA 90024
707. L. E. Temple, Construction Project Management Support Division, ER-15, Department of Energy, Washington, DC 20545
708. D. P. Tewari, Department of Physics, Indian Institute of Technology, New Delhi 10016, India
709. M. Thumm, Institut für Plasmaforschung, Pfaffenwaldring 31, D-7000 Stuttgart 80, Federal Republic of Germany
710. J. F. Traexler, Westinghouse Electric Corp., Quadrangle 2WII-203, Orlando, FL 32817
711. G. Vahala, Department of Physics, College of William and Mary, Williamsburg, VA 23185
712. T. C. Varljen, Westinghouse Hanford, P.O. Box 1970, Richland, WA 99352
713. R. Varma, Physical Research Laboratory, Navrangpura, Ahmedabad 380009, India
714. C. Walters, Technology Division, Building R25, Rutherford Laboratory, Chilton, Didcot, Oxon OX11 OQX, United Kingdom
715. C. N. Watson-Munro, University of Sydney, Wills Plasma Project, Sydney, N.S.W., Australia
716. J. Wong, Supercon, Inc., 9 Erie Drive, Natick, MA 01760
717. S. B. Woo, Department of Physics, University of Delaware, Newark, DE 19711
718. K. Yamamoto, Japan Atomic Energy Research Institute, 1-1-13 Shinbashi, Minato, Tokyo, Japan
719. H. Yoshikawa, Manager, Materials Engineering, Hanford Engineering Development Laboratory, P.O. Box 1970, Richland, WA 99352
720. G. A. Eliseev, I. V. Kurchatov Institute of Atomic Energy, P.O. Box 3402, 123182 Moscow, U.S.S.R.
721. V. A. Glukhikh, Scientific-Research Institute of Electro-Physical Apparatus, 188631 Leningrad, U.S.S.R.
722. D. D. Ryutov, Institute of Nuclear Physics, Siberian Branch of the Academy of Sciences of the U.S.S.R., Sovetskaya St. 5, 630090 Novosibirsk, U.S.S.R.

723. V. D. Shafranov, I. V. Kurchatov Institute of Atomic Energy, P.O. Box 3402, 123182 Moscow, U.S.S.R.

724. I. Shpigel, Institute of General Physics, U.S.S.R. Academy of Sciences, Ulitsa Vavilova 38, Moscow, U.S.S.R.

725. V. T. Tolok, Kharkov Physical-Technical Institute, Academical St. 1, 310108 Kharkov, U.S.S.R.

726. Library, Institute of Physics, Academia Sinica, Beijing, Peoples' Republic of China

727. M-L. Xue, Institute of Mechanics, Academia Sinica, Beijing, Peoples' Republic of China

728–835. Given distribution as shown in TID-4500, Magnetic Fusion Energy (Distribution Category UC-20)

*U. S. GOVERNMENT PRINTING OFFICE: 1985-544-045/20099